Mechanistic, interfacial and modeling studies of electro-precipitation during electrochemical advanced oxidation process in a thin-film reactor : case study with reclaimed municipal wastewater

Faidzul Hakim Adnan

Thèse

Présentée et soutenue publiquement pour l'obtention du titre de

DOCTEUR DE L'UNIVERSITÉ DE LORRAINE

Mention : GÉNIE DES PROCÉDÉS ET DES PRODUITS ET DES MOLÉCULES

par **Mohd Faidzul Hakim MOHD ADNAN**

Mechanistic, interfacial and modeling studies of electro-precipitation during electrochemical advanced oxidation process in a thin-film reactor: case study with reclaimed municipal wastewater

le 16 décembre 2021

Membres du jury :

Rapporteurs :	**M. Manuel RODRIGO**	Professeur, University of Castilla-La-Mancha (UCLM), Spain
	M. Alan HATTON	Professeur, Massachusetts Institute of Technology (MIT), USA
Examinateurs :	**Mme Karine GROENEN SERRANO**	Professeure, Université Toulouse III Paul Sabatier, France
	M. François LAPICQUE	Directeur de recherche, CNRS – Université de Lorraine, France
Directrice de thèse :	**Mme Marie-Noëlle PONS**	Directrice de recherche, CNRS – Université de Lorraine, France
Co-directeur de thèse :	**M. Emmanuel MOUSSET**	Chargé de recherche, CNRS – Université de Lorraine, France

Laboratoire Réaction et Génie des Procédés – Université de Lorraine – CNRS (UMR 7274)
1, rue Grandville – BP 20451 – F-54001 Nancy Cedex

ACKNOWLEDGEMENTS

To my dear supervisors, *Emmanuel Mousset* and *Marie-Noëlle Pons*, I thank you both for this opportunity and your warm, patient and enthusiastic guidance…

To the members of the panel, *Prof. Manuel Rodrigo, Prof. Alan Hatton, Dr. François Lapique* and *Prof. Karine Groenen Serrano*, I thank you for cultivating remarks and fruitful discussion during the defense…

To *Ministère de l'Enseignement Supérieur, de la Recherche et de l'Innovation, Institut Carnot, Zones Ateliers de la Moselle* and *European Regional Development Fund*, I could not be more grateful for the financial funds invested in this PhD work…

To *Steve Pontvianne*, I thank you for keeping up with all the analyses…

To my fellow friends, *you know who you are*, I thank you *all* for the cherish moment that we have had together…

and to my lovely wife, *Khaliesah*, I thank you for your priceless support…

-Faidzul-

ABSTRACT

Electrochemical advanced oxidation processes (EAOPs) have been receiving recognition to efficiently eliminate organics, especially micropollutants, in wastewater owing to continuous production of potent, quasi non-selective hydroxyl radicals *in situ*. The more recent application of thin-film reactor within the framework of EAOPs has spurred the capability to treat wastewater whereby mass transport and redox reactions are intensified. It comes with huge cut in total operational expense owing to significant drop in internal cell resistance. Nonetheless, EAOPs are still prone to electrode fouling due to the occurrence of local alkalization on cathode surface. The issue worsens while operating at industrial scale where the electrochemical cells are operated in continuous mode. Once the cathode is totally passivated by the scaling, the EAOPs efficacy is undoubtedly compromised. Polarity reversal has been a common practice in industries to periodically redissolve the deposition. Both cathode and anode materials need to be stable against corrosion/burning during the oxidation period, consequently the cathode material is often expensive. Therefore, in quest for limiting or even avoiding the polarity reversal, the objective of this thesis was to identify the optimal operating conditions by which minimal electro-precipitation was formed during an electro-oxidation of effluent to maximize the process efficacy. Decisive parameters on the kinetics of electro-precipitation were scrutinized, i.e., the applied current density (j_{app}), the interelectrode distance (d_{elec}), the matrix of effluent to be treated and the cathode material.

Under the operating conditions applied, only $Mg(OH)_2$, $CaCO_3$ and $Ca_3(PO_4)_2$ precipitates were present. Other deposits were not thermodynamically favorable. $Mg(OH)_2$ precipitation was highly dependent on j_{app} whilst $CaCO_3$ and $Ca_3(PO_4)_2$ easily occurred even at low applied current. Then, more scaling was observed in submillimetric range due to the involvement of more vigorous concomitant hydrogen gas evolution in macrometric setup. A mathematical model was proposed to predict electro-precipitation at varying d_{elec}, which account for scaling detachment due to the involvement of gas activity. The model would better allow estimating the rate of mineral scaling and could as well optimize the polarity reversal frequency. When the comparison was made with real wastewater, more electro-precipitation occurred due to co-precipitation of dissolved organics and inhibiting effect of sulfate in simulated effluent. When higher j_{app} was adopted, more organic mineralization, higher target pharmaceutical (tylosin) degradation and less mineral scaling were noticed. This was at the expense of higher power consumption and significantly higher release of undesirable byproducts. Finally, the use of porous carbonaceous cathodes only yielded in more electro-precipitation.

In perspective, the use of porous cathode in conjunction with micrometric d_{elec} would benefit from efficient electro-precipitation for value-added non-conducting mineral resources recovery. It could be implemented alongside EAOP to achieve simultaneous pollutant degradation and resource recovery in a single operation.

RÉSUMÉ

Les procédés électrochimiques d'oxydation avancés (PEOAs) sont de plus en plus reconnus pour éliminer efficacement les polluants organiques, y compris les micropolluants, dans les eaux usées. Les radicaux hydroxyles en tant qu'oxydants puissants et très peu sélectifs y sont générés *in situ* et en continu. L'application plus récente de réacteurs à couche mince dans le cadre des PEOAs a permis d'améliorer l'efficacité de traitement d'effluents aqueux, suite à l'intensification du transport de matière et des cinétiques de réactions d'oxydoréduction. A cela s'ajoute une baisse des coûts opérationnels grâce à la réduction significative de la résistance interne des cellules. Néanmoins, les PEOAs restent susceptibles à l'encrassement dû à l'alcalinisation locale sur la surface de la cathode. La problématique s'aggrave lors du fonctionnement à plus grande échelle, où les cellules s'opèrent en mode continu. Or, une fois que la cathode est complètement passivée par les dépôts minéraux, l'efficacité de l'oxydation devrait être compromise. En pratique, l'inversion de polarité est souvent plébiscitée en électrolyse industrielle pour redissoudre périodiquement les précipités. Par conséquent, les matériaux de cathode et d'anode doivent être stables contre la corrosion/l'incinération durant la période d'oxydation, et cela implique l'utilisation de matériaux de cathode coûteux. Afin de limiter, voire d'éviter cette inversion de polarité, l'objectif principal de cette thèse a été d'identifier les conditions opératoires optimales pour lesquelles l'entartrage soit minimal et la durée d'efficacité d'oxydation anodique maximale. Les paramètres impactant la cinétique d'électro-précipitation ont été examinés, tels que la densité de courant appliquée (j_{app}), la distance interélectrode (d_{elec}), la matrice de l'effluent à traiter et le matériau de cathode.

Dans les conditions de fonctionnement appliquées, seuls les précipités de $Mg(OH)_2$, $CaCO_3$ et $Ca_3(PO_4)_2$ étaient présents, les autres n'étant pas thermodynamiquement favorisés. L'électro-précipitation de $Mg(OH)_2$ dépendait fortement de j_{app} tandis que les précipités de $CaCO_3$ et de $Ca_3(PO_4)_2$ se produisaient facilement, même à faible courant. De plus, un dépôt plus important a été observé dans la condition microfluidique due à l'évolution concomitante plus vigoureuse de l'hydrogène gazeux dans la configuration millimétrique. Un modèle mathématique a été proposé pour prédire l'électro-précipitation aux différentes d_{elec}, en tenant compte du détachement des précipités lié à cette évolution de gaz. Ce modèle devrait permettre à l'avenir de pouvoir mieux estimer les rendements d'électro-précipitation tout en optimisant la fréquence d'inversion de polarité. De surcroît, lorsque la comparaison a été faite en utilisant des eaux usées traitées municipales, plus d'encrassement s'est produit avec la matrice réelle, en raison de la co-précipitation des matières organiques dissoutes et de l'effet inhibiteur des sulfates dans l'effluent simulé. Lorsque qu'une j_{app} élevée a été adoptée, les cinétiques de dégradation et de minéralisation du polluant pharmaceutique ciblé (tylosin) ont été augmentées et la quantité de dépôt cathodique diminuée. Cependant, cela s'est

accompagné d'une consommation énergétique significativement plus élevée et d’un relargage de sous-produits indésirables plus conséquent auquel il faudra remédier dans le futur. Enfin, l'utilisation de cathodes plus poreuses n'a fait qu’accroître le phénomène d’électro-précipitation.

En perspective, la porosité élevée de la cathode accompagnée d’une faible d_{elec} semblent être des conditions importantes dans un objectif de récupération cathodique optimale de minéraux non conducteurs à haute valeur ajoutée. Cette électro-précipitation pourrait se réaliser en complément des PEOAs qui permettraient d’éliminer en parallèle les composés organiques dans l’effluent.

TABLE OF CONTENTS

LIST OF TABLES

LIST OF FIGURES

ABBREVIATIONS

Symbol	Unit	Definition	Symbol	Unit	Definition
α	-	OH- hindrance factor	η	%	Current efficiency
A	m^2	Electroactive surface area	η_{O_2}	-	Efficiency of OH^- production from dissolved ORR
A_C	m^2	Cross-sectional area	η_{H_2}	-	Loss of faradaic current due to concomitant HER
Ag-AgCl	-	Saturated silver chloride reference electrode	η_{H_2O}	-	Efficiency of OH^- production from dissolved HER
BDD	-	Boron-doped diamond	I_P	A	Peak current
BE	-	Basic effluent	IOA	-	Index of agreement
γ	$V\ s^{-1}$	Scan rate	I	A	Applied current intensity
ΔC	$mol\ m^{-3}$	Difference in concentration	I_{lim}	A	Limiting current
C_i	$mol\ m^{-3}$	Concentration of ionic species in electrolyte	j_{app}	$A\ m^{-2}$	Applied current density
C_{DL}	F	Double layer capacitance	$j_{lim,0}$	$A\ m^{-2}$	Initial limiting current density
CE	-	Counter electrode	κ	$\mu S\ cm^{-1}$	Ionic conductivity containing dispersed gas bubble
C_F	F	Film capacitance	κ_0	$\mu S\ cm^{-1}$	Ionic conductivity free of gas bubble
CPE	F	Constant phase element	κ/κ_0	-	Electrolyte reduced conductivity
C_{SOL}	$mol\ m^{-3}$	Concentration of reactive species in the bulk	K_{Ai}	-	Acidity constant
Cl-volatile	$mol\ m^{-3}$	Volatile chlorinated species consisted of Cl_2, ClO_2 and Cl_2O	k_{CaCO_3}	$m^4\ mol^{-1}\ s^{-1}$	Heterogeneous second rate constant of $CaCO_3$ electro-precipitation
$[CO_3^{2-}]_{int}$	$mol\ m^{-3}$	Interfacial CO_3^{2-} concentration	$k_{Ca(OH)_2}$	$m^7\ mol^{-2}\ s^{-1}$	Heterogeneous second rate constant of $Ca(OH)_2$ electro-precipitation
COD	$mg\text{-}O_2\ L^{-1}$	Chemical oxygen demand	k_{inhib}	$m^4\ mol^{-1}\ s^{-1}$	Coefficient of Mg^{2+} inhibition by adsorption/incorporation
CV	-	Cyclic voltammetry	KKT	-	Kramers-Kronig Transform
d	m	Channel width (equivalent to W)	k_m	$m\ s^{-1}$	Mass transfer coefficient
DAC	-	Dimensionless applied current density	k_{MgCO_3}	$m^4\ mol^{-1}\ s^{-1}$	Heterogeneous second rate constant of $MgCO_3$ electro-precipitation
d_{DL}	m	Double layer thickness	$k_{Mg(OH)_2}$	$m^7\ mol^{-2}\ s^{-1}$	Heterogeneous second rate constant of $Mg(OH)_2$ electro-precipitation
d_{elec}	m	Interelectrode distance	$K_{S,i}$	-	Solubility constant
d_H	m	Hydraulic diameter	K_W	-	Water auto-ionization constant
D_L	$m^2\ s^{-1}$	Electrolyte diffusion coefficient	λ_i	$S\ m^2\ mol^{-1}$	Ionic molar conductivity
d_{elec}/W	-	Aspect ratio	L	m	Length of electrode
ε_0	F.m	Vacuum permittivity	Le	-	Dimensionless distance
ε_S	-	Solvent dielectric constant	L_{IND}	H	Inductance
E_A	V	Measured anode potential	LSV	-	Linear scan voltammetry
E_C	V	Measured cathode potential	m_i	g	Mass of element
EEC	-	Electrical equivalent circuit	ME	-	Model efficiency
$E^0_{Oxy/Red}$	V	Standard potential of a redox species	ν_{H_2}	-	Stoichiometry of H_2 in HER
E_L	m	Entry length	ν_{H_2O}	-	Stoichiometry of H_2O in HER

Symbol	Unit	Definition	Symbol	Unit	Definition
ν_{O_2}	-	Stoichiometry of dissolved O_2 in ORR	t	s	Electrolysis time
n	-	*CPE* parameter	t_i	-	Ionic transference number
N_i	mol	Molar quantity	TIC	mg-C L^{-1}	Total inorganic carbon
n_e	-	Number of electrons participated in considered reaction	TOC	mg-C L^{-1}	Total organic carbon
n_{H_2}	-	Number of e^- in HER	TN	mg-N L^{-1}	Total nitrogen
n_{H_2O}	-	Number of e^- in HER	ΔU	V	Cell voltage
n_{O_2}	-	Number of e^- in ORR	u_i	$m^2\ s^{-1}\ V^{-1}$	Ionic mobility
NOM	-	Natural organic matter	u_L	m s^{-1}	Cross-sectional electrolyte velocity
N-volatile	mol m^{-3}	Volatile nitrogenous species consisted of N_2 and NO_X	υ_L	$m^2\ s^{-1}$	Electrolyte kinematic viscosity
OER	-	O_2 evolution reaction	V	m^3	Treated volume
ORR	-	O_2 reduction reaction	$\dot{V}_F$	$m^3\ s^{-1}$	Volume flow rate
OH^-_{crit}	mol m^{-3}	Critical OH^- concentration	V_R	m^3	Reactor volume
PC	kWh m^{-3}	Specific power consumption	φ	-	Gas void
pH_{crit}	-	Critical pH	W	m	Width of electrode
Pt	-	Platinum	WE	-	Working electrode
ρ_L	kg m^{-3}	Electrolyte density	WWTP	-	Wastewater treatment plant
ρ/ρ_0	-	Electrolyte relative resistivity	X	%	Conversion rate
R	-	Gas constant	x_e	m	Electrode length (equivalent to L)
$\sum RI$	V	Internal ohmic resistance	z_i	-	Ionic valence number
Re	-	Reynolds number	ω	-	Constant relating C_{DL} and d_{elec}
R_{CT}	Ω	Charge transfer resistance			
R_{DES}	Ω	Adsorption/desorption resistance			
R_F	Ω	Film resistance			
r_i	mol $m^{-2}\ s^{-1}$	Heterogeneous rate of reaction			
RE	-	Reference electrode			
RMSE	-	Root mean square error			
R_{SOL}	Ω	Electronic transfer resistance in solution between WE and RE			
RW	-	Reclaimed wastewater			
S	m^2	Electrode surface area			
Sc	-	Schmidt number			
SCE	-	Saturated calomel electrode			
SD	-	Supersaturation degree			
SHE	-	Standard hydrogen potential			
SI	-	Supersaturation index			
SE	-	Saline effluent			
SPC	kWh g^{-1}	Specific power consumption			
SPCM	kWh g-TOC^{-1}	Specific power consumption per gram of TOC			
SPCP	kWh g-precipitate^{-1}	Specific power consumption per gram of electro-precipitate			
SPCT	kWh g-tylosin^{-1}	Specific power consumption per gram of tylosin			
SSE	-	Saturated sulfate electrode			
SW	-	Simulated wastewater			
τ	s	Electrolyte resistance time			
T	K	Temperature			

RÉSUMÉ ÉTENDU

I. Introduction générale

Ce travail de thèse a pour objectif la caractérisation et la quantification de l'électro-précipitation minérale cathodique ayant lieu au cours d'un traitement d'électro-oxydation d'eaux usées. Le procédé d'électro-oxydation a été appliqué dans un réacteur électrochimique submillimétrique ayant une surface d'électrode de 50 cm^2. La conception du réacteur submillimétrique, ou également appelé à couche mince, a été choisie en raison de l'énorme potentiel qu'il pourrait offrir pour des applications environnementales **[1, 2]**. Par exemple, le transport de matière et les réactions d'oxydoréduction sont intensifiés et les coûts opérationnels diminués grâce à une forte réduction de la résistance interne de la cellule **[3-5]**. En dépit de cet intérêt potentiel, peu de recherches ont été dirigées vers ce sujet. Plus précisément, aucune publication n'existe dans la littérature au regard de la formation d'électro-précipités dans une cellule électrochimique à couche mince, contrairement à celles faites dans le montage conventionnel à disque rotatif **[6-8]**. Une fois que la cathode est totalement passivée par l'électro-précipitation, l'efficacité de l'électro-oxydation est sans aucun doute compromise. C'est la raison pour laquelle les travaux de recherche de la thèse ont été menés sur cette problématique. La **Fig. R.I** illustre l'approche et le déroulement de la thèse.

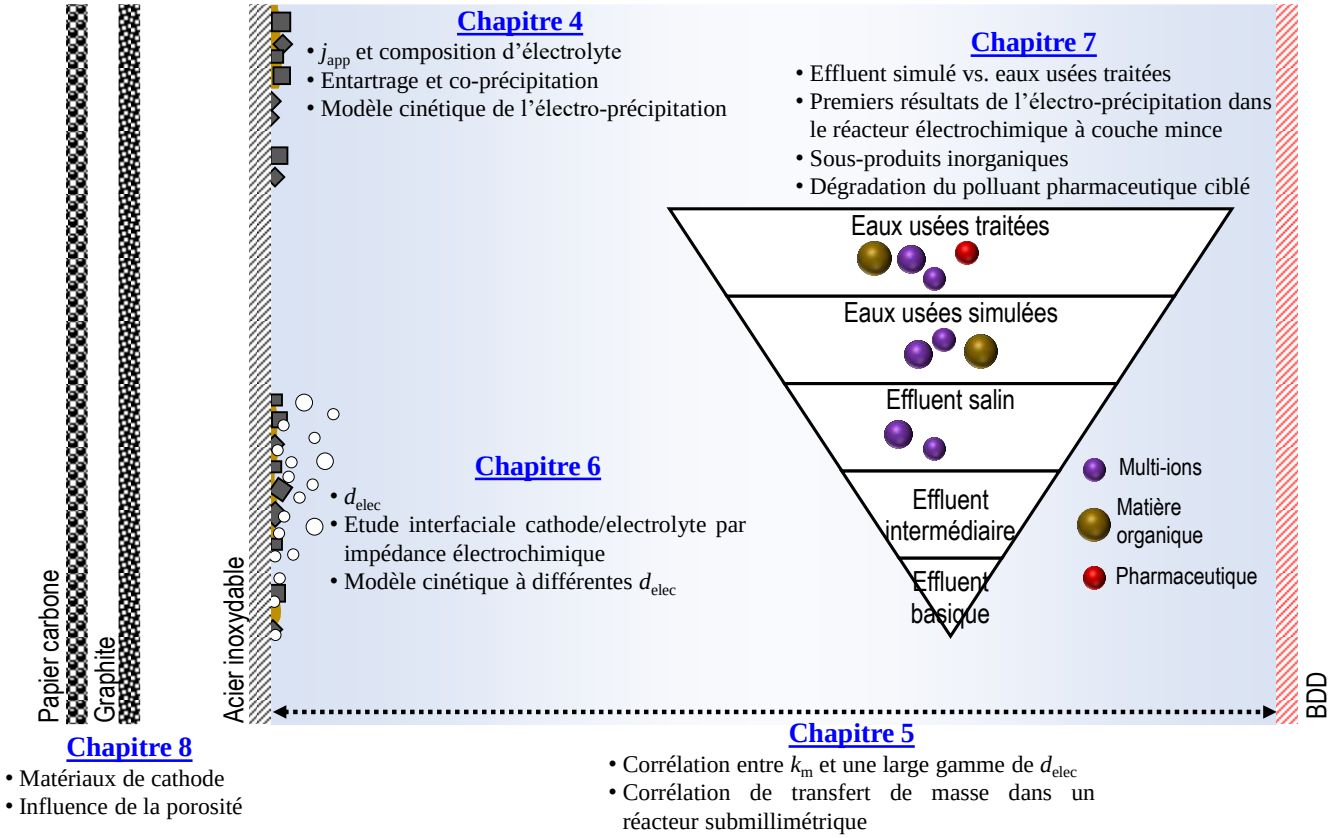

Fig. R.I. Schéma de l'approche et du déroulement de la thèse.

Selon la **Fig. R.I**, les paramètres déterminants sur la cinétique de l'électro-précipitation ont été examinés, tels que la densité de courant appliquée (j_{app}), la distance inter-électrode (d_{elec}), la matrice de l'effluent à traiter et le matériau de la cathode. Des modèles théoriques ont été proposés accompagnés des résultats expérimentaux. Du point de vue pratique, l'objectif a été d'établir les conditions opératoires pour lesquelles l'entartrage serait minimisé. Dans ce cas, l'impact sur l'efficacité de l'électro-oxydation serait minimisé et donc la durabilité du procédé serait assurée.

II. Influence de la densité de courant appliquée (j_{app})

Dans la gamme de j_{app} utilisée, l'alcalinisation locale sur la surface de la cathode s'est produite principalement par la réduction de l'eau au lieu de celle de l'O_2 dissous. L'entartrage était indépendant du phénomène d'électro-migration et était contrôlé par la diffusion du transport de matière. Dans toutes les conditions étudiées, seuls les précipités d'hydroxyde de magnésium ($Mg(OH)_2$), de carbonate de calcium ($CaCO_3$) et de phosphate de calcium ($Ca_3(PO_4)_2$) ont été formés. La formation d'hydroxyde de calcium ($Ca(OH)_2$), de carbonate de magnésium ($MgCO_3$), de struvite ($MgNH_4H_nPO_4^{3-n}$), de dolomite ($CaMg(CO_3)_2$) et de phosphate de magnésium ($Mg_3(PO_4)_2$) n'était pas favorisée. L'électro-précipitation de $Mg(OH)_2$ s'est avérée fortement dépendante de j_{app}, mais indépendante des autres espèces ioniques coprésentes dans l'électrolyte. $Mg(OH)_2$ précipitait dès que le pH interfacial de 10,2 était atteint. Le $CaCO_3$ se déposait facilement sur la surface de la cathode même sous une faible polarisation du courant. L'entartrage par $CaCO_3$ était plus important à faible j_{app} en raison de l'évolution concomitante du gaz plus intense à j_{app} élevée. Ensuite, les études ont été dirigées vers l'électro-précipitation au sein des réacteurs électrochimiques avec des d_{elec} variables.

III. Evolution de transport de matière d'une échelle macrométrique à l'échelle micrométrique

L'évolution du transport de matière en fonction de d_{elec} pour des variations de ce paramètre allant d'une échelle micrométrique (100 µm) à millimétrique (3000 µm) a été préalablement examinée et a été représentée dans la **Fig. R.II**. Un changement drastique de l'évolution de k_m a permis d'identifier de manière quantitative le début du comportement microfluidique, qui se situe en dessous de 1000 µm. Une corrélation a été proposée pour prédire k_m en fonction de la large gamme de d_{elec}. En écoulement laminaire (7 < Reynolds < 623) et pour une température comprise entre 10 et 50°C (532 < Schmidt < 3315), de nouvelles corrélations de transport de matière utilisant le nombre adimensionnel de Sherwood ont été obtenues pour les configurations microfluidiques et millimétriques. L'extrapolation de k_m pour la mise à l'échelle des réacteurs électrochimiques microfluidiques parait donc réalisable.

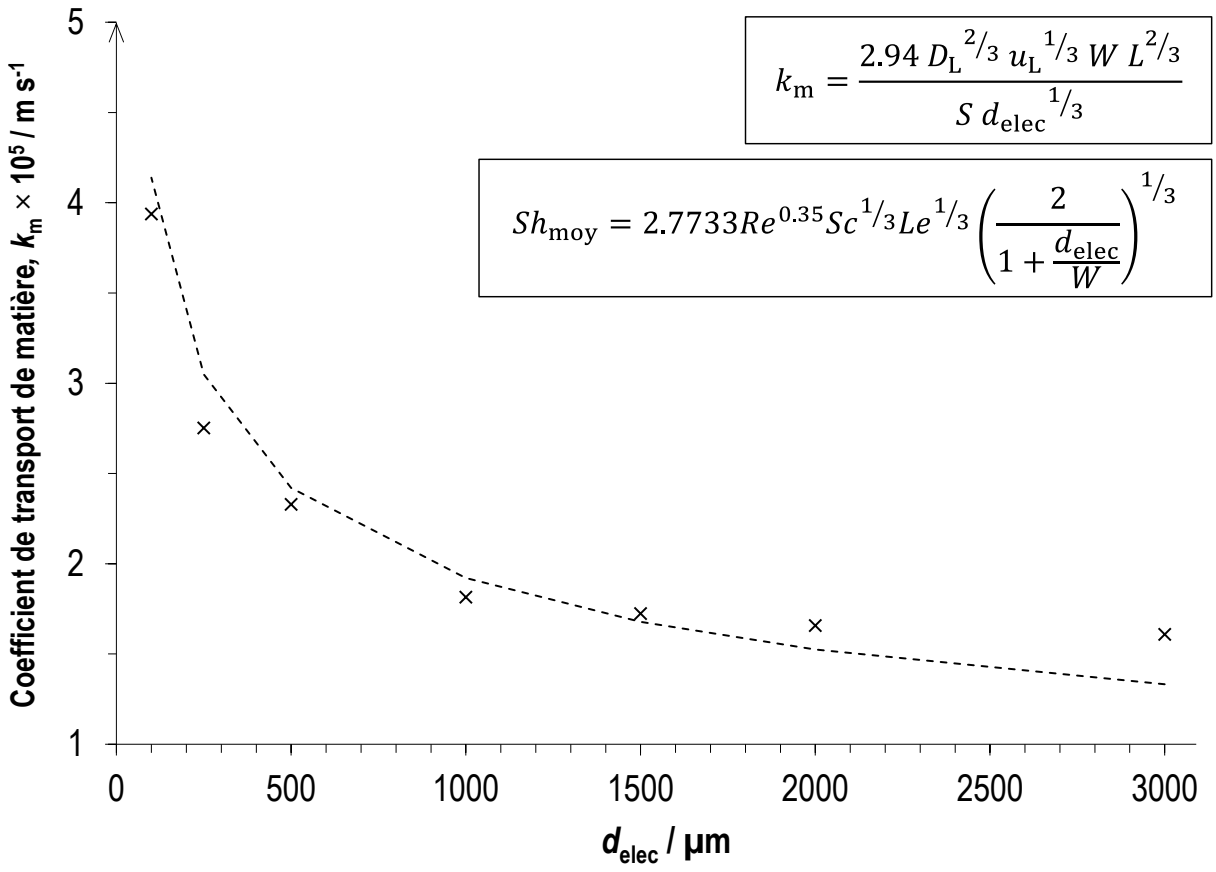

Fig. R.II. Corrélation de k_m en fonction de d_{elec} et corrélation obtenue avec le nombre adimensionnel de Sherwood.

IV. Rôle de la distance inter-électrode (d_{elec}) sur la formation d'électro-précipitation

Une fois la caractérisation du transport de matière en fonction de d_{elec} appréhendée, la recherche s'est orientée vers le rôle de d_{elec} sur la formation des électro-précipités dans la cellule électrochimique. Comme cela a été prédit par un nouveau modèle mathématique prenant en compte la réaction concomitante d'évolution de l'hydrogène (H_2) (HER), une précipitation plus intense a été observée par ordre décroissant de d_{elec} de 3 mm à 100 µm, en appliquant 4 mA cm^{-2}. En revanche, aucun dépôt n'était présent à la plus faible d_{elec} étudiée (50 µm), ce qui est dû à une condition non faradique. Le potentiel cathodique appliqué (E_C) a diminué avec l'augmentation de la d_{elec}, ce qui a intensifié la production de bulles de H_2 et minimisé l'électro-précipitation. Des études supplémentaires en appliquant un E_C identique ont mis en évidence la contribution anodique de l'oxygène (O_2) dissous produit à l'anode sur la cinétique d'électro-précipitation. Cet apport est encore plus intensifié à des distances submillimétriques. La concomitance de HER en fonction de d_{elec} a été évaluée plus en détail en accédant à la résistivité électrolytique relative (ρ/ρ_0) et à la fraction du gaz (φ) formé pendant l'électrolyse. Les résultats montrent que ρ/ρ_0 et φ augmentaient avec la diminution de d_{elec}. Malgré

l'évolution de HER en parallèle, lorsque d_{elec} diminuait, la résistance interne de la cellule électrochimique était réduite. Elle a diminué linéairement jusqu'à un d_{elec} de 100 µm, valeur en dessous de laquelle la linéarité a été interrompue. Enfin, une étude d'impédance électrochimique a été réalisée pour caractériser les processus électrochimiques à l'interface cathode/électrolyte. De nouveaux modèles mathématiques corrélant la résistance de transfert de charge (R_{CT}) et la capacitance de double couche électronique (C_{DL}) en fonction de d_{elec} ont été proposés. L'interrelation entre ces paramètres fondamentaux avec l'occurrence d'électro-précipitation est schématisée dans la **Fig. R.III**.

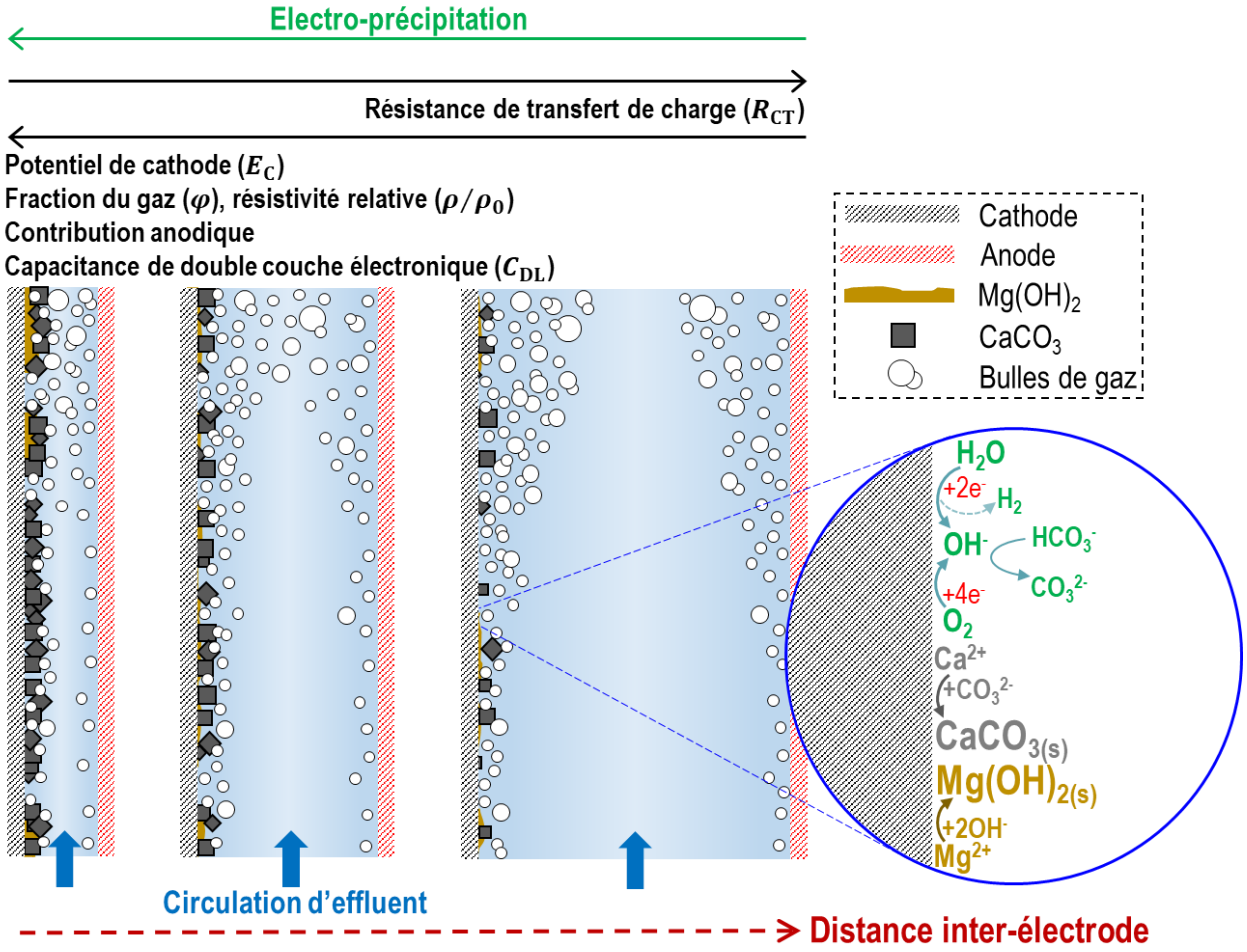

Fig. R.III. Schéma mécanistique de la formation d'électro-précipités sous l'influence de l'évolution concomitante du H_2 en fonction de d_{elec}.

V. Rôle de la matrice d'effluent : effluent simulé vs. eaux usées traitées

La thèse s'est poursuivie sur des études inédites concernant le rôle de la matrice de l'effluent sur l'électro-précipitation dans le réacteur électrochimique à couche mince. L'augmentation du degré de complexité de la matrice depuis l'effluent simulé jusqu'au système réel constitué d'eaux usées urbaines traitées a été abordée. En complément des phénomènes d'entartrage, la minéralisation de l'effluent, le

devenir des sous-produits inorganiques ainsi que la dégradation d'un polluant pharmaceutique représentatif (tylosine) ont été suivis. Il a été démontré dans des eaux simulées que la présence d'ions multiples (Ca^{2+}, Mg^{2+}, HCO_3^-/CO_3^{2-}, NH_4^+, $H_2PO_4^-/HPO_4^{2-}$, NO_3^-, NO_2^-, Cl^-, SO_4^{2-}, K^+ et Na^+) et de matière organique (peptone et extrait de viande) représentatifs de l'effluent réel ont peu d'influence sur la cinétique de formation d'électro-précipitation. Cette tendance a été attribuée à l'occurrence d'un pH local élevé sur la cathode qui pourrait atténuer l'effet d'inhibition des matières organiques sur la formation du dépôt **[9]**. Lorsque les dépôts ayant lieu dans l'effluent simulé sont comparés à ceux obtenus avec des eaux usées traitées, une quantité plus importante est observé dans ce dernier cas. Cela pourrait être dû, soit à la co-précipitation des matières organiques dissoutes - plus complexes dans les eaux usées réelles - avec Ca^{2+} et Mg^{2+} sur la surface de la cathode, soit à l'effet inhibiteur résultant de la teneur plus élevée en sulfates dans l'effluent simulé. Lors du traitement des eaux usées réelles, une minéralisation plus élevée est obtenue, mais elle s'accompagne d'une dégradation plus lente du polluant pharmaceutique ciblé. Cette dernière tendance est supposée liée à la compétition entre les substances organiques dissoutes dans l'effluent avec le polluant organique.

VI. Influence du matériau de la cathode et porosité

Enfin, l'influence des matériaux de cathode a été examinée. La cinétique et le mécanisme de formation d'électro-précipités sur l'acier inoxydable (non poreux) et des matériaux carbonés et poreux tel que le graphite et le papier carbone ont été comparés. Ils ont chacun une surface électroactive et une porosité différente. De plus, les propriétés interfaciales de ces trois cathodes, dans l'état initial ou après avoir subi un dépôt, ont été caractérisées par impédance électrochimique. Les résultats montrent que l'utilisation d'une cathode poreuse telle que le papier carbone entraînerait une précipitation plus rapide de $CaCO_3$, un taux plus élevé de conversion de Cl^- en sous-produits toxiques (ClO_3^- et ClO_4^-) ainsi qu'une acidification du milieu qui impliquerait un post-traitement. Par conséquent, ce n'était pas la cathode la plus appropriée pour répondre à l'objectif initial. L'électro-précipitation était légèrement plus favorisée sur le graphite que sur l'acier inox en raison du pH local plus élevé sur le premier. Par conséquent, même si le matériau carboné présente un avantage économique, son utilisation a entraîné plus d'électro-précipitation.

VIII. Conclusions et perspectives

En vue des résultats expérimentaux acquis au cours de la thèse, il a été démontré que l'acier inoxydable serait le matériau le plus adapté si la formation de précipités est à minimiser. Par ailleurs, les résultats suggèrent également que le papier carbone et d'autres matériaux poreux seraient les plus appropriés au cas où la précipitation cathodique est recherchée. Ils viendraient ainsi en prérequis du procédé d'électro-précipitation pour la récupération d'éléments à haute valeur ajoutée tel que le

phosphore. En termes de j_{app}, la valeur dans la gamme de 1 à 2 mA cm^{-2} pourrait être un bon compromis tenant compte la consommation d'énergie globale, l'électro-précipité formé, la minéralisation de l'effluent ainsi que l'évolution des sous-produits indésirables. La durée totale du traitement devrait être plus longue pour maximiser le taux d'élimination de polluants, mais cela ne poserait pas de contrainte énergétique lorsque des réacteurs à couche mince seront adoptés. Enfin, les modèles cinétiques de formation de précipités développés dans la thèse pourraient être utiles pour prédire les phénomènes d'électro-précipitation. Ces modèles sont applicables soit pour limiter l'entartrage lors du procédé de traitement par l'électro-oxydation, ou bien pour favoriser le dépôt lorsqu'il est souhaité, ce qui est par exemple le cas dans le procédé de valorisation des déchets par l'électro-précipitation.

Références

[1] S. Sabatino, A. Galia, O. Scialdone, Electrochemical abatement of organic pollutants in continuous-reaction systems through the assembly of microfluidic cells in series, ChemElectroChem, 3 (2016) 83-90.
[2] J.F. Pérez, J. Llanos, C. Sáez, C. López, P. Cañizares, M.A. Rodrigo, Towards the scale up of a pressurized-jet microfluidic flow-through reactor for cost-effective electro-generation of H_2O_2, Journal of Cleaner Production, 211 (2019) 1259-1267.
[3] J.F. Pérez, J. Llanos, C. Sáez, C. López, P. Cañizares, M.A. Rodrigo, Development of an innovative approach for low-impact wastewater treatment: A microfluidic flow-through electrochemical reactor, Chemical Engineering Journal, 351 (2018) 766-772.
[4] P. Ma, H. Ma, S. Sabatino, A. Galia, O. Scialdone, Electrochemical treatment of real wastewater. Part 1: Effluents with low conductivity, Chemical Engineering Journal, 336 (2018) 133-140.
[5] E. Mousset, Unprecedented reactive electro-mixing reactor: Towards synergy between micro- and macro-reactors?, Electrochemistry Communications, 118 (2020) 106787.
[6] C. Deslouis, D. Festy, O. Gil, G. Rius, S. Touzain, B. Tribollet, Characterization of calcareous deposits in artificial sea water by impedance techniques — 1. Deposit of $CaCO_3$ without $Mg(OH)_2$, Electrochimica Acta, 43 (1998) 1891-1901.
[7] C. Barchiche, C. Deslouis, O. Gil, S. Joiret, P. Refait, B. Tribollet, Role of sulphate ions on the formation of calcareous deposits on steel in artificial seawater; the formation of green rust compounds during cathodic protection, Electrochimica Acta, 54 (2009) 3580-3588.
[8] C. Barchiche, C. Deslouis, D. Festy, O. Gil, P. Refait, S. Touzain, B. Tribollet, Characterization of calcareous deposits in artificial seawater by impedance techniques: 3 — deposit of $CaCO_3$ in the presence of Mg(II), Electrochimica Acta, 48 (2003) 1645-1654.
[9] Y. Lei, M. Saakes, R.D. van der Weijden, C.J.N. Buisman, Effects of current density, bicarbonate and humic acid on electrochemical induced calcium phosphate precipitation, Chemical Engineering Journal, 342 (2018) 350-356.

SCIENTIFIC PRODUCTION

Papers in peer-reviewed journals

1. F.H. Adnan, E. Mousset, S. Pontvianne, M.-N. Pons, *Mineral cathodic electro-precipitation and its kinetic modelling in thin-film microfluidic reactor during advanced electro-oxidation process*, **Electrochimica Acta**, 387 (2021) 138487.
2. F.H. Adnan, M.-N. Pons, E. Mousset, *Mass transport evolution in microfluidic thin film electrochemical reactors: New correlations from millimetric to submillimetric interelectrode distances*, **Electrochemistry Communications**, 130 (2021) 107097.
3. F.H. Adnan, S. Pontvianne, M.-N. Pons, E. Mousset, *Unprecedented roles of submillimetric interelectrode distances and electrogenerated gas bubbles on mineral cathodic electro-precipitation: modeling and interface studies*, **Chemical Engineering Journal**, 431 (2022) 133413.

Oral presentations

1. F.H. Adnan, M.-N. Pons, E. Mousset, Mineral scaling on the surface of electrode during electrochemical advanced oxidation process in microfluidic thin film reactor, 1st ELO. WatR international workshop, Nancy, France (15th – 17th September 2020).
2. F.H. Adnan, M.-N. Pons, E. Mousset, Influence of micrometric interelectrode distances and cathode materials on mineral scaling during advanced oxidation process, 29th topical meeting ISE, Mikulov (online), Czech Republic (18th – 21st April 2021).
3. F.H. Adnan, M.-N. Pons, E. Mousset, Influence of micrometric interelectrode distance and water hardness on mineral scaling at electrode surface during electrochemical advanced oxidation process, 12th ESEE, Leeuwarden (online), the Netherlands (14th – 17th June 2021).
4. F.H. Adnan, M.-N. Pons, E. Mousset, Influence of electro-precipitation on pharmaceutical micropollutant degradation in simulated and reclaimed wastewater, 72nd annual meeting ISE, Jeju Island (online), South Korea (29th – 3rd September 2021).
5. F.H. Adnan, M.-N. Pons, E. Mousset, Influence de la dureté des eaux usées et des micro-distances sur l'efficacité d'un proceed électrochimique, 13th international conference GRUTTEE, Rennes, France (18th – 20th February 2020).

I. Introduction

Within the framework of water reuse as a countermeasure against water scarcity that might concern a magnitude number of countries across the globe, conventional biological and physicochemical treatments applied in wastewater treatment plants (WWTPs) do not suffice **[1, 2]**. In response, a variety of complementary treatments have been proposed across literature and some of them even have been applied at industrial scale **[3-6]**. The majority of them are based on the fundamentals of chemical oxidation, in which strong oxidants are involved in the degradation of pollutants **[7, 8]**. Classical processes such as chlorination, ozonation and advanced oxidation processes (AOPs) are to an extent well-established to be able to totally degrade organic contaminants present in aqueous media **[3, 9]**. Nevertheless, their efficiency comes first and foremost with high operational price. Secondly the addition of chemicals into the media to be treated is a prerequisite, be it H_2O_2, Cl_2, O_3, acid/base and/or ferrous sources. One might notice the contradictory practices between preserving the aquatic ecosystem receiving the treated wastewater against the admittance of unnatural element into it when chemical reagents are introduced into the media to be treated.

AOP techniques have been doped by the introduction of electrochemical advanced oxidation processes (EAOPs) **[10-12]**. The latter have been documented across literature to also be able to degrade organic pollutants into simpler organic compounds which are easier to be biodegraded **[13]**. A quasi-complete mineralization into CO_2 and inorganic species can be even obtained if required. A huge boost to the limitation of AOPs is that EAOPs do not necessarily require the addition of chemicals to electrogenerate strong, quasi non-selective oxidizing agent such as hydroxyl radicals ($^{\bullet}OH$) as well as hydrogen peroxide (H_2O_2) *in-situ*.

In addition to the advanced electro-oxidation by $^{\bullet}OH$ mentioned above, other indirect electro-oxidation (also called mediated electro-oxidation) can take place with active oxidants ($HClO/ClO^-$, Cl_2, O_3, etc) depending on the composition of electrolyte **[14, 15]**. It exists other variants of EAOPs such as those where photo-, solar photo- and sono- irradiation sources have been called upon in a way to optimize the processes **[12, 16-18]**. The coupling between EAOPs have also been explored to combine heterogeneous and homogeneous $^{\bullet}OH$ production to improve treatment capacity **[9, 19, 20]**.

Nevertheless, the phenomenon of electrode fouling during electrolysis, and particularly in EAOPs, is an inherent issue to be solved. The formation of irreversible polymeric film on anode **[14]** as well as polymeric and/or inorganic scaling **[21-23]** on cathode can hamper the process efficiency. Consequently, their durability under continuous operation, which is the ultimate goal in real field applications, is massively impacted, when regular and costly maintenance are not foreseen.

In recent years, the application of submillimetric reactors within the framework of EAOPs has spurred the capability of treatment of wastewater effluent using these techniques. The micrometric interelectrode distance (d_{elec}) significantly accommodates the limitation by mass transfer often encountered in macro-reactors. Furthermore, the redox reactions taking place on electrodes are intensified by bringing them very close to each other. While treating urban WWTPs effluents, their ionic conductivity (i.e., averagely 1000 µS cm^{-1}) is apparently too low for conventional undivided reactor (d_{elec} between 1 and 4 cm). This low value of electrical conductivity limits the efficiency and applicability of EAOPs in various terms; firstly, the huge ohmic drop in-between electrodes requires an application of significantly larger operating currents thus larger overall power consumption. Secondly, the oxidation of pollutants will quickly be limited by mass transfer towards the electrodes. Thus, the efficiency of pollutant degradation is critically impacted. Thirdly, to promote the mass transfer of pollutants, supporting electrolyte is added making the EAOPs less attracting as environmental-friendly processes and therefore real field applications. Fortunately, the use of microfluidic reactors would allow the treatment of reclaimed wastewater without the need for supporting electrolyte. As a consequence, microfluidic configuration would allow not only innate mass transfer enhancement, but also huge cut in operation cost while being environmentally friendly.

Considering the interest in the use of submillimetric electrochemical reactor to treat wastewater, this topic deserves more attention from research community. Moreover, no work has yet been reported in literature pertaining the occurrence of mineral scaling inside a microfluidic electrochemical reactor. Consequently, the lack of data on scaling formation during an EAOP to treat either synthetic or real wastewater inside submillimetric as well as millimetric reactor configurations was deemed a crucial research gap. Hence, this PhD thesis work aims at evaluating the kinetics of electro-precipitation formation on cathode in scalable conventional parallel-plate reactor subjected to a parametric investigation. Primordial variables such as applied current density (j_{app}), d_{elec}, matrices of effluent with increasing degree of complexity as well as cathode material were scrutinized. Theoretical predictive models have also been proposed accompanying the experimental results obtained. The mechanistic understanding on the formation of electro-precipitation at the cathode/electrolyte interface has been substantiated by means of electrochemical impedance studies. The practical and end objective is to establish the operating conditions by which less mineral scaling is formed, without impacting the EAOP efficiency to maximize the durability of the process.

The approach and structure of the thesis are schematized in **Fig. I.1**.

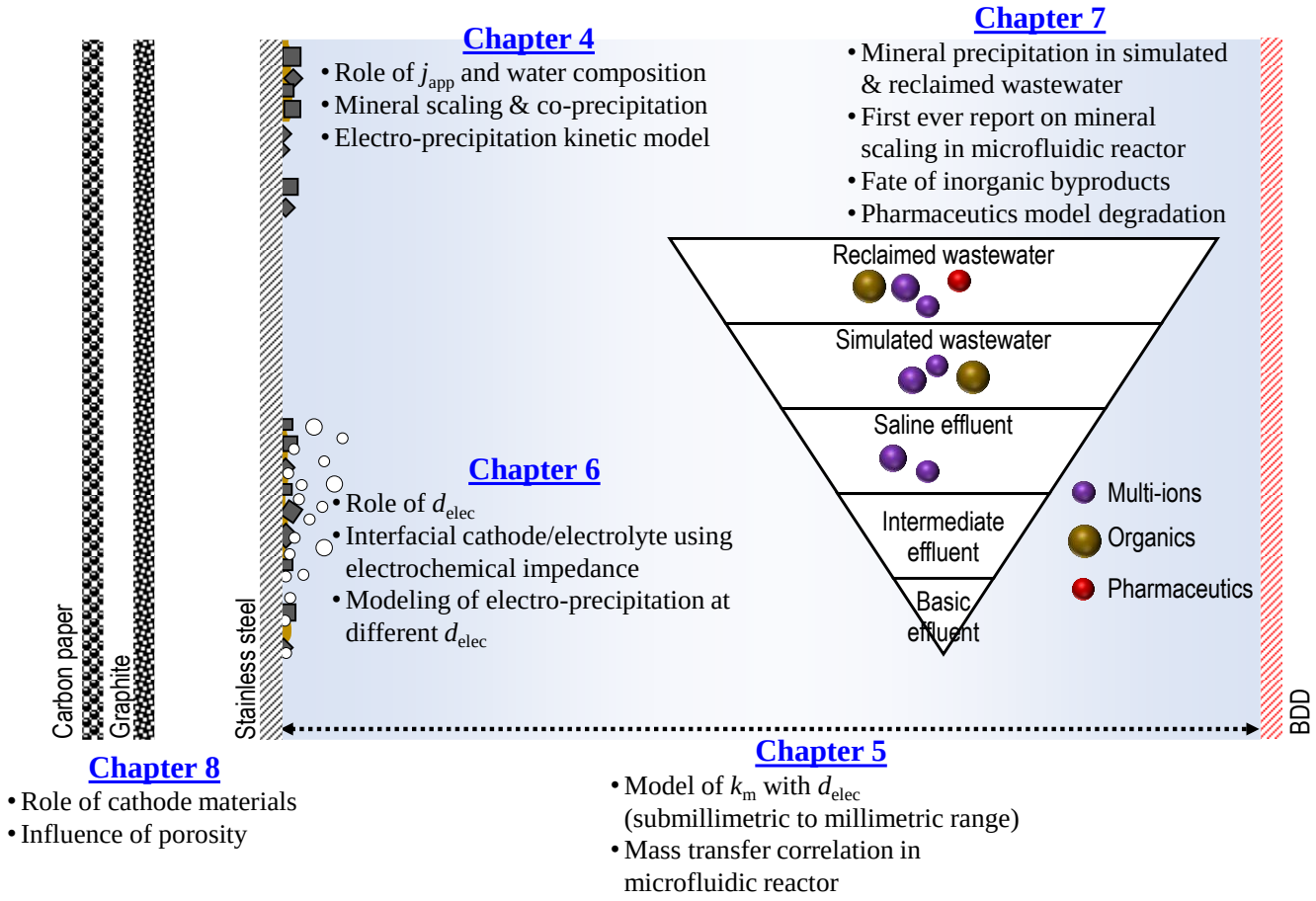

Fig. I.1. Thesis schematic chart and key parameters discussed in each chapter.

The manuscript starts with a bibliographical study in **Chapter 2** which lays out the background on the opportunity surrounding the microfluidic technology towards its application in water treatment domain. The study also points out the lack of mass transfer correlation in such reactor design for easy scale up or scale down application. Furthermore, the application of electrochemical methods for calcareous scaling investigation, pollutant removal and recovery as well as water softening have been highlighted. It ends with a discussion on vast application of EAOP to treat wastewater of various sources. **Chapter 3** details the technical aspects of experimental works including simulated and real wastewater effluent preparation, experimental pilot and electrochemical reactor setup, detailed analytical methods as well as modeling software. Next, the fundamental role of j_{app} and co-precipitation of mineral scaling in simulated effluent is discussed in **Chapter 4**. The simulated effluent mimicked the ionic properties of municipal reclaimed wastewater. The kinetics of electro-precipitation as function of j_{app} and the composition of effluent were depicted and modeled. **Chapter 5** involves the study on the development of mass transfer correlation inside an electrochemical reactor operated with wide range of d_{elec}. The interelectrode gap ranged between submillimetric to millimetric values. A theoretical model between mass transfer coefficient (k_m) and the large spectrum of d_{elec} is correlated. The established correlations are not only limited to water treatment domain but are also open to other various applications. **Chapter 6** presents the critical role of d_{elec} towards the quantity

and kinetics of mineral scaling from microfluidic up to millimetric reactor scale. Determining parameters as the outcome of varying d_{elec} were exposed. The underlying interfacial properties between partially blocked cathode surface in contact with the effluent was also discussed. The kinetics of electro-precipitation occurring under wide range of d_{elec} were substantiated using mathematical models. In the next chapter, systematic and scrupulous comparison between the formation of mineral scaling in simulated and real reclaimed wastewater was undertaken in **Chapter 7**. Particularly, the influence of the occurring electro-precipitation on simultaneous evolution of organics mineralization, chlorinated and nitrogenous inorganic byproducts as well as on pharmaceutical pollutant removal is discussed. Finally, **Chapter 8** inspects the role of cathode materials and porosity towards the formation of mineral deposition during the electro-oxidation of both simulated and reclaimed wastewater. Pioneering work was conducted on the comparison between the kinetics of electro-precipitation formed on different cathode materials during the electro-oxidation process operating inside a microfluidic cell. The manuscript ends with conclusions and perspectives in **Chapter 9**.

References

[1] S.D. Richardson, S.Y. Kimura, Water analysis: Emerging contaminants and current issues, Analytical Chemistry, 88 (2016) 546-582.
[2] M.S. Díaz-Cruz, D. Barceló, Determination of antimicrobial residues and metabolites in the aquatic environment by liquid chromatography tandem mass spectrometry, Analytical and Bioanalytical Chemistry, 386 (2006) 973-985.
[3] M.A. Oturan, J.-J. Aaron, Advanced oxidation processes in water/wastewater treatment: Principles and applications. A review, Critical Reviews in Environmental Science and Technology, 44 (2014) 2577-2641.
[4] I. Sirés, E. Brillas, Remediation of water pollution caused by pharmaceutical residues based on electrochemical separation and degradation technologies: A review, Environment International, 40 (2012) 212-229.
[5] V. Jegatheesan, B.K. Pramanik, J. Chen, D. Navaratna, C.-Y. Chang, L. Shu, Treatment of textile wastewater with membrane bioreactor: A critical review, Bioresource Technology, 204 (2016) 202-212.
[6] M. Panizza, Chapter 13 - Fine chemical industry, pulp and paper industry, petrochemical industry and pharmaceutical industry, in: C.A. Martínez-Huitle, M.A. Rodrigo, O. Scialdone (Eds.) Electrochemical Water and Wastewater Treatment, Butterworth-Heinemann2018, pp. 335-364.
[7] K. Groenen Serrano, Chapter 6 - Indirect electrochemical oxidation using hydroxyl radical, active chlorine, and peroxodisulfate, in: C.A. Martínez-Huitle, M.A. Rodrigo, O. Scialdone (Eds.) Electrochemical Water and Wastewater Treatment, Butterworth-Heinemann2018, pp. 133-164.
[8] C. Sáez, M.A. Rodrigo, A.S. Fajardo, C.A. Martínez-Huitle, Chapter 7 - Indirect electrochemical oxidation by using ozone, hydrogen peroxide, and ferrate, in: C.A. Martínez-Huitle, M.A. Rodrigo, O. Scialdone (Eds.) Electrochemical Water and Wastewater Treatment, Butterworth-Heinemann2018, pp. 165-192.
[9] E. Brillas, I. Sirés, Chapter 11 - Hybrid and sequential chemical and electrochemical processes for water decontamination, in: C.A. Martínez-Huitle, M.A. Rodrigo, O. Scialdone (Eds.) Electrochemical Water and Wastewater Treatment, Butterworth-Heinemann2018, pp. 267-304.
[10] P. Rychen, C. Provent, L. Pupunat, N. Hermant, Domestic and industrial water disinfection using boron-doped diamond electrodes, in: C. Comninellis, G. Chen (Eds.) Electrochemistry for the Environment, Springer New York, New York, NY, 2010, pp. 143-161.
[11] A. Kapałka, G. Fóti, C. Comninellis, Basic principles of the electrochemical mineralization of organic pollutants for wastewater treatment, in: C. Comninellis, G. Chen (Eds.) Electrochemistry for the Environment, Springer New York, New York, NY, 2010, pp. 1-23.
[12] O. Garcia-Rodriguez, E. Mousset, H. Olvera-Vargas, O. Lefebvre, Electrochemical treatment of highly concentrated wastewater: A review of experimental and modeling approaches from lab- to full-scale, Critical Reviews in Environmental Science and Technology, (2020) 1-70.
[13] F.C. Moreira, R.A.R. Boaventura, E. Brillas, V.J.P. Vilar, Electrochemical advanced oxidation processes: A review on their application to synthetic and real wastewaters, Applied Catalysis B: Environmental, 202 (2017) 217-261.
[14] C.A. Martínez-Huitle, M.A. Rodrigo, I. Sirés, O. Scialdone, Single and coupled electrochemical processes and reactors for the abatement of organic water pollutants: A critical review, Chemical Reviews, 115 (2015) 13362-13407.
[15] I. Sirés, E. Brillas, M.A. Oturan, M.A. Rodrigo, M. Panizza, Electrochemical advanced oxidation processes: Today and tomorrow. A review, Environmental Science and Pollution Research, 21 (2014) 8336-8367.
[16] E. Mousset, D.D. Dionysiou, Photoelectrochemical reactors for treatment of water and wastewater: A review, Environmental Chemistry Letters, 18 (2020) 1301-1318.
[17] A. Wang, Y.-Y. Li, A.L. Estrada, Mineralization of antibiotic sulfamethoxazole by photoelectro-Fenton treatment using activated carbon fiber cathode and under UVA irradiation, Applied Catalysis B: Environmental, 102 (2011) 378-386.
[18] M. Skoumal, R.M. Rodríguez, P.L. Cabot, F. Centellas, J.A. Garrido, C. Arias, E. Brillas, Electro-Fenton, UVA photoelectro-Fenton and solar photoelectro-Fenton degradation of the drug ibuprofen in acid aqueous medium using platinum and boron-doped diamond anodes, Electrochimica Acta, 54 (2009) 2077-2085.
[19] O. Scialdone, A. Galia, S. Sabatino, Abatement of Acid Orange 7 in macro and micro reactors. Effect of the electrocatalytic route, Applied Catalysis B: Environmental, 148-149 (2014) 473-483.
[20] S. Sabatino, A. Galia, O. Scialdone, Electrochemical abatement of organic pollutants in continuous-reaction systems through the assembly of microfluidic cells in series, ChemElectroChem, 3 (2016) 83-90.

[21] I. Sanjuán, D. Benavente, V. García-García, E. Expósito, V. Montiel, Electrochemical softening of concentrates from an electrodialysis brackish water desalination plant: Efficiency enhancement using a three-dimensional cathode, Separation and Purification Technology, 208 (2019) 217-226.
[22] Y. Yu, H. Jin, X. Quan, B. Hong, X. Chen, Continuous multistage electrochemical precipitation reactor for water softening, Industrial & Engineering Chemistry Research, 58 (2019) 461-468.
[23] Y. Yu, H. Jin, X. Jin, R. Yan, L. Zhang, X. Chen, Current pulsated electrochemical precipitation for water softening, Industrial & Engineering Chemistry Research, 57 (2018) 6585-6593.

II. State of the art

Introduction

The literature review is outlined in the following order: (1) the application of microfluidic reactors to treat wastewater, (2) electro-precipitation on cathode during electrochemical processes and (3) removal of pharmaceutical pollutants in various matrix of effluent by EAOPs. The chapter is ended with concluding remarks and perspectives that will be partly addressed through this thesis work.

II.1. Electrochemical microreactors for wastewater treatment application

The use of microfluidic electrochemical reactors has been introduced since the early 1980s, but their application in the field of wastewater treatment is relatively recent (2010). Only a handful of papers have been found on this topic (**Table II.1**), understandably due to the question of productivity to treat large volumes of water with a microfluidic technology. Nevertheless, promising results have been reported and the possibility of scale-up has also been explored.

II.1.1. Influence of applied current density

Applied current density is a crucial parameter in the application of electrochemical process to degrade organic pollutants. It is also closely related to the electrode potential through the Butler-Volmer relation **[1]**, which is the driving force for direct and indirect oxidation and reduction reactions **[2]**. An optimal range of j_{app} was systematically noticed, depending on the type of EAOP **[3-6]**, anode and cathode materials **[5, 6]**, on operating conditions (**Table II.1**) as well as on the configuration mode of microfluidic reactors **[5, 7, 8]**. This apparent optimal value of j_{app} occurs due to two main reasons; either the electrical current is too low to produce significant quantity of oxidants or, on the contrary, too much electrical charges are given to the system till the redundant charges are wasted to unwanted side-reactions. Hence, the current efficiency (η, in %) is commonly written under the form given in **Eq. (II.1) [5]**.

$$\eta = 100\,\frac{n_e F C_{SOL} \dot{V}_F X}{j_{app} S} \qquad \text{(II.1)}$$

where n_e is the number of required electrons for pollutant conversion, F is the Faraday constant (96485 C mol^{-1}), $\dot{V}_F$ is the flow rate (in m^3 s^{-1}), X is the conversion rate, j_{app} in A m^{-2}, C_{SOL} is the initial pollutant concentration (in mol m^{-3}) and S is the electrode surface area (in m^2).

Figure II.1 illustrates the percentages and η of chloroacetic acid removal by electro-oxidation at different current densities and flow rates. From **Fig. II.1(a)**, it was observed that at low current

density, organic abatement increased with applied current. The degradation was kinetically controlled by charge transfer and that was the reason why it increased with j_{app}, whereas in the region of high j_{app}, the percentage of abatement increased negligibly or remained constant with further increase in j_{app}. The degradation was kinetically controlled by organics mass transfer to the electrode. Excessive charge would be used for parasitic reactions. As a result, the η plot depicted a maximum where it increased with further increase in j_{app} (**Fig. II.1(b)**). Several other works have come up with similar deduction **[7-10]**.

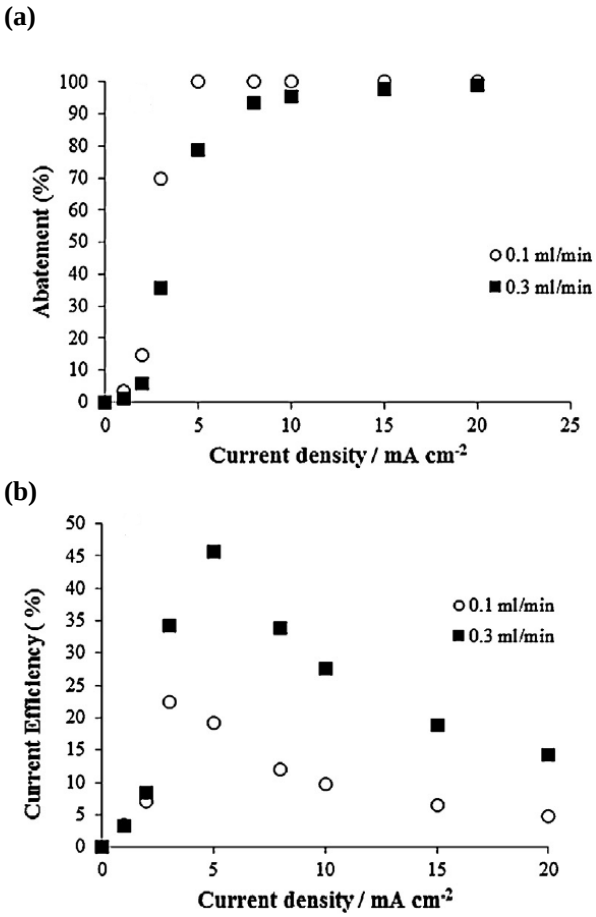

Fig. II.1. **(a)** Percentage and **(b)** current efficiency (η) of degradation of chloroacetic acid in microfluidic reactor as a function of j_{app} at different flow rates. Initial pollutant concentration: 5 mM, d_{elec}: 50 µm, anode: BDD, cathode: stainless steel, surface area: 5 cm^2. Adapted from Scialdone et al. **[5]**.

Finally, depending on how much electrical current is applied for the degradation of organics, specific energy consumption can be estimated for the process. Specific power consumption (*SPC*) has commonly been reported where the energy consumption was brought per gram of pollutant treated as defined in **Eq. II.2**.

$$SPC = \frac{\Delta U I t}{(\Delta C) V} \quad \text{(II.2)}$$

where *SPC* is generally in kWh per gram of pollutant, ΔU is the cell voltage (in V), *I* is applied current intensity (in A), *t* is the time of electrolysis (in s), ΔC is the decrease of pollutant concentration (in g L^{-1}) and *V* is the treated volume in the reactor (in L).

SPC is typically proportional to the applied current. A large advantage of the microfluidic reactor in comparison with conventional device is that, ΔU (**Eq. (II.2)**) is largely dropped owing to micrometric distance in-between electrodes **[7, 8, 11, 12]**. Consequently, *SPC* is significantly reduced hence the total EAOP operational cost could heavily be cut. Therefore, EAOP operating in microfluidic mode could then be competitive with respect to other conventional methods to treat wastewater, which is the reason why it has been scrutinized in this thesis.

II.1.2. Influence of flow rate

The effluent flow rate is an important parameter because it determines the residence time (τ) of the effluent to be treated in the electrolytic reactive zone. Generally, the influence of flow rate depends on the electrochemical process occurring on electrode surfaces. According to **Fig. II.1**, in the region where the process was kinetically controlled by charge transfer (lower j_{app}), organic removal was more efficient with lower flow rate. It was due to higher τ, thus there was a longer treatment of pollutant per charge applied. When the abatement of pollutant was controlled by mass transfer, the removal increased with the flow rate as a result of mass transfer intensification. *SPC* was also improved owing to similar reasons (**Fig. II.1**). Similar trend of conclusion has been documented in several works across literature **[4-7, 9, 13]**.

II.1.3. Influence of interelectrode distance

Despite being in micrometric conditions, the d_{elec} between anode and cathode still plays a determining role towards the reaction mechanism occurring inside the microfluidic reactor. **Figure II.2** plots the percentage of color and Chemical Oxygen Demand (COD) removal during an EF process to oxidize acid orange dye pollutant. The highest color (100%) (**Fig. II.2(b)**) and COD (80%) (**Fig. II.2(c)**) removals were achieved at lower d_{elec} (120 vs. 240 µm) at 20 A m^{-2} (2 mA cm^{-2}) **[3]**. It was attributed to higher H_2O_2 production (**Fig. II.2(a)**) with smaller d_{elec} **[3]**. Lower distance resulted in a higher contribution of dissolved oxygen (O_2) formed on anode via **Eq. (II.3)** to produce H_2O_2 via **Eq. (II.4)**. Furthermore, the lower distance also led to a more uniform distribution of dissolved O_2 thus favoring H_2O_2 formation **[3]**. Adversely, further decreasing in d_{elec} led to lower residence time in the reactor.

Thus, it led to lower accumulation of H_2O_2 and faster mass transfer of H_2O_2 towards the anode, before being oxidized back to dissolved O_2 (**Eq. (II.5)**).

$$2H_2O \rightarrow O_2 + 4H^+ + 4e^- \quad \text{(II.3)}$$

$$O_2 + 2H^+ + 2e^- \rightarrow H_2O_2 \quad \text{(II.4)}$$

$$H_2O_2 \rightarrow O_2 + 2H^+ + 2e^- \quad \text{(II.5)}$$

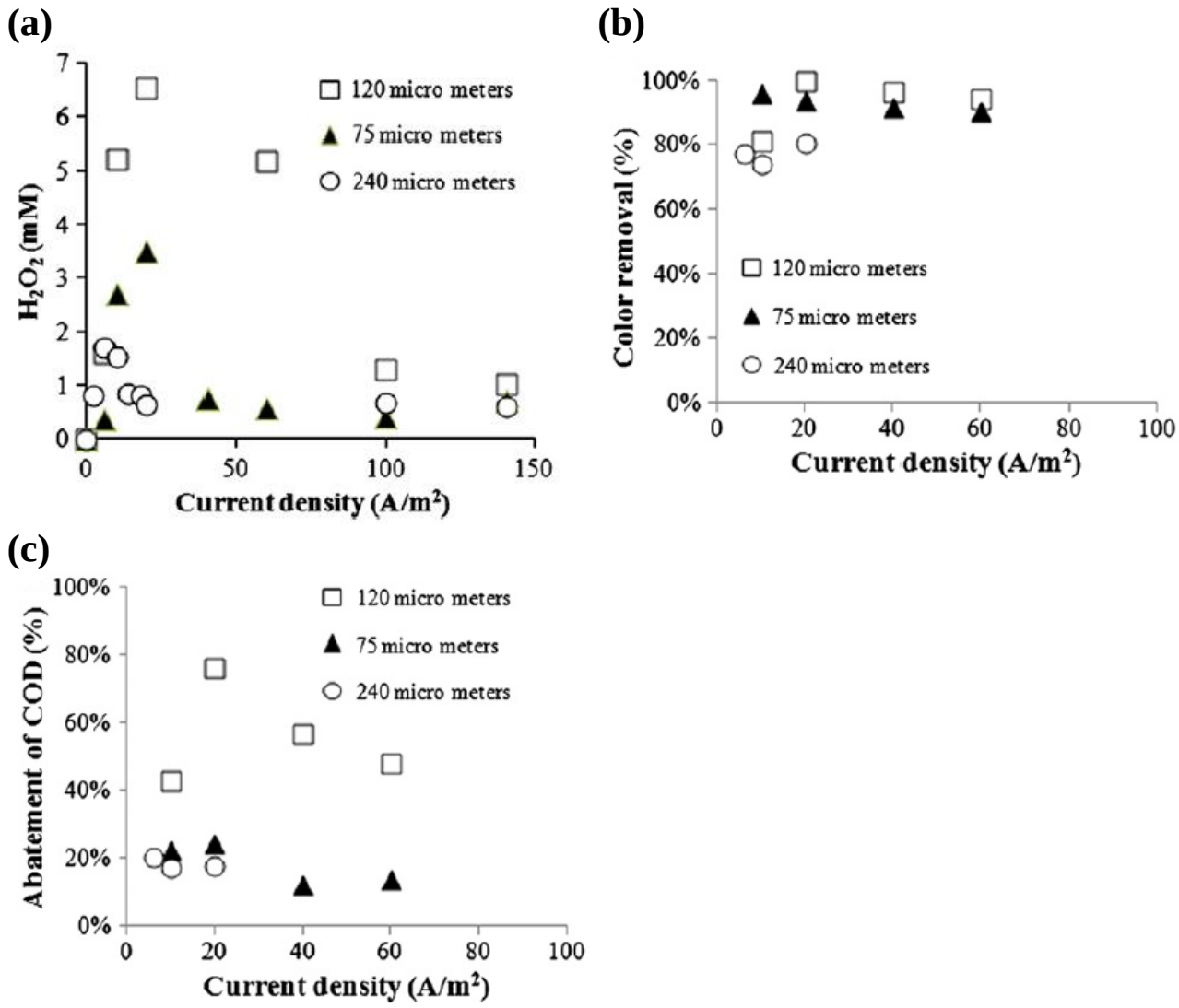

Fig. II.2. **(a)** Hydrogen peroxide (H_2O_2), percentage of **(a)** color removal and **(b)** COD removal of organic dye using EF inside microfluidic reactor with different d_{elec} at different j_{app}. Anode: IrO_2-Ta_2O_5/Ti, cathode: graphite. Initial dye concentration: 0.43 mM, Fe^{2+}: 0.5 mM. Adapted from Scialdone et al. **[3]**.

When the interelectrode gap decreases, redox reactions on both anode and cathode are intensified. Mass transfer towards both electrodes is also significantly improved. This has been demonstrated during the electro-oxidation of tetrachloroethane inside a microfluidic reactor operating using 50 and

75 µm d_{elec} **[14]**. Better abatement and η were noticed using lower d_{elec} and it was due to a better mass transfer of the pollutant towards the electrodes.

While progressively transitioning into the micrometric scale by reducing the interelectrode gap, the electrochemical cell voltage is reduced **[7]**. It occurs owing to the reduction of ohmic drop in-between electrodes. This phenomenon has clearly been presented in **Fig. II.3**. It illustrates the variation of ohmic resistance ($\sum R$) happening inside electrochemical reactors with large range of d_{elec} at different possible supporting electrolyte concentrations **[8]**. Considering for example the lowest supporting electrolyte (0.5 g L^{-1}), the $\sum R$ measured inside stirred tank reactor with 25000 µm (2.5 cm) d_{elec} was 346 Ω. The resistance was reduced to 6 Ω inside a microfluidic reactor operating using similar 0.5 g L^{-1} supporting electrolyte.

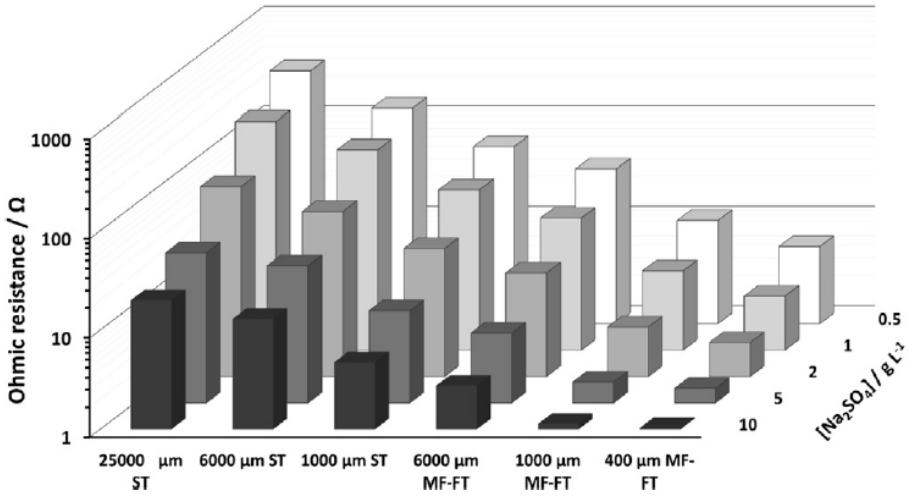

Fig. II.3. Variation of ohmic resistance as a function of d_{elec} and different concentrations of supporting electrolyte. Adopted from Pérez et al. **[8]**.

d_{elec} plays a determining role on the kinetics of reactions inside microfluidic reactor. Therefore, its role on the formation of electro-precipitation taking place inside such reactor will be investigated in details in the thesis. There has been a study conducted by Khongton et al. in which the EO experiments were performed at different d_{elec} (250 to 750 µm), while keeping the τ constant **[9]**. For that, the flow rate was adjusted according to the d_{elec} to keep the residence time identical. Similar approach will be adopted throughout this work except when the influence of flow rate is intended.

II.1.4. Influence of electrode material

Depending upon the type of EAOP intended, electrode materials are selected accordingly. Advanced EO normally operates with anode possessing high overpotential for O_2 evolution such as lead oxide (PbO_2), tin oxide (SnO_2) and BDD (boron-doped diamond), which possesses $E^0_{H_2O/O_2}$ of 1.8-2.0, 1.9-

2.2 and 2.2-2.6 V/SHE respectively **[15]**. It allows the generation of potent oxidant such as $^{\bullet}OH$ on its surface via **Eq. (II.6)**.

$$M + H_2O \rightarrow M(^{\bullet}OH) + H^+ + e^- \quad \text{(II.6)}$$

BDD has been receiving great attention due to its efficiency, stability, better life-span and high $E^0_{H_2O/O_2}$. These anodes are called non-active anodes, because the produced $^{\bullet}OH$ are loosely attached on anode surface by physisorption **[16]**. Hence, they can react quasi non-selectively with organic pollutants to oxidize them into simpler forms. When EO mode is solely intended, electrodes possessing high hydrogen (H_2) evolution potential (close to 0 V/SHE) such as stainless steel, platinum (Pt), titanium (Ti), nickel (Ni) or other metals are used **[17]**. Thus, H_2O_2 generation, which is as well an oxidant, is avoided.

When EF process is applied, cathode with low overpotential for H_2 evolution (towards negative potential values) is used. The most common cathodes are carbonaceous-based materials such as graphite, carbon sponge, activated carbon fiber, graphite felt and carbon felt **[15, 18]**. The purpose is to generate H_2O_2 *in-situ* from O_2 reduction via **Eq. (II.4)** which is one of the reagents (with Fe^{2+}) of Fenton process provided in **Eq. (II.7)**.

$$Fe^{2+} + H_2O_2 \rightarrow Fe^{3+} + {}^{\bullet}OH + OH^- \quad \text{(II.7)}$$

Furthermore, carbonaceous gas diffusion electrode has also been used to even improve H_2O_2 production by maximizing the contact between cathode, O_2 (by supplying air flow) and electrolyte **[15]**. An anode possessing low overpotential for O_2 evolution is used for EF, e.g., Pt, RuO_2 and/or IrO_2. These anodes are called active anodes, because $^{\bullet}OH$ are strongly abided to the metal by chemisorption **[17]**. The metal M may form higher oxide MO and its decomposition releases O_2. On an active anode, water oxidation produces dissolved O_2 which is the precursor of H_2O_2 following **Eq. (II.3)**. Thus, the EF reagents are electrocatalytically regenerated (**Eqs. (II.4)** and **II.8**) in the electrolytic cell.

$$Fe^{3+} + e^- \rightarrow Fe^{2+} \quad \text{(II.8)}$$

A coupling of EAOP can be done in a single electrochemical cell simply by changing the electrode material. Successive attempts have been made in submillimetric reactor configuration for example during the degradation of chloroacetic acid **[5]** and Acid Orange 7 organic dye **[6]** by coupled EO-EF using BDD and compact graphite as anode and cathode respectively. A summary of different electrode materials used in EAOPs operated in microfluidic condition is given in **Table I.1**.

II.1.5. Influence of initial concentration of pollutant

The concentration of pollutant to be treated in the effluent can have an impact on the kinetics and efficiency of its degradation **[4]**. The results of EO of formic acid in a microfluidic reactor at varying formic acid concentrations, as plotted in **Fig. II.4**, could explain the mechanism **[4]**. In the lower range of concentrations ($\leq$ 5 mmol L^{-1}), high pollutant oxidation was achieved and it was independent of applied current. The degradation process was supposed to be controlled by mass transfer. Contrastingly, using higher formic acid concentration ($\geq$ 15 mmol L^{-1}), a decrease of the degradation yield was noted but η increased (**Eq. (II.1)**). It suggested that the availability of pollutant near the anode surface was no longer the limiting factor, meaning that the kinetics was therefore limited by the charge transfer. Elsewhere, the degradation efficiency of organic dye was evaluated by either EO or EF process in microfluidic configurations **[13]**. Once again, lower organic abatement at higher concentration was observed but with drastic decrease in energy consumption (**Fig. II.4(c)**). The latter was attributed to lower impact of parasitic oxidation reactions and therefore to the higher η.

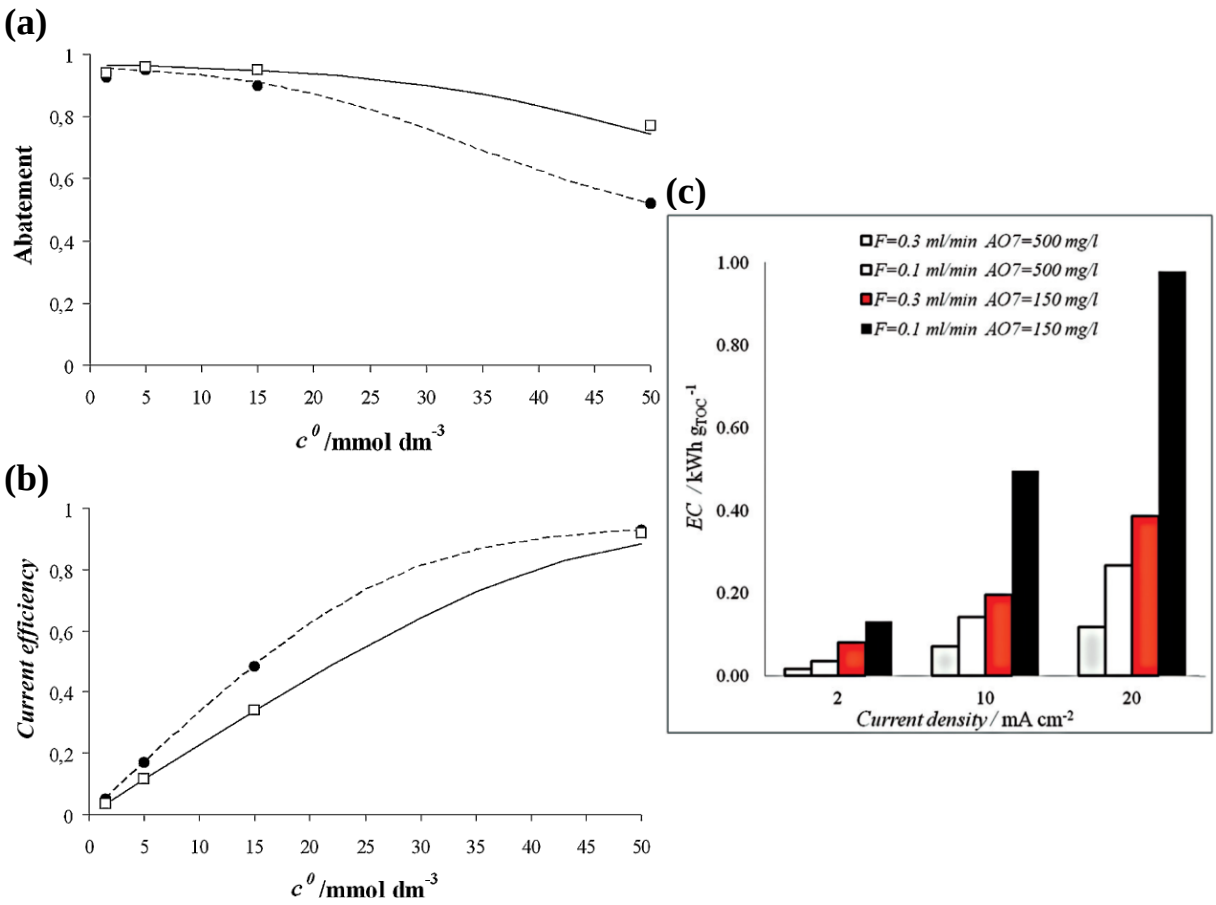

Fig. II.4. Formic acid removal **(a)** and the associated η values **(b)** at varying initial formic acid concentrations (adapted from Scialdone et al. **[4]**). (●): 6.7 and (□): 10 mA cm^{-2}. **(c)** Variation of *SPC* during organic dye (acid orange 7 (AO7)) degradation at different dye concentrations and j_{app} (adapted from Scialdone et al. **[13]**).

When high j_{app} was used to treat highly concentrated wastewater particularly using BDD as anode, the organic oxidation would be limited by mass transfer **[16]**. It is because sufficient electrical charge was supplied, which provided sufficient amount of $^{\bullet}OH$ to quickly and efficiently degrade the organics. **Figure II.5** gives an example of such case where landfill leachate waste was electro-oxidized using different anodes at 2 A **[19]**. Consequently, organic degradation followed and could be modeled using a pseudo first-order kinetic rate, when its oxidation was independent of initial organic content.

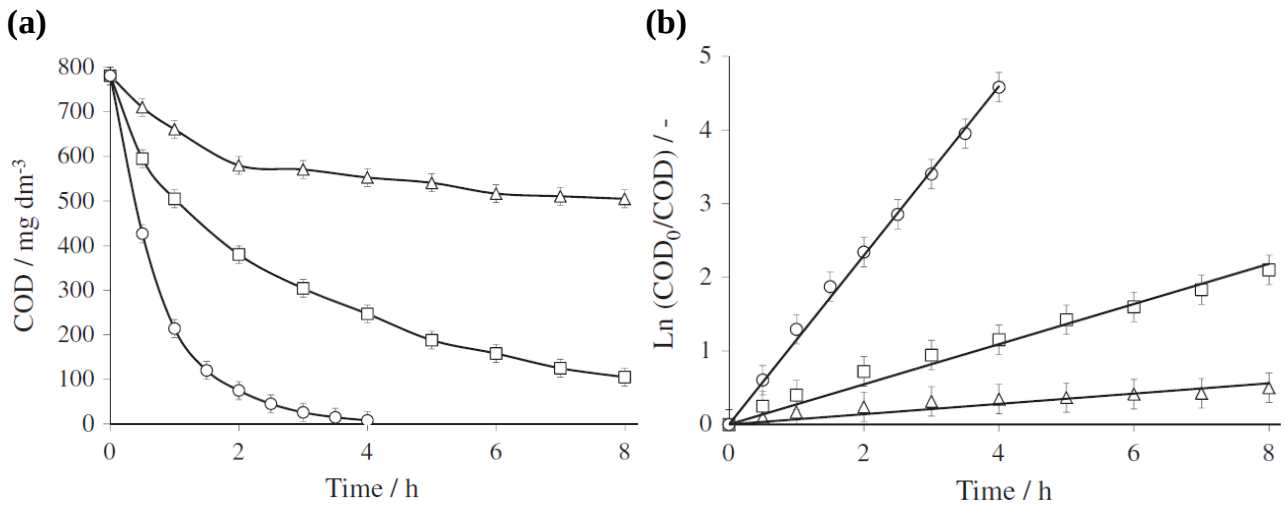

Fig. II.5. **(a)** COD abatement and **(b)** pseudo first-order kinetic plot during the EO of landfill leachate wastewater using (△): $TiRuSnO_2$, (□): PbO_2 and (○): BDD anodes. *I*: 2 A. Adapted from Panizza et al. **[19]**.

Table II.1. Literature review on the application of microfluidic reactors to treat wastewater.

Pollutant	EAOP	Mode	Electrode materials	d_{elec} / µm	Operating conditions	Ref
Oxalic acid	EO	Flow-by	Anode: BDD (9 cm^2) Cathode: Nickel (9 cm^2)	50, 360 and 750	Oxalic acid: 360 – 900 mg L^{-1} j_{app}: 4.44 – 1.67 mA cm^{-2} (40 – 150 mA) Flow rate: 0.5 mL min^{-1}, Na_2SO_4: 0 or 5 mg L^{-1}, pH: 2	[20]
Formic acid	EO	Flow-by	Anode: BDD (2.7 cm^2) Cathode: Nickel (2.7 cm^2)	50 and 75	Formic acid: 69 – 2300 mg L^{-1} j_{app}: 2.2 – 40 mA cm^{-2} (6 – 108 mA) Flow rate: 0.05 – 0.30 mL min^{-1}, pH: 2	[4]
Acid Orange 7	EF	Flow-by	Anode: Ti/IrO_2-Ta_2O_5 (5 cm^2) Cathode: Compact graphite (5 cm^2) or Carbon felt (5 – 6 cm^2)	7, 120 and 240	Acid orange 7: 150 mg L^{-1} j_{app}: 1 – 15 mA/cm^2 (5 – 75 mA) Flow rate: 0.1 mL min^{-1}, Na_2SO_4: 5 g L^{-1}, Fe^{2+}: 76 mg L^{-1}, volume: 50 mL	[3]
Chloroacetic acid	EO EF EO-EF	Flow-by	**EO**: Anode: BDD, Cathode: Stainless steel **EF**: Anode: Ti/IrO_2-Ta_2O_5, Cathode: Compact graphite **EO-EF**: Anode: BDD, Cathode: Compact graphite All electrode surface area: 5 cm^2	50 and 100	Chloroacetic acid: 473 mg L^{-1} j_{app}: 1 – 20 mA cm^{-2} (5 – 100 mA) Flow rate: 0.1 – 0.6 mL min^{-1}, EF: 0 or 76 mg L^{-1} Fe^{2+}, pH: 3 (EF)	[5]
Acid Orange 7	EO EF Indirect oxidation by active chlorine (IOAC)	Flow-by	**EO**: Anode: BDD, Cathode: Nickel **EF**: Anode: Ti/IrO_2-Ta_2O_5, Cathode: Compact graphite **IOAC**: Anode: Ti/IrO_2-Ta_2O_5, Cathode: Nickel All electrode surface area: 5 cm^2	50, 75, 120 and 240	Acid Orange 7: 150 mg L^{-1} j_{app}: 2 – 14 mA cm^{-2} (10 – 70 mA) Flow rate: 0.1 – 0.4 mL min^{-1}, EF: 34 – 152 mg L^{-1} Fe^{2+}, pH: 7 (EO, IOAC) and 3 (EF), NaCl: 993 mg L^{-1} (IOAC)	[6]

Pollutant	EAOP	Mode	Electrode materials	d_{elec} / µm	Operating conditions	Ref
Tetrachloroethane	EO ER EO-ER	Flow-by	**EO**: Anode: BDD, Cathode: Nickel **ER**: Anode: DSA, Cathode: Silver **EO-ER**: Anode: BDD, Cathode: Silver All electrode surface area: 3-4 cm^2	50 and 75	Tetrachloroethane: 151 – 285 mg L^{-1} j_{app}: 3 – 15 mA cm^{-2} (9 – 45 mA) Flow rate: 0.1 – 0.4 mL min^{-1}, pH: 2	[14]
Conversion of dichloroacetic acid to chloroacetic acid	ER	Flow-by	Anode: Ti/IrO_2-Ta_2O_5, Cathode: Compact graphite **Configuration in series**: Surface area: 4 cm^2 (each electrode) **Configuration in stack**: Surface area: 6 cm^2 (each chamber)	100	Dichloroacetic acid: 13 – 64.5 mg L^{-1} j_{app}: 10 – 48 mA cm^{-2} Flow rate: 0.05, 0.1 and 0.2 mL min^{-1}	[21]
Acid Orange 7	EO EF EF-EO	Flow-by	**EO**: Anode: BDD, Cathode: Nickel **EF**: Anode: DSA, Cathode: Graphite Configuration: single, 3 in series or in series with between 2 EAOPs All electrode surface area: 4 cm^2	EO: 50 EF: 120	Acid Orange 7: 150 and 500 mg L^{-1} **EO**: j_{app}: 2 – 20 mA cm^{-2} Flow rate: 0.1 – 0.3 mL min^{-1} **EF**: j_{app}: 1 – 20 mA cm^{-2} Flow rate: 0.1 mL min^{-1}, Fe^{2+}: 76 mg L^{-1}, pH: 3	[13]
Total organic carbon in reclaimed industrial WWTP effluent	EO	Flow-by	Anode: BDD (3.75 cm^2) Cathode: Nickel (3.75 cm^2)	50	TOC_0: 210 mg L^{-1} j_{app}: 5.3 – 53.3 mA cm^{-2} (20 – 200 mA) Flow rate: 0.1 – 0.5 mL min^{-1}, pH: 6.2, volume: 50 mL	[7]
Diuron herbicide	EO	Flow-by	Anode: Graphite sheet (3 cm^2) Cathode: Stainless steel (3 cm^2)	250 – 750	Diuron: 10 mg L^{-1} j_{app}: 0.16 – 0.64 mA cm^{-2} (0.5 – 2 mA) pH: 3–10, conductivity: 6.7 – 1000 µS cm^{-1}	[9]
Paracetamol in synthetic solution and reclaimed municipal WWTP effluent	EO	Flow-by	Anode: BDD (50 cm^2) Cathode: Carbon felt (50 cm^2)	50 – 1000	Paracetamol: 15 mg L^{-1} j_{app}: 2 to 12 mA cm^{-2} pH: 3 or neutral, Na_2SO_4: 0.14, 0.57 and 1.42 g L^{-1}, conductivity: 230 to 2000 µS cm^{-1}, flow rate: 0.43 L min^{-1}, volume: 200 or 500 mL	[11]

Pollutant	EAOP	Mode	Electrode materials	d_{elec} / µm	Operating conditions	Ref
Paracetamol in synthetic solution	EO	Flow-through	Anode: Perforated BDD (14 cm^2) Cathode: Carbon felt (14 cm^2)	500	Paracetamol: 15 mg L^{-1} j_{app}: 4 mA cm^{-2} Na_2SO_4: 570 mg L^{-1} (850 µS cm^{-1}), pH: neutral, volume: 4 L	[12]
Clopyralid in simulated soil washing effluent	EO	Flow-through	Anode: BDD mesh (33 cm^2) Cathode: Perforated plate stainless steel (33 cm^2)	400	Clopyralid: 100 mg L^{-1} j_{app}: 10 mA cm^{-2} Flow rate: 1.67 L min^{-1}, volume: 1 L	[22]
Clopyralid in simulated soil washing effluent	EO	Flow-through	Anode: BDD (50 cm^2) or Ti/RuO_2-IrO_2 MMO mesh (53 cm^2) Cathode: Perforated stainless steel plate (33 cm^2)	400	Clopyralid: 100 mg L^{-1} j_{app}: 10 and 100 mA cm^{-2} Flow rate: 1.67 L min^{-1}, volume: 1 L	[8]
Clopyralid in simulated soil washing effluent	EF	Flow-through	Anode: Ti/RuO_2-IrO_2 MMO (53 cm^2) or BDD mesh (50 cm^2) Cathode: CB/PTFE-RVC or CB/PTFE-Al (33 cm^2)	400	Clopyralid: 100 mg L^{-1} j_{app}: 20, 30 and 50 mA cm^{-3} Flow rate: 1.17 L min^{-1}, Fe^{2+}: 28 and 112 mg L^{-1}, Na_2SO_4: 1 or 7.1 g L^{-1}, pH: 3, volume: 750 mL	[23]
Clopyralid in simulated soil washing effluent	EF	Flow-through	Anode: Ti/RuO_2-IrO_2 MMO (33 cm^2) Cathode: CB/PTFE-Al foam (33 cm^2), Al foam thickness: 5 mm. For scale-up study: 10 and 15 mm	150	Clopyralid: 100 mg L^{-1} j_{app}: 10 – 60 mA cm^{-3} Flow rate: 2.67 L min^{-1}, Na_2SO_4: 7.1 g L^{-1}, volume: 2.25 L, pressurized air: 6 bars	[24]
Pretreated soil washing wastewater containing clopyralid herbicide	EO EF	Flow-through	**EO**: Anode: BDD mesh, Cathode: perforated stainless steel plate **EF**: Anode: BDD mesh, Cathode: CB/PTFE-Al foam All electrode surface area: 33 cm^2	150	400 g of soil polluted with 100 g kg^{-1} of clopyralid washed with 1 L water j_{app}: 10 – 100 mA cm^{-2} Flow rate: 0.4 – 1.6 L min^{-1}, EF: 28 mg L^{-1} Fe^{2+}, pH: 3 (EF)	[10]

Abbreviations: EO: Electro-oxidation, ER: electro-reduction, EF: electro-Fenton, BDD: boron-doped diamond, DSA: dimensionally stable anode, CB: carbon black, PTFE: polytetrafluoroethylene, RVC: reticulated vitreous carbon, Al: aluminum, d_{elec}: interelectrode distance, j_{app}: applied current density, TOC: total organic carbon.

II.1.6. Design and modularity of microfluidic electrochemical cell

II.1.6.1. Mass transfer in submillimetric electrochemical reactors

The application of submillimetric reactor configurations requires further in-depth understanding regarding the mass transfer phenomenon at the core of the electrochemical cell. Thin film reactors **[25-27]** introduced in the early 80s consisted of a plate electrode (i.e., the working electrode) most of the time positioned horizontally and were equipped with a counter electrode at the downstream of the reactor (**Fig. II.6(a)**). The reference electrode RE was positioned close to the working electrode, upstream if a 3-electrode configuration was adopted **[27]**. This thin film setup is not appropriate to receive wastewater effluent. Flow-by filter-press or flow-through reactor design is more apt for wastewater application at pilot or even industrial scale (e.g., **Figs. II.6(b)-(c)**).

Correlation in the form of $Sh = aRe^{b}Sc^{c}Le^{d}$ assuming Lévêque approximation is common in parallel-plate electrochemical reactors in the literature. It allows a dimensionless expression of the mass transfer coefficient (k_m) with dimensionless fluid properties as well as dimensionless reactor configurations under respective hydrodynamic regime of liquid flow. As a result, the extrapolation of k_m for a given reactor dimension during a scale up or scale down is possible. **Table II.2** regroups the coefficients of *a*, *b*, *c* and *d* of *Sh* correlation in parallel-plate reactor design under laminar regime. Some of the cited works used turbulence promoter to enhance mass transfer but the flow regime remained laminar **[28-31]**. **Table II.3** groups the values of k_m determined in parallel-plate electrochemical cells. Surprisingly, there is lack of data with regard to the k_m values under submillimetric electrochemical design. To the best of authors' knowledge, only Scialdone et al. **[4]** and Pérez et al. **[8]** evaluated the k_m value in their respective submillimetric reactor setup.

Hence, the establishment of mass transfer correlations under submillimetric condition would be beneficial to the body of knowledge since it concerns not only the application in environmental field but also in other electrochemistry areas. It would allow a convenient estimation of k_m for a scale up or scale down of an electrochemical reactor operated in comparable hydrodynamic regime. Since the correlation is expressed in dimensionless form, the correlation remains valid to other microfluidic reactor geometries of interest.

(a)

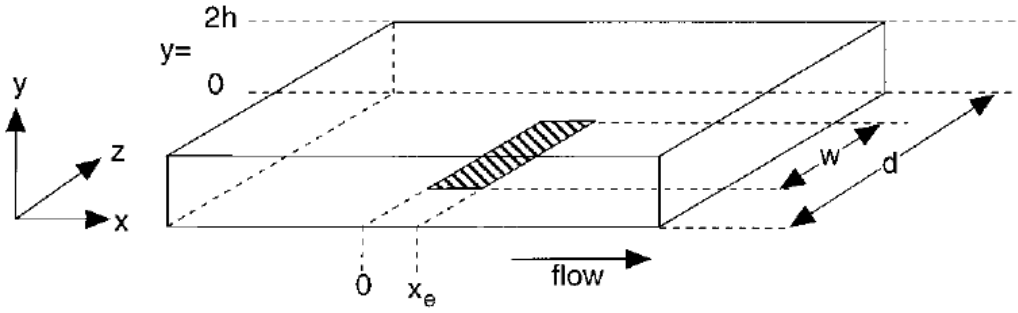

(b)

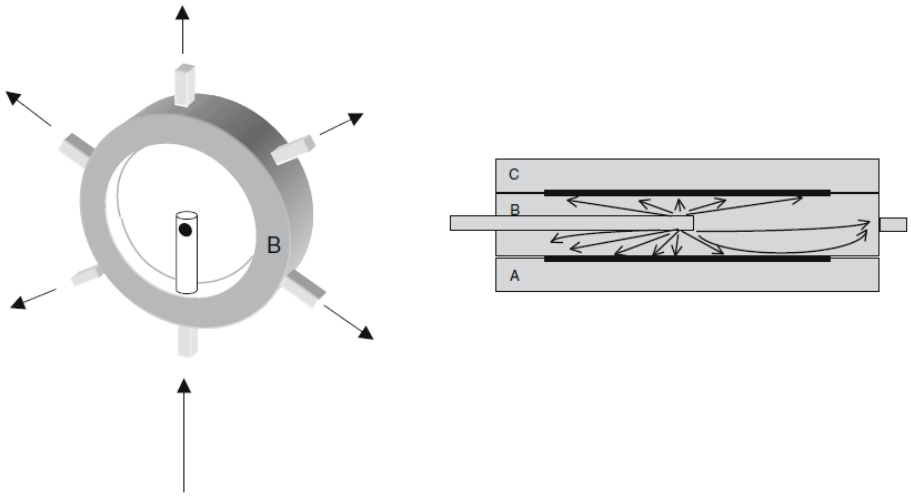

(c)

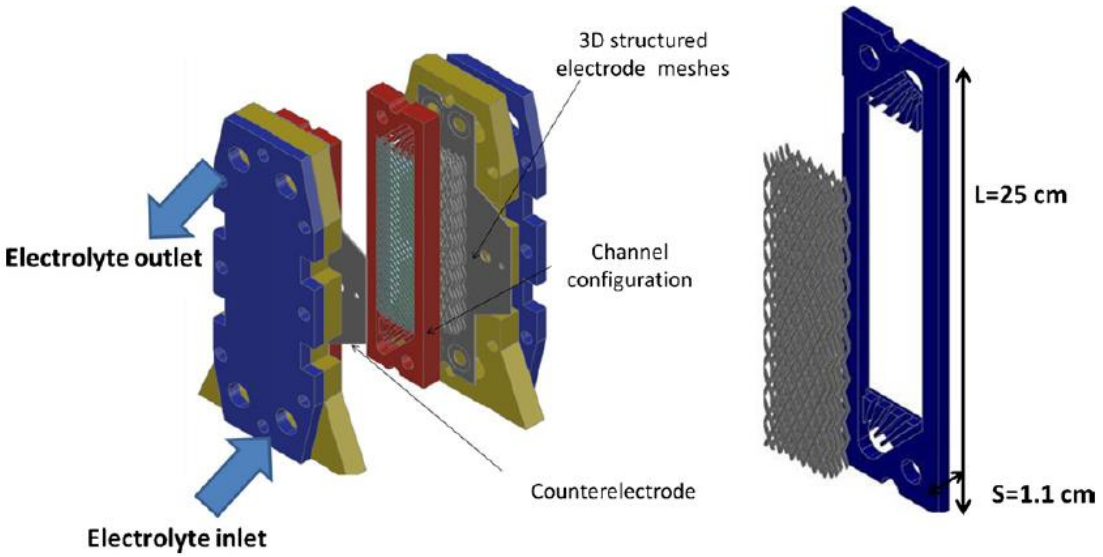

Fig. II.6. **(a)** Thin-film channel flow cell from reproduced from Cooper et al. **[27]** and more recent parallel-plate electrochemical reactors such as **(b)** parallel-plate with impinging inlet reproduced from Martínez-Huitle et al. **[32]** and **(c)** commercial parallel-plate filter-press type reactor reproduced from Cruz-Díaz et al. **[30]**.

Table II.2. Coefficients for *Sh* correlation in millimetric parallel-plate electrochemical reactors within the given range of *Re* and *Sc* numbers.

Configuration	*a*	*b*	*c*	*d*	*Re* validity ranges	*Sc* validity ranges	Ref.
Parallel plate without turbulence promoter	0.18	0.73	0.33	-	500 - 2200	1494	[28]
Parallel plate with turbulence promoter	0.71	0.55	0.33	-	500 - 2200	1494	[28]
Parallel-plate reactor	2.54	0.33	0.33	-	< 2300	-	[33]
Parallel-plate reactor	2.54	0.33	0.29	0.33	200 - 2000	960 - 3300	[34, 35]
Parallel-plate reactor without turbulence promoter	0.28	0.70	0.33	-	148 - 6109	1588	[36]
Flow cell Diacell®	0.69	0.36	0.33	-	25 - 100	1780	[37]
Flow cell Diacell®	0.14	0.70	0.33	-	100 - 2500	1780	[37]
Parallel-plate reactor	0.56 – 0.71	0.36 – 0.37	0.33	-	125 - 3550	1469	[38]
Parallel-plate reactor with turbulence promoter	2.77	0.41	0.41	0.41	839 - 1525	1420	[29]
Parallel-plate reactor with turbulence promoter	0.076	0.25	0.33	-	90 - 180	3774	[30]
Parallel-plate reactor with turbulence promoter	0.14 – 0.27	0.67	0.33	-	55 - 2100	1633	[31]
Parallel-plate reactor without turbulence promoter	0.19	0.81	0.33	-	1250 - 6900	1633	[39]

Table II.3. Reactor designs and their evaluated range of k_m values.

Type of reactor	Cell configuration	k_m / m s^{-1}	Ref.
Parallel-plate / flow-by	d_{elec}: 32 mm Geometry: Rectangular Area: 100 cm^2 Flow rate: 4 to 24.7 L min^{-1}	0.86 – 3.11 × 10^{-5}	**[36]**
Parallel-plate / flow-by	d_{elec}: 11 mm Geometry: Rectangular Area: 247.5 cm^2 Flow rate: 0.05 – 0.6 L min^{-1}	1.44 – 1.75 × 10^{-6}	**[30]**
Parallel-plate / flow-by	d_{elec}: 10 mm Geometry: Circular Area: 63.5 cm^2 Flow rate: 2.75 L min^{-1}	2.10 × 10^{-5}	**[40]**
Parallel-plate with impinging inlet	d_{elec}: 10 mm Geometry: Circular Area: 63.5 cm^2 Flow rate: 1.10 L min^{-1}	2.97 × 10^{-5}	**[32]**
Parallel-plate / flow-by	d_{elec}: 10 mm Geometry: Circular Area: 63.5 cm^2 Flow rate: 9.1 L min^{-1}	2.00 × 10^{-5}	**[41]**
Parallel-plate / flow-by	d_{elec}: 9 mm Geometry: Circular Area: 78 cm^2 Flow rate: 1.25 L min^{-1}	2.83 × 10^{-5}	**[42]**
Parallel-plate / flow-by	d_{elec}: 7 mm Geometry: Circular Area: 63.2 cm^2 Flow rate: 1.4 - 135 L min^{-1}	0.23 – 3.3 × 10^{-5}	**[37]**
Parallel-plate / flow-by	d_{elec}: 5.5 mm Geometry: Porous or non-porous rectangular Volumetric area: 30, 58 and 517 cm^{-1} Flow rate: 1.52 – 3 L min^{-1}	5.42 – 579 × 10^{-8}	**[43]**
Parallel-plate / flow-by	d_{elec}: 5 mm Geometry: Rectangular Area: 80 cm^2 Flow rate: 27 to 84 L min^{-1}	0.30 – 1.20 × 10^{-5}	**[44]**
Parallel-plate / flow-by	d_{elec}: 1 mm Geometry: Circular Area: 70 cm^2 Flow rate: 5.6 to 18.3 L min^{-1}	1.60 × 10^{-5}	**[45]**
Parallel-plate / flow-by	d_{elec}: 0.05 – 0.075 mm Geometry: Rectangular Area: 2.7 cm^2 Flow rate: 0.05 to 0.3 × 10^{-3} L min^{-1}	*2.15 – 3.22 × 10^{-5}	**[4]**
Parallel-plate / flow-through	d_{elec}: 0.4 mm Geometry: Porous, circular Area: 52.8 cm^2 Flow rate: 0.5 to 1.5 L min^{-1}	1.45 × 10^{-5}	**[8]**

*estimated from *Sh* number used in their work

II.1.6.2. Microfluidic electrochemical reactor in wastewater treatment application

To date, two electrochemical reactor designs have been adopted to treat wastewater in microfluidic conditions as summarized in **Table II.1**. The first one is a flow-by design and the other one is a flow-through configuration as illustrated in **Fig. II.7**.

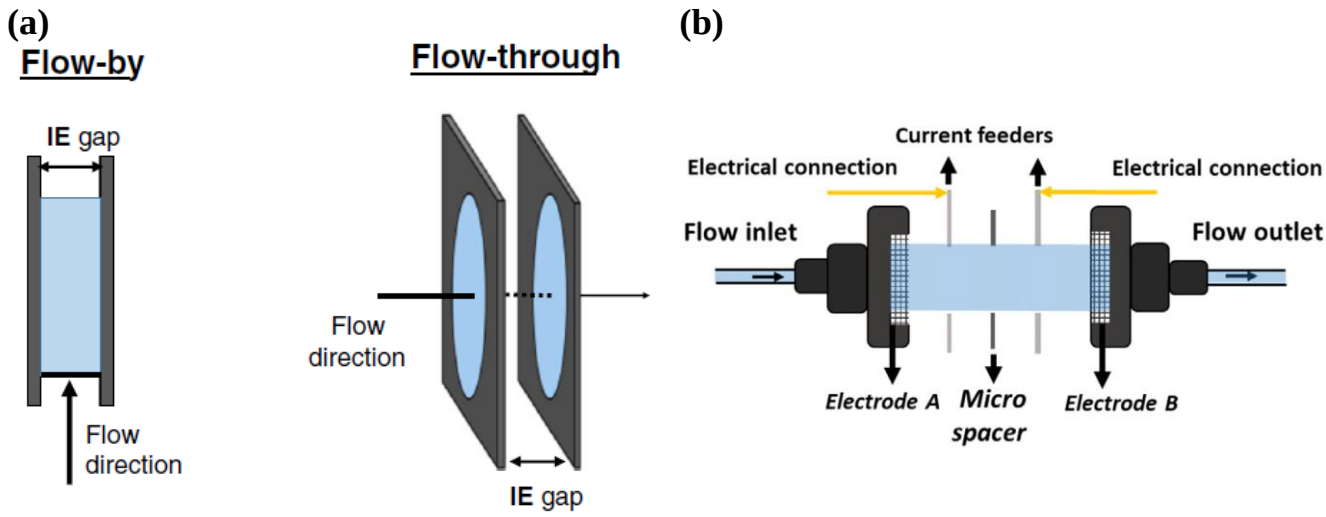

Fig. II.7. **(a)** Difference between flow-by and flow-through electrolytic flow and **(b)** scheme of flow-through microfluidic cell adopted by Pérez et al. **[22]**.

In the flow-by configuration, the electrolyte flowed in between two planar electrodes separated by a micrometric distance **[22]**. In the flow-through mode, the electrodes were porous, typically meshes, which allowed the electrolyte to pass through them **[22]**. The two meshes of anode and cathode were separated by a spacer, micrometric in thickness, which gave microfluidic characteristics to the reactor **[22]**.

A comparison in terms of pollutant degradation as well as economic performance between the two designs has been performed and it has been illustrated in **Fig. II.8**. It can be observed that both degradation of clopyralid and the mineralization of Total Organic Carbon (TOC) were faster using flow-through mode at both applied current investigated (**Figs. II.8(a)-II.8(b)**). At 10 mA cm^{-2}, complete removal of clopyralid and TOC were obtained after 10.1 and 11.4 Ah dm^{-3} respectively using flow-by mode, whilst they required 2.4 and 2.7 Ah dm^{-3} in flow-through mode. Lower *SPC* was also obtained in the flow-through configuration, which was evaluated at 12 kWh m^{-3} using 10 mA cm^{-2} against 61 kWh m^{-3} in flow-by mode working at similar j_{app}. Better energetic performance was attributed not only to lower cell voltage but also to improved mass transfer **[8, 22]**. With 3-dimensional mesh electrodes in flow-through cell, higher geometric area and specific surface of

electrode could be achieved over planar electrodes and more local turbulence occurred in the mesh. Therefore, the reactor design was more compact and k_m was higher compared to the flow-by design.

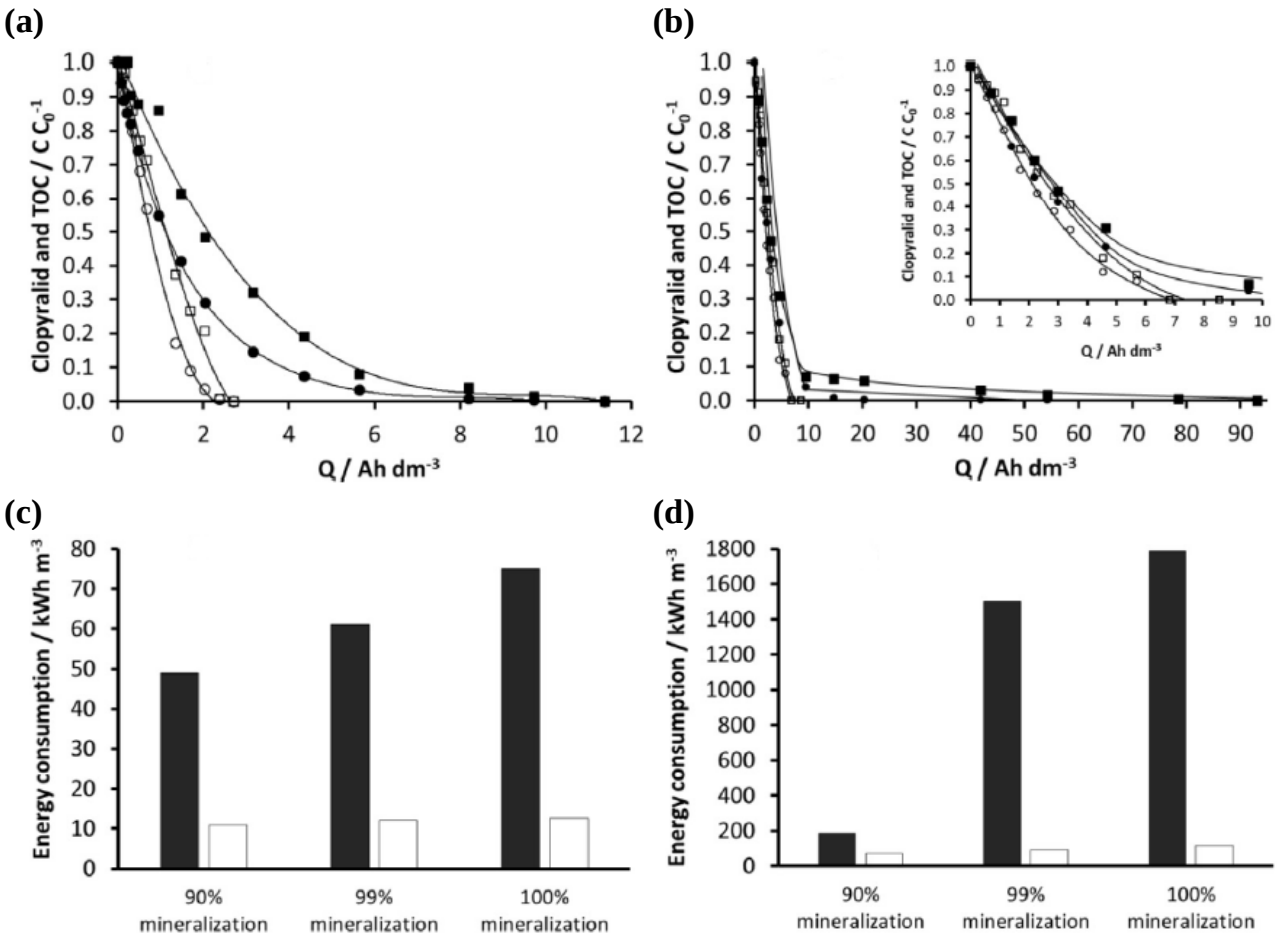

Fig. II.8. Comparison of clopyralid pesticide (●, ○) and TOC (■, □) removal using flow-by (●, ■) and flow-through (○, □) microfluidic reactors by applying 10 (**(a)**, **(c)**) and 100 (**(b)**, **(d)**) mA cm^{-2}. Power consumption of flow-by (black bar) and flow-through (white bar) during the process to reach different mineralization degrees at 10 mA cm^{-2} **(c)** and 100 mA cm^{-2} **(d)**. Flow-by d_{elec}: 3000 µm and flow-through d_{elec}: 400 µm. Anode: BDD and cathode: stainless steel. Adapted from Pérez et al. **[8]**.

The fact that the electrochemical microreactor implies small volume within the cell, the productivity of the process using such reactor design is often questionable. To address this problem, several authors have tempted operating the reactors in series. For example, up to three flow-by microfluidic reactors were operated in series (**Fig. II.9(a)**) to degrade an organic dye up to 500 mg L^{-1} in concentration **[13]**. The results are presented in **Fig. II.10**. It was shown that color and organics removal as well as treatment productivity could effectively be improved by operating the cells in series as expected. A coupling of two microfluidic reactors combining EF and EO were as well modulated. The first process of EF was aimed to reduce organic content using cheap electrodes while using low energy consumption, whilst from the second EO process, the strong oxidation by $^{\bullet}OH$ was intended to achieve total organics degradation. Optimal coupling was obtained by adapting different

applied parameters required by each operation **[13]**. An assay has also been made to increase H_2O_2 production in a flow-through microfluidic cell **[24]**. It was done by using thicker cathode materials (5, 10 and 15 mm in length, which gave 16.5 to 49.5 cm^3 in volume (depicted in **Fig. II.9(b)**)) hence sizing up the geometrical volume of electrochemical reactor. The authors reported having a proportional increase in H_2O_2 production rate with the increasing cathode thickness. However, ohmic resistance was reported to increase slightly when the thickness of cathode was increased. Cell voltage also increased with electrode thickness. As a result, higher cell voltage entailed an increase in *SPC*.

(a)

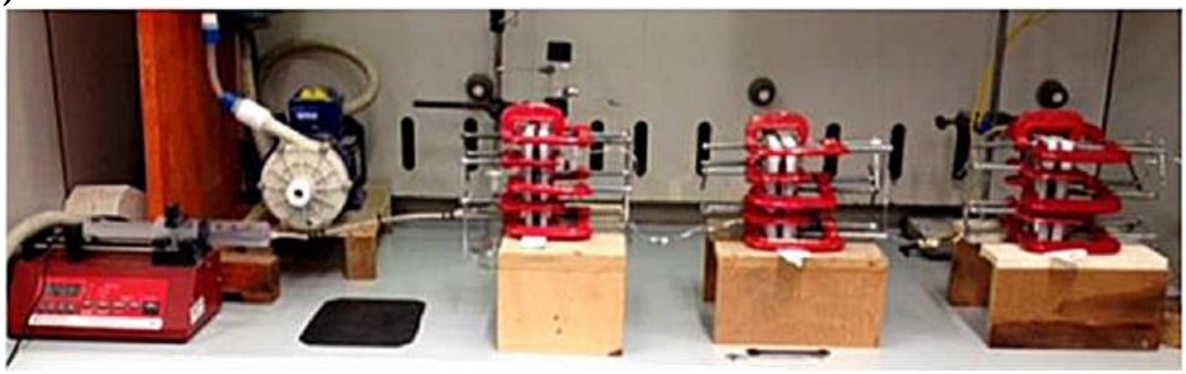

(b)

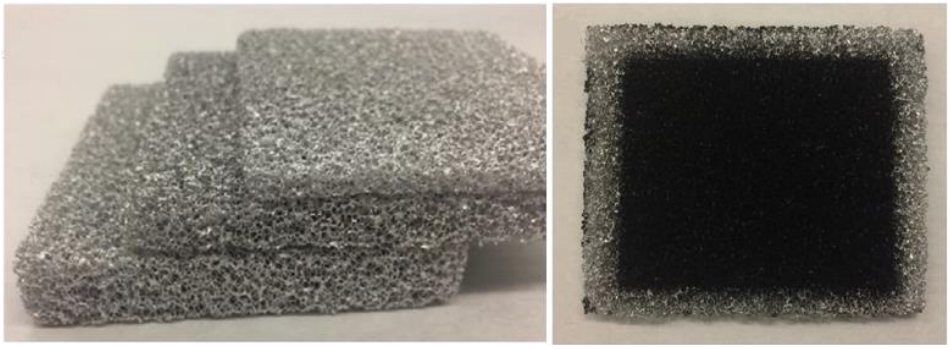

Fig. II.9. **(a)** Flow-by microfluidic reactors operating in series (adapted from Sabatino et al **[13]**) and **(b)** cathode material thicknesses used in flow-through microfluidic cell from Pérez et al **[24]**.

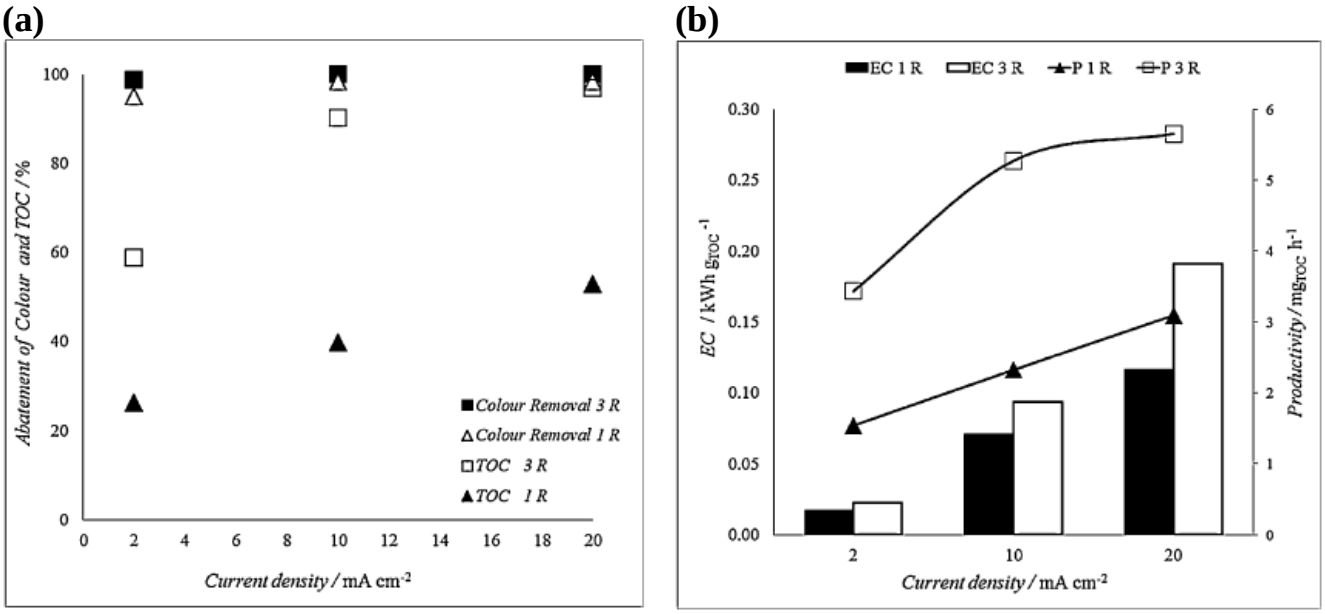

Fig. II.10. **(a)** Color and TOC removal as well as **(b)** energy consumption and productivity for flow-by microfluidic reactor working in single or in series at different j_{app}. Adapted from Sabatino et al. **[13]**.

Recently, another innovative microreactor design has been introduced, which could be particularly applicable in the field of wastewater treatment **[12]**. The reactor is illustrated in **Fig. II.11**. This design was proposed to reduce the mass transfer limitation often encountered in conventional macroreactors as well as to address the low treatment capacity and the clogging issue related to microfluidic reactors. It has been called reactive electro-mixing reactor and it consists of impellers, which themselves are composed of thin film electrochemical reactors. The reactors were set on motion with the rotation of the reactive electro-blades. One reactor can accommodate several impellers, which thus means several microreactors in one macroreactor. In the meanwhile, the macroreactors could be operated in series to significantly increase the productivity.

In summary, only a handful of publications exist in the literature regarding the use of microfluidic reactors in the field of water and wastewater treatments. Low productivity and clogging issues remain a big hurdle for the application of submillimetric reactors in large scale. These challenges are more present when real wastewater is to be treated. In the scope of reclaimed municipal or industrial wastewater treatments for water reuse, the effluent often contains colloidal and suspended solids that would need a preliminary separation step. Moreover, the organic content in the effluent is low. When the degradation of micropollutant is intended, these low concentrations could quickly reduce the process efficacy. This is where the applicability of electrochemical microreactors in the field of environmental engineering would be of interest. It could lift the mass transfer constraint encountered in conventional reactors while avoiding the use of external chemical reagents. Thus, the investigation of different behaviors between millimetric and microfluidic configuration is the grand theme of the

thesis. The occurrence of electro-precipitation, particularly in microfluidic features, has never been investigated yet. It will be the subject of discussion in the incoming sections.

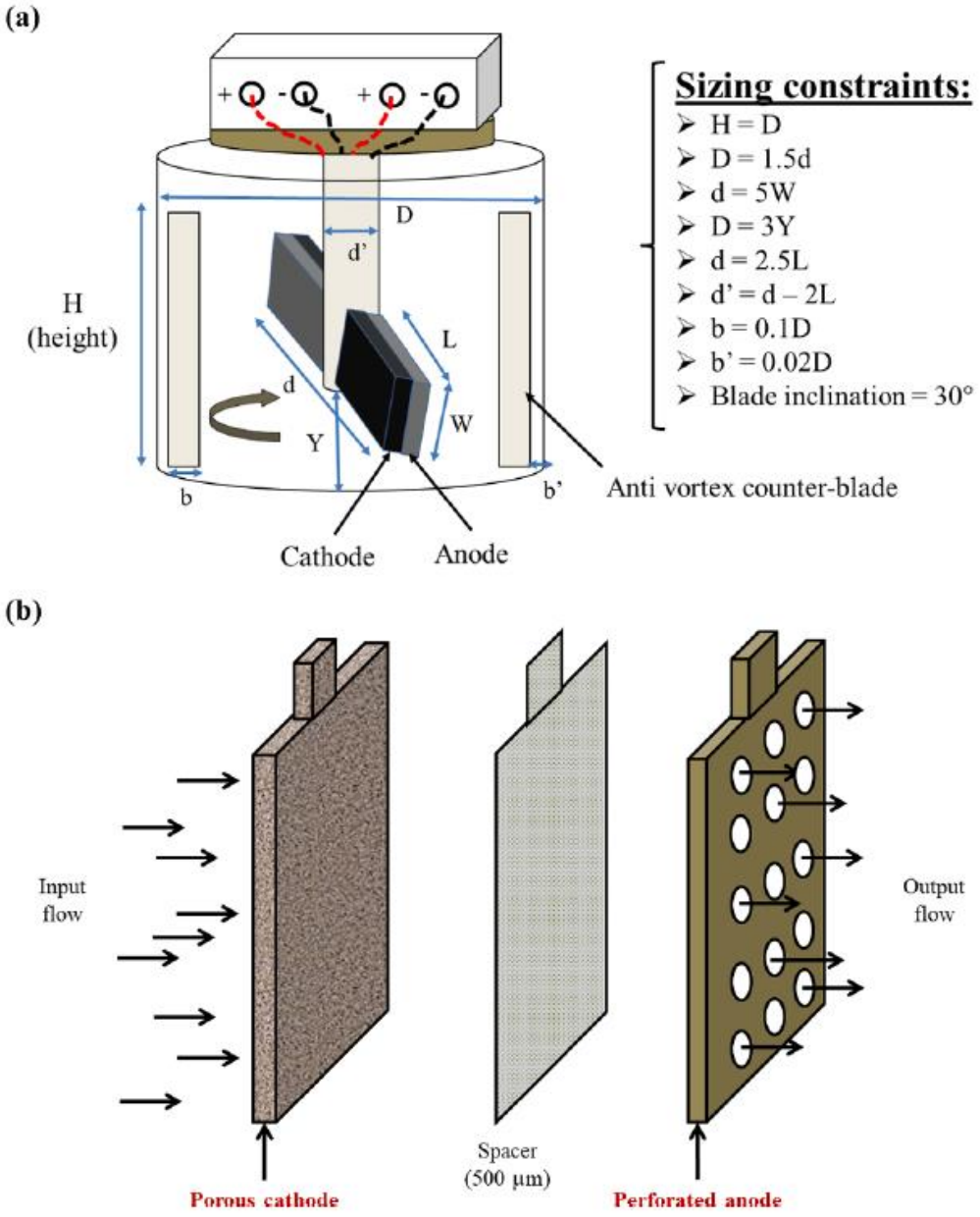

Fig. II.11. **(a)** Schematic diagram of reactive electro-mixing reactor and **(b)** an reactive electro-blade acting as flow-through microreactor. Reproduced from Mousset **[12]**.

II.2. Concomitant cathodic electro-precipitation during an electrolytic process

Calcareous scaling deposition that takes place naturally due to Ca^{2+} and Mg^{2+} content of natural water (water hardness) is a permanent problem. Technical and economic issues pertaining calcareous scaling in industrial plants and domestic equipment have triggered researches on this topic in early ages, including via electrochemical methods which has also been called accelerated scaling process **[46-50]**. This method implies the reduction of dissolved O_2 (**Eq. (II.9)**) and water (**Eq. (II.10)**) to favor the mineral deposition on cathode of an electrochemical cell **[51, 52]**.

$$O_2 + 2H_2O + 4e^- \rightarrow 4OH^- \quad \text{(II.9)}$$

$$2H_2O + 2e^- \rightarrow H_2 + 2OH^- \quad \text{(II.10)}$$

Ever since, the cathodic electrochemical precipitation has been widely documented in the literature and it concerns three major domains of application namely cathodic protection (**Table II.4**), phosphorus recovery (**Table II.5**) and water softening (**Table II.6**). On one hand, the deposition on cathode is deliberate to achieve the intended goal. On the other hand, such as in the case with EAOPs, the cathodic deposition is a major drawback, which would decrease the process efficiency during a long operation. Mineral scaling could result in economic challenges in all kinds of electrochemical reactors and the main influencing parameters are exposed hereinafter including the submillimetric features that will be adopted in this thesis.

II.2.1. Applied cathode potential/current density

II.2.1.1. Relation between cathode potential, local alkalization and mineral scaling

Corrosion of a metal occurs when the metal (M) spontaneously releases its ion (M^{Z+}) into the solution that it is in contact with. It is a spontaneous reaction when two metal elements are present, with one having more tendency to release electrons (less noble metal) acting as anode. Corroded metal loses its tensile strength, becomes brittle and has short life span. That is the reason why several authors have investigated the corrosion behavior of soft metal and carbon metal that have widely been used in marine infrastructure since they present more economic value. For instance, the formation of corrosion product by applying a corrosion potential has been investigated by Rakitin et al. **[53]** and Gabrielli et al. **[46]** on ferrous metal and also by Ben Amor et al. **[54]**, Bousselmi et al. **[55]** and Marin-Cruz et al. **[56]** on carbon steel. Furthermore, by applying a more negative potential that corresponds to the potential of the reduction of dissolved O_2 or water (**Eqs. (II.9)-(II.10)**), the reduction reactions producing OH^- are accelerated. This continuous production of OH^- induces high

local pH increase at the cathode vicinity. In the presence of carbonates, Ca^{2+} and Mg^{2+} in solution, mineral deposits are therefore formed on the cathode surface (**Eqs. (II.11)-(II.13)**) **[50, 57-59]**.

$$Mg^{2+} + 2OH^- \leftrightarrow Mg(OH)_2 \quad \text{(II.11)}$$

$$OH^- + HCO_3^- \leftrightarrow H_2O + CO_3^{2-} \quad \text{(II.12)}$$

$$Ca^{2+} + CO_3^{2-} \leftrightarrow CaCO_3 \quad \text{(II.13)}$$

These precipitates, also referred as scaling, serve as the basis for cathodic protection application, which has vastly been applied in underwater pipelines, marine transportation and above/under water infrastructures. It offers an excellent barrier towards further degradation of metal in contact with water. It significantly reduces the diffusion of dissolved O_2 towards the metal surface hence hindering further corrosion.

It has been shown across literature that the kinetics, quantity and crystallography of calcareous deposit are heavily dependent on the applied potential **[57, 59-61]**. **Figure II.12** plots normalized chronoamperometric curves during the formation of calcareous scaling at different applied potentials. According to **Figs. II.12(b)-II.12(c)** a potential of -1.2 V vs. saturated calomel electrode (SCE) represented a potential threshold **[59, 60]**. From -0.9 to -1.1 V/SCE, the applied potentials were on the plateau of the O_2 reduction producing OH^- (**Eq. (II.9)**) according to the voltammogram plotted in **Fig. II.12(a) [62]**. The lower the potential, the higher the rate of OH^- production, hence faster scaling (**Eq. (II.13)**) occurred. As a result, cathode surface was completely covered by the passivated film, thus the residual current at the end of the electrolysis was almost nil. At -1.2 V/SCE and below, the applied potential reached the region of water reduction (**Eq. (II.10)**) **[62]**. OH^- production occurred with concurrent HER. The evolved H_2 on the cathode surface induced partial detachment of calcareous scaling **[60, 61]**. It also led to a porous morphology of the scaling, which made the cathode surface not totally covered by the deposition. Consequently, higher residual current was noticed at the end of electrolysis (**Figs. II.12(b)-II.12(d)**).

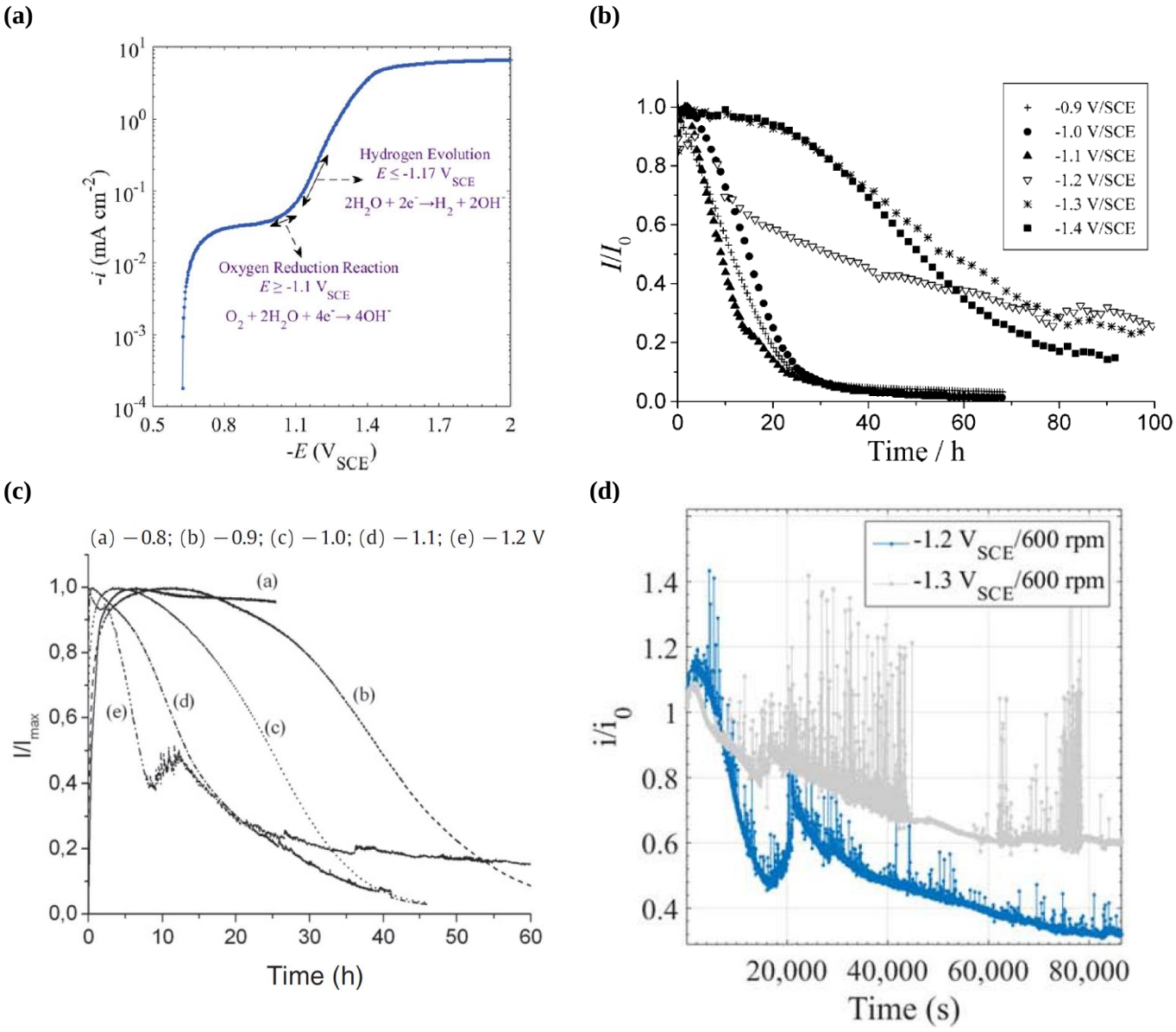

Fig. II.12. **(a)** Voltammogram on steel in synthetic seawater from **[62]** and chronoamperometric curves during the formation of calcareous scaling at different applied potential, adapted from **(b)** Barchiche et al. **[59]**, **(c)** Karoui et al. **[60]** and **(d)** Hoseinieh et al. **[61]**.

II.2.1.2. Gas evolution activity on electrode surface

When the applied potentials on cathode and anode surpass the potential of water reduction and oxidation respectively, HER (**Eq. (II.10)**) and O_2 evolution reaction (OER) (**(Eq. (II.3)**) occur. In the lower region of applied current, i.e., under the condition where HER and OER are already reached, the majority of gases are in dissolved form **[63]**. On a gas evolving electrode, it has been reported that there are periodic nucleation, growth and detachment of bubbles from electrode surface **[63-65]**. These periodic evolving and departing gas bubbles have been documented to enhance mass transfer locally on electrode surface **[63, 64, 66-68]**. The enhancement takes place firstly via microconvection owing to the evolving and departing gas bubbles from the electrode surface (**Fig. II.13**). Secondly,

the displacement of bubbles over the electrode surface induces a mechanism known as forced convection or macroconvection **[63-65, 67, 68]**. As the applied current density increases, the production of gases becomes more intense. The supersaturation of dissolved gas in the vicinity of electrodes increases too. The adhering gas bubbles could coalesce between each other to produce a film of gas bubbles, so-called gas curtain on electrode surface **[66]**. It can result in a significant increase in ohmic drop under certain configurations especially when the electrodes are brought close to each other **[69-73]**. The coalescence of dispersed gas bubbles might contribute towards gas film formation **[74]**. In such cases, slug flow (no longer dispersion) of bubbles, whose thicknesses were below 5 mm, was reported for example in a duct, **[69]**. The appearance of slug flow of gas bubbles was fact-driven and even more would be expected under the microfluidic setup **[75]**.

The characterization and mechanistic understanding on electro-precipitation taking place inside submillimetric up to millimetric cells lack studies taking into account the gas evolution reactions in the precipitates stability. This will therefore be one of the objectives of the PhD thesis.

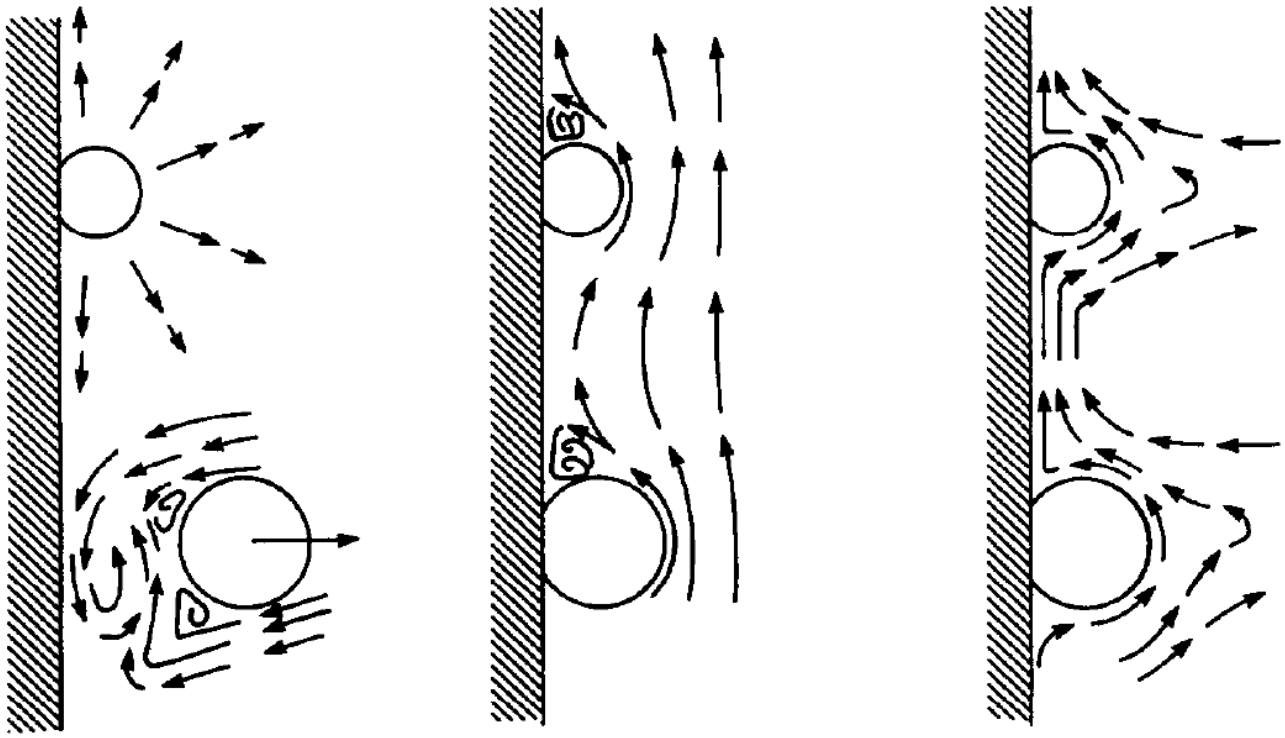

Fig. II.13. Bubbles flow pattern inducing mass transfer enhancement through **(a)** microconvection, **(b)** macroconvection and **(c)** free convection. Reproduced from Vogt et al. **[66]**.

II.2.1.3. Current distribution on gas evolving electrode

The current distribution on electrode surface could be affected by the evolving gas. However, it has been reported a homogeneity of the current density distribution on large (64 cm^2; 16 × 14 cm × cm) flat anode surface inside a commercial filter-press reactor with a pair of BDD and platinized titanium

electrodes with d_{elec} of 5 mm **[76]**. The result is depicted in **Fig. II.14** in which it is affirmed a negligible drop of 10^{-5} relative current density very closely to the border, where the electrolyte was in contact with anode-cathode separator.

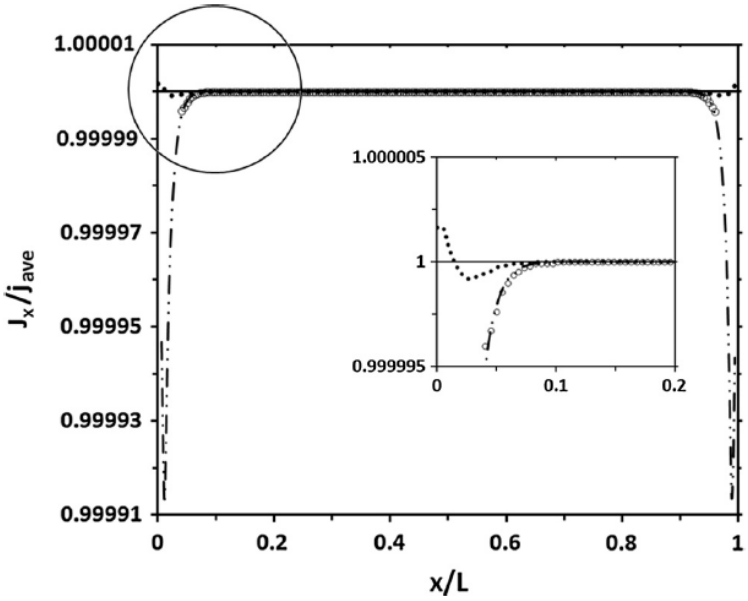

Fig. II.14. Simulation of current density distribution during a typical EO operation producing •OH on BDD anode during water oxidation in 1 M H_2SO_4. Potential sweep between 0.66 to 3 V/SHE to identify the region of •OH production from H_2O oxidation. Reproduced from Pérez et al. **[76]**.

Then, microfluidic reactors might behave differently compared to millimetic reactors due to changes in interelectrode gap and hydrodynamic behavior. Thus, an investigation on the homogeneity of current distribution on electrode surface as well as the impact that it could have towards electrochemical reaction selectivity was performed **[75]**. The study was conducted in a microfluidic setup with the involvement of gas evolution in between electrodes. It was reported that the formation of bubbles inside the micrometric interelectrode space can perturb the spread of current density line across electrode surface unlike in the case with larger interelectrode gap. However, as long as the electrolyte flow was reasonably high (i.e., above 2.5 mL min^{-1}) and that the bubble size was less than 50% of the d_{elec} for fast-kinetic electrochemical reactions, the disturbance on the homogeneity of current density distribution was minimal. Thus, the selectivity of the desired reaction on electrode surface was ensured. Moreover, an average diameter of H_2 bubbles that evolved on electrode surface under the polarization of less than 10 mA cm^{-2} was 26 µm **[74]**. The average diameter of gas bubble varied as function of j_{app} with eventual possibility of gas bubbles coalescence at relatively higher j_{app} (> 30 mA cm^{-2}). Therefore, in function of j_{app}, adopted d_{elec} and electrolytic flow rate, the current distribution homogeneity and reaction selectivity could be impacted by the evolving gas. These features would then be looked upon during the selection of operating parameters.

Table II.4. Literature review on $CaCO_3$ and $Mg(OH)_2$ electro-precipitates on cathode surface.

Application	Precipitation	Electrochemical system	Electrolyte	Potential	Allotropy	Parameter	Ref
Calcareous scaling	$CaCO_3$	WE: Fe disk (2 cm^2) CE: Pt RE: Ag/AgCl Volume: 80 mL	$CaCl_2$ or $Ca(NO_3)_2$: 0.05 M NaCl, NaI, NaBr or $NaNO_3$: 1 M NaHCO3: 2.1 g L^{-1} Volume: 80 mL	Open circuit (corrosion potential)	Aragonite	• Anions (Cl^-, I^-, Br^- and NO_3^-) • Bicarbonates	**[53]**
Calcareous scaling	$CaCO_3$	WE: Fe disk CE: unspecified RE: Saturated sulfate electrode (SSE)	Carbonically pure water, Ca^{2+}: 200 mg L^{-1}, Mineral drinking water, Ca^{2+}: 468 mg L^{-1} Scaling inhibitor: aminotris(methylene-phosphonic) (ATMP): 1 mg L^{-1}	Open circuit (corrosion potential)	Aragonite	• Ca^{2+} concentration • Scaling inhibitor	**[46]**
Calcareous scaling	$CaCO_3$	WE: Pt disk (0.2 cm^2) CE: unspecified RE: Saturated sulfate electrode (SSE)	Carbonically pure water, Ca^{2+}: 20, 120 and 160 mg L^{-1} KCl: 10^{-4} to 10^{-2} M K_2SO_4: 1 mM (blank)	Open circuit (corrosion potential) -1 and -1.5 V/SSE	Calcite	• Ionic strength • Rotational speed	**[47]**
Calcareous scaling	$CaCO_3$	WE: Gold disk (0.2 cm^2) CE: Pt RE: Saturated sulfate electrode (SSE)	Carbonically pure water, Ca^{2+}: 40, 80, 120 and mg L^{-1} $NaSO_4$: 218 mg L^{-1} NaCl: 120 mg L^{-1} $NaNO_3$: 50 – 680 mg L^{-1} $MgCO_3$: 100 – 300 mg L^{-1}	-0.8 to -1.4 V/SSE	Calcite Aragonite	• Flow rate • Ca^{2+} concentration • Anions: SO_4^{2-}, Cl^-, NO_3^- • Mg^{2+}	**[48]**
Calcareous scaling	$CaCO_3$	WE: Gold disk (0.2 cm^2) CE: Pt grid RE: Saturated calomel electrode (SCE)	Carbonically pure water, Ca^{2+}: 40 – 200 mg L^{-1} Dissolved O_2: 2.4 to 4.8 mg L^{-1} (mixture of O_2 and N_2), temperature: 25 and 50 °C, pH: 7	-1 V/SCE	Vaterite Spherulite Calcite	• Dissolved O_2 concentration • Flow rate • Degree of hardness • Temperature	**[49]**

Application	Precipitation	Electrochemical system	Electrolyte	Potential	Allotropy	Parameter	Ref
Calcareous scaling	$CaCO_3$	WE: Gold disk (0.2 cm^2)	Carbonically pure water Ca^{2+}: 40 and 200 mg L^{-1} Dissolved O_2: 5 or 100% (mixture of O_2 in N_2), flow rate: 60 and 1000 mL min^{-1}	-1.2 V/SCE	Calcite Vaterite	• Surface treatment • Dissolved O_2 concentration • Ca^{2+} concentration • Flow rate	[50]
Calcareous scaling	$CaCO_3$	WE: Soft steel, stainless steel or copper disk (1 cm^2) CE: Tin oxide film coated conductive glass (transparent) RE: Ag-AgCl	Commercial mineral water, Ca^{2+}: 108 mg L^{-1}, Mg^{2+}: 14 mg L^{-1}, HCO_3^-: 350 mg L^{-1}, Na^+: 3 mg L^{-1}, K^+: < 1 mg L^{-1}, Cl^-: 9 mg L^{-1}, SO_4^{2-}: 61 mg L^{-1}, pH: 7.4	-1 V/Ag-AgCl	Calcite	• Nature of metallic substrate • Surface energy of substrate	[77]
Calcareous scaling	$CaCO_3$	WE: Gold (0.2 cm^2), bronze or stainless steel (1.5 cm^2) CE: unspecified RE: Saturated copper sulfate electrode (SSE)	Carbonically pure water, Ca^{2+}: 40 and 200 mg L^{-1} Simulated seawater, $CaCl_2$: 1.54 g L^{-1}, $NaHCO_3$: 168 mg L^{-1}, Na_2CO_3: 21 mg L^{-1}, NaCl: 30 g L^{-1}, $MgSO_4$: 3.48 g L^{-1}, $MgCl_2$: 8.31 g L^{-1}, pH: 7 – 8	-0.9 to -1 V/SSE	Vaterite Calcite Aragonite	• Composition of scaling water • Impedance study at different water composition • Electrode substrate	[78]
Calcareous scaling	$CaCO_3$	WE: Carbon steel disk (0.2 cm^2) CE: Pt plate RE: Saturated calomel electrode (SCE)	Synthetic solution corresponding to underground natural water (Tunisia) Ca^{2+}: 100 mg L^{-1}, CO_3^{2-}: 4.2 – 5.1 mg L^{-1}, SO_4^{2-}: 500 – 1500 mg L^{-1}	Open circuit (corrosion potential)	Calcite Fe_2O_3	• SO_4^{2-} concentration • Rotation speed	[54]
Calcareous scaling	$CaCO_3$ $Mg(OH)_2$	WE: Carbon steel disk (0.2 cm^2) CE: Pt plate RE: Saturated calomel electrode (SCE)	Synthetic solution corresponding to underground natural water (Tunisia) Ca^{2+}: 100 mg L^{-1}, Cl^-: 996 mg L^{-1}, HCO_3^-/CO_3^{2-}: unspecified, Mg^{2+}: 30 – 142 mg L^{-1}, pH: 7.0 – 7.5	-0.9 to -1.1 V/SCE	Calcite Mixture aragonite calcite Aragonite	• Mg^{2+} concentration	[79]

Application	Precipitation	Electrochemical system	Electrolyte	Potential	Allotropy	Parameter	Ref
Calcareous scaling	$CaCO_3$	WE: Carbon steel disk (0.2 cm^2) CE: Pt plate RE: Saturated calomel electrode (SCE)	Synthetic solution corresponding to underground natural water (Tunisia) Ca^{2+}: 400 mg L^{-1}, Cl^-: 1000 mg L^{-1}, CO_3^{2-}: 150 mg L^{-1}, SO_4^{2-}: 480 – 3842 mg L^{-1}, pH: 7.0 – 7.5	-0.95 V/SCE	Calcite Vaterite	• SO_4^{2-} concentration	**[80]**
Calcareous scaling	$CaCO_3$	WE: Carbon steel disk (0.2 cm^2) CE: unspecified RE: Saturated calomel electrode (SCE)	Natural underground water, Ca^{2+}: 606 mg L^{-1}, Mg^{2+}: 279 mg L^{-1}, HCO_3^-: 133 mg L^{-1}, Na^+: 1.3 g L^{-1}, K^+: 24 mg L^{-1}, Cl^-: 2.3 g L^{-1}, SO_4^{2-}: 2.3 g L^{-1}, Si: 5.8 mg L^{-1}, pH: 7.2	Open circuit (corrosion potential)	-	• Long immersion time • Rotation speed	**[55]**
Calcareous scaling	$CaCO_3$	WE: Carbon steel disk (0.5 cm^2) CE: Graphite bar RE: Saturated calomel electrode (SCE)	Simulated cooling water in refineries cooling towers Ca^{2+}:120 (low) or 360 (high) mg L^{-1}, CO_3^{2-}: 180 (low) or 540 (high) mg L^{-1}, Mg^{2+}: 37 mg L^{-1}, SiO_2: 50 mg L^{-1}, SO_4^{2-}: 200 mg L^{-1}, Cl^-: 200 mg L^{-1}, PO_4^{3-}: 10 mg L^{-1}, Fe^{2+}: 0.1 mg L^{-1} pH: 7.8, temperature: 40 °C	-1.1 to -1.75 V/SCE	Aragonite Mixture aragonite calcite Calcite	• Applied potential • Concentrations of Ca^{2+} and CO_3^{2-} • Role of existing scale deposition on $CaCO_3$ crystals growth	**[81]**
Calcareous scaling	$CaCO_3$	WE: Carbon steel disk (0.5 cm^2) CE: Graphite bar RE: Saturated calomel electrode (SCE)	Simulated cooling water in refineries cooling towers Ca^{2+}: 360 mg L^{-1}, CO_3^{2-}: 540 mg L^{-1}, Mg^{2+}: 150 mg L^{-1}, SiO_2: 50 mg L^{-1}, SO_4^{2-}: 200 mg L^{-1}, Cl^-: 200 mg L^{-1}, PO_4^{3-}: 10 mg L^{-1}, Fe^{2+}: 0.1 mg L^{-1} pH: 7.8, temperature: 40 °C	-1.1, -1.3 and -1.75 V/SCE	Aragonite Mixture aragonite calcite Calcite	• Role of existing scale deposition on $CaCO_3$ crystals growth	**[82]**

Application	Precipitation	Electrochemical system	Electrolyte	Potential	Allotropy	Parameter	Ref
Calcareous scaling	$CaCO_3$ $Mg(OH)_2$	WE: Nickel foil or nickel film on Si substrate CE: Pt wire RE: Saturated calomel electrode	Synthetic industrial cooling water, $CaCl_2$: 600 mg L^{-1}, $NaHCO_3$: 600 mg L^{-1}, $MgCl_2$: 300 mg L^{-1}, organic inhibitor: 20 mg L^{-1} either phosphonobutane tricarboxylic acid (PBTC) or ethane diphosphonic acid (EDPA), temperature: 25 – 65 °C	-0.5 to -0.9 V/SCE -0.8 to -1.4 V/SCE	Calcite Aragonite	• Temperature • Water composition • Presence of organic inhibitors	[83]
Calcareous scaling	$CaCO_3$	WE: Carbon steel disk (0.5 cm^2) CE: Graphite bar RE: Saturated calomel electrode (SCE)	Simulated cooling water in refineries cooling towers Ca^{2+}:120 mg L^{-1}, Mg^{2+}: 150 mg L^{-1}, SiO_2: 50 mg L^{-1}, SO_4^{2-}: 200 mg L^{-1}, Cl^-: 200 mg L^{-1}, PO_4^{3-}: 10 mg L^{-1}, Fe^{2+}: 0.1 mg L^{-1}, Corrosion inhibitor, hydroxyphosphono acetic acid (HPA): 3 mg L^{-1} Scale inhibitor, hydroxyethane diphosphonic acid (HEDP): 3 mg L^{-1}, pH: 7.8	Open circuit (corrosion potential)	No crystals but corrosion products	• Presence of corrosion inhibitor, scale inhibitor or a mixture of both	[56]
Calcareous scaling	$CaCO_3$	WE: Carbon steel disk (0.2 cm^2) CE: Pt grid RE: Saturated calomel electrode (SCE)	Mineral potable water, Ca^{2+}: 112 mg L^{-1}, Mg^{2+}: 28 mg L^{-1}, HCO_3^-: 430 mg L^{-1}, Na^+: 6.6 mg L^{-1}, K^+: 1.8 mg L^{-1}, Cl^-: 8 mg L^{-1}, F^-: 0.6 mg L^{-1}, SO_4^{2-}: 61 mg L^{-1}, NO_3^-: < 1 mg L^{-1}, pH: 7.3, temperature: 40 °C Green inhibitor: *Paronychia Argentea* (PA): 0 to 108 mg L^{-1}	-1 V/SCE	Calcite Deformed calcite	• Presence of green inhibitor	[84]

Application	Precipitation	Electrochemical system	Electrolyte	Potential	Allotropy	Parameter	Ref
Calcareous scaling	$CaCO_3$	WE: Stainless steel (1 cm^2) CE: unspecified RE: unspecified	Simulated seawater, $CaCl_2$: 28.45 g L^{-1}, $MgCl_2$: 5.75 g L^{-1}, $NaHCO_3$: 1.55 g L^{-1}, NaCl: 63 – 64 g L^{-1}, KCl: 2.25 g L^{-1}, SrCl: 0.8 g L^{-1}, inhibitors: 1 – 30 mg L^{-1}	Unspecified	Vaterite Aragonite Calcite	• Impact of 3 green inhibitors and 1 non-green inhibitor	[85]
Cathodic protection	$CaCO_3$	WE: Gold disk (0.2 cm^2) CE: Pt grid RE: Saturated calomel electrode (SCE)	Simulated seawater $CaCl_2$: 1.2 g L^{-1}, NaCl: 29 g L^{-1}, $NaHCO_3$: 168 mg L^{-1}, Na_2CO_3: 21 mg L^{-1}, pH: 8.2, stirring rate: 120 – 4900 rpm	-0.8 to -1.2 V/SCE	Calcite Aragonite	• Stirring rate	[57]
Cathodic protection	$Mg(OH)_2$	WE: Gold disk (0.2 cm^2) CE: Pt grid RE: Saturated calomel electrode (SCE)	Simulated seawater $MgCl_2$: 5.2 g L^{-1}, NaCl: 29 g L^{-1}, $NaHCO_3$: 168 mg L^{-1}, Na_2CO_3: 21 mg L^{-1}, pH: 8.2, stirring rate: 120 – 1200 rpm	-0.8 to -1.2 V/SCE	Brucite	• Stirring rate	[58]
Cathodic protection	$CaCO_3$ $Mg(OH)_2$	WE: Carbon steel (2 cm^2) and gold disk (0.2 cm^2) CE: Pt grid RE: Saturated calomel electrode (SCE)	Simulated seawater $CaCl_2$: 1.2 g L^{-1}, $MgCl_2$: 5.2 g L^{-1}, NaCl: 25 g L^{-1}, Na_2SO_4: 4.1 g L^{-1}, $NaHCO_3$: 234 mg L^{-1}, KCl: 695 mg L^{-1}, pH: 8.2, $[Mg^{2+}]$: 0 – 200% of $[Mg^{2+}]_0$	-0.9 to -1.4 V/SCE	Aragonite Mixture aragonite brucite Brucite	• Metal substrate: steel and gold • Mg^{2+} concentration • Applied potential	[59]
Cathodic protection	$CaCO_3$ $Mg(OH)_2$	WE: Carbon steel (2 cm^2) CE: Pt grid RE: Saturated calomel electrode (SCE)	Simulated seawater $CaCl_2$: 1.2 g L^{-1}, $MgCl_2$: 5.2 g L^{-1}, NaCl: 25 g L^{-1}, Na_2SO_4: 4.1 g L^{-1}, $NaHCO_3$: 234 mg L^{-1}, KCl: 695 mg L^{-1}, pH: 8.2, temperature: 10 – 30 °C, SO_4^{2-}: 0 or 2.77 g L^{-1}, $[Ca^{2+}]$: 0 – 100% of $[Ca^{2+}]_0$	-1 and -1.2 V/SCE	Aragonite Mixture aragonite brucite	• Temperature • Ca^{2+} concentration • Presence of SO_4^{2-}	[86]

Application	Precipitation	Electrochemical system	Electrolyte	Potential	Allotropy	Parameter	Ref
Cathodic protection	$CaCO_3$ $Mg(OH)_2$	WE: Carbon steel (2 cm^2) CE: Pt grid RE: Saturated calomel electrode (SCE)	Simulated seawater $CaCl_2$: 1.2 g L^{-1}, $MgCl_2$: 5.2 g L^{-1}, NaCl: 25 g L^{-1}, Na_2SO_4: 4.1 g L^{-1}, $NaHCO_3$: 234 mg L^{-1}, 695 mg L^{-1}, pH: 8.2, Ca^{2+}: 0 or 421 mg L^{-1}, Mg^{2+}: 0 – 2.65 g L^{-1}, SO_4^{2-}: 0 – 8.3 g L^{-1}	-1 V/SCE	Aragonite Brucite Corrosion products	• SO_4^{2-} concentration • Mg^2 concentration	[87]
Cathodic protection	$CaCO_3$ $Mg(OH)_2$	WE: Gold rod (0.2 cm^2) CE: Pt grid RE: Saturated calomel electrode (SCE)	Simulated seawater $MgCl_2$: 5.2 g L^{-1}, $CaCl_2$: 1.2 g L^{-1}, NaCl: 29 g L^{-1}, $NaHCO_3$: 168 mg L^{-1}, Na_2CO_3: 21 mg L^{-1}, pH: 8.2, Na^+-montmorillonite clay: 0 – 0.2 g L^{-1}, Kaolinite clay: 0 – 0.2 g L^{-1}	-1.1 V/SCE	Aragonite Calcite Deformed calcite	• Presence of clays in simulated seawater	[88]
Cathodic protection	$CaCO_3$	WE: Transparent chromium-gold coated glass (0.4 cm^2) CE: Pt grid RE: Saturated calomel electrode (SCE)	Carbonically pure water, Ca^{2+}: 160 mg L^{-1} pH: 6.6	-1 V/SCE	Calcite Vaterite	-	[89]
Cathodic protection	$CaCO_3$ $Mg(OH)_2$	WE: Steel (10 cm^2) CE: Pt foil RE: Saturated calomel electrode (SCE)	Simulated seawater, NaCl: 41 g L^{-1}, $NaHCO_3$: 210 mg L^{-1}, Na_2SO_4: 4 g L^{-1}, $CaCl_2$: 1.1 g L^{-1}, $MgCl_2$: 5.2 g L^{-1}, temp.: 0 – 25 °C	-0.906 V/SCE	Aragonite Calcite	• Temperature • Water composition	[90]
Cathodic protection	$CaCO_3$ $Mg(OH)_2$	WE: Cylindrical different steel samples (20 cm^2) CE: Pt coated mesh RE: Saturated calomel electrode (SCE)	Real seawater (sand filtered), Flow rate: 20 to 380 mL min^{-1}	-0.9 V/SCE	Aragonite	• Different steel substrates and surface roughness • Long polarization time	[91]

Application	Precipitation	Electrochemical system	Electrolyte	Potential	Allotropy	Parameter	Ref
Cathodic protection	$CaCO_3$ $Mg(OH)_2$	WE: Stainless steel (0.785 cm^2) CE: Pt grid RE: Ag-AgCl	Simulated seawater, $CaCl_2$: 1.2 g L^{-1}, $MgCl_2$: 5.2 g L^{-1}, NaCl: 25 g L^{-1}, Na_2SO_4: 4 g L^{-1}, $NaHCO_3$: 235 mg L^{-1}, KCl: 703 mg L^{-1}, pH: 8.2	-0.8 to -1.2 V/Ag-AgCl	Brucite Aragonite	• Temperature • Applied potential	[60]
Cathodic protection	$CaCO_3$ $Mg(OH)_2$	WE: Carbon steel disk (1 cm^2) CE: Pt RE: Saturated calomel electrode (SCE)	Simulated seawater, $CaCl_2$: 1.2 g L^{-1}, $MgCl_2$: 5.2 g L^{-1}, NaCl: 24.5 g L^{-1}, Na_2SO_4: 4.1 g L^{-1}, $NaHCO_3$: 201 mg L^{-1}, KCl: 700 mg L^{-1}, pH: 8.2, rotational speed: 120 – 600 rpm	-0.9 to -1.3 V/SCE	Aragonite Brucite	• Rotational speed • Applied potential	[61]
Cathodic protection	$CaCO_3$ $Mg(OH)_2$	WE: Stainless steel disk (1 cm^2) CE: Pt RE: saturated calomel electrode (SCE)	Simulated seawater, $CaCl_2$: 1.2 g L^{-1}, $MgCl_2$: 5.2 g L^{-1}, NaCl: 24.5 g L^{-1}, Na_2SO_4: 4.1 g L^{-1}, $NaHCO_3$: 200 mg L^{-1}, KCl: 700 mg L^{-1}, pH: 8.2 SO_4^{2-}: 0 – 200% $[SO_4^{2-}]_0$ Mg^{2+}: 0 – 200% $[Mg^{2+}]_0$ Ca^{2+}: 0 – 200% $[Ca^{2+}]_0$	-1.1 V/SCE	Calcite Aragonite	• Water composition • SO_4^{2-} concentration • Mg^{2+} concentration • Ca^{2+} concentration	[62]

Abbreviations: WE: working electrode, CE: counter electrode, RE: reference electrode, Pt: platinum, Ti: titanium, Si: silicon.

II.2.2. Electrolytic properties and composition

Simple Ca^{2+} containing solution saturated by carbonate using CO_2 bubbling has been used in early stages to investigate calcareous kinetics and nuclei growth mechanism **[46-48, 50, 78]**. From there onwards, more complex matrices of solutions have been explored (**Table II.4**) such as simulated groundwater **[54, 79, 80]**, simulated seawater **[57-62, 85-87]**, simulated industrial cooling water **[56, 81-83]**, natural groundwater **[55]** and real seawater **[88, 90, 91]** as well as mineral drinking water **[77, 84]**. This transition from simple matrix into real natural water matrix is necessary to investigate several possible parameters that could alter the kinetics of mineral scaling.

While treating real wastewater of multiple origins, the wastewater is often composed of multi-ions having various concentrations depending on their source. It means that several precipitations could occur once their thermodynamic constant of precipitation have been reached **[92]**. Consequently, cathodic precipitation is done deliberately to retain specific species from the bulk and the retained product could be recovered if it has an added value **[93]**. A clear example is the phosphorus nutrient recovery. Phosphorus is a nonrenewable resource and, in the meanwhile, the emission of phosphorus into the waste streams represents a rich unrecovered phosphorus source **[94]**. That is the motivation behind the phosphorus recovery via electrochemical precipitation method which has been attempted as electrochemical phosphorus recovery **[95]**. This technique is currently under optimization to replace chemical dosing method (e.g. with NaOH or $Mg(OH)_2$ to precipitate PO_4^{3-} under the form of struvite ($MgNH_4H_nPO_4^{3-n}$) in the waste streams rich with P and N nutrients) **[93, 96]**. A literature review about the recovery via electro-precipitation routes is provided in **Table II.6**.

II.2.2.1. Presence of multi-ions in solution

Among the ionic species which are jointly present in the natural water body, Mg^{2+} and SO_4^{2-} are the two most reported species to inhibit the growth of scaling **[59-62, 86]**. Their inhibiting effect can be clearly seen from **Figs. II.15-II.16** in which the chronoamperograms and scanning electron micrographs are respectively shown at varying concentrations of Mg^{2+} and SO_4^{2-}. Both chronoamperograms indicated an increase in residual currents as a result of lesser calcareous scaling on electrode surface. They were supported by scanning electron microscopy (SEM) images showing significantly bare electrode surface at the highest Mg^{2+} and SO_4^{2-} concentrations. According to literature, Mg^{2+} hinders the growth of $CaCO_3$ by its incorporation into the $CaCO_3$ crystal lattice **[79, 97, 98]**. The growth of the most stable $CaCO_3$ crystal (calcite, cubic form as shown in **Fig. II.15(b-I)**) was then slowed down. It promoted aragonite crystallography (needle-like form as in **Figs. II.15(b-II)** to **II.15(b-IV)**) instead, as a result of incorporation of Mg^{2+} into $CaCO_3$ deposit. As for

the SO_4^{2-} ions, they could impede the $CaCO_3$ growth, either by lowering the cathode local pH **[86, 87]**, adsorbing into the $CaCO_3$ crystal lattice **[99]**, or by increasing the $CaCO_3$ solubility **[62, 100]**.

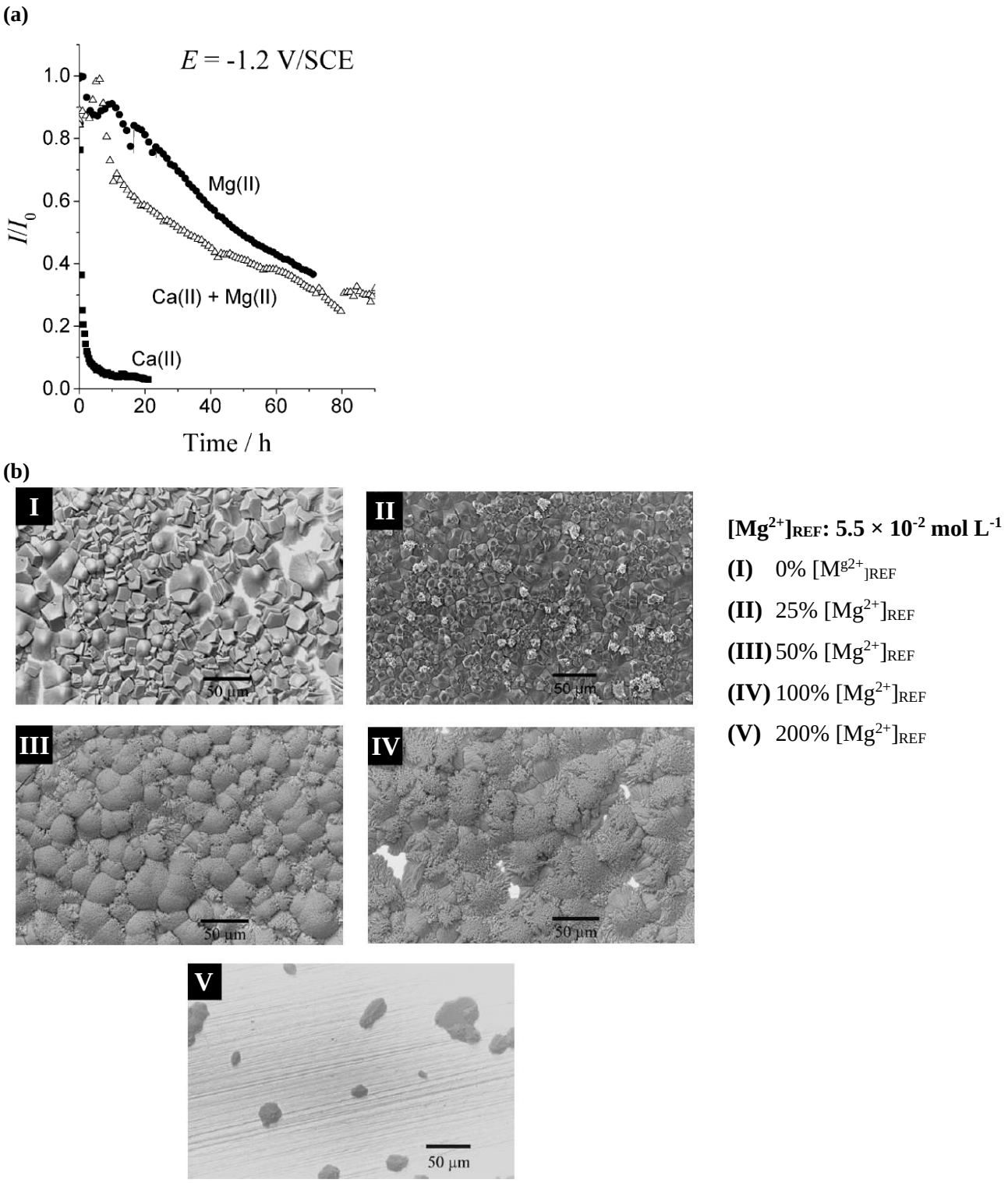

Fig. II.15. **(a)** Chronoamperometric curves in the absence and presence of Mg^{2+} and **(b)** SEM of cathodic electro-precipitates at varying concentrations of Mg^{2+}. Adapted from Barchiche et al. **[59]**.

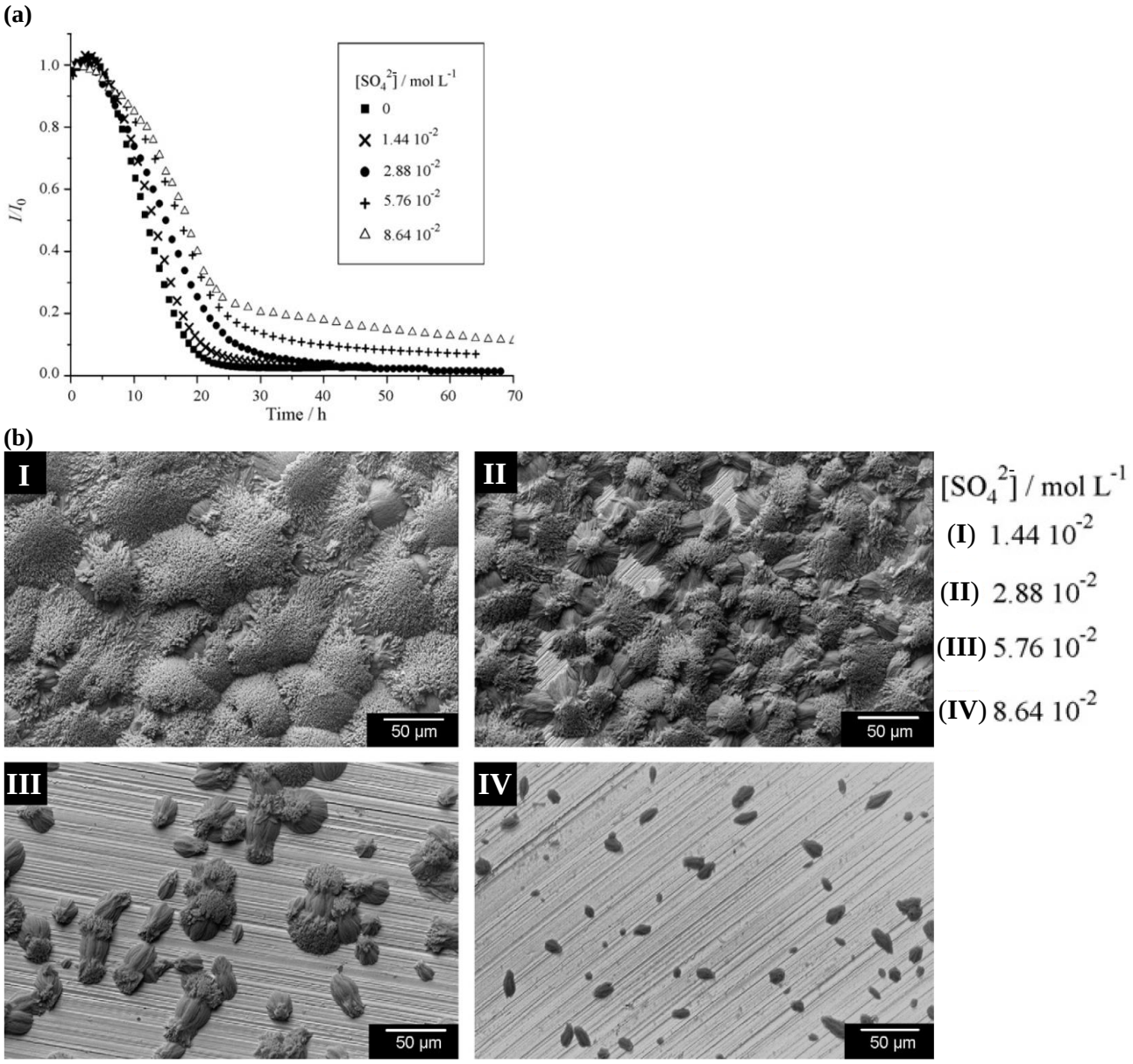

Fig. II.16. **(a)** Chronoamperometric curves in the presence of varying sulfate content and **(b)** SEM of cathodic electro-precipitates at the corresponding SO_4^{2-} concentration. Adapted from Barchiche et al. **[87]**.

In the presence of other ionic species representative of typical raw **[92, 96, 101, 102]** and pretreated **[103-106]** wastewater, the occurrence of struvite ($MgNH_4H_nPO_4^{3-n}$), calcium phosphates and other precipitates might occur. It has been documented that under the conditions where molar ratio of Mg^{2+}, NH_4^+ and PO_4^{3-} is adequate (1:1:1), struvite recovery via electro-precipitation was possible. Then, as depicted in **Fig. II.17**, when Ca^{2+}, Mg^{2+} and HPO_4^{2-}/PO_4^{3-} were simultaneously present in the effluent, the co-precipitation of Mg, Ca and phosphate might happen. Their concentrations decreased during the electrolysis treatment and it resulted in precipitates with regular morphologies and element distribution as shown in **Fig. II.17(c)**. Where Ca was dominant, the precipitate took rhombohedral form (**Fig. II.17(c-A)**), while it presented lamella-like (**Fig. II.17(c-B)**) and spherical shapes (**Fig. II.17(c-C)**) when Mg and P element were predominantly present **[92]**.

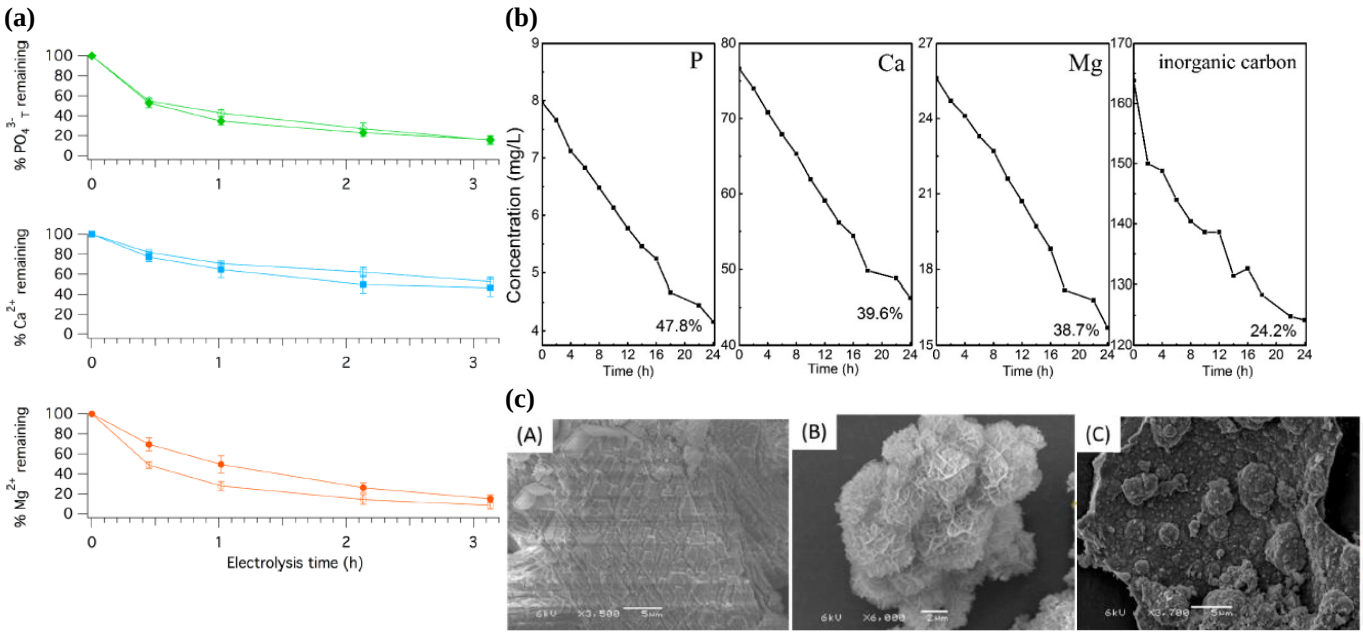

Fig. II.17. Evolution of PO_4^{3-}, Ca^{2+}, Mg^{2+} and inorganic carbon during electro-precipitation process for their recovery when they were simultaneously present in the bulk. Treatment of **(a)** public wastewater reproduced from Cid et al. **[101]** and **(b)** influent of municipal wastewater treatment plant adapted from Lei et al. **[92]**. Their co-precipitation resulted in irregular morphologies as well as element distribution as shown from SEM images **[92]** in **(c)**.

II.2.2.2. Presence of organics

Electro-oxidation is applied to treat waste streams often containing organics and/or inorganic pollutants. The presence of organic compounds could somehow influence on the kinetics and the type of scaling formed on electrode surface. In the case where the organic pollutant itself is to be degraded (thus valueless) but it bears recoverable valuable resources, simultaneous organic abatement and resource recovery via electro-precipitation could be tempted. That was the essay conducted by Ning et al. **[107]** where organophosphorus pesticide was degraded via EO process using BDD on anode and simultaneous phosphorus recovery by cathodic precipitation in a single cell. Orthophosphate (PO_4^{3-}) was released during the oxidation of the pesticide and it was later deposited on cathode via electro-precipitation with Ca^{2+}. As a result, total phosphorus in the bulk decreased, PO_4^{3-} increased and later decreased with Ca^{2+} due to their co-precipitation on cathode (**Fig. II.18**). It could be deduced that depending on the composition of effluent to be treated, it could alter the degree of deposition occurring on anode or cathode.

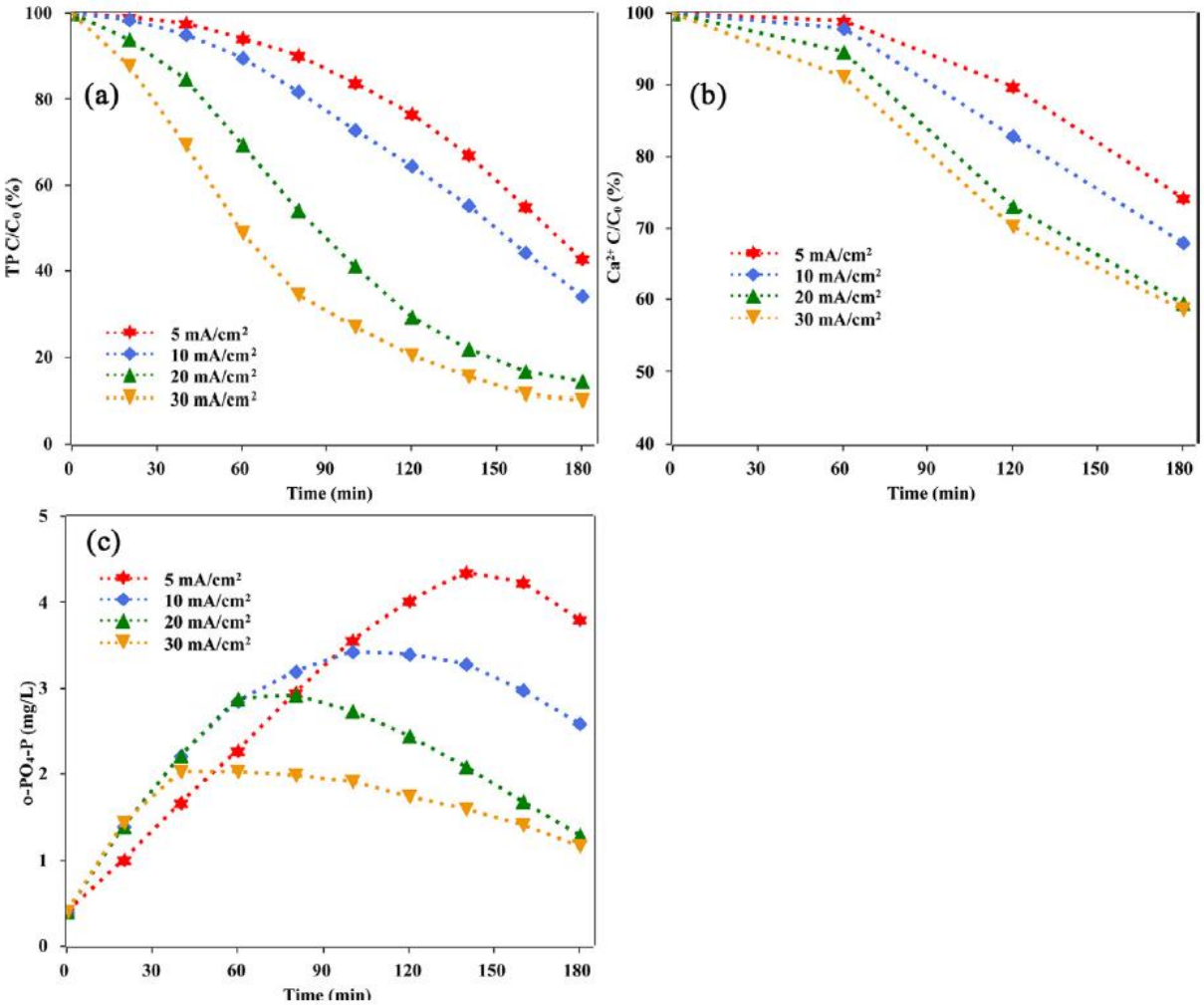

Fig. II.18. Simultaneous electro-oxidation process of organophosphorus pesticide (acephate) on BDD anode and phosphorus recovery on Ti mesh cathode at different j_{app} **[107]**. The evolutions of **(a)** total phosphorus (TP), **(b)** Ca^{2+} and **(c)** PO_4^{3-} concentration during the treatment.

Anthropogenic dissolved organic matter (DOM) is omnipresent in wastewater and its content varies with anthropogenic activities and waste stream treatment level. When EAOP is to be used to treat wastewater as pretreatment or post-treatment, DOM will also be the subject of treatment in the electrochemical system. The interaction of DOM with precipitated compounds during an electrochemical recovery process has been systematically investigated in a millimetric reactor configuration **[108, 109]**. As opposed to the interaction of DOM with $Ca_3(PO_4)_2$ during chemical precipitation, more electro-precipitation of calcium phosphate was observed with increasing concentration of DOM during an electrochemical process as illustrated in **Fig. II.19 [109]**. It has been attributed to the rise of cathodic local pH that lifted the inhibition effect of DOM on calcium phosphate precipitation.

Consequently, the presence of DOM in the effluent could induce co-precipitation during an EAOP in general. Its behavior during the EO process under microfluidic condition using either synthetic or real wastewater will then be checked in the PhD thesis.

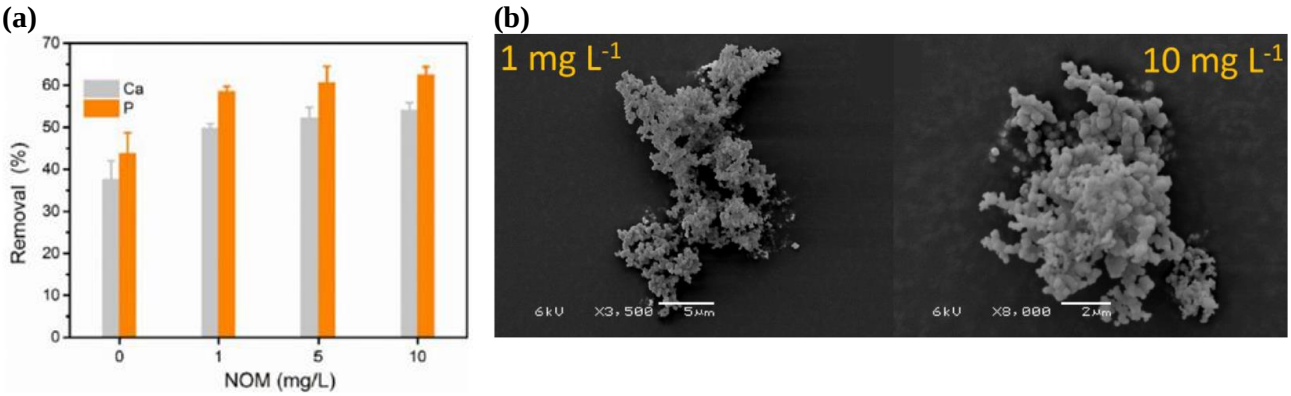

Fig. II.19. **(a)** Removal of Ca^{2+} and phosphorus as a function of NOM concentration and **(b)** amorphous calcium phosphates precipitate. Adapted from Lei et al. **[109]**.

II.2.2.3. Presence of scaling/corrosion inhibitors

In the objective to reduce scaling tendency, the addition of inhibitors has been tested. Various studies have been devoted to the kinetic growth of $CaCO_3$ in the presence of inhibitors **(Table II.4)**. The inhibitors could be either organic or inorganic compounds. As the name suggests, the growth of calcareous scaling was impeded in their presence. It can be affirmed by the plots of chronoamperometric and EIS curves in **Figs. II.20(a) [84]** and **II.20(b) [56]**. In the former, the curve did not decrease in the presence of optimal scale inhibitor (**Figs. II.20(a)**). In the latter, high charge transfer resistance (R_{CT}) was measured (diameter of the demi-sphere) in the presence of inhibitors, which described significant corrosion activity of carbon steel (**Fig. II.20(b)**). Moreover, in the absence of scaling inhibitor, the $CaCO_3$ took typical cubic shape calcite crystallography (**Fig. II.20(c) [84]**). In the presence of inhibitors, deformed and irregular $CaCO_3$ morphologies have been documented (**Figs. II.20(d)-II.20(g) [83, 84]**). It has been proposed that the inhibitors inhibited the growth of calcareous scaling by adsorbing or co-precipitating with the calcareous layer **[56, 83, 84]**.

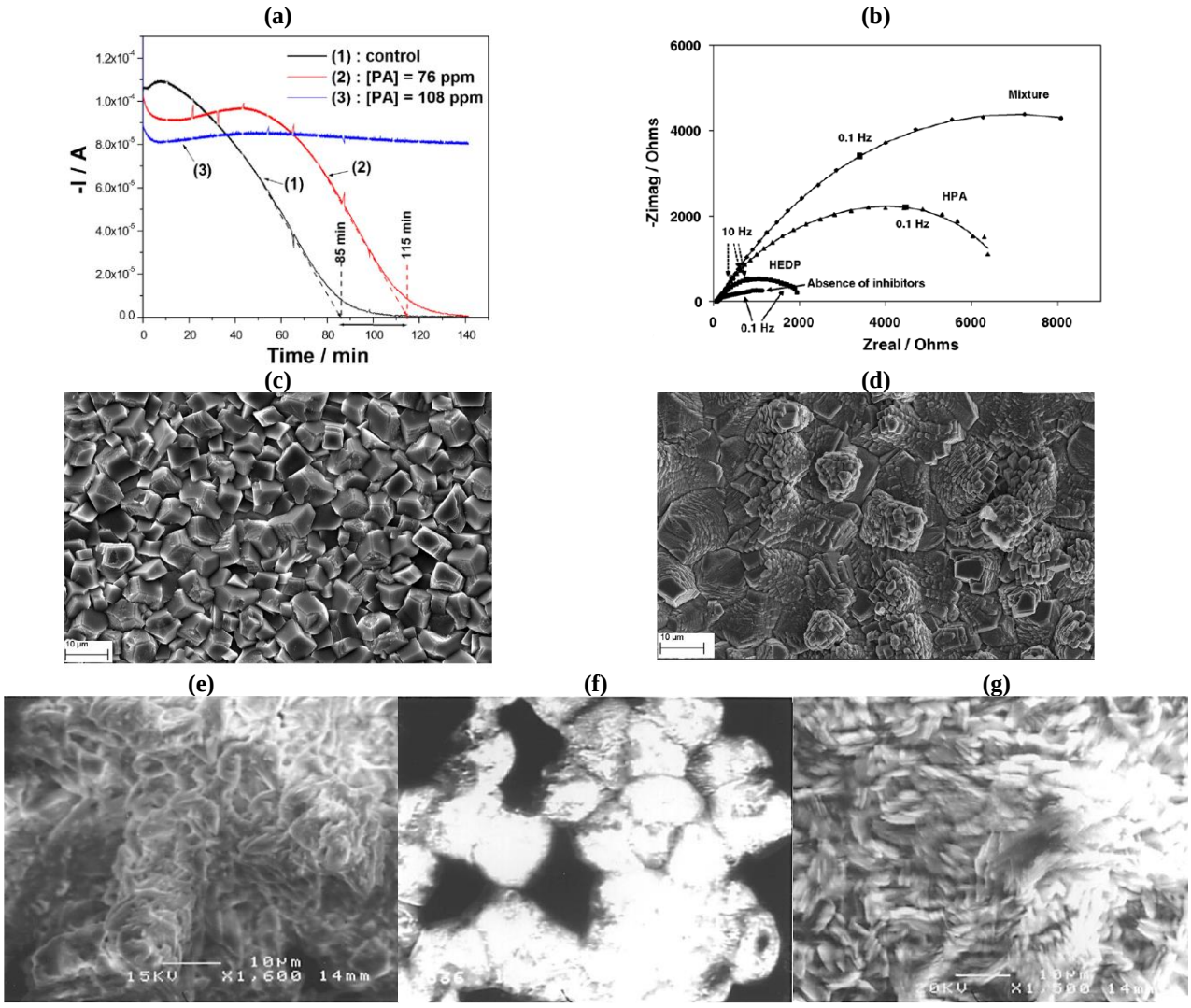

Fig. II.20. **(a)** Chronoamperometric curves in the absence and presence of green inhibitor *Paronychia Argentea* **[84]**, **(b)** EIS spectra during carbon steel corrosion in the presence of corrosion inhibitor (hydroxyphosphonoacetic acid), scale inhibitor (hydroxyethane diphosphonic acid) or both **[56]**. SEM of calcareous deposit in the absence of inhibitor **(c)** and in the presence of **(d)** PA inhibitor **[84]**, **(e)** phosphonobutane tricarboxylic acid, **(f)** 1,1 ethane diphosphonic acid and **(g)** 1,2 ethane diphosphonic acid **[83]**.

II.2.2.4. Temperature and pH

The influence of water temperature has also been scrutinized, because it could have an impact on the solubility of calcareous scaling, dissolved O_2 solubility and diffusivity **[60, 86, 90]**. **Figure II.21** illustrates the chronoamperograms during the formation of scaling at different solution temperatures and applied potentials. As the temperature increased, the solubility of $CaCO_3$ crystals decreased and the diffusivity of O_2 towards cathode increased **[60, 86]**. These two phenomenons explained the faster kinetics of deposition noticed in **Figs. II.21(a)** and **II.21(b)**. Nonetheless, when a more cathodic potential was applied (-1.2 V/SCE), where H_2 evolution was significant, the influence of temperature was negligible (**Fig. II.21(c)**) **[86]**.

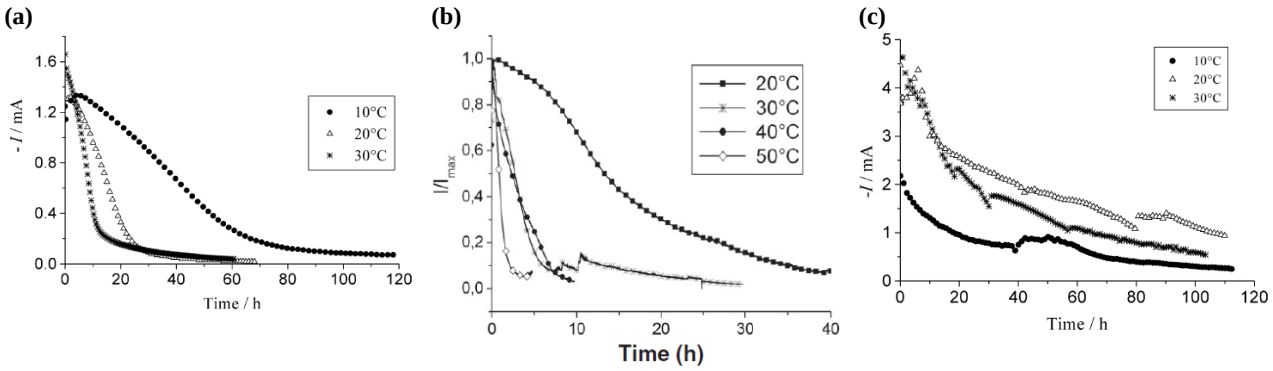

Fig. II.21. Chronoamperograms during the formation of calcareous deposit at different solution temperatures. The experiments were performed at (a) -1.0 **[86]**, (b) -1.1 **[60]** and (c) -1.2 V/SCE **[86]**.

Bulk pH has primordial impact on the thermodynamic equilibrium of ionic species in the solution. EAOPs have different optimal operating pH notably those involving EF mechanism. According to **Fig. II.22(a)**, the cathodic precipitation of Mg and phosphorus were less dependent on initial bulk pH, on the contrary to Ca precipitation **[110]**. It was ascribed to inorganic carbon speciation as function of pH, while alkaline pH promoted more Ca^{2+} precipitation given the fact carbonate being the predominant form. It is also interesting to note that final effluent pH after electrochemical treatment is dependent on the initial pH of the effluent as schematized in **Fig. II.22(b) [110]**. Within the framework of EAOP treatment of reclaimed wastewater, the effluent pH is buffered by the presence of ionic species. Thus, the pH is often neutral.

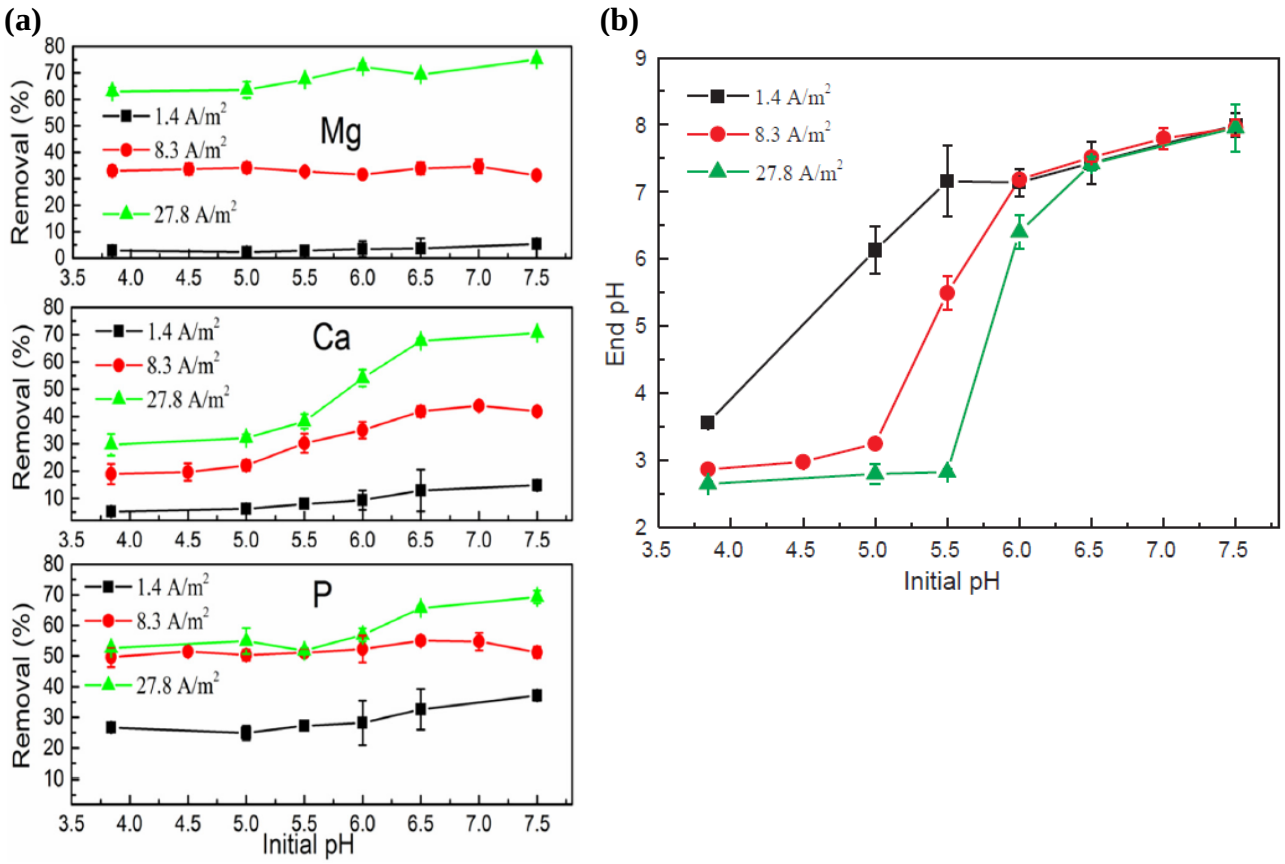

Fig. II.22. **(a)** Precipitation of Mg, Ca and phosphorus as function of varying initial bulk pH and j_{app} as well as **(b)** dependency of final pH after electrolysis on initial bulk pH. Adapted from Lei et al. **[110]**.

II.2.3. Electrode materials

Studies using different electrode materials as substrate for mineral scaling have been reported in literature and some of them have been listed in **Table II.4**. The electrode materials have diverse electrochemical responses under current/potential polarization. For example, as indicated in **Figs. II.23(a)-II.23(b)**, the voltammograms between electrode materials were distinct **[59, 77]**. From **Fig. II.23(a)**, faster O_2 reduction into OH^- took place in respective order of copper, soft steel and stainless steel and the overpotential for HER were almost identical across all three **[77]**. In **Fig. II.23(b)**, O_2 reduction was firstly observed on gold but the potential window before H_2 evolution was larger on gold than on steel **[59]**. As a result, it was observed in **Fig. II.23(c)** that the scaling on gold was not yet perturbed by HER gas at similar applied potential compared with the steel **[59]**. Hence faster, more scaling and less residual current were noticed on gold.

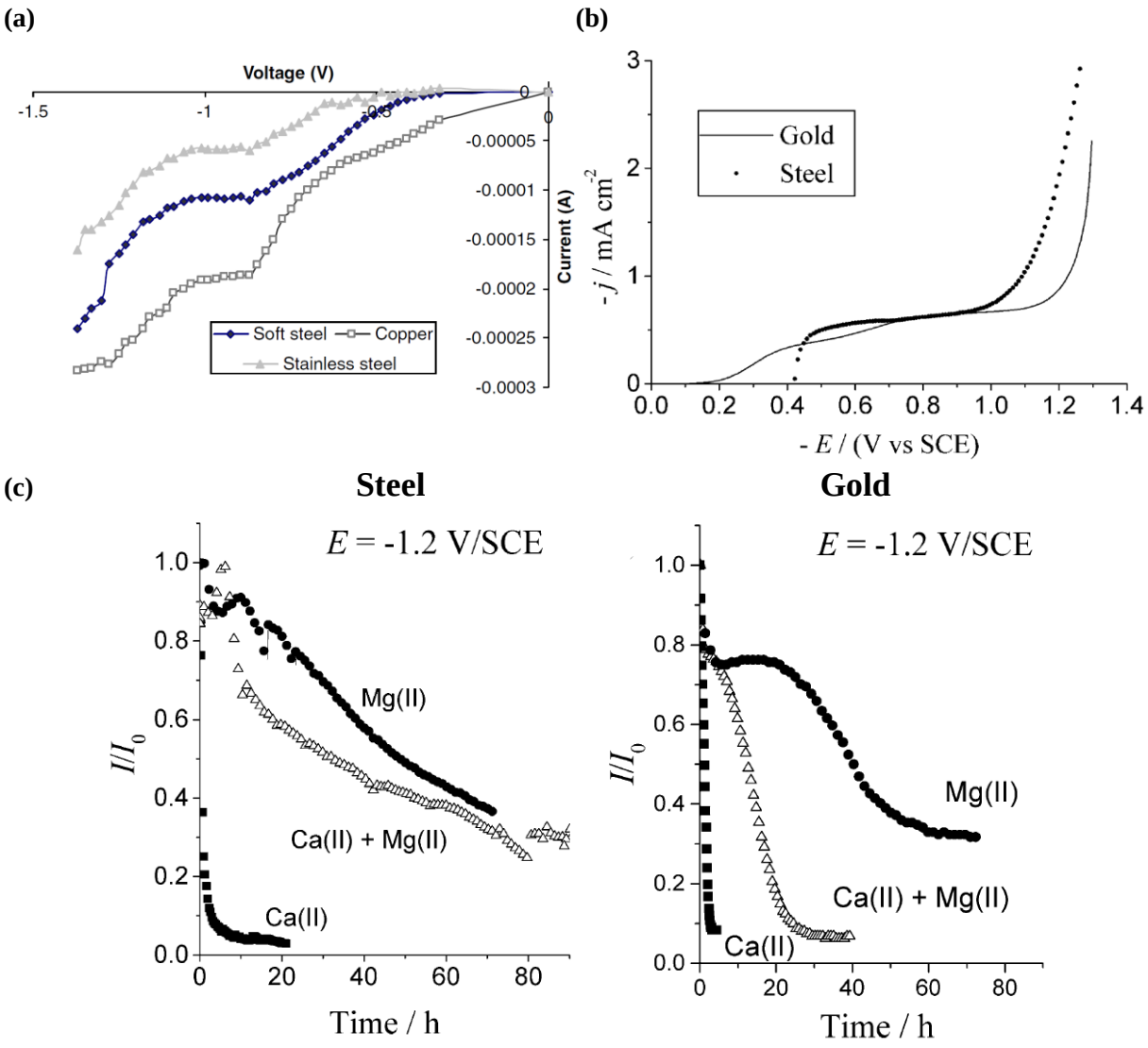

Fig. II.23. **(a, b)** Voltammograms of different electrode materials polarized in cathodic region of synthetic solution containing precipitating elements **[59, 77]** and **(c)** chronoamperometric curves of precipitating Ca^{2+} and/or Mg^{2+} at different applied potentials **[59]**. Adapted from Euvrard et al. **[77]** and Barchiche et al. **[59]**.

Elsewhere, carbonaceous graphite felt was compared to non-porous Pt-Ti electrode during the electro-precipitation process to remove and recover phosphorus (**Fig. II.24**) **[111]**. Better phosphorus deposition was noted on graphite felt in comparison to the Pt-Ti and it occurred with more acidic bulk pH. The authors have attributed the phenomenon towards higher accumulation of OH^- in porous cathode resulting in higher precipitation.

Thus, porous cathode has indeed a crucial role on the electro-precipitation but yet little report has been made on this parameter. For that reason, it will be a parameter to investigate in the study of mineral scaling in submillimetric EAOP condition, as particularly done during the PhD thesis.

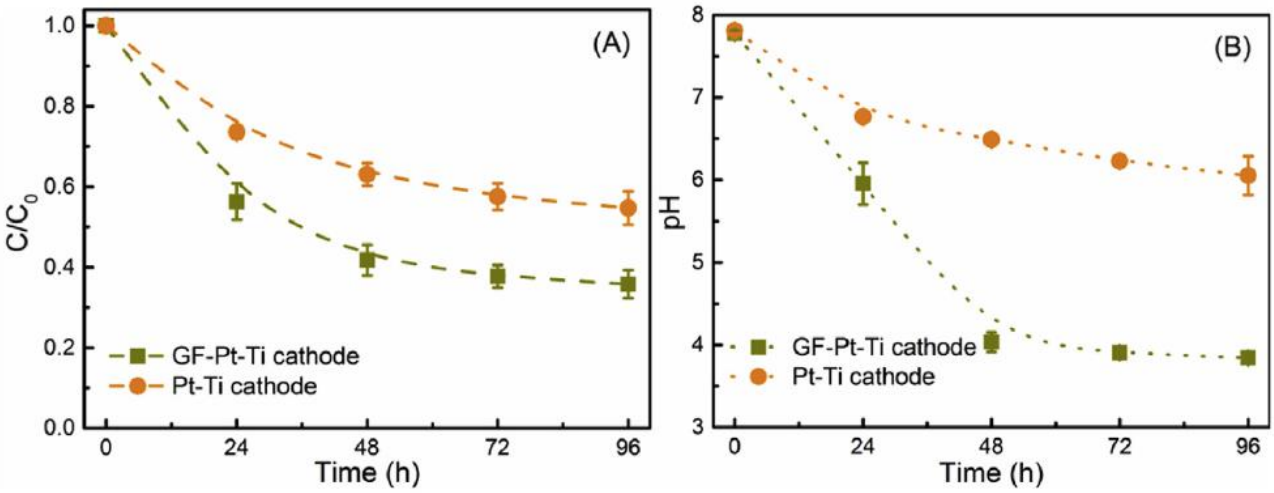

Fig. II.24. **(a)** Phosphorus concentration and **(b)** bulk pH evolution during electrochemical recovery using different cathode materials. Reproduced from Lei at. **[111]**.

Table II.5. Struvite and phosphorus recovery as well as simultaneous pollutant removal using electrochemical recovery process.

Electro-precipitate	Electrochemical system	Effluent / electrolyte	j_{app} or E	Parameters	Ref
Struvite ($MgNH_4PO_4$)	WE: Nickel rod (1 cm^2) CE: unidentified RE: Saturated Hg-$HgSO_4$ (SSE)	Representative of ionic properties of manure wastewater after sludge treatment NH_4^+: 69.5 mg L^{-1}, $H_2PO_4^-/HPO_4^{2-}$: 377.3 mg L^{-1}, Mg^{2+}: 93.6 mg L^{-1}	-0.6 to -2 V/SSE	• Bulk pH	**[103]**
Struvite ($MgNH_4PO_4$)	Anode: Pt sheet (24 cm^2) Cathode: Nickel sheet (24 cm^2) or Pt sheet, Ru-Ir-alloy net (24 cm^2) and low porosity graphite rod (∅ 0.5 cm × 12 cm), d_{elec}: 2 cm	Representative of ionic properties of waste stream from anaerobic digesters PO_4^{3-}: 483 mg L^{-1}, NH_4^+: 90 mg L^{-1}, Mg^{2+}: 121 mg L^{-1}, pH: 7 – 7.5	3 to 12 V	-	**[104]**
Struvite ($MgNH_4PO_4$)	WE: Stainless steel cylinder (5.39 cm^2) CE: Pt grid RE: Ag-AgCl	Representative of ionic properties of animal manure PO_4^{3-}: 760 mg L^{-1}, NH_4^+: 141 mg L^{-1}, Mg^{2+}: 260 mg L^{-1}, Ca^{2+}: 0 – 210 mg L^{-1}, pH: 7.6, volume: 250 mL	-0.6 to -1.1 V/Ag-AgCl	• Applied potential • Rotational speed • Ca^{2+} concentration • Electrolyte temperature	**[105]**
Phosphorus	Anode: BDD (37.5 cm^2) Cathode: Two Ti mesh (anode inserted in between) d_{elec}: 1 cm	Synthetic solution, Acephate (organaphosphorus pesticide) giving out the total phosphorus content of: 10 mg L^{-1} Na_2SO_4: 14 g L^{-1} (supporting electrolyte), volume: 250 mL, pH: 4 – 9, Ca^{2+}: 0 – 65 mg L^{-1}, Mg^{2+}: 0 or 25 mg L^{-1}, HCO_3^-/CO_3^{2-}: 0 or 150 mg L^{-1}	5 to 30 mA cm^{-2}	• Applied current density • Ca^{2+} concentration • Mg^{2+} and co-precipitation of brucite • HCO_3^- and co-precipitation of calcite • Cl^- ($^{\bullet}OH$ scavenger)	**[107]**
Phosphorus	Divided cell, Anodic compartment: Pt (22 cm^2), 200 mL Cathodic compartment: Steel (22 cm^2), 200 mL	Nanofiltration concentrate from a dead-end filtration. This NF module treated the permeate of a pilot scale aerobic membrane bioreactor which was fed with domestic wastewater from local WWTP Ca^{2+}: 83 mg L^{-1}, Mg^{2+}: 22 mg L^{-1}, HCO_3^-/CO_3^{2-}: 58 mg L^{-1}, PO_4^{3-}: 23 mg L^{-1}, Na^+: 130 mg L^{-1}, K^+: 22 mg L^{-1}, pH: 7.8	0.46 mA cm^{-2} (10 mA) 2.27 mA cm^{-2} (50 mA)	• Bulk pH • Applied current density	**[106]**

Electro-precipitate	Electrochemical system	Effluent / electrolyte	j_{app} or E	Parameters	Ref
Phosphorus	Anode: MMO of Bi_2O_3-TiO_2-$Ir_XTa_YO_2$/Ti Cathode: Stainless steel **Pilot scale**: Volume: 22 L, recirculation flow rate: 10 L min^{-1}, configuration: 7 anodes and 8 cathodes, separated by 3 mm distance. Surface area: 1.8 m^2 giving reactor surface to volume ratio of 80 m^2 m^{-3} **Bench scale configuration**: Electrode spacing: 3 mm, reactor surface to volume ratio: 35 m^2 m^{-3}	Public toilet wastewater: Ca^{2+}: 40 mg L^{-1}, Mg^{2+}: 19.4 mg L^{-1} COD: 320-380 mg-O_2 L^{-1}, HCO_3^-/CO_3^{2-}: 1.04 g L^{-1}, Cl^-: 851 mg L^{-1}, PO_4^{3-}: 57 mg L^{-1}, NH_4^+: 235 mg L^{-1}, SO_4^{2-}: 288 mg L^{-1}, Na^+: 621 mg L^{-1}, K^+: 238 mg L^{-1}, pH: 8.3 Synthetic wastewater replicating the ionic and pH properties of public toilet waste water (for both pilot and bench scale): Ca^{2+}: 6 – 58 mg L^{-1}, Mg^{2+}: 0 – 26 mg L^{-1}, PO_4^{3-}: 43 – 123 mg L^{-1}, HCO_3^-/CO_3^{2-}: 0.98 – 3.66 g L^{-1}	**Pilot scale**: Potentio static: 3.3 and 3.5 V **Bench scale**: Potentio static: 3.5 V Galvano static: 3 - 52 mA cm^{-2}	• Real vs. simulated wastewater • Ca^{2+} concentration • Mg^{2+} concentration • PO_4^{3-} concentration • HCO_3^-/CO_3^{2-} concentration • Applied current density	[101]
Phosphorus	Two cell compartments, 500 mL for electro-precipitation and another 500 mL for sampling mixing. Anode: Pt-coated Ti mesh Cathode: Ti plate (53 cm^2)	Synthetic solution, P: 18.6 mg L^{-1}, Ca^{2+}: 40.1 mg L^{-1}, Na_2SO_4: 7.1 g L^{-1}, volume: 1000 mL (total of both cell compartments) recirculation flow rate: 100 mL min^{-1}, pH: 4 - 10	0.4 mA cm^{-2} (20 mA)	• Bulk pH • Comparison with chemical precipitation method	[112]
Phosphorus	Two cell compartments, 500 mL for electro-precipitation and another 500 mL for sampling mixing. Anode: Pt-coated Ti mesh Cathode: Ti plate (53 cm^2) d_{elec}: 2.7 cm	Synthetic solution representative of domestic wastewater, P: 6.2 – 46.5 mg L^{-1}, Ca^{2+}: 20 to 100.2 mg L^{-1}, Na_2SO_4: 7.1 g L^{-1}, pH: 8.2 HCO_3^-/CO_3^{2-}: 61 – 610 mg L^{-1} Humic acid: 0 – 10 mg L^{-1} Volume: 1000 mL	Open circuit and 0.19 to 1.89 mA cm^{-2} (10 to 100 mA)	• Applied current density • Ca/P ratio for phosphorus recovery • HCO_3^-/CO_3^{2-} concentration • Presence of humic acid	[108]

Electro-precipitate	Electrochemical system	Effluent / electrolyte	j_{app} or E	Parameters	Ref
Phosphorus	Undivided cell, Anode: Ru-Ir coated Ti disk Cathode: Ti disk Surface area: 50 cm^2	Synthetic solution, Ca^{2+}: 40 mg L^{-1}, P: 7.4 mg L^{-1}, Na_2SO_4: 7.1 g L^{-1}, volume: 800 mL, pH: 4–10, flow rate: 70 mL min^{-1}, Natural organic matter: 1 – 10 mg L^{-1} NOM_1: natural anionic polyelectrolyte, NOM_2: mixture of hydrophilic non-humic with hydrophobic humic matter NOM_3: representative of fuvic acid	0.4 mA cm^{-2} (20 mA)	• Type and concentration of natural organic matter (NOM) • Bulk pH	[109]
Phosphorus, $CaCO_3$, $Mg(OH)_2$	Undivided cell, Anode: Pt-coated Ti disk (50 cm^2), Cathode: Square Ti (4, 16 and 36 cm^2), d_{elec}: 3 cm	Real wastewater influent of domestic WWTP (Leeuwarden, the Netherlands), Ca^{2+}: 75 mg L^{-1}, Mg^{2+}: 27 mg L^{-1}, organic carbon: 40 mg L^{-1}, inorganic carbon: 137 mg L^{-1}, Cl^-: 338 mg L^{-1}, PO_4^{3-}: 7.7 mg L^{-1}, NH_4^+: 66 mg L^{-1}, SO_4^{2-}: 30 mg L^{-1}, Na^+: 299 mg L^{-1}, K^+: 24 mg L^{-1}, NO_3^- and NO_2^-: each < 0.1 mg L^{-1}, pH: 8.3	5, 30 and 100 mA	• Applied current • Cathodic surface area / applied current density	[92]
Phosphorus, $CaCO_3$, $Mg(OH)_2$	Undivided cell, Anode: Pt-coated Ti disk (50 cm^2), Cathode: Square Ti (36 cm^2), d_{elec}: 3 cm	Real wastewater influent of domestic WWTP (Leeuwarden, the Netherlands), Ca^{2+}: 81 mg L^{-1}, Mg^{2+}: 19 mg L^{-1}, inorganic carbon: 138 mg L^{-1}, Cl^-: 223 mg L^{-1}, PO_4^{3-}: 7.5 mg L^{-1}, NH_4^+: 59 mg L^{-1}, SO_4^{2-}: 26 mg L^{-1}, Na^+: 253 mg L^{-1}, K^+: 21 mg L^{-1}, pH: 7.5, volume: 1000 mL, flow rate: 60 mL min^{-1}, pH: 3.8 – 7.5 (HNO_3)	5, 30 and 100 mA (0.14, 0.83 and 2.78 mA cm^{-2})	• Bulk pH • Applied current density	[110]

Electro-precipitate	Electrochemical system	Effluent / electrolyte	j_{app} or E	Parameters	Ref
Phosphorus, $CaCO_3$, $Mg(OH)_2$	Undivided cell batch and continuous cell, Anode: Pt-coated Ti disk (50 cm^2), Cathode: Square Ti or stainless steel (36 cm^2) d_{elec}: 0.5, 3 and 6 cm	Real wastewater influent of domestic WWTP (Leeuwarden, the Netherlands), Ca^{2+}: 75 mg L^{-1}, Mg^{2+}: 27 mg L^{-1}, organic carbon: 40 mg L^{-1}, inorganic carbon: 137 mg L^{-1}, Cl^-: 338 mg L^{-1}, PO_4^{3-}: 7.7 mg L^{-1}, NH_4^+: 66 mg L^{-1}, SO_4^{2-}: 30 mg L^{-1}, Na^+: 299 mg L^{-1}, K^+: 24 mg L^{-1}, NO_3^- and NO_2^-: each < 0.1 mg L^{-1}, pH: 8.3 Volume: 1000 mL and 1.2 mL min^{-1} (both batch and continuous mode), electrolysis of 1 to 4 days	5, 30 and 100 mA (0.14, 0.83 and 2.78 mA cm^{-2})	• Applied current • Electrolysis time, including long-term experiments • Interelectrode distance	[113]
Phosphorus	Microbial electrolysis cell, WE: Bio-anode, i.e., inoculated electroactive bacteria on graphite felt connected to Pt-coated Ti disk (50 cm^2) CE: Ti plate (36 cm^2), RE: Ag-AgCl d_{elec}: 1 cm NaAc substrate replacement every 24 h	Inoculation synthetic wastewater: $NaCH_3COO$ (NaAc): 0.82 g L^{-1}, KCl: 0.74 g L^{-1}, NaCl: 0.58 g L^{-1}, KH_2PO_4: 3.4 g L^{-1}, K_2HPO_4: 4.35 g L^{-1}, NH_4Cl: 0.28 g L^{-1}, $MgSO_4$: 0.1 g L^{-1}, $CaCl_2$: 0.1 g/L Biomass collected from active microbial recharge battery cell. Real wastewater influent of domestic WWTP (Leeuwarden, the Netherlands), Ca^{2+}: 81 mg L^{-1}, Mg^{2+}: 20 mg L^{-1}, COD: 236 mg L^{-1}, inorganic carbon: 121 mg L^{-1}, organic carbon: 72 mg L^{-1}, Cl^-: 213 mg L^{-1}, PO_4^{3-}: 7 mg L^{-1}, NH_4^+: 52 mg L^{-1}, SO_4^{2-}: 27 mg L^{-1}, Na^+: 249 mg L^{-1}, K^+: 21 mg L^{-1}, pH: 7.5, volume: 900 mL	-0.35 V/Ag-AgCl (potential slightly higher than the oxidation potential of NaAc substrate)	• NaAC substrate concentration • Operation duration • Initial phosphate concentration	[114]

Electro-precipitate	Electrochemical system	Effluent / electrolyte	j_{app} or E	Parameters	Ref
Phosphorus	Column electrochemical reactor containing $CaCO_3$ particles, Anode: Pt-coated Ti rod (14 cm^2), Cathode: Ti rod (14 cm^2), d_{elec}: 1 cm Continuous flow mode $CaCO_3$ particle size: < 0.5, 0.5-1, 1-2 and 2-3 mm	Synthetic solution, P: 18.6 mg L^{-1} and 1 mg L^{-1} (for low P system) Na_2SO_4: 1.42 g L^{-1} Real wastewater influent of domestic WWTP (Leeuwarden, the Netherlands) Flow rate: 0.4 – 2.4 L day^{-1}	5, 10 and 20 mA (0.36, 0.71 and 1.43 mA cm^{-2})	• Applied current density • $CaCO_3$ particle sizes • Batch vs. continuous mode • Initial P content • Synthetic vs real wastewater • Long term test	[115]
Phosphorus	Undivided cell, Anode: Pt-coated Ti disk (50 cm^2) Cathode: Graphite felt (50 cm^2) attached to Pt-Ti disk d_{elec}: 3 cm	Synthetic solution, P: 18.6 mg L^{-1}, Ca^{2+}: 20 – 80.2 mg L^{-1}, Na_2SO_4: 1.42 – 7.1 g L^{-1} Real wastewater influent of domestic WWTP (Leeuwarden, the Netherlands) Volume: 900 mL, flow rate: 120 mL min^{-1}	0.2 mA (low) 1 mA (highest)	• Applied current • Initial Ca^{2+} concentration • Synthetic vs. real wastewater	[111]
Phosphorus	Undivided cell, Anode: Pt-coated nickel, Ru-Ir MMO or Pt-Ir MMO (50 cm^2) Cathode: Ti square plate (36 cm^2) d_{elec}: 3 cm	Synthetic solution, Ca^{2+}: 40 mg L^{-1}, Na_2SO_4: 7.1 g L^{-1} (50 mM) or NaCl: 50 mM or $NaClO_4$: 50 mM, Nitrilotris (methylene phosphonic acid) (NTMP) (non-orthophosphates source): 30 mg L^{-1} (0.3 mM P), Volume: 1000 mL Real wastewater influent of domestic WWTP (Leeuwarden, the Netherlands) spiked with 30 mg L^{-1} NTMP	2.8 mA cm^{-2} (100 mA)	• Anode material • Electrolyte composition • Synthetic vs. real wastewater	[116]

Electro-precipitate	Electrochemical system	Effluent / electrolyte	j_{app} or E	Parameters	Ref
Phosphorus	Undivided cell, Anode: Pt-coated Ti (50 cm^2), Cathode: Pt-coated Ti (50 cm^2), d_{elec}: 3 cm	Raw cheese wastewater from industrial WWTP (Groningen, the Netherlands) Ca^{2+}: 2.2 g L^{-1}, Mg^{2+}: 138 mg L^{-1}, COD: 19.8 g L^{-1}, soluble P: 827 mg L^{-1}, total carbon: 7.72 g L^{-1}, organic carbon: 7.71 g L^{-1}, Cl^-: 107 mg L^{-1}, PO_4^{3-}: 2.4 g L^{-1}, NH_4^+: 77 mg L^{-1}, total N: 496 mg L^{-1}, SO_4^{2-}: 257 mg L^{-1}, Na^+: 87 g L^{-1}, K^+: 21 mg L^{-1}, pH: 4.4, conductivity: 209 mS cm^{-1}, volume: 900 mL, flow rate: 150 mL min^{-1}	1 to 6 mA cm-2 (50 to 300 mA)	• Chemical (NaOH dosage) vs. electrochemical precipitation tests • Bulk pH • Applied current density	[96]
Phosphorus	Scale-up study **Prototype 1** Volume: 4 L, Anode: Ru-Ir MMO placed in the center of reactor Cathode: Tubular stainless steel positioned adjacent to the inner wall of reactor **Prototype 2** Volume: 2.8 L, Anode: Pt-coated Ti, Cathode: Tubular stainless steel with 35% less surface area (economical reason). Closed system, H_2 (cathode) and Cl_2 (anode) were sent to gas collector (1 M NaOH) Flow rate: 0.93 L day^{-1} (0.65 mL min^{-1}) in long run test	Raw cheese wastewater from industrial WWTP (Groningen, the Netherlands) **Prototype 1** Parametric investigation: Retention time: 1, 1.5 and 3 days P concentration: 1×, 2× and 10× dilution factor **Prototype 2** Long term experiment Applied current: 600 mA, retention time: 3-day, flow rate: 0.93 L day^{-1} (0.65 mL min^{-1})	200 – 800 mA	• Applied current • Residence time, including long-term experiments • Phosphate concentration	[102]

Abbreviations: BDD: boron-doped diamond, MMO: mixed metal oxide, Pt: platinum, Ti: titanium, Ir: iridium, Ru: ruthenium, COD: chemical oxygen demand, P: phosphorus, d_{elec}: interelectrode distance and j_{app}: applied current density.

II.2.4. Electrochemical reactor design, scale up and maintenance

The electro-precipitation for nutrient recovery has been receiving increasing attention in recent years, owing to its promising possibility to recover valuable products. Therefore, several reactors have been designed at large scale to increase the treatment capacity as depicted in **Figs. II.25(a)-II.25(c)**. Takabe et al. used a batch electrochemical reactor to precipitate phosphorus using 4-pairs of electrodes working in series to treat up to 5 L of effluent (**Fig. II.25(a)**) **[117]**. Lei et al. started the parametric studies in a reactor up to 1 L capacity using Pt-coated Ti electrodes having 50 cm^2 surface area **[92, 109, 113]** (**Fig. II.25(b)**). They recently came up with a pilot scale reactor unit with tubular stainless steel cathode with a capacity to treat up to 4 L in continuous mode (**Fig. II.25(c)**) **[102]**. Here, after long operation hours, the cathode was totally/almost passivated by the precipitates. As a countermeasure, Takabe et al. operated their reactors with polarity reversal to improve the process durability.

In regard to mineral scaling, most of the studies listed in **Table II.4** involve the use of a classical rotating disk electrode with varying exposed surface area up to 2 cm^2. The use of such electrodes is only adequate to conduct mechanistic studies on the kinetics of precipitation. However, the fundamental of scaling deposition remains valid, while operating the electrolysis to treat wastewater at an industrial scale, for example in water softening technology. Due to the precipitation on the cathode, Mg- and Ca-based precipitates were formed and the water was softened. Water softening technique has been widely adopted to treat a large spectrum of effluent according to the list provided in **Table II.6**. The electro-precipitation concept for water softening has received huge success and it has been employed from laboratory up to big scale industrial projects. For example, it has been applied in a case study where a commercial filter-press reactor (**Fig. II.25(d)**) **[118]** and a multistage electrochemical precipitation reactor (**Fig. II.25(e)**) **[119]** have been employed to induce mineral scaling for water softening purpose. Elsewhere, at relatively larger scale, water hardness, COD and total nitrogen (TN) of the secondary effluent of a nonradioactive WWTP of nuclear power plant (South Korea) were treated using integrated electrodialysis reversal coupled to EO process **[120]**. Another one involved water hardness and trihalomethanes treatment of brackish Llobregat River (Barcelona, Spain) by electrodialysis with polarity reversal technology **[121]**.

These successful industrial scale water treatment and water softening have only been made possible owing to the implementation of periodically self-cleaning electrodes and/or membranes so that the total passivation of electrodes did not occur. For that reason, the most realistic, cost effective and on-the-field proven technique is the periodic reversal. However, this technique might not suit most of EAOPs. Efficient descaling using this technique could only be obtained by applying high applied

current (**Table II.6**), which means an increase of the overall operation cost. Furthermore, only stable electrodes should be used (refer **Table II.6**) such as DSA (IrO_2-RuO_2/Ti), MMO (IrO_2-RuO_2-SnO_2/Ti), Pt-coated Ti or BDD that could resist high current polarization at both cathode and anode configurations. Certain electrode materials are corroded upon anodic polarization at high current, releasing ions into the solution (e.g., most steels and less noble metals). Carbonaceous materials are even burnt when they are used as anode under medium and high current densities. Therefore, one of the objectives of this thesis work is to check whether an alternative for polarity reversal technique would be possible.

Upon deep literature survey on the topic of cathodic electro-precipitation, there has not yet been a study that reports on the precipitation occurring inside submillimetric electrochemical reactors. It is indeed a step backward with respect to the scale up attempt aforementioned. Given the interesting advantages that could offer microfluidic reactors and the fact that they are susceptible for scale up (**Section II.1.2**), the scaling phenomenon inside submillimetric configuration represents a research gap. Only a couple of studies have attempted to investigate the role of d_{elec} towards the kinetics of electro-precipitation. Lei et al. observed a decrease in precipitation of phosphorus going from 30 mm to 5 mm and they attributed it to the compensation of anodic H^+ on cathodic OH^- thus lowering the precipitating capacity **[113]**. Takabe et al. went slightly below to 1 mm from 10 mm and 5 mm as they also noticed less electro-precipitation on cathode at the lowest investigated d_{elec} **[117]**. However, they observed that the phosphorus precipitation followed a different trend with 1 mm d_{elec}, whereby more precipitation on the bulk was noticed as a result of higher bulk pH. Therefore, an interesting observation has been made at lower d_{elec}.

Since no approach has yet been attempted on the occurrence of electro-precipitation in microfluidic cells, this PhD thesis intends to serve as a reference for the sequencing works in the future. The involvement of anodic activity would be supposedly more marked and it might play significant role towards the mechanism of electro-precipitation on cathode as well as pollutant degradation via BDD($^{\bullet}OH$) or mediated oxidants in the bulk in-between electrodes. Moreover, the kinetic model to estimate and predict mineral scaling is lacking in the current literature. Hence, it will be another quest invoked in this thesis.

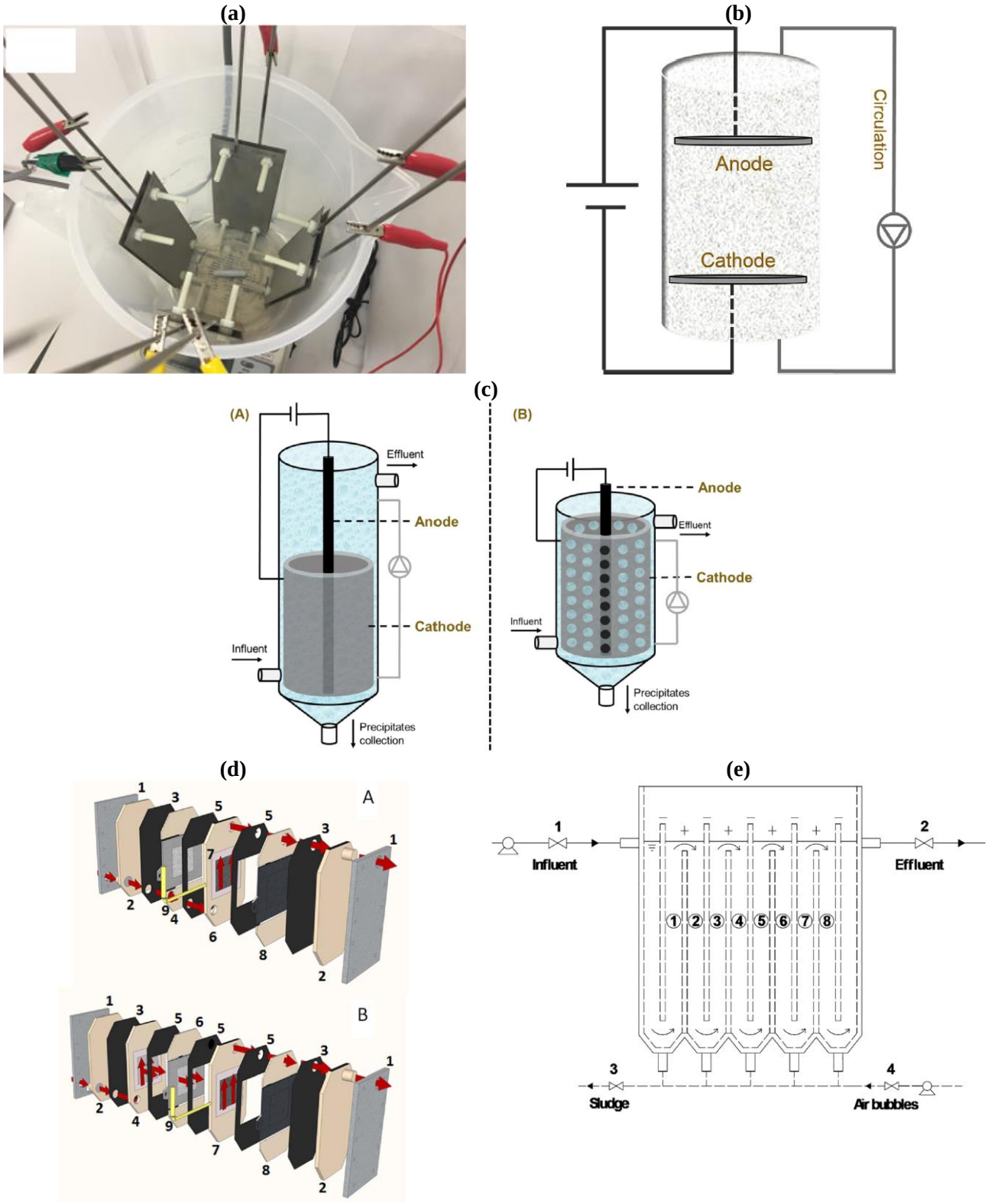

Fig. II.25. **(a)** 4-pair of electrodes working in series by Takabe et al. **[117]**, **(b)** horizontal parallel-plate reactor **[116]** and **(c)** scaled up electrochemical reactor with large tubular cathode for phosphorus electro-precipitation recovery **[102]** adapted from Lei et al., **(d)** commercial filter-press type reactor by Sanjuán et al. **[118]** and **(e)** multistage electro-precipitation reactor for water softening technology by Yu et al. **[119]**.

Table II.6. Electro-precipitation for water softening technology and successive implementation of polarity reversal to minimize total passivation.

Process	Electrochemical system	Effluent / electrolyte	j_{app} or E	Parameters	Ref
Water softening Polarity reversal	Electro-deionization with periodic polarity change (EDIR) 6 pairs of EDIR stacks consisting of cationic and anionic exchange membranes in 3 stages Anode = Cathode = Ti-coated Pt Surface area: 100 cm^2	Synthetic solution, Total hardness: 250 – 1250 mg-$CaCO_3$ L^{-1} Flow concentrate: 25 – 500 mL min^{-1} Flow diluate: 20 mL min^{-1} (constant) Polarity reversal: 10 – 60 min	20 V	• Flow rate • Polarity reversal period • Water hardness • Comparison on long term operation using homogenous and heterogeneous membrane	[122]
Removal of COD and TN Polarity reversal	Integrated electrodialysis reversal (EDR) with electro-oxidation (EO) processes **Electrodialysis reversal** 2-stack in series each containing 250 cell pairs. Each pair consisted of diluting compartment, cation membrane, concentrating compartment and anion membrane Membrane area: 1440 cm^2 **Electro-oxidation** Bipolar electrolyzer, parallel flow, 23 electrodes of RuO_2-SnO_2-IrO_2/Ti MMO, d_{elec}: 1.4 cm, effective surface area: 1800 cm^2	Effluent of secondary nonradioactive WWTP of nuclear power plant (South Korea) Turbidity: 0.57 NTU, pH: 7.78, conductivity: 2.5 mS cm^{-1}, suspended solid: 35 mg L^{-1}, COD: 33 mg L^{-1}, TN: 36 mg L^{-1}, Ca^{2+}: 41 mg L^{-1}, Mg^{2+}: 66 mg L^{-1}, Fe^{2+}: 1.6 mg L^{-1}, Al^{3+}: 2.2 mg L^{-1}, Mn^{2+}: 0.06 mg L^{-1}, Na^+: 566 mg L^{-1}, K^+: 18 mg L^{-1}, NH_4^+: 8.2 mg L^{-1}, Cl^-: 557 mg L^{-1}, SO_4^{2-}: 695 mg L^{-1}, NO_3^-: 0.05 mg L^{-1}, SiO_2: 2.7 mg L^{-1}, total dissolved solid: 1.25 g L^{-1}	**EDR** Product 13 L min^{-1} Concentrate 2.8 L min^{-1} **Stage I** 60 V – 77 A **Stage II** 60 V – 3.7 A **EO** 6 L min^{-1} 126 A (70 mA cm^{-2})	• Industrial application	[120]

Process	Electrochemical system	Effluent / electrolyte	j_{app} or E	Parameters	Ref
Tri-halomethane (THM) removal and desalination Polarity reversal	Electrodialysis with electrode polarity reversal (EDR) to automatically clean membrane surface as the tertiary treatment. Cartridge filter of 10 µm before going into the EDR unit. Electrode material: unspecified **Pilot plant** 2-stage stacks with 200 cell pairs each stack, maximum DWTP flow of 3 m^3 s^{-1} **Up-scale unit** Industrial pilot scale with 2 stacks of 600 cell each, maximum DWTP flow of 4 m^3 s^{-1}	Brackish river water (Llobregat, Barcelona) after conventional treatment (pre-oxidation using potassium permanganate, coagulation, flocculation, oxidation with ClO_2, sand filtration, granulated active carbon filtration and final chlorination using chlorine gas) at drinking water treatment plant (DWTP)	unspecified	• Industrial application	[121]
Scaling detachment using pulsed applied current	Flow plant with undivided cell, Anode: DSA sheet, cathode: mirror stainless steel Surface area: 147 cm^2 d_{elec}: 5 mm	Simulated properties of industrial recirculated cooling water, $CaCl_2$: 333 mg L^{-1}, $NaHCO_3$: 504 mg L^{-1}, $MgCl_2$: 101.5 mg L^{-1}, anti-scalant: 2 mg L^{-1}, pH: 8.5, conductivity: 1400 µs cm^{-1}, V: 100 mL, Flow rate: 0.08 – 0.33 L min^{-1}	10 to 60 mA cm^{-2}	• Water softening performance • Applied current density • Flow rate	[123]
Water softening	Multistage electrochemical precipitation reactor, 8-stage cell, Anode: 4× DSA, Cathode: 5× stainless steel, d_{elec}: 1 cm, total effective surface area: 800 cm^2 Single stage surface area: 100 cm^2	Simulated properties of industrial recirculated cooling water Hardness: 350 mg L^{-1}, alkalinity: 300 mg L^{-1}, pH: 8.2, anti-scalant: 1 – 6 mg L^{-1} Periodic scale detachment by sending air bubbles from the bottom of the cell	2 to 12 mA cm^{-2} Single cell: 0.2 to 1.2 A Multistage: 1.6 to 9.6 A	• Applied current density • Flow rate • Anti-scalant concentration	[119]
Water softening Polarity reversal	Flow plant with undivided cell, Anode = Cathode = IrO_2-RuO_2/Ti DSA (147 cm^2) d_{elec}: 5 mm	Simulated properties of recirculating cooling water, $CaCl_2$: 333 mg L^{-1}, $NaHCO_3$: 504 mg L^{-1}, $MgCl_2$: 102 mg L^{-1}, pH: 8.5, conductivity: 1600 µS cm^{-1}, volume: 100 mL Flow rate: 0.17 – 0.5 L min^{-1}	10 to 25 mA cm^{-2}	• Polarity reversal time • Flow rate • Long cycle for stability test	[124]

Process	Electrochemical system	Effluent / electrolyte	j_{app} or E	Parameters	Ref
Water softening Polarity reversal	Flow plant with undivided cell, Anode = Cathode = DSA (200 cm^2), 4 membranes (8 mm thickness each) and 5 plastic grids were placed in between electrodes	Simulated properties of recirculating cooling water, $CaCl_2$: 555 mg L^{-1}, $NaHCO_3$: 840 mg L^{-1} Flow rate: 0.33 – 3 L min^{-1}	10 mA cm^{-2}	• Heterogeneous vs. homogenous exchange membrane • Ca^{2+} concentration • Mg^{2+} concentration • Alkalinity • Ionic conductivity • Membrane spacing • Scale detachment and operation stability tests	[125]
Phosphorus recovery Polarity reversal	Electrochemical batch reactor, Anode = Cathode = Pt-coated Ti 2 pairs of electrodes were used connected in parallel d_{elec}: 1 cm Polarity inversion period: 1 – 10 min	Real anaerobic digestion effluent pretreated with cationic organic polymer coagulant and centrifugally dehydrated Total phosphorus: 74 mg L^{-1}, dissolved phosphorus: 57 mg L^{-1}, PO_4^{3-}: 51 mg L^{-1}, Ca^{2+}: 44 mg L^{-1}, Mg^{2+}: 16 mg L^{-1}, NH_4^+: 502 mg L^{-1}, suspended solid: 816 mg L^{-1}, pH: 7.83, volume: 5 L	1 to 4 A	• Applied current • Polarity inversion duration	[126]
Phosphorus recovery Polarity reversal	Electrochemical batch reactor, Anode = Cathode = Pt-coated Ti 4 pairs of electrodes were used Effective surface area: 126 cm^2 d_{elec}: 1, 5 or 10 mm Polarity inversion period: 3 min	Real anaerobic digestion effluent pretreated with cationic organic polymer coagulant and centrifugally dehydrated Total phosphorus: 83 mg L^{-1}, dissolved phosphorus: 75 mg L^{-1}, PO_4^{3-}: 75 mg L^{-1}, Ca^{2+}: 42 mg L^{-1}, Mg^{2+}: 20 mg L^{-1}, NH_4^+: 443 mg L^{-1}, suspended solid: 196 mg L^{-1}, K^+: 48 mg L-1, Na^+: 66 mg L^{-1}, Fe^{2+}: 0.08 mg L^{-1}, pH: 7.69, 8.0 or 8.4.	4 A (32 mA cm^{-2})	• Interelectrode distance	[117]

Process	Electrochemical system	Effluent / electrolyte	j_{app} or E	Parameters	Ref
Water softening	Flow plant with undivided cell, Anode: IrO_2/Ti DSA (100 cm^2) Cathode: 2D Ti mesh or 3D stainless steel mesh Geometric cathode surface area: 100 cm^2 (taken for current density calculation) d_{elec}: 0.8 cm (flow-by) d_{elec}: 0.3 cm (flow-through) Configuration flow-by vs. flow-through was compared	Simulated brackish water from electrodialysis concentrate, Ca^{2+}: 600 mg L^{-1}, Mg^{2+}: 200 mg L^{-1}, HCO_3^-: 850 mg L^{-1}, Cl^-: 1000 mg L^{-1}, NO_3^-: 800 mg L^{-1}, SO_4^{2-}: 770 mg L^{-1}, Na^+: 400 mg L^{-1} Flow rate: 0.003 – 0.045 L min^{-1} HCO_3^-: 0 – 5500 mg L^{-1} Water hardness: 300 – 2380 mg L^{-1} $CaCO_3$ Sodium hexametaphosphate (HMP) (scale inhibitor): 0.2 mg L^{-1}	2.5 to 20 mA cm^{-2}	• Flow-through vs. flow-by mode • Flow rate • Applied current density • Bicarbonates concentration and water hardness • Presence of inhibitor • Coupling vs. cascade mode to test scale-up for productivity	[118]

Abbreviations: DSA: dimensionally stable anode, MMO: mixed metal oxide, Sn: tin, Pt: platinum, Ti: titanium, Ir: iridium, Ru: ruthenium, COD: chemical oxygen demand, TN: total nitrogen, d_{elec}: interelectrode distance and j_{app}: applied current density.

II.3. Pharmaceuticals removal by EAOPs

Once the deposits/fouling dominantly cover the electrode surfaces, without proper intervention, the efficiency of EAOP decreases. The capacity of the EAOP to mineralize pollutant as well as micropollutant decreases. In this thesis, tylosin, an antibiotic for veterinary use, was chosen as model micropollutant to check on the influence of electro-precipitation towards its removal.

The occurrence of pharmaceutical micropollutants in the effluent of WWTPs has been raising concern amongst different stakeholders. More and more pharmaceutical substances traceable in the wastewater have been categorized as emerging pollutants due to their potential hazard not only to human but also to other living organisms. Their detection in aquatic environment varies with the geographical activities: < 1 µg L^{-1} at the outlet of municipal WWTP **[127, 128]**, 6 µg L^{-1} in the waste stream of dairy industry and reaching 30 µg L^{-1} at the outlet of hospital waste **[127]**. Their continuous emission at very low concentration leads to accumulation in soil and aquatic environment. Prolonged and persistent exposure of aquatic life to the pharmaceutical substances has caused the development of antibiotic-resistant bacteria **[129]** as well as endocrine disruption, genotoxicity and wildlife poisoning **[130, 131]**. Thus, the occurrence of pharmaceutics in soils and water needs to be regarded with serious note. That is the reason why pharmaceutical micropollutants have been the case study of various degradation techniques including EAOPs.

Several pharmaceutical groups have been subjected to EAOP treatment in literature and some of them are recorded in **Table II.7**. Among them are (1) sulfonamides (sulfanilamide **[132, 133]**, sulfamethazine **[134-137]**, sulfamethoxazole **[138, 139]** and sulfachloropyridazine **[140]**), (2) tetracyclines **[141]**, (3) betalactams (amoxicillin **[142]** and penicillin G **[143]**), (4) amphenicols (chloramphenicol **[144, 145]**), (5) bacteriostatic drugs (trimethoprim **[146]**), (6) nitro-imidazoles (metronidazole **[147]**), (7) macrolides (tylosin **[148]**), (8) quinolones (ciprofloxacin **[149]**), (9) nonsteroidal anti-inflammatory drugs (NSAID) (diclofenac **[150]** and ibuprofen **[151]**), (10) analgesic drugs (paracetamol **[11, 12, 152]**), (11) betablockers (atenolol, metoprolol and propranolol **[153]**), (12) timoprazoles (omeprazole **[154]**), (13) histamines (ranitidine **[155]**) and (14) bronchodilators (salbutamol **[149]**).

These pharmaceutical micropollutants were treated by various EAOPs such as EO, EF, coupled EF-EO, photo electro-Fenton via ultraviolet-A irradiation (PEF-UVA) and solar photo electro-Fenton (SPEF). Most of the investigations were done in synthetic solutions, in which the pharmaceuticals were spiked at the intended concentration. Still, several authors have used real wastewater matrices to take into consideration the real matrix influence (**Table II.7**).

Treatment of tylosin compound by EAOP has scarcely been reported in literature. Tylosin is an antibiotic drug commonly used to treat bacterial infection in small domestic animals such as cats, dogs and ferrets as well as livestock animals like sheep, goats and cows. Tylosin degradation by other techniques for example electrocoagulation **[156]**, ozonation **[157]**, photolysis **[158]** and advanced oxidation process such as photocatalyst **[159-161]**, O_3/H_2O_2 **[162]** and nanosilver catalyst/peroxydisulfate **[163, 164]** have been documented. However, only one work from Ferrag-Siagh et al. **[148]** was found to report on the application of EAOP using EF as pretreatment to increase the biodegradability of tylosin. The treatment was proven efficient. Moreover, EAOPs such as EO and EF are much easier to setup as they operate in mild conditions with small footprint, without the need for stringent supply of UV source, O_3 or external H_2O_2. Furthermore, when EAOP is carried out in microfluidic reactor setup, operational cost of the treatment is significantly advantageous as compared to other AOPs. Due to this reason, tylosin degradation and mineralization using EO using submillimetric reactor will be performed in this PhD thesis. Compared to the EF, no addition of Fe^{2+} catalyst as well as pH acidification are required. Moreover, microfluidic feature would offer mass transfer intensification advantage to the process which would be beneficial to oxidize pollutant of very low concentration. Eventually, some more insight on EAOP to oxidize tylosin will be elucidated, particularly in the matrix of real wastewater effluent.

Table II.7. Literature review on the EAOP treatments of different pharmaceutical pollutants.

Group	Pollutant	EAOP	Electrochemical system	Electrolyte	j_{app}	Parameters	Ref
Sulfonamide	Sulfanilamide	EO	Undivided and divided cylindrical cell, Anode: BDD (3 cm^2), Cathode: Stainless steel (3 cm^2), d_{elec}: 1 cm	Synthetic solution, Sulfanilamide: 239 – 2390 mg L^{-1}, Na_2SO_4: 7 g L^{-1} (undivided) and 70 g L^{-1} (divided cell), pH: 2 – 6, volume: 100 mL	33 to 150 mA cm^{-2}	• Bulk pH • Applied current density • Initial sulfanilamide concentration	[132]
Sulfonamide	Sulfanilamide	EF SPEF	Flow pilot plant with undivided cell coupled to solar photo reactor, Anode: Pt sheet (20 cm^2), Cathode: Carbon-PTFE-air diffusion (20 cm^2), d_{elec}: 1.2 cm, flow rate: 3.33 L min^{-1}	Synthetic solution, Sulfanilamide: 239 – 1195 mg L^{-1}, Na_2SO_4: 7 g L^{-1}, pH: 3, Fe^{2+}: 14 – 279 mg L^{-1} (catalyst), volume: 100 mL	50, 100 and 150 mA cm^{-2}	• Fe^{2+} concentration • Applied current density • Initial concentration	[133]
Sulfonamide	Sulfamethazine	EF PEF-UVA	Undivided cylindrical glass cell, Anode: BDD (3 cm^2), Cathode: Carbon-PTFE-air diffusion (3 cm^2), d_{elec}: 1 cm, air flow rate: 300 mL min^{-1}	Synthetic solution, Sulfamethazine: 193 – 1930 mg L^{-1}, Na_2SO_4: 7 g L^{-1}, Fe^{2+}: 11 – 84 mg L^{-1} (catalyst), pH: 2 – 6, volume: 100 mL	33 to 100 mA cm^{-2}	• Bulk pH • Fe^{2+} concentration • Applied current density • Initial sulfamethazine concentration	[134]
Sulfonamide	Sulfamethazine	EO EF	Undivided cell, Anode: Pt (20 cm^2), Cathode: Carbon felt (208 cm^2)	Synthetic solution, Sulfamethazine: 25 – 198 mg L^{-1}, Na_2SO_4: 7 g L^{-1}, Fe^{2+}: 2.8 – 56 mg L^{-1}, pH: 3, temp.: 18 – 45 °C, flow rate: 2 L min^{-1}, V: 1 L	0.24 to 2.9 mA cm^{-2}	• Applied current density • Fe^{2+} concentration • Initial sulfamethazine concentration • Operating temperature • Biodegradability test	[135]
Sulfonamide	Sulfamethazine	EO EO EF	Undivided cell, Anode: Pt, BDD, IrO_2-RuO_2/Ti or graphite felt (24 cm^2), Cathode: Graphite felt	Synthetic solution, Sulfamethazine: 29 mg L^{-1}, Na_2SO_4: 7 g L^{-1}, Fe^{2+}: 11 mg L^{-1}, pH: 3, volume: 300 mL	2.1 to 42 mA cm^{-2}	• Anode material • Applied current density • Comparison of EAOPs	[136]

Group	Pollutant	EAOP	Electrochemical system	Electrolyte	j_{app}	Parameters	Ref
Sulfonamide	Sulfamethazine	EF	Undivided cell, Anode: Pt Cathode: Carbon felt, carbon sponges (with different pore sizes) and stainless steel All geometric surface area: 21 cm^2, d_{elec}: 2.5 cm	Synthetic solution, Sulfamethazine: 29 mg L^{-1}, Na_2SO_4: 7 g L^{-1}, Fe^{2+}: 11 mg L^{-1}, pH: 3, volume: 250 mL	50 to 500 mA	• Applied current • Cathode material	[137]
Sulfonamide	Sulfa-methoxazole	EO EF	Undivided cell, Anode: Pt mesh (EO) and Pt mesh or BDD (EF) (25 cm^2) Cathode: Carbon felt (70 cm^2)	Synthetic solution, Sulfamethoxazole: 21 – 329 mg L^{-1}, Na_2SO_4: 7 g L^{-1}, Fe catalyst: 11 mg L^{-1} Fe^{2+}, or 11 mg L^{-1} Fe^{2+} + 13 mg L^{-1} Cu^{2+} or 13 mg L^{-1} Cu^{2+}, pH: 3, volume: 220 mL	30 to 450 mA	• Applied current • Initial sulfamethoxazole concentration • Type of Fenton catalyst Fe^{2+} and/or Cu^{2+}	[138]
Sulfonamide	Sulfa-methoxazole	EO EF PEF-UVA	Undivided cell, Anode: RuO_2/Ti mesh (16 cm^2) Cathode: EO: RuO_2/Ti (16 cm^2) Others: activated carbon fiber (ACF) felt (16 cm^2)	Synthetic solution, Sulfamethoxazole: 50 – 300 mg L^{-1}, Na_2SO_4: 7 g L^{-1}, Fe^{2+}: 28 – 112 mg L^{-1}, pH: 3, volume: 125 mL	7.5 to 31 mA cm^{-2}	• Comparison between EAOPs • Applied current density • Fe^{2+} concentration • Initial sulfamethoxazole concentration	[139]
Sulfonamide	Sulfachloro-pyridazine	EF	Undivided cell, Anode: Pt mesh or BDD (25 cm^2) Cathode: Carbon felt (70 cm^2)	Synthetic solution, Sulfachloropyridazine: 25 – 60 mg L^{-1}, Na_2SO_4: 7 g L^{-1}, Fe^{2+}: 11 mg L^{-1}, pH: 3, volume: 220 mL	30 to 350 mA	• Applied current • Anode material	[140]
Tetracycline	Tetracycline	EO	Undivided cell, Anode: IrO_2-RuO_2/Ti DSA, Cathode: Carbon felt (240 cm^2)	Synthetic solution, Tetracycline: 100 – 300 mg L^{-1}, Na_2SO_4: 14 g L^{-1}, pH: 3 – 9, volume: 0.4 L	500 to 1500 mA	• Applied current • Bulk pH • Initial tetracycline concentration	[141]

Group	Pollutant	EAOP	Electrochemical system	Electrolyte	j_{app}	Parameters	Ref
Betalactam	Amoxicilin	EO	Undivided cell, Anode: Carbon felt, carbon fiber, graphite, Pt, PbO_2, IrO_2-RuO_2/Ti DSA or BDD (24 cm^2), Cathode: Stainless steel (24 cm^2), d_{elec}: 3 cm	Synthetic solution, Amoxicilin: 36 mg L^{-1}, Na_2SO_4: 7 g L^{-1}, pH: 5.3, volume: 250 mL	2.1 to 42 mA cm^{-2}	• Anode material • Applied current density	[142]
Nonsteroidal anti-inflammatory drug	Diclofenac	EO	Undivided cell, Anode: Pt or BDD (3 cm^2), Cathode: Stainless steel (3 cm^2) d_{elec}: 1 cm	Synthetic solution, Diclofenac: 175 mg L^{-1}, Na_2SO_4: 7 g L^{-1} KH_2PO_4: 7 g L^{-1} pH: 6.5 or without adjustment, volume: 0.1 L	17 to 150 mA cm^{-2} (50 to 450 mA)	• Bulk pH • Applied current density	[150]
Nonsteroidal anti-inflammatory drug	Ibuprofen	EF PEF-UVA SPEF	Undivided cell, Anode: Pt or BDD (3 cm2), Cathode: Carbon-PTFE-air diffusion (3 cm^2) O_2 flow rate: 20 mL min^{-1}	Synthetic solution, Ibuprofen: 41 mg L^{-1}, Na_2SO_4: 7 g L^{-1}, pH: 2 – 6, Fe^{2+}: 5.6 – 112 mg L^{-1}, volume: 100 mL	3.3 to 100 mA cm^{-2}	• Comparison between EAOPs • Applied current density • Fe^{2+} concentration	[151]
Analgesic	Paracetamol	EF EF-EO	Undivided cylindrical cell, Anode: Ti_4O_7 plate (EO) or Pt/Ti mesh (EF) (24 cm^2) Cathode: Carbon felt (126 cm^2) Continuous air bubble: 1 L min^{-1}	• Real WWTP effluent with conventional activated sludge process • Real WWTP effluent with membrane bioreactor (MBR) • Real-source urine treated with lab-scale MBR • Synthetic solution in 7 g L^{-1} Na_2SO_4 All matrices were spiked with 10 mg L^{-1} paracetamol Fe^{2+}: 11 mg L^{-1}, pH: 3, volume: 250 mL	100, 250 and 300 mA	• Comparison between different background matrices of real wastewater effluent to mineralize acetaminophen • Toxicity evaluation of different treated effluents	[152]

Group	Pollutant	EAOP	Electrochemical system	Electrolyte	j_{app}	Parameters	Ref
Analgesic	Paracetamol	EO	Flow plant with undivided flow cell, Anode: BDD (50 cm^2), Cathode: Carbon felt (50 cm^2) d_{elec}: 50 – 1000 µm	• Synthetic solution in 0.14, 0.57 and 1.42 g L^{-1} Na_2SO_4 Volume: 200 mL • Real effluent of municipal WWTP (Reims, France) Volume: 500 mL Both effluents were spiked with 15 mg L^{-1} paracetamol, pH: 3 or neutral, flow rate: 0.43 L min^{-1}	2 to 12 mA cm^{-2}	• Applied current density • Interelectrode distance • Electrolytic conductivity • Synthetic vs. real wastewater effluent • Bulk pH	[11]
Analgesic	Paracetamol	EO	Electro-mixing reactor, Anode: perforated BDD (14 cm^2), Cathode: Carbon felt (14 cm^2), d_{elec}: 500 µm	Synthetic solution, Paracetamol: 15 mg L^{-1}, Na_2SO_4: 570 mg L^{-1}, pH: neutral volume: 4 L	4 mA cm^{-2}	• Proof of concept • Electro-mixing vs. conventional flow-by reactor	[12]
Beta blocker	Atenolol, metoprolol and propranolol	EF SPEF	Recirculated flow electrochemical cell coupled to solar photo reactor, Anode: Pt or BDD (90.3 cm^2), Cathode: Carbon-PTFE-air diffusion or carbon felt (90.3 cm^2) 1 or 2 pairs of electrodes were tested, d_{elec}: 1.2 cm	Synthetic solution, Atenolol: 158 mg L^{-1}, Metoprolol: 66 mg L^{-1} Propranolol: 135 mg L^{-1} Na_2SO_4: 14 g L^{-1}, Fe^{2+}: 28 mg L^{-1}, temperature: 35 °C, pH: 3, flow rate: 4.2 L min^{-1}, volume: 10 L	Carbon-PTFE-AD: 17 to 55 mA cm^{-2} Carbon felt: 4.4 mA cm^{-2}	• Number of pairs of electrodes setting • EF vs. SPEF	[153]
Amphenicol	Chlor-amphenicol	EO	Flow plant with undivided cell Anode: BDD or RuO_2 based MMO (78 cm^2), Cathode: Stainless steel (78 cm^2), d_{elec}: 9 mm	Simulated urine waste of hospital effluent spiked with 100 mg L^{-1} chloramphenicol	1.25 to 5 mA cm^{-2}	• Applied current density • Anode material	[144]

Group	Pollutant	EAOP	Electrochemical system	Electrolyte	j_{app}	Parameters	Ref
Amphenicol	Chlor-amphenicol	EO EF PEF-UVA SPEF	**Bench scale** Undivided cylindrical cell Anode: Pt or BDD (3 cm^2) Cathode: Carbon-PTFE-air diffusion (3 cm^2), d_{elec}: 1 cm **Pilot scale** Flow plant with undivided cell coupled to photo reactor Anode: Pt (90.2 cm^2) Cathode: Carbon-PTFE-air diffusion (90.2 cm^2) d_{elec}: 1.2 cm	Synthetic solution, Chloramphenicol: 25 – 245 mg L^{-1} Na_2SO_4: 7 g L^{-1} Temperature: 35 °C pH: 3, Fe^{2+}: 28 mg L^{-1} **Bench scale** Volume: 100 mL, flow: magnetic stirring (800 rpm), air flow: 0.3 L min^{-1} **Pilot scale** Volume: 10 L, flow rate: 3.3 L min^{-1}, air flow: 4.5 L min^{-1}	33 to 100 mA cm^{-2}	• Comparison between EAOPs • Applied current density • Initial chloramphenicol concentration • Bench scale vs. pilot scale up scale	[145]
Bacterio-static	Trimethoprim	EO EF PEF-UVA SPEF	Flow plant consisted of undivided electrochemical cell coupled to compound parabolic collectors and solar photo reactor Anode: Pt or BDD (10 cm^2) Cathode: Carbon-PTFE-air diffusion (10 cm^2), d_{elec}: 5 mm	Volume: 1.25 L Flow rate: 0.67 L min^{-1} • Synthetic solution, Na_2SO_4: 7 g L^{-1}, Fe^{2+}: 2 – 8 mg L^{-1}, pH: 3 – 4.5 • Real wastewater effluent of urban WWTP Both effluents were spiked with 20 mg L^{-1} trimethoprim	2.5 to 150 mA cm^{-2}	• Comparison of different EAOPs • Fe^{2+} concentration • Applied current density • Bulk pH • Synthetic vs. real effluent	[146]
Nitro-imidazole	Metronidazole	EF	Undivided cell, Anode: Pt (32 cm^2), Cathode: Graphite felt	Synthetic solution, Metronidazole: 100 – 500 mg L^{-1}, Na_2SO_4: 7 g L^{-1}, Fe^{2+}: 2.8 – 56 mg L^{-1}, pH: 2 – 9, volume: 250 mL	0.04 to 0.45 mA cm^{-2}	• Applied current density • Bulk pH • Initial metronidazole and Fe^{2+}concentration	[147]

Group	Pollutant	EAOP	Electrochemical system	Electrolyte	j_{app}	Parameters	Ref
Timoprazole	Omeprazole	EO	Undivided cell, Anode: Pt or BDD (3 cm^2), Cathode: Carbon-PTFE-air diffusion (3 cm^2), air flow rate: 300 mL min^{-1} d_{elec}: 1 cm	Synthetic solution, Omeprazole: 17 – 169 mg L^{-1}, NaH_2PO_4: 18 mg L^{-1} H_3PO_4: 2.4 mg L^{-1}, pH: 7, temperature: 35 °C, volume: 100 mL	33 to 150 mA cm^{-2}	• Anode material • Applied current density • Initial omeprazole concentration	[154]
Histamine	Ranitidine	EO EF	Undivided cell, Anode: Pt (42 cm^2), BDD (25 cm^2) or IrO_2-RuO_2/Ti DSA (25 cm^2) Cathode: Carbon felt (60 cm^2)	Synthetic solution, Ranitidine: 31 mg L^{-1}, Na_2SO_4: 7 g L^{-1}, Fe^{2+}: 6 mg L^{-1}, pH: 3, temperature: 20 °C, volume: 230 mL	100 to 500 mA	• Applied current • Comparison between EAOPs	[155]
Macrolide	Tylosin	EF	Undivided cell, Anode: Cylindrical Pt Cathode: Carbon felt (194 cm^2)	Synthetic solution, Tylosin: 100 mg L^{-1}, Na_2SO_4: 7.1 g L^{-1}, Fe^{2+}: 6 mg L^{-1}, pH: 3, V: 0.6 L	300 mA	-	[148]
Quinolone Sulfonamide Brancho-dilator Urea	Ciprofloxacin Sulfa-methoxazole Salbutamol Urea	EO	Flow plant with undivided cell Anode: BDD (69 cm^2) Cathode: Zirconium (69 m^2)	Synthetic solution, Ciprofloxacin: 14 – 25 mg L^{-1} Sulfamethoxazole: 15 mg L^{-1} Salbutamol: 16 mg L^{-1} Urea: 5 – 38 mg L^{-1} K_2SO_4: 17 g L^{-1} (pH: 4) K_2SO_4: 3.5 g L^{-1} (pH: 6) Flow rate: 6 L min^{-1}	1.4 to 7.2 mA cm^{-2}	• Applied current density • Electroactivity of compound to be treated • Bulk pH • Urea concentration • Initial pollutant concentration	[149]

Abbreviations: EO: Electro-oxidation, EF: electro-Fenton, PEF: photo electro-Fenton, SPEF: solar photo electro-Fenton, UVA: ultraviolet A, BDD: boron-doped diamond, DSA: dimensionally stable anode, PTFE: polytetrafluoroethylene, j_{app}: applied current density, MMO: mixed metal oxide, Pt: platinum, Ti: titanium, Ir: iridium, Ru: ruthenium, d_{elec}: interelectrode distance and WWTP: wastewater treatment plant.

II.4. Concluding remarks

Listed below are the critical subjects of experimentation, discussion and interpretation throughout this thesis:

- No mass transfer correlation in submillimetric parallel-plate electrochemical reactors has yet been established in literature either in laminar or turbulent regime.
- In a classical EAOP, mineral electro-precipitation is occuring on cathode. Under continuous operation without maintenance, the electrode surface will be totally passivated.
- No publication yet exists pertaining the formation of mineral scaling inside a microfluidic electrochemical reactor.
- The kinetic model to predict mineral electro-precipitation on cathode is scarcely available.
- Important parameters on mineral scaling for example interelectrode gap and electrode materials ought to be investigated in further details.
- The use of microfluidic reactors to treat wastewater merits more attention from scientific communities.
- No report has yet been made on the simultaneous fate of chlorinated and nitrogenous byproducts during wastewater treatment in submillimetric condition.

References

[1] S. Fransen, J. Fransaer, S. Kuhn, Current and concentration distributions in electrochemical microreactors: Numerical calculations and asymptotic approximations for self-supported paired synthesis, Electrochimica Acta, 292 (2018) 914-934.
[2] E. Mousset, Y. Pechaud, N. Oturan, M.A. Oturan, Charge transfer/mass transport competition in advanced hybrid electrocatalytic wastewater treatment: Development of a new current efficiency relation, Applied Catalysis B: Environmental, 240 (2019) 102-111.
[3] O. Scialdone, A. Galia, S. Sabatino, Electro-generation of H_2O_2 and abatement of organic pollutant in water by an electro-Fenton process in a microfluidic reactor, Electrochemistry Communications, 26 (2013) 45-47.
[4] O. Scialdone, C. Guarisco, A. Galia, Oxidation of organics in water in microfluidic electrochemical reactors: Theoretical model and experiments, Electrochimica Acta, 58 (2011) 463-473.
[5] O. Scialdone, E. Corrado, A. Galia, I. Sirés, Electrochemical processes in macro and microfluidic cells for the abatement of chloroacetic acid from water, Electrochimica Acta, 132 (2014) 15-24.
[6] O. Scialdone, A. Galia, S. Sabatino, Abatement of Acid Orange 7 in macro and micro reactors. Effect of the electrocatalytic route, Applied Catalysis B: Environmental, 148-149 (2014) 473-483.
[7] P. Ma, H. Ma, S. Sabatino, A. Galia, O. Scialdone, Electrochemical treatment of real wastewater. Part 1: Effluents with low conductivity, Chemical Engineering Journal, 336 (2018) 133-140.
[8] J.F. Pérez, J. Llanos, C. Sáez, C. López, P. Cañizares, M.A. Rodrigo, Development of an innovative approach for low-impact wastewater treatment: A microfluidic flow-through electrochemical reactor, Chemical Engineering Journal, 351 (2018) 766-772.
[9] W. Khongthon, G. Jovanovic, A. Yokochi, P. Sangvanich, V. Pavarajarn, Degradation of diuron via an electrochemical advanced oxidation process in a microscale-based reactor, Chemical Engineering Journal, 292 (2016) 298-307.
[10] M. Rodríguez, M. Muñoz-Morales, J.F. Perez, C. Saez, P. Cañizares, C.E. Barrera-Díaz, M.A. Rodrigo, Toward the development of efficient electro-Fenton reactors for soil washing wastes through microfluidic cells, Industrial & Engineering Chemistry Research, 57 (2018) 10709-10717.
[11] E. Mousset, M. Puce, M.N. Pons, Advanced electro-oxidation with boron-doped diamond for acetaminophen removal from real wastewater in a microfluidic reactor: Kinetics and mass-transfer studies, ChemElectroChem, 6 (2019) 2908-2916.
[12] E. Mousset, Unprecedented reactive electro-mixing reactor: Towards synergy between micro- and macro-reactors?, Electrochemistry Communications, 118 (2020) 106787.
[13] S. Sabatino, A. Galia, O. Scialdone, Electrochemical abatement of organic pollutants in continuous-reaction systems through the assembly of microfluidic cells in series, ChemElectroChem, 3 (2016) 83-90.
[14] O. Scialdone, A. Galia, C. Guarisco, S. La Mantia, Abatement of 1,1,2,2-tetrachloroethane in water by reduction at silver cathode and oxidation at boron doped diamond anode in micro reactors, Chemical Engineering Journal, 189-190 (2012) 229-236.
[15] F.C. Moreira, R.A.R. Boaventura, E. Brillas, V.J.P. Vilar, Electrochemical advanced oxidation processes: A review on their application to synthetic and real wastewaters, Applied Catalysis B: Environmental, 202 (2017) 217-261.
[16] M. Panizza, G. Cerisola, Direct and mediated anodic oxidation of organic pollutants, Chemical Reviews, 109 (2009) 6541-6569.
[17] C.A. Martínez-Huitle, M.A. Rodrigo, I. Sirés, O. Scialdone, Single and coupled electrochemical processes and reactors for the abatement of organic water pollutants: A critical review, Chemical Reviews, 115 (2015) 13362-13407.
[18] I. Sirés, E. Brillas, M.A. Oturan, M.A. Rodrigo, M. Panizza, Electrochemical advanced oxidation processes: Today and tomorrow. A review, Environmental Science and Pollution Research, 21 (2014) 8336-8367.
[19] M. Panizza, C.A. Martinez-Huitle, Role of electrode materials for the anodic oxidation of a real landfill leachate – Comparison between Ti–Ru–Sn ternary oxide, PbO_2 and boron-doped diamond anode, Chemosphere, 90 (2013) 1455-1460.
[20] O. Scialdone, C. Guarisco, A. Galia, G. Filardo, G. Silvestri, C. Amatore, C. Sella, L. Thouin, Anodic abatement of organic pollutants in water in micro reactors, Journal of Electroanalytical Chemistry, 638 (2010) 293-296.

[21] O. Scialdone, A. Galia, S. Sabatino, D. Mira, C. Amatore, Electrochemical conversion of dichloroacetic acid to chloroacetic acid in a microfluidic stack and in a series of microfluidic reactors, ChemElectroChem, 2 (2015) 684-690.
[22] J.F. Pérez, J. Llanos, C. Sáez, C. López, P. Cañizares, M.A. Rodrigo, A microfluidic flow-through electrochemical reactor for wastewater treatment: A proof-of-concept, Electrochemistry Communications, 82 (2017) 85-88.
[23] J.F. Pérez, J. Llanos, C. Sáez, C. López, P. Cañizares, M.A. Rodrigo, On the design of a jet-aerated microfluidic flow-through reactor for wastewater treatment by electro-Fenton, Separation and Purification Technology, 208 (2019) 123-129.
[24] J.F. Pérez, J. Llanos, C. Sáez, C. López, P. Cañizares, M.A. Rodrigo, Towards the scale up of a pressurized-jet microfluidic flow-through reactor for cost-effective electro-generation of H_2O_2, Journal of Cleaner Production, 211 (2019) 1259-1267.
[25] J.A. Alden, R.G. Compton, Hydrodynamic voltammetry with channel microband electrodes: axial diffusion effects, Journal of Electroanalytical Chemistry, 404 (1996) 27-35.
[26] R.G. Compton, P.R. Unwin, Channel and tubular electrodes, Journal of Electroanalytical Chemistry and Interfacial Electrochemistry, 205 (1986) 1-20.
[27] J.A. Cooper, R.G. Compton, Channel electrodes — A review, Electroanalysis, 10 (1998) 141-155.
[28] M. Griffiths, C.P. de León, F.C. Walsh, Mass transport in the rectangular channel of a filter-press electrolyzer (the FM01-LC reactor), American Institute of Chemical Engineers, 51 (2005) 682-687.
[29] S.J. Coleman, S. Roy, Design of an ultrasonic tank reactor for copper deposition at electrodes separated by a narrow gap, Ultrasonics Sonochemistry, 42 (2018) 445-451.
[30] M. Cruz-Díaz, F.F. Rivera, E.P. Rivero, I. González, The FM01-LC reactor modeling using axial dispersion model with a reaction term coupled with a continuous stirred tank (CST), Electrochimica Acta, 63 (2012) 47-54.
[31] C.F. Oduoza, A.A. Wragg, M.A. Patrick, The effects of a variety of wall obstructions on local mass transfer in a parallel plate electrochemical flow cell, Chemical Engineering Journal, 68 (1997) 145-155.
[32] C.A. Martinez-Huitle, S. Ferro, A. De Battisti, Electrochemical incineration of oxalic acid: Reactivity and engineering parameters, Journal of Applied Electrochemistry, 35 (2005) 1087-1093.
[33] T.P. Szanto A., White I., Walsh F. C., Electrosynthesis and mass transport measurements in a laboratory filter-press electrolyzer, 4th european symposium on electrochemical engineering, Prague, Czech Republic, 1996, pp. 273.
[34] D.J. Pickett, B.R. Stanmore, Ionic mass transfer in parallel plate electrochemical cells, Journal of Applied Electrochemistry, 2 (1972) 151-156.
[35] D.J. Pickett, K.L. Ong, The influence of hydrodynamic and mass transfer entrance effects on the operation of a parallel plate electrolytic cell, Electrochimica Acta, 19 (1974) 875-882.
[36] T.R. Ralph, M.L. Hitchman, J.P. Millington, F.C. Walsh, Mass transport in an electrochemical laboratory filterpress reactor and its enhancement by turbulence promoters, Electrochimica Acta, 41 (1996) 591-603.
[37] J.L.C. Santos, V. Geraldes, S. Velizarov, J.G. Crespo, Characterization of fluid dynamics and mass-transfer in an electrochemical oxidation cell by experimental and CFD studies, Chemical Engineering Journal, 157 (2010) 379-392.
[38] N. Tzanetakis, K. Scott, W.M. Taama, R.J.J. Jachuck, Mass transfer characteristics of corrugated surfaces, Applied Thermal Engineering, 24 (2004) 1865-1875.
[39] A.A. Wragg, A.A. Leontaritis, Local mass transfer and current distribution in baffled and unbaffled parallel plate electrochemical reactors, Chemical Engineering Journal, 66 (1997) 1-10.
[40] M.A. Quiroz, U.A. Martínez-Huitle, C.A. Martínez-Huitle, Mass transfer measurements in a parallel disk cell using the limiting current technique, Journal of the Mexican Chemical Society, 49 (2005) 279-283.
[41] E.V. dos Santos, S.F.M. Sena, D.R. da Silva, S. Ferro, A. De Battisti, C.A. Martínez-Huitle, Scale-up of electrochemical oxidation system for treatment of produced water generated by Brazilian petrochemical industry, Environmental Science and Pollution Research, 21 (2014) 8466-8475.
[42] P. Cañizares, J. García-Gómez, J. Lobato, M.A. Rodrigo, Electrochemical oxidation of aqueous carboxylic acid wastes using diamond thin-film electrodes, Industrial & Engineering Chemistry Research, 42 (2003) 956-962.
[43] G. Coria, T. Pérez, I. Sirés, J.L. Nava, Mass transport studies during dissolved oxygen reduction to hydrogen peroxide in a filter-press electrolyzer using graphite felt, reticulated vitreous carbon and boron-doped diamond as cathodes, Journal of Electroanalytical Chemistry, 757 (2015) 225-229.

[44] A.M. Polcaro, A. Vacca, M. Mascia, S. Palmas, J. Rodiguez Ruiz, Electrochemical treatment of waters with BDD anodes: kinetics of the reactions involving chlorides, Journal of Applied Electrochemistry, 39 (2009) 2083.
[45] Á. Anglada, A.M. Urtiaga, I. Ortiz, Laboratory and pilot plant scale study on the electrochemical oxidation of landfill leachate, Journal of Hazardous Materials, 181 (2010) 729-735.
[46] C. Gabrielli, M. Keddam, G. Maurin, H. Perrot, R. Rosset, M. Zidoune, Estimation of the deposition rate of thermal calcareous scaling by the electrochemical impedance technique, Journal of Electroanalytical Chemistry, 412 (1996) 189-193.
[47] C. Gabrielli, M. Keddam, A. Khalil, R. Rosset, M. Zidoune, Study of calcium carbonate scales by electrochemical impedance spectroscopy, Electrochimica Acta, 42 (1997) 1207-1218.
[48] C. Gabrielli, Quartz crystal microbalance investigation of electrochemical calcium carbonate scaling, Journal of The Electrochemical Society, 145 (1998) 2386.
[49] C. Gabrielli, G. Maurin, G. Poindessous, R. Rosset, Nucleation and growth of calcium carbonate by an electrochemical scaling process, Journal of Crystal Growth, 200 (1999) 236-250.
[50] L. Beaunier, C. Gabrielli, G. Poindessous, G. Maurin, R. Rosset, Investigation of electrochemical calcareous scaling: Nuclei counting and morphology, Journal of Electroanalytical Chemistry, 501 (2001) 41-53.
[51] C. Deslouis, I. Frateur, G. Maurin, B. Tribollet, Interfacial pH measurement during the reduction of dissolved oxygen in a submerged impinging jet cell, Journal of Applied Electrochemistry, 27 (1997) 482-492.
[52] M.M. Tlili, M. Benamor, C. Gabrielli, H. Perrot, B. Tribollet, Influence of the interfacial pH on electrochemical $CaCO_3$ precipitation, Journal of The Electrochemical Society, 150 (2003) C765.
[53] A.R. Rakitin, V.I. Kichigin, Electrochemical study of calcium carbonate deposition on iron. Effect of the anion, Electrochimica Acta, 54 (2009) 2647-2654.
[54] Y. Ben Amor, L. Bousselmi, H. Takenouti, E. Triki, Influence of sulphate ions on corrosion mechanism of carbon steel in calcareous media, Corrosion Engineering, Science and Technology, 40 (2005) 129-136.
[55] L. Bousselmi, C. Fiaud, B. Tribollet, E. Triki, Impedance spectroscopic study of a steel electrode in condition of scaling and corrosion: Interphase model, Electrochimica Acta, 44 (1999) 4357-4363.
[56] J. Marin-Cruz, R. Cabrera-Sierra, M. Pech-Canul, I. Gonzalez, EIS study on corrosion and scale processes and their inhibition in cooling system media, Electrochimica Acta, 51 (2006) 1847-1854.
[57] C. Deslouis, D. Festy, O. Gil, G. Rius, S. Touzain, B. Tribollet, Characterization of calcareous deposits in artificial sea water by impedance techniques — 1. Deposit of $CaCO_3$ without $Mg(OH)_2$, Electrochimica Acta, 43 (1998) 1891-1901.
[58] C. Deslouis, D. Festy, O. Gil, V. Maillot, S. Touzain, B. Tribollet, Characterization of calcareous deposits in artificial sea water by impedances techniques: 2-deposit of $Mg(OH)_2$ without $CaCO_3$, Electrochimica Acta, 45 (2000) 1837-1845.
[59] C. Barchiche, C. Deslouis, D. Festy, O. Gil, P. Refait, S. Touzain, B. Tribollet, Characterization of calcareous deposits in artificial seawater by impedance techniques: 3 — deposit of $CaCO_3$ in the presence of Mg(II), Electrochimica Acta, 48 (2003) 1645-1654.
[60] H. Karoui, B. Riffault, M. Jeannin, A. Kahoul, O. Gil, M. Ben Amor, M.M. Tlili, Electrochemical scaling of stainless steel in artificial seawater: Role of experimental conditions on $CaCO_3$ and $Mg(OH)_2$ formation, Desalination, 311 (2013) 234-240.
[61] S.M. Hoseinieh, T. Shahrabi, B. Ramezanzadeh, M.F. Rad, The role of porosity and surface morphology of calcium carbonate deposits on the corrosion behavior of unprotected API 5L X52 rotating disk electrodes in artificial seawater, Journal of The Electrochemical Society, 163 (2016) C515-C529.
[62] S.M. Hoseinieh, T. Shahrabi, Influence of ionic species on scaling and corrosion performance of AISI 316L rotating disk electrodes in artificial seawater, Desalination, 409 (2017) 32-46.
[63] H. Vogt, Gas-evolving electrodes, in: E. Yeager, J.O.M. Bockris, B.E. Conway, S. Sarangapani (Eds.) Comprehensive Treatise of Electrochemistry: Electrodics: Transport, Springer US, Boston, MA, 1983, pp. 445-489.
[64] L.J.J. Janssen, Behaviour of and mass transfer at gas-evolving electrodes, Electrochimica Acta, 34 (1989) 161-169.
[65] H. Vogt, R.J. Balzer, The bubble coverage of gas-evolving electrodes in stagnant electrolytes, Electrochimica Acta, 50 (2005) 2073-2079.
[66] H. Vogt, The role of single-phase free convection in mass transfer at gas evolving electrodes — 1. Theoretical, Electrochimica Acta, 38 (1993) 1421-1426.
[67] M.G. Fouad, G.H. Sedahmed, Mass transfer at gas evolving screen electrodes, Electrochimica Acta, 20 (1975) 615-618.

[68] H. Vogt, Mass transfer at gas evolving electrodes with superposition of hydrodynamic flow, Electrochimica Acta, 23 (1978) 203-205.
[69] F. Hine, Bubble effects on the solution ir drop in a vertical electrolyzer under free and forced convection, Journal of The Electrochemical Society, 127 (1980) 292.
[70] F. Hine, Hydrodynamic studies of bubble effects on the IR-drops in a vertical rectangular cell, Journal of The Electrochemical Society, 122 (1975) 1185.
[71] H. Vogt, A hydrodynamic model for the ohmic interelectrode resistance of cells with vertical gas evolving electrodes, Electrochimica Acta, 26 (1981) 1311-1317.
[72] C.W. Tobias, Effect of gas evolution on current distribution and ohmic resistance in electrolyzers, Journal of The Electrochemical Society, 106 (1959) 833.
[73] N. Nagai, M. Takeuchi, T. Kimura, T. Oka, Existence of optimum space between electrodes on hydrogen production by water electrolysis, International Journal of Hydrogen Energy, 28 (2003) 35-41.
[74] L.J.J. Janssen, J.G. Hoogland, The effect of electrolytically evolved gas bubbles on the thickness of the diffusion layer — II, Electrochimica Acta, 18 (1973) 543-550.
[75] J. Křišťál, R. Kodým, K. Bouzek, V. Jiřičný, Electrochemical microreactor and gas-evolving reactions, Electrochemistry Communications, 10 (2008) 204-207.
[76] T. Pérez, M.I. León, J.L. Nava, Numerical simulation of current distribution along the boron-doped diamond anode of a filter-press-type FM01-LC reactor during the oxidation of water, Journal of Electroanalytical Chemistry, 707 (2013) 1-6.
[77] M. Euvrard, F. Membrey, C. Filiatre, C. Pignolet, A. Foissy, Kinetic study of the electrocrystallization of calcium carbonate on metallic substrates, Journal of Crystal Growth, 291 (2006) 428-435.
[78] R. Jaouhari, A. Benbachir, A. Guenbour, C. Gabrielli, J. Garcia-Jareno, G. Maurin, Influence of water composition and substrate on electrochemical scaling, Journal of The Electrochemical Society, 147 (2000) 2151-2161.
[79] Y. Ben Amor, L. Bousselmi, B. Tribollet, E. Triki, Study of the effect of magnesium concentration on the deposit of allotropic forms of calcium carbonate and related carbon steel interface behavior, Electrochimica Acta, 55 (2010) 4820-4826.
[80] Y. Ben Amor, L. Bousselmi, M.C. Bernard, B. Tribollet, Nucleation-growth process of calcium carbonate electrodeposition in artificial water — influence of the sulfate ions, Journal of Crystal Growth, 320 (2011) 69-77.
[81] J. Marin-Cruz, E. Garcia-Figueroa, M. Miranda-Hernández, I. Gonzalez, Electrochemical treatments for selective growth of different calcium carbonate allotropic forms on carbon steel, Water Research, 38 (2004) 173-183.
[82] J. Marin-Cruz, R. Cabrera-Sierra, M. Pech-Canul, I. Gonzalez, Characterization of different allotropic forms of calcium carbonate scales on carbon steel by electrochemical impedance spectroscopy, Journal of Applied Electrochemistry, 34 (2004) 337-343.
[83] S. Xu, Structure and morphology of electrodeposited $CaCO_3$: X-ray diffraction and microscopy studies, Journal of The Electrochemical Society, 146 (1999) 3315.
[84] Z. Belarbi, B. Sotta, L. Makhloufi, B. Tribollet, J. Gamby, Modelling of delay effect of calcium carbonate deposition kinetics on rotating disk electrode in the presence of green inhibitor, Electrochimica Acta, 189 (2016) 118-127.
[85] A. Martinod, A. Neville, M. Euvrad, K. Sorbie, Electrodeposition of a calcareous layer: Effects of green inhibitors, Chemical Engineering Science, 64 (2009) 2413-2421.
[86] C. Barchiche, C. Deslouis, O. Gil, P. Refait, B. Tribollet, Characterisation of calcareous deposits by electrochemical methods: Role of sulphates, calcium concentration and temperature, Electrochimica Acta, 49 (2004) 2833-2839.
[87] C. Barchiche, C. Deslouis, O. Gil, S. Joiret, P. Refait, B. Tribollet, Role of sulphate ions on the formation of calcareous deposits on steel in artificial seawater; the formation of green rust compounds during cathodic protection, Electrochimica Acta, 54 (2009) 3580-3588.
[88] C. Deslouis, P. Falaras, O. Gil, M. Jeannin, V. Maillot, B. Tribollet, Influence of clay on calcareous deposit in natural and artificial sea water, Electrochimica Acta, 51 (2006) 3173-3180.
[89] O. Devos, C. Gabrielli, B. Tribollet, Simultaneous EIS and in situ microscope observation on a partially blocked electrode application to scale electrodeposition, Electrochimica Acta, 51 (2006) 1413-1422.
[90] S.-H. Lin, S.C. Dexter, Effects of temperature and magnesium ions on calcareous deposition, Corrosion, 44 (1988) 615-622.
[91] K.E. Mantel, W.H. Hartt, T.-Y. Chen, Substrate, surface finish, and flow rate influences on calcareous deposit structure, Corrosion, 48 (1992) 489-500.

[92] Y. Lei, J.C. Remmers, M. Saakes, R.D. van der Weijden, C.J.N. Buisman, Is there a precipitation sequence in municipal wastewater induced by electrolysis?, Environmental Science & Technology, 52 (2018) 8399-8407.
[93] L. Kong, X. Liu, Emerging electrochemical processes for materials recovery from wastewater: Mechanisms and prospects, Frontiers of Environmental Science & Engineering, 14 (2020) 90.
[94] S. Sarvajayakesavalu, Y. Lu, P.J.A. Withers, P.S. Pavinato, G. Pan, P. Chareonsudjai, Phosphorus recovery: a need for an integrated approach, Ecosystem Health and Sustainability, 4 (2018) 48-57.
[95] Y. Liu, Y.-Y. Deng, Q. Zhang, H. Liu, Overview of recent developments of resource recovery from wastewater via electrochemistry-based technologies, Science of the Total Environment, 757 (2021) 143901.
[96] Y. Lei, Z. Zhan, M. Saakes, R.D. van der Weijden, C.J.N. Buisman, Electrochemical recovery of phosphorus from acidic cheese wastewater: Feasibility, quality of products, and comparison with chemical precipitation, ACS ES&T Water, 1 (2021) 1002-1013.
[97] Y. Zhang, R.A. Dawe, Influence of Mg^{2+} on the kinetics of calcite precipitation and calcite crystal morphology, Chemical Geology, 163 (2000) 129-138.
[98] M. Kitamura, Crystallization and transformation mechanism of calcium carbonate polymorphs and the effect of magnesium ion, Journal of Colloid and Interface Science, 236 (2001) 318-327.
[99] Y. Tang, F. Zhang, Z. Cao, W. Jing, Y. Chen, Crystallization of $CaCO_3$ in the presence of sulfate and additives: Experimental and molecular dynamics simulation studies, Journal of Colloid and Interface Science, 377 (2012) 430-437.
[100] L. Fernández-Díaz, Á. Fernández-González, M. Prieto, The role of sulfate groups in controlling $CaCO_3$ polymorphism, Geochimica et Cosmochimica Acta, 74 (2010) 6064-6076.
[101] C.A. Cid, J.T. Jasper, M.R. Hoffmann, Phosphate recovery from human waste via the formation of hydroxyapatite during electrochemical wastewater treatment, ACS Sustainable Chemistry & Engineering, 6 (2018) 3135-3142.
[102] Y. Lei, Z. Zhan, M. Saakes, R.D. van der Weijden, C.J.N. Buisman, Electrochemical recovery of phosphorus from wastewater using tubular stainless-steel cathode for a scalable long-term operation, Water Research, 199 (2021) 117199.
[103] S. Ben Moussa, G. Maurin, C. Gabrielli, M. Ben Amor, Electrochemical precipitation of struvite, Electrochemical and Solid-State Letters, 9 (2006) C97.
[104] C.C. Wang, X.D. Hao, G.S. Guo, M.C.M. van Loosdrecht, Formation of pure struvite at neutral pH by electrochemical deposition, Chemical Engineering Journal, 159 (2010) 280-283.
[105] Z. Belarbi, J. Trembly, Electrochemical processing to capture phosphorus from simulated concentrated animal feeding operations waste, Journal of The Electrochemical Society, 165 (2018) E685-E693.
[106] C. Kappel, K. Yasadi, H. Temmink, S.J. Metz, A.J.B. Kemperman, K. Nijmeijer, A. Zwijnenburg, G.J. Witkamp, H.H.M. Rijnaarts, Electrochemical phosphate recovery from nanofiltration concentrates, Separation and Purification Technology, 120 (2013) 437-444.
[107] Y. Ning, K. Li, Z. Zhao, D. Chen, Y. Li, Y. Liu, Q. Yang, B. Jiang, Simultaneous electrochemical degradation of organophosphorus pesticides and recovery of phosphorus: Synergistic effect of anodic oxidation and cathodic precipitation, Journal of the Taiwan Institute of Chemical Engineers, 125 (2021) 267-275.
[108] Y. Lei, M. Saakes, R.D. van der Weijden, C.J.N. Buisman, Effects of current density, bicarbonate and humic acid on electrochemical induced calcium phosphate precipitation, Chemical Engineering Journal, 342 (2018) 350-356.
[109] Y. Lei, B. Song, M. Saakes, R.D. van der Weijden, C.J.N. Buisman, Interaction of calcium, phosphorus and natural organic matter in electrochemical recovery of phosphate, Water Research, 142 (2018) 10-17.
[110] Y. Lei, I. Hidayat, M. Saakes, R. van der Weijden, C.J.N. Buisman, Fate of calcium, magnesium and inorganic carbon in electrochemical phosphorus recovery from domestic wastewater, Chemical Engineering Journal, 362 (2019) 453-459.
[111] Y. Lei, E. Geraets, M. Saakes, R.D. van der Weijden, C.J.N. Buisman, Electrochemical removal of phosphate in the presence of calcium at low current density: Precipitation or adsorption?, Water Research, 169 (2020) 115207.
[112] Y. Lei, B. Song, R.D. van der Weijden, M. Saakes, C.J.N. Buisman, Electrochemical induced calcium phosphate precipitation: Importance of local pH, Environmental Science & Technology, 51 (2017) 11156-11164.
[113] Y. Lei, J.C. Remmers, M. Saakes, R.D. van der Weijden, C.J.N. Buisman, Influence of cell configuration and long-term operation on electrochemical phosphorus recovery from domestic wastewater, ACS Sustainable Chemistry & Engineering, 7 (2019) 7362-7368.

[114] Y. Lei, M. Du, P. Kuntke, M. Saakes, R. van der Weijden, C.J.N. Buisman, Energy efficient phosphorus recovery by microbial electrolysis cell induced calcium phosphate precipitation, ACS Sustainable Chemistry & Engineering, 7 (2019) 8860-8867.
[115] Y. Lei, S. Narsing, M. Saakes, R.D. van der Weijden, C.J.N. Buisman, Calcium carbonate packed electrochemical precipitation column: New concept of phosphate removal and recovery, Environmental Science & Technology, 53 (2019) 10774-10780.
[116] Y. Lei, M. Saakes, R.D. van der Weijden, C.J.N. Buisman, Electrochemically mediated calcium phosphate precipitation from phosphonates: Implications on phosphorus recovery from non-orthophosphate, Water Research, 169 (2020) 115206.
[117] Y. Takabe, M. Fujiyama, Y. Yamasaki, T. Masuda, Influences of electrode distance and electrolysis time on phosphorus precipitation and composition during electrolysis of anaerobic digestion effluent, Science of the Total Environment, 803 (2022) 150114.
[118] I. Sanjuán, D. Benavente, V. García-García, E. Expósito, V. Montiel, Electrochemical softening of concentrates from an electrodialysis brackish water desalination plant: Efficiency enhancement using a three-dimensional cathode, Separation and Purification Technology, 208 (2019) 217-226.
[119] Y. Yu, H. Jin, X. Quan, B. Hong, X. Chen, Continuous multistage electrochemical precipitation reactor for water softening, Industrial & Engineering Chemistry Research, 58 (2019) 461-468.
[120] K.-H. Yeon, J.-H. Song, J. Shim, S.-H. Moon, Y.-U. Jeong, H.-Y. Joo, Integrating electrochemical processes with electrodialysis reversal and electro-oxidation to minimize COD and T-N at wastewater treatment facilities of power plants, Desalination, 202 (2007) 400-410.
[121] F. Valero, R. Arbós, Desalination of brackish river water using Electrodialysis Reversal (EDR): Control of the THMs formation in the Barcelona (NE Spain) area, Desalination, 253 (2010) 170-174.
[122] H.-J. Lee, M.-K. Hong, S.-H. Moon, A feasibility study on water softening by electrodeionization with the periodic polarity change, Desalination, 284 (2012) 221-227.
[123] Y. Yu, H. Jin, X. Jin, R. Yan, L. Zhang, X. Chen, Current pulsated electrochemical precipitation for water softening, Industrial & Engineering Chemistry Research, 57 (2018) 6585-6593.
[124] H. Jin, Y. Yu, L. Zhang, R. Yan, X. Chen, Polarity reversal electrochemical process for water softening, Separation and Purification Technology, 210 (2019) 943-949.
[125] H. Jin, Y. Yu, X. Chen, Membrane-based electrochemical precipitation for water softening, Journal of Membrane Science, 597 (2020) 117639.
[126] Y. Takabe, N. Ota, M. Fujiyama, Y. Okayasu, Y. Yamasaki, M. Minamiyama, Utilisation of polarity inversion for phosphorus recovery in electrochemical precipitation with anaerobic digestion effluent, Science of the Total Environment, 706 (2020) 136090.
[127] K.D. Brown, J. Kulis, B. Thomson, T.H. Chapman, D.B. Mawhinney, Occurrence of antibiotics in hospital, residential, and dairy effluent, municipal wastewater, and the Rio Grande in New Mexico, Science of the Total Environment, 366 (2006) 772-783.
[128] N.A. Sabri, H. Schmitt, B.M. van der Zaan, H.W. Gerritsen, H.H.M. Rijnaarts, A.A.M. Langenhoff, Performance of full scale constructed wetlands in removing antibiotics and antibiotic resistance genes, Science of tTotal Environment, 786 (2021) 147368.
[129] N.A. Sabri, H. Schmitt, B. Van der Zaan, H.W. Gerritsen, T. Zuidema, H.H.M. Rijnaarts, A.A.M. Langenhoff, Prevalence of antibiotics and antibiotic resistance genes in a wastewater effluent-receiving river in the Netherlands, Journal of Environmental Chemical Engineering, 8 (2020) 102245.
[130] S.D. Richardson, S.Y. Kimura, Water analysis: Emerging contaminants and current issues, Analytical Chemistry, 88 (2016) 546-582.
[131] B. Petrie, R. Barden, B. Kasprzyk-Hordern, A review on emerging contaminants in wastewaters and the environment: Current knowledge, understudied areas and recommendations for future monitoring, Water Research, 72 (2015) 3-27.
[132] A. El-Ghenymy, J.A. Garrido, R.M. Rodríguez, P.L. Cabot, F. Centellas, C. Arias, E. Brillas, Degradation of sulfanilamide in acidic medium by anodic oxidation with a boron-doped diamond anode, Journal of Electroanalytical Chemistry, 689 (2013) 149-157.
[133] A. El-Ghenymy, P.L. Cabot, F. Centellas, J.A. Garrido, R.M. Rodríguez, C. Arias, E. Brillas, Mineralization of sulfanilamide by electro-Fenton and solar photoelectro-Fenton in a pre-pilot plant with a Pt/air-diffusion cell, Chemosphere, 91 (2013) 1324-1331.
[134] A. El-Ghenymy, R.M. Rodríguez, C. Arias, F. Centellas, J.A. Garrido, P.L. Cabot, E. Brillas, Electro-Fenton and photoelectro-Fenton degradation of the antimicrobial sulfamethazine using a boron-doped diamond anode and an air-diffusion cathode, Journal of Electroanalytical Chemistry, 701 (2013) 7-13.

[135] D. Mansour, F. Fourcade, N. Bellakhal, M. Dachraoui, D. Hauchard, A. Amrane, Biodegradability improvement of sulfamethazine solutions by means of an electro-Fenton process, Water, Air & Soil Pollution, 223 (2012) 2023-2034.
[136] F. Sopaj, N. Oturan, J. Pinson, F. Podvorica, M.A. Oturan, Effect of the anode materials on the efficiency of the electro-Fenton process for the mineralization of the antibiotic sulfamethazine, Applied Catalysis B: Environmental, 199 (2016) 331-341.
[137] F. Sopaj, N. Oturan, J. Pinson, F.I. Podvorica, M.A. Oturan, Effect of cathode material on electro-Fenton process efficiency for electrocatalytic mineralization of the antibiotic sulfamethazine, Chemical Engineering Journal, 384 (2020) 123249.
[138] A. Dirany, I. Sirés, N. Oturan, M.A. Oturan, Electrochemical abatement of the antibiotic sulfamethoxazole from water, Chemosphere, 81 (2010) 594-602.
[139] A. Wang, Y.-Y. Li, A.L. Estrada, Mineralization of antibiotic sulfamethoxazole by photoelectro-Fenton treatment using activated carbon fiber cathode and under UVA irradiation, Applied Catalysis B: Environmental, 102 (2011) 378-386.
[140] A. Dirany, I. Sirés, N. Oturan, A. Özcan, M.A. Oturan, Electrochemical treatment of the antibiotic sulfachloropyridazine: Kinetics, reaction pathways, and toxicity evolution, Environmental Science & Technology, 46 (2012) 4074-4082.
[141] J. Wu, H. Zhang, N. Oturan, Y. Wang, L. Chen, M.A. Oturan, Application of response surface methodology to the removal of the antibiotic tetracycline by electrochemical process using carbon-felt cathode and DSA ($Ti/RuO_2–IrO_2$) anode, Chemosphere, 87 (2012) 614-620.
[142] F. Sopaj, M.A. Rodrigo, N. Oturan, F.I. Podvorica, J. Pinson, M.A. Oturan, Influence of the anode materials on the electrochemical oxidation efficiency. Application to oxidative degradation of the pharmaceutical amoxicillin, Chemical Engineering Journal, 262 (2015) 286-294.
[143] S. Cotillas, E. Lacasa, M. Herraiz, C. Sáez, P. Cañizares, M.A. Rodrigo, The role of the anode material in selective penicillin G oxidation in urine, ChemElectroChem, 6 (2019) 1376-1384.
[144] M. Herraiz-Carboné, S. Cotillas, E. Lacasa, Á. Moratalla, P. Cañizares, M.A. Rodrigo, C. Sáez, Improving the biodegradability of hospital urines polluted with chloramphenicol by the application of electrochemical oxidation, Science of the Total Environment, 725 (2020) 138430.
[145] S. Garcia-Segura, E.B. Cavalcanti, E. Brillas, Mineralization of the antibiotic chloramphenicol by solar photoelectro-Fenton: From stirred tank reactor to solar pre-pilot plant, Applied Catalysis B: Environmental, 144 (2014) 588-598.
[146] F.C. Moreira, S. Garcia-Segura, R.A.R. Boaventura, E. Brillas, V.J.P. Vilar, Degradation of the antibiotic trimethoprim by electrochemical advanced oxidation processes using a carbon-PTFE air-diffusion cathode and a boron-doped diamond or platinum anode, Applied Catalysis B: Environmental, 160-161 (2014) 492-505.
[147] A. Aboudalle, F. Fourcade, A.A. Assadi, L. Domergue, H. Djelal, T. Lendormi, S. Taha, A. Amrane, Reactive oxygen and iron species monitoring to investigate the electro-Fenton performances. Impact of the electrochemical process on the biodegradability of metronidazole and its by-products, Chemosphere, 199 (2018) 486-494.
[148] F. Ferrag-Siagh, F. Fourcade, I. Soutrel, H. Aït-Amar, H. Djelal, A. Amrane, Electro-Fenton pretreatment for the improvement of tylosin biodegradability, Environmental Science and Pollution Research, 21 (2014) 8534-8542.
[149] Y. Lan, C. Coetsier, C. Causserand, K. Groenen Serrano, An experimental and modelling study of the electrochemical oxidation of pharmaceuticals using a boron-doped diamond anode, Chemical Engineering Journal, 333 (2018) 486-494.
[150] E. Brillas, S. Garcia-Segura, M. Skoumal, C. Arias, Electrochemical incineration of diclofenac in neutral aqueous medium by anodic oxidation using Pt and boron-doped diamond anodes, Chemosphere, 79 (2010) 605-612.
[151] M. Skoumal, R.M. Rodríguez, P.L. Cabot, F. Centellas, J.A. Garrido, C. Arias, E. Brillas, Electro-Fenton, UVA photoelectro-Fenton and solar photoelectro-Fenton degradation of the drug ibuprofen in acid aqueous medium using platinum and boron-doped diamond anodes, Electrochimica Acta, 54 (2009) 2077-2085.
[152] Y. Ouarda, C. Trellu, G. Lesage, M. Rivallin, P. Drogui, M. Cretin, Electro-oxidation of secondary effluents from various wastewater plants for the removal of acetaminophen and dissolved organic matter, Science of the Total Environment, 738 (2020) 140352.
[153] E. Isarain-Chávez, R.M. Rodríguez, P.L. Cabot, F. Centellas, C. Arias, J.A. Garrido, E. Brillas, Degradation of pharmaceutical beta-blockers by electrochemical advanced oxidation processes using a flow plant with a solar compound parabolic collector, Water Research, 45 (2011) 4119-4130.

[154] E.B. Cavalcanti, S.G. Segura, F. Centellas, E. Brillas, Electrochemical incineration of omeprazole in neutral aqueous medium using a platinum or boron-doped diamond anode: Degradation kinetics and oxidation products, Water Research, 47 (2013) 1803-1815.
[155] H. Olvera-Vargas, N. Oturan, E. Brillas, D. Buisson, G. Esposito, M.A. Oturan, Electrochemical advanced oxidation for cold incineration of the pharmaceutical ranitidine: Mineralization pathway and toxicity evolution, Chemosphere, 117 (2014) 644-651.
[156] W. Baran, E. Adamek, M. Jajko, A. Sobczak, Removal of veterinary antibiotics from wastewater by electrocoagulation, Chemosphere, 194 (2018) 381-389.
[157] M.C. Dodd, M.-O. Buffle, U. von Gunten, Oxidation of antibacterial molecules by aqueous ozone: Moiety-specific reaction kinetics and application to ozone-based wastewater treatment, Environmental Science & Technology, 40 (2006) 1969-1977.
[158] M. Voigt, M. Jaeger, On the photodegradation of azithromycin, erythromycin and tylosin and their transformation products – A kinetic study, Sustainable Chemistry and Pharmacy, 5 (2017) 131-140.
[159] S. Babić, L. Ćurković, D. Ljubas, M. Čizmić, TiO_2 assisted photocatalytic degradation of macrolide antibiotics, Current Opinion in Green and Sustainable Chemistry, 6 (2017) 34-41.
[160] H. Dong, X. Guo, C. Yang, Z. Ouyang, Synthesis of g-C_3N_4 by different precursors under burning explosion effect and its photocatalytic degradation for tylosin, Applied Catalysis B: Environmental, 230 (2018) 65-76.
[161] X. Guo, H. Dong, T. Xia, T. Wang, H. Jia, L. Zhu, Highly efficient degradation toward tylosin in the aqueous solution by carbon spheres/g-C_3N_4 composites under simulated sunlight irradiation, ACS Sustainable Chemistry & Engineering, 6 (2018) 12776-12786.
[162] A.Y.-C. Lin, C.-F. Lin, J.-M. Chiou, P.K.A. Hong, O_3 and O_3/H_2O_2 treatment of sulfonamide and macrolide antibiotics in wastewater, Journal of Hazardous Materials, 171 (2009) 452-458.
[163] S. Kamali Moghaddam, M.H. Rasoulifard, M. Vahedpour, M.R. Eskandarian, Kinetic study on degradation of tylosin in aqueous media using potassium peroxydisulfate in the presence of immobilized nanosilver, Desalination and Water Treatment, 57 (2016) 3552-3558.
[164] S. Kamali Moghaddam, M.H. Rasoulifard, M. Vahedpour, M.R. Eskandarian, Removal of tylosin from aqueous solution by UV/nano Ag/$S_2O_8^{2-}$ process: Influence of operational parameters and kinetic study, Korean Journal of Chemical Engineering, 31 (2014) 1577-1581.

III. Material and methods

In this chapter, technical details on the chemical reagents used, the preparation of simulated effluents, the experimental pilot and electrochemical reactor setup are discussed. Moreover, the pre- and post-treatment procedures, analytical methods as well as the utilization of software are exposed.

III.1. Chemical reagents

III.1.1. Preparation of effluents

Calcium sulfate dihydrate (>90%), magnesium sulfate heptahydrate (>98%), sodium hydrogenocarbonate (>99.5%), sodium sulfate (>97%), sodium chloride (>99%) and potassium chloride (>99%) were purchased from VWR International (Fontenay-sous-Bois, France). Tylosin tartrate T6134 and sulfuric acid (95-97%) were obtained from Sigma Aldrich (Saint-Quentin-Fallavier, France). Ammonium sulfate (>99.5%) and ammonium sulfate (>99.5%) were supplied by Fluka Honeywell (Fontenay-sous-Bois, France). Peptone P and meat extract (lab-lemco) powders were provided from Thermo Fisher Scientific (Illkirch, France). These chemical reagents were used as purchased without further treatment.

III.1.2. Analysis

Acetonitrile of high performance liquid chromatography – mass spectroscopy (HPLC LC-MS) grade (>99.9%) was purchased from VWR International (Fontenay-sous-Bois, France). Formic acid (>98%), titanium (IV) oxysulfate-sulfuric acid (27-31%) solution and H_2O_2 standard solution (30% (w/w)) were obtained from Sigma Aldrich (Saint-Quentin-Fallavier, France). Nessler reagent, mineral stabilizer and polyvinyl alcohol dispersing agent were provided by HACH (Düsseldorf, Germany). Multi-element standard solution containing calcium (Ca), potassium (K), magnesium (Mg) and sodium (Na) of 1000 µg mL^{-1} each was supplied by SCP Science (Courtabœuf, France). TIC, TOC and TN 1000 µg mL^{-1} standard solutions were purchased from TechLab (Metz, France). Nitrate (NO_3^-), sulfate (SO_4^{2-}) and chloride (Cl^-) 1000 mg L^{-1} standard solutions were also provided by Techlab (Metz, France). Nitrite (NO_2^-), chlorite (ClO_2^-), chlorate (ClO_3^-) and perchlorate (ClO_4^-) 1000 mg L^{-1} standard solutions were purchased from Sigma Aldrich (Saint-Quentin-Fallavier, France).

III.1.3. Electrochemical cell characterization

Potassium hexacyanoferrate (II) trihydrate (98.5-102.0%), potassium hexacyanoferrate (III) (>99%) and sodium carbonate (>99.5%) were purchased from Sigma Aldrich (Saint-Quentin-Fallavier, France).

III.2. Preparation of effluent

III.2.1. Simulated effluents

Ion concentrations of simulated effluents were characteristic of reclaimed wastewater (RW) properties (**Table III.1**). The average pH of simulated effluents was adjusted to ~7.6. They all have an ionic strength of 0.02 mol L^{-1}. In 2 L of ultrapure water (PureLab ELGA Classic, Veolia Water, Antony, France), basic effluent (BE) was prepared by dissolving 0.1014 g $MgSO_4.7H_2O$, 1.2887 g $CaSO_4.2H_2O$ and 0.8400 g $NaHCO_3$. 650 µL of H_2SO_4 1 M was added to adjust the pH. BE effluent without carbonates was prepared following the similar procedure by replacing $NaHCO_3$ with 0.4000 g Na_2SO_4. Intermediate effluent (IE) was prepared by dissolving 0.1014 g $MgSO_4.7H_2O$, 1.2887 g $CaSO_4.2H_2O$, 0.8400 g $NaHCO_3$, 0.0132 g $(NH_4)_2SO_4$ and 0.0062 g $NaH_2PO_4.2H_2O$ in 2 L ultrapure water. 650 µL of H_2SO_4 1 M was added to adjust the pH. In 2 L ultrapure water, saline effluent (SE) was prepared by dissolving 1.2887 g $CaSO_4.2H_2O$, 0.0896 g $MgSO_4.7H_2O$, 0.8400 g $NaHCO_3$, 0.0124 g $Mg(NO_3)_2.6H_2O$, 0.0132 g $(NH_4)_2SO_4$, 0.0062 g $NaH_2PO_4.2H_2O$, 0.3810 g NaCl, 0.0650 g KCl and 800 µL of NO_2^- 1000 µg mL^{-1} standard solution. 650 µL of H_2SO_4 1 M was added to adjust the pH. Simulated wastewater (SW) consisted of similar salts composition as SE only with the addition of 32 mg L^{-1} peptone and 22 mg L^{-1} meat extract. 20 mg of tylosin tartrate was added in 2 L of effluent (10 mg L^{-1}) in case where simulated effluent was spiked with tylosin.

III.2.2. Reclaimed wastewater effluent (RW)

RW was sampled at the outlet of Reims urban WWTP receiving a mixture of domestic and industrial waste streams. The plant treats 65,000 m^3 of wastewater daily and has a treatment capacity of 470,000 people equivalents. The effluent was stored at -4 °C before usage and it was filtered with standard filter paper (Dutscher, Brumath, France) (~10 µm pore diameter) prior to experimentations.

Table III.1. Physicochemical properties of the effluent of municipal WWTP (Reims, France).

pH	IC / µS cm^{-1}	Ca^{2+} / mg L^{-1}	Mg^{2+} / mg L^{-1}	TIC / mg-C L^{-1}	TOC / mg-C L^{-1}	TN / mg-N L^{-1}
7.57 ± 0.21	1,021 ± 74	133 ± 8	4.2 ± 0.5	68 ± 4	4.5 ± 0.5	2.1 ± 0.5

NH_4^+ / mg L^{-1}	NO_3^- / mg L^{-1}	NO_2^- / mg L^{-1}	PO_4^{3-} / mg L^{-1}	Cl^- / mg L^{-1}	SO_4^{2-} / mg L^{-1}	K^+ / mg L^{-1}	Na^+ / mg L^{-1}
1.6 ± 0.5	2.2 ± 1.2	0.5 ± 0.4	1.6 ± 0.5	129 ± 38	66 ± 7	17 ± 1.7	76 ± 24

III.2.3. Electrolyte for electrochemical reactor characterizations

Mass transfer characterization of the electrochemical reactors as well as the determination of electroactive surface of electrodes were performed using electrochemical methods. They involved the use of ferro-ferricyanide solution prepared as follow: 84.4776 g of $K_4Fe(CN)_6$, 32.9240 g of $K_3Fe(CN)_6$ and 105.99 g of Na_2CO_3 were dissolved in 2 L of ultrapure water. It gave out a solution containing 0.05 mol L^{-1} of $K_3Fe(CN)_6$, 0.1 mol L^{-1} of $K_4Fe(CN)_6$ and 0.5 mol L^{-1} Na_2CO_3 buffer.

III.3. Experimental setup

III.3.1. Electrochemical system

0.5 L of effluent was used in every experiment. The effluent was stored in a double-jacket stainless steel reservoir connected to a thermostatic bath (Bioblock Scientific, PolyScience, Niles, IL, USA) which can regulate the working temperature of experiments. A peristaltic pump (Masterflex, Cole-Parmer, Vernon Hills, IL, USA) was used to circulate the effluent at the desired flow rate (10 to 800 mL min^{-1}) in batch recirculation mode. The electrochemical setup consisted of a parallel-plate reactor (**Fig. III.1**). Its body was made of poly (methyl methacrylate) (PMMA), a material chemically and thermally resistant in the applied operating conditions. Rubber seals were designed, built-in, to provide tightness and avoid leakage. Both anode and cathode were planar rectangles, facing one another. BDD (DiaCCon, Fürth, Germany), 2 mm in thickness, was coated on both sides with a Niobium substrate by 12 µm. BDD was always employed as anode. Pure platinum plate (Ögussa, Vienna, Austria) was adopted as anode in some preliminary studies. 316L stainless steel (Gantois Industries, Saint-Dié-des-Vosges, France), graphite plate (Final Advanced Materials, Didenheim, France) and carbon paper (Ion Power, München, Germany) were used as cathode. The width (W) and length (L) of the planar electrodes in contact with the electrolyte were 5 and 10 cm respectively giving out a geometric surface area of 50 cm^2. A spacer made of polytetrafluoroethylene (PTFE) with varying thicknesses of 100, 250, 500, 1000, 1500, 2000 and 3000 µm (Bohlender, Grünsfeld, Germany) was used to separate the cathode and anode. Thus, they defined the varying d_{elec} investigated in this work, distinguished from micrometric progressively into a typical millimetric

configuration. A HMP4040 model current generator (Rohde & Schwarz, Meudon-la-Forêt, France) was used to run the electrochemical reactor under galvanostatic mode. A range of 20 to 800 mA applied current (corresponding to 0.4 to 16 mA cm^{-2} current density) was tested throughout the study. For the experiments using a potentiostat (Ametek, Massy, France), the electrochemical cell was connected to the potentiostat under a 3-electrode configuration. Silver-saturated silver chloride (Ag-AgCl) was used as reference electrode (RE). It was inserted into the cell at the bottom part, near the electrolyte inlet stream as depicted in **Fig. III.2**. The electrolyte was introduced by forced convection from the bottom of the cell flowing upward. The positioning of the RE (lower part of the cell) took advantage of the gravitational force to ensure stable measurement conditions by avoiding: firstly, engorgement in the case of unstable effluent flow and secondly, perturbation due to gas evolution. Furthermore, the Ag-AgCl reference electrode was positioned very close to the working electrode (500 ± 100 µm) in order to avoid ohmic loss in solution.

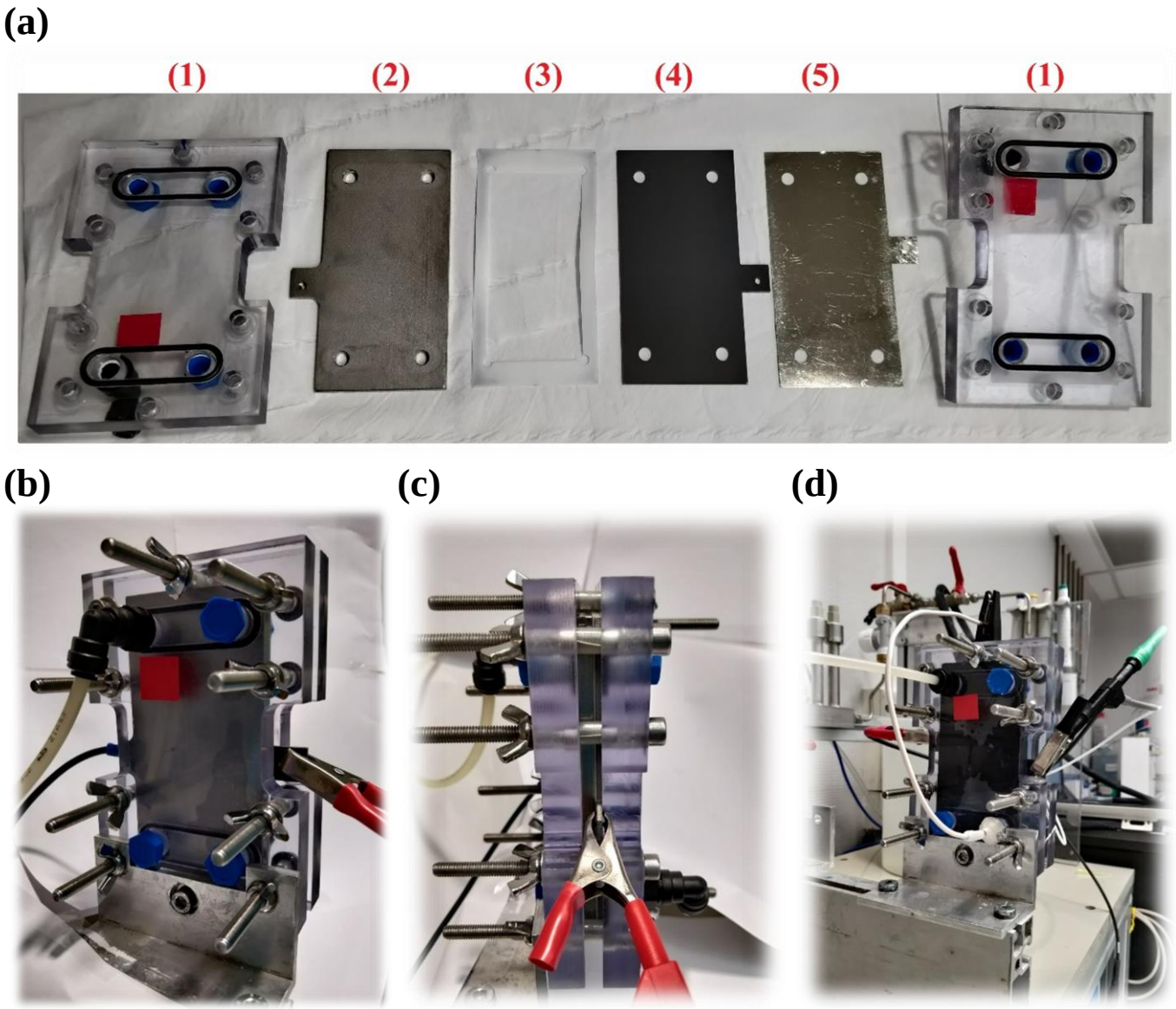

Fig. III.1. **(a)** Disassembled parallel-plate cell with 1: PMMA cell plate, 2: stainless steel cathode, 3: PTFE spacer, 4: BDD plate anode or 5: Pt plate anode, **(b)** side view of assembled electrochemical cell working in 2-electrode configuration, **(c)** front view of thin-film electrochemical reactor working in 2-electrode configuration and **(d)** side view of the cell working under 3-electrode configuration.

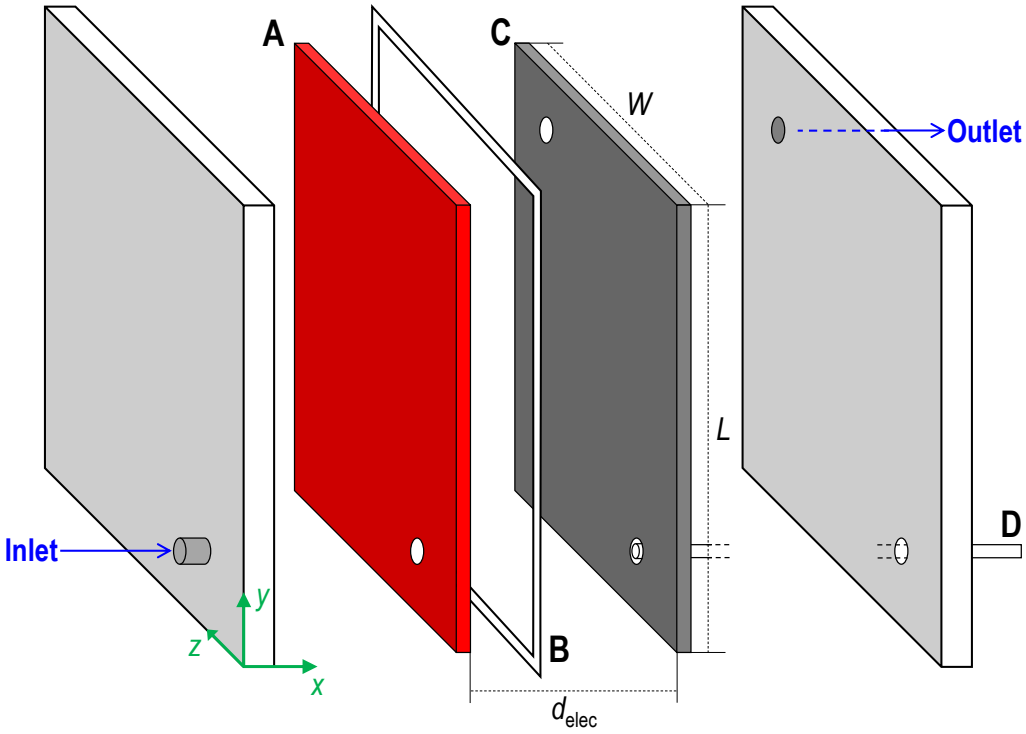

Fig. III.2. An exploded view of the parallel-plate electrochemical reactor. A: anode or counter electrode, B: PTFE spacer acting as interelectrode separator, C: cathode or working electrode, D: Ag-AgCl reference electrode, d_{elec}: interelectrode distance, *W*: width and *L*: length of electrodes.

III.3.2. Pretreatment of electrodes

Prior to utilization, stainless steel and graphite plates were preconditioned chemically by soaking them in 300 mL of sulfuric acid solution at 0.25 M overnight to get rid of possible remaining electro-precipitate. Additionally, the graphite was pretreated electrochemically to remove plausible deposition residue in the pores. 0.25 M of sulfuric acid was used as electrolyte, the graphite plate was positioned as anode, whilst a carbon felt (Mersen, Gennevilliers, France) served as cathode. The graphite anode was oxidized at 300 mA using a current generator and the oxidation pretreatment lasted an hour. Meanwhile, the carbon paper was used as received without pretreatment. Carbon paper was cut to take similar form as other cathodes as illustrated in **Fig. III.3**. Each carbon paper electrode was used only once, to ensure repeatability.

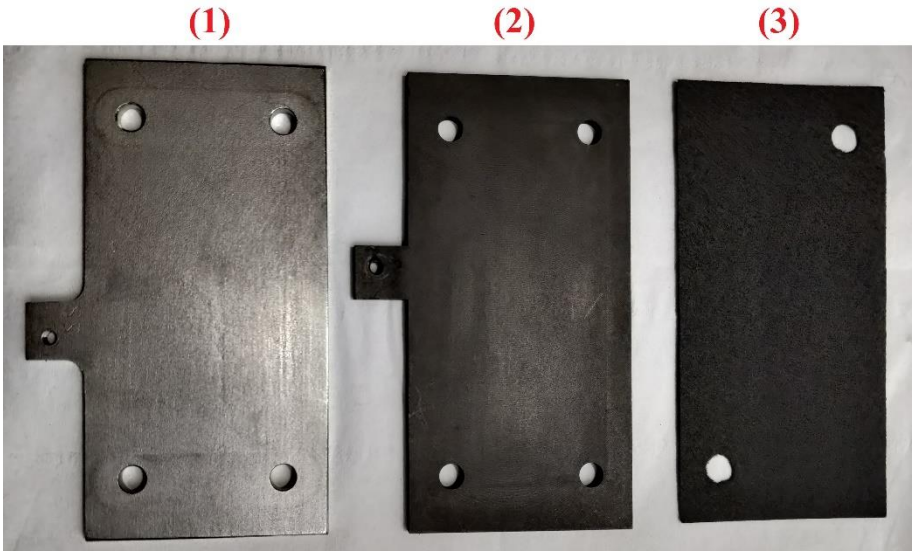

Fig. III.3. **(1)** Stainless steel, **(2)** graphite and **(3)** carbon paper cathodes.

III.3.3. Post treatment and recovery process

After each experiment, sulfuric acid solution of 0.25 M was used to thoroughly wash and recover precipitates occurring in different compartments of the experimental pilot. Anode was immersed in 50 mL of the acidic solution for 30 min. 300 mL of acidic solution was recirculated inside the experimental pilot plant during 1 h. Another 300 mL of 0.25 M sulfuric acid solution was used to immerse cathode overnight. This step served as both post-treatment as well as pretreatment of the cathode regeneration for the next experiment. The purpose was to re-dissolve the mineral deposits back into ionic form by lowering the pH. For recovery process, the acid washing solution of different compartments were then filtered through Phenex^{TM} regenerated cellulose 0.45 µm filter (Phenomenex, Le Pecq, France) and were analyzed by inductively coupled plasma optical emission spectroscopy (ICP-OES) to measure the Ca and Mg concentrations. Knowing different concentrations of cations in different compartments of experimental pilot, mass balance of cations was performed to observe the distribution of mineral precipitates formed in and out of the electrochemical reactor in addition to attesting a quasi-complete recovery of cations.

Mass balance and percentage recovery of *i* elements (Ca and Mg) are defined in **Eq. (III.1)** and **Eq. (III.2)**:

$$m_{i,recovered} = m_{i,fin} + m_{i,anode} + m_{i,cathode} + m_{i,tube} \quad \text{(III.1)}$$

$$\left(m_{i,recovered} \,/\, m_{i,init}\right) \times 100 = \%\, recovery \quad \text{(III.2)}$$

where $m_{i,recovered}$ is the total mass (in mg) of *i* recovered from different compartments, $m_{i,init}$ the initial mass of *i* element in electrolyte before electrolysis, $m_{i,fin}$ the mass of *i* that remains in the

electrolyte at the end of electrolysis, $m_{i,anode}$ the mass of *i* recovered from the surface of anode, $m_{i,cathode}$ the mass of *i* recovered from the surface of cathode and $m_{i,tube}$ the mass of *i* recovered from the surface of pilot tubing.

III.4. Analytical methods

III.4.1. Inductively coupled plasma optical emission spectrometry (ICP-OES)

Ca and Mg elemental concentrations were monitored using ICP-OES Thermo iCAP 6000 (Thermo Fisher, Noisy-Le-Grand, France). Collected samples were filtered using Phenex^{TM} 0.45 µm filter and were dissolved in 0.5 M H_2SO_4 background matrix inside ICP tube with 10 mL capacity. Using ICP-OES, the samples were nebulized, vaporized, atomized, ionized and excited thermally by means of argon plasma and ceramic torch. A radio-frequency generator produced a frequency of 1,100 kHz to attain a temperature up to 10,000 K. They were then detected and quantified by optical emission spectrometer at wavelengths of 279.55 nm, 280.27 nm and 285.21 nm for Mg and 317.93 nm, 318.12 nm and 422.67 nm for Ca. The calibration was done using external calibration method. Standard solutions ranging from 0.5 to 5 mg L^{-1} Mg as well as from 5 to 50 mg L^{-1} Ca were prepared from the Ca, K, Mg and Na multi-element 1000 µg mL^{-1} standard solution. Control solutions with known concentrations of Mg and Ca were analyzed every 10 analyses of samples to check for any drift in instrument measurement.

III.4.2. TOC/TN analysis

Total inorganic carbon (TIC), total organic carbon (TOC) and total nitrogen (TN) were measured using Shimadzu V_{CSH} TOC coupled to TNM-1 analyzer (Marne-La-Vallée, France). The analyzer was equipped with Shimadzu ASI-V autosampler (Marne-La-Vallée, France) that could accommodate 68 40 mL vials and automate analysis process. The samples were filtered and diluted accordingly before being stored in TOC glass vial (40 mL capacity). TIC was programmed to be analyzed separately with the TOC and TN. For the TIC analysis, a small amount of hydrochloric acid was added to acidify the sample (pH < 3). All carbonates in the sample were then converted to carbon dioxide (CO_2). The acidified sample was sparged with carrier gas (purified air) to volatilize the converted CO_2. It was dehumidified in a dehumidifier before passing through halogen scrubber into a sample cell of a non-dispersive infrared detector (NDIR). The NDIR analog signal was converted to TIC concentration by intermediary of TIC calibration curve. A calibration curve was previously performed via an autodilution program of the V_{CSH} TOC instrument. A series of TIC standard solutions varying between 1, 2, 5, 10, 12.5, 25 and 50 mg-C L^{-1} were analyzed to establish the curve. Next, the measurement of TOC and TN were carried out simultaneously. Due to relatively elevated

inorganic carbon content in comparison to organic carbon in all investigated effluents throughout this thesis, TOC was analyzed following the non-purgeable organic carbon (NPOC) procedure. Furthermore, volatile organic species was not present in the synthetic effluent as well as in the WWTP effluent. Using this method, a small quantity of hydrochloric acid was added into the sample and it was sparged with purified air to chase out the CO_2. As a result, all inorganic carbon content of the sample was eliminated. The remaining organic carbon was carried by the carrier gas (purified air) into a catalyst-filled combustion tube and heated to 720 °C. The sample was decomposed into CO_2. The combustion products were cooled, dehumidified and passed through the halogen scrubber. The CO_2 was measured by NDIR and the signal was converted into NPOC concentration by means of NPOC calibration curve. A NPOC calibration curve was established between 0.5 and 10 mg-C L^{-1} employing TOC commercial standard solution and using autodilution program. When the sample was introduced into the catalytic combustion chamber at 720 °C, if nitrogenous compounds were present, they were decomposed into nitrogen monoxide. The carrier gas then containing nitrogen monoxide was cooled and dehumidified before being sent into a chemiluminescence gas analyzer. The nitrogen monoxide detection signal was converted into TN quantification by intermediary of a TN calibration curve. It was previously established using TN standard solutions, whose concentrations varied between 1, 2, 5, 10, 16.67, 25 and 30 mg-N L^{-1} autodiluted by the instrument.

III.4.3. Chromatography

III.4.3.1. Ionic chromatography

NO_2^-, NO_3^-, Cl^-, ClO_2^-, ClO_3^-, ClO_4^- and SO_4^{2-} anion concentrations were measured via ionic chromatography Dionex™ ICS-6000 Capillary HPIC™ (Thermo Scientific, Noisy-Le-Grand, France). Standard solutions containing each anion of known concentrations were prepared from their corresponding commercial standard solution of 1000 µg mL^{-1}. The range of calibration for each anion is given as follow. NO_2^-, ClO_2^- and ClO_3^- were calibrated from 0.5 to 40 mg L^{-1}, NO_3^- from 0.5 to 30 mg L^{-1}, Cl^- was calibrated from 1 to 300 mg L^{-1} while SO_4^{2-} from 1 to 480 mg L^{-1}. AS19 IC Dionex™ IonPac™ anion-exchange column (25 cm × 4 mm) (Thermo Scientific, Noisy-Le-Grand, France) equipped with AG19 Dionex™ IonPac™ column guard (Thermo Scientific, Noisy-Le-Grand, France) was used. The pump worked in isocratic mode and the eluent flow rate was set at 1 mL min^{-1}. The autosampler tray was regulated at 20 °C, the column of detector compartment was maintained at 30 °C and the suppressor of conductivity detector was regulated at 35 °C. All samples were filtered using Phenex™ 0.45 µm filter and kept inside HPLC 1.5 mL vial prior to analysis.

III.4.3.2. High performance liquid chromatography – photo diode array detection (HPLC-PDA)

HPLC-PDA was employed to quantify the evolution of tylosin concentration during the EAOP treatment. The collected sample was filtered using Phenex^{TM} 0.45 µm filter, undiluted and stored in HPLC 1.5 mL vial. Tylosin calibration curve was established using tylosin solution containing 0.5, 1, 2, 5, 7.5, 10 and 20 mg L^{-1} tylosin. The HPLC chain consisted of pump unit, column oven, autosampler section and detection unit. Kinetex® reversed phase C18 column with 2.6 µm and 100 Å particle and pore sizes respectively, 4.6 mm in internal diameter and 100 mm in length (Phenomenex, Le Pecq, France) was the core of the separation technique. The pump worked in binary gradient mode pumping 35% of solvent A (ultrapure water plus 1% v/v formic acid) and 65% of solvent B (acetonitrile). The eluent flow rate was 0.6 mL min^{-1}. The oven, in which the column was kept, was operated at 25 °C. A thermo-regulated rack was used for sampling. Needle rinse mode was programmed before and after aspiration and each dip lasted 3 s. Autosampler chamber was set at 20 °C during analysis and it switched to 4 °C when the analysis ended for proper samples storage. 50 µL of sample was injected for tylosin concentration analysis. The HPLC was coupled to a PDA detector. The detector cell unit was set at 30 °C. UV absorbances at the wavelengths ranging from 190 to 350 nm were registered. The maximal absorbance of tylosin molecule was recorded at 290 nm.

III.4.4. Spectrophotometry

Quantification of NH_4^+, active chlorine and PO_4^{3-} were performed using a HACH spectrophotometer (Lognes, France). The colorimetric quantification of NH_4^+ was done with the Nessler method (Method 8038, 0.02 to 2.50 mg NH_3-N L^{-1}) and that of free chlorine by DPD method (N,N diethyl-p-phenylenediamine) (Method 8021, 0.02 to 2.00 mg-Cl_2 L^{-1}). The PhosVer3 method (ascorbic acid) (Method 8048, 0.02 to 2.50 mg-PO_4^{3-} L^{-1}) was used to dose PO_4^{3-}.

Hydrogen peroxide (H_2O_2) concentration was measured via H_2O_2-Ti^{4+} complexation method **[1]**. 100 µL of titanium (IV) oxysulfate sulfuric acid solution was put inside a glass vial tube before adding 4 mL of sample to be analyzed. If H_2O_2 was present, the mixture gave out a yellowish color. A UV-2600 spectrophotometer (Shimadzu, Marne-La-Vallée, France) was used to detect maximum absorbance of the complex at 410 nm wavelength. H_2O_2 concentration was deduced according to the Beer-Lambert law (H_2O_2 molar extinction coefficient of 43 M^{-1} cm^{-1}) from a calibration curve established using a series of H_2O_2 standard solutions with concentrations varying from 0.01 to 1 mM.

Fluorescence spectrophotometry was performed to inspect the presence of dissolved organic matter in the tested effluent. Fluorescence spectrophotometer F-2500 (Hitachi, Düsseldorf, Germany) was

used to achieve the purpose. 5 mL of sample was filled inside quartz cuvette for the analysis. Wavelength scan operation, in synchronous scan mode between 230 to 600 nm at 300 nm min^{-1}, was performed for each sample. The fluorescence intensity of organic content of the effluent in function of excitation wavelength was then captured.

III.4.5. Scanning electronic microscopy (SEM) coupled to energy dispersive X-ray (EDX) analysis

Images of electro-precipitates on carbon paper cathode were taken using a SEM JEOL JSM-6490 (Croissy-sur-Seine, France) coupled with EDX analysis. The latter allowed determining the elemental analysis of electro-precipitates. The SEM scan was done on carbon paper because only this cathode material could be cut to follow the 3 cm diameter SEM metal sampler, without affecting the deposits. Prior to SEM scan, a cut carbon paper sample was fixed onto the metal sampler with the help of a double-sided carbon adhesive. The sample surface was then metalized by means of gold nanoparticles using JEOL JFC-1100 Ion Sputter (Croissy-sur-Seine, France). During SEM measurements, the electronic beam was set at 5 kV accelerator volt. The image magnification varied between 80× to 1500×. For EDX elemental analysis, the accelerator volt was set to 20 kV using a magnification factor of 400×.

III.4.6. Electrochemical methods

A potentiostat (Ametek, Massy, France) was equipped with a PMC-1000 channel. It could perform both direct current (DC) and alternative current (AC) experiments up to $\pm$10 V and $\pm$2 A respectively. Owing to the integration of frequency response analyzer (FRA) to the potentiostat, electrochemical impedance spectroscopy (EIS) could be carried out between 10 µHz to 1 MHz. It offered AC voltage amplitude between 0.1 to 1000 mV root mean square (RMS).

III.4.6.1. Chronoamperometry and chronopotentiometry

The PMC-1000 potentiostat allowed chronoamperometry and chronopotentiometry experiments by applying either fixed potential or fixed current, respectively. In either case, Ag-AgCl reference electrode was used. Chronoamperometry experiments were conducted by applying a constant potential of -1.6 V/Ag-AgCl under different electrochemical reactor setups. The role of the applied electrode potential was investigated during the study. Meanwhile, chronopotentiometry experiments were performed under multiple reactor configurations by varying pairs of electrodes as well as d_{elec}. The purpose was to get the corresponding values of cathode and anode applied potentials. For that

purpose, a fixed current of either -200 or +200 mA was applied on the targeted working electrode under the tested cell configuration.

III.4.6.2. Cyclic voltammetry (CV) and linear scan voltammetry (LSV)

CV and LSV are powerful tools to study the electrochemical behavior of an electrolyte inside a specific electrochemical reactor. They involve a sweeping of a range of potential, at a certain scan rate and the intensity response of the electrochemical system is recorded. A voltammogram is the outcome of a CV or LSV measurement. Different ranges of potential sweeping as well as different scan rates were used depending on the objective of the study. In the mass transfer characterization study from submillimetric into millimetric electrochemical reactor, the potential was swept between 0.2 to -1.6 V/Ag-AgCl at a scan rate of 2.5 mV s^{-1} **[2, 3]**. The electrochemical behavior of investigated effluents inside different electrochemical reactor configurations, LSV was performed sweeping a potential range of 0.5 to -1.8 V/Ag-AgCl at 10 mV s^{-1} scan rate. Elsewhere, during the estimation of electroactive surface of electrodes, CV was carried out between 0.6 to -0.8 V/Ag-AgCl with using a scan rate of 10 mV s^{-1} **[4, 5]**.

III.4.6.3. Electrochemical impedance spectroscopy (EIS)

The EIS technique is based on small amplitude AC perturbations at different AC frequencies and the analysis of the system response gives out the information on electrochemical and physical parameters, reactions kinetic as well as the surface morphology at the electrode/electrolyte interface. In this thesis, EIS was conducted in galvanostatic mode covering a frequency range between 100 kHz to 100 mHz. The perturbation amplitude (ΔI_{AC}) varied between 5 and 10 mA RMS according to EIS spectra with 10 points per decade (ppd). The EIS analysis was programmed before electrolysis (t = 0) as well as at 0.5, 1, 2, 3, 4 and 5 h of galvanostatic electrolysis at an applied 200 mA (i.e. 4 mA cm^{-2}) DC. The EIS parameters were extracted by means of equivalent electrical circuit (EEC) model using ZSimpwin® commercial software.

III.5. Modeling software

III.5.1. Kramers-Kronig test

Kramers-Kronig transform (KKT) method was used to check the applicability of EIS technique by comparing the experimental EIS plot with a mathematical-conformed spectrum. To run the KKT test, two software were used: (1) KKT program offered by the Zsimpwin® and (2) the KKT program developed by Dr. Bernard Boukamp from the University of Twente **[6, 7]**. If the two spectra coincided

within acceptable deviation margin (evaluated by the software in chi-squared residues (χ^2)), the experimental EIS spectra were validated.

III.5.2. Zsimpwin®

EIS raw data were collected from VersaStudio® which was the interface for Ametek® potentiostat. Using Zsimpwin®, the EIS parameters were extracted from the raw data by intermediary of EEC model.

III.5.3. Aquasim©

Aquasim© provides an interface where chemical reactions, physicochemical equilibriums and constants, mathematical equations as well as kinetic laws of multiple species can be easily inserted and accounted for **[8]**. Furthermore, the software already comes with the embedded codes to visualize the plot of the resulting model curve and can be compared directly with the experimental one. Thus, Aquasim© was used to complement the mathematical models developed in this thesis. It was used to simulate the evolution of Ca^{2+} and Mg^{2+} concentrations during their participation in the electro-precipitating reactions.

III.6. Fitting evaluation criteria between experimental and modeling data

The fitting between experimental data and theoretical model was evaluated using either root mean square error (RMSE), model efficiency (ME) and/or index of agreement (IOA) given as **Eq. (III.3)**, **Eq. (III.4)** and **Eq. (III.5)**, respectively **[9]**:

$$RMSE = \sqrt{\frac{\sum_{i=1}^{K}(y_i - y_i')^2}{K}} \quad \text{(III.3)}$$

$$ME = 1 - \frac{\sum_{i=1}^{K}(y_i - y_i')^2}{\sum_{i=1}^{K}(y_i - y_M)^2} \quad \text{(III.4)}$$

$$IOA = 1 - \frac{\sum_{i=1}^{K}(y_i - y_i')^2}{\sum_{i=1}^{K}(|y_i' - y_M| + |y_i - y_M|)^2} \quad \text{(III.5)}$$

where K is the number of steps of checked values, y_i' is the experimental value, y_i is the corresponding simulated value and y_M is the average of simulated value.

References

[1] F. Sopaj, N. Oturan, J. Pinson, F.I. Podvorica, M.A. Oturan, Effect of cathode material on electro-Fenton process efficiency for electrocatalytic mineralization of the antibiotic sulfamethazine, Chemical Engineering Journal, 384 (2020) 123249.
[2] J.R. Selman, C.W. Tobias, Mass-transfer measurements by the limiting-current technique, in: T.B. Drew, G.R. Cokelet, J.W. Hoopes, T. Vermeulen (Eds.) Advances in Chemical Engineering, Academic Press, 1978, pp. 211-318.
[3] P. Cañizares, J. García-Gómez, I. Fernández de Marcos, M.A. Rodrigo, J. Lobato, Measurement of mass-transfer coefficients by an electrochemical technique, Journal of Chemical Education, 83 (2006) 1204.
[4] T.X.H. Le, M. Bechelany, S. Lacour, N. Oturan, M.A. Oturan, M. Cretin, High removal efficiency of dye pollutants by electron-Fenton process using a graphene based cathode, Carbon, 94 (2015) 1003-1011.
[5] E. Mousset, Z. Wang, J. Hammaker, O. Lefebvre, Physico-chemical properties of pristine graphene and its performance as electrode material for electro-Fenton treatment of wastewater, Electrochimica Acta, 214 (2016) 217-230.
[6] B.A. Boukamp, A linear Kronig-Kramers transform test for immittance data validation, Journal of The Electrochemical Society, 142 (1995) 1885-1894.
[7] B.A. Boukamp, Electrochemical impedance spectroscopy in solid state ionics: recent advances, Solid State Ionics, 169 (2004) 65-73.
[8] P. Reichert, AQUASIM - a tool for simulation and data analysis of aquatic systems, Water Science and Technology, 30 (1994) 21.
[9] E. Mousset, S. Pontvianne, M.-N. Pons, Fate of inorganic nitrogen species under homogeneous Fenton combined with electro-oxidation/reduction treatments in synthetic solutions and reclaimed municipal wastewater, Chemosphere, 201 (2018) 6-12.

IV. Mineral cathodic electro-precipitation and its kinetic modeling in thin-film microfluidic reactor during advanced electro-oxidation process

(Published as scientific article, reference: *Electrochimica Acta 387 (2021) 138487*)

IV.1. Introduction

The occurrence of electro-precipitation is a major drawback within the application of EAOPs and more generally electrolysis to treat wastewater. While treating water of varying concentrations of calcium (Ca^{2+}) and magnesium (Mg^{2+}) ions), a layer of insulating deposit can be formed on the surface of cathode. Despite low concentration of Ca^{2+} and Mg^{2+} in an effluent, in case of the operation of electrochemical cells in continuous-mode such, most of the time, encountered in industrial applications, the deposit progressively passivates the whole electrode surface. Sequencing polarity inversion might be applied as counter-measure but it might take a toll on treatment efficacy, duration of operation and overall operational cost. Furthermore, cathode in operation must be able to tolerate high anodic current during the inverted polarization step given the fact that some cathode materials have been reported to be corroded in such conditions **[1]**. Upon treating water with high Ca^{2+} and Mg^{2+} content, sequencing inversion of polarity might not be the best strategy since the passivation of electrode occurs anyhow. Eventually, without regular intervention, electrochemical cells become very inefficient or probably are no longer operational.

The mechanism of formation of deposits has been well established in the literature **[2, 3]**. When the electrode is polarized at a sufficiently negative potential, dissolved O_2 is reduced to hydroxide ions (OH^-) according to **Eq. (II.9)** resulting in an increase of local pH **[4, 5]**.

$$O_2 + 2H_2O + 4e^- \rightarrow 4OH^- \qquad \text{(II.9)}$$

At a more cathodic potential, reduction of solvent (H_2O) can take place according to **Eq. (II.10)**, which also produces hydroxide ions as well as H_2.

$$2H_2O + 2e^- \rightarrow H_2 + 2OH^- \qquad \text{(II.10)}$$

As shown in **Eqs. (I.11)** and **(IV.1)**, in the presence of Mg^{2+} and Ca^{2+}, deposits of hydroxide can be produced. Moreover, the pH increment also shifts thermodynamic ratio of carbonates/bicarbonates (**Eq. (I.12)**) favoring the production of carbonate scales as written in **Eqs. (I.13)** and **(IV.2)**.

$$Mg^{2+} + 2OH^- \leftrightarrow Mg(OH)_2 \quad \text{(II.11)}$$

$$OH^- + HCO_3^- \leftrightarrow H_2O + CO_3^{2-} \quad \text{(II.12)}$$

$$Ca^{2+} + CO_3^{2-} \leftrightarrow CaCO_3 \quad \text{(II.13)}$$

$$Ca^{2+} + 2OH^- \leftrightarrow Ca(OH)_2 \quad \text{(IV.1)}$$

$$Mg^{2+} + CO_3^{2-} \leftrightarrow MgCO_3 \quad \text{(IV.2)}$$

Different studies have already demonstrated the formation of aforementioned deposits in electrochemical cell while operating with different types of water with varying contents of Ca^{2+} and Mg^{2+}. They are characterized by their source and application domain: synthetic water for cooling system in cooling towers and oil refineries **[6, 7]**, artificial **[8, 9]** and natural groundwater **[10, 11]**, mineral potable water **[12, 13]**, artificial **[3, 14-16]** and real seawater **[17, 18]**. Interestingly, the reported works were all conducted on the classical rotating disk electrode (RDE) possessing effective exposed surface area of 0.2 cm^2 **[3, 8-12, 14, 17]**, 0.5 cm^2 **[6, 7, 19]**, 1 cm^2 **[16, 20, 21]** and 1.5 cm^2 **[15]**. Either carbon steel, gold or stainless steel was used as the working electrode playing the role of cathode. To the best of authors' knowledge, the study of electro-precipitation outside aforementioned configuration is scarce.

Due to the omnipresence of calcium and magnesium in water, further study to understand and more particularly to avoid the formation of insulating deposition at larger scale seems primordial. It is within this context that a detailed investigation has been carried out to understand the influence of electrolytic composition towards the formation of mineral deposits on electrode surface during EAOP. The objective is to establish operating conditions in-which scaling does not occur, or, is minimized owing to the benefits attributed by a microfluidic cell. Moreover, addition of chemical reagents is no longer compulsory in microreactor; hence, interference possibly originating from the supporting electrolyte is avoided. Magnesium hydroxide ($Mg(OH)_2$), calcium carbonate ($CaCO_3$) and magnesium carbonate ($MgCO_3$) deposits are studied due to the ubiquity of Mg^{2+}, Ca^{2+} and HCO_3^- /CO_3^{2-} ions in water sources. Results presented in this chapter are the first to elucidate the phenomenon of passivation in microfluidic reactor, a configuration very distinctive to those reported in the literature where RDE were used as working electrode. The geometry and configuration of microfluidic cell adopted in this work are closely representative to reactors used in industries. Notably, the difference between electrode surface in this present study is 25 to 250 times bigger compared to RDEs (0.2 to 2 cm^2) used in the literature. The present design is more adapted for further applications on a larger scale. Synthetic water is used in this work, but it closely mimics the average characteristic of effluent of municipal WWTPs particularly the concentration of Ca^{2+}, Mg^{2+} and

carbonates as well as pH and ionic conductivity. Furthermore, it is the first time that the influence on electro-precipitation of hydroxyl radicals produced at high O_2 evolution overvoltage anode is studied. Novel theoretical models are developed in this paper where the objectives are two-fold; first, assumptions made to establish the models lead to a better understanding of the mechanism of mineral electro-precipitation if they occur. Second, these models are the first to be reported to predict the evolution of electro-precipitating ions, particularly under the configuration of thin-film microfluidic reactor.

IV.2. Experimental section

Parallel-plate electrochemical cell with BDD and stainless steel as anode and cathode respectively was used. It was configured under submillimetric condition by using 500 µm d_{elec} between anode and cathode. The electrolyte was recirculated at 100 mL min^{-1}. Effluent with and without carbonates contained sources of Ca^{2+} (150 mg L^{-1}) and Mg^{2+} (5 mg L^{-1}) dissolved in ultrapure water. Effluent with carbonates contained a concentration of 60 mg-C L^{-1}. Initial values of pH and ionic conductivity were always adjusted to 7.6 and 1000 µS cm^{-1} respectively. A small quantity of sodium sulfate (1.4 to 5 mmol L^{-1}) was added when required in order to reach a constant ionic conductivity and strength (0.02 mol L^{-1}) for suitable comparison. The synthetic solution was representative to the average characteristics of municipal WWTP effluent.

Evolutions of Ca and Mg elements concentration were monitored using ICP-OES, SO_4^{2-} evolution was followed using ionic chromatography and total inorganic carbon (TIC) was measured using TOC/TN analyzer. H_2O_2 concentration was dosed using complexing H_2O_2-Ti^{4+} spectrophotometry method. LSV, chronoamperometry and chronopotentiometry were carried out via Ametek potentiostat connected to the electrochemical cell. The electrode potential was reported against Ag-AgCl RE.

IV.3. Modeling

IV.3.1. Electrolyte containing Mg^{2+} and Ca^{2+}

Mg^{2+} and Ca^{2+} react with OH^- to produce precipitates of $Mg(OH)_2$ and $Ca(OH)_2$ when the product of concentrations of both cations with OH^- exceeds the constants of solubility of $Mg(OH)_2$ ($K_{S,Mg(OH)_2}$) ($K_{S,Mg(OH)_2}$ = 5.61 × 10^{-12} **[22, 23]**) and of $Ca(OH)_2$ ($K_{S,Ca(OH)_2}$) ($K_{S,Ca(OH)_2}$ = 5.00 × 10^{-6} **[22, 23]**) respectively. Knowing Mg^{2+} and Ca^{2+} concentrations in the system, the concentration of OH^- at which its product reaches the $K_{S,Mg(OH)_2}$ and $K_{S,Ca(OH)_2}$ values, respectively, can be calculated. It is noted as critical OH^- concentration (OH^-_{crit}). During the electrolysis, OH^- ions are produced on cathode by

reduction of either dissolved O_2 via 4-electrons reaction (**Eq. (II.9)**) and/or water via 2-electrons reaction (**Eq. (II.10)**). Since both reactions took place in parallel on cathode in our system under the applied current densities, they have been considered as competing reactions. η_{O_2} and η_{H_2O} terms were used to proportionate the current efficiency as a result of the reduction of O_2 and H_2O respectively. The rate of production of OH^- (r_{OH^-}, in mol m^{-2} s^{-1}) on cathode in batch mode can thus be written as in **Eq. (IV.3)**:

$$r_{OH^-} = + \frac{d[OH^-]}{dt} = \frac{\nu_{O_2}\, j_{app}}{n_{O_2}\, F}\eta_{O_2} + \frac{\alpha\, \nu_{H_2O}\, j_{app}}{n_{H_2O}\, F}\eta_{H_2O} \qquad \text{(IV.3)}$$

where ν_{O_2} and ν_{H_2O} are the stoichiometry coefficient of OH^- via reaction of reduction of O_2 (**Eq. (II.9)**) and H_2O (**Eq. (II.10)**) respectively, while n_{O_2} and n_{H_2O} are their number of electrons involved in those faradaic reactions, j_{app} is the applied current density in A m^{-2} and F is the Faraday constant (96485 C mol^{-1}). α is denoted as OH^- hindrance factor ($\alpha < 1$) assigned to the faradaic production of OH^- which occurs concomitantly with physical evolution of gas bubbles on cathode surface at high j_{app}. In accordance to **Eq. (II.10)**, H_2 gas also evolves when H_2O is reduced to OH^-. H_2 gas evolution is more intense when higher current density value is used, according to the Faraday's law. Gas evolution on cathode surface contributes to two major consequences; firstly, less surface area could be available for mineral deposition on cathode surface **[24]**. Secondly, it could promote detachment of deposits occurring on the electrode **[25, 26]**.

On the surface of cathode, OH^- ions are produced abundantly and continuously. Water is the solvent of electrolyte thus its electrochemical reduction is limitless. Meanwhile, dissolved O_2 are not only consumed on cathode (**Eq. (II.9)**), but it is also concomitantly produced on anode through water oxidation (**Eq. (II.3)**).

$$2H_2O \rightarrow O_2 + 4H^+ + 4e^- \qquad \text{(II.3)}$$

In microfluidic configuration, the distance between cathode and anode is very small thus the replenishment of dissolved O_2 could take place continuously **[27]**. As a result, once OH^-_{crit} is reached, OH^- concentration is considered constant and it does not vary whilst reacting with Mg^{2+} and Ca^{2+} because the concentration of OH^- is significantly larger and in excess compared to the cations concentrations. In addition, it is assumed that Mg^{2+} and Ca^{2+} were not reduced or oxidized by direct electrochemical reduction or oxidation, so that their oxidation state remained constant all along the electrolysis **[28]**.

Hence, according to **Eqs. (I.11)** and **(IV.1)**, the rates of reaction of Mg^{2+} and Ca^{2+} (in mol m^{-2} s^{-1}) can be written according to **Eq. (IV.4)** and **Eq. (IV.5)** respectively:

$$r_{Mg^{2+}} = -r_{Mg(OH)_2} = -k_{Mg(OH)_2}[Mg^{2+}][OH^-]^2 \quad \text{(IV.4)}$$

$$r_{Ca^{2+}} = -r_{Ca(OH)_2} = -k_{Ca(OH)_2}[Ca^{2+}][OH^-]^2 \quad \text{(IV.5)}$$

where $k_{Mg(OH)_2}$ and $k_{Ca(OH)_2}$ are the heterogeneous third order rate constants regarding the reaction of precipitation of $Mg(OH)_2$ and $Ca(OH)_2$ respectively in $m^7\ mol^{-2}\ s^{-1}$, while $[Mg^{2+}]$, $[Ca^{2+}]$ and $[OH^-]$ are the molar concentration (in $mol\ m^{-3}$) of Mg^{2+}, Ca^{2+} and OH^- ions, respectively.

IV.3.2. Electrolyte containing Ca^{2+} and CO_3^{2-}

Ca^{2+} reacts with CO_3^{2-} to form $CaCO_3$ precipitates when the product of concentrations of both ions exceeds the constant of solubility of $CaCO_3$ ($K_{S,CaCO_3}$) ($K_{S,CaCO_3}$ = 3.36 × 10^{-9} **[23, 29-31]**). Supersaturation degree (*SD*) of $CaCO_3$ is defined in **Eq. (IV.6)** and follows by its supersaturation index (*SI*) in **Eq. (IV.7) [32, 33]**.

$$SD = \frac{[Ca^{2+}]\,[CO_3^{2-}]}{K_{S,CaCO_3}} \quad \text{(IV.6)}$$

$$SI = log_{10}(SD) \quad \text{(IV.7)}$$

Thermodynamically, $CaCO_3$ can precipitate when *SD* > 1 (or *SI* > 0). Carbonates concentration can be estimated from TIC measurement that corresponds to the sum of all forms of inorganic carbon (**Eq. (IV.8)**):

$$\text{TIC} = [H_2CO_3] + [HCO_3^-] + [CO_3^{2-}] \quad \text{(IV.8)}$$

where H_2CO_3 is carbonic acid and HCO_3^- is bicarbonate ion.

The inorganic carbon species are linked together by acid dissociation constants K_{A1} and K_{A2} given in **Eqs. (IV.9)**–**(IV.10)**, respectively.

$$K_{A1} = \frac{[H^+]\,[HCO_3^-]}{[H_2CO_3]} \quad \text{(IV.9)}$$

$$K_{A2} = \frac{[H^+]\,[CO_3^{2-}]}{[HCO_3^-]} \quad \text{(IV.10)}$$

Their ratios are therefore governed by the solution pH. pK_{A1} and pK_{A2} values are 6.3 and 10.4 **[34]**, respectively. Under the range of our pH operating conditions and at the proximity of cathode surface, the quantity of H_2CO_3 is negligible and the expression of TIC can be simplified into **Eq. (IV.11)**.

$$\text{TIC} = [HCO_3^-] + [CO_3^{2-}] \quad \text{(IV.11)}$$

CO_3^{2-} concentration is related to the concentration of OH^- produced on cathode surface by its equilibrium with HCO_3^- in agreement with **Eq. (II.12)** and **Eq. (II.13)**. Hence, the evolution of interfacial CO_3^{2-} concentration ($[CO_3^{2-}]_{\text{int,t}}$) can be estimated from TIC values by combining **Eqs. (IV.3)**, **(IV.10)** and **(IV.11)** giving out an expression in **Eq. (IV.12)**.

$$[CO_3^{2-}]_{\text{int,t}} = \frac{K_{A2} \times TIC_t}{\frac{K_W}{[OH^-]_t} + K_{A2}} \quad \text{(IV.12)}$$

where K_{A2} and the concentration of interfacial CO_3^{2-}, OH^- and TIC are expressed in mol L^{-1} while the equilibrium constant of auto-ionization of water (K_W) is considered equaled to 10^{-14} at 25°C.

According to **Eq. (II.13)**, the rate of reaction of Ca^{2+} and CO_3^{2-} producing $CaCO_3$ can be defined as indicated in **Eq. (IV.13)**:

$$r_{Ca^{2+}} = r_{CO_3^{2-}} = -r_{CaCO_3} = -k_{CaCO_3}[Ca^{2+}][CO_3^{2-}]_{int} \quad \text{(IV.13)}$$

where r_i is in mol m^{-2} s^{-1}, k_{CaCO_3} is the heterogenous second order rate constant (in m^4 mol^{-1} s^{-1}) regarding the reaction of precipitation of $CaCO_3$. Identically to the Mg^{2+}/Ca^{2+} system (**Section IV.3.1**), OH^- accumulates at the vicinity of cathode during the electrolysis.

IV.3.3. Electrolyte containing Mg^{2+} and CO_3^{2-}

In absence of Ca^{2+}, Mg^{2+} can precipitate in the form of $Mg(OH)_2$ upon reaching OH^-_{crit} as well as $MgCO_3$ when the product of concentrations of Mg^{2+} and CO_3^{2-} exceeds thermodynamic solubility constant of $MgCO_3$ ($K_{S,MgCO_3}$) ($K_{S,MgCO_3}$ = 1.59 × 10^{-8} **[35]**). Local alkalization remains valid at the surface of cathode. Knowing the fact that Mg^{2+} could participate in the precipitation reactions of $Mg(OH)_2$ and $MgCO_3$, on top of kinetic law defined in **Eq. (IV.4)**, the rate of reaction of Mg^{2+} (in mol m^{-2} s^{-1}) can be rewritten in **Eq. (IV.14)** as follow:

$$r_{Mg^{2+}} = -r_{Mg(OH)_2} - r_{MgCO_3} = -k_{Mg(OH)_2}[Mg^{2+}][OH^-]^2 - k_{MgCO_3}[Mg^{2+}][CO_3^{2-}] \quad \text{(IV.14)}$$

where k_{MgCO_3} is the heterogeneous second order rate constant (in m^4 mol^{-1} s^{-1}) regarding the reaction of precipitation of $MgCO_3$.

IV.3.4. Electrolyte containing Mg^{2+}, Ca^{2+} and CO_3^{2-}

In the matrix of electrolyte containing Mg^{2+}, Ca^{2+} and CO_3^{2-}, both Mg^{2+} and Ca^{2+} can undergo precipitation in accordance to **Eqs. (II.11)** and **(IV.1)** and **Eqs. (II.13)** and **(IV.2)**. The phenomenon of local alkalization remains valid in this system.

In the presence of Mg^{2+}, depositing $Mg(OH)_2$ consumes OH^- over time. The cathodic production of OH^- in **Eq. (IV.3)** is modified taking into account this event as indicated in **Eq. (IV.15)**:

$$r_{OH^-} = + \frac{d[OH^-]}{dt} = \frac{\nu_{O_2}\, j_{app}}{n_{O_2}\, F}\eta_{O_2} + \frac{\alpha\, \nu_{H_2O}\, j_{app}}{n_{H_2O}\, F}\eta_{H_2O} - 2\, k_{Mg(OH)_2}[Mg^{2+}][OH^-]^2 \qquad \text{(IV.15)}$$

IV.3.5. Modeling software and fitting evaluation

Aquasim **[36]** was used to model the evolution of Mg^{2+}, Ca^{2+} and CO_3^{2-}. The fitting between experimental and modeled curve was evaluated using RMSE (**Eq. (III.3)**), ME (**Eq. (III.4)**) and IOA (**Eq. (III.5)**) provided in **Chapter 3**.

IV.4. Results and discussion

IV.4.1. Stability of anions in blank solutions using BDD or Pt anode

Preliminary experiments were conducted in the microfluidic reactor to check on the behavior of anions (SO_4^{2-} and HCO_3^-/CO_3^{2-}) during electro-oxidation in the absence of depositing elements. BDD and Pt anodes were used to verify the involvement of $^{\bullet}OH$ towards any oxidation of anions. The former is well-known for its high overpotential for oxygen evolution reaction (OER). Consequently, physi-sorbed $^{\bullet}OH$ are produced at anode vicinity **[37, 38]**. Contrastingly, the overpotential for OER with Pt anode is low. Thus $^{\bullet}OH$ is chemi-sorbed on the anode surface, making the radical not available **[39]**.

The evolution of concentration of SO_4^{2-} and TIC are depicted in **Fig. IV.1**. It has been noticed that the concentration of both anions remained constant throughout the entire electro-oxidation experiments whether BDD or Pt was used as anode. First deduction that can be made is that SO_4^{2-} and HCO_3^-/CO_3^{2-} anions were stable during the electro-oxidation process whatever the anode employed. It means that they will not interfere if there is occurrence of electro-precipitation on cathode surface. Secondly, under these applied conditions, the formation of oxidizing agent of $^{\bullet}OH$ did not inflict towards the degradation of SO_4^{2-} and HCO_3^-/CO_3^{2-} anions. Anode potential was measured to be +2.40 V/Ag-AgCl (or +2.60 V/SHE), which already hit the standard potential of formation of $^{\bullet}OH$ when 4 mA cm^{-2} is applied. The oxidation conditions were not strong enough to

oxidize SO_4^{2-} into peroxydisulfates ($S_2O_8^{2-}$) **[40]** and CO_3^{2-} into peroxydicarbonates ($C_2O_6^{2-}$) **[41, 42]** with $SO_4^{\bullet-}$ and $CO_3^{\bullet-}$ as intermediates, respectively. Moreover, anion of strong acid such as SO_4^{2-} is very unlikely to form complex with alkaline-earth cations such as Ca^{2+} and Mg^{2+} **[43]**. In overall, $^{\bullet}OH$ involvement in microfluidic reactor set-up did not lead to the oxidation of SO_4^{2-} and HCO_3^- /CO_3^{2-} anions in blank electrolytes during electro-oxidation experiments. In overall, the presence of $^{\bullet}OH$ in our applied microfluidic reactor conditions could thus be omitted from the developed theoretical models and was confirmed further in the next sections.

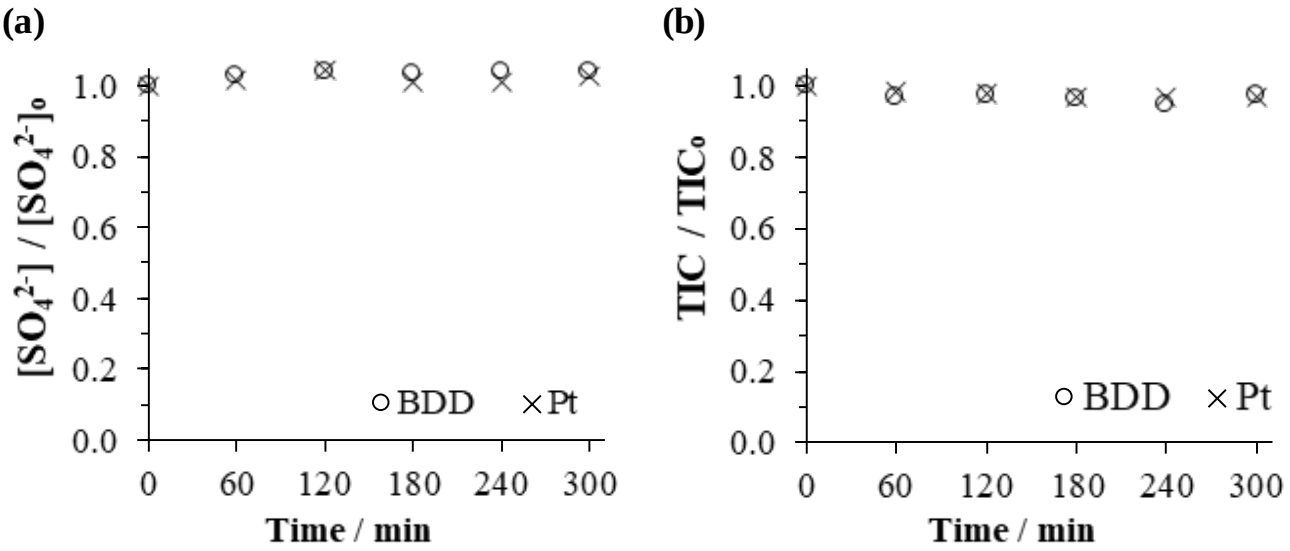

Fig. IV.1. Evolution of concentration of **(a)** SO_4^{2-} (in blank solution containing sulfates only) and **(b)** TIC (in blank solution containing carbonates only) during the electrolysis of blank solutions using BDD (○) or Pt (×) as anode. Cathode: stainless steel, ionic strength of both blank solutions: 0.02 mol L^{-1}, j_{app}: 4 mA cm^{-2} and d_{elec}: 500 µm.

IV.4.2. Local alkalization on cathode surface: reactions' selectivity between reduction of dissolved O_2 and water

According to **Eq. (II.9)** and **Eq. (II.10)** respectively, both dissolved O_2 and H_2O can undergo faradaic reduction generating OH^- (**Eq. (II.3)**). To identify the weight of contribution of dissolved O_2 to produce OH^- with respect to local alkalization phenomenon, tests in presence and absence of dissolved O_2 were conducted. Under the investigated micrometric distance, anodic activity might be involved in this selectivity, since H_2O could be also oxidized to O_2.

Figure IV.2 plots the evolution of concentration of Mg^{2+}, Ca^{2+} and TIC in the experiments with and without dissolved O_2. In both cases, the concentration of all species decreased regardless of presence of dissolved O_2. This indicates that the initial presence of dissolved O_2 was insignificant towards the phenomenon of local alkalization, and consequently towards the formation of deposits on cathode surface. Notably from **Fig. IV.2(a)** and **Fig. IV.2(b)**, it has been deduced that the source of OH^- ions

came mainly from reduction of water and not from dissolved O_2. A slight decrease in the electro-precipitation of Ca^{2+} in absence of dissolved O_2 was due to slightly lesser amount of OH^- participating in thermodynamic shift of HCO_3^-/CO_3^{2-} towards the formation of CO_3^{2-} (**Fig. IV.2(b)**). Thus, lesser extent of electro-precipitating $CaCO_3$ was observed.

Under theses setups, the concentration of electrogenerated H_2O_2 was measured to further study the contribution of dissolved O_2 reduction producing OH^- ions in accordance with **Eq. (II.4)**.

$$O_2 + 2H_2O + 2e^- \leftrightarrow H_2O_2 + 2OH^- \quad \text{(II.4)}$$

The H_2O_2 production was found to be very small (maximum concentration went up to 1.8 µmol L^{-1}, data not shown), whatever the applied current density. Most of H_2O_2 concentration values fell below the limit of quantification of the method, determined to be 0.8 µmol L^{-1}. This observation was attributed to the low H_2 evolution overvoltage on stainless steel cathode **[44]**. Similar poor production of H_2O_2 on stainless cathode was reported by Sopaj et al. **[45]**. They measured approximately 40 µmol L^{-1} of H_2O_2 under their experimental setup when 4.8 mA cm^{-2} was applied **[45]**. Unlike the configuration presented in our work, compressed air was continuously bubbled under their experimental setup to supply dissolved O_2 to promote the Fenton reaction, which explains the difference in measured H_2O_2 concentration.

η_{O_2} and η_{H_2O} in **Eq. (IV.3)** and **Eq. (IV.15)** were estimated via **Eqs. (IV.16)-(IV.17)** at each value of current density investigated in this work.

$$\eta_{O_2} = \frac{n_e F N_{O_2}}{I t} \quad \text{(IV.16)}$$

$$\eta_{H_2O} = 1 - \eta_{O_2} \quad \text{(IV.17)}$$

where n_e is the number of electrons exchanged in **Eq. (II.4)** (i.e., 2), N_{O_2} is the quantity of dissolved O_2 (in mol) reduced to H_2O_2 in **Eq. (II.4)**, I is the applied current (in A) and t is the electrolysis time (in s).

At 4 mA cm^{-2} (or 200 mA), the highest concentration of H_2O_2 (1.8 µmol L^{-1}) was found after 1 h of electrolysis. In 500 mL of electrolyte, knowing the fact that same number of moles of dissolved O_2 (N_{O_2}, in mol) is consumed to produce the number of moles of H_2O_2 ($N_{H_2O_2}$, in mol):

$$\eta_{O_2} = \frac{n_e F N_{O_2}}{I t} = \frac{2 \times 96485 \times 0.9 \times 10^{-6}}{0.2 \times 3600} \times 100 = 0.02\%$$

$$\eta_{H_2O} = 100 - \eta_{O_2} = 99.98\%$$

While at 0.4 mA cm^{-2} (or 20 mA), the highest concentration of H_2O_2 (1.18 µmol L^{-1}) was found after 1 h of electrolysis.

$$\eta_{O_2} = \frac{2 \times 96485 \times 0.59 \times 10^{-6}}{0.02 \times 3600} \times 100 = 0.16\%$$

$$\eta_{H_2O} = 100 - \eta_{O_2} = 99.84\%$$

Their values are regrouped in **Table IV.1**.

Table IV.1. Estimation of η_{O_2} and η_{H_2O} in faradaic production of OH^- on cathode.

j_{app} / mA cm^{-2}	N_{O_2} / µmol	CE_{O_2} / %	CE_{H_2O} / %
0.4	0.6	0.16	99.84
4	0.9	0.02	99.98

To conclude, local alkalization on cathode surface principally occurred due to the reduction of H_2O with only slight involvement of dissolved O_2 under our experimental setup. The latter was electrocatalytically reduced to OH^- with negligible production of H_2O_2 on stainless steel. Our proposed model takes into consideration this observed selectivity given by higher faradaic yield of η_{H_2O} in producing OH^- as deduced in **Table IV.1** when applied to **Eq. (IV.3)** and **Eq. (IV.15)**.

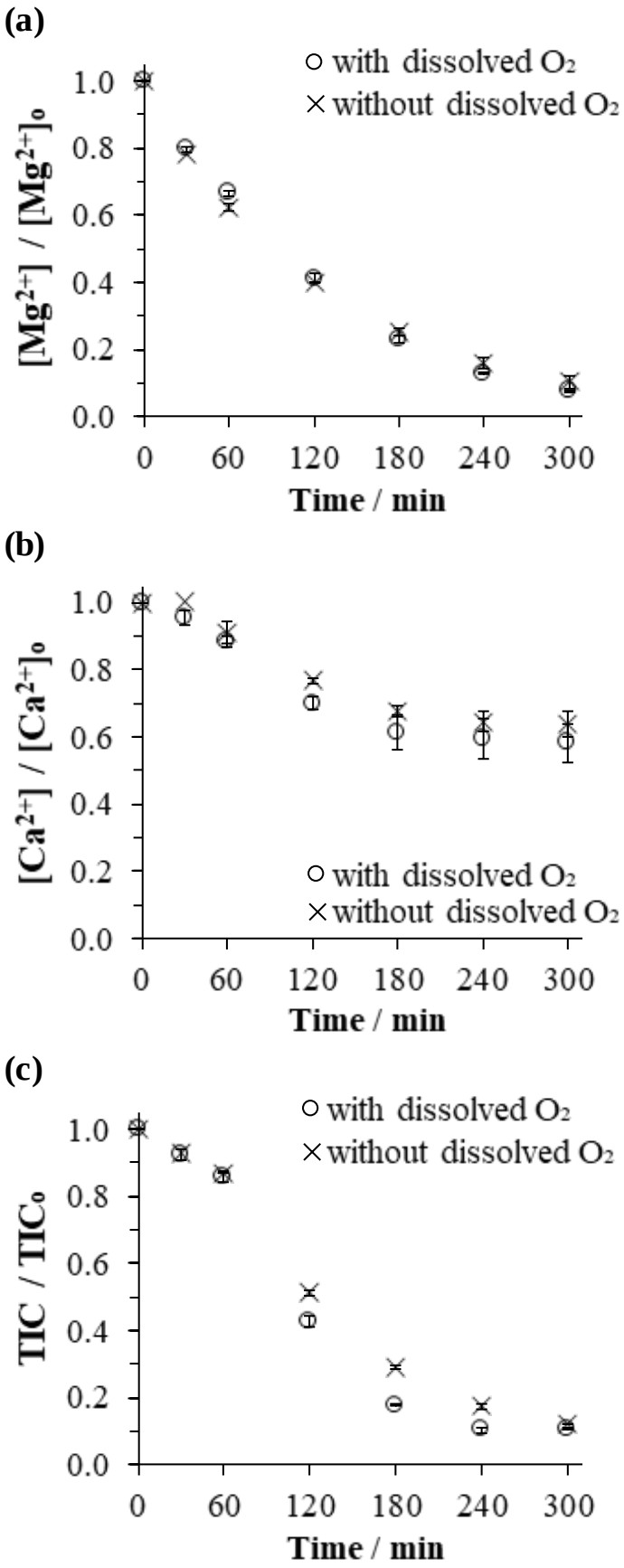

Fig. IV.2. Evolution of concentration of **(a)** Mg^{2+}, **(b)** Ca^{2+} and **(c)** TIC during the electrolysis of artificial effluent containing 150 mg L^{-1} of Ca^{2+}, 5 mg L^{-1} of Mg^{2+} and 60 mg-C L^{-1} of HCO_3^-/CO_3^{2-} in absence (×) (via bubbling with N_2 gas) and presence (○) of dissolved O_2 throughout the experiment. Anode: BDD, cathode: stainless steel, j_{app}: 4 mA cm^{-2} and d_{elec}: 500 µm.

IV.4.3. Influence of electromigration of ionic species

Although calcium and magnesium deposits are formed on the surface of cathode during electrolysis, Ca^{2+} and Mg^{2+} do not participate in direct electron transfer to yield Ca metal (Ca(s)) and Mg metal (Mg(s)) respectively. The reduction of Ca^{2+} and Mg^{2+} each by two electrons need to overcome a strong thermodynamic barrier ($E^0_{Ca^{2+}/Ca_{(s)}}$ = -2.84 V/SHE and $E^0_{Mg^{2+}/Mg_{(s)}}$ = -2.356 V/SHE **[46]**), and these strong reduction conditions are not involved in the present study (cathode potential determined to be -1.34 V/SHE). Instead, they reacted chemically with respective counter-ions on the surface of cathode, producing scaling when solubility constant of precipitates was achieved. Despite not being electroactive elements in regard to driving force of potential difference across electrochemical reactor, Ca^{2+} and Mg^{2+} mobility towards cathode surface might be involved in the displacement of ionic species jointly present in the bulk. In agreement with the Nernst-Planck equation, Ca^{2+} and Mg^{2+} were transported by forced convection thanks to electrolyte flow in-between electrodes. Under stationary conditions, they underwent diffusion from electrolyte bulk through finite boundary layer (i.e. diffusion layer), towards reactive zone at the proximity of cathode surface. Then through migration, they were mobilized to fulfill electroneutrality on cathode surface as the consequence of local alkalization **[47-49]**.

The initial limiting current density ($j_{\mathrm{lim},0}$) for the adopted electrochemical design operating with the working synthetic effluent is calculated using **Eq. (IV.18) [50, 51]**.

$$I_{\mathrm{lim}} = n_{\mathrm{e}}\, F\, S\, k_{\mathrm{m}}\, C_{\mathrm{SOL}} \qquad \text{(IV.18)}$$

where n_{e} is the number of electrons participating in the limiting reaction of **Eq. (II.9)**, S the effective surface of cathode (m^2), k_{m} the mass transfer coefficient for the assigned electrochemical cell from the bulk towards the cathode (m s^{-1}) and C_{SOL} the molar concentration of considered reactive species in the bulk (mol m^{-3}).

Reaction of dissolved O_2 reduction via 4-electrons producing OH^- (**Eq. (II.9)**) was selected as limiting step in agreement to the very high η_{H_2O} value. n_{e} is thus equal to 4. The stainless steel cathode possesses an effective surface area of 50 cm^{-2}. k_{m} equals to 2.33 × 10^{-5} m s^{-1} (**Chapter 5**). The concentration of dissolved O_2 was taken at 25°C, which is 2.81 × 10^{-4} mol L^{-1}. Computing **Eq. (IV.18)** gave $I_{\mathrm{lim},0}$ equals to 0.013 A, which lead to a $j_{\mathrm{lim},0}$ of 0.25 mA cm^{-2}. $I_{\mathrm{lim},0}$ value was ascertained experimentally with the plateau of limiting current density spotted on the voltammogram of the experimental setup. Therefore, the two current densities investigated in this study were both above the evaluated $j_{\mathrm{lim},0}$. As a result, the electrochemical reactions occurring on the surface of cathode were considered limited by mass transfer.

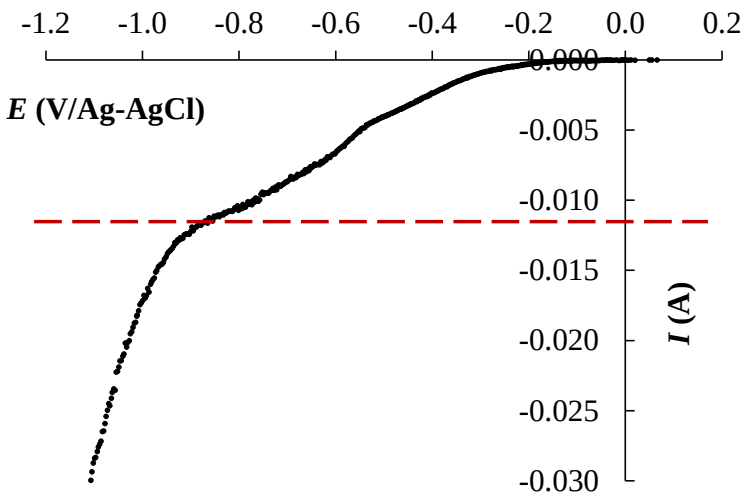

Fig. IV.3. Linear scan voltammetry (LSV) on stainless steel working electrode under cathodic polarization at a scan rate of 10 mV s^{-1}. BDD was used as CE. d_{elec}: 500 µm. 0.5 L of electrolyte containing 150 mg L^{-1} Ca^{2+}, 5 mg L^{-1} Mg^{2+} and carbonates of 60 mg-C L^{-1} with ionic strength of 0.02 mol L^{-1}.

In this section, under constant hydrodynamic parameters, the influence of electromigration of ionic species was investigated by varying the ionic strength of artificial effluent using Na_2SO_4 as supporting electrolyte. **Table IV.2** summarizes the values of ionic transference number for the different cases. They were calculated using **Eqs. (IV.19)-(IV.20) [52]** under the assumption that our electrolytic system complied with the restriction of infinite dilution where interaction between ions was not occurring.

$$t_i = \frac{z_i\, C_i\, u_i}{\sum_i z_i\, C_i\, u_i} \qquad \text{(IV.19)}$$

with

$$u_i = \frac{\lambda_i}{z_i\, F} \qquad \text{(IV.20)}$$

where t_i is the transference number, z_i the ionic charges, u_i the ionic mobility (in $m^2\ s^{-1}\ V^{-1}$), C_i the molar concentrations of ionic species (in mol L^{-1}) and λ_i the ionic molar conductivity (in S m^2 mol^{-1}).

Table IV.2. Ionic transference number for artificial effluent containing 150 mg L^{-1} of Ca^{2+}, 5 mg L^{-1} of Mg^{2+} and 60 mg-C L^{-1} of TIC without and with addition of Na_2SO_4 at different concentrations.

Ionic strength / mol L^{-1}	Ionic transference number				
	Ca^{2+}	Mg^{2+}	Na^{+}	HCO_3^-	SO_4^{2-}
0.02 (without Na_2SO_4)	0.218	0.011	0.123	0.339	0.309
0.04	0.120	0.006	0.241	0.187	0.447
0.10	0.050	0.002	0.325	0.077	0.545

As can be seen from **Table IV.2**, the more Na_2SO_4 was added to increase the ionic strength of artificial effluent, the more ionic mobility of Ca^{2+}, Mg^{2+} and HCO_3^-/ CO_3^{2-} were minimized by increasing transport activity of Na^+ and SO_4^{2-}.

Fig. IV.4 depicts the trend of evolution of concentrations of Mg^{2+}, Ca^{2+} and TIC when the investigated artificial effluent had different ionic strengths. The concentration of each ion decreased over time regardless of value of ionic strength. It seemed to have very little impact on the variation of the concentrations of Ca^{2+} and TIC as previously suggested by Tlili et al., where migration might play some role with respect to only more concentrated species in the system **[47]**. Standard deviations were calculated between results obtained with the electrolytes with enhanced ionic mobility in comparison to the one without supporting electrolyte. The average values are listed in **Table IV.3**. The two highest deviations were obtained in Mg^{2+} and TIC concentrations with evaluated deviation as low as 0.049 and 0.042, respectively. Therefore, the ionic strength of electrolyte had minor effect within the range of studied electrolyte concentrations towards the occurring mineral deposition on cathode surface. Electromigration of ionic species other than Ca^{2+}, Mg^{2+} and HCO_3^-/CO_3^{2-} did not influence the mobility of the precipitating elements in-between electrodes inside microfluidic electrochemical reactor. Mass transfer by diffusion was then the rate-limiting factor. Based on these results, the effect of electromigration could be omitted from the theoretical model proposed in **Section IV.3**. The addition of small quantity of supporting electrolyte (from 1.4 to 5 mmol L^{-1}) to achieve constant ionic strength across different investigated matrices of electrolyte will not influence the kinetics of mineral electro-precipitation in experimental results presented onwards.

Table IV.3. Average standard deviations calculated for electrolytes having enhanced ionic strengths (0.04 and 0.10 mol L^{-1}).

Element	Average standard deviation	
	0.04 mol L^{-1}	0.10 mol L^{-1}
Mg^{2+}	0.030	0.049
Ca^{2+}	0.018	0.021
TIC	0.029	0.042

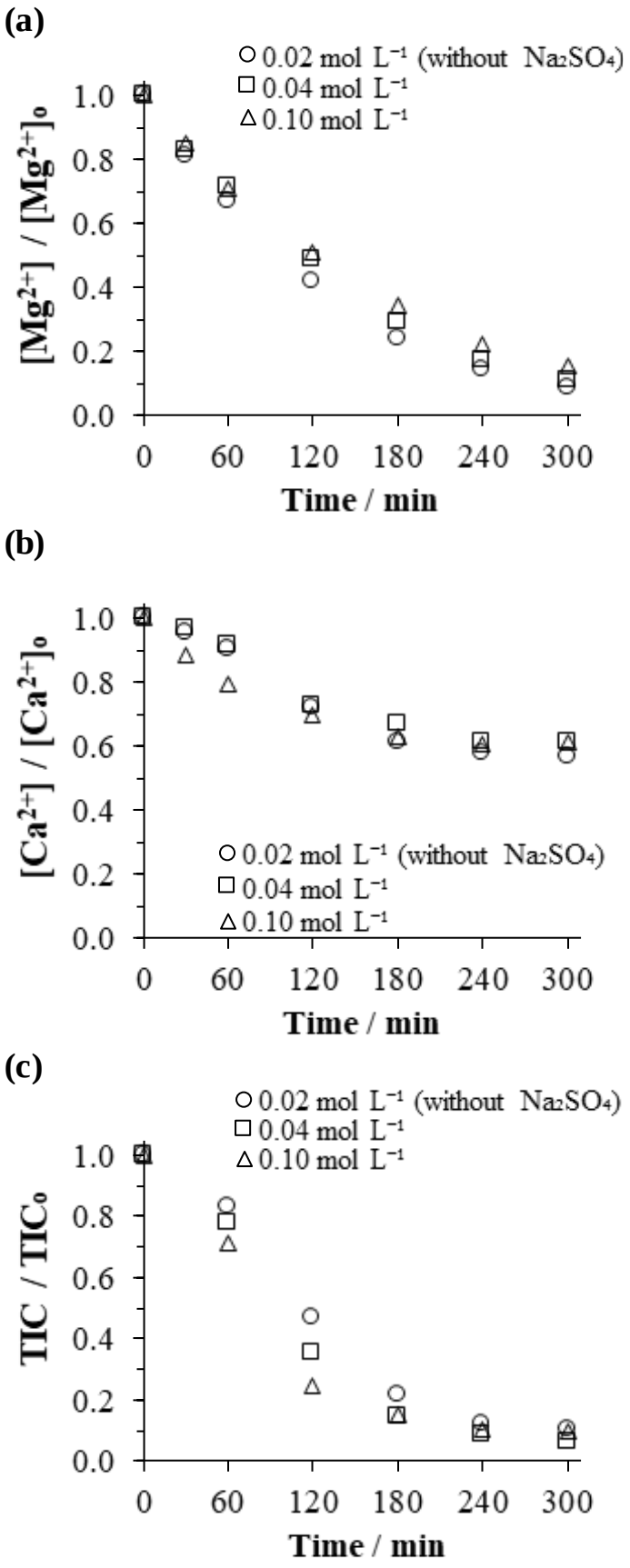

Fig. IV.4. Evolution of concentrations of **(a)** Mg^{2+}, **(b)** Ca^{2+} and **(c)** TIC during the electrolysis of artificial effluents bearing different ionic strengths of 0.02 (○) (without the addition of supporting electrolyte), 0.04 (□) and 0.10 (△) mol L^{-1}. Anode: BDD, cathode: stainless steel, j_{app}: 4 mA cm^{-2} and d_{elec}: 500 µm.

IV.4.4. Influence of matrix of electrolyte

IV.4.4.1. Influence of CO_3^{2-} towards the mineral electro-precipitation

Electrolysis of electrolyte containing Mg^{2+} and Ca^{2+}, in presence and absence of CO_3^{2-}, in the microfluidic flow-by reactor were carried out by applying 0.4 and 4 mA cm^{-2} and the results are plotted in **Fig. IV.5** and **Fig. IV.6**. From **Fig. IV.5**, it could firstly be observed that Ca^{2+} did not precipitate in the electrolyte without carbonate at both current densities. It precipitated only in presence of carbonate. Thus, it has been concluded that $Ca(OH)_2$ was not produced throughout these series of experiment and Ca^{2+} only electro-precipitated to form $CaCO_3$. This observation can be supported by the value of thermodynamic constant of solubility of $Ca(OH)_2$ that is high (5.00×10^{-6} **[22, 23]**) - thus highly soluble -, hence the interfacial pH never reached the OH^-_{crit} (i.e. 36.6 mol m^{-3}, pH = 12.6) to precipitate with Ca^{2+}. Secondly, according to **Fig. IV.6**, Mg^{2+} only precipitated at 4 mA cm^{-2} and no Mg^{2+}-based deposition occurred at 0.4 mA cm^{-2}. At low current density, since no decrease of Mg^{2+} was observed, it can be concluded that $Mg(OH)_2$ was not electro-precipitated. Same remark was given by Deslouis et al. **[14]** where they did not observe precipitation of $Mg(OH)_2$ when interfacial pH of 9.3 was not yet reached. Our result tells that there was a plateau at 4 mA cm^{-2} at the very beginning of electrolysis up to 7 min before Mg^{2+} started to deposit forming $Mg(OH)_2$, as soon as OH^-_{crit} (0.16 mol m^{-3}, interfacial pH = 10.2) was reached (**Fig. IV.6**). Then, during the first hour of electrolysis at 4 mA cm^{-2}, a slightly higher kinetics of $Mg(OH)_2$ deposition was observed in the electrolyte without carbonate. In the presence of CO_3^{2-}, there was perhaps a weak competition between $Mg(OH)_2$ and $CaCO_3$ for active site on the surface of cathode **[20, 53]**. However, it was not accounted for $MgCO_3$, otherwise the kinetics of precipitation with the electrolyte containing CO_3^{2-} would be faster and not slower than the one without CO_3^{2-}. To conclude, Mg^{2+} electro-precipitated independently with regard to carbonate ions.

Moreover, it can be seen in **Fig. IV.5** that $CaCO_3$ was already deposited at low current density, unlike $Mg(OH)_2$ even though the thermodynamic constant of solubility of $Mg(OH)_2$ is lower than that of $CaCO_3$. Similar observation was reported by Okstad et al. **[54]**. The higher initial concentration of Ca^{2+} - implemented to simulate the composition of reclaimed wastewater from urban WWTPs - can be one of the reasons of this observation, whereby supersaturation degree was already high. On top of that, experimental results showed that 7.2% more $CaCO_3$ deposition occurred at 0.4 mA cm^{-2} in comparison to higher applied current density of 4 mA cm^{-2}. To our understanding, once $CaCO_3$ electro-precipitation started to occur, it took place regardless of applied current density as long as the current density was equal or higher than the starting point of the nucleation of $CaCO_3$ crystal. In case of low and high applied current densities investigated in this work, $CaCO_3$ already formed at the low

j_{app} (0.4 mA cm^{-2}). It would behave similarly at higher applied current density except that within the latter, oxidation and reduction of solvent on the surface of electrodes were occurring at higher rates leading to higher amount of electro-generated gas. Given the fact that at 0.4 mA cm^{-2} it was already exceeding the limiting current density (0.25 mA cm^{-2}, see **Section IV.4.3**), gas production was therefore occurring at both applied conditions. It means that the influence of gas evolution was taking place concomitantly with the electro-precipitation on cathode surface **[55]**, but in an antagonist way according to the level of gas production. At 0.4 mA cm^{-2}, the lower evolution of gas on the surface of electrode could enhance the mass transfer of species towards the electrodes **[56-59]**. This enhancement would be attributed to firstly micro-convection, even at small value of current density **[56]**, due to evolving and departing gas bubbles from the electrode surface. Secondly, forced convection or macro-convection owing to movement and displacement of bubbles over the electrode surface could also occur **[57-59]**. Therefore, transport of Ca^{2+} and Mg^{2+} towards cathode surface for precipitating reaction were enhanced at the low j_{app} condition. This could explain why slightly more $CaCO_3$ was obtained at lower j_{app}. Contrastingly, higher intensity of gas evolution is expected over the surface of cathode at high j_{app} (4 mA cm^{-2}). Therefore, bubble coverage at the electrode surface should have increased as described by Vogt et al. **[24]**. Therefore, the more intense gas evolution at higher j_{app} could have disturbed the layer of $CaCO_3$ nuclei and in-parallel promoted the detachment of $CaCO_3$ deposit **[25, 26, 44]**. Consequently, less electro-precipitation of $CaCO_3$ was observed at higher j_{app}.

Furthermore, in presence of Ca^{2+} (150 mg L^{-1}) and carbonates (TIC of 60 mg-C L^{-1}), *SI* defined in **Eq. (IV.7)** equaled to 0.89 in the initial electrolyte. It means that Ca^{2+} and CO_3^{2-} concentrations in the bulk were already above their equilibrium state in water (where $SI = 0$) initially **[32]**. From the thermodynamic point of view, $CaCO_3$ precipitation in the bulk and scaling on metal substrate could occur. However, the induction time for homogenous and heterogeneous $CaCO_3$ nucleation varies in function of physicochemical component of bulk liquid as well as metal substrate **[13, 33, 60]**. According to Gabrielli et al., thermodynamics requires a 40-fold supersaturation before the precipitation in the bulk can be observed, i.e., equivalent to *SI* value around 1.6 **[2, 60, 61]**. It has also been demonstrated that under low supersaturation conditions, very long induction time (12 h) was required before observing scaling on metal substrate **[62]**. This might be one of the reasons sluggish kinetics of electro-precipitation of $CaCO_3$ was observed at the very beginning of electrolysis in **Fig. IV.5**. With respect to the evolution of experimental TIC concentrations (**Fig. IV.7(a-d)**) as well as to the modeled interfacial CO_3^{2-} concentrations illustrated in **Fig. IV.8**, this slow initial kinetics were also noticed. From **Fig. IV.8**, it can be noticed that on cathode surface, CO_3^{2-} departed from its initial bulk concentration and rapidly increased owing to electrogenerated OH^- once the electrolysis started. With increasing quantity of interfacial CO_3^{2-}, more CO_3^{2-} was readily available to react with Ca^{2+} to

form $CaCO_3$ scaling. The supersaturation degree quickly increased, thus promoting the deposition of $CaCO_3$. The concentration of interfacial CO_3^{2-} kept increasing as long as the rate of production of OH^- was superior to the rate of production of $CaCO_3$ (or CO_3^{2-} consumption at the interface). During this period, more CO_3^{2-} was shifted from HCO_3^- form since the OH^- concentration also increased, the phenomenon that contributed towards local alkalization. A peak was attained when the rate of OH^- production equaled that of CO_3^{2-} consumed. Beyond this peak, the rate of electro-precipitation of $CaCO_3$ declined due to decreasing concentration of both Ca^{2+} and CO_3^{2-} in the electrolyte at later stage of electrolysis as can be observed in **Fig. IV.5**. When comparing the evolution of interfacial CO_3^{2-} concentration modeled at 4 mA cm^{-2} (**Fig. IV.8(a)**) against 0.4 mA cm^{-2} (**Fig. IV.8(b)**), three remarks can be made; firstly, longer time was needed to reach the peak at $r_{OH^-} = r_{CaCO_3}$. Secondly, smaller concentration of interfacial CO_3^{2-} was produced at higher current density and thirdly, $CaCO_3$ electro-precipitation occurred at relatively slower rate after the peak of equivalence. The involvement of gas evolution might explain the described behaviors. As above-mentioned, intensified evolving H_2 gas on cathode surface at higher j_{app} decreased significantly the effective surface area of cathode even though the OH^- production was enhanced in the meantime. Consequently, longer buffer time was observed in **Fig. IV.5(a)** (**inset** curve) at the beginning of electrolysis in comparison to **Fig. IV.5(b)**. Lesser amount of interfacial CO_3^{2-} was also expected at the proximity of cathode surface due to the intervention of evolving gas. This disturbance on cathode took place throughout the electrolysis and consequently, plausible detachment of $CaCO_3$ scaling occurred along the way. In overall, slower kinetics of $CaCO_3$ deposition was observed under high current density, affirmed by the trend depicted in **Fig. IV.5**.

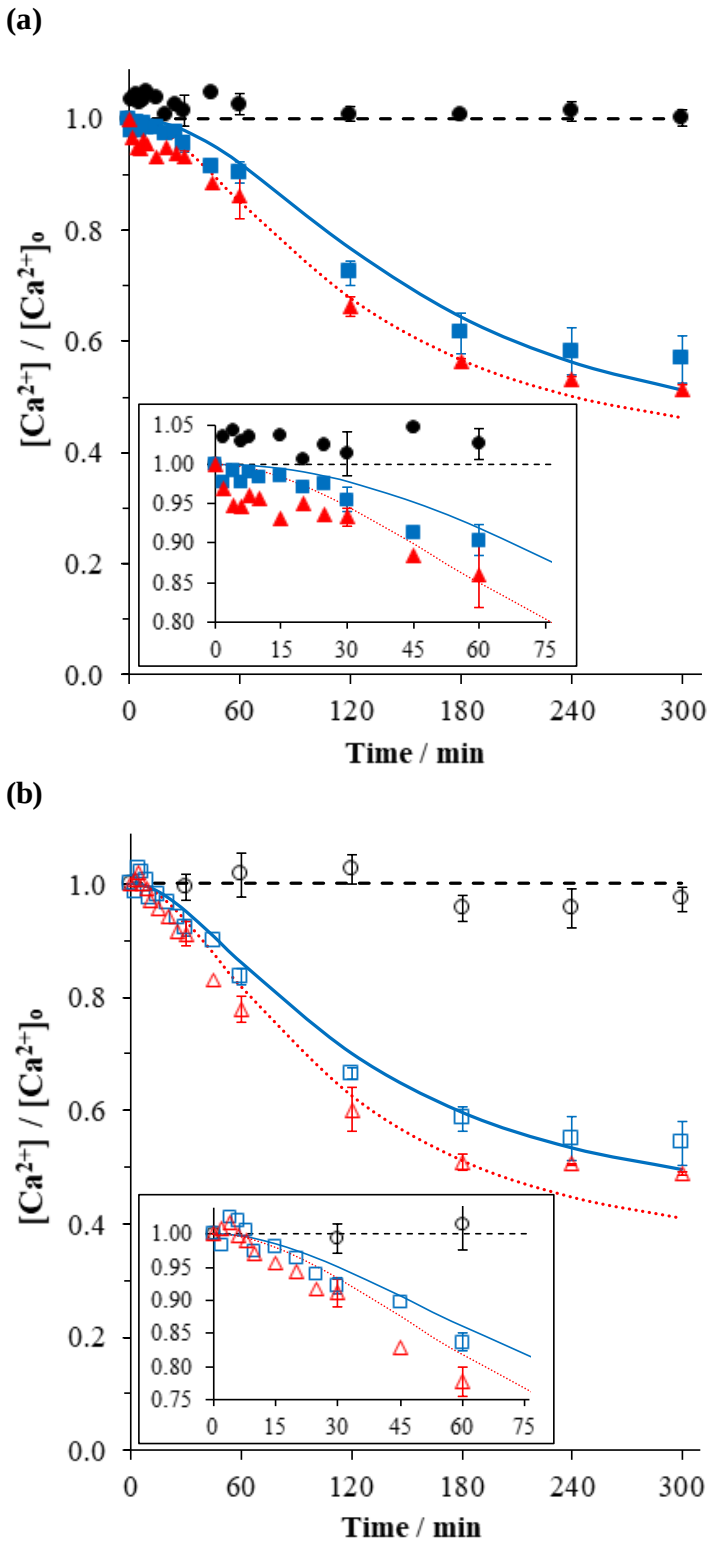

Fig. IV.5. Evolution of Ca^{2+} concentration during the electrolysis of different matrices of electrolyte ((●, ○): Ca^{2+} and Mg^{2+} without CO_3^{2-}, (■, □): Ca^{2+}, Mg^{2+} and CO_3^{2-} and (▲, △): Ca^{2+} and CO_3^{2-} without Mg^{2+}) at **(a)** 4 mA cm^{-2} (●, ■, ▲) and **(b)** 0.4 mA cm^{-2} (○, □, △). (– – –): model curve for Ca^{2+} and Mg^{2+} electrolyte without CO_3^{2-}, (——): model curve for Ca^{2+}, Mg^{2+} and CO_3^{2-} electrolyte and (·····): model curve for Ca^{2+} and CO_3^{2-} without Mg^{2+} electrolyte. **Inset**: zoom of the initial kinetics evolution of Ca^{2+}. Anode: BDD, cathode: stainless steel and d_{elec}: 500 µm.

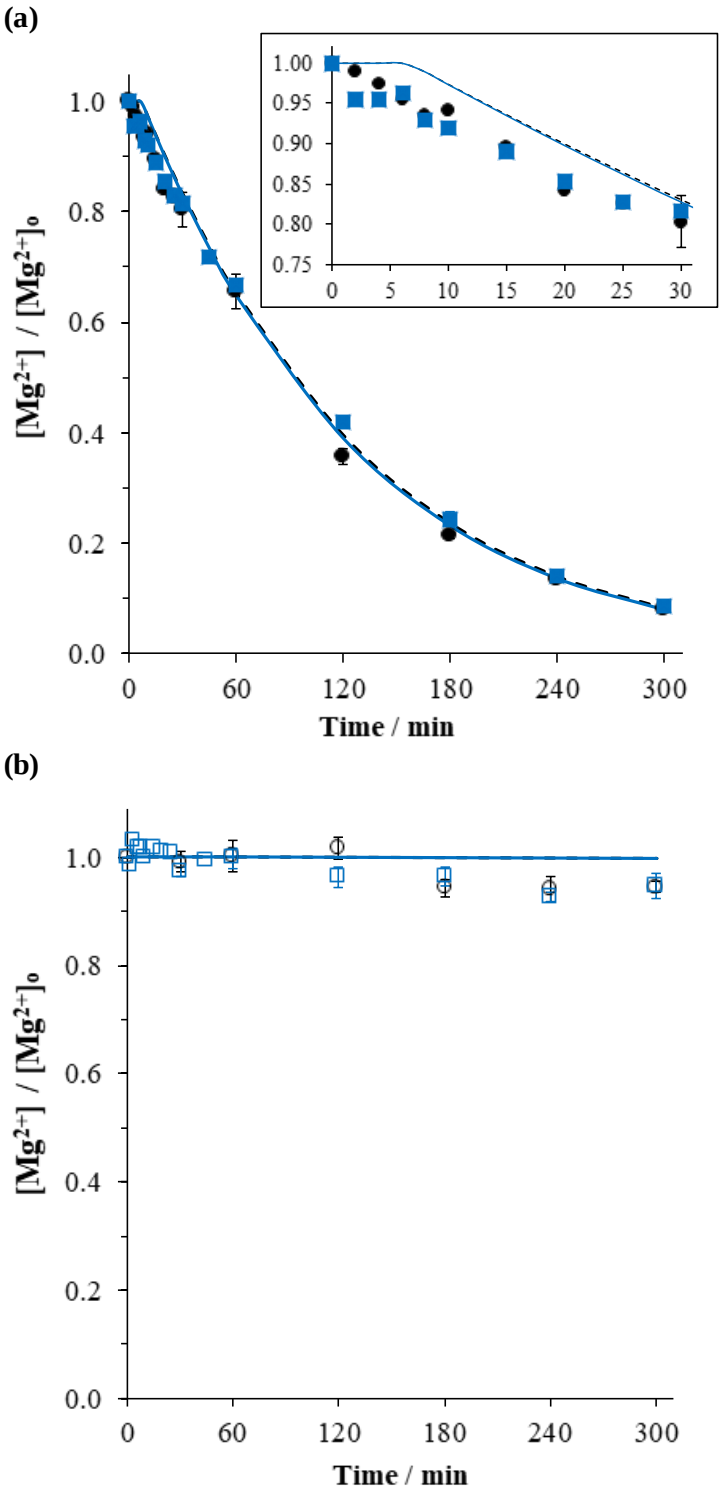

Fig. IV.6. Evolution of Mg^{2+} concentration during the electrolysis of different matrices of electrolyte ((●, ○): Ca^{2+} and Mg^{2+} without CO_3^{2-} and (■, □): Ca^{2+}, Mg^{2+} and CO_3^{2-}) at **(a)** 4 mA cm^{-2} (●, ■) and **(b)** 0.4 mA cm^{-2} (○, □). (– – –): model curve for Ca^{2+} and Mg^{2+} electrolyte without CO_3^{2-} and (——): model curve for Ca^{2+}, Mg^{2+} and CO_3^{2-} electrolyte. **Inset**: zoom of the initial kinetics evolution of Mg^{2+}. Anode: BDD, cathode: stainless steel and d_{elec}: 500 µm.

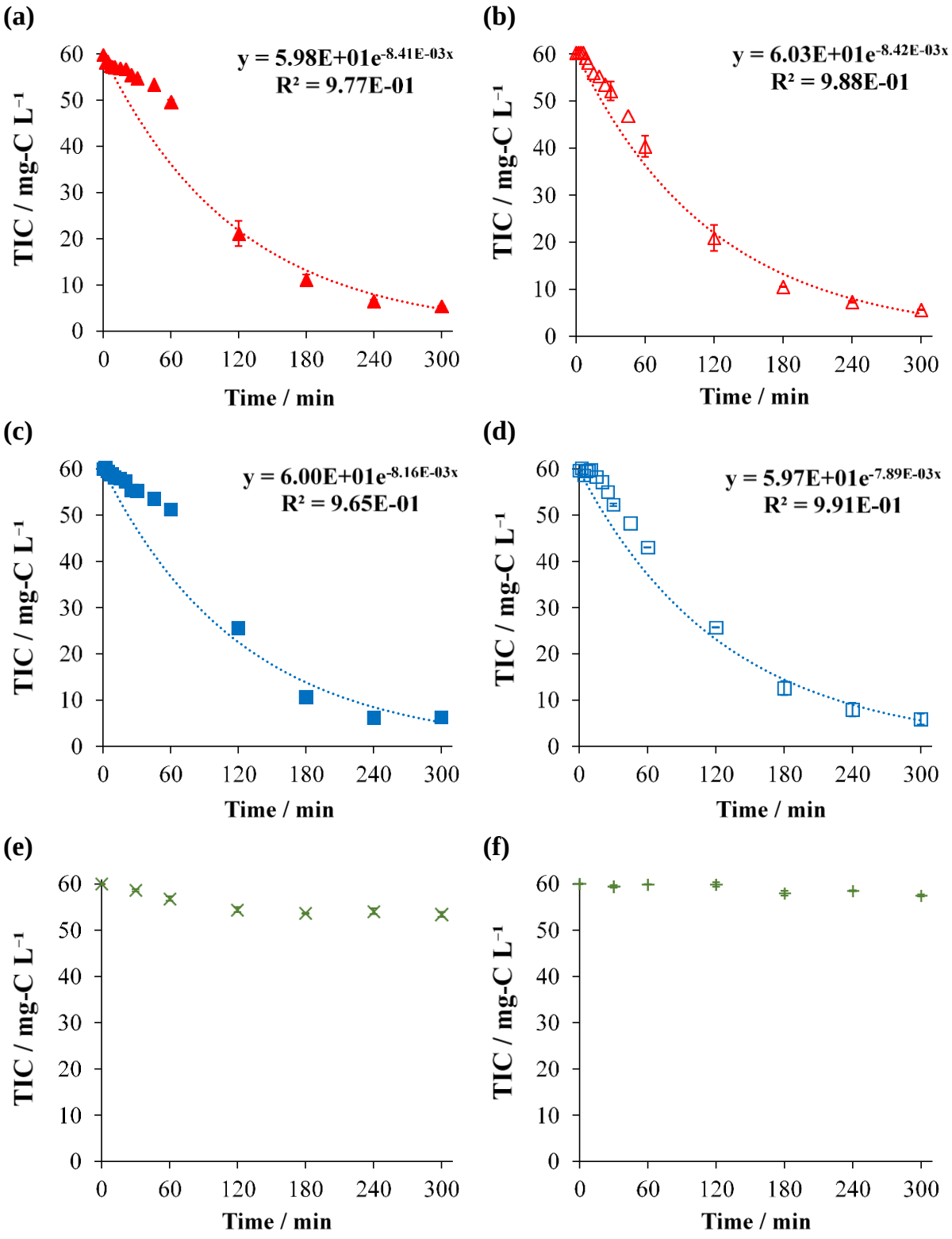

Fig. IV.7. Evolution of experimental TIC concentration over time over the course of electrolysis at 4 mA cm^{-2} (**a**, **c**, **e**) and 0.4 mA cm^{-2} (**b**, **d**, **f**) using (■, □): Ca^{2+}, Mg^{2+} and CO_3^{2-} electrolyte, (▲, △): Ca^{2+} and CO_3^{2-} without Mg^{2+} electrolyte and (×, +) Mg^{2+} and CO_3^{2-} without Ca^{2+} electrolyte. Dotted line corresponds to pseudo-first order kinetics of TIC decay. Anode: BDD, cathode: stainless steel, d_{elec}: 500 µm.

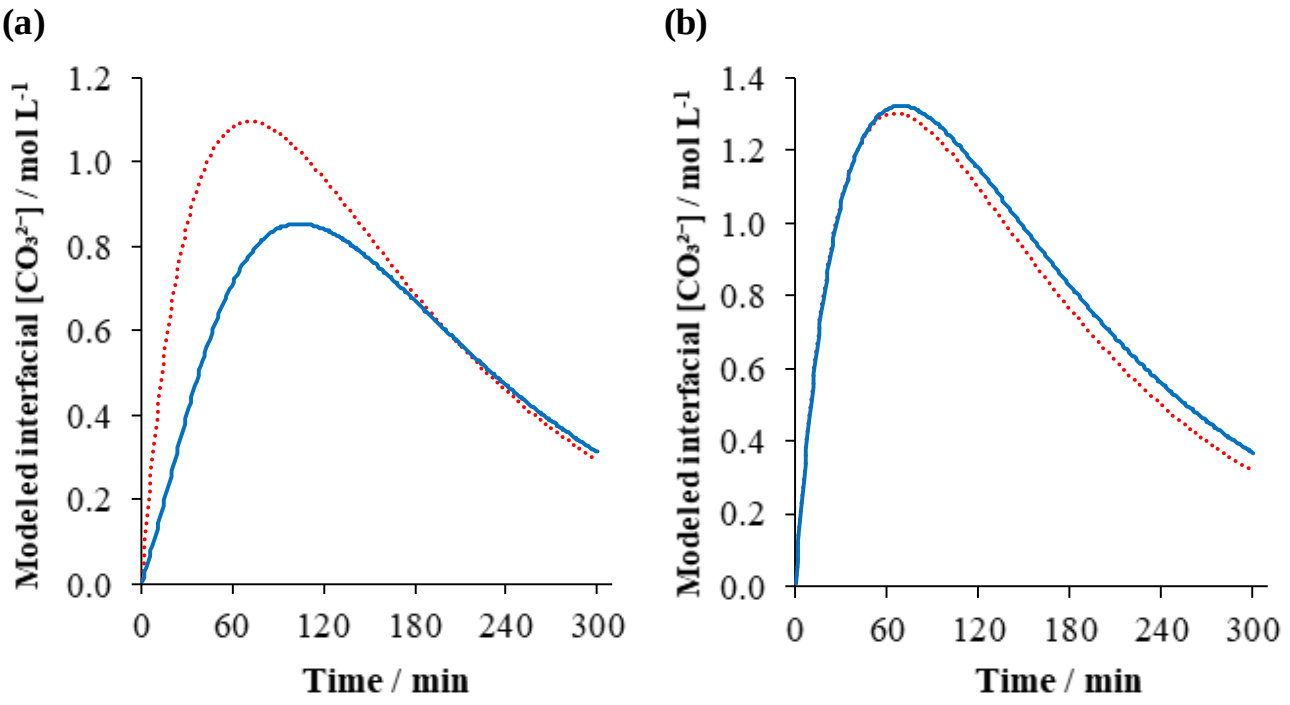

Fig. IV.8. Modeled concentration of interfacial CO_3^{2-} concentration during the electrolysis of electrolyte containing Ca^{2+}, Mg^{2+} and CO_3^{2-} (——) and electrolyte containing: Ca^{2+} and CO_3^{2-} without Mg^{2+} (·····) under the polarization of **(a)** 4 mA cm^{-2} and **(b)** 0.4 mA cm^{-2}. Anode: BDD, cathode: stainless steel and d_{elec}: 500 µm.

IV.4.4.2. Influence of Mg^{2+} towards the mineral electro-precipitation

To investigate the role of Mg^{2+} towards $CaCO_3$ deposition in microfluidic reactor, two electrolytes, both consisting of Ca^{2+} and CO_3^{2-} but only one contained Mg^{2+}, were compared. According to **Fig. IV.5**, at both applied current densities, concentrations of Ca^{2+} decreased over time. In both cases, higher degree of $CaCO_3$ electro-precipitation (12%) was observed in the system in absence of Mg^{2+}. This difference was even more significant when the electrochemical cell was polarized with lower current density where the interface was less perturbed by evolving gas (**Fig. IV.5(b)**). This finding can be attributed to the inhibition effect of Mg^{2+} during $CaCO_3$ deposition **[9, 14, 18, 25, 32]**. Mg^{2+} can either incorporate into the $CaCO_3$ lattices lowering their growth kinetics on cathode surface **[9, 32, 63]**, or, a thin layer of magnesian gel-like film **[25, 53, 64]** - which was formed prior to the $CaCO_3$ deposition **[21, 64]** - partially limited the surface reactivity of cathode towards the scaling of $CaCO_3$. Nonetheless, it has been reported that $CaCO_3$ crystal can still develop and grow on the layer of $Mg(OH)_2$ as confirmed by mixture of brucite and aragonite crystals from microscopic techniques **[25, 64-66]**. With regard to the competing reaction of gas evolution on the surface of cathode at higher current density, it remained true while working with electrolyte without Mg^{2+}. More intense H_2 gas evolution led to less $CaCO_3$ electro-precipitation (**Fig. IV.5**) as previously described. A slight difference was found in terms of $CaCO_3$ crystallography according to literature. When cathode potential was relatively low in the region of solvent reduction, $CaCO_3$ deposit has been reported to

crystallize under cubic calcite allotropy. Whilst in presence of Mg^{2+}, $CaCO_3$ takes aragonite form **[2, 7, 21, 25, 44]**. Under strong evolving gas activity, porous structure of $CaCO_3$ deposit has been reported **[19-21, 26, 67]**.

In addition, the trends of modeled interfacial CO_3^{2-} concentration depicted on **Fig. IV.8** complement the deduction made on the inhibiting role of Mg^{2+} towards $CaCO_3$ electro-precipitation. At higher j_{app} (4 mA cm^{-2}, **Fig. IV.8(a)**), $Mg(OH)_2$ deposit was formed in the electrolyte containing Mg^{2+}. The formation of $Mg(OH)_2$ deposit partly consumed interfacial OH^-. As a result, r_{OH^-} decreased as accounted in the model (**Eq. (IV.21)**). Together with H_2 gas evolution at higher current polarization, the increment of interfacial CO_3^{2-} concentration was slower in the electrolyte in presence of Mg^{2+} relatively to the one without Mg^{2+}. Smaller interfacial CO_3^{2-} concentration was expected at cathode surface therefore lowering kinetic rate of $CaCO_3$ electro-precipitation. Contrastingly, $Mg(OH)_2$ electro-precipitation did not take place at lower j_{app}. Gas evolution was significantly lower at 0.4 mA cm^{-2}. Consequently, the evolution of modeled interfacial CO_3^{2-} concentrations (**Fig. IV.8(b)**) for both electrolytes in absence and presence of Mg^{2+} were quite similar. It means that the availability of interfacial CO_3^{2-} on cathode surface was about the same for either electrolyte. Hence, it was then confirmed from **Fig. IV.5(b)** that the lower growth rate of $CaCO_3$ deposition obtained in the presence of Mg^{2+} at lower current density was due to the decrease of supersaturation degree of $CaCO_3$ in the presence of Mg^{2+} **[68]**. As previously discussed, it can adsorb or incorporate into $CaCO_3$ crystal lattice inhibiting its growth during the electrolysis **[32, 63]**.

IV.4.4.3. Influence of Ca^{2+} towards the mineral electro-precipitation

Fig. IV.9 illustrates the behavior of mineral deposition during electrolysis in the presence or absence of Ca^{2+} at 4 and 0.4 mA cm^{-2}. From **Fig. IV.9(a)**, it was observed that Mg^{2+} underwent electro-precipitation independently of Ca^{2+}. The evolution of concentration of Mg^{2+} in presence of Ca^{2+} followed exactly the trend given in absence of Ca^{2+}. This observation indicated indifferent role of Ca^{2+} towards the deposition of Mg^{2+}. From **Fig. IV.9(b)**, it was noticed that Mg^{2+} did not precipitate at lower applied current density (0.4 mA cm^{-2}) in both matrices of electrolyte. The evolution of TIC in **Fig. IV.7(e-f)** suggested that the concentration of CO_3^{2-} declined negligibly over time in the matrix without Ca^{2+} relatively to the behavior in the presence of Ca^{2+}. This tendency coupled with the observation made in **Fig. IV.9(a)** allowed deducing on the absence of electro-precipitation of $MgCO_3$ in our operated microfluidic cell configuration. In addition, considering the fact that CO_3^{2-} did not precipitate in the absence of Ca^{2+}, the results in this section corroborated with those in **Section IV.4.4.1** in which CO_3^{2-} only underwent precipitation with Ca^{2+} to form $CaCO_3$ deposit. The evolution of modeled interfacial CO_3^{2-} concentration in the case without Ca^{2+} plotted in **Figs. IV.9(c)**

and **IV.9(d)** might as well come into similar conclusion. Interfacial CO_3^{2-} concentration increased in conjunction to OH^- production on electrode surface. No CO_3^{2-} was consumed at the vicinity of cathode in the absence of Ca^{2+} allowing a continuous and quicker shift into CO_3^{2-} form at cathode interface. The interfacial CO_3^{2-} concentration arrived at a quasi-plateau at the end of electrolysis when the majority of carbon was converted into CO_3^{2-} form. Slower rate of OH^- production at higher applied current was due to involvement of H_2 evolution activity.

To summarize, Mg^{2+} deposited under the form of $Mg(OH)_2$ and it was not influenced by the presence of Ca^{2+} nor CO_3^{2-}. Only applied current density influenced the electro-precipitation of $Mg(OH)_2$ as already described in **Section IV.4.4.1**. According to Bénézeth et al. **[35]**, $MgCO_3$ or commonly known as magnesite, possesses very slow kinetics of crystallization. Other hydrated Mg-carbonates forms are plausible owing to slow precipitation kinetics of the former, but they are rather unstable due to strong hydrated character of Mg^{2+} **[35, 69, 70]**. As a result, direct electro-precipitation of $MgCO_3$ would be realizable but only under stringent conditions, i.e., elevated departing supersaturated solution, elevated temperature and very high CO_2 partial pressure **[71]**. Hence, based on our experimental results supported by the work of other authors, $MgCO_3$ was not formed under our experimental conditions.

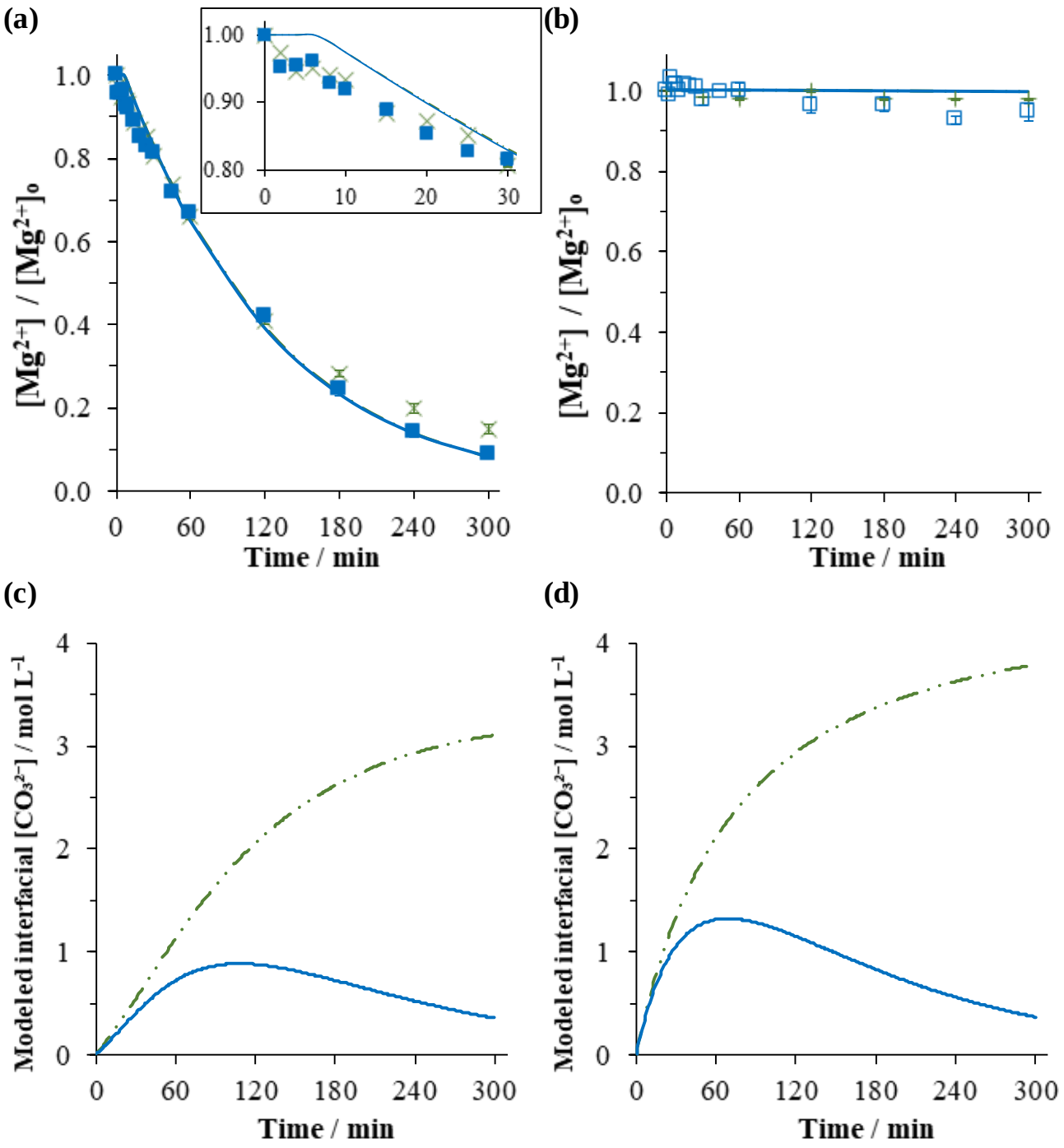

Fig. IV.9. Evolution of Mg^{2+} (**a**, **b**) and modeled interfacial CO_3^{2-} (**c**, **d**) concentrations during the electrolysis of electrolyte containing Ca^{2+} (■, □) or without Ca^{2+} (×, +) at 4 mA cm^{-2} (**a**, **c**) and 0.4 mA cm^{-2} (**b**, **d**). Model curves of electrolyte in presence of Ca^{2+} (——) or in absence of Ca^{2+} (— · ·). **Inset (a)**: zoom of the initial kinetic evolution of Mg^{2+}. Anode: BDD, cathode: stainless steel and d_{elec}: 500 µm.

IV.4.5. Evolution of pH and conductivity

In **Fig. IV.10** are plotted the graphs of variation of bulk solution pH and ionic conductivity throughout the electrolysis of all investigated matrices of electrolyte at both high and low applied current densities. Few general trends can be drawn from these curves. Firstly, solution pH and ionic conductivity tended to decrease in the bulk during the electro-precipitation process. The decrease in pH was the most remarkable in the electrolyte without carbonates since no buffer effect of HCO_3^-/CO_3^{2-} was present in this matrix. Similar remark was also made by other authors, Tlili et al. **[47]** and Piri et al. **[26]**, when they checked upon the variation of pH in bulk solution during the formation of $CaCO_3$. This drop of pH value was ascribed to the consumption of OH^- that partake in the reaction of $Mg(OH)_2$ deposition according to **Eq. (II.11)**. It could also be attributed to the pH participation towards the thermodynamic equilibrium shift of HCO_3^-/CO_3^{2-} in favor of CO_3^{2-} formation in **Eq. (I1.12)**, while consuming OH^-. Net concentration of OH^- in the bulk therefore declined, indicated by the decrease of measured bulk pH. The only case where bulk pH did not decrease was during the electrolysis of electrolyte in absence of Ca^{2+}. At both applied current densities, $CaCO_3$ deposit was not formed. Meanwhile, OH^- was continuously electro-generated on the surface of cathode. OH^- diffusing from cathode surface to the bulk only reacted with existing HCO_3^- until complete conversion into the basic form, i.e. CO_3^{2-}(**Eq. (II.12)**). Then, the accumulation of OH^- in the bulk yielded in an increase of pH value. Moreover, the only electro-precipitation that occurred in the electrolyte in absence of Ca^{2+} was $Mg(OH)_2$ and it was only seen at higher range of j_{app}. However, as demonstrated in **Fig. IV.10(a)**, OH^- consumed for the deposition of $Mg(OH)_2$ on cathode surface contributed trivially towards the diminishing pattern of pH in the bulk unlike during the deposition of $CaCO_3$.

Similar argument can be done towards the trend of ionic conductivity in the bulk. Knowing the fact that OH^- possesses high value of ionic conductivity despite not being the highest relatively to H^+, its consumption throughout the electro-precipitating event of $CaCO_3$ manifested a decline in overall bulk ionic conductivity as shown in **Figs. IV.10(c)** and **IV.10(d)**.

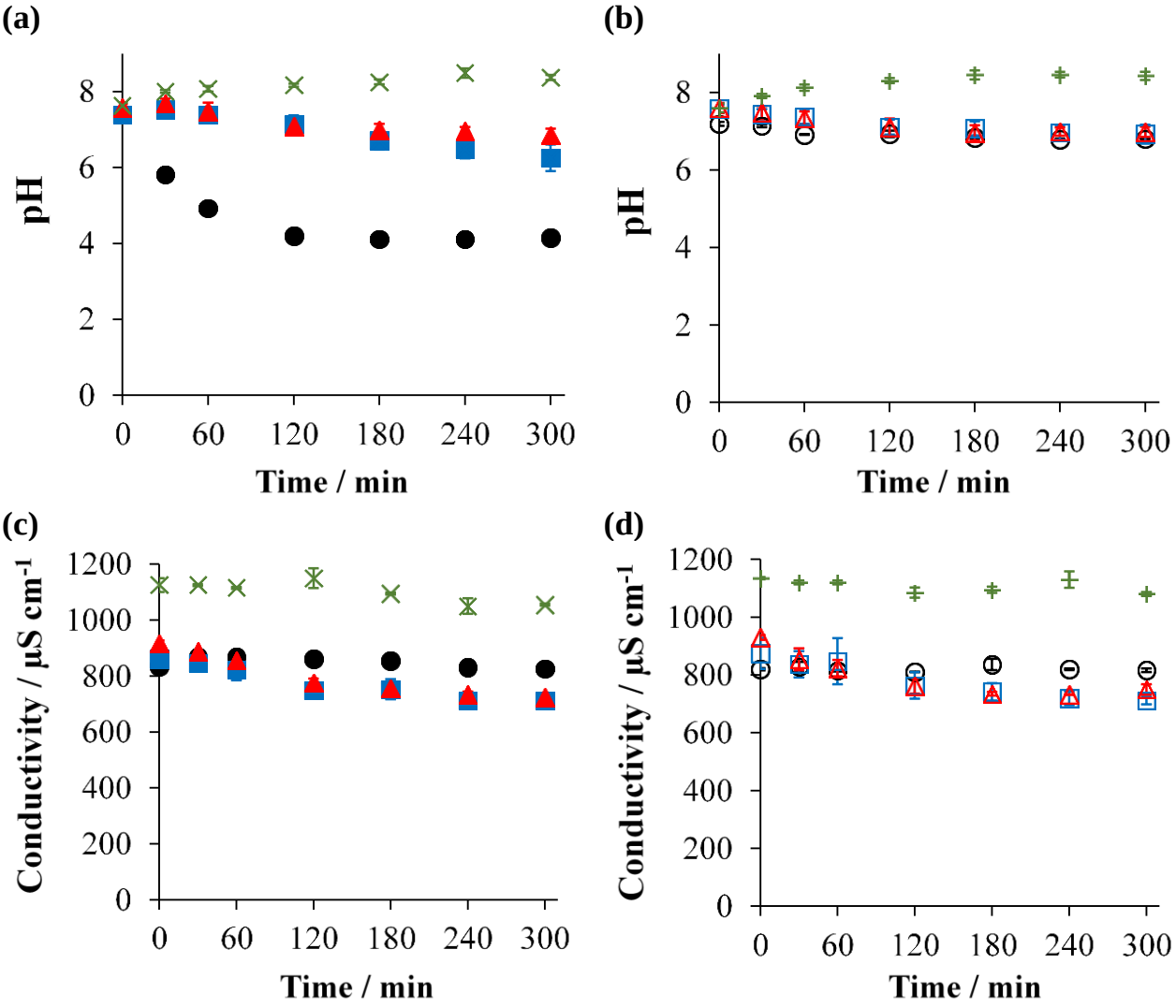

Fig. IV.10. Evolution of pH (**a**,**b**) and ionic conductivity (**c**,**d**) during the electrolysis of different matrices of electrolyte (Ca^{2+} and Mg^{2+} without CO_3^{2-} (●, ○), Ca^{2+}, Mg^{2+} and CO_3^{2-} (■, □), Ca^{2+} and CO_3^{2-} without Mg^{2+} (▲, △), and Mg^{2+} and CO_3^{2-} without Ca^{2+} (×, +)) at 4 mA cm^{-2} (●, ■, ▲, ×) and 0.4 mA cm^{-2} (○, □, △, ×). Anode: BDD, cathode: stainless steel, d_{elec}: 500 µm.

IV.4.6. Mass balance and elements recovery

Figure IV.11 depicts the recovery of Mg and Ca from the different electrochemical reactor compartments at the end of experiment for different matrices of electrolyte at both current densities investigated. Very high percentage of Mg and Ca recovery across all experiments was verified with the lowest being 90%. The percentage of recovery across all electrolysis took an average value of 95%. From **Fig. IV.11**, in the case where electro-precipitation occurred, high percentage of Mg and Ca were recovered from cathode while negligible quantity was found in tubing and from anode surface. It is important to note that high Mg and Ca recovery means negligible loss of the elements was ensured. Mass balance of Mg and Ca from different compartment was conserved. Consequently, the trends of cation concentrations depicted in previous figures were reliable. Their decay from

electrolyte bulk, coupled to high mass recovery from cathode surface was indicative of mineral precipitations occurring on the cathode.

Looking at **Fig. IV.11(b)**, percentages of mass of Ca recovered from cathode in both matrices of electrolyte were higher at 0.4 mA cm^{-2} as compared to 4 mA cm^{-2}, confirming the relative influence of evolving gas activity on cathode surface. Moreover, the percentage of Ca recovery from cathode was always lower in the matrix in presence of Mg^{2+}, whatever the current density applied. It is in agreement with the fact that less Ca^{2+} was electro-precipitated in presence of Mg^{2+} demonstrating the inhibition effect of the latter towards $CaCO_3$ co-precipitation with $Mg(OH)_2$.

On the other hand, the recovery of Mg in all electrolytes under study illustrated in **Fig. IV.11(a)** confirmed that the Mg^{2+}-based deposit only took place under high current density. It further corroborated the fact that the formation of $Mg(OH)_2$ deposit was not influenced by other ionic species co-present in the electrolyte.

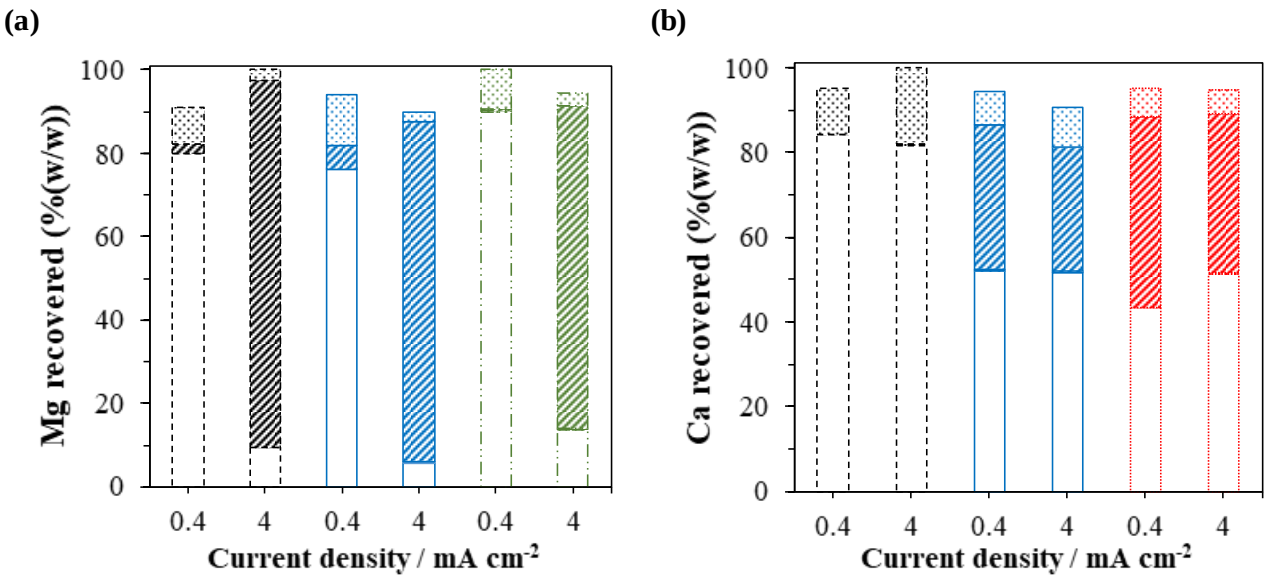

Fig. IV.11. Percentages (w/w) of **(a)** Mg and **(b)** Ca recovered from different parts of experimental pilot (☐: electrolyte, ▨: cathode, ⊞: anode and ⚄: tube) after 300 min-electrolysis at 0.4 and 4 mA cm^{-2} of different matrices of electrolyte ((- - - - -): Ca^{2+} and Mg^{2+} without CO_3^{2-}, (———): Ca^{2+}, Mg^{2+} and CO_3^{2-}, (·····): Ca^{2+} and CO_3^{2-} without Mg^{2+}, and (- · — · -): Mg^{2+} and CO_3^{2-} without Ca^{2+}).

IV.4.7. Theoretical evolution of Ca^{2+}, Mg^{2+} and interfacial CO_3^{2-} during electrolysis in different matrices

Simulations of evolution of Mg^{2+} concentration during the electrolysis of all matrices of electrolyte depicted in **Figs. IV.6(a)**, **Fig. IV.6(b)**, **Fig. IV.9(a)** and **Fig. IV.9(b)** fitted very well with their corresponding experimental curves. Their RMSE values stayed underneath 0.0078 as summarized in **Table IV.4** whilst ME and IOA values remained above 0.9849 and 0.9956 respectively under all case study. The modeling indicated that under the polarization of 4 mA cm^{-2}, it took approximately 7 min for the electrochemical system to reach interfacial OH^-_{crit} (0.16 mol m^{-3}, interfacial pH_{crit} = 10.2) before Mg^{2+} started to precipitate. This lag time was also observed experimentally as illustrated in **inset** of **Fig. IV.6(a)** and **Fig. IV.9(a)**. The models of Mg^{2+} concentrations decreased over time following the calibrated empirical value of $k_{Mg(OH)_2}$ of 0.330 m^7 mol^{-2} min^{-1}. Exactly same trend was observed across all matrices of electrolyte containing Mg^{2+} since $Mg(OH)_2$ deposition was independent of CO_3^{2-} and Ca^{2+} ions. Accordingly, similar procedures were carried out for $Ca(OH)_2$ deposit. However, due to high solubility of $Ca(OH)_2$, the OH^-_{crit} concentration that needed to be reached was as high as 36.6 mol m^{-3} (pH = 12.6). Under our investigated experimental setup, this OH^-_{crit} value was not achieved by either j_{app}. Maximum theoretical interfacial OH^- concentration was obtained under 4 mA cm^{-2} at 7.43 mol m^{-3} (pH = 11.8). As a consequence, no precipitation of $Ca(OH)_2$ was observed.

The modeling of interfacial CO_3^{2-} concentration at cathode surface was rather accurate as extensively discussed from **Sections IV.4.4.1** to **IV.4.4.3**. In agreement with **Eq. (IV.12)** and **Eq. (IV.15)**, interfacial CO_3^{2-} was proven to be dependent on j_{app}; hence H_2 gas evolution activity on cathode. Its concentration was as well influenced by the consumption of interfacial OH^-. Taking into account these matters, **Eq. (IV.13)** yields reliable models of evolution of Ca^{2+} concentration across multiple matrices of electrolyte investigated. The calibrated empirical value of constant rate of $CaCO_3$ electro-precipitation (k_{CaCO_3}) was 3.6 × 10^{-3} m^4 mol^{-1} min^{-1}. Ca^{2+} model curves fitted their experimental counterparts well. In agreement to listed values in **Table IV.4**, the lowest RMSE was 0.0761 in the system containing Mg^{2+}, Ca^{2+} and CO_3^{2-} at low j_{app}. Other RMSE values ranged from 0.0828 to 0.1163 and the Ca^{2+} model fitting remained reliable in accordance to other model fitting criteria such as ME and IOA. Their respective values obtained for the case with worst RMSE fitting (i.e., matrix containing Ca^{2+} and CO_3^{2-} without Mg^{2+} at 0.4 mA cm^{-2}) were 0.9758 and 0.9934.

In order to account for intensive concomitant H_2 gas evolution at high j_{app}, the OH^- hindrance factor α introduced in **Eq. (IV.3)** and **Eq. (IV.15)** was taken at 7.5% to fit experimental results. This tells that approximately only 7.5% of cathode surface was effective for mineral electro-precipitation

including the detachment of deposits already formed by the evolving gas. The α value was found to approximately match the observed experimental decrease of $CaCO_3$ scaling (7.2%) between the two regions of applied current densities investigated. In addition, it has also been observed that at lower applied current, the applied current density already surpassed limiting current density (**Section IV.4.2**). This means that secondary reaction like concurrent gas evolution was already present but it did not influence on the availability of interfacial CO_3^{2-} on cathode (**Fig. IV.8(b)**) but rather improving the mass transfer of Ca^{2+} and Mg^{2+} towards cathode surface (**Section IV.4.4.1**). The hindrance of $CaCO_3$ growth kinetics in this case was purely attributed to steric inhibition of Mg^{2+} in solution since no $Mg(OH)_2$ was produced under this condition **[64]**. Therefore, the kinetic law of depositing $CaCO_3$ was slightly modified taking into account this effect as defined in **Eq. (IV.21)**:

$$r_{Ca^{2+}} = -r_{CaCO_3} = -(k_{CaCO_3} - k_{inhib})\,[Ca^{2+}][CO_3^{2-}]_{int,t} \qquad \text{(IV.21)}$$

where k_{inhib} (in m^4 mol^{-1} min^{-1}) is the steric inhibition of Mg^{2+} ion either by adsorption or incorporation into $CaCO_3$ lattices as previously discussed in **Section IV.4.4.2**. By fitting the modeled Ca^{2+} concentration with its experimental data (the matrix in presence of Mg^{2+}) at low j_{app}, k_{inhib} was evaluated to be 9.0×10^{-4} m^3 mol^{-1} min^{-1}. This value is about 25% of the empirical $CaCO_3$ electro-precipitation constant of k_{CaCO_3}. It suggests that in the presence of 5 mg L^{-1} of Mg^{2+} (in the system containing 150 mg L^{-1} of Ca^{2+}), 25% less $CaCO_3$ electro-precipitation should have been observed due to the inhibition effect. However, experimental results indicated only 12% less $CaCO_3$ scaling after 5 h of electrolysis, which is about half the theoretical value. This discrepancy was attributed to the enhancement of Ca^{2+}, CO_3^{2-} and Mg^{2+} transport by micro- and macro-convection towards cathode interface **[56-59]** which could favor the electro-precipitation reactions.

Table IV.4. Model fitting evaluation between simulated and experimental evolution of Mg^{2+} and Ca^{2+} concentrations in all investigated matrices of electrolyte, considering RMSE, ME and IOA at both 0.4 and 4 mA cm^{-2}. (N/A: division by 0 values. Appeared when evaluating the model in the case where no deposition occurs).

Electrolyte	**Ionic species**	**Model fitting criteria**	**Applied current density**	
			0.4 mA cm^{-2}	**4 mA cm^{-2}**
Ca^{2+} and Mg^{2+} without CO_3^{2-}	Mg^{2+}	RMSE	0.0073	0.0064
		ME	N/A	0.9901
		IOA	N/A	0.9975
	Ca^{2+}	RMSE	0.0999	0.1036
		ME	N/A	N/A
		IOA	N/A	N/A
Ca^{2+} and CO_3^{2-} without Mg^{2+}	Ca^{2+}	RMSE	0.1163	0.1136
		ME	0.9758	0.9710
		IOA	0.9934	0.9918
Mg^{2+} and CO_3^{2-} without Ca^{2+}	Mg^{2+}	RMSE	0.0034	0.0078
		ME	N/A	0.9849
		IOA	N/A	0.9956
Ca^{2+}, Mg^{2+} and CO_3^{2-}	Mg^{2+}	RMSE	0.0056	0.0060
		ME	N/A	0.9883
		IOA	N/A	0.9969
	Ca^{2+}	RMSE	0.0761	0.0828
		ME	0.9844	0.9767
		IOA	0.9960	0.9938

IV.5. Conclusions

The occurrence of mineral electro-precipitation inside a microfluidic reactor was newly investigated in this work. Due to the existence of precipitating agents in water resources of natural or anthropogenic origin, electro-precipitates can be formed during advanced electro-oxidation processes and they might compromise the efficiency of such processes. Inside a scalable microfluidic reactor, the phenomenon of local alkalization on cathode surface originated principally from reduction of water and not dissolved O_2 under investigated conditions. The reaction kinetics at the proximity of cathode surface were limited by mass transfer. Upon further investigation, the influence of electromigration towards the occurrence of electro-precipitation was negligible, meaning that diffusion was the main limiting factor.

$MgCO_3$ deposit was not observed throughout this work, while $Mg(OH)_2$ precipitate was highly dependent on j_{app}, because the local pH value was the decisive parameter upon its formation. Thus $Mg(OH)_2$ was hardly formed at low j_{app}. In addition, $Mg(OH)_2$ deposition was independent of ionic species jointly present in the electrolyte bulk. Regarding Ca-based precipitates, $Ca(OH)_2$ was not formed under our investigated configuration, while $CaCO_3$ was easily deposited on cathode surface even under small current polarization. More electro-precipitation of $CaCO_3$ was recovered at lower j_{app} (0.4 mA cm^{-2}) owing to vigorous gas evolution at higher j_{app} (4 mA cm^{-2}). $CaCO_3$ scaling was proven to be impeded by the presence of Mg^{2+} ion. A novel mathematical model was proposed to simulate and predict the evolution of depositing species of Mg^{2+}, Ca^{2+} and interfacial CO_3^{2-} in presence or absence of co-deposition within the microfluidic reactor. The models fitted well with experimental data given the RMSE, ME and IOA values.

It could be deduced eventually that $^{\bullet}OH$ continuously produced on BDD anode did not influence towards the electro-precipitation occurring on cathode counterpart in the applied condition despite micrometric distance separating them. In order to minimize scaling formation, a compromise with respect to degradation efficiency of pollutant needs to be accommodated for upcoming research. Lower j_{app} could be used, but lower degradation of pollutant via direct electron transfer or indirect oxidation would be consequently expected due to lower overpotential. Alternatively, electro-precipitation could be minimized by applying high current density, benefiting the intensified evolving gas on cathode surface to un-do the deposits. However, energy consumption would be deemed deal-breaker for its application at industrial scale. Nonetheless, since micrometric range of d_{elec} extensively cut down the internal resistance of electrochemical cells, cell voltage would not be eventually so high at such high current densities. Further studies are required to test microfluidic configuration in order

to concomitantly yield high degradation efficiency while minimizing the resulting mineral electro-precipitation.

References

[1] F. Sopaj, N. Oturan, J. Pinson, F. Podvorica, M.A. Oturan, Effect of the anode materials on the efficiency of the electro-Fenton process for the mineralization of the antibiotic sulfamethazine, Applied Catalysis B: Environmental, 199 (2016) 331-341.
[2] L. Beaunier, C. Gabrielli, G. Poindessous, G. Maurin, R. Rosset, Investigation of electrochemical calcareous scaling: Nuclei counting and morphology, Journal of Electroanalytical Chemistry, 501 (2001) 41-53.
[3] C. Deslouis, D. Festy, O. Gil, G. Rius, S. Touzain, B. Tribollet, Characterization of calcareous deposits in artificial sea water by impedance techniques — 1. Deposit of $CaCO_3$ without $Mg(OH)_2$, Electrochimica Acta, 43 (1998) 1891-1901.
[4] C. Deslouis, I. Frateur, G. Maurin, B. Tribollet, Interfacial pH measurement during the reduction of dissolved oxygen in a submerged impinging jet cell, Journal of Applied Electrochemistry, 27 (1997) 482-492.
[5] H. Deligianni, L.T. Romankiw, In situ surface pH measurement during electrolysis using a rotating pH electrode, IBM Journal of Research and Development, 37 (1993) 85-95.
[6] J. Marin-Cruz, R. Cabrera-Sierra, M. Pech-Canul, I. Gonzalez, EIS study on corrosion and scale processes and their inhibition in cooling system media, Electrochimica Acta, 51 (2006) 1847-1854.
[7] J. Marin-Cruz, E. Garcia-Figueroa, M. Miranda-Hernández, I. Gonzalez, Electrochemical treatments for selective growth of different calcium carbonate allotropic forms on carbon steel, Water Research, 38 (2004) 173-183.
[8] Y. Ben Amor, L. Bousselmi, H. Takenouti, E. Triki, Influence of sulphate ions on corrosion mechanism of carbon steel in calcareous media, Corrosion Engineering, Science and Technology, 40 (2005) 129-136.
[9] Y. Ben Amor, L. Bousselmi, B. Tribollet, E. Triki, Study of the effect of magnesium concentration on the deposit of allotropic forms of calcium carbonate and related carbon steel interface behavior, Electrochimica Acta, 55 (2010) 4820-4826.
[10] L. Bousselmi, C. Fiaud, B. Tribollet, E. Triki, Impedance spectroscopic study of a steel electrode in condition of scaling and corrosion: Interphase model, Electrochimica Acta, 44 (1999) 4357-4363.
[11] L. Bousselmi, C. Fiaud, B. Tribollet, E. Triki, The characterisation of the coated layer at the interface carbon steel-natural salt water by impedance spectroscopy, Corrosion Science, 39 (1997) 1711-1724.
[12] Z. Belarbi, B. Sotta, L. Makhloufi, B. Tribollet, J. Gamby, Modelling of delay effect of calcium carbonate deposition kinetics on rotating disk electrode in the presence of green inhibitor, Electrochimica Acta, 189 (2016) 118-127.
[13] M. Euvrard, F. Membrey, C. Filiatre, C. Pignolet, A. Foissy, Kinetic study of the electrocrystallization of calcium carbonate on metallic substrates, Journal of Crystal Growth, 291 (2006) 428-435.
[14] C. Deslouis, D. Festy, O. Gil, V. Maillot, S. Touzain, B. Tribollet, Characterization of calcareous deposits in artificial sea water by impedances techniques: 2-deposit of $Mg(OH)_2$ without $CaCO_3$, Electrochimica Acta, 45 (2000) 1837-1845.
[15] R. Jaouhari, A. Benbachir, A. Guenbour, C. Gabrielli, J. Garcia-Jareno, G. Maurin, Influence of water composition and substrate on electrochemical scaling, Journal of The Electrochemical Society, 147 (2000) 2151-2161.
[16] A. Martinod, A. Neville, M. Euvrad, K. Sorbie, Electrodeposition of a calcareous layer: Effects of green inhibitors, Chemical Engineering Science, 64 (2009) 2413-2421.
[17] C. Deslouis, P. Falaras, O. Gil, M. Jeannin, V. Maillot, B. Tribollet, Influence of clay on calcareous deposit in natural and artificial sea water, Electrochimica Acta, 51 (2006) 3173-3180.
[18] S.-H. Lin, S.C. Dexter, Effects of temperature and magnesium ions on calcareous deposition, Corrosion, 44 (1988) 615-622.
[19] J. Marin-Cruz, R. Cabrera-Sierra, M. Pech-Canul, I. Gonzalez, Characterization of different allotropic forms of calcium carbonate scales on carbon steel by electrochemical impedance spectroscopy, Journal of Applied Electrochemistry, 34 (2004) 337-343.
[20] S.M. Hoseinieh, T. Shahrabi, Influence of ionic species on scaling and corrosion performance of AISI 316L rotating disk electrodes in artificial seawater, Desalination, 409 (2017) 32-46.

[21] S.M. Hoseinieh, T. Shahrabi, B. Ramezanzadeh, M.F. Rad, The role of porosity and surface morphology of calcium carbonate deposits on the corrosion behavior of unprotected API 5L X52 rotating disk electrodes in artificial seawater, Journal of The Electrochemical Society, 163 (2016) C515-C529.
[22] S. Mathé, Chimie des solutions, Dunod, 2018.
[23] W.M. Haynes, CRC Handbook of chemistry and physics, 97th ed., CRC press2017.
[24] H. Vogt, R.J. Balzer, The bubble coverage of gas-evolving electrodes in stagnant electrolytes, Electrochimica Acta, 50 (2005) 2073-2079.
[25] C. Barchiche, C. Deslouis, D. Festy, O. Gil, P. Refait, S. Touzain, B. Tribollet, Characterization of calcareous deposits in artificial seawater by impedance techniques: 3 — deposit of $CaCO_3$ in the presence of Mg(II), Electrochimica Acta, 48 (2003) 1645-1654.
[26] M. Piri, R. Arefinia, Investigation of the hydrogen evolution phenomenon on $CaCO_3$ precipitation in artificial seawater, Desalination, 444 (2018) 142-150.
[27] O. Scialdone, A. Galia, S. Sabatino, Electro-generation of H_2O_2 and abatement of organic pollutant in water by an electro-Fenton process in a microfluidic reactor, Electrochemistry Communications, 26 (2013) 45.
[28] J. Newman, K.E. Thomas-Alyea, Electrochemical systems, 3rd ed., John Wiley & Sons, 2012.
[29] O. Velts, M. Uibu, J. Kallas, R. Kuusik, CO_2 mineral trapping: Modeling of calcium carbonate precipitation in a semi-batch reactor, Energy Procedia, 4 (2011) 771-778.
[30] S.J. Kakaraniya, A. Mehra, Reactive precipitation in gas−liquid systems, Industrial & Engineering Chemistry Research, 46 (2007) 1125-1137.
[31] C. Kazadi Mbamba, D.J. Batstone, X. Flores-Alsina, S. Tait, A generalised chemical precipitation modelling approach in wastewater treatment applied to calcite, Water Research, 68 (2015) 342-353.
[32] Y. Zhang, R.A. Dawe, Influence of Mg^{2+} on the kinetics of calcite precipitation and calcite crystal morphology, Chemical Geology, 163 (2000) 129-138.
[33] M. Ben Amor, D. Zgolli, M.M. Tlili, A.S. Manzola, Influence of water hardness, substrate nature and temperature on heterogeneous calcium carbonate nucleation, Desalination, 166 (2004) 79-84.
[34] J.N. Butler, Carbon dioxide equilibria and their applications, 1st ed., Taylor & Francis Group, New York: Routledge, 1991.
[35] P. Bénézeth, G.D. Saldi, J.-L. Dandurand, J. Schott, Experimental determination of the solubility product of magnesite at 50 to 200°C, Chemical Geology, 286 (2011) 21-31.
[36] P. Reichert, AQUASIM - a tool for simulation and data analysis of aquatic systems, Water Science and Technology, 30 (1994) 21.
[37] C.A. Martínez-Huitle, M. Panizza, Electrochemical oxidation of organic pollutants for wastewater treatment, Current Opinion in Electrochemistry, 11 (2018) 62-71.
[38] E. Mousset, L. Quackenbush, C. Schondek, A. Gerardin-Vergne, S. Pontvianne, S. Kmiotek, M.-N. Pons, Effect of homogeneous Fenton combined with electron transfer on the fate of inorganic chlorinated species in synthetic and reclaimed municipal wastewater, Electrochimica Acta, 334 (2020) 135608.
[39] E. Mousset, D.D. Dionysiou, Photoelectrochemical reactors for treatment of water and wastewater: A review, Environmental Chemistry Letters, 18 (2020) 1301-1318.
[40] N. Vatistas, C. Comninellis, The persulfate process for the mediated oxidation of organic pollutants, in: C. Comninellis, G. Chen (Eds.) Electrochemistry for the Environment, Springer New York, New York, NY, 2010, pp. 229-244.
[41] B.P. Chaplin, Critical review of electrochemical advanced oxidation processes for water treatment applications, Environmental Science: Processes & Impacts, 16 (2014) 1182-1203.
[42] B.P. Chaplin, Chapter 17 - Advantages, disadvantages, and future challenges of the use of electrochemical technologies for water and wastewater treatment, in: C.A. Martínez-Huitle, M.A. Rodrigo, O. Scialdone (Eds.) Electrochemical Water and Wastewater Treatment, Butterworth-Heinemann, 2018, pp. 451-494.
[43] A.R. Despić, Deposition and dissolution of metals and alloys. Part B: Mechanisms, kinetics, texture, and morphology, in: B.E. Conway, J.O.M. Bockris, E. Yeager, S.U.M. Khan, R.E. White (Eds.) Comprehensive Treatise of Electrochemistry: Volume 7 Kinetics and Mechanisms of Electrode Processes, Springer US, Boston, MA, 1983, pp. 451-528.
[44] H. Karoui, B. Riffault, M. Jeannin, A. Kahoul, O. Gil, M. Ben Amor, M.M. Tlili, Electrochemical scaling of stainless steel in artificial seawater: Role of experimental conditions on $CaCO_3$ and $Mg(OH)_2$ formation, Desalination, 311 (2013) 234-240.
[45] F. Sopaj, N. Oturan, J. Pinson, F.I. Podvorica, M.A. Oturan, Effect of cathode material on electro-Fenton process efficiency for electrocatalytic mineralization of the antibiotic sulfamethazine, Chemical Engineering Journal, 384 (2020) 123249.

[46] A.J. Bard, L.R. Faulkner, Electrochemical methods: Fundamentals and applications, John Wiley & Sons2001.
[47] M.M. Tlili, M. Benamor, C. Gabrielli, H. Perrot, B. Tribollet, Influence of the interfacial pH on electrochemical $CaCO_3$ precipitation, Journal of The Electrochemical Society, 150 (2003) C765.
[48] S. Sarkar, W. Aquino, Electroneutrality and ionic interactions in the modeling of mass transport in dilute electrochemical systems, Electrochimica Acta, 56 (2011) 8969-8978.
[49] T. Li, T.C. Keener, L. Cheng, Carbon dioxide removal by using $Mg(OH)_2$ in a bubble column: Effects of various operating parameters, International Journal of Greenhouse Gas Control, 31 (2014) 67-76.
[50] M. Panizza, P.A. Michaud, G. Cerisola, C. Comninellis, Anodic oxidation of 2-naphthol at boron-doped diamond electrodes, Journal of Electroanalytical Chemistry, 507 (2001) 206-214.
[51] P. Cañizares, J. García-Gómez, I. Fernández de Marcos, M.A. Rodrigo, J. Lobato, Measurement of mass-transfer coefficients by an electrochemical technique, Journal of Chemical Education, 83 (2006) 1204.
[52] R.A.W. Dryfe, 20 - Liquid junction potentials, in: C.G. Zoski (Ed.) Handbook of Electrochemistry, Elsevier, Amsterdam, 2007, pp. 849-877.
[53] C. Barchiche, C. Deslouis, O. Gil, P. Refait, B. Tribollet, Characterisation of calcareous deposits by electrochemical methods: Role of sulphates, calcium concentration and temperature, Electrochimica Acta, 49 (2004) 2833-2839.
[54] T. Okstad, Ø. Rannestad, R. Johnsen, K. Nisancioglu, Significance of hydrogen evolution during cathodic protection of carbon steel in seawater, Corrosion, 63 (2007) 857-865.
[55] C. Arkam, Quartz crystal electrogravimetry with controlled hydrodynamics, Journal of The Electrochemical Society, 141 (1994) L103.
[56] H. Vogt, The role of single-phase free convection in mass transfer at gas evolving electrodes — 1. Theoretical, Electrochimica Acta, 38 (1993) 1421-1426.
[57] H. Vogt, Gas-evolving electrodes, in: E. Yeager, J.O.M. Bockris, B.E. Conway, S. Sarangapani (Eds.) Comprehensive Treatise of Electrochemistry: Electrodics: Transport, Springer US, Boston, MA, 1983, pp. 445-489.
[58] L.J.J. Janssen, Behaviour of and mass transfer at gas-evolving electrodes, Electrochimica Acta, 34 (1989) 161-169.
[59] M.G. Fouad, G.H. Sedahmed, Mass transfer at gas evolving screen electrodes, Electrochimica Acta, 20 (1975) 615-618.
[60] C. Gabrielli, G. Maurin, G. Poindessous, R. Rosset, Nucleation and growth of calcium carbonate by an electrochemical scaling process, Journal of Crystal Growth, 200 (1999) 236-250.
[61] Y. Ben Amor, L. Bousselmi, M.C. Bernard, B. Tribollet, Nucleation-growth process of calcium carbonate electrodeposition in artificial water — influence of the sulfate ions, Journal of Crystal Growth, 320 (2011) 69-77.
[62] T. Chen, A. Neville, M. Yuan, Calcium carbonate scale formation — assessing the initial stages of precipitation and deposition, Journal of Petroleum Science and Engineering, 46 (2005) 185-194.
[63] M. Kitamura, Crystallization and transformation mechanism of calcium carbonate polymorphs and the effect of magnesium ion, Journal of Colloid and Interface Science, 236 (2001) 318-327.
[64] K.E. Mantel, W.H. Hartt, T.-Y. Chen, Substrate, surface finish, and flow rate influences on calcareous deposit structure, Corrosion, 48 (1992) 489-500.
[65] C. Gabrielli, Quartz crystal microbalance investigation of electrochemical calcium carbonate scaling, Journal of The Electrochemical Society, 145 (1998) 2386.
[66] S. Xu, Structure and morphology of electrodeposited $CaCO_3$: X-ray diffraction and microscopy studies, Journal of The Electrochemical Society, 146 (1999) 3315.
[67] C. Gabrielli, M. Keddam, A. Khalil, R. Rosset, M. Zidoune, Study of calcium carbonate scales by electrochemical impedance spectroscopy, Electrochimica Acta, 42 (1997) 1207-1218.
[68] H.J. Meyer, The influence of impurities on the growth rate of calcite, Journal of Crystal Growth, 66 (1984) 639-646.
[69] F.L. Sayles, W.S. Fyfe, The crystallization of magnesite from aqueous solution, Geochimica et Cosmochimica Acta, 37 (1973) 87-99.
[70] L. Hopkinson, K. Rutt, G. Cressey, The transformation of nesquehonite to hydromagnesite in the system CaO-MgO-H_2O-CO_2: An experimental spectroscopic study, The Journal of Geology, 116 (2008) 387-400.
[71] M. Hänchen, V. Prigiobbe, R. Baciocchi, M. Mazzotti, Precipitation in the Mg-carbonate system — effects of temperature and CO_2 pressure, Chemical Engineering Science, 63 (2008) 1012-1028.

V. Mass transfer evolution in microfluidic thin film electrochemical reactor: New correlations from millimetric to submillimetric interelectrode distances

(Published as scientific article, reference: *Electrochemistry Communications 130 (2021) 107097*)

V.1. Introduction

Electrochemical reactor with micrometric feature has brought interesting approach in multiple disciplines such as electrosynthesis **[1-5]**, electrodeposition **[6, 7]**, sensor development **[8, 9]** and wastewater treatments **[10-15]**. Versatility, small footprint, suitability for fast kinetic reactions, easily thermoregulated, independence of supporting electrolyte, mass transfer intensification and huge energy saver are amongst the leverages that are sought from the microfluidic flow reactor technology **[16-18]**. Mass transfer characterization in submillimetric range has already been scrutinized since the early 70's with the development of flow rectangular channel, tubular and granular bed electrochemical reactors **[19-27]**. Estimating the average k_m is particularly crucial for sizing the electrochemical reactors and for scale-up studies **[28]**. Regarding millimetric scale reactors, mass transfer correlations of different geometries with or without turbulence promoters **[28-33]**, electrodes morphology **[34, 35]** as well as innovative electrolyte inlet **[36, 37]** and agitation system **[38, 39]** have been widely investigated in literature. However, more data are required on the mass transfer evolution and correlation in microfluidic parallel-plate reactors which are applicable at larger scale **[40]**. It could be due to challenging experimentation in different hydrodynamics conditions and temperature as well as to the difficulty to configure 3-electrode setups under narrow gap **[38, 39]**. Hence, it has been reported for the first time here-in the mass transfer evolution over a wide range of d_{elec} from millimetric (3 mm) down to submillimetric value (100 µm) in a flow-by parallel-plate reactor with a large effective surface area. Its design is more apt for scale-up application in industries. A model has been proposed to evaluate k_m as function of d_{elec}. Finally, mass transfer correlation involving dimensionless numbers in microfluidic and millimetric feature has been proposed.

V.2. Experimental section

V.2.1. Electrochemical system

The electrochemical setup consisted of a parallel-plate reactor and its exploded view is illustrated in **Fig. III.2** in **Chapter 3**. Both working and counter electrodes were planar rectangles, facing one another. Stainless steel was the WE while BDD served as CE. Their W and L were 5 and 10 cm respectively giving out an effective surface area of 50 cm^2. A spacer made of PTFE with varying

thicknesses of 100, 250, 500, 1000, 1500, 2000 and 3000 µm was used to separate the WE and CE. Thus, they defined the varying d_{elec} investigated in this work, distinguished from micrometric progressively into a typical millimetric configuration. Ag-AgCl was used as the RE.

V.2.2. Mass transfer characterization

The characterization of mass transfer in the electrochemical cells was carried out following the widely adopted limiting current technique method as described elsewhere **[41, 42]**. 0.5 L of electrolytic solution containing 0.05 M $K_3Fe(CN)_6$, 0.10 M $K_4Fe(CN)_6$ and 0.50 M Na_2CO_3 as supporting electrolyte was employed. High concentration of supporting electrolyte was used to avoid electro-migration effect **[41, 43]**. Using this technique, the reduction of ferricyanide ($Fe(CN)_6^{3-}$) was brought to a maximum rate (limiting current plateau) so that its reduction was purely controlled by mass transfer regime. The physical properties of electrolyte at different investigated temperatures **[29, 30, 44]** are given in **Table V.1**. LSV was swept in the region of cathodic potential activity of ferri-ferrocyanide electrolyte over a range of potentials from 0.2 to -1.6 V versus Ag-AgCl reference electrode at 2.5 mV s^{-1} scan rate. Within the adopted range of flow rates, the scan rate was sufficiently slow to attain steady-state **[45]**. The BDD CE features a wide potential window of water stability with O_2 evolution reaction (OER) occuring at 2.5-2.7 V/SHE. At this high OER potential, negligible interference of O_2 evolved on the CE was expected in the range of investigated cathodic potential. Moreover, to further confirm the influence of the presence of dissolved O_2 in the electrolyte, preliminary experiments were conducted at both extremities (i.e., 100 and 3000 µm) as well as using 500 µm interelectrode gap under the condition free of dissolved O_2. The electrolyte in the reservoir was aerated with N_2 gas for 30 min before LSV was performed. The results indicated that the limiting current plateau (just before the reduction of solvent) were not influenced by the presence of dissolved O_2. The outcoming limiting current values (I_{lim} in A) under d_{elec} and investigated operating conditions were related to average k_{m} (m s^{-1}) via **Eq. (V.1) [42]**:

$$k_{\mathrm{m}} = \frac{I_{\mathrm{lim}}}{n_{\mathrm{e}}\, F\, S\, C_{\mathrm{SOL}}} \qquad \text{(V.1)}$$

where n_{e} is the number of electrons involved in the reduction reaction of ferri- to ferrocyanide (i.e., 1), F the Faraday's constant (96485 C mol^{-1}), S the effective surface area of working electrode (m^2) and C_{SOL} the molar concentration of ferricyanide in the bulk (mol m^{-3}).

During the characterization of k_{m} over the range of d_{elec}, electrolyte cross-sectional velocity, u_{L}, in m min^{-1} (**Eq. (V.2)**) inside electrochemical reactors was kept constant (4 m min^{-1}) from one distance to another.

$$u_{\mathrm{L}} = \frac{\dot{V}_{\mathrm{F}}}{A_{\mathrm{C}}} \quad \text{(V.2)}$$

$$A_{\mathrm{C}} = d_{\mathrm{elec}} W \quad \text{(V.3)}$$

where $\dot{V}_{\mathrm{F}}$ is the volumetric flow rate (in m^3 min^{-1}), W is the electrode width (in m), A_{C} is the cross-sectional area of electrolyte passage (in m^2) and d_{elec} is the interelectrode distance (in m).

This was to investigate the influence of d_{elec} on k_{m}, without considering the enhancement of mass transfer related to convective flow of electrolyte. To achieve the purpose, the electrolyte flow rate was adjusted accordingly to the volume of reactor. Consequently, not only the superficial velocity was identical, but electrolyte residence time (τ) in min (**Eq. (V.4)**) was also kept identical (0.025 min) from one configuration to another.

$$\tau = \frac{\dot{V}_{\mathrm{F}}}{V_{\mathrm{R}}} \quad \text{(V.4)}$$

$$V_{\mathrm{R}} = d_{\mathrm{elec}} W L \quad \text{(V.5)}$$

where V_{R} is the cell volume (in m^3) and L is the electrode length (in m).

The flow rate varied from 10 to 600 mL min^{-1}, when d_{elec} increased from 100 to 3000 µm. Across all investigated d_{elec} and for relevant comparison, electrolyte flow was kept under laminar regime according to the following range of Reynolds (*Re*) values: 7 to 623. Owing to the entrance manifolds of tube-type entry of the electrochemical cell, under similar hydrodynamic regimes, electrolyte recirculating zone in the reactor was considered minimal in all investigated configurations **[36, 46, 47]**.

Table V.1. Physical properties of ferri-ferrocyanide electrolytic solution at 10, 25 and 50 °C.

Temperature / °C	**Density, ρ_{L} / kg m^{-3}**	**Kinematic viscosity, ν_{L} / m^2 s^{-1}**	**Diffusion coefficient, D_{L} / m^2 s^{-1}**
10	1042.06	14.28×10^{-7}	4.31×10^{-10}
25	1038.04	9.82×10^{-7}	6.48×10^{-10}
50	1028.87	6.06×10^{-7}	11.39×10^{-10}

V.3. Results and discussion

V.3.1. Mass transfer behavior over a wide range of interelectrode distances

Voltammograms of electrochemical reactors with different d_{elec} study were illustrated in **Fig. V.1**. From the plateau of I_{lim} identified on the voltammograms, average k_m values over the wide range of d_{elec} are shown in **Fig. V.2**. Interestingly, two distinct behaviors of k_m were observed as a first approach. The increase of k_m in the millimetric range from 3000 µm down to 1000 µm seemed linear (slope: -10^{-3} s^{-1}, coefficient of determination $R^2 = 0.91$). Beneath 1000 µm, k_m increased drastically with decreasing d_{elec} further down into the micrometric ranges. This trend demonstrates that the mass transfer was massively enhanced while transitioning from millimetric to micrometric gap, which confirms the interest of microfluidic reactors for transfer intensification **[14, 16, 48-53]**. The range of k_m determined under both millimetric and micrometric configurations in this work are in close agreement with those reported in literature (**Table II.3** in **Chapter 2**). In millimetric ranges, k_m values of 1.61×10^{-5} m s^{-1} and 1.82×10^{-5} m s^{-1} were obtained respectively for 3000 µm and 1000 µm, in comparison to reported values of k_m between $0.30 - 1.20 \times 10^{-5}$ m s^{-1} using 5000 µm **[54]** and 1.60×10^{-5} m s^{-1} using 1000 µm **[28]**.

Levich equation (**Eq. (V.6)**) has been widely adopted in literature to relate I_{lim} to electrolyte volume flow rate in thin rectangular channel electrode reactors **[19, 55, 56]**.

$$I_{lim} = 0.925 n_e F W C_{SOL} (D_L x_e)^{2/3} \left(\frac{\dot{V}_F}{h^2 d}\right)^{1/3} \quad \text{(V.6)}$$

where

$$\dot{V}_F = u_L W d_{elec} \quad \text{(V.7)}$$

$$h = \frac{d_{elec}}{2} \quad \text{(V.8)}$$

W is the electrode width (in cm), x_e is the electrode length (equivalent to L, in cm), $\dot{V}_F$ in cm^3 s^{-1}, h is half the cell depth (in cm), d is the channel width (equivalent to W in this work, in cm) and u_L in cm s^{-1}. **Equation (V.6)** is ideally applicable under conditions where $h \ll d$, sufficiently large electrode area, the electrolyte flow rate is not too low and the profile of electrolyte flow velocity in the channel is parabolic **[19]**. Relating **Eq. (V.1)** and **Eq. (V.6)** gives out an expression of average k_m in function of d_{elec} (**Eq. (V.9)**):

$$k_{\mathrm{m}} = \frac{2.94\, {D_{\mathrm{L}}}^{2/3}\, {u_{\mathrm{L}}}^{1/3}\, W\, L^{2/3}}{S\, {d_{\mathrm{elec}}}^{1/3}} \qquad \text{(V.9)}$$

Slight adjustment of **Eq. (V.6)** coefficient (2.94) was done to match the experimental data and this deviation could be due to the non-ideality of direct application of **Eq. (V.6)** under the condition where electrode width and channel width are identical ($W = d$), i.e. in which an edge effect could not be neglected **[19, 40]**. The plot of experimental and theoretical k_{m} versus d_{elec} is given in **Fig. V.2**. The theoretical curve matches well with the experimental counterpart with a deviation of 0.000187 when they were subjected to RMSE (**Eq. (III.3)**).

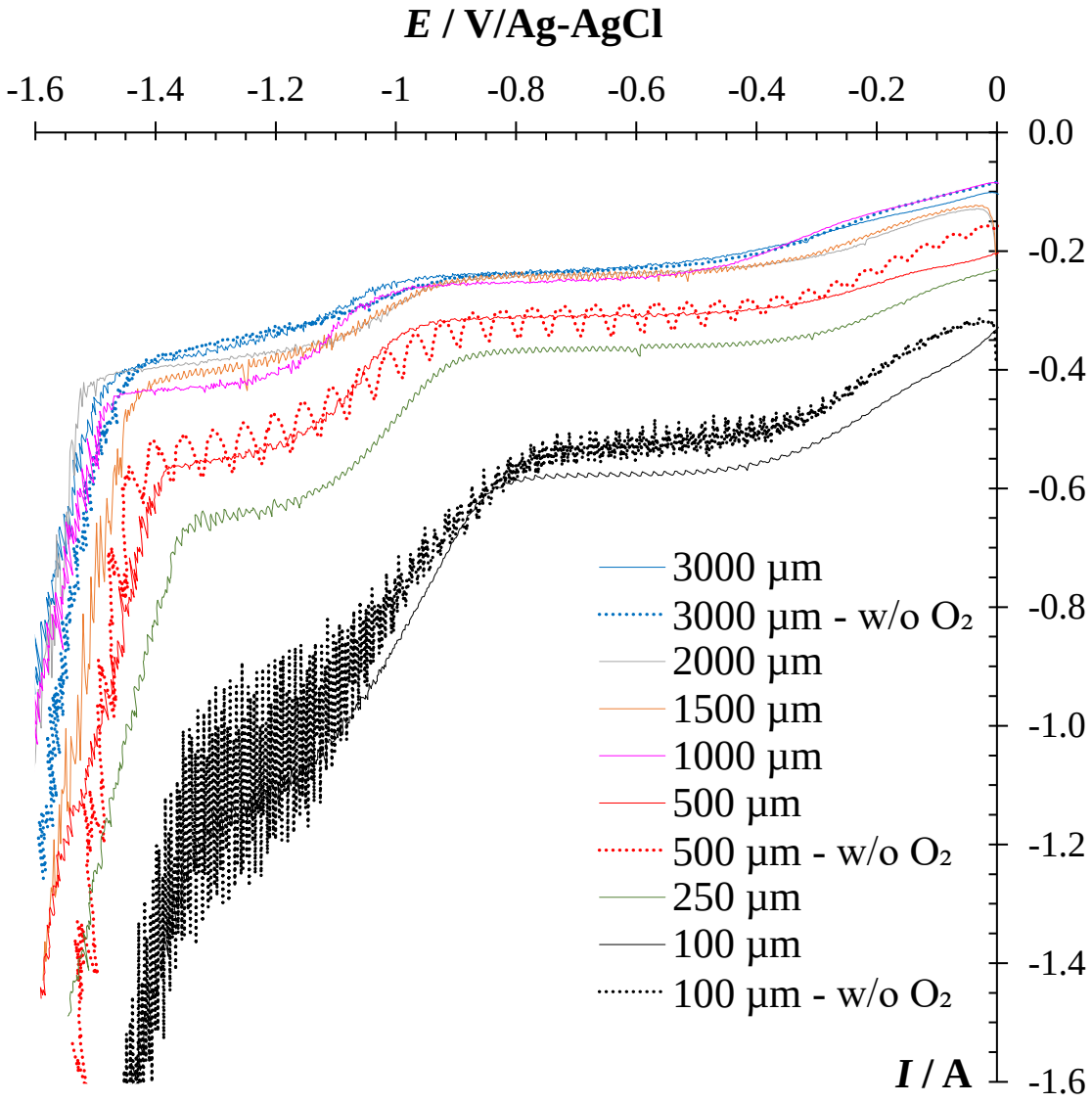

Fig. V.1. LSV of the electrochemical cell with all investigated d_{elec}. WE: stainless steel, CE: BDD and RE: Ag/AgCl. 0.5 L of electrolyte consisted of 0.05 M $K_3Fe(CN)_6$, 0.10 M $K_4Fe(CN)_6$ and 0.50 M Na_2CO_3. Cathodic potential ranges from 0.2 to -1.6 V vs. Ag-AgCl at 2.5 mV s^{-1} scan rate. Dotted line: experiments in the absence of dissolved O_2 by purging with N_2 gas in the feed tank.

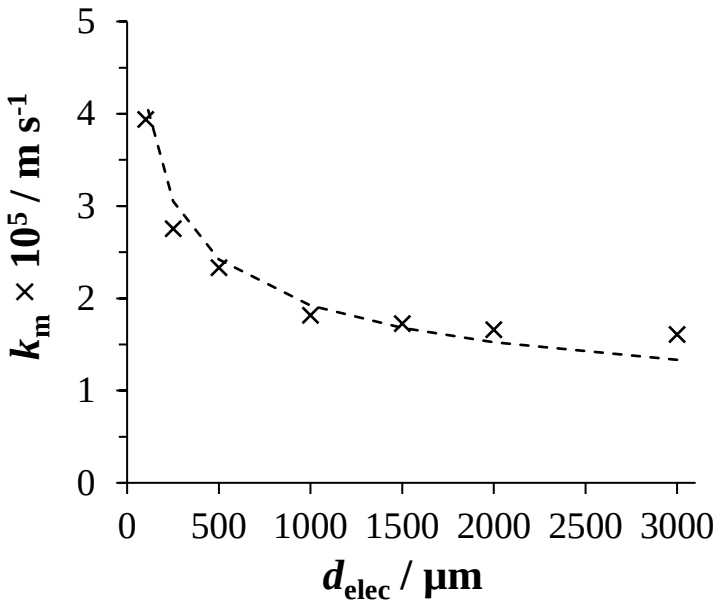

Fig. V.2. Variation of experimental and theoretical average k_m as function of d_{elec}. **Operating conditions**: Flow rate: 10 – 600 mL min^{-1}, temperature: 25 °C, u_L: 4 m min^{-1} and τ: 0.025 min.

V.3.2. Mass transfer correlations in microfluidic and millimetric parallel-plate electrochemical reactors

Evaluation of mass transfer correlations were conducted on electrochemical reactors with 100 and 500 µm (representing micrometric setup) and 3000 µm (representing millimetric setup). The variation of mass transfer with fluid hydrodynamics, fluid physicochemical properties and eventually electrochemical reactor geometry can be expressed using theoretical dimensionless Sherwood (*Sh*) correlation accounting for *Re*, Schmidt (*Sc*), dimensionless distance (*Le*) numbers as well as d_{elec}/W aspect ratio written in **Eq. (V.10) [57]**.

$$Sh = aRe^b Sc^c Le^d \left(\frac{2}{1+\frac{d_{elec}}{W}}\right)^{1/3} \quad \text{(V.10)}$$

The form of expression in **Eq. (V.10)** is valid with strict respect to the Lévêque approximation **[55, 58]**, which imposes that (i) the electrolyte is incompressible having constant physical properties, (ii) the flow is in laminar steady-state, becomes fully developed after a certain entry length for a given reactor geometry, (iii) mass transfer is due to convection and diffusion, (iv) electrolyte flow is treated as bidimensional in *x*-*y* planes (**Fig. III.2**), (v) molecular diffusion of reactive species only occurs in *x*-axis (normal to the electrodes), (vi) friction at walls induced retardation and produces parabolic velocity profile with maximum velocity at the center of the channel and (vii) diffusional double-layer is a lot smaller than hydrodynamic boundary layer. This dimensionless expression is particularly useful to estimate the average k_m values during scale-up or scale-down of an electrochemical reactor

at the operating conditions of interest. The entry length (E_L) was evaluated via **Eq. (V.11) [58, 59]** and they were plotted in **Fig. V.3**. It increased from 0.027 to 21.7 mm when d_{elec} increased from 100 to 3000 µm.

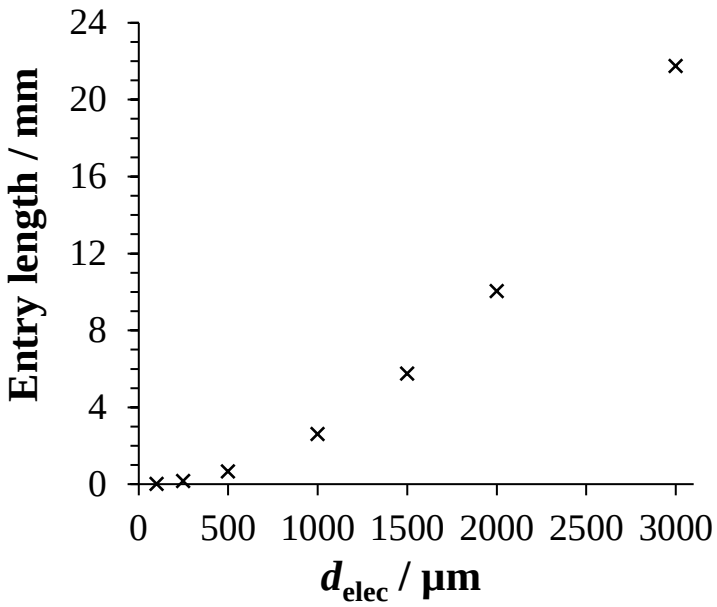

Fig. V.3. Variation of entry length of electrochemical cell with different d_{elec}.

Re, *Sc* and *Le* are defined by **Eqs. (V.12)-(V.14)** whilst *a*, *b*, *c* and *d* are constant parameters.

$$E_L = 0.01\, d_H\, Re \tag{V.11}$$

$$Re = \frac{u_L\, d_H}{\upsilon_L} \tag{V.12}$$

$$Sc = \frac{\upsilon_L}{D_L} \tag{V.13}$$

$$Le = \frac{d_H}{L} \tag{V.14}$$

$$d_H = \frac{2\, W\, d_{elec}}{W + d_{elec}} \tag{V.15}$$

D_L and υ_L are diffusion coefficient and kinematic viscosity respectively both in $m^2\ s^{-1}$ taken at the operated temperature **[29, 30, 44]** (**Table V.1**). d_H is hydraulic diameter in m.

To establish the theoretical *Sh* correlation, k_m values were measured at different electrolytic flow rates and temperatures. Experimental *Sh* were computed using **Eq. (V.16) [42]** and they were plotted against varying investigated *Re* and *Sc* numbers. The coefficients *a*, *b*, *c* and *d* were extracted from the best fitting between theoretical and experimental *Sh* plots.

$$Sh = \frac{k_m \, d_H}{D_L} \quad \text{(V.16)}$$

The influence of electrolyte flow rate and temperature on k_m for each selected configuration is presented in **Fig. V.4**. k_m increased with increasing flow rate across both configurations at constant temperature (**Fig. V.4(a)**). This finding is expected owing to the enhancement of mass transfer brought to the $Fe(CN)_6^{3-}$ reduction reaction, when higher flow rate was tested. It can be noticed that the k_m increase with increasing electrolyte flow rate was markedly pronounced in microfluidic device (100 and 500 µm) in comparison to the distance of 3000 µm (**Fig. V.4(a)**). The highest k_m (5.06×10^{-5} m s^{-1} at 0.05 L min^{-1}) was achieved when the electrochemical reactor was used with 100 µm interelectrode gap. In addition, when the temperature varied from 10 to 50°C, k_m increased from 3.28×10^{-5} to 5.22×10^{-5} m s^{-1} for the 100 µm, from 1.66×10^{-5} to 3.11×10^{-5} m s^{-1} for the 500 µm and from 1.20×10^{-5} to 2.41×10^{-5} m s^{-1} for the 3000 µm gap (**Fig. V.4(b)**). These trends were due to the increase in diffusivity of $Fe(CN)_6^{3-}$ reducing species with temperature **[44, 60, 61]**.

Using the k_m values obtained under different operating conditions, experimental *Sh* were evaluated as illustrated in **Fig. V.5**. The best fitting of **Eq. (10)** to the experimental data of each submillimetric and millimetric configuration were achieved when the coefficients *a*, *b*, c and *d* took the values provided in **Table V.2**. The coefficient *a* slightly varied: it decreased from 3.00 to 2.31 from 100 µm to 500 µm d_{elec} before rising up again to 3.01 using 3000 µm configuration. The values were within the range reported in literature **[57, 62]**. *b* variation between 0.32 and 0.37 corroborated the reported *Re* exponent value close to 0.30 in literature that corresponds to fully developed laminar flow **[34, 37, 57, 62, 63]**. The widely reported 1/3 ratio of *Sc* exponent *c* as well as of *Le* exponent *d* were obtained to match the experimental data under all three setups **[30, 32, 34, 37, 57, 62, 63]**.

The fitting of theoretical *Sh* correlations with experimental data for all three d_{elec} configurations were evaluated using RMSE (**Eq. (III.3)**). Deviation of 0.038, 0.056 and 0.024 were calculated between logarithmic plots of theoretical-experimental *Sh* against *Re* for 100, 500 and 3000 µm configurations respectively. In function of *Sc*, theoretical plot deviated from the experimental data by 0.070, 0.047 and 0.026 in respective order of 100, 500 and 3000 µm. Therefore, theoretical *Sh* correlations fitted very well with their experimental counterparts.

Given the trend of *a*, *b*, c and *d* coefficients under the large spectrum of investigated d_{elec}, under fully developed laminar regime, an average *Sh* correlation written in **Eq. (V.17)** can be proposed.

$$Sh_{\text{ave}} = 2.7733 Re^{0.35} Sc^{1/3} Le^{1/3} \left(\frac{2}{1+\frac{d_{\text{elec}}}{w}} \right)^{1/3} \quad \text{(V.17)}$$

The average *Sh* correlation is in close agreement with the one proposed by Pickett et al. **[57]** with the *a* coefficient slightly higher in this present work. It could be attributed to a larger surface area used here (50 cm^2 vs. 16 cm^2 in **[57]**) as well as enhancement of mass transfer brought to the microfluidic reactor.

Table V.2. Fitted values of *a*, *b*, *c* and *d* of theoretical *Sh* correlation in parallel-plate electrochemical reactors under microfluidic and millimetric configurations under laminar regime.

Configuration	***a***	***b***	***c***	***d***	***Re* range**	***Sc* range**
Thin film reactor (distance: 100 µm)	3.00	0.32	0.33	0.33	7 - 34	532 - 3315
Thin film reactor (distance: 500 µm)	2.31	0.37	0.33	0.33	34 - 269	532 - 3315
Parallel-plate (distance: 3000 µm)	3.01	0.37	0.33	0.33	128 - 623	532 - 3315

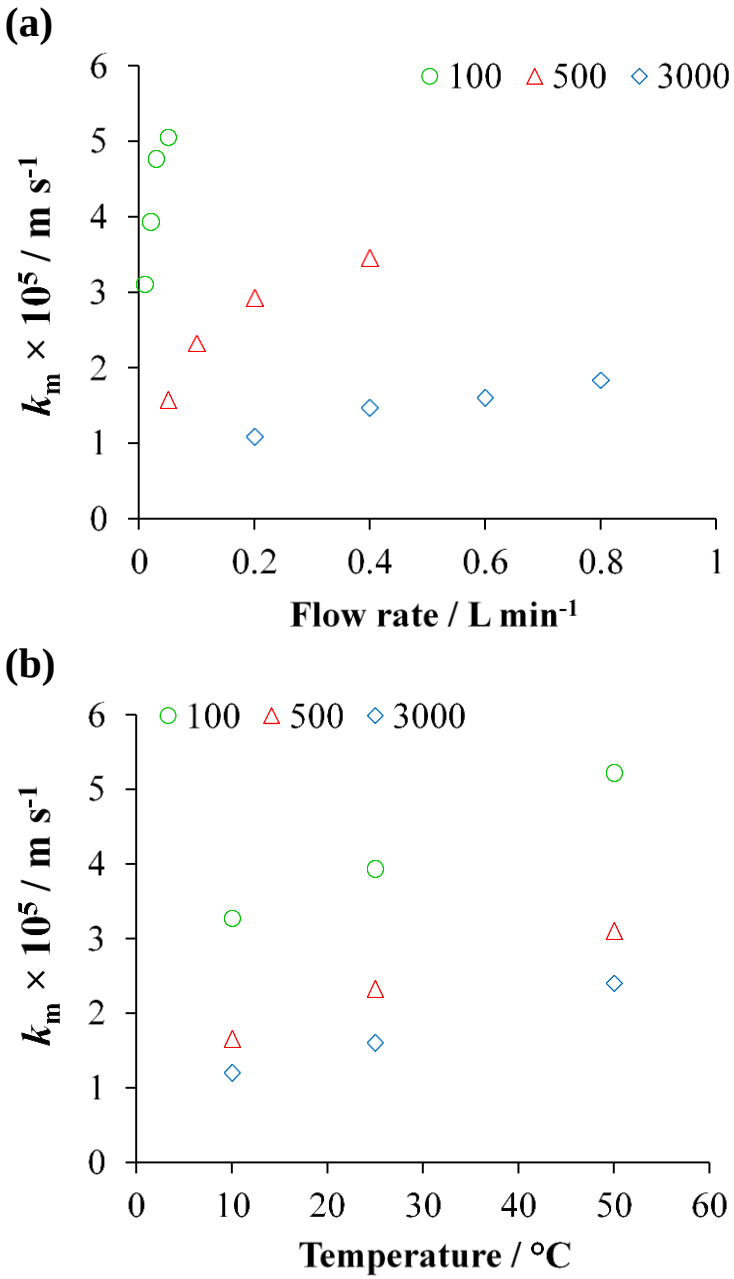

Fig. V.4. k_m as function of **(a)** electrolyte flow rate and **(b)** temperature for d_{elec} of 100, 500 and 3000 µm. **Operating conditions**: **(a)** Temperature = 25 °C and **(b)** flow rate = 0.02, 0.10 and 0.60 L min^{-1} for d_{elec} of 100, 500 and 3000 µm respectively.

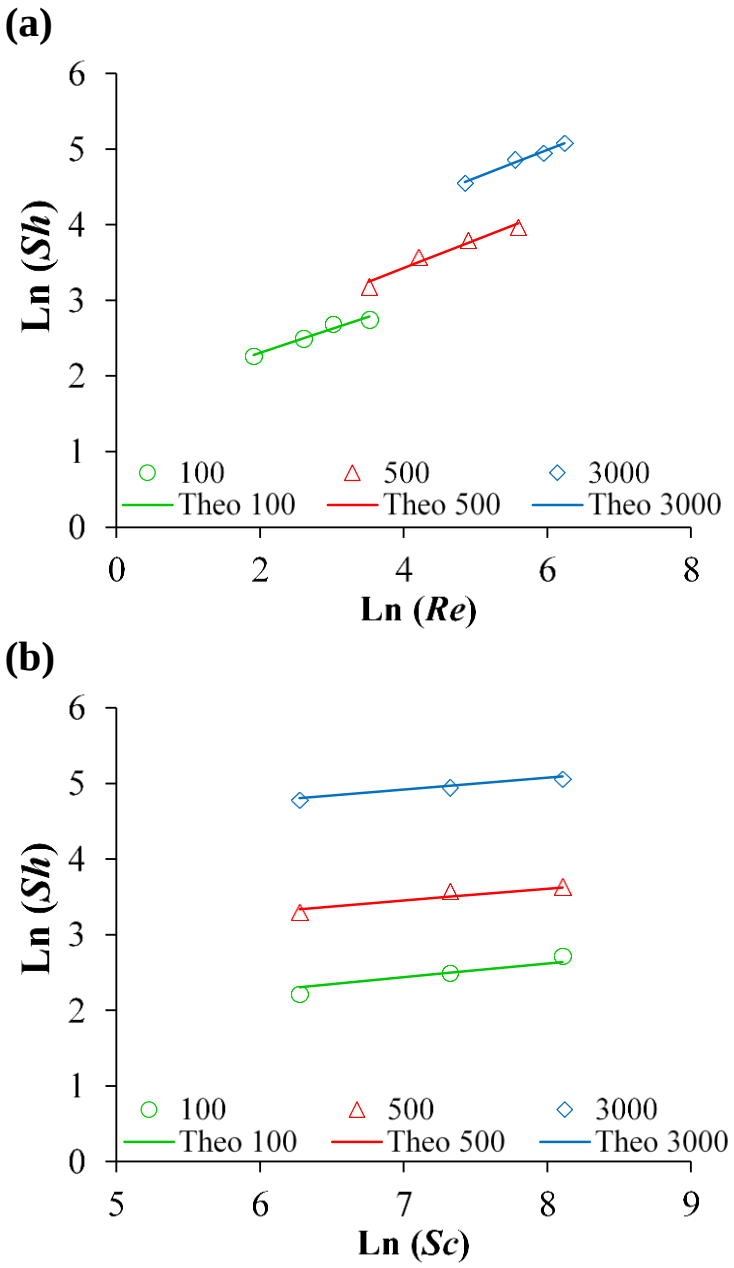

Fig. V.5. Experimental (symbol) versus theoretical *Sh* correlation (continuous line) as function of **(a)** *Re* and **(b)** *Sc* numbers. **Operating conditions**: **(a)** Temperature = 25 °C and **(b)** flow rate = 0.02, 0.10 and 0.60 L min^{-1} for d_{elec} of 100, 500 and 3000 µm respectively.

V.4. Conclusions

The variation of k_m as function of d_{elec} from millimetric to micrometric range has been newly reported. A novel single equation to estimate k_m over a wide range of d_{elec} has been proposed. It highlights the inverse relationship between k_m and d_{elec}, which makes k_m values greatly increased at distances below 1000 µm. Using experimental k_m data in submillimetric as well as millimetric configurations at varying flow rates ($7<Re<623$) and temperatures ($532<Sc<3315$), mass transfer correlations taking into consideration not only fluid properties but also electrochemical reactor hydrodynamic and geometry, have been established. The theoretical *Sh* number plots matched very well with their corresponding experimental values. The newly established *Sh* correlation in this work covered a wide interval of interelectrode distances. They were obtained using an electrochemical cell whose design is more adapted for multidisciplinary applications at larger scale whilst the robustness of the *Sh* correlation was experimentally justified. The results presented here-in will be particularly helpful for k_m estimation in a parallel-plate reactor under wide range of d_{elec} (i.e., from several tens of micrometers to several millimeters) at given applied operating conditions. These expressions can be particularly suitable for micro-distances that can be useful for great mass transfer intensification, unlike millimetric or even centimetric distances often implemented.

References

[1] C.A. Paddon, M. Atobe, T. Fuchigami, P. He, P. Watts, S.J. Haswell, G.J. Pritchard, S.D. Bull, F. Marken, Towards paired and coupled electrode reactions for clean organic microreactor electrosyntheses, Journal of Applied Electrochemistry, 36 (2006) 617.
[2] A.A. Folgueiras-Amador, K. Philipps, S. Guilbaud, J. Poelakker, T. Wirth, An easy-to-machine electrochemical flow microreactor: Efficient synthesis of isoindolinone and flow functionalization, Angewandte Chemie International Edition, 56 (2017) 15446-15450.
[3] C. Renault, J. Roche, M.R. Ciumag, T. Tzedakis, S. Colin, K. Serrano, O. Reynes, C. André-Barrès, P. Winterton, Design and optimization of electrochemical microreactors for continuous electrosynthesis, Journal of Applied Electrochemistry, 42 (2012) 667-677.
[4] M. Atobe, H. Tateno, Y. Matsumura, Applications of flow microreactors in electrosynthetic processes, Chemical Reviews, 118 (2018) 4541-4572.
[5] A. Ziogas, G. Kolb, M. O'Connell, A. Attour, F. Lapicque, M. Matlosz, S. Rode, Electrochemical microstructured reactors: design and application in organic synthesis, Journal of Applied Electrochemistry, 39 (2009) 2297.
[6] C. Léger, J. Elezgaray, F. Argoul, Probing interfacial dynamics by phase-shift interferometry in thin cell electrodeposition, Journal of Electroanalytical Chemistry, 486 (2000) 204-219.
[7] M. Rosso, E. Chassaing, J.N. Chazalviel, T. Gobron, Onset of current-driven concentration instabilities in thin cell electrodeposition with small inter-electrode distance, Electrochimica Acta, 47 (2002) 1267-1273.
[8] S. Park, J.H. Park, S. Hwang, J. Kwak, Bench-top fabrication and electrochemical applications of a micro-gap electrode using a microbead spacer, Electrochemistry Communications, 68 (2016) 76-80.
[9] H. Lee, T.K. Choi, Y.B. Lee, H.R. Cho, R. Ghaffari, L. Wang, H.J. Choi, T.D. Chung, N. Lu, T. Hyeon, S.H. Choi, D.-H. Kim, A graphene-based electrochemical device with thermoresponsive microneedles for diabetes monitoring and therapy, Nature Nanotechnology, 11 (2016) 566-572.
[10] S. Zhang, M. Sun, T. Hedtke, A. Deshmukh, X. Zhou, S. Weon, M. Elimelech, J.-H. Kim, Mechanism of heterogeneous Fenton reaction kinetics enhancement under nanoscale spatial confinement, Environmental Science & Technology, 54 (2020) 10868-10875.
[11] M. Rodríguez, M. Muñoz-Morales, J.F. Perez, C. Saez, P. Cañizares, C.E. Barrera-Díaz, M.A. Rodrigo, Toward the development of efficient electro-Fenton reactors for soil washing wastes through microfluidic cells, Industrial & Engineering Chemistry Research, 57 (2018) 10709-10717.
[12] O. Scialdone, A. Galia, S. Sabatino, Abatement of Acid Orange 7 in macro and micro reactors. Effect of the electrocatalytic route, Applied Catalysis B: Environmental, 148-149 (2014) 473-483.
[13] S. Sabatino, A. Galia, O. Scialdone, Electrochemical abatement of organic pollutants in continuous-reaction systems through the assembly of microfluidic cells in series, ChemElectroChem, 3 (2016) 83-90.
[14] E. Mousset, Unprecedented reactive electro-mixing reactor: Towards synergy between micro- and macro-reactors?, Electrochemistry Communications, 118 (2020) 106787.
[15] M.L. Satuf, J. Macagno, A. Manassero, G. Bernal, P.A. Kler, C.L.A. Berli, Simple method for the assessment of intrinsic kinetic constants in photocatalytic microreactors, Applied Catalysis B: Environmental, 241 (2019) 8-17.
[16] H.S. White, K. McKelvey, Redox cycling in nanogap electrochemical cells, Current Opinion in Electrochemistry, 7 (2018) 48-53.
[17] W.B. Zimmerman, Electrochemical microfluidics, Chemical Engineering Science, 66 (2011) 1412-1425.
[18] K. Jähnisch, V. Hessel, H. Löwe, M. Baerns, Chemistry in microstructured reactors, Angewandte Chemie International Edition, 43 (2004) 406-446.
[19] R.G. Compton, P.R. Unwin, Channel and tubular electrodes, Journal of Electroanalytical Chemistry and Interfacial Electrochemistry, 205 (1986) 1-20.
[20] J.A. Cooper, R.G. Compton, Channel electrodes — A review, Electroanalysis, 10 (1998) 141-155.
[21] M.D. Birkett, A. Kuhn, Combined effects in mass transfer to a planar electrode, Electrochimica Acta, 22 (1977) 1427-1429.

[22] I. Roušar, J. Hostomsky, V. Cezner, B. tverák, Limiting local current densities for electrodes located on the walls of a rectangular channel with laminar flow; Asymptotic solution and experimental verification, Journal of The Electrochemical Society, 118 (1971) 881.
[23] K. Aoki, K. Tokuda, H. Matsuda, Hydrodynamic voltammetry at channel electrodes: Part VIII. Theory of reversible voltammograms for chronoamperometry and linear sweep voltammetry, Journal of Electroanalytical Chemistry and Interfacial Electrochemistry, 209 (1986) 247-258.
[24] K. Yunus, A.C. Fisher, Voltammetry under microfluidic control, a flow cell aproach, Electroanalysis, 15 (2003) 1782-1786.
[25] P.R. Unwin, R.G. Compton, The use of channel electrodes in the investigation of interfacial reaction mechanisms (Chapter 6), in: R.G. Compton (Ed.) Comprehensive Chemical Kinetics, Elsevier (1989), pp. 173-296.
[26] D.J. Pickett, Design of plug flow electrochemical reactors, Electrochemical reactor design, Elsevier Science Publishing Company (1979), pp. 171-280.
[27] D.R. Gabe, D.J. Robinson, Mass transfer in a rotating cylinder cell—I. Laminar flow, Electrochimica Acta, 17 (1972) 1121-1127.
[28] Á. Anglada, A.M. Urtiaga, I. Ortiz, Laboratory and pilot plant scale study on the electrochemical oxidation of landfill leachate, Journal of Hazardous Materials, 181 (2010) 729-735.
[29] A.A. Wragg, A.A. Leontaritis, Local mass transfer and current distribution in baffled and unbaffled parallel plate electrochemical reactors, Chemical Engineering Journal, 66 (1997) 1-10.
[30] M. Griffiths, C.P. de León, F.C. Walsh, Mass transport in the rectangular channel of a filter-press electrolyzer (the FM01-LC reactor), American Institute of Chemical Engineers, 51 (2005) 682-687.
[31] C.A. Martinez-Huitle, S. Ferro, A. De Battisti, Electrochemical incineration of oxalic acid: Reactivity and engineering parameters, Journal of Applied Electrochemistry, 35 (2005) 1087-1093.
[32] T.R. Ralph, M.L. Hitchman, J.P. Millington, F.C. Walsh, Mass transport in an electrochemical laboratory filterpress reactor and its enhancement by turbulence promoters, Electrochimica Acta, 41 (1996) 591-603.
[33] F.C. Walsh, C. Ponce de León, Progress in electrochemical flow reactors for laboratory and pilot scale processing, Electrochimica Acta, 280 (2018) 121-148.
[34] N. Tzanetakis, K. Scott, W.M. Taama, R.J.J. Jachuck, Mass transfer characteristics of corrugated surfaces, Applied Thermal Engineering, 24 (2004) 1865-1875.
[35] M. Cruz-Díaz, F.F. Rivera, E.P. Rivero, I. González, The FM01-LC reactor modeling using axial dispersion model with a reaction term coupled with a continuous stirred tank (CST), Electrochimica Acta, 63 (2012) 47-54.
[36] A. Djati, M. Brahimi, J. Legrand, B. Saidani, Entrance effect on mass transfer in a parallel plate electrochemical reactor, Journal of Applied Electrochemistry, 31 (2001) 833-837.
[37] D.J. Pickett, K.L. Ong, The influence of hydrodynamic and mass transfer entrance effects on the operation of a parallel plate electrolytic cell, Electrochimica Acta, 19 (1974) 875-882.
[38] S. Coleman, S. Roy, Effect of ultrasound on mass transfer during electrodeposition for electrodes separated by a narrow gap, Chemical Engineering Science, 113 (2014) 35-44.
[39] S.J. Coleman, S. Roy, Design of an ultrasonic tank reactor for copper deposition at electrodes separated by a narrow gap, Ultrasonics Sonochemistry, 42 (2018) 445-451.
[40] D. Pauwels, B. Geboes, J. Hereijgers, D. Choukroun, K. De Wael, T. Breugelmans, The application of an electrochemical microflow reactor for the electrosynthetic aldol reaction of acetone to diacetone alcohol, Chemical Engineering Research and Design, 128 (2017) 205-213.
[41] J.R. Selman, C.W. Tobias, Mass-transfer measurements by the limiting-current technique, in: T.B. Drew, G.R. Cokelet, J.W. Hoopes, T. Vermeulen (Eds.) Advances in Chemical Engineering, Academic Press (1978), pp. 211-318.
[42] P. Cañizares, J. García-Gómez, I. Fernández de Marcos, M.A. Rodrigo, J. Lobato, Measurement of mass-transfer coefficients by an electrochemical technique, Journal of Chemical Education, 83 (2006) 1204.
[43] F.H. Adnan, E. Mousset, S. Pontvianne, M.-N. Pons, Mineral cathodic electro-precipitation and its kinetic modelling in thin-film microfluidic reactor during advanced electro-oxidation process, Electrochimica Acta, (2021) 138487.

[44] H. Saraç, M.A. Patrick, A.A. Wragg, Physical properties of the ternary electrolyte potassium ferri-ferrocyanide in aqueous sodium hydroxide solution in the range 10–90°C, Journal of Applied Electrochemistry, 23 (1993) 51-55.
[45] A.C. Fisher, R.G. Compton, A general computational approach to linear sweep voltammetry at channel electrodes, Journal of Applied Electrochemistry, 22 (1992) 38-42.
[46] A.A. Wragg, D.J. Tagg, M.A. Patrick, Diffusion-controlled current distributions near cell entries and corners, Journal of Applied Electrochemistry, 10 (1980) 43-47.
[47] J.E. Terrazas-Rodríguez, S. Gutiérrez-Granados, M.A. Alatorre-Ordaz, C. Ponce de León, F.C. Walsh, A comparison of the electrochemical recovery of palladium using a parallel flat plate flow-by reactor and a rotating cylinder electrode reactor, Electrochimica Acta, 56 (2011) 9357-9363.
[48] G. Gao, Q. Zhang, Z. Hao, C.D. Vecitis, Carbon nanotube membrane stack for flow-through sequential regenerative electro-Fenton, Environmental Science & Technology, 49 (2015) 2375-2383.
[49] S. Fransen, J. Fransaer, S. Kuhn, Current and concentration distributions in electrochemical microreactors: Numerical calculations and asymptotic approximations for self-supported paired synthesis, Electrochimica Acta, 292 (2018) 914-934.
[50] P. Ma, H. Ma, S. Sabatino, A. Galia, O. Scialdone, Electrochemical treatment of real wastewater. Part 1: Effluents with low conductivity, Chemical Engineering Journal, 336 (2018) 133-140.
[51] J.F. Pérez, J. Llanos, C. Sáez, C. López, P. Cañizares, M.A. Rodrigo, Development of an innovative approach for low-impact wastewater treatment: A microfluidic flow-through electrochemical reactor, Chemical Engineering Journal, 351 (2018) 766-772.
[52] J.F. Pérez, J. Llanos, C. Sáez, C. López, P. Cañizares, M.A. Rodrigo, On the design of a jet-aerated microfluidic flow-through reactor for wastewater treatment by electro-Fenton, Separation and Purification Technology, 208 (2019) 123-129.
[53] E. Mousset, M. Puce, M.N. Pons, Advanced electro-oxidation with boron-doped diamond for acetaminophen removal from real wastewater in a microfluidic reactor: Kinetics and mass-transfer studies, ChemElectroChem, 6 (2019) 2908-2916.
[54] A.M. Polcaro, A. Vacca, M. Mascia, S. Palmas, J. Rodiguez Ruiz, Electrochemical treatment of waters with BDD anodes: kinetics of the reactions involving chlorides, Journal of Applied Electrochemistry, 39 (2009) 2083.
[55] J.C. Eklund, A.M. Bond, J.A. Alden, R.G. Compton, Perspectives in modern voltammetry: Basic concepts and mechanistic analysis, in: D. Bethell (Ed.) Advances in Physical Organic Chemistry, Academic Press (1999), pp. 1-120.
[56] C.A. Paddon, G.J. Pritchard, T. Thiemann, F. Marken, Paired electrosynthesis: Micro-flow cell processes with and without added electrolyte, Electrochemistry Communications, 4 (2002) 825-831.
[57] D.J. Pickett, B.R. Stanmore, Ionic mass transfer in parallel plate electrochemical cells, Journal of Applied Electrochemistry, 2 (1972) 151-156.
[58] F. Cœuret, A. Storck, Revue des corrélations, Eléments de génie électrochimique, Lavoisier, Paris (1993), pp. 129-165.
[59] L.S. Han, Hydrodynamic entrance lengths for incompressible laminar flow in rectangular ducts, Journal of Applied Mechanics, 27 (1960) 403-409.
[60] E. Eroğlu, S. Yapici, O.N. Şara, Some transport properties of potassium ferri/ferro-cyanide solutions in a wide range of schmidt numbers, Journal of Chemical & Engineering Data, 56 (2011) 3312-3317.
[61] A.J. Arvía, S.L. Marchiano, J.J. Podestá, The diffusion of ferrocyanide and ferricyanide ions in aqueous solutions of potassium hydroxide, Electrochimica Acta, 12 (1967) 259-266.
[62] T.P. Szanto A., White I., Walsh F. C., Electrosynthesis and mass transport measurements in a laboratory filter-press electrolyzer, 4th european symposium on electrochemical engineering, Prague, Czech Republic, (1996), pp. 273.
[63] J.L.C. Santos, V. Geraldes, S. Velizarov, J.G. Crespo, Characterization of fluid dynamics and mass-transfer in an electrochemical oxidation cell by experimental and CFD studies, Chemical Engineering Journal, 157 (2010) 379-392.

VI. Role of interelectrode distance and electrogenerated gas bubbles on mineral electro-precipitation

(Published as scientific article, reference: *Chemical Engineering Journal 431 (2022) 133413*)

VI.1. Introduction

The application of microfluidic reactors within the framework of EAOPs has offered another viewpoint in terms of wastewater treatment capability **[1-4]**. Coupled to the development of diamond-based anode or other high overpotential for OER, higher degree of electrochemical oxidation of organic contaminants has been reached **[5-8]**. The micrometric d_{elec} not only allow mineralization of organic pollutants without the addition of supporting electrolyte but it also vastly accommodates the phenomenon of limitation by mass transfer and ohmic resistance **[9]**. This is particularly adequate with solutions having low ionic conductivity, which is typical of the effluent at outlet of municipal WWTPs **[10-12]**.

Numerous studies have already been reported on the formation of mineral scaling in electrochemical cells while treating different water sources originated from different domains of application: artificial water for cooling system in cooling towers and oil refineries **[13, 14]**, artificial **[15, 16]** and natural underground water **[17, 18]**, mineral potable water **[19, 20]**, artificial **[21-24]** and real seawater **[25, 26]**. Most of the works were carried out using rotating disk electrodes (RDE) possessing effective surface area of 0.2 cm^2 **[15-19, 21, 22, 25]**, 0.5 cm^2 **[13, 14, 27]**, 1 cm^2 **[24, 28, 29]** and 1.5 cm^2 **[23]**. Recently, more scalable electrochemical cell geometries were suggested to study the occurrence of mineral electro-precipitation. Artificial brine solution (25 mL) was used to precipitate Ca and Mg deposits on cathode with 0.75 cm^2 effective surface area in a parallel-plate electrochemical cell working in discontinuous mode **[30, 31]**. The cathode and anode were separated by a 5 mm gap. In another series of work, horizontal parallel-plate cell with higher geometric surface area (i.e., 36 cm^2) was used to electrochemically precipitate calcium, magnesium and phosphorus **[32-35]**. 0.8 to 1 L wastewater effluent was electrolyzed in recirculation mode and the distance separating anode and cathode in these works was 30 mm. Elsewhere, Sanjuán et al. in their work conducted a water hardness treatment of simulated electrodialysis concentrate **[36]**. The studies were done in a pilot plant working in flow mode using commercial undivided cell with 100 cm^2 surface area electrodes. Amongst the list, our recent work **[37]** was the first to illustrate the occurrence of mineral scaling inside a parallel-plate microfluidic reactor with 50 cm^2 surface area and 500 µm d_{elec}. The influence of electrolytic composition and current density were scrutinized. To the best of authors' knowledge, no report has yet been published to discuss the variation of mineral deposition with d_{elec} lower than 5

mm, especially at submillimetric distances that imply a different mass transfer behavior (**Chapter 4**). Moreover, it is known that electro-precipitation often takes place with concomitant HER **[28, 29, 38-40]**. It results in calcareous deposit with porous morphology and is also the reason for partial deposit detachment from cathode surface **[27, 29, 39, 41]**. However, the role of gas evolution on electro-precipitation in submillimetric distances has never been explored. Furthermore, mass transfer intensification would promote the involvement of O_2 gas generated from OER at anode under micrometric configuration.

For the first time, the influence of a wide range of d_{elec} (50-3000 µm) with regard to the occurrence of cathodic mineral deposition was therefore investigated in details. The involvement of HER while varying d_{elec} and its effect towards the quantity of mineral scaling were further scrutinized. A new kinetic model has been proposed to predict the electro-precipitation at the different d_{elec}, by incorporating the gas evolution. To reinforce the mechanistic understanding at the cathode/electrolyte interface over the wide range of investigated d_{elec}, EIS analysis were performed.

VI.2. Experimental section

Synthetic effluent contained fixed concentrations of Ca^{2+} (150 mg L^{-1}), Mg^{2+} (5 mg L^{-1}) and 60 mg-C L^{-1} carbonates, which were dissolved in ultrapure water. The initial value of pH was adjusted to 7.6 by the addition of sulfuric acid when necessary. The mixture of salts including pH adjustment yielded an ionic conductivity of around 1000 µS cm^{-1} and ionic strength of 0.02 mol L^{-1}. These properties correspond to the average characteristic of effluent at the outlet of municipal WWTPs. BDD (50 cm^2) and stainless steel (50 cm^2) were used as anode and cathode respectively. PTFE spacer with various thicknesses of 50, 100, 250 and 500 µm for micrometric distances as well as 1000 and 3000 µm for millimetric distances were implemented. Unless mentioned otherwise, electrolysis was carried out in galvanostatic mode under the polarization of 4 mA cm^{-2} (200 mA).

Concentration of Ca and Mg were monitored using ICP-OES. TIC was measured using a TOC-meter V_{CSH} TC/TN. LSV, chronoamperometry and chronopotentiometry were performed by intermediary of a potentiostat connected to the electrochemical cell. The electrode potentials were reported as function of Ag-AgCl RE. LSV was carried out sweeping the range of cathodic potentials from 0 to -1.6 V/Ag-AgCl using a scan rate of 10 mV s^{-1}. EIS was conducted in galvanostatic mode covering the frequency ranges between 100 kHz to 100 mHz. The perturbation amplitude varied between 5 and 10 mA RMS according to EIS spectra with 10 ppd. The EIS analysis was programmed at regular interval during galvanostatic electrolysis at applied direct current of 200 mA (i.e., 4 mA cm^{-2}). The EIS parameters were extracted by means of EEC model using ZSimpwin® commercial software.

Throughout the series of experiments, the j_{app} was always higher than all $j_{lim,0}$ values (**Table VI.1**), whatever the configurations used. The $j_{lim,0}$ value for each electrochemical cell setup was evaluated in similar way as described in **Chapter 4** using **Eq. (IV.18)**. The values of k_m specific for each cell configuration were obtained as a result of mass transfer characterization studies conducted in **Chapter 5**. Therefore, across all configurations from millimetric to submillimetric inspected in this chapter, the electrochemical processes were diffusional mass-transfer controlled. It is worth mentioning that while varying d_{elec}, the liquid flow rate was also adjusted to have identical electrolyte residence time across different volumes of electrochemical reactors for relevant comparison. The flow rate of 10, 20, 50, 100, 200 and 600 mL min^{-1} were used for 50, 100, 250, 500, 1000 and 3000 µm d_{elec} respectively. A residence time of 0.025 min was maintained across all configurations. Since the electrolyte flow rate was adapted accordingly to the volume of reactor, cross-sectional electrolyte velocity was also kept constant, i.e. in this work 4 m min^{-1}, from one configuration to another. Knowing the fact that the d_H (**Eq. (V.15)**) was modified from one d_{elec} to another, Reynolds number (*Re*) (**Eq. (V.12)**) also increased with the d_{elec} as summarized in **Table VI.1**. *Re* values could be calculated by considering the physicochemical properties of the effluent provided in the caption of **Table V.1**. *Re* values ranged from 7 (50 µm) to 377 (3000 µm), meaning that the hydrodynamic flow of electrolyte was maintained under laminar regime in all investigated cases **[42-45]**. This could ensure reliable comparisons of the results obtained under different d_{elec} setups.

Table VI.1. The values of $j_{lim,0}/j_{app}$ ratio, k_m, d_H and *Re* number associated to the investigated d_{elec}. j_{app}= 4 mA cm^{-2}, cathode: stainless steel and anode: BDD. $C_{O_2,25°C}$ = 2.81 × 10^{-4} mmol L^{-1} and $\upsilon_{L,25°C}$ = 10^{-6} m^2 s^{-1}.

d_{elec} / µm	k_m / m s^{-1}	$j_{lim,0}/j_{app}$ (≪ 1)	d_H / mm	*Re*
50	6.44 × 10^{-5}	0.1746	0.10	7
100	3.94 × 10^{-5}	0.1068	0.20	16
250	2.75 × 10^{-5}	0.0746	0.50	33
500	2.33 × 10^{-5}	0.0632	0.99	66
1000	1.82 × 10^{-5}	0.0492	1.96	130
3000	1.61 × 10^{-5}	0.0436	5.66	377

VI.3. Modeling

VI.3.1. Kinetics of $Mg(OH)_2$ and $CaCO_3$ electro-precipitation

A kinetic model has been proposed to predict the electro-precipitation by considering the influence of d_{elec}. The methodology adopted for a single d_{elec} (500 µm) in our previous work has been followed and adapted to take into account the electrodes gap **[37]**. Local alkalization on cathode surface

occurred due to faradaic reactions of reduction of dissolved O_2 (**Eq. (II.9)**) and H_2O (**Eq. (II.10)**), while the OH^- production can be estimated by Faraday's law (**Eq. (VI.1)**):

$$O_2 + 2H_2O + 4e^- \rightarrow 4OH^- \quad \text{(II.9)}$$

$$2H_2O + 2e^- \rightarrow H_2 + 2OH^- \quad \text{(II.10)}$$

$$r_{OH^-} = +\frac{d[OH^-]}{dt} = \frac{\nu_{O_2} j_{app}}{n_{O_2} F}\eta_{O_2} + \left(\nu_{H_2O}\frac{\eta_{H_2O}}{n_{H_2O}} - \nu_{H_2}\frac{\eta_{H_2}}{n_{H_2}}\right)\frac{j_{app}}{F} - 2k_{Mg(OH)_2}[Mg^{2+}][OH^-]^2 \quad \text{(VI.1)}$$

where r_{OH^-} is the heterogeneous production rate of OH^- (mol m^{-2} min^{-1}), $k_{Mg(OH)_2}$ is the heterogenous third order rate constant associated to the reaction of electro-precipitation of $Mg(OH)_2$ (0.33 m^7 mol^{-2} min^{-1} **[37]**) on cathode surface, n_{O_2} and n_{H_2O} are the numbers of electrons participating in **Eq. (II.9)** and **Eq. (II.10)** respectively whilst ν_{O_2} and ν_{H_2O} are the stoichiometric coefficient of OH^- production from **Eq. (II.9)** and **Eq. (II.10)** respectively. n_{H_2} and ν_{H_2} are respectively the number of electrons reacted and stoichiometry to produce H_2 with respect to the stoichiometry of OH^- production from H_2O reduction in **Eq. (II.10)**. $[OH^-]$ and $[Mg^{2+}]$ are the molar concentrations of OH^- and Mg^{2+} ions respectively (mol m^{-3}), j_{app} is the applied current density (A m^{-2}), F is the Faraday's constant, η_{O_2} and η_{H_2O} are the current efficiencies attributed to faradaic reactions (**Eq. (II.9)** and **Eq. (II.10)**). Under the polarization of 4 mA cm^{-2}, their values are taken as 0.02% and 99.98% respectively in accordance to **Chapter 4**. η_{H_2} is the loss of faradaic current efficiency related to concurrent H_2 evolution in **Eq. (II.10)** on cathode surface. This contribution was introduced through a term denoted as OH^- hindrance factor (α) due to gas bubbles and is defined in **Eq. (VI.2)**:

$$\alpha = \nu_{H_2O}\frac{\eta_{H_2O}}{n_{H_2O}} - \nu_{H_2}\frac{\eta_{H_2}}{n_{H_2}} \quad \text{(VI.2)}$$

Equation (VI.1) can then be simplified into **Eq. (VI.3)**:

$$r_{OH^-} = +\frac{d[OH^-]}{dt} = \frac{\nu_{O_2} j_{app}}{n_{O_2} F}\eta_{O_2} + \alpha\frac{j_{app}}{F} - 2k_{Mg(OH)_2}[Mg^{2+}][OH^-]^2 \quad \text{(VI.3)}$$

The precipitation rate of $Mg(OH)_2$ could be estimated using **Eq. (IV.4)**. The electro-precipitation of $CaCO_3$ was modeled following the theoretical concentration of interfacial carbonates $[CO_3^{2-}]_{int}$ (in mol m^{-3}) as previously defined as **Eq. (IV.12)**. The rate of precipitation of $CaCO_3$ could then be modeled by its kinetic law expressed in **Eq. (IV.13)** where the heterogeneous second order rate constant of heterogeneous electro-precipitation k_{CaCO_3} was taken as 3.6×10^{-3} m^4 mol^{-1} min^{-1} **[37]** (**Chapter 4**).

VI.3.2. Relationship between double layer capacitance, double layer thickness and interelectrode distance

The double layer capacitance (C_{DL}) can be expressed in terms of the thickness of electronic double layer (d_{DL}) by **Eq. (VI.4)** [46, 47]:

$$C_{DL} = \frac{\varepsilon_S \, \varepsilon_0}{d_{DL}} \quad \text{(VI.4)}$$

where C_{DL} is expressed in F, ε_S the dielectric constant of solvent in bulk (here water, the value was taken at 80 **[48-50]**), ε_0 the vacuum permittivity (8.854×10^{-12} F.m **[49, 51]**) and d_{DL} is expressed in m.

It is proposed to relate d_{elec} with d_{DL} using the following expression of **Eq. (VI.5)**:

$$d_{elec} = \omega \, (d_{DL,A} + d_{DL,C}) \quad \text{(VI.5)}$$

where ω is a constant ($\omega \gg 1$), $d_{DL,A}$ and $d_{DL,C}$ are the double layer thicknesses on anode and cathode, respectively. Supposing the double layer thickness is identical on both anode and cathode ($d_{DL,A} = d_{DL,C}$), **Eq. (VI.5)** is simplified into **Eq. (VI.6)** and then into **Eq. (VI.7)**.

$$d_{elec} = 2 \, \omega \, d_{DL} \quad \text{(VI.6)}$$

$$d_{DL} = d_{elec}/(2\omega) \quad \text{(VI.7)}$$

Inserting the expression of d_{DL} from **Eq. (VI.7)** into **Eq. (VI.4)** gives out a novel equation (**Eq. (VI.8)**):

$$C_{DL} = \frac{\varepsilon_S \, \varepsilon_0 \, 2 \, \omega}{d_{elec}} \quad \text{(VI.8)}$$

VI.3.3. Modeling and fitting evaluation

The modeling of the evolution of Mg^{2+} and Ca^{2+} concentrations were done using Aquasim© **[52]**. The validity of experimental impedance spectra was controlled using linear KKT method performed using Zsimpwin® and KKT program developed by University of Twente **[53, 54]**. The fitting between experimental data and the kinetic models were evaluated using RMSE (**Eq. (III.3)**) as well as ME (**Eq. (III.4)**).

VI.4. Results and discussion

VI.4.1. Kinetics and modeling of mineral electro-precipitation at various interelectrode distances

The evolution of concentrations of Mg^{2+}, Ca^{2+} and TIC at different d_{elec} are illustrated in **Fig. VI.1**. From **Fig. VI.1(a)**, $Mg(OH)_2$ was noticed to electro-precipitate the most at 100, 250 and 500 µm. As the d_{elec} increased, less $Mg(OH)_2$ precipitation occurred. It was observed that Mg^{2+} in electrolyte precipitated by 85.7 ± 1.3, 91.0 ± 0.1, 91.2 ± 0.9, 87.7 ± 0.5 and 81.0 ± 0.1% after 5-hour electrolysis for d_{elec} of 100, 250, 500, 1000 and 3000 µm respectively. **Figures VI.1(b)** and **VI.1(c)** plot the evolution of Ca^{2+} and TIC concentrations respectively, across multiple d_{elec} investigated. It can be observed that the $CaCO_3$ electro-precipitated the most at 100 µm and lesser precipitation of $CaCO_3$ was obtained with increasing d_{elec} (**Fig. VI.1(b)** and **Fig. VI.1(c)**). 55.1 ± 1.1 and 94.8 ± 0.8% of Ca^{2+} and TIC, respectively, were deposited on cathode using 100 µm. These percentages of precipitation decreased to 36.2 ± 2.8 and 82.1 ± 0.4% of Ca^{2+} and TIC, respectively, when the electrochemical cell was used with 3000 µm d_{elec}. Interestingly, it was noticed that there were no mineral electro-precipitation of $Mg(OH)_2$ and $CaCO_3$ at the lowest d_{elec} investigated (50 µm) (**Fig. VI.1**). These results suggested that the mineral electro-precipitation tended to occur easier when shifting progressively from millimetric into microfluidic setup, except at the lowest d_{elec} investigated (50 µm).

The Mg and Ca mass balances recovery have been estimated to ensure that not only there was no loss of electrolyte during electrolysis (i.e. via leakage or dead volume in the pilot), but also to verify that the trend of the occurrence of mineral cathodic depositions was correct. **Figure VI.2** shows the mass balances of Mg and Ca successively recovered from different parts of experimental pilot after 5 h of electrolysis under all investigated d_{elec}. The sum of the remaining Mg and Ca in solution with their mass recovered from anode, cathode and tubing remained above 84 ± 5% with the average recovery of 91.2 ± 2.2% for Mg and 99.7 ± 4.1% for Ca across all d_{elec} investigated. The majority of Mg and Ca precipitated from electrolyte was found on cathode, while little mass was recovered from tubing and anode surface. This observation can confirm the cathodic precipitation of $Mg(OH)_2$ and $CaCO_3$ induced by the phenomenon of local alkalization on cathode surface **[55-57]** and validate the results presented in **Fig. VI.1**.

As can be observed in **Fig. VI.1**, the model curves of Mg^{2+}, Ca^{2+} and TIC fitted well with their experimental counterparts at different d_{elec} under study, which confirmed the need to consider gas bubbles evolution through α parameter as discussed in **Section VI.4.3**. The calculated RMSE values

for Mg^{2+}, Ca^{2+} and TIC curves fitting across all d_{elec} are tabulated in **Table VI.2**. RMSE values for Mg^{2+} curves fitting was as low as 0.0028 under 500 µm configuration, whilst the highest error (0.0149) was found under the 3000 µm setup (**Table VI.2**). The lowest and highest RMSE values in Ca^{2+} curves fitting were 0.0996 and 0.1983, corresponding to d_{elec} of 250 µm and 1000 µm respectively. The kinetics of TIC evolution in the bulk under all d_{elec} were pseudo first-order rates, as already previously noticed **[37]**. The lowest RMSE (0.0818) was found for 50 µm, whereas the highest RMSE (0.4658) corresponded to the configuration of 500 µm.

Table VI.2. Model fitting evaluation by RMSE between modeled and experimental curves of Mg^{2+}, Ca^{2+} and TIC concentrations in all investigated d_{elec} configurations. j_{app}: 4 mA cm^{-2}, cathode: stainless steel and anode: BDD.

d_{elec} / µm	RMSE		
	Mg^{2+}	Ca^{2+}	TIC
50	0.0095	0.1041	0.0818
100	0.0086	0.1352	0.2677
250	0.0068	0.0996	0.2810
500	0.0028	0.1026	0.4658
1000	0.0038	0.1983	0.2716
3000	0.0149	0.1704	0.2231

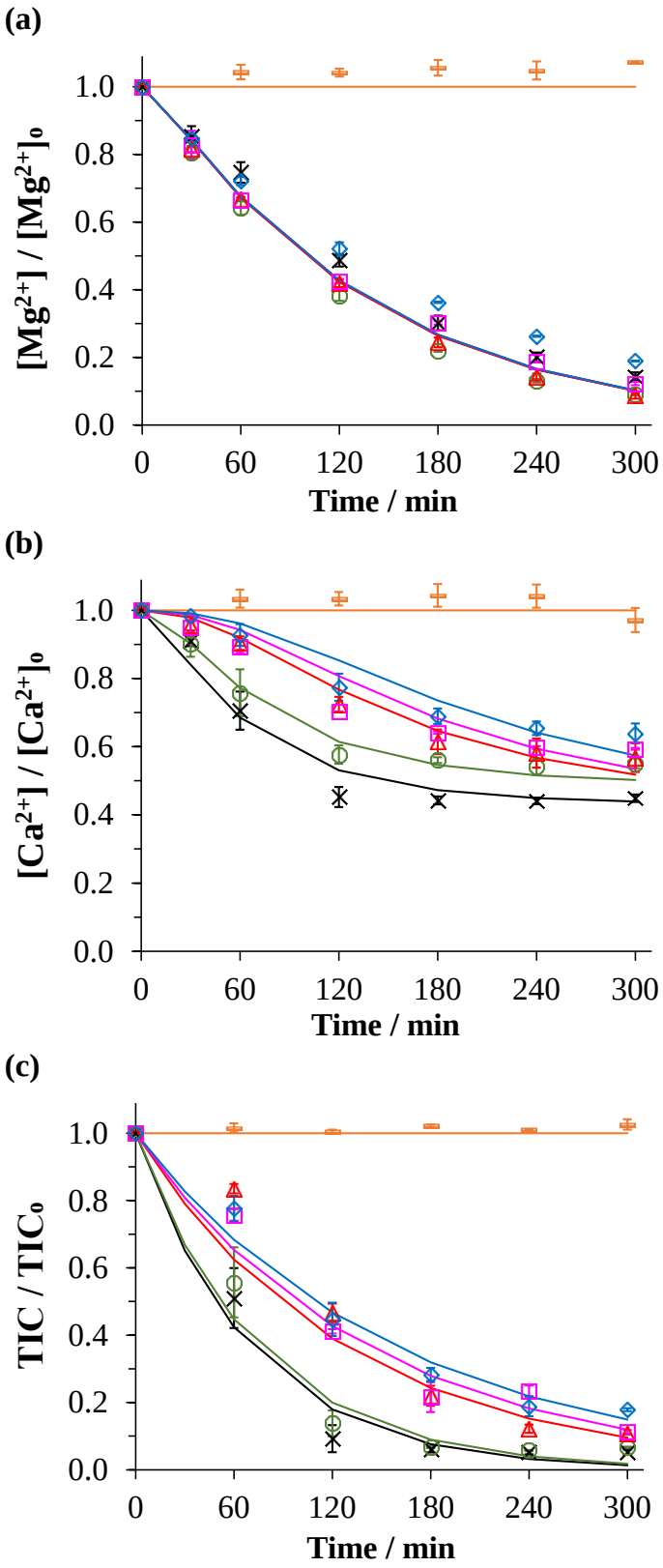

Fig. VI.1. Evolution of experimental and modeled concentrations of **(a)** Mg^{2+}, **(b)** Ca^{2+} and **(c)** TIC during the electrolysis at 4 mA cm^{-2} for different d_{elec} (—: 50 µm, ✕: 100 µm, ○: 250 µm, △: 500 µm, □: 1000 µm and ◇: 3000 µm). Cathode: stainless steel and anode: BDD. Solution containing 150 mg L^{-1} of Ca^{2+}, 5 mg L^{-1} of Mg^{2+} and 60 mg L^{-1} of TIC.

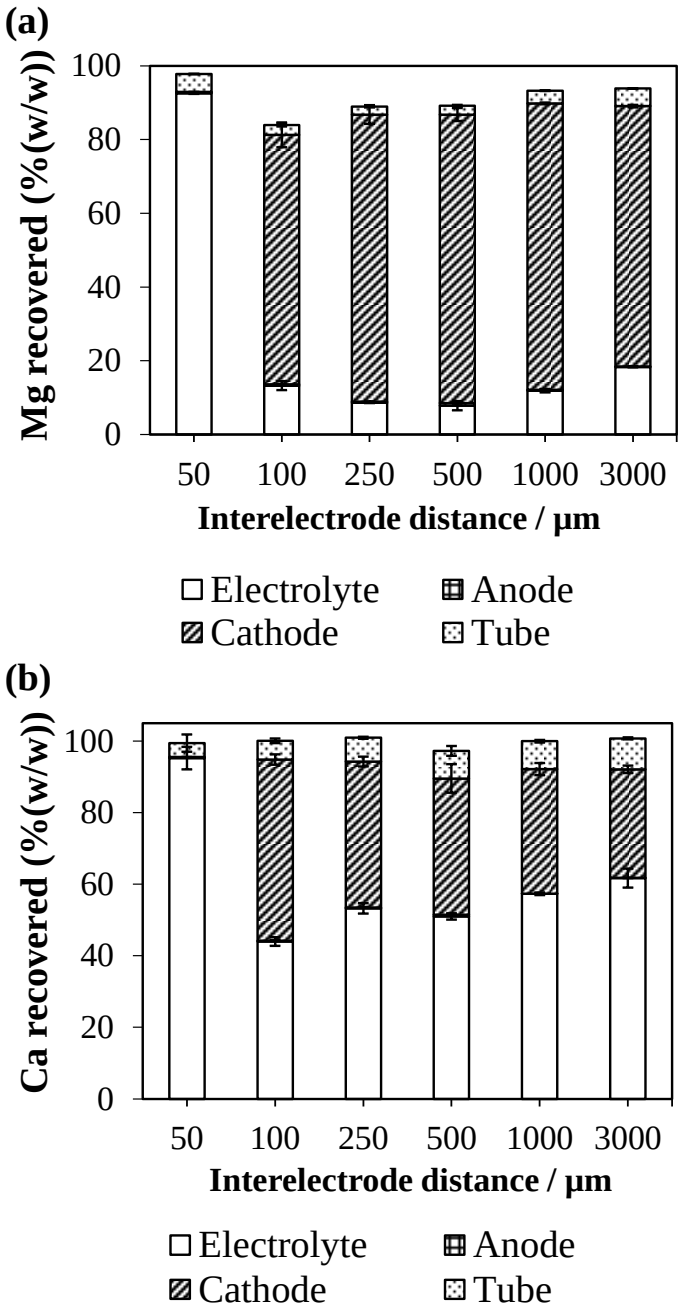

Fig. VI.2. Mass balance of **(a)** Mg and **(b)** Ca recovered from different parts of experimental pilot (☐: electrolyte, ▨: cathode, ⊞: anode and ⁘: tube) after 5 h of electrolysis under different configurations of d_{elec}. j_{app}: 4 mA cm^{-2}, cathode: stainless steel, anode: BDD and solution: 150 mg L^{-1} of Ca^{2+}, 5 mg L^{-1} of Mg^{2+} and 60 mg L^{-1} of TIC.

VI.4.2. Impact of cathode potential on mineral electro-precipitations at different interelectrode distances

The trends observed in **Section VI.4.1** can be elucidated by the values of the cathode potential (E_C) measured using the potentiostat, when 4 mA cm^{-2} current density was applied to the different electrochemical cell configurations. E_C values along with the average percentages of mass of Mg, Ca and TIC electro-precipitated after 5 h of electrolysis at 4 mA cm^{-2} for each d_{elec} are illustrated in **Fig. VI.3(a)**. It can be noticed that the E_C values dropped significantly from 0.202 ± 0.024 V/Ag-AgCl (50 µm) to -1.453 ± 0.021 V/Ag-AgCl (100 µm). The diminishing trend continued further down to -1.915 ± 0.030 V/Ag-AgCl when 3000 µm was used. LSV curves corresponding to all investigated d_{elec} are presented in **Fig. VI.4**. Across all interelectrode gaps, the plateau of limiting current of reduction of dissolved O_2 into OH^- ions (**Eq. (II.9)**) were noticeable in the potential range of -0.7 to -1.10 V/Ag-AgCl (**Fig. VI.4**). Comparable range of values have been reported in literature **[16, 23, 27-29, 38, 40]**. Within these ranges of applied potential, OH^- production via 4-electron of ORR was the most selective with minimal concomitant gas evolution on electrodes surface. The E_C measured with 100 µm (-1.453 ± 0.021 V/Ag-AgCl) was the closest to the potential of ORR into OH^- (-0.7 to -1.10 V/Ag-AgCl). As a consequence, amongst the various d_{elec} under study, the electro-precipitation of $Mg(OH)_2$ (**Eq. (II.11)**) and $CaCO_3$ (**Eq. (II.13)**) took place with minimal evolving H_2 perturbation when the electrochemical cell was used with d_{elec} of 100 µm. As the d_{elec} increased, E_C progressively moved farther away into the region of potential of H_2O reduction which started at about -1.10 V/Ag-AgCl according to **Fig. VI.4**. Within this region, the OH^- production still occurred but concomitantly with HER **[14, 38-40, 58-60]**. As a result, lesser production of mineral electro-precipitation was observed with the increasing interelectrode gap. Furthermore, using the LSV curves plotted in **Fig. 4**, Tafel slopes **[61, 62]** corresponding to the region of measured E_C for all d_{elec} configurations were determined and they are illustrated in **Fig. VI.5**. Tafel slope corresponding to d_{elec} of 3000 µm depicted the highest slope (-1.57 V dec^{-1}) amongst all the investigated d_{elec}, which accentuated the fact that the highest overpotential was obtained while operating with 3000 µm in comparison with the micrometric distances (-0.38 V dec^{-1} using 100 µm).

The higher concurrent H_2 evolution activity when d_{elec} increased can be further justified by the ratio of $j_{lim,0}$ over the adopted j_{app}. The ratios are plotted in **Fig. VI.3(b)**. When the j_{app} value is inferior or equal to $j_{lim,0}$ (i.e., $j_{lim,0}/j_{app} \geq 1$), it represents a condition in which OH^- is produced from the 4-electron ORR of **Eq. (II.9)** without any parasitic HER (**Eq. (II.10)**) **[63, 64]**. When j_{app} was greater than $j_{lim,0}$ ($j_{lim,0}/j_{app} < 1$), it means that OH^- production was accompanied by concomitant HER due to mass transfer limitation of dissolved O_2. From **Fig. VI.3(b)**, it can be observed that the $j_{lim,0}$ values

decreased when d_{elec} increased. Hence, the $j_{lim,0}/j_{app}$ was further reduced with increasing d_{elec} and remained below 1 whatever the distance (**Table VI.1**). Consequently, parasitic HER was more pronounced with increasing d_{elec}. Contrastingly, under the 50 µm d_{elec} setup, the E_C measured was too low for the 4-electron ORR yet to occur. This enlightened the reason why no precipitation was spotted at this minimum d_{elec} investigated.

To further confirm the role of E_C in electro-precipitation phenomena at different d_{elec}, experiments were performed in potentiostatic mode at the same E_C (-1.6 V/Ag-AgCl) - the applied E_C measured on cathode when 4 mA cm^{-2} was applied under 500 µm setup - for 500 and 3000 µm interelectrode gap configurations. The electrolyte contained 150 mg L^{-1} of Ca^{2+}, 5 mg L^{-1} of Mg^{2+} and 60 mg L^{-1} of TIC, identical to that used in **Fig. VI.1** and **Fig. VI.3**. The resulting evolution of Mg^{2+}, Ca^{2+} and TIC concentrations under the potentiostatic electrolysis are given in **Fig. VI.6**. It was observed that after 5 h of electrolysis, 85.2 ± 2.0% of Mg^{2+} precipitated on cathode under submillimetric setup whereas only 59.2 ± 0.9% of Mg^{2+} from electrolyte was deposited under millimetric setup (**Fig. VI.6(a)**). At the end of the electrolysis, it was noticed a similar amount of Ca^{2+} deposited using 500 µm (50.6 ± 0.1%) in comparison to 3000 µm (49.4 ± 0.6%) with however slightly faster kinetics of Ca^{2+} precipitation under microfluidic configuration up till 4 h of electrolysis (**Fig. VI.6(b)**). The TIC evolution in **Fig. VI.6(c)** suggested that faster consumption of carbonates species occurred under microfluidic setup leading to 93.5 ± 0.2% of CO_3^{2-} precipitated with Ca^{2+} forming $CaCO_3$ at 500 µm against 89.0 ± 0.6% of CO_3^{2-} precipitation occurring at 3000 µm. The difference of electro-precipitation observed at both distances and at the same applied E_C indicated that E_C was not the sole influencing factor. The influence of the electrochemical reactor geometry could be also involved. The dissimilarity observed in **Fig. VI.6** could then be explained by a difference that could have been brought while transitioning into the microfluidic configuration. Using micrometric d_{elec}, the rate of OH^- production in **Eq. VI.(3)** was intensified by external provision of dissolved O_2 coming from the oxidation of solvent on anode (**Eq. (II.3)**), producing more OH^- in comparison to the millimetric d_{elec}.

$$2H_2O \rightarrow O_2 + 4H^+ + 4e^- \qquad \text{(II.3)}$$

Consequently, interfacial OH^- concentration was higher under microfluidic than millimetric setup. Subsequently, thermodynamics of **Eq. (II.11)** and **Eq. (II.12)** were shifted to the right to favor the precipitation reaction of $Mg(OH)_2$ and the production of CO_3^{2-} respectively. Therefore, quicker kinetics and more electro-precipitations of $Mg(OH)_2$ and $CaCO_3$ perceived in **Fig. VI.6** are justified. This anodic provision of dissolved O_2 could occur using 3000 µm as well, but it did at much lesser extent. One could question that the production of protons in **Eq. (II.3)** could compensate in the

meantime the interfacial OH^- at cathode vicinity under microfluidic configuration to produce H_2O (**Eq. (VI.9)**), which could however be reduced back to OH^- following **Eq. (II.10)**.

$$H^+ + OH^- \rightarrow H_2O \quad \text{(VI.9)}$$

Furthermore, the evolution of bulk pH during the electrolysis using different cell configurations is depicted in **Fig. VI.7**. From a practical point of view, it was noticed that within the case where no mineral precipitation was observed, i.e., at 50 µm (**Fig. VI.7**), the bulk pH tended to increase. This behavior was also observed in the previous work when the operating conditions allowed to avoid electro-precipitation at 500 µm interelectrode gap **[37]**. This shows that the intensification of OH^- production due to the anodic source of dissolved O_2 was more predominant than the compensation of protons with OH^-, at both interface and in the bulk.

Again, in term of practicability, electrolysis in galvanostatic mode has more interest for the application in the real field. The incoming sections are devoted to further enlighten the mechanism of mineral scaling evolution at different d_{elec} by exploiting the concomitant gas evolution and characterizing the electrode/electrolyte interface through impedance studies.

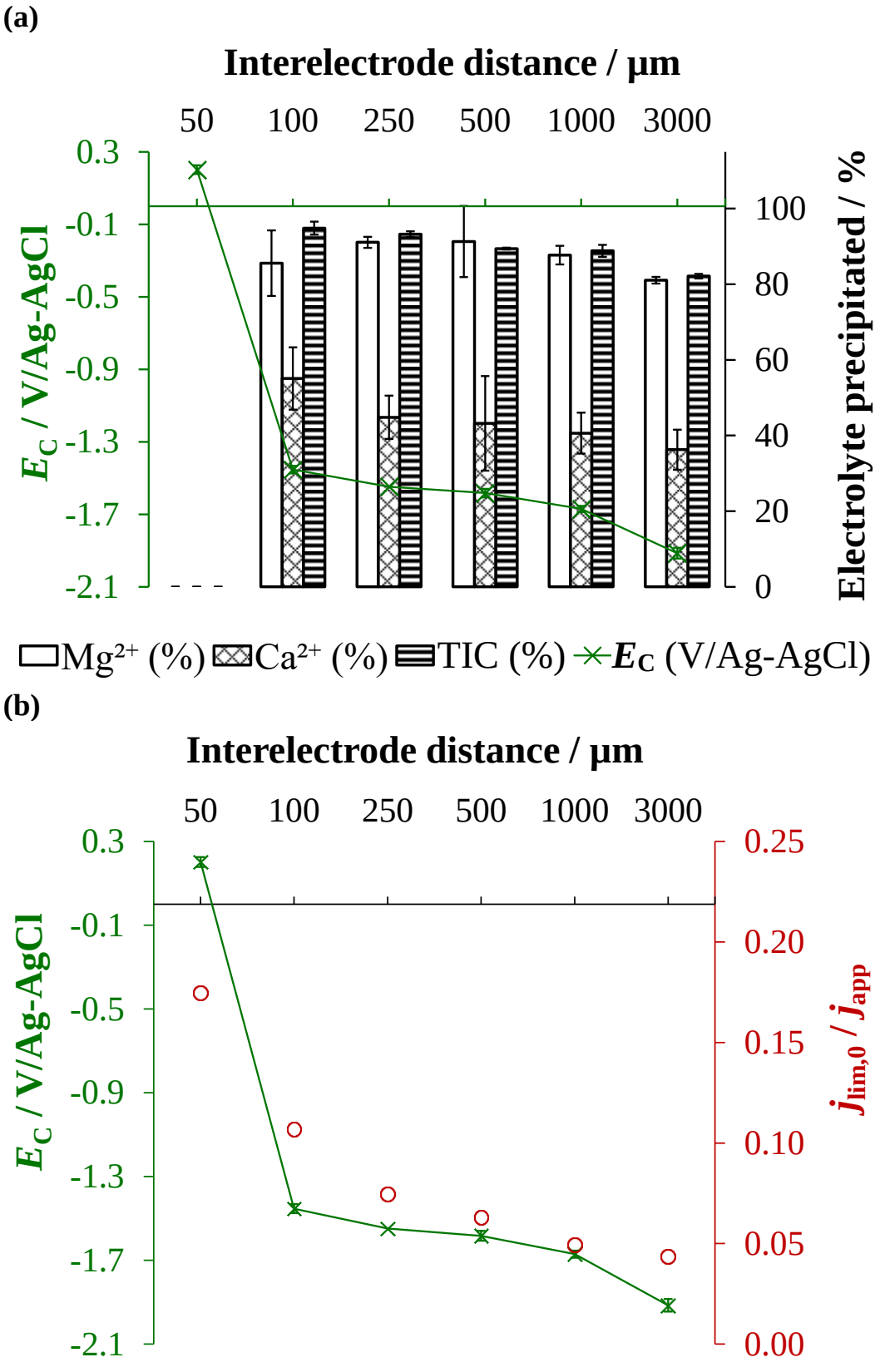

Fig. VI.3. Influence of d_{elec} on the evolution of **(a)** E_C (×) and average percentage of Mg (▭), Ca (▨) and TIC (▬) electro-precipitated, and **(b)** $j_{lim,0}/j_{app}$ (○). Cathode: stainless steel, anode: BDD, j_{app}: 4 mA cm^{-2}. Solution contained 150 mg L^{-1} of Ca^{2+}, 5 mg L^{-1} of Mg^{2+} and 60 mg-C L^{-1} of TIC.

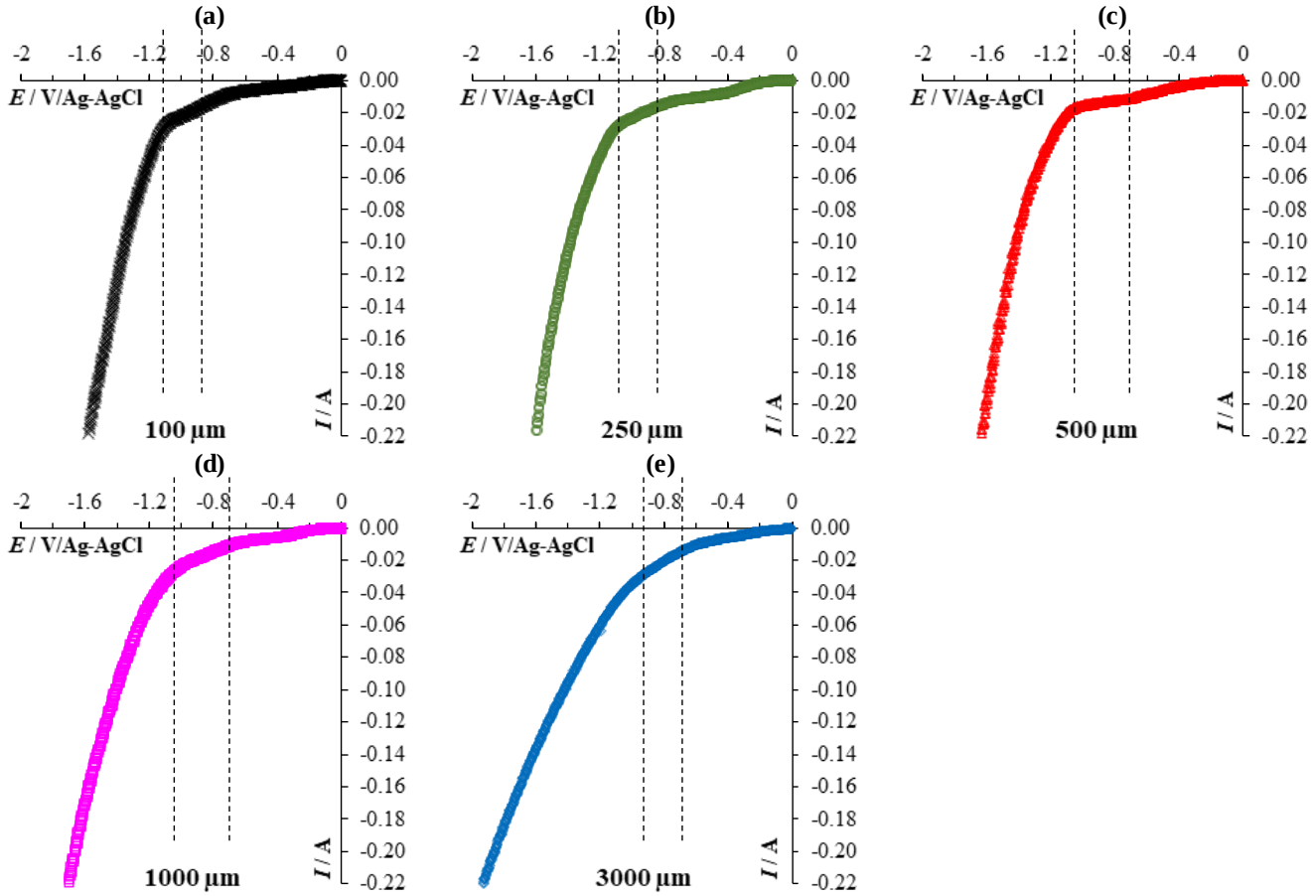

Fig. VI.4. LSV of electrochemical reactors with **(a)** 100 µm, **(b)** 250 µm, **(c)** 500 µm, **(d)** 1000 µm and **(e)** 3000 µm d_{elec} in solution containing 150 mg L^{-1} Ca^{2+}, 5 mg L^{-1} Mg^{2+} and 60 mg-C L^{-1} TIC. Scan rate: 10 mV s^{-1}, WE: stainless steel and CE: BDD.

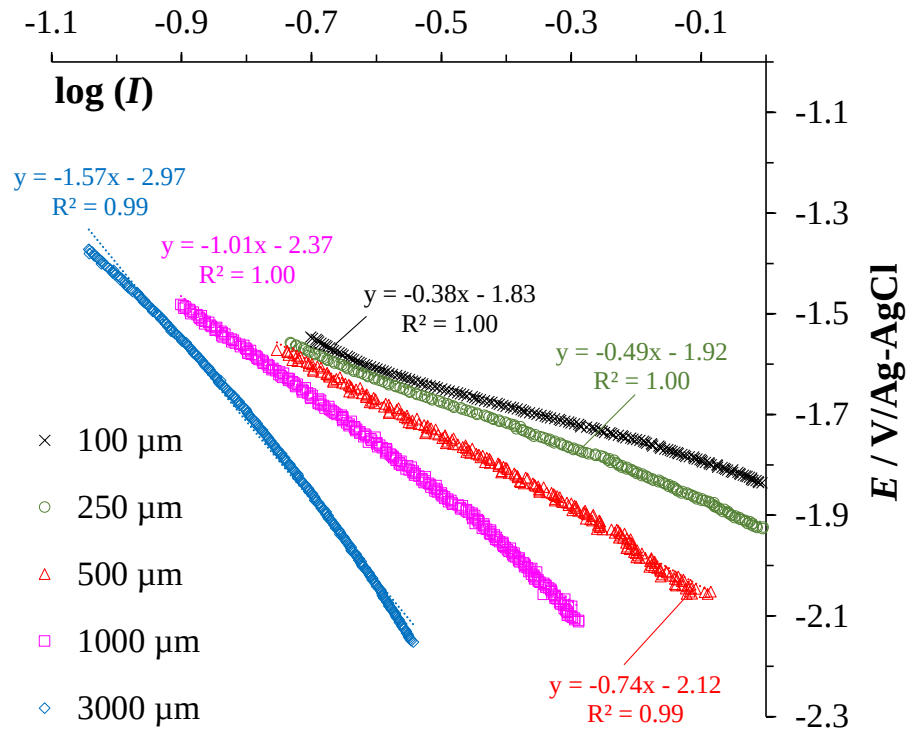

Fig. VI.5. Tafel slopes in the range of investigated j_{app} (4 mA cm^{-2}) across different d_{elec} configurations. Solution contained 150 mg L^{-1} of Ca^{2+}, 5 mg L^{-1} of Mg^{2+} and 60 mg-C L^{-1} of TIC. WE (cathode): stainless steel and CE (anode): BDD.

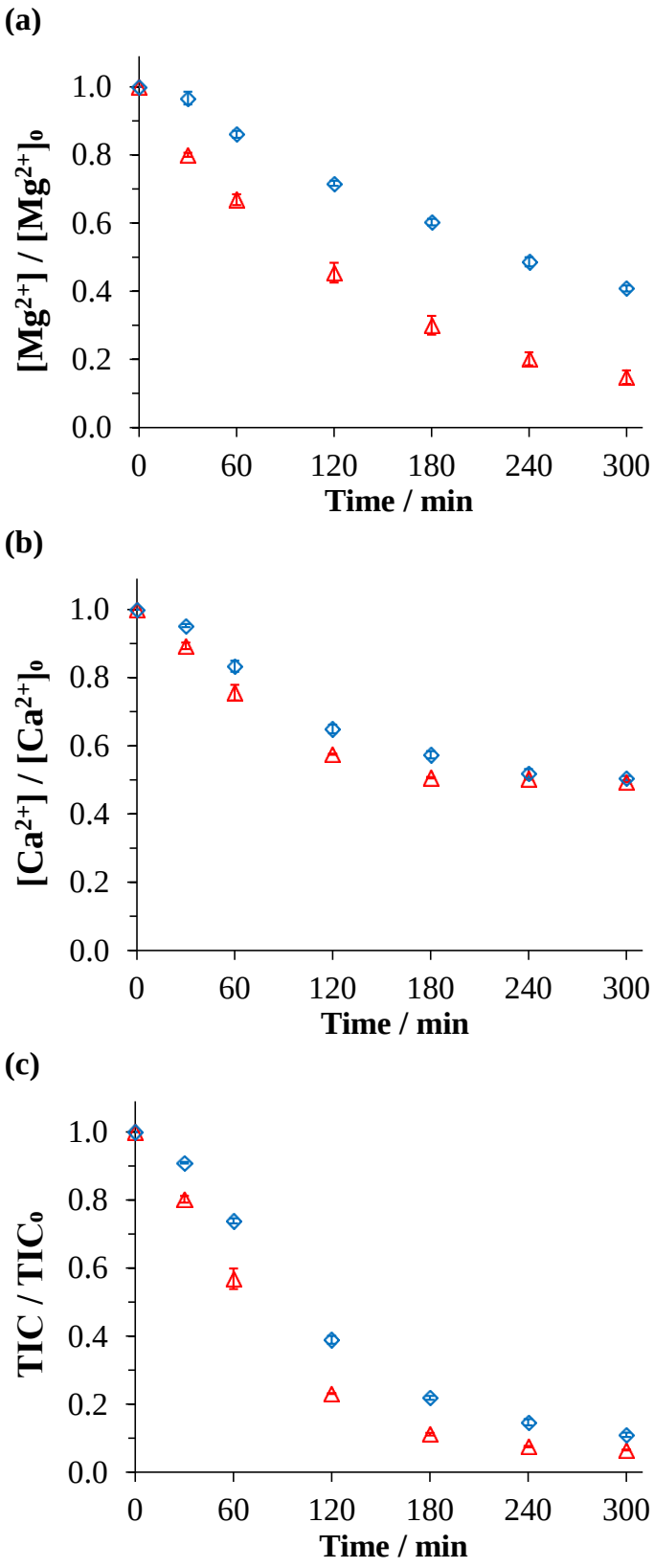

Fig. VI.6. Evolution of Mg^{2+}, Ca^{2+} and TIC concentrations during the electrolysis of solution containing 150 mg L^{-1} of Ca^{2+}, 5 mg L^{-1} of Mg^{2+} and 60 mg L^{-1} of TIC at constant E_C of -1.6 V/Ag-AgCl under microfluidic (500 µm, △) and millimetric (3000 µm, ◇) configurations. WE: stainless steel and CE: BDD.

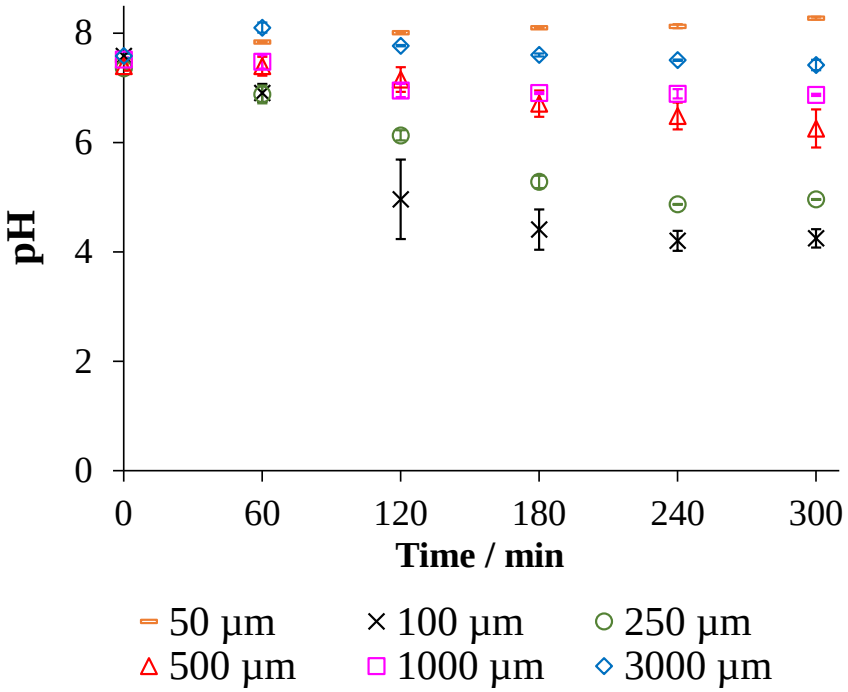

Fig. VI.7. The evolution of bulk pH over time for different d_{elec} under study. j_{app}: 4 mA cm^{-2}, cathode: stainless steel, anode: BDD and solution: 150 mg L^{-1} of Ca^{2+}, 5 mg L^{-1} of Mg^{2+} and 60 mg L^{-1} of TIC.

VI.4.3. The influence of gas evolution on the formation of mineral electro-precipitation

It has been shown that α, the parmeter accounting for physical gas evolution on cathode surface (**Eqs. (VI.2)-(VI.3)**), was primordial to yield reliable model fittings to the Mg^{2+}, Ca^{2+} and TIC experimental curves (**Section VI.4.1**). It was also demonstrated that the more d_{elec} increased, the more the ratio of $j_{lim,0}/j_{app}$ decreased due to decreasing $j_{lim,0}$ with increasing d_{elec} (**Section VI.4.2**). As a consequence, the secondary HER was more vigorous when the d_{elec} increased. Subsequently, the mineral electro-precipitation decreased with d_{elec}. This feature was also supported by the evolution of E_C values that decreased progressively farther into the region of water reduction with increasing d_{elec} (**Fig. VI.2**). This new interesting insight indicates the impactful influence that the gas evolution has on the formation of mineral electro-precipitation at various d_{elec}. Thus, it merits further in-depth investigations as discussed in this sub-section.

The evolution of reduced conductivity of electrolyte (κ/κ_0), which is the ratio of ionic conductivity of electrolyte containing dispersed gas bubbles (κ) over ionic conductivity of electrolyte free of gas bubbles (κ_0) **[65]**, is plotted as function of time for different d_{elec} in **Fig. VI.8(a)**. It has been noticed that κ/κ_0 decreased the most under the configuration of 100 µm, while it increased progressively with d_{elec}. Therefore, κ/κ_0 decreased the most under the configuration where the mineral electro-precipitation occurred the most (i.e., 100 µm), while when no mineral precipitation was observed (i.e., at 50 µm), κ/κ_0 remained constant over the course of electrolysis. Due to the non-conducting nature of gas bubbles **[66, 67]**, the ionic conductivity of electrolyte is reduced. Using the experimental data of κ/κ_0, the equation of Bruggeman written in **Eq. (VI.10)** allows estimating the gas void (φ) - the fraction of gas volume over the total volume of liquid and gas - for different d_{elec} at 4 mA cm^{-2}.

$$\varphi = 1 - \left(\frac{\kappa}{\kappa_0}\right)^{2/3} \qquad \text{(VI.10)}$$

The φ values are plotted against the interelectrode gap in **Fig. VI.8(b)**. φ was noticed to decrease as function of d_{elec}, which agreed with the above-mentioned trend of κ/κ_0 with d_{elec} (**Fig. VI.8(a)**). It means, the resistivity due to non-conducting gas bubbles was at the highest under the configuration of 100 µm and it decreased progressively with increasing order of d_{elec}. The higher values of φ obtained in smaller interelectrode gaps was confirmed by several works in literature **[66, 68]**.

The term relative resistivity (ρ/ρ_0) (**Eq. (VI.11)**) is also used in literature to depict the evolution of electrolyte resistivity, which is simply the inverse of κ/κ_0. The ρ/ρ_0 is plotted in function of d_{elec} in **Fig. VI.8(c)**.

$$\frac{\rho}{\rho_0} = {}^{1}\Big/\left({}^{\kappa}/_{\kappa_0}\right) \quad \text{(VI.11)}$$

ρ/ρ_0 decreased in the increasing order of d_{elec}. Comparable trend of the evolution of relative resistivity as function of interelectrode gap has also been highlighted in the work of Hine et al. **[69, 70]** and Vogt et al. **[71]** but in a larger range of interelectrode gap (5 to 70 mm) and relatively larger applied current densities (75 to 375 mA cm^{-2}). To further assess the relation between the gas evolution, the electrolyte resistivity and α coefficient, the α values are plotted against d_{elec} in **Fig. VI.8(c)**. It can be observed that α decreased with the increasing d_{elec}. In agreement with the plots in **Fig. VI.8**, α followed the trends of φ and ρ/ρ_0 with d_{elec}. Therefore, it strengthens the significance of introducing the α factor to account for physical H_2 evolution during the mineral scaling. In the nutshell, the relationship between the gas evolution, gas void and relative resistivity with the formation of mineral scaling on cathode surface at different interelectrode gaps can be schematized in **Fig. VI.9**. The least electro-deposition took place at the highest d_{elec} under study (3000 µm) owing to vigorous evolving gas whilst the mineral scaling occurred the most under the 100 µm configuration.

The internal ohmic resistance due to ohmic drop ($\sum RI$) in an electrochemical cell not only varies with the variation of interelectrode gap but is also affected by the evolving gas bubbles which act as moving electrical insulators in-between electrodes **[67]**. Therefore, it appears also interesting to study the evolution $\sum RI$ that can be evaluated by **Eq. (VI.12)**.

$$\sum RI = \Delta U - |E_C| - |E_A| \quad \text{(VI.12)}$$

where $\sum RI$ is the ohmic drop (V), while $|E_C|$ and $|E_A|$ are the absolute values of cathode and anode potentials (V) respectively.

The plots of $\sum RI$ and overall ΔU as function of d_{elec} are given in **Fig. VI.10**. It can be clearly observed that, as the d_{elec} decreased, the ohmic drop and cell voltage decreased linearly down to 100 µm. Interestingly, the decrease of $\sum RI$ occurred abruptly below 100 µm, breaking the linearity observed in the range of 100 µm to 3000 µm configuration. This is the first time that the non-linearity of ohmic resistance is assessed under the microfluidic setup unlike the linear decrease of $\sum RI$ usually observed using millimetric distances in literature (**Eq. (VI.13)**) **[72]**.

$$\sum RI = \frac{j_{app}\, d_{elec}}{\kappa_0} \quad \text{(VI.13)}$$

In the presence of gas bubbles, **Eq. (VI.13)** is slightly modified to take into consideration the gas void fraction as shown in **Eq. (VI.14) [69, 71]**:

$$\sum RI = \frac{j_{\text{app}}}{\kappa_0 \, (1-\varphi)^{3/2}} \, d_{\text{elec}} \qquad \text{(VI.14)}$$

The slope value obtained from the linear trend in **Fig. VI.10**, for distances ranging from 100 to 3000 µm, equaled 0.2435 V mm^{-1} (R^2 = 0.95).

In conclusion, the $\sum RI$ decreased with decreasing d_{elec} and higher φ fraction in submillimetric region made the $\sum RI$ decrease non-linearly. A decrease in electrolytic $\sum RI$ reduces indeed the energy consumption of an EAOP, nevertheless it does not promise a decrease in mineral scaling formation as practically proven in this work. More mineral precipitation occurred, while the $\sum RI$ decreased in descending order of d_{elec} down to 100 µm.

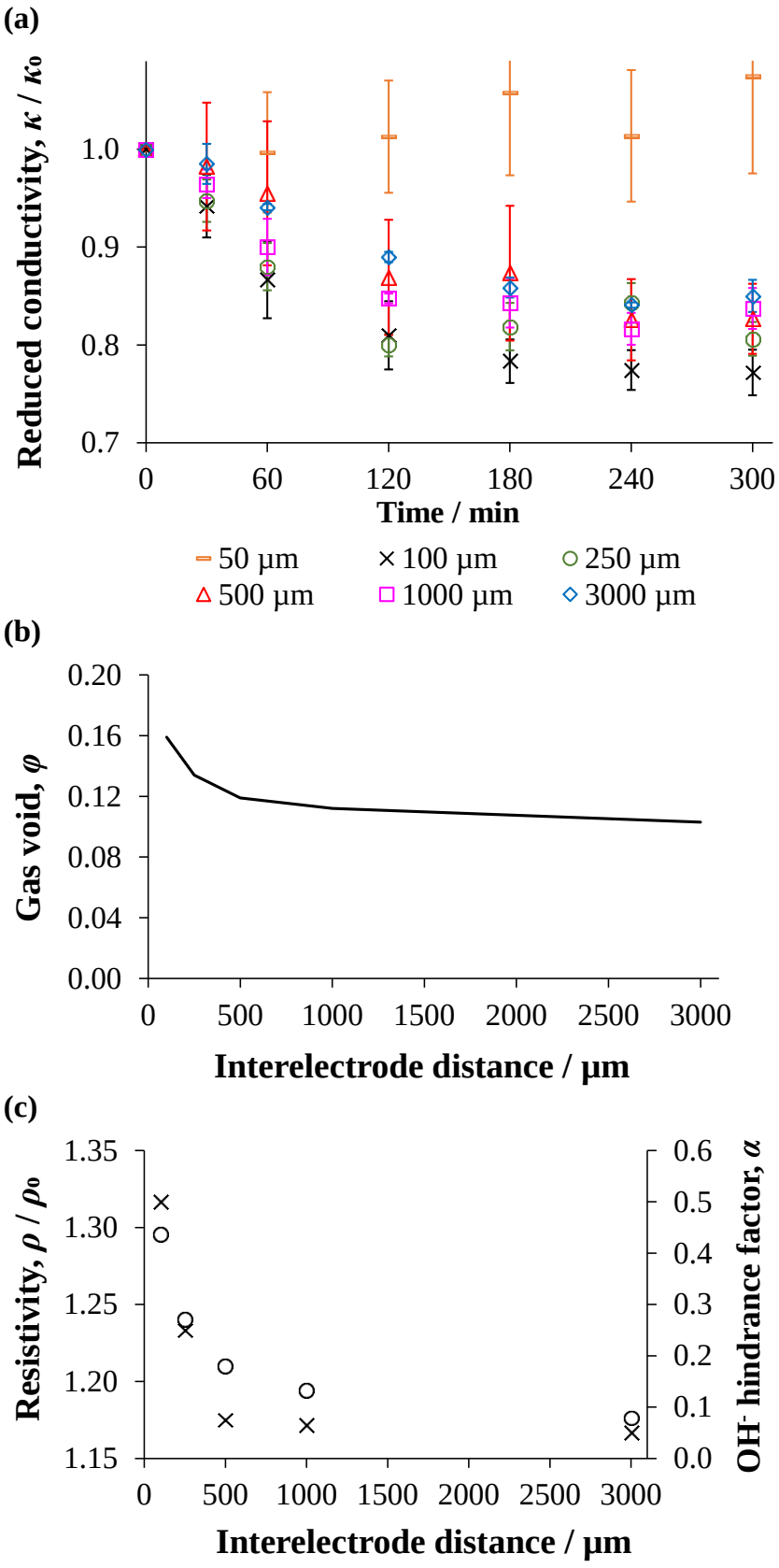

Fig. VI.8. **(a)** Evolution of κ/κ_0 of electrolyte in-between different d_{elec}, **(b)** influence of d_{elec} on the estimated φ fraction and **(c)** variation of ρ/ρ_0 (○) and α (×) with d_{elec}. Cathode: stainless steel, anode: BDD and j_{app} = 4 mA cm^{-2}.

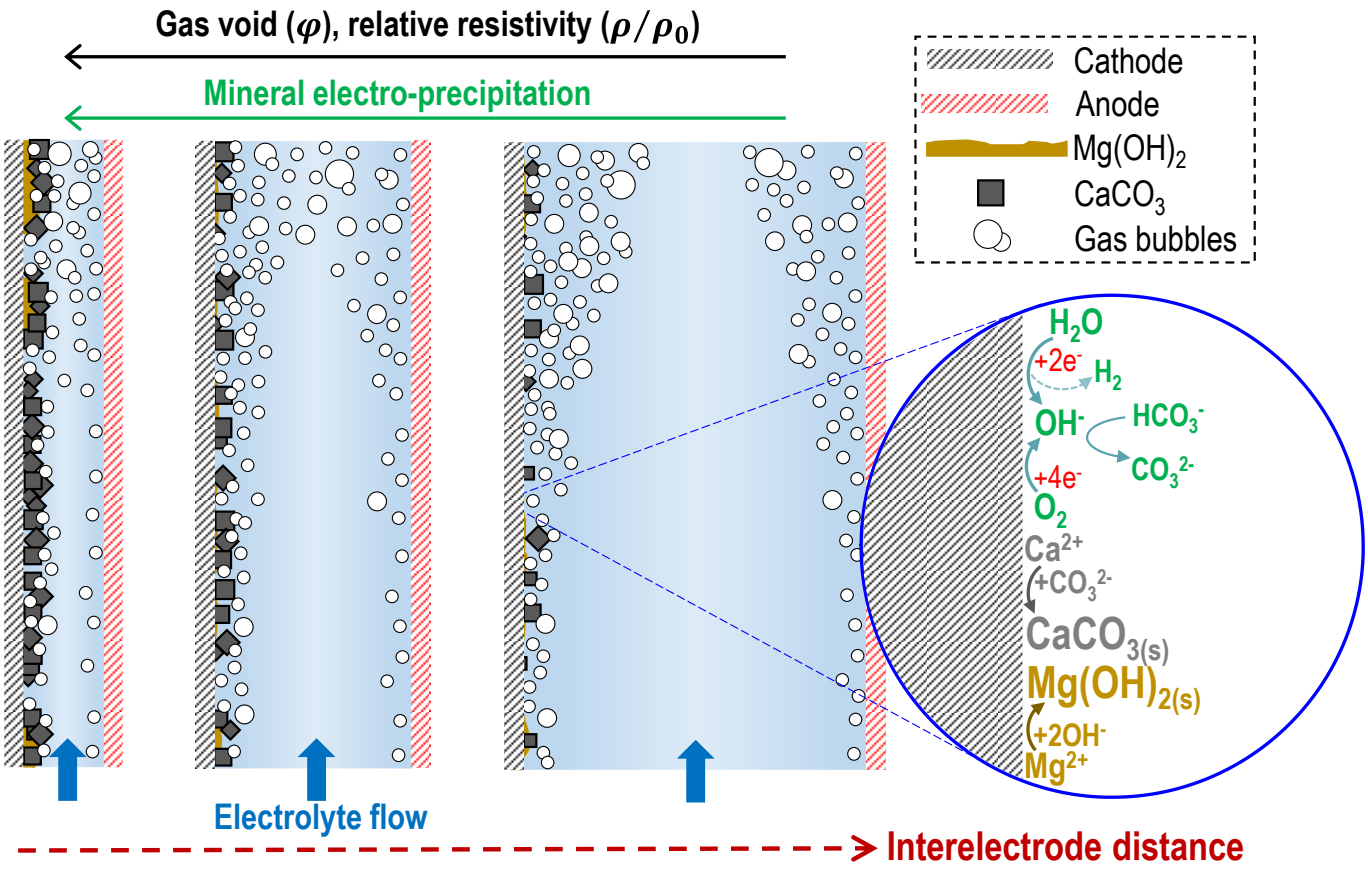

Fig. VI.9. Mechanistic scheme describing the relationship between mineral electro-precipitation with the occurring concurrent gas evolution on cathode surface under different d_{elec} configurations.

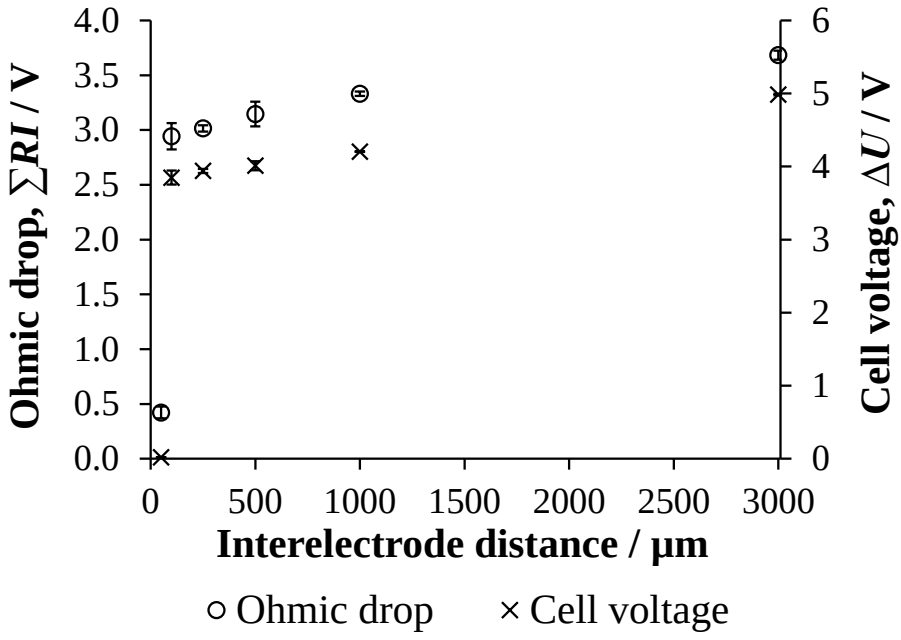

Fig. VI.10. Ohmic drop ($\sum RI$) of electrolyte (○) and cell voltage (ΔU) (×) as a function of d_{elec}. Cathode: stainless steel, anode: BDD and j_{app} = 4 mA cm^{-2}.

VI.4.4. Cathode/electrolyte interface impedance study of electro-precipitation at different interelectrode distances

It is presented here-in for the first time, the interfacial parameters acquired by EIS analysis of a scalable electrochemical reactor in the aim at better understanding the cathode/electrolyte interface mechanism under electro-precipitation condition considering wide ranges of d_{elec}. The EIS extracted parameters under distinct configurations of millimetric into submillimetric setup are compared and discussed. A mechanistic scheme of mineral electro-precipitation on cathode surface is proposed with the integrated EEC to characterize the precipitation using EIS (**Fig. VI.11**). R_F and C_F corresponded respectively to the resistance and capacitance of porous non-conductive precipitation film. Charge transfer resistance (R_{CT}) was attributed to the difficulty of electronic transfer for electrochemical reactions to occur on cathode surface as the mineral electro-precipitation grew over time. R_{SOL} was attributed to the resistance of electronic transfer in electrolyte between cathode (as working electrode) and reference electrode. Instead of pure capacitor circuit element, constant phase element (CPE_{DL}) was used to model the charging of non-faradaic capacitive electronic behavior that occurred on bare cathode surface - the area where there was no electro-precipitation - with ions present in electrolyte. This capacitive response was due to the electronic double-layer formed at the polarized interface. CPE_{DL} was more apt to account for not only the non-homogeneity of distribution of metallic elements that composed stainless steel cathode **[73-75]** but also non-ideality of capacitive response due to uneven coverage of porous electro-precipitation and evolving gas on cathode surface **[28, 29, 76, 77]**. The value of C_{DL} is linked with CPE_{DL} (in F) by **Eq. (VI.15) [74, 76-78]**:

$$CPE_{DL} = C_{DL}{}^{n}\left[R_{SOL}{}^{-1} + R_{CT}{}^{-1}\right]^{(1-n)} \quad \text{(VI.15)}$$

where n ($0 < n < 1$) is the constant phase element parameter and R_{SOL} as well as R_{CT} are expressed in Ohms.

Another time-constant, L_{IND}-R_{DES} (L in Henry and R_{DES} in Ohms) was added to complete the equivalent circuit. This pair of time constant is ascribed to R_i-C_i couple when R_i and C_i take negative values, as the outcome of mathematical fitting of equivalent circuit to experimental data. This is often used when induction loop appears in the experimental data, which was also noticed previously not only in batteries, fuel cells and corrosion study but also in water electrolysis system with gas evolving electrodes **[79-83]**. Consequently, the inductive loop in our experimental spectra has been attributed to the possible adsorption/desorption of mineral electro-precipitate at the cathode surface.

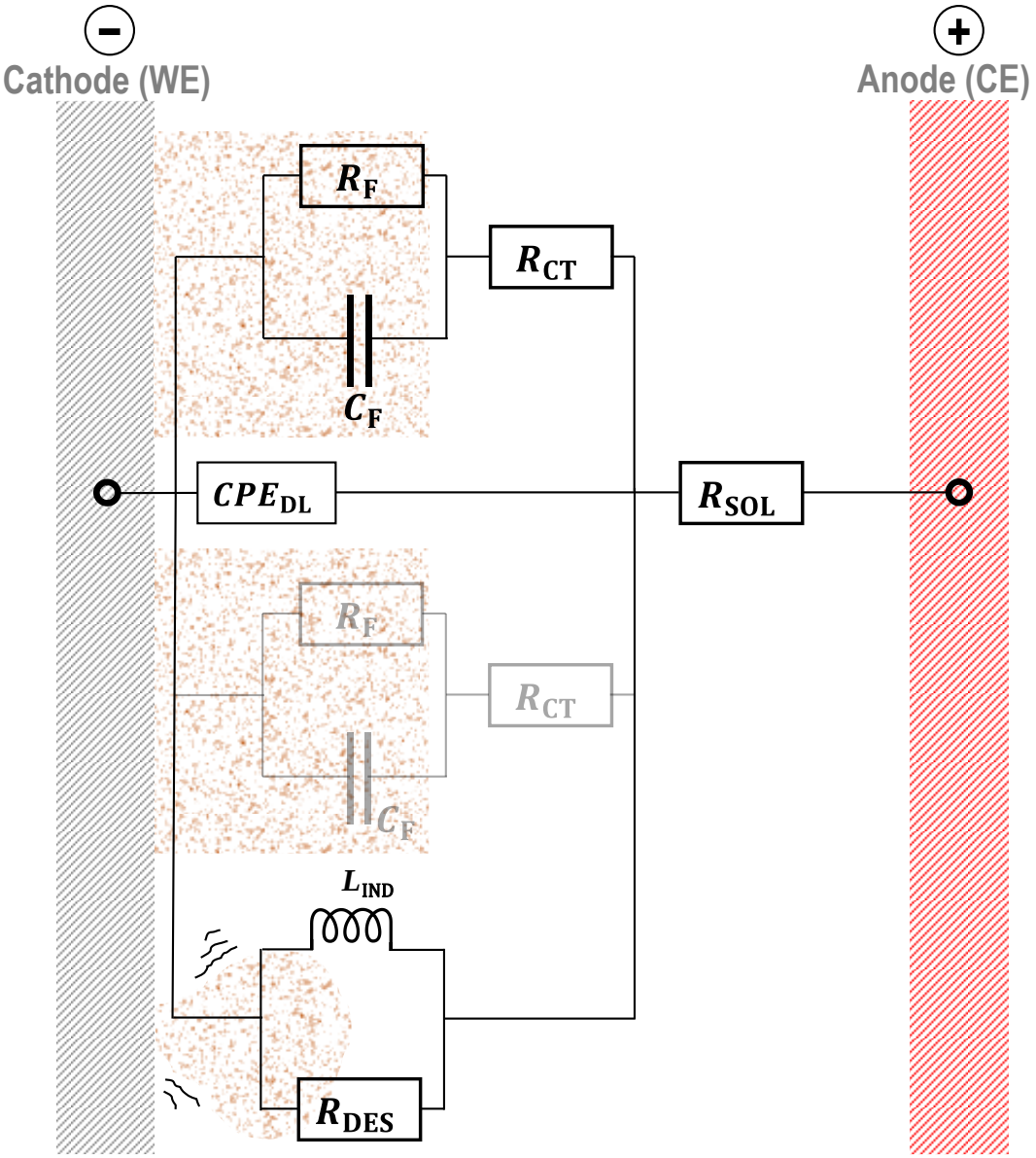

Fig. VI.11. Mechanistic scheme of mineral electro-precipitation on cathode surface including the representation of EEC used in EIS modeling. WE: stainless steel and CE: BDD.

The validity of the impedance spectra obtained in our experiments was checked and validated by the linear KKT method **[84-87]** and they were plotted against the experimental data at varying d_{elec} as shown in **Fig. VI.12**. Negative impedance values obtained in high frequency regions were not considered as they were the outcome of instrumental artifacts. The chi-squared residues χ^2 between linear KKT and EEC model fitting curves against experimental data are tabulated in **Table VI.3**. The experimental curves complied well with the KKT plots considering the highest χ^2 deviation of 0.0017, whereas the modeled curves fitted the experimental counterparts very well with the highest χ^2 of 0.0103. The conformity of experimental EIS spectra with KKT standard confirmed the proposed EEC model (**Fig. VI.11**).

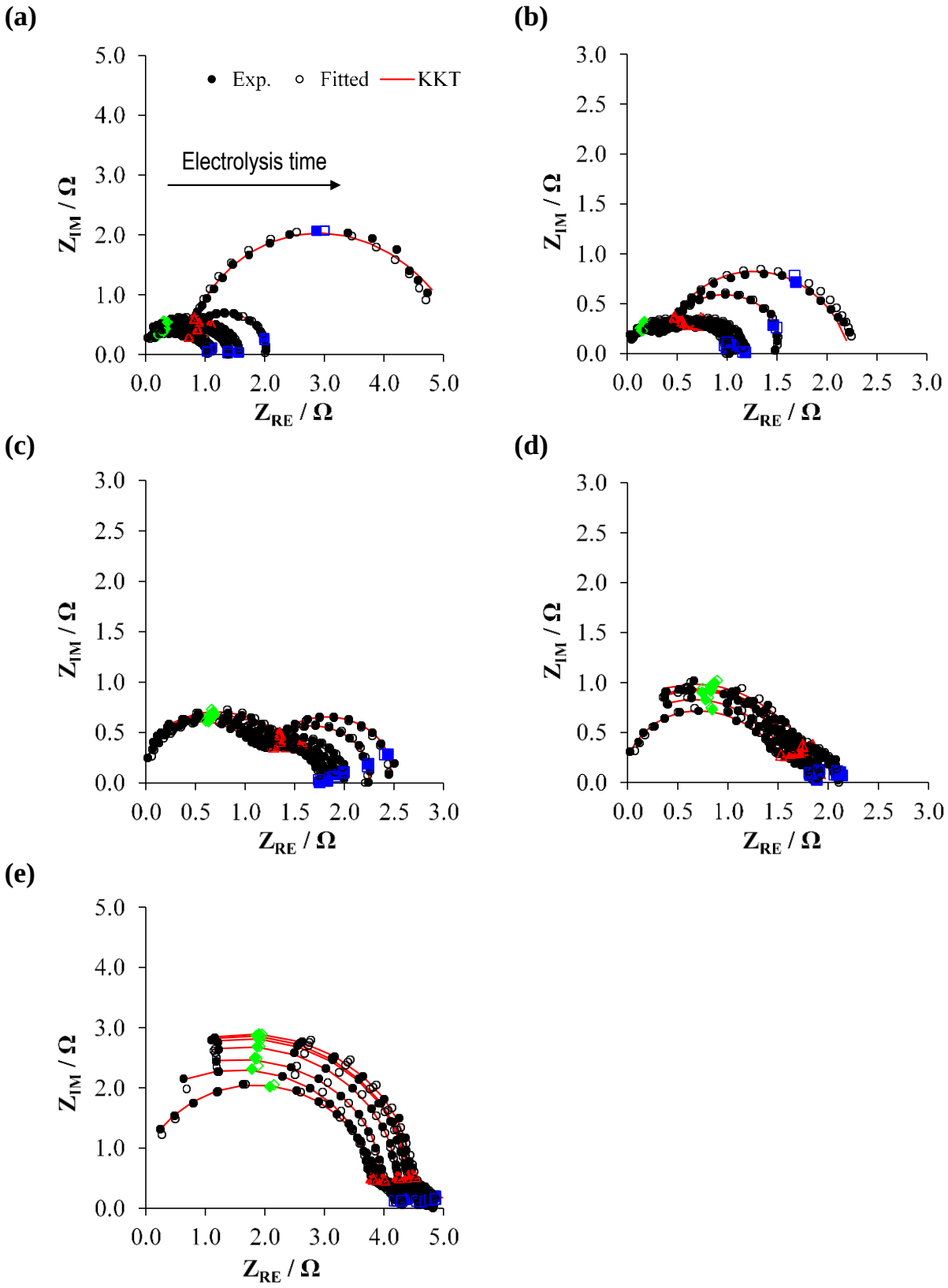

Fig. VI.12. Plots of linear KKT (—), experimental (●) and EEC theoretical (○) impedance spectra for d_{elec} of **(a)** 100 µm, **(b)** 250 µm, **(c)** 500 µm, **(d)** 1000 µm and **(e)** 3000 µm. (◆, ◇): high frequency (20 kHz), (▲, △): middle frequency (2 kHz) and (■, □): low frequency (0.2 kHz) impedance samples. Electrolysis time: 0, 0.5, 1, 2, 3, 4 and 5 h.

Table VI.3. Chi-squared (χ^2) residues between EIS experimental spectra with linear KKT control and EEC theoretical plots for different investigated d_{elec}.

Time / h	100 µm		250 µm		500 µm		1000 µm		3000 µm	
	KKT	EEC	KKT	EEC	KKT	EEC	KKT	EEC	KKT	EEC
0	0.00043	0.00187	0.00058	0.01028	0.00016	0.00188	0.00048	0.00256	0.00002	0.00082
0.5	0.00011	0.00389	0.00058	0.00537	0.00011	0.00284	0.00018	0.00121	0.00003	0.00238
1	0.00029	0.00362	0.00063	0.00418	0.00005	0.00352	0.00016	0.00431	0.00003	0.00128
2	0.00031	0.00450	0.00071	0.00708	0.00007	0.00716	0.00010	0.00165	0.00003	0.00181
3	0.00031	0.00337	0.00060	0.00441	0.00007	0.00203	0.00026	0.00249	0.00004	0.00229
4	0.00023	0.00285	0.00170	0.00950	0.00004	0.00544	0.00016	0.00163	0.00004	0.00298
5	0.00033	0.00220	0.00130	0.00610	0.00007	0.00494	0.00010	0.00162	0.00004	0.00656

Figure VI.13 depicts the evolution of R_{CT}, R_F, C_{DL} and C_F over time for all the investigated d_{elec}. C_{DL} values estimated correspond well to the average values widely reported in literature (4-60 µF) **[27, 39, 41, 51, 78, 88, 89]**. An interesting feature is that R_{CT} and C_{DL} values were seen to be constant over the course of experiment, whatever the d_{elec} adopted (**Fig. VI.13**). The average values of R_{CT} were 0.79±0.04 Ω, 0.55±0.05 Ω, 1.1±0.14 Ω, 1.6±0.06 Ω and 4.4±0.18 Ω for 100, 250, 500, 1000 and 3000 µm d_{elec} respectively. The average C_{DL} values were 25±1.7 µF, 21±2.4 µF, 8±1.3 µF, 6.2±0.2 µF and 2.6±0.1 µF for respective distances of 100, 250, 500, 1000 and 3000 µm. In literature, R_{CT} and C_{DL} have been reported to respectively increase and decrease as function of electrolysis time **[17, 21, 22, 27, 41, 78, 79]**, due to non-conductive nature of $CaCO_3$ and $Mg(OH)_2$ deposits which progressively cover the effective surface of electrode. Contrastingly, under this experimental setup, the progressive formation of mineral electro-precipitate did not significantly impede the electrochemical reactions occurring on the electrode/electrolyte interface. This observation could be attributed to the large cathode surface used in these experiments, which was about 25 to 250 times bigger than the classic rotating disk electrodes used by others **[37]**. The cathode surface was not fully covered by the precipitate and hence offered adequate sites for electronic exchanges at electrode/electrolyte interface. Moreover, owing to concomitant gas evolution on the cathode, the morphology of electro-precipitate is known to be porous which hindered the complete coverage of cathode surface **[39, 90]**. Lastly, the overall trend of the impedance response attributed to the faradaic resistance of non-conducting porous layer (R_F) was found to increase over time according to **Fig. VI.13**. The increase was more pronounced under the configuration in which more mineral electro-precipitation occurred, i.e., when d_{elec} was decreasing. After 5 h of electrolysis, there was an increase of about 1.1, 1.3, 2.1, 2.5 and 3.7 times of R_F relatively to their initial values before electrolysis for the respective distances of 3000, 1000, 500, 250 and 100 µm. In the meantime, C_F appeared to be rather constant during the electrolysis considering standard deviations, similarly to the evolution of C_{DL} with electrolysis time (**Fig. VI.13**).

Fig. VI.14 illustrates the experimental and modeled plots of R_{CT} and C_{DL} as a function of d_{elec} at the beginning and after 1, 3 and 5 h of electrolysis. Interestingly, R_{CT} increased linearly with increasing d_{elec} according to **Figs. VI.14(a), VI.14(c), VI.14(e)** and **VI.14(g)**. At t = 0, the linear curve has a slope of 1.20 Ω mm^{-1} (R^2 = 0.99) and after 5 h electrolysis, the slope was evaluated at 1.43 Ω mm^{-1} (R^2 = 0.98). One could expect that the more the electrode is covered by non-conducting film, the more the R_{CT} resistance for faradaic electron exchange at electrode/electrolyte is enhanced. This reverse trend can be firstly explained by the manifestation of varying the d_{elec}. It has been elaborated from **Fig. VI.6** that the involvement of anodic activity producing dissolved O_2 was more pronounced in microfluidic configuration. As a result, R_{CT} measured by EIS at narrow interelectrode gap was lower. Secondly, as depicted in **Fig. VI.3**, when d_{elec} increased, the E_C measured on cathode surface decreased lower into the water reduction region. More vigorous HER occurring at higher d_{elec} impeded more effectively the electronic charge transfer. As a result, R_{CT} increased as the interelectrode gap increased. Those are the reasons why largest R_{CT} was characterized with 3000 µm setup in **Fig. VI.14** despite the least mineral scaling occurred under this configuration. Moreover, the fact that R_{CT} decreased when E_C increased (i.e., when d_{elec} decreased) does corroborate the result obtained by Hoseinieh et al. **[29]**. Eventually, the trend of R_{CT} as function of d_{elec} offers a new interesting insight, since it has never been studied elsewhere in the literature and therefore constitutes a baseline for future investigation.

To further explore the trend between R_{CT} and the d_{elec}, the slopes of R_{CT} curves (R_{CT}/d_{elec}) obtained in **Figs. VI.14(a), VI.14(c), VI.14(e)** and **VI.14(g)** have been plotted as function of electrolysis time (**Fig. VI.15**). It was noticed that the R_{CT}/d_{elec} ratio remained practically constant and it took an average value of 1.32 ± 0.11 Ω mm^{-1} during the electrolysis. This finding suggested that the electrochemical setup adopted in this work was not prone to prompt total electrode passivation by mineral scaling, at least after 5 h of electrolysis. This is probably due to the large effective surface area employed in this work and further highlights its interest for the application at larger scale.

Looking at the redistribution of charges at the electrode/electrolyte interface (**Fig. VI.14(b), VI.14(d), VI.14(f)** and **VI.14(h)**), another new interesting insight was noticed. C_{DL} values decreased drastically with increasing d_{elec}. This could partly be attributed to the decrease in the applied E_C on cathode. As the consequence of more vigorous gas evolution at lower E_C, the distribution of charges at cathode/electrolyte interface was perturbed and ionic species and their solvated forms could undergo rearrangement at the interface **[91-93]**. As a result, the capacitance response via EIS measurement was smaller. The apparent decreasing trend of C_{DL} values with decreasing E_C was supported by the literature **[39, 76, 77, 81, 94]**. Furthermore, a new model is proposed to establish the relationship

between C_{DL} and d_{elec}. C_{DL} model curves are plotted as a function of d_{elec} in **Fig. VI.14(b), VI.14(d), VI.14(f)** and **VI.14(h)** before (t = 0) and after 1, 3 and 5 h of electrolysis using **Eq. (VI.16)**.

$$C_{DL} = 5.0305 \pm 0.6073 \times \frac{1}{d_{elec}} \quad \text{(VI.16)}$$

In **Eq. (VI.16)**, C_{DL} is expressed in µF and d_{elec} is in mm. It can be observed that C_{DL} varied linearly with $1/d_{elec}$ from millimetric distances down to 250 µm. Within this range of d_{elec}, the theoretical C_{DL} curves matched well the experimental plots. Using ME fitting criterion (**Eq. (III.4)**), the ME was evaluated as high as 97.93% with the worst fitting scenario calculated to be 95.46%. Below 250 µm, the evolution of C_{DL} was no longer proportional to the inverse of d_{elec}. More mineral scaling occurring under this condition might be the factor that broke the linearity with $1/d_{elec}$. By identification between **Eq. (VI.16)** and **Eq. (VI.8)**, the slope of the former equals to $2\varepsilon_S\varepsilon_0\omega$. Thus, the constant ω can be estimated and equaled to 3.55×10^6. Computing **Eq. (VI.16)** with the approximated ω yielded d_{DL} values of 0.07, 0.14, 0.28 and 0.85 nm when the electrochemical cell was equipped with 250, 500, 1000 and 3000 µm d_{elec} respectively. These values were lower than 3 to 5 nm reported in diluted aqueous solution (electrolyte of 10 mM) at 25°C **[48, 95]**. This difference might be explained by the concurrent gas evolution taking place in the present case on both cathode and anode surfaces through the entire electrolysis.

Contrastingly, the evolutions of R_F and C_F which are characteristic of insulating deposit films formed on cathode surface in function of d_{elec} (**Fig. VI.16**) were more straightforward. Both resistance and capacitance related to the film formation (i.e., R_F and C_F, respectively) decreased in the increasing order of d_{elec}. As depicted in **Fig. VI.1**, less mineral deposition took place in the increasing order of interelectrode gap. Consequently, fitted R_F and C_F values decreased owing to lesser mineral electro-precipitation formed in ascending order of d_{elec}. This further emphasizes the decreasing trends of R_F and C_F values with decreasing applied potential which have been reported in literature **[27, 39, 76, 78, 81]**.

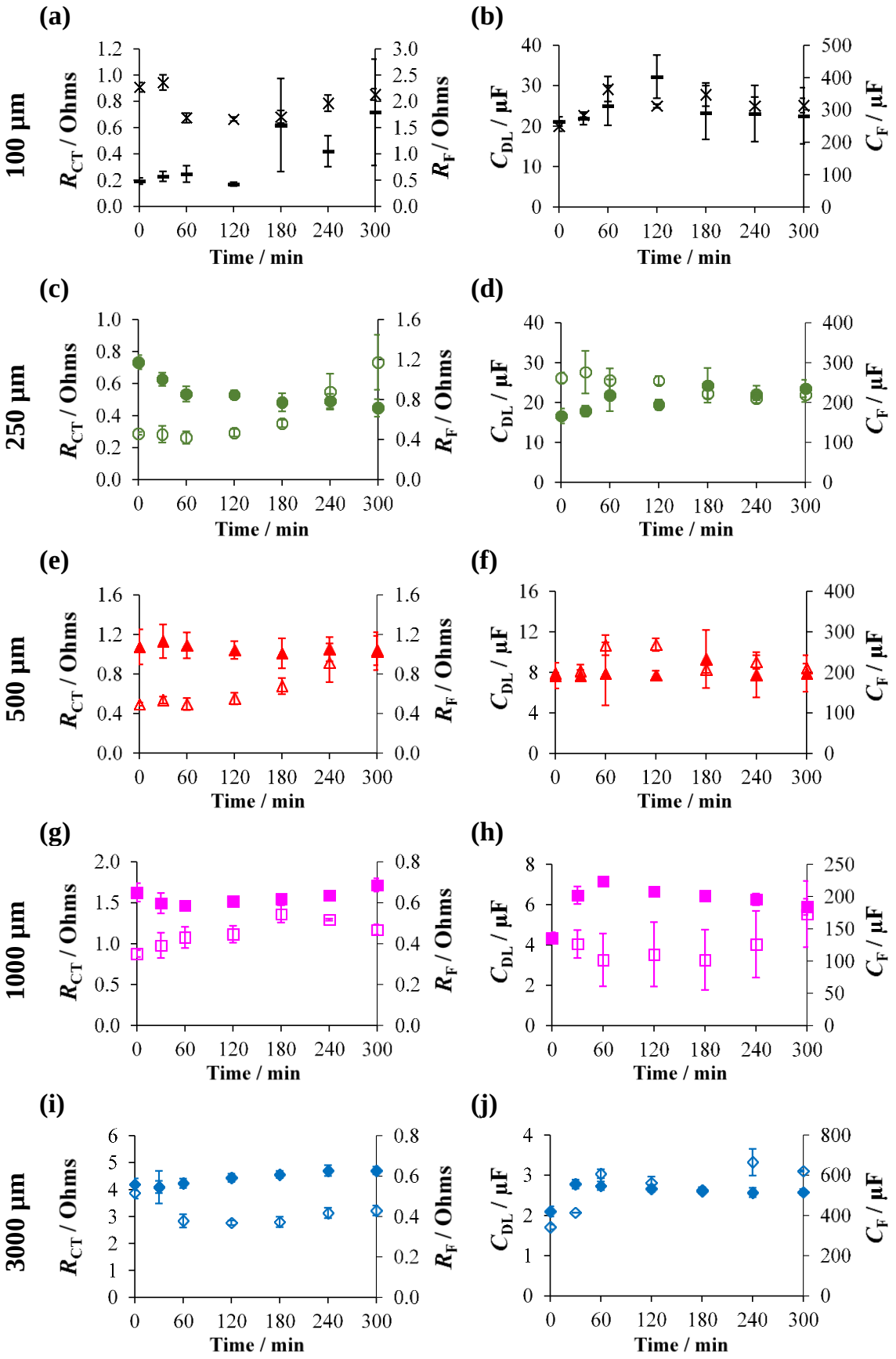

Fig. VI.13. Evolutions of R_{CT} (✕, ●, ▲, ■, ◆), R_F (—, ○, △, □, ◇) in **(a)**, **(c)**, **(e)**, **(g)**, **(i)** as well as C_{DL} (✕, ●, ▲, ■, ◆) and C_F (—, ○, △, □, ◇) in **(b)**, **(d)**, **(f)**, **(h)**, **(j)** during 5 h of electrolysis using different d_{elec}. Cathode: stainless steel, anode: BDD and j_{app}: 4 mA cm^{-2}. Solution containing 150 mg L^{-1} of Ca^{2+}, 5 mg L^{-1} of Mg^{2+} and 60 mg L^{-1} of TIC.

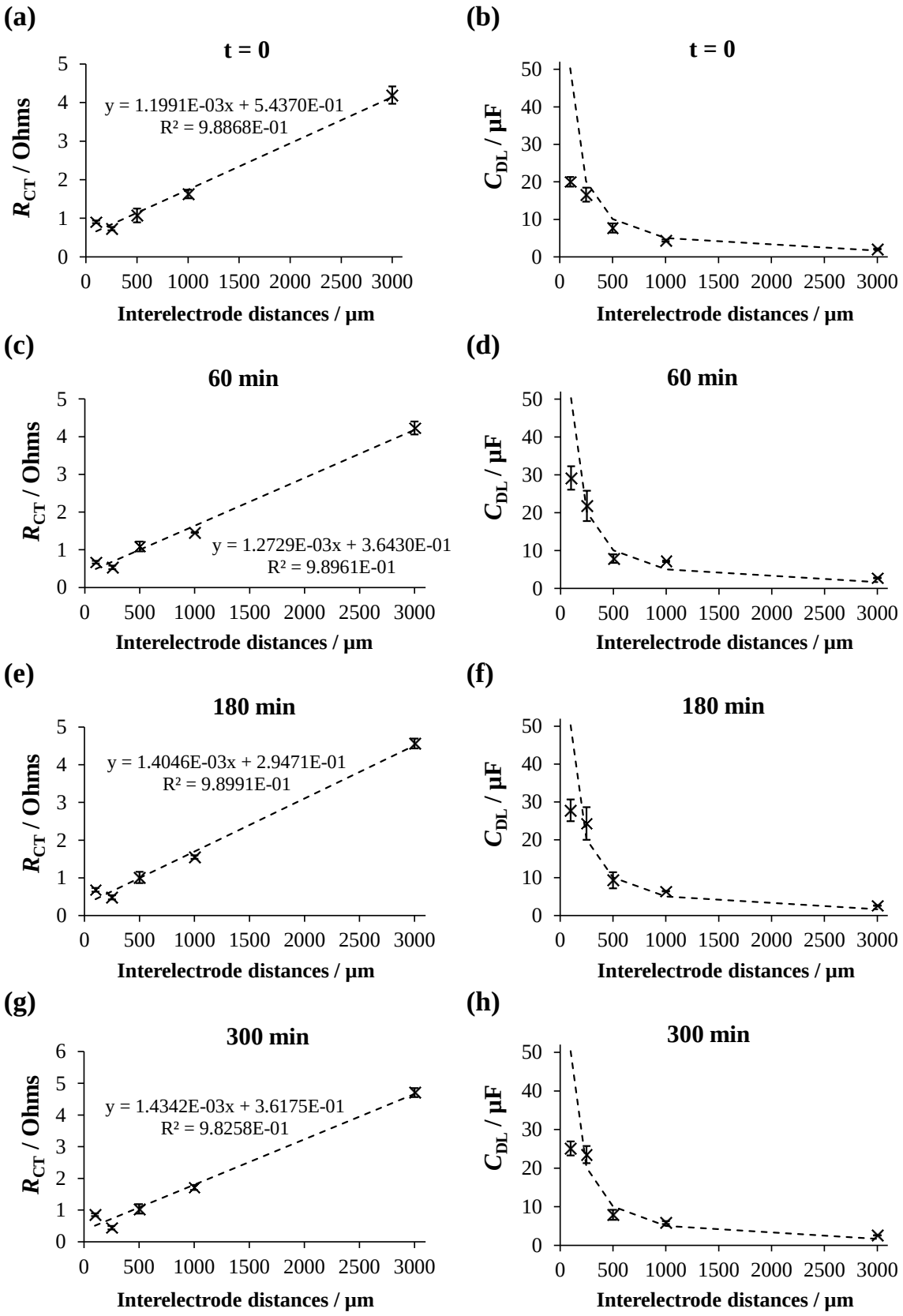

Fig. VI.14. Experimental and modeled curves of R_{CT} in **(a)**, **(c)**, **(e)** and **(g)** as well as C_{DL} in **(b)**, **(d)**, **(f)** and **(h)** as a function of d_{elec} at the initial time and after 1, 3 and 5 h of electrolysis. Cathode: stainless steel, anode: BDD and j_{app}: 4 mA cm^{-2}. Solution containing 150 mg L^{-1} of Ca^{2+}, 5 mg L^{-1} of Mg^{2+} and 60 mg L^{-1} of TIC.

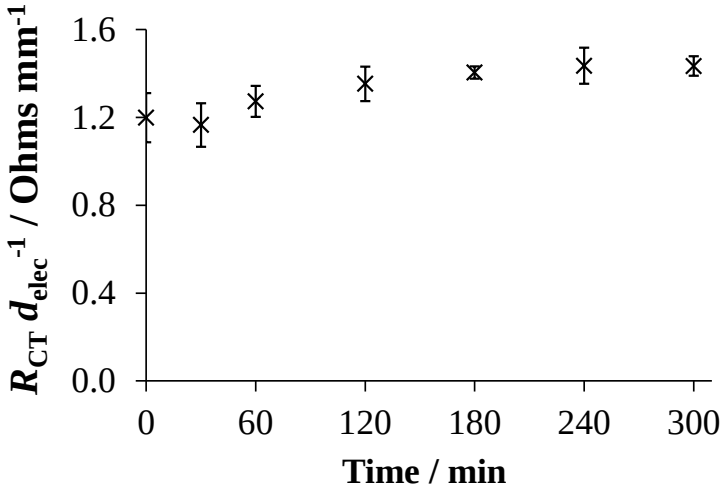

Fig. VI.15. R_{CT}/d_{elec} slope as a function of electrolysis time.

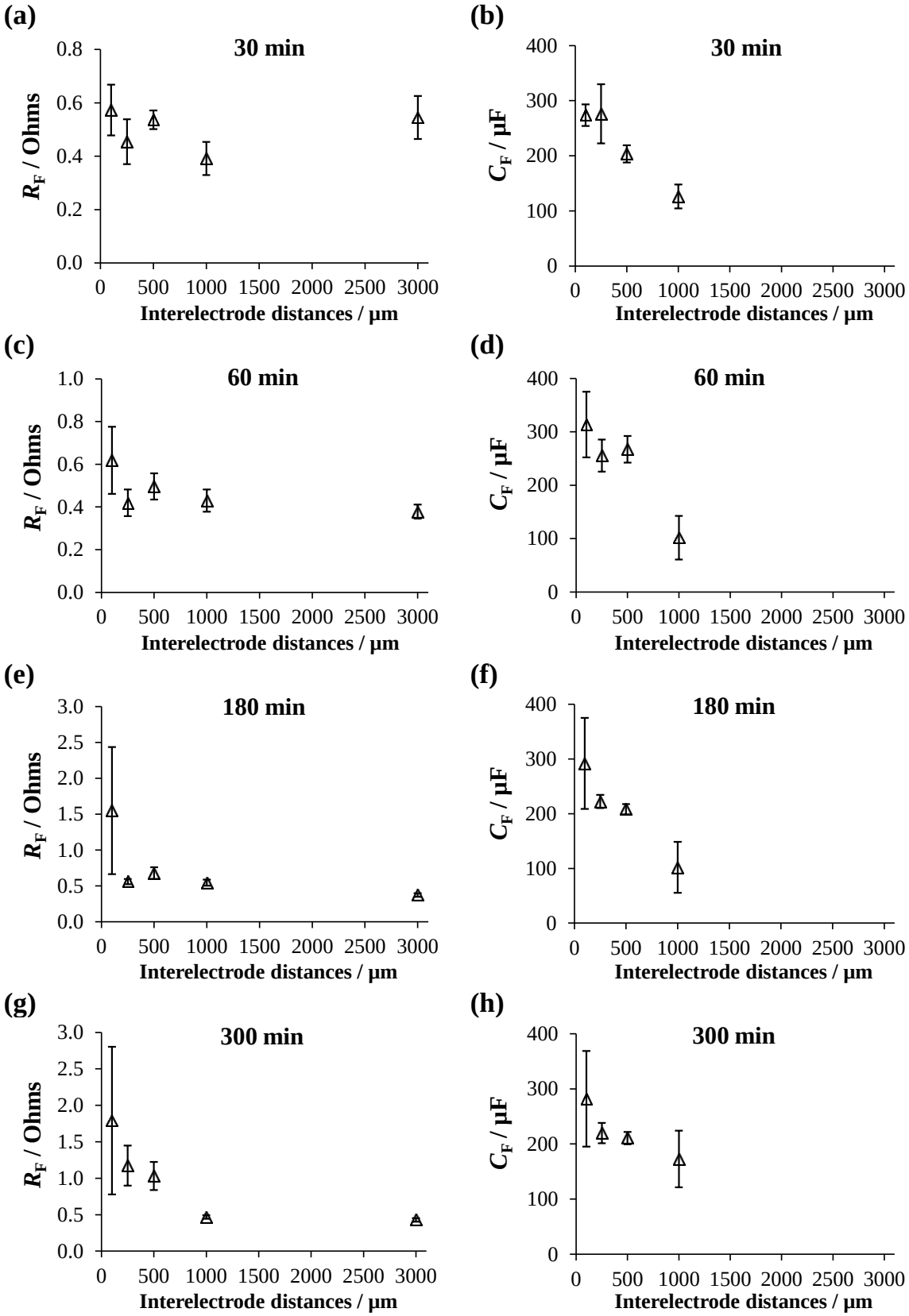

Fig. VI.16. Evolutions of R_F in **(a)**, **(c)**, **(e)** and **(g)** as well as C_F in **(b)**, **(d)**, **(f)** and **(h)** as a function of d_{elec} after 0.5, 1, 3 and 5 h of electrolysis. Cathode: stainless steel, anode: BDD, j_{app}: 4 mA cm^{-2} and solution: Ca^{2+} 150 mg L^{-1}, Mg^{2+} 5 mg L^{-1} and TIC 60 mg L^{-1}.

VI.5. Conclusions

The influence of a wide range of d_{elec} (50-3000 µm) towards the occurrence of mineral electro-precipitation has been elucidated for the first time. Under similar diffusional mass transfer regime and laminar hydrodynamic regime from one configuration to the others, more deposition of $Mg(OH)_2$ and $CaCO_3$ were observed in decreasing order of d_{elec} from 3000 to 100 µm, whilst no deposit was present at the lowest d_{elec} investigated (50 µm). This new insight was mostly accounted for the applied E_C when the electrochemical cells were polarized at 4 mA cm^{-2}. No OH^- was yet produced under the 50 µm configuration, due to the high E_C value (0.202 $\pm$ 0.024 V/Ag-AgCl). From 100 µm d_{elec} upwards, the OH^- production occurred concomitantly with HER and it was more intense at higher interelectrode gap. This finding was in line with the decreasing measured E_C in ascending order of d_{elec}. In this case, the parasitic HER reduced the current efficiency of the formation of OH^- via dissolved O_2 and H_2O reduction reactions and also induced detachment of mineral scaling occurring on cathode surface. When identical E_C was applied under millimetric and microfluidic configurations, a difference of electro-precipitation related to the electrochemical reactor design was emphasized. More provision of dissolved O_2 produced from OER on anode contributed towards the formation of mineral scaling on cathode under microfluidic than millimetric configuration. A novel mathematical modeling taking into account the concomitant H_2 evolution to model the kinetics of Mg and Ca electro-precipitation has been proposed. It fitted well with the experimental data (RMSE < 0.0149 for Mg^{2+} and RMSE < 0.1983 for Ca^{2+}). The concurrent gas bubbles formed while varying d_{elec} showed that both relative resistivity and gas void fraction increased when d_{elec} decreased from 3000 µm to 100 µm. Despite the concomitant HER, when d_{elec} was reduced, the internal ohmic resistance dropped linearly with decreasing interelectrode gap from millimetric down to 100 µm, but below 100 µm, the linear trend was no longer observed.

Electrochemical processes taking place at the cathode/electrolyte interface were accessed by EIS method. Under the configurations where mineral deposition were observed, it was noticed that the R_{CT} and C_{DL} values were constant during the 5 h of electrolysis whatever the d_{elec} adopted. It was attributed to the large effective surface area of the cathode whereby it was not fully passivated under the applied operating conditions in this work. Contrastingly, R_{CT} and C_{DL} values increased and decreased respectively with increasing d_{elec}. Under microfluidic setups, R_{CT} values were lower owing firstly to the facility of OH^- production due to external provision of dissolved O_2 from the oxidation of water on anode, and secondly to the less evolving H_2 at lower d_{elec}. Using higher d_{elec}, higher intensity of HER provoked more perturbation of charge distribution at electrode/electrolyte interface, which resulted in lower C_{DL} values. Novel mathematical relations to assess R_{CT} and C_{DL} as a function of d_{elec} have been proposed to predict their evolution.

Finally, it has been newly demonstrated the importance of d_{elec} on the formation of mineral scaling on the cathode surface. Both the effects of H_2 overpotential and electrochemical design (i.e., the contribution of anode under micrometric distances) have been proven influential to hinder or minimize the occurrence of mineral precipitation on cathode surface through the occurrence or not of gas bubbles electrogeneration. Due to primordial role of gas evolution taking an effect on mineral electro-precipitation observed in this work, the overpotential of H_2 evolution offered by other cathode materials could either minimize or maximize the electro-precipitation, which will be the subject of research in incoming chapter.

References

[1] O. Scialdone, A. Galia, C. Guarisco, S. Randazzo, G. Filardo, Electrochemical incineration of oxalic acid at boron doped diamond anodes: Role of operative parameters, Electrochimica Acta, 53 (2008) 2095-2108.
[2] O. Scialdone, E. Corrado, A. Galia, I. Sirés, Electrochemical processes in macro and microfluidic cells for the abatement of chloroacetic acid from water, Electrochimica Acta, 132 (2014) 15-24.
[3] O. Scialdone, A. Galia, S. Sabatino, D. Mira, C. Amatore, Electrochemical conversion of dichloroacetic acid to chloroacetic acid in a microfluidic stack and in a series of microfluidic reactors, ChemElectroChem, 2 (2015) 684-690.
[4] E. Mousset, Unprecedented reactive electro-mixing reactor: Towards synergy between micro- and macro-reactors?, Electrochemistry Communications, 118 (2020) 106787.
[5] P.V. Nidheesh, G. Divyapriya, N. Oturan, C. Trellu, M.A. Oturan, Environmental applications of boron-doped diamond electrodes: 1. Applications in water and wastewater treatment, ChemElectroChem, 6 (2019) 2124-2142.
[6] S.O. Ganiyu, C.A. Martínez-Huitle, Nature, mechanisms and reactivity of electrogenerated reactive species at thin-film boron-doped diamond (BDD) electrodes during electrochemical wastewater treatment, ChemElectroChem, 6 (2019) 2379-2392.
[7] E. Mousset, N. Oturan, M.A. Oturan, An unprecedented route of OH radical reactivity evidenced by an electrocatalytical process: Ipso-substitution with perhalogenocarbon compounds, Applied Catalysis B: Environmental, 226 (2018) 135-146.
[8] X. Du, M.A. Oturan, M. Zhou, N. Belkessa, P. Su, J. Cai, C. Trellu, E. Mousset, Nanostructured electrodes for electrocatalytic advanced oxidation processes: From materials preparation to mechanisms understanding and wastewater treatment applications, Applied Catalysis B: Environmental, 296 (2021) 120332.
[9] P. Ma, H. Ma, S. Sabatino, A. Galia, O. Scialdone, Electrochemical treatment of real wastewater. Part 1: Effluents with low conductivity, Chemical Engineering Journal, 336 (2018) 133-140.
[10] E. Mousset, M. Puce, M.N. Pons, Advanced electro-oxidation with boron-doped diamond for acetaminophen removal from real wastewater in a microfluidic reactor: Kinetics and mass-transfer studies, ChemElectroChem, 6 (2019) 2908-2916.
[11] E. Mousset, L. Quackenbush, C. Schondek, A. Gerardin-Vergne, S. Pontvianne, S. Kmiotek, M.-N. Pons, Effect of homogeneous Fenton combined with electron transfer on the fate of inorganic chlorinated species in synthetic and reclaimed municipal wastewater, Electrochimica Acta, 334 (2020) 135608.
[12] E. Mousset, S. Pontvianne, M.-N. Pons, Fate of inorganic nitrogen species under homogeneous Fenton combined with electro-oxidation/reduction treatments in synthetic solutions and reclaimed municipal wastewater, Chemosphere, 201 (2018) 6-12.
[13] J. Marin-Cruz, R. Cabrera-Sierra, M. Pech-Canul, I. Gonzalez, EIS study on corrosion and scale processes and their inhibition in cooling system media, Electrochimica Acta, 51 (2006) 1847-1854.
[14] J. Marin-Cruz, E. Garcia-Figueroa, M. Miranda-Hernández, I. Gonzalez, Electrochemical treatments for selective growth of different calcium carbonate allotropic forms on carbon steel, Water Research, 38 (2004) 173-183.
[15] Y. Ben Amor, L. Bousselmi, H. Takenouti, E. Triki, Influence of sulphate ions on corrosion mechanism of carbon steel in calcareous media, Corrosion Engineering, Science and Technology, 40 (2005) 129-136.
[16] Y. Ben Amor, L. Bousselmi, B. Tribollet, E. Triki, Study of the effect of magnesium concentration on the deposit of allotropic forms of calcium carbonate and related carbon steel interface behavior, Electrochimica Acta, 55 (2010) 4820-4826.
[17] L. Bousselmi, C. Fiaud, B. Tribollet, E. Triki, Impedance spectroscopic study of a steel electrode in condition of scaling and corrosion: Interphase model, Electrochimica Acta, 44 (1999) 4357-4363.
[18] L. Bousselmi, C. Fiaud, B. Tribollet, E. Triki, The characterisation of the coated layer at the interface carbon steel-natural salt water by impedance spectroscopy, Corrosion Science, 39 (1997) 1711-1724.
[19] Z. Belarbi, B. Sotta, L. Makhloufi, B. Tribollet, J. Gamby, Modelling of delay effect of calcium carbonate deposition kinetics on rotating disk electrode in the presence of green inhibitor, Electrochimica Acta, 189 (2016) 118-127.
[20] M. Euvrard, F. Membrey, C. Filiatre, C. Pignolet, A. Foissy, Kinetic study of the electrocrystallization of calcium carbonate on metallic substrates, Journal of Crystal Growth, 291 (2006) 428-435.
[21] C. Deslouis, D. Festy, O. Gil, G. Rius, S. Touzain, B. Tribollet, Characterization of calcareous deposits in artificial sea water by impedance techniques — 1. Deposit of $CaCO_3$ without $Mg(OH)_2$, Electrochimica Acta, 43 (1998) 1891-1901.

[22] C. Deslouis, D. Festy, O. Gil, V. Maillot, S. Touzain, B. Tribollet, Characterization of calcareous deposits in artificial sea water by impedances techniques: 2-deposit of $Mg(OH)_2$ without $CaCO_3$, Electrochimica Acta, 45 (2000) 1837-1845.
[23] R. Jaouhari, A. Benbachir, A. Guenbour, C. Gabrielli, J. Garcia-Jareno, G. Maurin, Influence of water composition and substrate on electrochemical scaling, Journal of The Electrochemical Society, 147 (2000) 2151-2161.
[24] A. Martinod, A. Neville, M. Euvrad, K. Sorbie, Electrodeposition of a calcareous layer: Effects of green inhibitors, Chemical Engineering Science, 64 (2009) 2413-2421.
[25] C. Deslouis, P. Falaras, O. Gil, M. Jeannin, V. Maillot, B. Tribollet, Influence of clay on calcareous deposit in natural and artificial sea water, Electrochimica Acta, 51 (2006) 3173-3180.
[26] S.-H. Lin, S.C. Dexter, Effects of temperature and magnesium ions on calcareous deposition, Corrosion, 44 (1988) 615-622.
[27] J. Marin-Cruz, R. Cabrera-Sierra, M. Pech-Canul, I. Gonzalez, Characterization of different allotropic forms of calcium carbonate scales on carbon steel by electrochemical impedance spectroscopy, Journal of Applied Electrochemistry, 34 (2004) 337-343.
[28] S.M. Hoseinieh, T. Shahrabi, Influence of ionic species on scaling and corrosion performance of AISI 316L rotating disk electrodes in artificial seawater, Desalination, 409 (2017) 32-46.
[29] S.M. Hoseinieh, T. Shahrabi, B. Ramezanzadeh, M.F. Rad, The role of porosity and surface morphology of calcium carbonate deposits on the corrosion behavior of unprotected API 5L X52 rotating disk electrodes in artificial seawater, Journal of The Electrochemical Society, 163 (2016) C515-C529.
[30] B.S. Lalia, A. Khalil, R. Hashaikeh, Selective electrochemical separation and recovery of calcium and magnesium from brine, Separation and Purification Technology, 264 (2021) 118416.
[31] B.S. Lalia, R. Hashaikeh, Electrochemical precipitation to reduce waste brine salinity, Desalination, 498 (2021) 114796.
[32] Y. Lei, J.C. Remmers, M. Saakes, R.D. van der Weijden, C.J.N. Buisman, Is there a precipitation sequence in municipal wastewater induced by electrolysis?, Environmental Science & Technology, 52 (2018) 8399-8407.
[33] Y. Lei, B. Song, M. Saakes, R.D. van der Weijden, C.J.N. Buisman, Interaction of calcium, phosphorus and natural organic matter in electrochemical recovery of phosphate, Water Research, 142 (2018) 10-17.
[34] Y. Lei, I. Hidayat, M. Saakes, R. van der Weijden, C.J.N. Buisman, Fate of calcium, magnesium and inorganic carbon in electrochemical phosphorus recovery from domestic wastewater, Chemical Engineering Journal, 362 (2019) 453-459.
[35] Y. Lei, E. Geraets, M. Saakes, R.D. van der Weijden, C.J.N. Buisman, Electrochemical removal of phosphate in the presence of calcium at low current density: Precipitation or adsorption?, Water Research, 169 (2020) 115207.
[36] I. Sanjuán, D. Benavente, V. García-García, E. Expósito, V. Montiel, Electrochemical softening of concentrates from an electrodialysis brackish water desalination plant: Efficiency enhancement using a three-dimensional cathode, Separation and Purification Technology, 208 (2019) 217-226.
[37] F.H. Adnan, E. Mousset, S. Pontvianne, M.-N. Pons, Mineral cathodic electro-precipitation and its kinetic modelling in thin-film microfluidic reactor during advanced electro-oxidation process, Electrochimica Acta, (2021) 138487.
[38] C. Barchiche, C. Deslouis, D. Festy, O. Gil, P. Refait, S. Touzain, B. Tribollet, Characterization of calcareous deposits in artificial seawater by impedance techniques: 3 — deposit of $CaCO_3$ in the presence of Mg(II), Electrochimica Acta, 48 (2003) 1645-1654.
[39] M. Piri, R. Arefinia, Investigation of the hydrogen evolution phenomenon on $CaCO_3$ precipitation in artificial seawater, Desalination, 444 (2018) 142-150.
[40] H. Karoui, B. Riffault, M. Jeannin, A. Kahoul, O. Gil, M. Ben Amor, M.M. Tlili, Electrochemical scaling of stainless steel in artificial seawater: Role of experimental conditions on $CaCO_3$ and $Mg(OH)_2$ formation, Desalination, 311 (2013) 234-240.
[41] C. Gabrielli, M. Keddam, A. Khalil, R. Rosset, M. Zidoune, Study of calcium carbonate scales by electrochemical impedance spectroscopy, Electrochimica Acta, 42 (1997) 1207-1218.
[42] J.C. Eklund, A.M. Bond, J.A. Alden, R.G. Compton, Perspectives in modern voltammetry: Basic concepts and mechanistic analysis, in: D. Bethell (Ed.) Advances in Physical Organic Chemistry, Academic Press, (1999), pp. 1-120.
[43] D.J. Pickett, B.R. Stanmore, Ionic mass transfer in parallel plate electrochemical cells, Journal of Applied Electrochemistry, 2 (1972) 151-156.

[44] F. Cœuret, A. Storck, Hydrodynamique et transfert de matière par diffusion, Eléments de génie électrochimique, Lavoisier, Paris, 1993, pp. 91-128.
[45] F.H. Adnan, M.-N. Pons, E. Mousset, Mass transport evolution in microfluidic thin film electrochemical reactors: New correlations from millimetric to submillimetric interelectrode distances, Electrochemistry Communications, 130 (2021) 107097.
[46] N. Xu, J. Riley, Nonlinear analysis of a classical system: The double-layer capacitor, Electrochemistry Communications, 13 (2011) 1077-1081.
[47] A.J. Bard, Faulkner, L.R., Double-layer structure and adsorption, in: J.W.S. Inc. (Ed.) Electrochemical methods: Fundamentals and applications (2001), pp. 534.
[48] B.E. Conway, J.O.M. Bockris, I.A. Ammar, The dielectric constant of the solution in the diffuse and Helmholtz double layers at a charged interface in aqueous solution, Transactions of the Faraday Society, 47 (1951) 756-766.
[49] O. Teschke, G. Ceotto, E.F. de Souza, Interfacial water dielectric-permittivity-profile measurements using atomic force microscopy, Physical Review E, 64 (2001) 011605.
[50] M.C.F. Wander, A.E. Clark, Structural and dielectric properties of quartz−water interfaces, The Journal of Physical Chemistry C, 112 (2008) 19986-19994.
[51] M.E. Orazem, Tribollet, B., Electrochemistry, in: E.-E. Society (Ed.) Electrochemical Impedance Spectroscopy2017, pp. 122-124.
[52] P. Reichert, AQUASIM - a tool for simulation and data analysis of aquatic systems, Water Science and Technology, 30 (1994) 21.
[53] B.A. Boukamp, A linear Kronig-Kramers transform test for immittance data validation, Journal of The Electrochemical Society, 142 (1995) 1885-1894.
[54] B.A. Boukamp, Electrochemical impedance spectroscopy in solid state ionics: recent advances, Solid State Ionics, 169 (2004) 65-73.
[55] M.M. Tlili, M. Benamor, C. Gabrielli, H. Perrot, B. Tribollet, Influence of the interfacial pH on electrochemical CaCO3 precipitation, Journal of The Electrochemical Society, 150 (2003) C765.
[56] C. Deslouis, I. Frateur, G. Maurin, B. Tribollet, Interfacial pH measurement during the reduction of dissolved oxygen in a submerged impinging jet cell, Journal of Applied Electrochemistry, 27 (1997) 482-492.
[57] H. Deligianni, L.T. Romankiw, In situ surface pH measurement during electrolysis using a rotating pH electrode, IBM Journal of Research and Development, 37 (1993) 85-95.
[58] C. Carré, A. Zanibellato, M. Jeannin, R. Sabot, P. Gunkel-Grillon, A. Serres, Electrochemical calcareous deposition in seawater. A review, Environmental Chemistry Letters, 18 (2020) 1193-1208.
[59] C. Arkam, Quartz crystal electrogravimetry with controlled hydrodynamics, Journal of The Electrochemical Society, 141 (1994) L103.
[60] H. Vogt, R.J. Balzer, The bubble coverage of gas-evolving electrodes in stagnant electrolytes, Electrochimica Acta, 50 (2005) 2073-2079.
[61] X. Hu, X. Tian, Y.-W. Lin, Z. Wang, Nickel foam and stainless steel mesh as electrocatalysts for hydrogen evolution reaction, oxygen evolution reaction and overall water splitting in alkaline media, RSC Advances, 9 (2019) 31563-31571.
[62] M. Wang, W. Fu, L. Du, Y. Wei, P. Rao, L. Wei, X. Zhao, Y. Wang, S. Sun, Surface engineering by doping manganese into cobalt phosphide towards highly efficient bifunctional HER and OER electrocatalysis, Applied Surface Science, 515 (2020) 146059.
[63] E. Mousset, Y. Pechaud, N. Oturan, M.A. Oturan, Charge transfer/mass transport competition in advanced hybrid electrocatalytic wastewater treatment: Development of a new current efficiency relation, Applied Catalysis B: Environmental, 240 (2019) 102-111.
[64] O. Scialdone, C. Guarisco, A. Galia, Oxidation of organics in water in microfluidic electrochemical reactors: Theoretical model and experiments, Electrochimica Acta, 58 (2011) 463-473.
[65] P. Mandin, Z. Derhoumi, H. Roustan, W. Rolf, Bubble over-potential during two-phase alkaline water electrolysis, Electrochimica Acta, 128 (2014) 248-258.
[66] R. Hreiz, L. Abdelouahed, D. Fünfschilling, F. Lapicque, Electrogenerated bubbles induced convection in narrow vertical cells: A review, Chemical Engineering Research and Design, 100 (2015) 268-281.
[67] R. Hreiz, L. Abdelouahed, D. Fünfschilling, F. Lapicque, Electrogenerated bubbles induced convection in narrow vertical cells: PIV measurements and Euler–Lagrange CFD simulation, Chemical Engineering Science, 134 (2015) 138-152.
[68] L. Abdelouahed, G. Valentin, S. Poncin, F. Lapicque, Current density distribution and gas volume fraction in the gap of lantern blade electrodes, Chemical Engineering Research and Design, 92 (2014) 559-570.

[69] F. Hine, Bubble effects on the solution IR drop in a vertical electrolyzer under free and forced convection, Journal of The Electrochemical Society, 127 (1980) 292.
[70] F. Hine, Hydrodynamic studies of bubble effects on the IR-drops in a vertical rectangular cell, Journal of The Electrochemical Society, 122 (1975) 1185.
[71] H. Vogt, A hydrodynamic model for the ohmic interelectrode resistance of cells with vertical gas evolving electrodes, Electrochimica Acta, 26 (1981) 1311-1317.
[72] X. Chen, G. Chen, P.L. Yue, Investigation on the electrolysis voltage of electrocoagulation, Chemical Engineering Science, 57 (2002) 2449-2455.
[73] G.J. Brug, A.L.G. van den Eeden, M. Sluyters-Rehbach, J.H. Sluyters, The analysis of electrode impedances complicated by the presence of a constant phase element, Journal of Electroanalytical Chemistry and Interfacial Electrochemistry, 176 (1984) 275-295.
[74] B. Hirschorn, M.E. Orazem, B. Tribollet, V. Vivier, I. Frateur, M. Musiani, Determination of effective capacitance and film thickness from constant-phase-element parameters, Electrochimica Acta, 55 (2010) 6218-6227.
[75] M.E. Orazem, Tribollet, B., Time-constant dispersion, in: E.-E. Society (Ed.) Electrochemical Impedance Spectroscopy, John Wiley & Sons, Inc2017, pp. 349-355.
[76] X. Cao, C. Jin, F. Lu, Z. Yang, M. Shen, R. Yang, Electrochemical properties of $MnCo_2O_4$ spinel bifunctional catalyst for oxygen reduction and evolution reaction, Journal of The Electrochemical Society, 161 (2014) H296-H300.
[77] Y. Lai, Y. Li, L. Jiang, W. Xu, X. Lv, J. Li, Y. Liu, Electrochemical behaviors of co-deposited Pb/Pb–MnO_2 composite anode in sulfuric acid solution – Tafel and EIS investigations, Journal of Electroanalytical Chemistry, 671 (2012) 16-23.
[78] O. Devos, C. Gabrielli, B. Tribollet, Simultaneous EIS and in situ microscope observation on a partially blocked electrode application to scale electrodeposition, Electrochimica Acta, 51 (2006) 1413-1422.
[79] X.-M. Wang, J.-M. Hu, J.-Q. Zhang, C.-N. Cao, Characterization of surface fouling of Ti/IrO_2 electrodes in 4-chlorophenol aqueous solutions by electrochemical impedance spectroscopy, Electrochimica Acta, 53 (2008) 3386-3394.
[80] L.A. da Silva, V.A. Alves, M.A.P. da Silva, S. Trasatti, J.F.C. Boodts, Electrochemical impedance, SEM, EDX and voltammetric study of oxygen evolution on Ir + Ti + Pt ternary-oxide electrodes in alkaline solution, Electrochimica Acta, 41 (1996) 1279-1285.
[81] L.A. da Silva, V.A. Alves, M.A.P. da Silva, S. Trasatti, J.F.C. Boodts, Oxygen evolution in acid solution on IrO_2 + TiO_2 ceramic films. A study by impedance, voltammetry and SEM, Electrochimica Acta, 42 (1997) 271-281.
[82] J.-M. Hu, J.-Q. Zhang, C.-N. Cao, I.M. Hsing, Kinetics investigation of H_2/CO electrooxidation in PEFCs by the combined use of equivalent circuit fitting and mathematical modeling of the faradaic impedance, Electrochimica Acta, 49 (2004) 5227-5234.
[83] E. Rasten, G. Hagen, R. Tunold, Electrocatalysis in water electrolysis with solid polymer electrolyte, Electrochimica Acta, 48 (2003) 3945-3952.
[84] M. Urquidi-Macdonald, S. Real, D.D. Macdonald, Applications of Kramers—Kronig transforms in the analysis of electrochemical impedance data—III. Stability and linearity, Electrochimica Acta, 35 (1990) 1559-1566.
[85] M.E. Orazem, Tribollet, B., The Kramers–Kronig relations, in: E.-E. Society (Ed.) Electrochemical Impedance Spectroscopy, John Wiley & Sons, Inc2017, pp. 595-614.
[86] M.C.H. McKubre, D.D. Macdonald, B. Sayers, J.R. Macdonald, Measuring techniques and data analysis, Impedance Spectroscopy2018, pp. 124-126.
[87] R. Pachimatla, M. Thomas, S.R. Oc, R. Srinivasan, Analysis of instabilities in electrochemical systems using nonlinear electrochemical impedance spectroscopy, Journal of The Electrochemical Society, 166 (2019) H304-H312.
[88] C. Cachet, R. Wiart, Zinc electrowinning in acidic sulfate electrolytes: Impedance analysis and modeling of the influence on Nickel impurities, Journal of The Electrochemical Society, 141 (1994) 131-140.
[89] Y. Ge, X. Xie, J. Roscher, R. Holze, Q. Qu, How to measure and report the capacity of electrochemical double layers, supercapacitors, and their electrode materials, Journal of Solid State Electrochemistry, 24 (2020) 3215-3230.
[90] C. Gabrielli, Quartz crystal microbalance investigation of electrochemical calcium carbonate scaling, Journal of The Electrochemical Society, 145 (1998) 2386.
[91] R.W. Impey, P.A. Madden, I.R. McDonald, Hydration and mobility of ions in solution, The Journal of Physical Chemistry, 87 (1983) 5071-5083.

[92] C. Zhong, Y. Deng, W. Hu, J. Qiao, L. Zhang, J. Zhang, A review of electrolyte materials and compositions for electrochemical supercapacitors, Chemical Society Reviews, 44 (2015) 7484-7539.
[93] G. Bai, H.-B. Yi, H.-J. Li, J.-J. Xu, Hydration characteristics of Ca^{2+} and Mg^{2+}: a density functional theory, polarized continuum model and molecular dynamics investigation, Molecular Physics, 111 (2013) 553-568.
[94] O. Gharbi, M.T.T. Tran, B. Tribollet, M. Turmine, V. Vivier, Revisiting cyclic voltammetry and electrochemical impedance spectroscopy analysis for capacitance measurements, Electrochimica Acta, 343 (2020) 136109.
[95] A. Doroszkowski, The physical chemistry of dispersion, in: R. Lambourne, T.A. Strivens (Eds.) Paint and Surface Coatings (Second Edition), Woodhead Publishing1999, pp. 198-242.

VII. Effect of simulated and real wastewaters on the occurrence of electro-precipitation and organic pollutants degradation

VII.1. Introduction

In previous chapters, parametric and modeling studies have been carried out in the electrolyte consisting of only Ca^{2+}, Mg^{2+} and TIC (except **Chapter 5**) during electro-oxidation conducted in submillimetric and millimetric interelectrode distances. It was deliberately done for the sake of detailed mechanistic study on the electro-precipitation of $Mg(OH)_2$ and $CaCO_3$ without the interference of external parameters.

In this chapter, the influence of additional compounds is the main topic of discussion. Understanding the influence of complex matrices of electrolyte mimicking the reclaimed wastewater (RW) properties towards both the formation of several possible electro-precipitation and the removal efficiency of a representative biorecalcitrant organic pollutant is the motivation of the study. To achieve that purpose, bottom-up approach has been adopted. It started with a comparison between basic effluent (BE) (Ca^{2+}, Mg^{2+} and TIC) and intermediate effluent (IE) (Ca^{2+}, Mg^{2+}, HCO_3^-/CO_3^{2-}, NH_4^+ and $H_2PO_4^-/HPO_4^{2-}$). The potential addition of electro-precipitate that could be thermodynamically favored or not during the electro-oxidation has been identified at this stage. The study continued with further complexation of IE with the addition of multi-ion species (NO_3^-, NO_2^-, Cl^-, SO_4^{2-}, K^+ and Na^+) whose concentrations are characteristics of those detected in reclaimed municipal wastewater. At this stage, the role of these ionic species on electro-precipitation is investigated in the electrolytic system called saline effluent (SE). Further down, the influence of the presence of organic matter towards the occurrence of electro-precipitate is characterized by adding organics (peptone and meat extract) into the SE to complete the simulated wastewater (SW). Eventually, the difference in electro-precipitate formation during the electro-oxidation process of SE and RW is compared. Finally, to put the research outcome into the practical perspective, the presence of electro-precipitation on the degradation of tylosin as model micropollutant in RW at different applied currents was evaluated.

VII.2. Experimental section

In **Chapter 6**, it has been shown eventually that the formation of mineral scaling was favored under submillimetric configuration. This was attributed to the lesser degree of HER evolution as well as anodic contribution of dissolved O_2 production towards cathode reduction activity. However, the systematic study of electro-precipitation occurrence under a microfluidic setup was still pursued in this chapter because the characterization of mineral scaling occurring under such configuration has

not yet been done in complex matrices. Furthermore, more data are needed regarding the analysis on the fate of N and Cl species during an electro-oxidation process under submillimetric condition. For that purpose, a d_{elec} of 500 µm was chosen for this chapter. It corresponds to the microfluidic configuration where the least mineral scaling was observed. Undivided parallel-plate electrochemical cell with BDD as anode (50 cm^2) and stainless steel as cathode (50 cm^2) was used to perform the electro-oxidation experiments. 500 mL of the effluent to be electro-oxidized was used and the effluent was recirculated with a flow rate of 100 mL min^{-1} such as in **Chapter 6**. The applied j_{app} was 4 mA cm^{-2} throughout the series of experiment except for **Section VII.3.5** where different applied currents were intended: 0.8 and 16 mA cm^{-2} were added.

Analytical methods have been described in detail in **Chapter 3**. Cation concentrations (Mg^{2+} and Ca^{2+}, supposedly identical to Mg and Ca element) were measured using ICP-OES, anion concentrations (NO_3^-, NO_2^-, SO_4^{2-}, Cl^-, ClO_2^-, ClO_3^- and ClO_4^-) were measured using ionic chromatography. NH_4^+ was measured with HACH spectrophotometer (Nessler method, Method 8038 (0.02 – 2.50 mg L^{-1} NH_3-N)), PO_4^{3-} was quantified using PhosVer 3 method (HACH, Method 8048 (0.02 – 2.50 mg L^{-1} PO_4^{3-})) and free chlorine was dosed using DPD method (HACH, Method 8021 (0.02 – 2.00 mg L^{-1})). TOC, TN and TIC were analyzed using TOC-TN analyzer (Shimadzu). Tylosin concentration was measured by HPLC-UV (wavelength 290 nm).

The average characteristics of all systematic simulated effluents (BE, IE, SE and SW) as well as the RW used in this work are represented in **Table VII.1**. Prior to the experiment with RW, it was filtered with standard filter paper (~10 µm pore diameter) to remove suspended solids in the effluent.

Table VII.1. Average physicochemical properties of simulated and reclaimed wastewaters. Reclaimed effluent was sampled from the outlet of Reims municipal wastewater treatment plant.

Parameter / unit	Basic effluent (BE)	Intermediate effluent (IE)	Saline effluent (SE)	Simulated wastewater (SW)	Reclaimed wastewater (RW)
pH	7.47 ± 0.08	7.41 ± 0.04	7.36 ± 0.04	7.50 ± 0.07	7.57 ± 0.21
Ionic conductivity / µS cm^{-1}	1,209 ± 21	1,220 ± 14	1,660 ± 1	1,640 ± 14	1,021 ± 74
NH_4^+ / mg L^{-1}	-	1.80	1.9 ± 0.1	2.2 ± 0.1	1.6 ± 0.5
NO_3^- / mg L^{-1}	-	-	1.9	2.0 ± 0.2	2.2 ± 1.2
NO_2^- / mg L^{-1}	-	-	0.40	0.40	0.46 ± 0.4
PO_4^{3-} / mg L^{-1}	-	1.94	2.2 ± 0.1	1.8 ± 0.1	1.6 ± 0.5
SO_4^{2-} / mg L^{-1}	-	-	403 ± 2	401 ± 3	66 ± 7
Cl^- / mg L^{-1}	-	-	124 ± 2	134 ± 1	129 ± 38
Ca^{2+} / mg L^{-1}	150	155	157 ± 0.1	152 ± 3	133 ± 8
Mg^{2+} / mg L^{-1}	5	5.4	5.3 ± 0.1	5.2 ± 0.1	4.2 ± 0.5
K^+ / mg L^{-1}	-	-	17	17	17 ± 1.7
Na^+ / mg L^{-1}	-	-	75	75	76 ± 24
TIC / mg-C L^{-1}	68 ± 0.1	64 ± 1	68 ± 1	64 ± 2	68 ± 4
TN / mg-N L^{-1}	-	1.80	4.6	5.0 ± 0.6	2.1 ± 0.5
TOC / mg-C L^{-1}	-	-	-	8.2 ± 0.9	4.5 ± 0.5

VII.3. Results and discussion

VII.3.1. Electro-precipitation in electrolyte consisting of only precipitating elements

Ca^{2+}, Mg^{2+}, HCO_3^-/CO_3^{2-}, NH_4^+ and $H_2PO_4^-/HPO_4^{2-}$ could undergo electro-precipitation, either in simulated or real wastewater. Their plausible precipitations under the applied operating conditions are discussed in this section.

In slightly alkaline initial pH environment, which is the case of the present experimental conditions (pH = 7-8), bicarbonates (HCO_3^-) and hydrogenophosphate (HPO_4^{2-}) were the dominant forms of inorganic carbon and phosphorus respectively, following the value of pK_A of the acid-base couples written in **Eqs. (VII.1)-(VII.2) [1, 2]**:

$$K_{A1} = \frac{[H^+][HCO_3^-]}{[H_2CO_3]}, \text{ pK}_{A1} = 6.3 \quad \text{(VII.1)}$$

$$K_{A2} = \frac{[H^+][HPO_4^{2-}]}{[H_2PO_4^-]}, \text{ pK}_{A2} = 7.2 \quad \text{(VII.2)}$$

However, due to high local pH induced on cathode surface during electrolysis owing to the reduction reactions of dissolved O_2 and water (**Eqs. (II.9)-(II.10)**) **[3-5]**, carbonate (CO_3^{2-}) and phosphate (PO_4^{3-}) ions can instantaneously become the dominant species at cathode surface, in agreement with **Eqs. (VII.3)-(VII.4)** following their respective pK_A values **[1, 2]**.

$$K_{A3} = \frac{[H^+][CO_3^{2-}]}{[HCO_3^-]}, \text{ pK}_{A3} = 10.4 \quad \text{(VII.3)}$$

$$K_{A4} = \frac{[H^+][PO_4^{3-}]}{[HPO_4^{2-}]}, \text{ pK}_{A4} = 12.4 \quad \text{(VII.4)}$$

The evolution of concentration of ionic species during the electro-oxidation of BE and IE is given in **Fig. VII.1**. According to **Figs. VII.1(a)-VII.1(c)**, Mg^{2+} and Ca^{2+} concentrations decreased similarly regardless of the presence of PO_4^{3-} and NH_4^+ ions under our operating conditions. It indicated the formation of $Mg(OH)_2$ and $CaCO_3$ precipitates. It has been demonstrated in a previous work that $MgCO_3$ was not formed under similar experimental setup as in this present work **[5]**. Mg precipitated independently in the presence of carbonates, while a similar amount of $Mg(OH)_2$ was obtained in a system without carbonates **[5]**. This has been further confirmed by the work of Lei et al. **[6]** and these authors have also ruled out the formation of dolomite ($MgCa(CO_3)_2$) after having demonstrated that Ca and Mg precipitated independently of CO_3^{2-} in wide range of solution pH. In **Fig. VII.1(d)**, it was observed that the NH_4^+ concentration did not decrease when it was added into the electrolyte

containing Mg^{2+}, Ca^{2+}, HCO_3^-/CO_3^{2-} and $H_2PO_4^-/HPO_4^{2-}$. It allows deducing that struvite ($MgNH_4H_nPO_4^{3-n}$) precipitation were not thermodynamically favored under current conditions. This was due to the fact that 1:1:1 molar ratio of Mg^{2+} (0.21 mM):NH_4^+ (0.10 mM):PO_4^{3-} (0.015 mM) was not achieved **[7]**, across all investigated matrices. Similar behavior was documented from the work of Lei et al. **[8]**.

Next, when $H_2PO_4^-/HPO_4^{2-}$ was added into the BE, PO_4^{3-} concentration diminished (**Fig. VII.1(e)**). Since $^{\bullet}OH$ was involved in such conditions of electro-oxidation treatment, phosphate might react with $^{\bullet}OH$ to produce phosphate radicals **[9]**. To check on the stability of PO_4^{3-} ion under the electro-oxidation environment, an electrolysis of phosphate blank solution (1.9 mg-PO_4^{3-} L^{-1} with Na_2SO_4 as supporting electrolyte) was performed under comparable operating conditions as the electro-oxidation experiment. **Figure VII.1(f)** illustrates the evolution of PO_4^{3-} concentration during the 5 h electrolysis. A slight decrease of PO_4^{3-} by 13% after the electrolysis was observed. Hence, the production of phosphate radicals (**Eqs. (VII.5)-(VII.7)**) **[9]** as well as perphosphate ($P_2O_8^{4-}$) (**Eq. (VII.8)**) **[10]** might happen, but did not represent the dominant PO_4^{3-} degradation route.

$$PO_4^{3-} + {}^{\bullet}OH \rightarrow PO_4^{\bullet 2-} + OH^- \quad \text{(VII.5)}$$

$$HPO_4^{2-} + {}^{\bullet}OH \rightarrow HPO_4^{\bullet -} + OH^- \quad \text{(VII.6)}$$

$$H_2PO_4^- + {}^{\bullet}OH \rightarrow H_2PO_4^{\bullet} + OH^- \quad \text{(VII.7)}$$

$$2PO_4^{\bullet 2-} \rightarrow P_2O_8^{4-} \quad \text{(VII.8)}$$

Another reaction mechanism could occur via electro-precipitation and could explain the decay of PO_4^{3-} noticed in **Fig. VII.1(e)**. Following the trend of Mg^{2+} concentration illustrated in **Fig. VII.1(a)**, Mg precipitated indifferently with regard to the presence or absence of phosphate. This suggests that $Mg_3(PO_4)_2$ or its other hydrated forms were not produced. It is in agreement with the fact that the formation of magnesium phosphates was not thermodynamically feasible under present circumstances as proposed by Lei et al. **[8]**. Consequently, the decrease in PO_4^{3-} concentration was rather attributed to its precipitation with Ca^{2+} to form $Ca_3(PO_4)_2$. This was relevant due to the low thermodynamic solubility constant of $Ca_3(PO_4)_2$ ($K_{S,Ca_3(PO_4)_2} = 10^{-26}$ **[11]**), which is even lower than that of $CaCO_3$ ($K_{S,CaCO_3} = 10^{-9}$) and $Mg(OH)_2$ ($K_{S,Mg(OH)_2} = 10^{-12}$) **[5]**. Nonetheless, the concentration of phosphate was too low compared with carbonate to yield an impact on Ca precipitation, as illustrated in **Fig. VII.1(b)**. In the presence of phosphate, slightly more carbonate was present in the bulk (**Fig. VII.1(c)**), because small proportion of Ca^{2+} reacted with phosphate to produce $Ca_3(PO_4)_2$.

To sum up, the only feasible electro-precipitates under the present operating conditions were $Mg(OH)_2$, $CaCO_3$ and $Ca_3(PO_4)_2$. The formation of struvite, $MgCO_3$, $CaMg(CO_3)_2$ and $Mg_3(PO_4)_2$ were not favoured. In comparison with the literature, comparable electro-precipitate elements formed during an electrochemical process either in submillimetric (this section) or centimetric configuration was found **[6, 8, 12]**. This fact suggests that the anodic activity inside the micrometric reactor only contributed towards higher kinetics of mineral scaling but not on the nature of the precipitates.

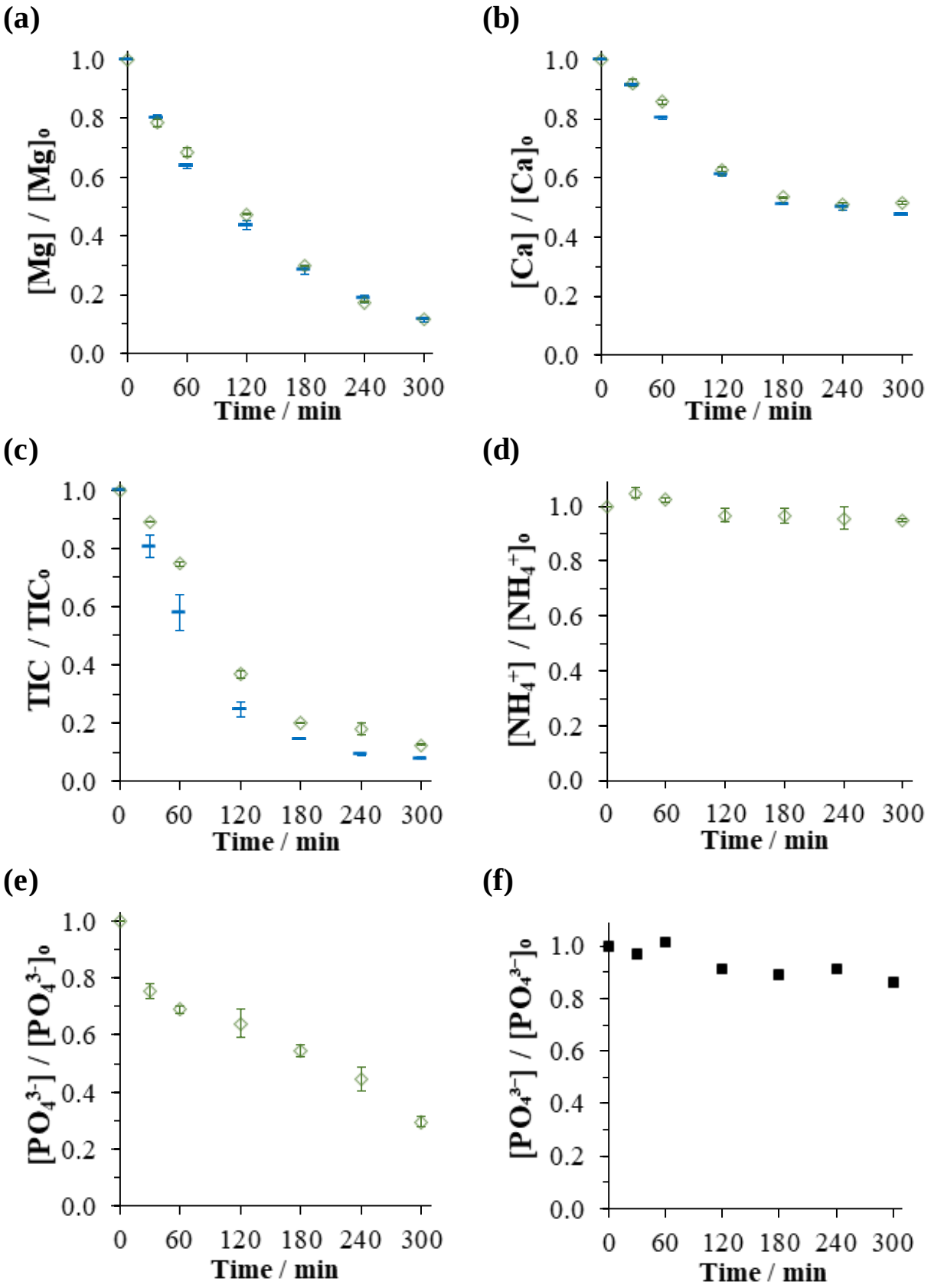

Fig. VII.1. Concentrations of **(a)** Mg^{2+}, **(b)** Ca^{2+}, **(c)** TIC, **(d)** NH_4^+ and PO_4^{3-} (**(e)**, **(f)**) during the electrolysis of (—): Ca^{2+}, Mg^{2+}, HCO_3^-/CO_3^{2-} (BE), (◇): Ca^{2+}, Mg^{2+}, HCO_3^-/CO_3^{2-}, NH_4^+, $H_2PO_4^-/HPO_4^{2-}$ (IE) and (■): PO_4^{3-} blank electrolytes. Anode: BDD, cathode: stainless steel and j_{app}: 4 mA cm^{-2}.

VII.3.2. Electro-precipitation in the presence of multi-ions representative of reclaimed wastewater

In this section, the influence of the presence of ionic species (NO_3^-, NO_2^-, SO_4^{2-}, Cl^-, K^+ and Na^+) jointly present in RW in addition to those investigated in **Section VII.3.1** (i.e., Ca^{2+}, Mg^{2+}, HCO_3^-/CO_3^{2-}, NH_4^+, $H_2PO_4^-$/HPO_4^{2-} in IE) have been scrutinized. The added multi-ions do not form direct precipitations with the deposits possibly formed in the system but they could play indirect role towards the occurrence of electro-precipitation.

From **Fig. VII.2**, it can be observed that the addition of other ionic species into the IE did not result in significant difference under the applied conditions. From **Figs. VII.2(a)-VII.2(d)**, Mg^{2+}, Ca^{2+}, TIC and PO_4^{3-} precipitated by 88.2 ± 0.3, 48.5 ± 1.2, 87.5 ± 0.6 and 70.4 ± 4.1% respectively in IE compared to 90.6, 51.0 ± 0.4, 89.9 ± 0.1 and 72.3 ± 6.4% in SE. In addition, NO_3^- concentration decreased from 1.9 mg L^{-1} to 1 mg L^{-1} after 1 h of electrolysis and it remained constant until the end of the process. The decrease suggested that the reduction of NO_3^- to NO_2^-, NH_4^+ and N_2 (**Eqs. (VII.9)-(VII.11)**) **[13-16]** was more dominant relatively to its production (**Eqs. (VII.12)-(VII.14)**) **[13-16]**.

$$NO_3^- + 10H^+ + 8e^- \rightarrow NH_4^+ + 3H_2O \qquad E^0 = -0.12\ V/SHE \qquad (VII.9)$$

$$NO_3^- + 6H^+ + 5e^- \rightarrow \frac{1}{2}N_2 + 3H_2O \qquad E^0 = 1.17\ V/SHE \qquad (VII.10)$$

$$NO_3^- + 2H^+ + 2e^- \rightarrow NO_2^- + H_2O \qquad E^0 = 0.01\ V/SHE \qquad (VII.11)$$

$$NO_2^- + H_2O \rightarrow NO_3^- + 2H^+ + 2e^- \qquad (VII.12)$$

$$NH_4^+ + 3H_2O \rightarrow NO_3^- + 10H^+ + 8e^- \qquad (VII.13)$$

$$\frac{1}{2}N_2 + 3H_2O \rightarrow NO_3^- + 6H^+ + 5e^- \qquad (VII.14)$$

Furthermore, under anodic oxidation conditions, the physisorbed $^{\bullet}OH$ could also play its role via **Eqs. (VII.15)-(VII.17) [14]**:

$$NH_4^+ + {}^{\bullet}OH + 3H_2O \leftrightarrow NO_3^- + 10H^+ + 8e^- \qquad (VII.15)$$

$$NO_2^- + {}^{\bullet}OH + H_2O \leftrightarrow NO_3^- + 2H^+ + 2e^- \qquad (VII.16)$$

$$NH_4^+ + 3{}^{\bullet}OH + OH^- \leftrightarrow \frac{1}{2}N_2 + 4H_2O + 3e^- \qquad (VII.17)$$

Nonetheless, the reduction of NO_3^- was not complete since it remained about 55% in the effluent. It means an equilibrium was reached between its rate of consumption and production.

NO_2^- initially present (0.40 mg L^{-1}) was not detected over the course of electrolysis. It suggests that **Eqs. (VII.12)**, **(VII.16)**, **(VII.18)** and **(VII.19)** were faster **[14, 17]** than **Eqs. (VII.11)**, **(VII.20)** and **(VII.21)**, which resulted in non-accumulation of it in the bulk. Furthermore, NO_2^- was initially relatively lower than NO_3^- in the bulk.

$$NO_2^- + 4H^+ + 3e^- \rightarrow \frac{1}{2}N_2 + 2H_2O \quad \text{(VII.18)}$$

$$NO_2^- + 8H^+ + 6e^- \rightarrow NH_4^+ + 3H_2O \quad \text{(VII.19)}$$

$$\frac{1}{2}N_2 + 2H_2O \rightarrow NO_2^- + 4H^+ + 3e^- \quad \text{(VII.20)}$$

$$NH_4^+ + 3H_2O \rightarrow NO_2^- + 8H^+ + 6e^- \quad \text{(VII.21)}$$

In IE, the concentration of NH_4^+ decreased negligibly (5.0 $\pm$ 0.9%) (**Fig. VII.2(e)**). Hence the reduction of NH_4^+ into NO_3^- (**Eqs. (VII.13)** and **(VII.15)**), into NO_2^- (**Eq. (VII.21)**) as well as direct oxidation of NH_4^+ into N_2 (**Eqs. (VII.17)** and **(VII.22)**) were insignificant under our investigated conditions.

$$NH_4^+ \rightarrow \frac{1}{2}N_2 + 4H^+ + 3e^- \quad \text{(VII.22)}$$

The slight NH_4^+ increase in the first hour of electrolysis could be ascribed to NO_3^- reduction (**Eq. (VII.9)**).

Contrastingly, the evolution of NH_4^+ concentration changed dramatically in multi-ions electrolyte (SE), as can be reckoned from **Fig. VII.2(e)**, where 99.0 $\pm$ 4.8% NH_4^+ was removed. This quasi-complete removal of NH_4^+ was associated with the presence of Cl^-: there was a fast reaction between NH_4^+ with HClO producing inorganic chloramines **[15, 17-21]** as listed in **Eqs. (VII.23)-(VII.29)**.

$$2Cl^- \rightarrow Cl_2 + 2e^- \qquad E^0 = 1.36\ V/SHE \qquad (VII.23)$$

$$Cl_2 + H_2O \rightarrow HClO + H^+ + Cl^- \qquad (VII.24)$$

$$\frac{1}{2}Cl_2 + H_2O \rightarrow HClO + H^+ + e^- \qquad E^0 = 1.61\ V/SHE \qquad (VII.25)$$

$$HClO + NH_4^+ \rightarrow NH_2Cl + H_2O + H^+ \qquad (VII.26)$$

$$NH_2Cl + HClO \rightarrow NHCl_2 + H_2O \qquad (VII.27)$$

$$NH_2Cl + HClO \rightarrow NCl_3 + H_2O \qquad (VII.28)$$

$$NH_2Cl + H^+ \rightarrow HClO + NH_4^+ \qquad (VII.29)$$

This deduction can be justified by the oxidation of Cl^- to Cl_2 (**Eq. (VII.23)**) and fast conversion of Cl_2 to hypochloric acid (HClO) (**Eqs. (VII.24)-(VII.25)**), which led to the decrease of Cl^- concentration in **Fig. VII.3(a)** and increasing trend of HClO in **Fig. VII.3(b)**. The quick conversion from Cl^- into Cl_2 and HClO was relevant given higher applied anode potential (E_A = 2.40 V/Ag-AgCl or 2.60 V/SHE) relatively to $E^0_{Cl_2/Cl^-}$ (1.36 V/SHE) (**Eq. (VII.23)**) and E^0_{HClO/Cl_2} (1.61 V/SHE) (**Eq. (VII.25)**). HClO further reacted with NH_4^+ producing $NHCl_2$, NH_2Cl and NCl_3 (**Eqs. (VII.26)-(VII.28)**). Moreover, NH_4^+ reacted with HClO not only to form inorganic chloramines, but also to generate NO_3^- and N_2 as shown in **Eqs. (VII.30)-(VII.31)**.

$$NH_4^+ + 4HClO \rightarrow NO_3^- + H_2O + 6H^+ + 4Cl^- \qquad (VII.30)$$

$$2NH_4^+ + 3HClO \rightarrow N_2 + 3H_2O + 5H^+ + 3Cl^- \qquad (VII.31)$$

In excess of chlorides with respect to molar ratio of NH_4^+ ($Cl^-/NH_4^+ > 7.6$), the so-called break point can be reached. In our condition, the ratio $N_{Cl^-}/N_{NH_4^+}$ was higher than 25, so the produced inorganic chloramines in effluent bulk could be further oxidized to form gaseous N_2 and nitrogen oxides (NO_X) (**Eqs. (VII.32)-(VII.33)**) **[18, 19]**. The group of N_2 and NO_X has been called volatile N (N-volatile) **[13, 22]**. The formation of N-volatile while treating N-species in multi-ions electrolyte was confirmed by the drop of TN concentration in **Fig. VII.2(f)**.

$$4NH_2Cl + 3Cl_2 + H_2O \rightarrow N_2 + N_2O + 10HCl \quad \text{(VII.32)}$$

$$NH_2Cl + NHCl_2 \rightarrow N_2 + 3HCl \quad \text{(VII.33)}$$

$$NH_2Cl + NHCl_2 + HClO \rightarrow N_2O + 4HCl \quad \text{(VII.34)}$$

$$2NH_2Cl + HClO \rightarrow N_2O + 3HCl \quad \text{(VII.35)}$$

The intermediary behavior of the production of HClO was not only due to the reactions with N-species, but also to its conversion back into Cl_2 (**Eq. (VII.36)**). Furthermore, its direct reaction into chlorate (ClO_3^-) (**Eqs. (VII.37)-(VII.39)**) **[10, 17]** as well as by intermediary of chlorite (ClO_2^-) (**Eqs. (VII.40)-(VII.41)**) **[10]** have commonly been documented. This was proven by the increasing concentration of ClO_3^- over the course of electrolysis depicted in **Fig. VII.3(c)**. Not only was the chemical conversion of HClO to ClO_3^- quick (**Eqs. (VII.38)-(VII.39)**), its standard potential of reduction is also low E^0_{HClO/ClO_3^-} (0.46 V/SHE) (**Eq. (VII.37)**). The conversion to ClO_3^- in presence of HClO was highly favorable.

$$HClO + H^+ + e^- \rightarrow \frac{1}{2}Cl_2 + H_2O \quad \text{(VII.36)}$$

$$6HClO + 3H_2O \rightarrow 2ClO_3^- + 4Cl^- + \frac{3}{2}O_2 + 12H^+ + 6e^- \quad E^0 = 0.46 \text{ V/SHE} \quad \text{(VII.37)}$$

$$HClO + 2ClO_2 + H_2O \rightarrow 2ClO_3^- + HCl + 2H^+ \quad \text{(VII.38)}$$

$$HClO \rightarrow ClO_3^- + HCl + Cl^- \quad \text{(VII.39)}$$

$$HClO + H_2O \rightarrow ClO_2^- + 3H^+ + 2e^- \quad \text{(VII.40)}$$

$$ClO_2^- + 2H_2O \rightarrow ClO_3^- + 2H^+ + 2e^- \quad E^0 = 0.33 \text{ V/SHE} \quad \text{(VII.41)}$$

Furthermore, ClO_3^- can also be produced directly from Cl^- and Cl_2 as shown in **Eqs. (VII.42)-(VII.44)** **[10]**. The applied E_A (2.60 V/SHE) was relatively larger than both the $E^0_{Cl_2/ClO_3^-}$ (1.45 V/SHE) (**Eq. (VII.42)**) and E^0_{HClO/ClO_3^-} (1.47 V/SHE) (**Eq. (VII.43)**).

$$Cl^- + 3H_2O \rightarrow ClO_3^- + 6H^+ + 6e^- \quad E^0 = 1.45 \text{ V/SHE} \quad \text{(VII.42)}$$

$$\frac{1}{2}Cl_2 + 3H_2O \rightarrow ClO_3^- + 6H^+ + 5e^- \quad E^0 = 1.47 \text{ V/SHE} \quad \text{(VII.43)}$$

$$3Cl_2 + 3H_2O \rightarrow ClO_3^- + 5Cl^- + 6H^+ \quad \text{(VII.44)}$$

Perchlorates (ClO_4^-) were also produced in the treated effluent as can be observed in **Fig. VII.3(d)**. The generation of ClO_4^- has been well documented when BDD was used as anode **[16, 23, 24]**. The

oxidation of ClO_3^- led to ClO_4^- as written in **Eq. (VII.45)**. This conversion was thermodynamically favorable given by the value of $E^0_{ClO_4^-/ClO_3^-}$ (1.20 V/SHE) which was lower than the applied E_A (2.60 V/SHE). This explains progressively slower production rate of ClO_3^- (**Fig. VII.3(c)**) as a function of electrolysis time, in contrast with the increasing production rate of ClO_4^- (**Fig. VII.3(d)**).

$$ClO_3^- + H_2O \rightarrow ClO_4^- + 2H^+ + 2e^- \qquad E^0 = 1.20 \text{ V/SHE} \qquad \text{(VII.45)}$$

The accumulation of ClO_3^- and ClO_4^- indicated that their decomposition rates corresponding to **Eqs. (VII.46)-(VII.50)** were much slower in comparison to their production rate.

$$ClO_3^- + 5Cl^- + 6H^+ \rightarrow 3Cl_2 + 3H_2O \qquad \text{(VII.46)}$$

$$ClO_3^- + 6H^+ + 5e^- \rightarrow \frac{1}{2}Cl_2 + 3H_2O \qquad \text{(VII.47)}$$

$$ClO_3^- + 2H^+ + 2e^- \rightarrow ClO_2^- + 3H_2O \qquad \text{(VII.48)}$$

$$2ClO_3^- + 4Cl^- + \frac{3}{2}O_2 + 12H^+ + 6e^- \rightarrow 6HClO + 3H_2O \qquad \text{(VII.49)}$$

$$ClO_3^- + 6H^+ + 6e^- \rightarrow Cl^- + 3H_2O \qquad \text{(VII.50)}$$

The accumulation of ClO_2^- remained below the detection limit throughout the electrolysis owing to its fast oxidation rate to ClO_3^- (**Eq. (VII.41)**) and reduction to HClO (**Eq. (VII.51)**) **[10, 16]**.

$$ClO_2^- + 3H^+ + 2e^- \rightarrow HClO + H_2O \qquad \text{(VII.51)}$$

In addition, the decrease of Cl^- (**Fig. VII.3(a)**) was partly due to the concurrent conversion towards volatile Cl (Cl-volatile), which is ascribed as Cl_2, ClO_2 and Cl_2O following **Eqs. (VII.52)-(VII.59) [10, 25]**:

$Cl^- + 2H_2O \rightarrow ClO_2 + 4H^+ + 5e^-$ E^0 = 1.60 V/SHE (VII.52)

$Cl_2 + 4H_2O \rightarrow 2ClO_2 + 8e^-$ E^0 = 1.54 V/SHE (VII.53)

$\frac{1}{2}Cl_2 + 2H_2O \rightarrow HClO_2 + 3H^+ + 3e^-$ E^0 = 1.63 V/SHE (VII.54)

$2Cl^- + H_2O \rightarrow Cl_2O + 2H^+ + 4e^-$ (VII.55)

$HClO + H_2O \rightarrow HClO_2 + 2H^+ + 2e^-$ E^0 = 1.68 V/SHE (VII.56)

$HClO_2 \rightarrow ClO_2 + H^+ + e^-$ E^0 = 1.28 V/SHE (VII.57)

$ClO_3^- + H_2O + e^- \rightarrow ClO_2 + 2OH^-$ E^0 = 1.17 V/SHE (VII.58)

$ClO_2^- \rightarrow ClO_2 + e^-$ E^0 = 0.95 V/SHE (VII.59)

Their occurrence was electrochemically feasible since the applied E_A (2.60 V/SHE) was superior to all redox couples of Cl-volatile species listed in **Eqs. (VII.52)-(VII.59)**.

Moreover, as it was the case with N-species, Cl-species that diffused close to BDD surface would react with $^{\bullet}$OH (**Eqs. (VII.60)-(VII.68)**) **[10, 19]**:

$HClO + {}^{\bullet}OH \rightarrow {}^{\bullet}ClO + H_2O$ (VII.60)

${}^{\bullet}ClO + {}^{\bullet}OH \rightarrow ClO_2^- + H^+$ (VII.61)

$ClO_2^- + {}^{\bullet}OH \rightarrow {}^{\bullet}ClO_2$ (VII.62)

${}^{\bullet}ClO_2 + {}^{\bullet}OH \rightarrow ClO_3^- + H^+$ (VII.63)

$H_2O \rightarrow {}^{\bullet}OH + H^+ + e^-$ (VII.64)

$Cl^- + {}^{\bullet}OH \rightarrow ClO^- + HClO$ (VII.65)

$ClO^- + {}^{\bullet}OH \rightarrow ClO_2^- + H^+ + e^-$ (VII.66)

$ClO_2^- + {}^{\bullet}OH \rightarrow ClO_3^- + H^+ + e^-$ (VII.67)

$ClO_3^- + {}^{\bullet}OH \rightarrow ClO_4^- + H^+ + e^-$ (VII.68)

SO_4^{2-} concentrations during the electrolysis of IE as well as SW and RW are plotted in **Fig. VII.3(e)**. They remained constant throughout the process. This proved that negligible amount of SO_4^{2-} was decomposed to peroxodisulfate ($S_2O_8^{2-}$) and sulfate radical ($SO_4^{\bullet-}$) according to **Eqs. (VII.69)-(VII.71) [5, 26, 27]** under all investigated conditions throughout this chapter.

$$2SO_4^{2-} \rightarrow S_2O_8^{2-} + 2e^- \quad \text{(VII.69)}$$

$$\bullet OH + 2SO_4^{2-} \rightarrow SO_4^{\bullet -} + OH^- \quad \text{(VII.70)}$$

$$SO_4^{\bullet -} + SO_4^{\bullet -} \rightarrow S_2O_8^{2-} \quad \text{(VII.71)}$$

To summarize, the presence of multi-ions whose concentrations were representative to those present in RW yielded insignificant influence towards the quantity of $Mg(OH)_2$, $CaCO_3$ and $Ca_3(PO_4)_2$ precipitations under simulated environment. However, the fate of other inorganic species during the electro-oxidation process could be followed. A mechanistic scheme involving the interrelation of the proposed half-equations of N and Cl species together with their reactions with $^{\bullet}$OH has been proposed in **Fig. VII.4**. In the absence of Cl^-, the oxidation of NH_4^+ into NO_3^- and N-volatile was inefficient since 95% of NH_4^+ (1.7 mg-NH_4^+ L^{-1}) remained in the electrolyte. It suggested that the physisorbed $^{\bullet}$OH was not effective to oxidize NH_4^+. In the presence of Cl^-, mediated oxidant HClO played central role towards the degradation of NH_4^+ principally into dissolved chloramines as well as N-volatile. The interrelation of reduction and oxidation reactions involving radicals yielded ClO_3^- and ClO_4^- as principal chlorinated byproducts. Despite the presence of Cl^-, intricate redox reactions including radical activities of N species only resulted in partial reduction of NO_3^- into NH_4^+ and N-volatile. Total denitrification did not occur in the present experimented reactor design since it remained 55% of NO_3^- (i.e., 1 mg-NO_3^- L^{-1}) in the treated media.

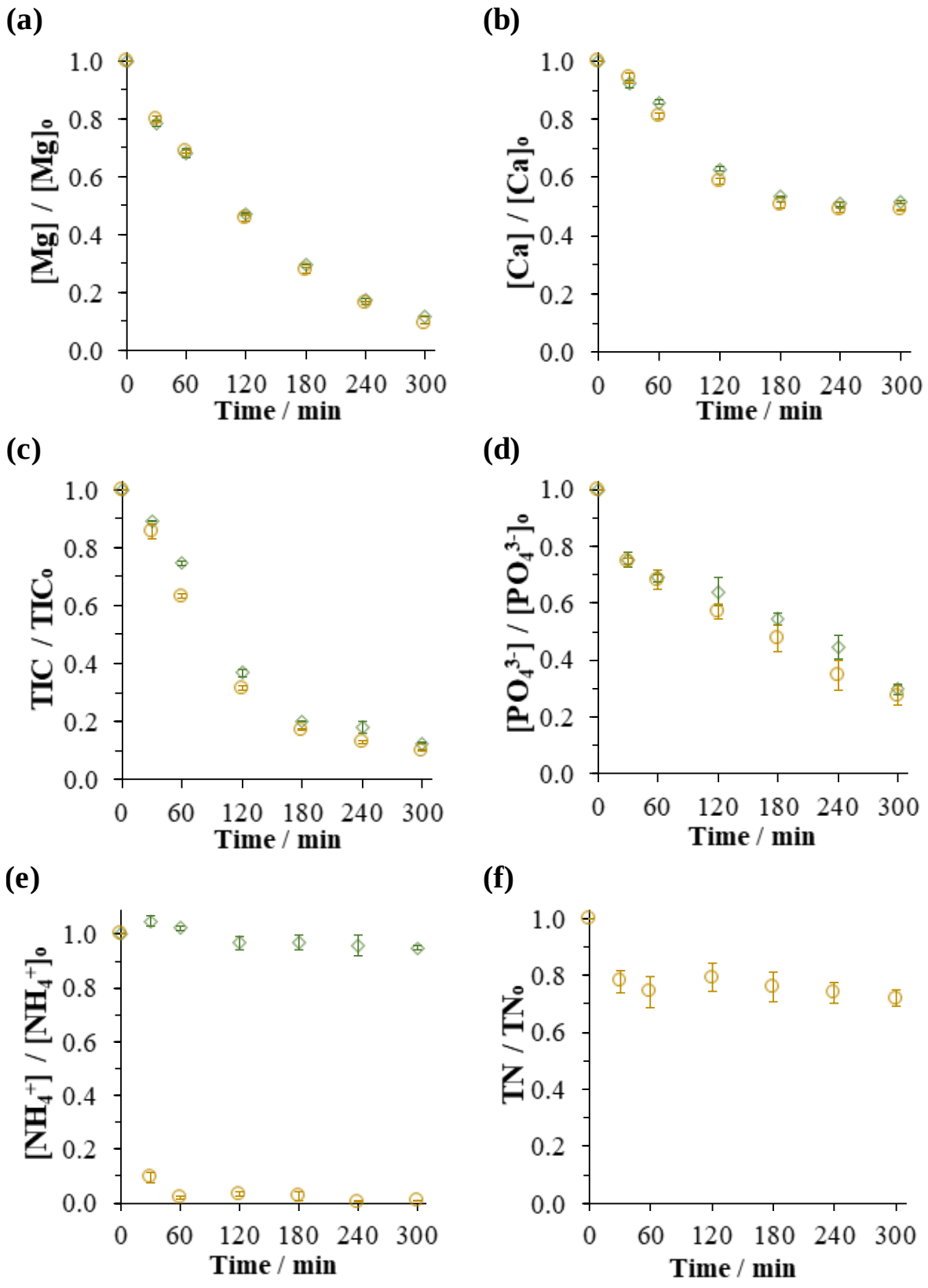

Fig. VII.2. Concentrations of **(a)** Mg^{2+}, **(b)** Ca^{2+}, **(c)** TIC, **(d)** PO_4^{3-}, **(e)** NH_4^+ and **(f)** TN during the electrolysis of (◇): Ca^{2+}, Mg^{2+}, HCO_3^-/CO_3^{2-}, NH_4^+, $H_2PO_4^-/HPO_4^{2-}$ (IE) and (○): SE (without organics) electrolytes. Anode: BDD, cathode: stainless steel and j_{app}: 4 mA cm^{-2}.

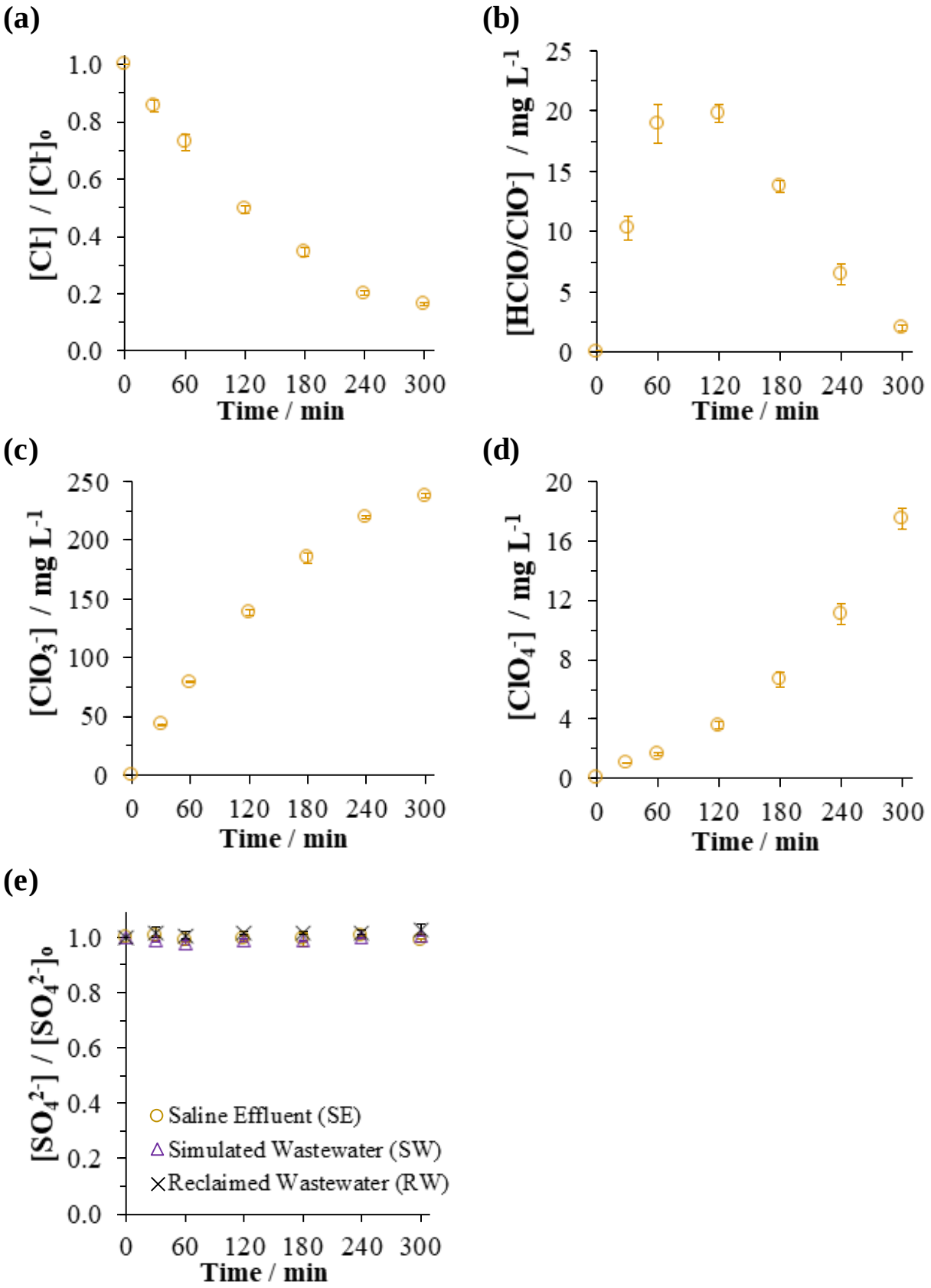

Fig. VII.3. Concentrations of **(a)** Cl^-, **(b)** $HClO/ClO^-$, **(c)** ClO_3^-, **(d)** ClO_4^- and **(e)** SO_4^{2-} during the electrolysis of SE. Anode: BDD, cathode: stainless steel and j_{app}: 4 mA cm^{-2}.

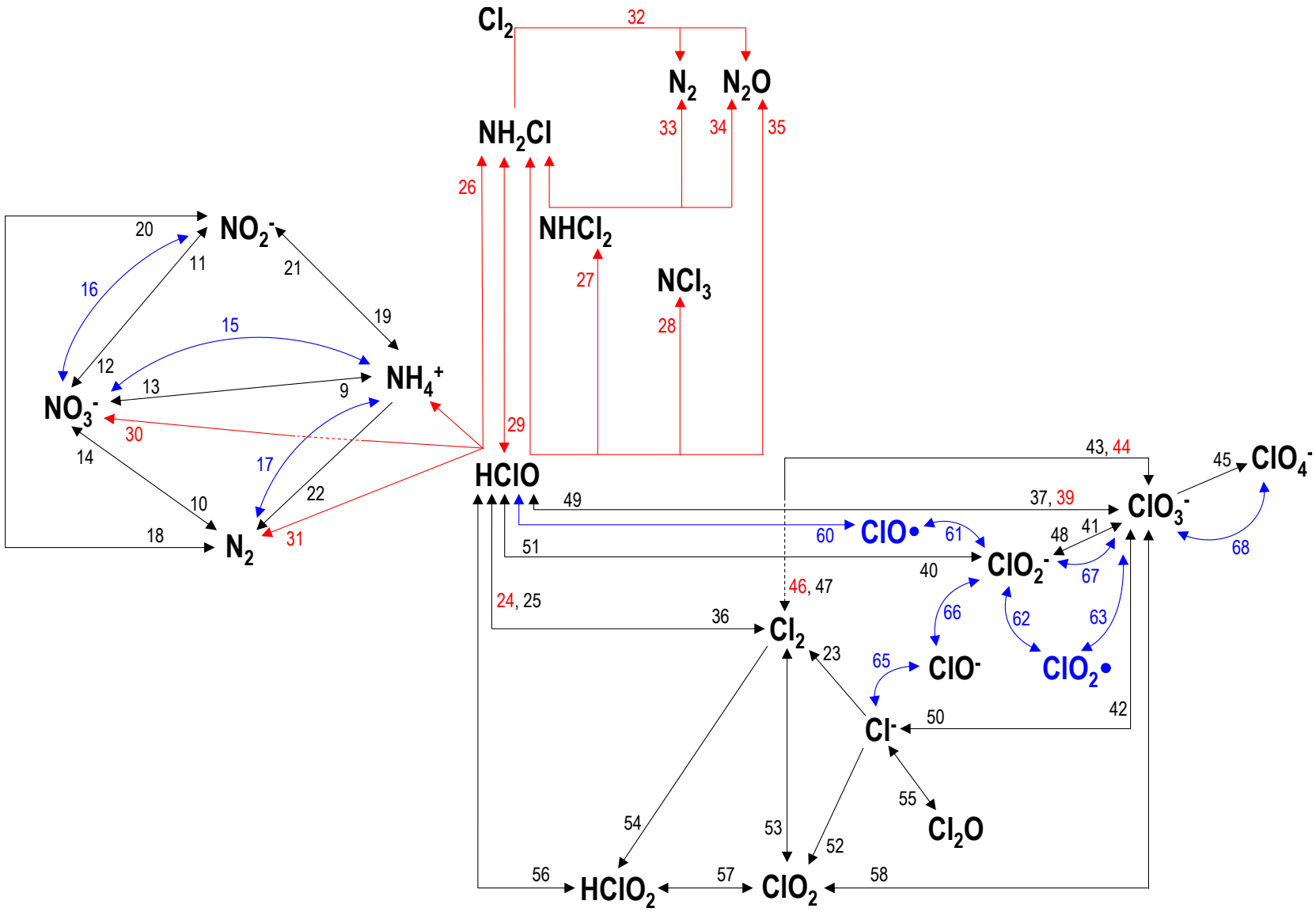

Fig. VII.4. Mechanistic scheme of the evolution of N and Cl species during the electro-oxidation process. The numbers are referred to the equations cited in the text. **Black**: direct electron transfer, **blue**: reactions involving radicals and **red**: chemical reactions and/or hydrolysis.

VII.3.3. Electro-precipitation in the presence of organic matter in simulated wastewater

The organic content of RW was simulated by adding 32 mg L^{-1} of peptone and 22 mg L^{-1} of meat extract following the procedure carried out elsewhere **[28, 29]**. The difference in the evolution of ionic and organic species during an electro-oxidation process of simulated electrolyte in the absence and presence of organics can be found in **Figs. VII.5** and **VII.6**. In overall, by adding organic matter into the simulated inorganic effluent, no significant effect on the occurrence of electro-precipitation was observed under these applied conditions. The difference between the precipitation of Mg, Ca, TIC and PO_4^{3-} in **Figs. VII.5(a)-VII.5(d)** was only about 0.5, 1.3, 0.2 and 4.8 % respectively. This trend could be due to high local pH **[5]** at the proximity of cathode that could lift the inhibitory effect of organics including humic acids **[30, 31]**. Our results corroborated with those documented by Lei et al. in which they did not observe any inhibiting effect of humic acids on calcium phosphate deposition under macro-reactor **[12, 32]**. At an appropriate humic acid concentration, it rather formed complexes with calcium and phosphate to favor calcium phosphate precipitation **[12, 32]**. **Figure VII.5(e)** depicts the evolution of NO_3^- during the electro-oxidation of SE and SW. It can be noticed that less NO_3^- was reduced to NH_4^+ under current applied conditions. This observation could be attributed to the presence of organics in the electrolyte. Due to competition for electronic exchanges, less NO_3^- was converted to NH_4^+. From **Fig. VII.5(f)**, NH_4^+ concentration was observed to already disappear after 0.5 h of electrolysis. As discussed in **Section VII.3.2**, in the presence of excess Cl^- in the effluent, NH_4^+ instantaneously reacted with mediated chlorinated oxidants to yield chloramines, N_2 and NO_2 (**Eqs. (VII.26)-(VII.35)**). Furthermore, in the presence of organics, organochloride species might as well be produced as a result of reactions between organics with mediated oxidants and $^{\bullet}OH$ **[22, 33]**. The evolution of TOC plotted in **Fig. VII.6(a)** could support the aforementioned reasoning whereby the TOC dropped by about 14% during the electro-oxidation treatment. In conjunction with the decrease of organic content (**Fig. VII.6(a)**), the concentration of Cl^- decreased more in the simulated effluent containing organics compared to the one without organics. This suggested that there was an additional consumption of Cl-mediated oxidants in the presence of organic matter. The hypothesis could be further affirmed by the plot of $HClO/ClO^-$ in **Fig. VII.6(c)**. The $HClO/ClO^-$ concentration was lower in the system containing organics as a consequence of its reaction with not only NH_4^+ but additionally organic matter. Eventually, slightly less Cl^-, ClO^- and ClO_2^- were available for their conversion towards ClO_3^- and ClO_4^-, which explained lower ClO_3^- and ClO_4^- transformation depicted in **Figs. VII.6(d)** and **VII.6(e)**.

To conclude, the presence of organics contributed to trivial difference in the occurrence of electro-precipitation during the electro-oxidation treatment of simulated effluent. It has been shown here that the inhibition of cathodic deposition by organics was not present due to high local pH. Comparable results have been obtained under both microfluidic and macrometric setups.

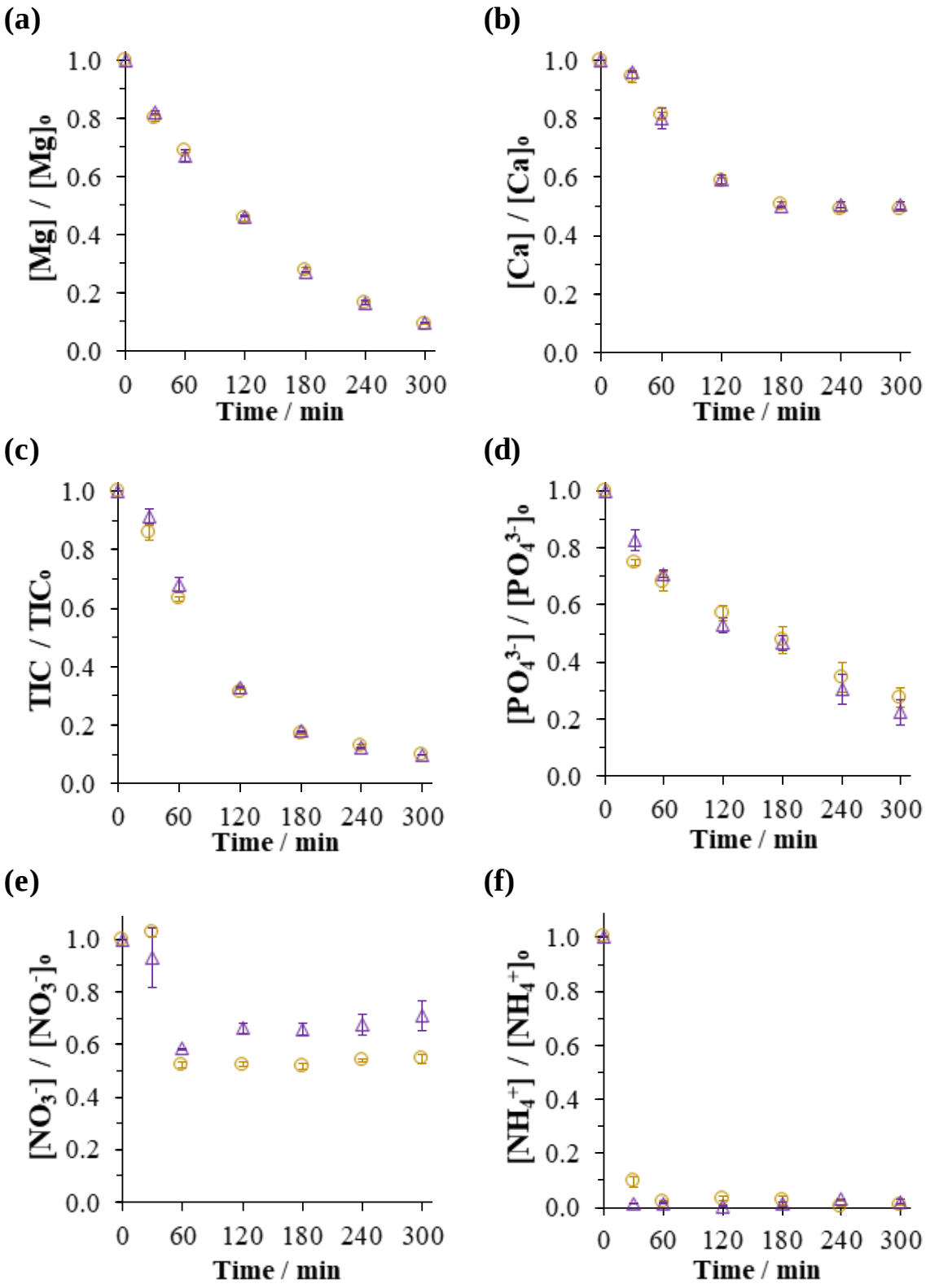

Fig. VII.5. Concentrations of **(a)** Mg^{2+}, **(b)** Ca^{2+}, **(c)** TIC, **(d)** PO_4^{3-}, **(e)** NH_4^+ and **(f)** NO_3^- during the electrolysis of (○): SE and (△): SW. Anode: BDD, cathode: stainless steel and j_{app}: 4 mA cm^{-2}.

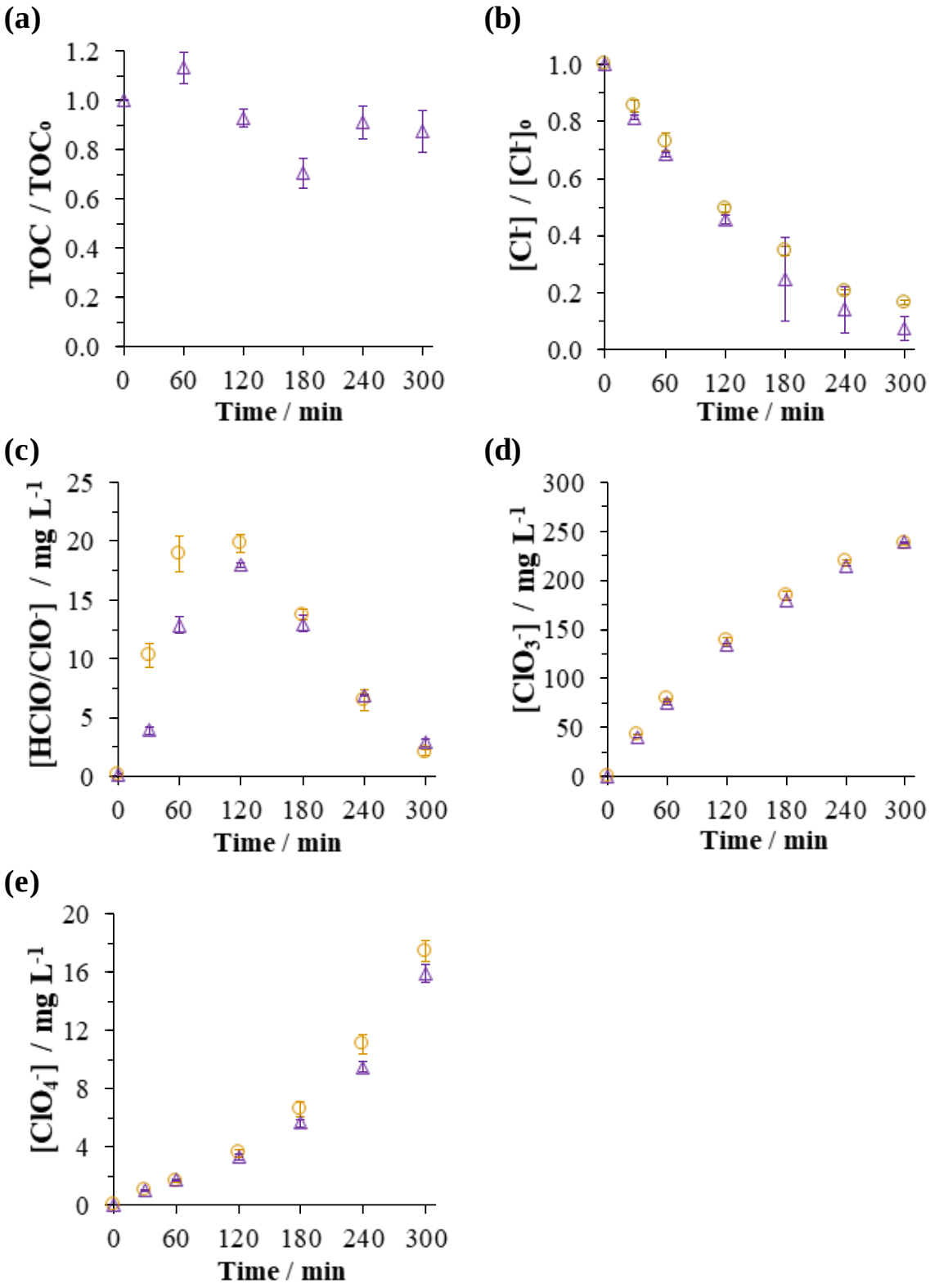

Fig. VII.6. Concentrations of **(a)** TOC, **(b)** Cl^-, **(c)** $HClO/ClO^-$, **(d)** ClO_3^- and **(e)** ClO_4^- during the electrolysis of (○): SE and (△): SW. Anode: BDD, cathode: stainless steel and j_{app}: 4 mA cm^{-2}.

VII.3.4. Electro-precipitation in simulated versus reclaimed wastewater effluent

The formation of electro-precipitates during the electro-oxidation of simulated and real effluent is compared in **Fig. VII.7**. It can be noticed from **Figs. VII.7(a)** and **VII.7(b)** that more precipitation of Mg and Ca were obtained in the matrix of real effluent in comparison with the simulated counterpart. Mg and Ca precipitated by 92.7 ± 3.1% and 70.0 ± 0.4% respectively in real effluent, whilst they precipitated by 90.1 ± 0.1% and 49.7 ± 2.7% in simulated effluent respectively. Two possible reasons could be given to justify the observed trend. Firstly, though best effort has been done to achieve close characteristics in overall aspects between both effluents (**Table VII.1**), there could have been in reality more organic substances that could co-precipitate with Mg^{2+} and/or Ca^{2+} on electrode surfaces which would reduce the cations in the bulk. **Fig. VII.8** illustrates the fluorescence spectra of both the simulated and real RW. It clearly shows a significant fluorescence response with RW, from 290 to 360 nm excitation wavelength bands (raw intensity of 424 to 352), in comparison to the response given by SW with low intensity peaks of 43 and 61 at 285 and 359 nm, respectively. Higher fluorescence response in RW was due to its higher fluorophore contents, which should be composed of several combined aromatic and/or cyclic groups with π-bonds. These are the characteristics of colloidal and dissolved organic matter in the RW which are recalcitrant since they are the residue in the effluent of WWTPs **[34]**. This proved that RW effluent contained more complex matrices of dissolved organics compared to the simulated effluent. They could form complexes with Ca^{2+} and/or Mg^{2+} at the proximity of electrodes or even undergo co-precipitation with Ca and Mg on cathode surface, as suggested by other authors **[12, 32, 35]**. Secondly, there was about six-time higher concentration of SO_4^{2-} between the simulated and real wastewater effluent. Higher SO_4^{2-} content in the SW was unavoidable, since it was the counter ion of several salts used to prepare the effluent including the sulfuric acid to slightly adjust effluent pH to a comparable value. SO_4^{2-} was selected since it was inactive with regards to anodic decomposition in the applied current condition as well as to the precipitating reactions of electrodeposition (**Section VII.3.2** and **Reference [5]**). Nonetheless, the excess presence of SO_4^{2-} might result in a passive inhibiting effect towards the formation of electro-precipitation as demonstrated in literature. Some authors who found similar finding suggested that the impedance of $CaCO_3$ growth occurred due to: (1) lower cathodic local pH which comes with increasing SO_4^{2-} concentration **[36, 37]**, (2) adsorption/incorporation of SO_4^{2-} on $CaCO_3$ crystals **[38]** or (3) higher solubility of $CaCO_3$ in the presence of SO_4^{2-} **[39, 40]**.

Then, as the Ca^{2+} precipitated more in the real effluent, it would correspondingly be expected that more TIC in the bulk decreased. However, it was not the case according to the evolution of bulk TIC depicted in **Fig. VII.7(c)**. Surely, more $CaCO_3$ was formed on cathode given relatively lower concentration of PO_4^{3-} versus TIC (1.6 mg-PO_4^{3-} L^{-1} vs. 68 mg-C L^{-1}) in the effluent. Consequently,

the precipitation of phosphate only took a small portion of free Ca^{2+}. Lower TIC in the bulk could then be explained by higher buffering capacity in the real effluent compared to simulated effluent. It can be justified by the evolution of bulk pH provided in **Fig. VII.7(d)**. The trend of PO_4^{3-} evolution is plotted in **Fig. VII.7(e)** and it corroborated with the higher Ca precipitation which led to higher precipitation with phosphate. Then, according to **Fig. VII.7(f)**, it can be seen that higher mineralization occurred in real matrix effluent as compared to the simulated effluent (28.3% vs. 14.4%), which indicated that more organic compound was degraded in the former.

Figure VII.9 presents the percentage of distributions of N species and Cl species during the electro-oxidation of simulated and real effluent experiments. The evolutions of NO_3^- and NH_4^+ species observed previously remained valid; in both effluents, there was a slight decrease in NO_3^- before it remained practically constant till the end of electrolysis. NH_4^+ concentration decreased abruptly from the beginning of electrolysis using both effluents, also following the trend deduced in previous sections. N-volatile (i.e. N_2 and NO_X) was calculated from mass balance between initial TN and the evolved TN during electrolysis. From **Figs. VII.9(a)** and **VII.9(b)**, it is interesting to note that more N-volatile was produced while treating simulated effluent (34%) relatively to N-volatile generated from real effluent (< 2%). Contrastingly, the N-combined, which regroups inorganic chloramine and organochloride species, was found to be higher in real effluent (87%) than in simulated effluent (57%). It could be therefore concluded that in both simulated and real effluents, the byproduct of N-species after 5 h electro-oxidation treatment consisted of inorganic chloramines and organochloride compound, but with high N-volatile produced in simulated in comparison to the real effluent. The discussion on the distribution percentage of Cl-species would help to conclude on this trend.

Figures VII.9(c) and **VII.9(d)** depict the percentage of distribution of Cl-species over the course of electrolysis in simulated and real effluents, respectively. It can be noticed that 92.6 $\pm$ 8.0% of Cl^- in simulated effluent was converted to soluble chlorinated byproducts and Cl-volatile via chain reactions discussed in **Section VII.3.2**, while lower Cl^- conversion of 76.7 $\pm$ 4.2% was evaluated using real effluent. Cl-volatile was determined through mass balance between initial Cl content subtracted with all dissolved chlorinated species during the electro-oxidation process. Then, according to **Figs. VII.9(c)** and **VII.9(d)**, lower $HClO/ClO^-$ was measured in the simulated system (18 mg-Cl_2 L^{-1}) after 2 h of electrolysis in comparison with the real system (27.5 mg-Cl_2 L^{-1}). These two differences could be explained by the fate of Cl^- decomposition pathway in both investigated electrolyte matrices. Less Cl^- degradation by about 16% in the real effluent indicated that there were much more competitive reactions present in the system, which slowed down the kinetics of Cl^- consumption. This statement could be supported by the accumulation of $HClO/ClO^-$ in the bulk, where the reactions of free chlorine with organics (in real effluent) possibly with cyclic bonds and/or aromatic compounds were

kinetically slower than the decomposition and electronic transfer of HClO/ClO^- to ClO_3^-, ClO_4^- and Cl-volatile **[33, 41]**. Consequently, since the SW contained simpler organic matrix, greater conversion of Cl^- into HClO/ClO^- was possible, which favored the oxidation into ClO_3^-, ClO_4^- and Cl-volatile, measured at 238 mg L^{-1}, 16 mg L^{-1} and 12% of total chlorine, respectively, after 5 h of electrolysis. Due to competitive reactions of Cl^- oxidation and degradation of organics by electron transfer and $^{\bullet}OH$, Cl^- conversion towards ClO_3^-, ClO_4^- and Cl-volatile in real matrix was delayed **[41-43]**. It led to their respective lower concentrations in the bulk, i.e., 193 mg L^{-1}, 4.7 mg L^{-1} and below 2% of total chlorine, after 5 h of treatment.

In summary, after 5 h of electro-oxidation treatment of simulated and real wastewater, more electro-precipitation was observed using real wastewater. This was probably due to a more complex organic matrix that could favor co-precipitation with Mg^{2+} and Ca^{2+} in real effluent and/or inhibiting effect of SO_4^{2-} in simulated wastewater. Less decomposition of Cl^- was observed in real effluent owing to concurrent organic reactions on anode surface. Cl-mediated oxidants rather reacted with organic pollutants in the bulk of reclaimed effluent, which led to a delay into the conversion of inorganic chlorinated end-products.

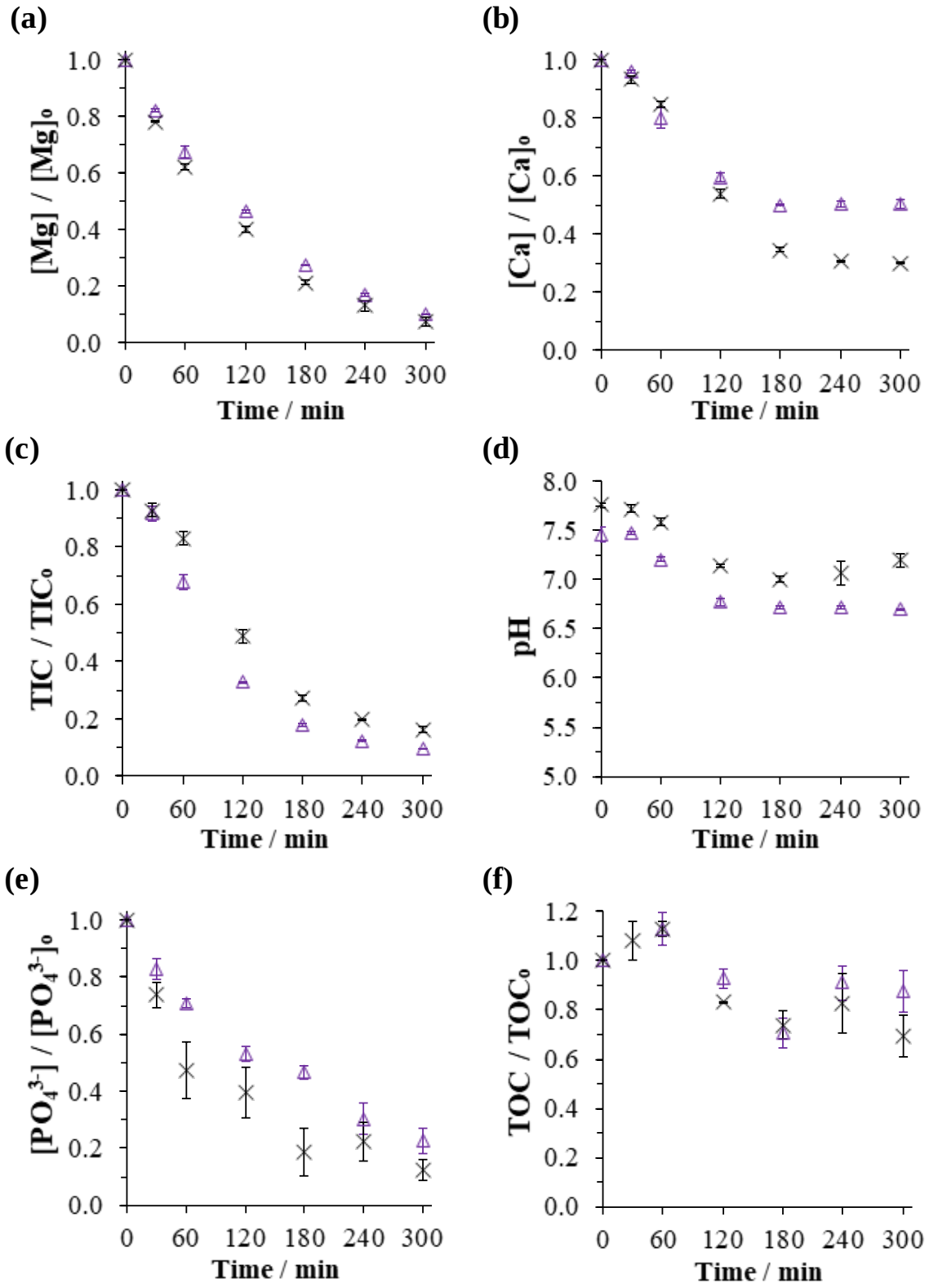

Fig. VII.7. Concentrations of **(a)** Mg^{2+}, **(b)** Ca^{2+}, **(c)** TIC, **(d)** pH, **(e)** PO_4^{3-} and **(f)** TOC during the electrolysis of (△): simulated (SW) and (×): real effluent (RW). Anode: BDD, cathode: stainless steel and j_{app}: 4 mA cm^{-2}.

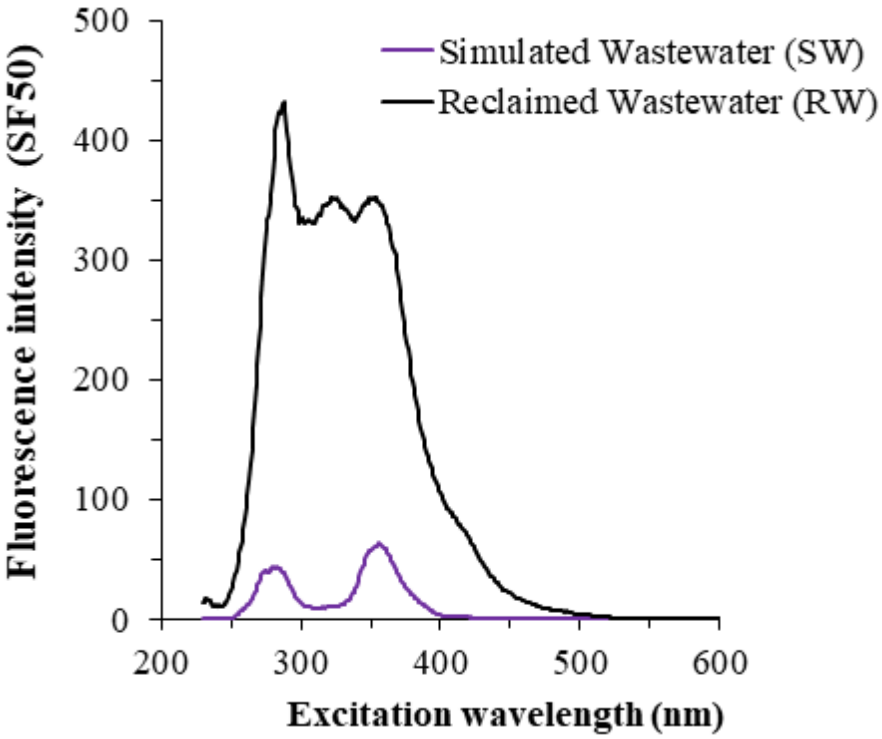

Fig. VII.8. Fluorescence spectra of simulated (SW) and reclaimed (RW) wastewater.

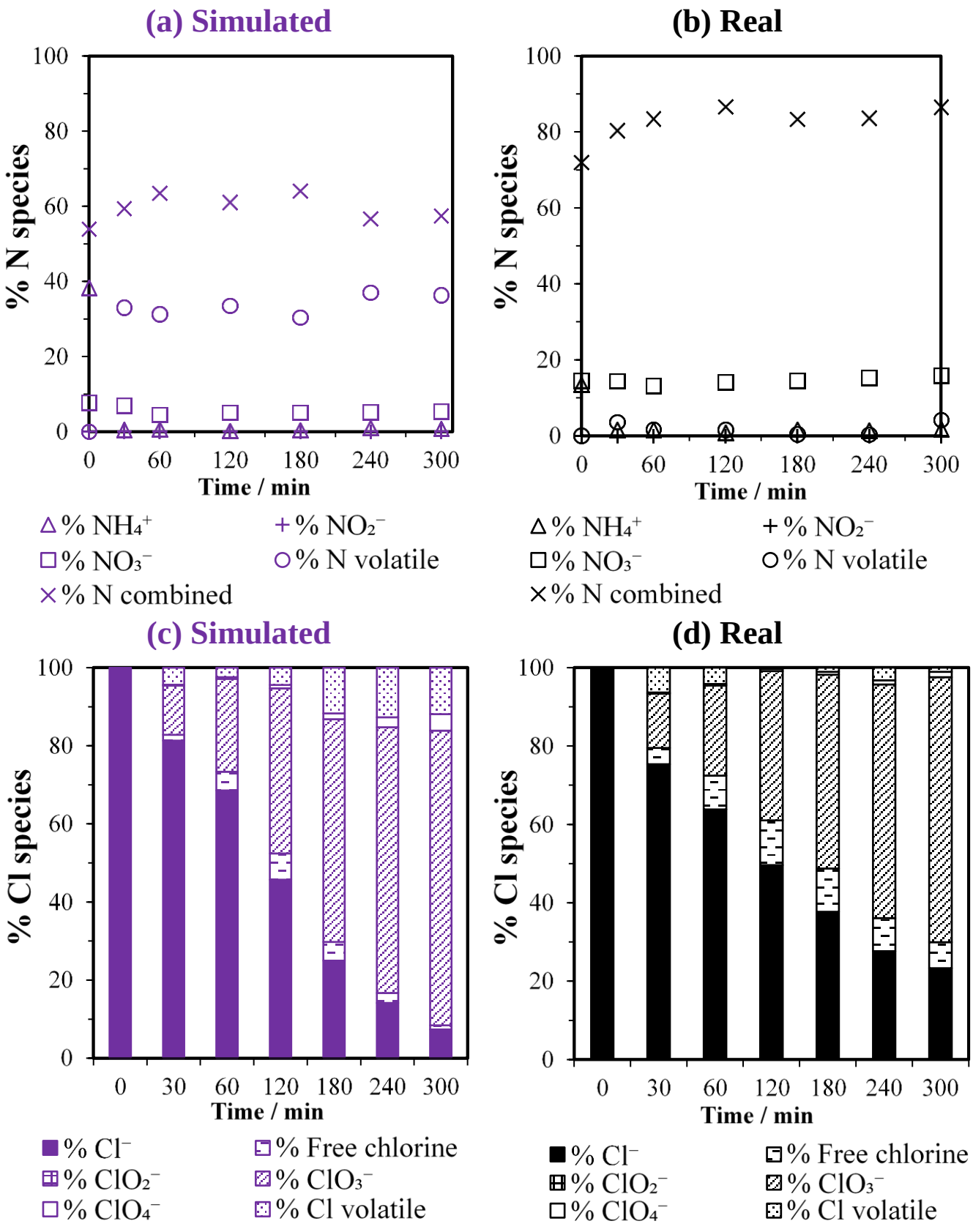

Fig. VII.9. Percentage distributions of N species in **(a)** simulated (SW) and **(b)** real effluent (RW) as well as Cl species in **(c)** simulated (SW) and **(d)** real effluent (RW) during the electro-oxidation treatment. Anode: BDD, cathode: stainless steel and j_{app}: 4 mA cm^{-2}.

VII.3.5. Role of electro-precipitation on the degradation of tylosin as model micropollutant in real wastewater effluent

The influence of occurring electro-precipitation on cathode surface towards the organic mineralization and tylosin degradation as model micropollutant in real wastewater effluent is investigated in this section. Tylosin was selected as model compound as it is a common pharmaceutical micropollutant found at the outlet of WWTP receiving industrial dairy and livestock farming wastes since tylosin is used as a veterinary antibiotic **[44-49]**. Since it is not found in typical domestic wastewater at the out stream of treatment plant, such as our sampled wastewater (Reims municipal WWTP, France), our sampled effluent was spiked with 10 mg L^{-1} of tylosin. The spiked concentration was larger than the average concentration of pharmaceutical compounds detected in the treated waste stream (< 0.5 µg L^{-1} **[50, 51]**). However, it would help to better characterize the influence of electro-precipitation on the degradation kinetics of tylosin compound. The chosen tylosin concentration seemed appropriate because comparable concentrations of pharmaceuticals were also used elsewhere to spike RW **[34, 52-54]**. In section **VII.3.5.1**, the occurrence of electro-precipitation was investigated over the course of electro-oxidation treatment at different j_{app}. The fate of inorganic species during these processes has been evaluated. The next sub-section was devoted to discuss the influence of electro-precipitation at different investigated j_{app} on tylosin degradation and total organic mineralization.

VII.3.5.1. Evolution of electro-precipitation at different applied current densities

The values of j_{app} were determined as function of initial dimensionless applied current density (*DAC*) with respect to the chemical oxygen demand (*COD*), considering the external source of COD brought by the added tylosin. The *DAC* is defined in **Eq. (VII.72) [55-57]**:

$$DAC = \frac{j_{app}}{j_{lim,0}} = \frac{j_{app}}{4Fk_m COD_{tot}} \quad \text{(VII.72)}$$

where $j_{lim,0}$ in A m^{-2}, k_m equaled to 2.33×10^{-5} m s^{-1} **[58]** and COD_{tot} is the sum of COD of wastewater (20.0 mg-O_2 L^{-1}) and that of tylosin (8.8 mg-O_2 L^{-1}) expressed in mol m^{-3}.

Thus, $j_{lim,0}$ of the investigated effluent equaled to 0.8 mA cm^{-2} (or 8 A m^{-2}). Hence, the *DAC* of 1, 5 and 20 corresponded to the j_{app} of 0.8, 4 and 16 mA cm^{-2} respectively, and they have been selected for this work.

Figure VII.10 depicts the evolution of inorganic species during the electro-oxidation of real wastewater at the three investigated *DAC*. From **Fig. VII.10(a)**, it was observed that the least

$Mg(OH)_2$ precipitation occurred at the lowest applied current (23.7 ± 2.1%) and it increased to 95.8 ± 2.9% at 4 mA cm^{-2}. Using 16 mA cm^{-2}, the kinetics of $Mg(OH)_2$ precipitation was higher until 4 h of electrolysis before the Mg settled at slightly lower overall precipitation (81.9 ± 2.7%). Looking at the Ca precipitation in **Fig. VII.10(b)**, Ca precipitated by about 70.0 ± 6.2% using j_{app} of 0.8 mA cm^{-2}, increased to 73.2 ± 1.1% using 4 mA cm^{-2} and it dropped down to 60.6 ± 2.8% using 16 mA cm^{-2}. Reproducible trend was found between the occurrence of Mg and Ca precipitates in the RW in function of *DAC*. They increased with increasing j_{app}. It could be due to more production of OH^- on cathode surface via the reduction reactions of dissolved O_2 and water **[5]**. Nevertheless, when the j_{app} was too high, the overpotential on cathode became largely superior to the standard potential of dissolved O_2 reduction, and consequently, the H_2O reduction reaction was dominant. The latter took place with concomitant HER; the higher the applied current, the higher the HER intensity. As a result, more H_2 bubbles evolved on cathode surface. On one hand, less active surface was available for: (1) the production of OH^- to further react with Mg^{2+} forming $Mg(OH)_2$ and (2): the production of OH^- to shift HCO_3^- to CO_3^{2-} for subsequent reaction with Ca^{2+} to produce $CaCO_3$. Both resulted in lesser amount of Mg and Ca precipitations. On the other hand, vigorous concomitant H_2 evolution could also provoke the detachment of electro-precipitate already formed on cathode surface **[5, 59, 60]**. These reasoning explained why lesser electro-precipitate was formed at the highest j_{app}. Comparable trend can be reckoned from the evolution of TIC in **Fig. VII.10(c)** owing to its precipitation reaction with Ca^{2+}. Nevertheless, it is worth mentioning that at high applied current density, carbonates could play the role of $^{\bullet}OH$ scavenger under the form of $CO_3^{\bullet-}$ **[61]**. It would cause less carbonates present under the form of CO_3^{2-} at the proximity of cathode to precipitate with Ca^{2+}. This might also be the reason why less $CaCO_3$ was noticed at 16 mA cm^{-2}. Next, **Fig. VII.10(d)** plots the evolution of PO_4^{3-} concentration during the electro-oxidation at all three applied currents. No significant difference was noted at the three investigated applied current. After 5 h of experiments, 76.4 ± 1.7%, 73.9 ± 4.2% and 83.0 ± 9.6% of PO_4^{3-} precipitated in the increasing order of j_{app}. Lei et al. have shown that better $Ca_3(PO_4)_2$ could be recovered by applying lower current, owing to lesser degree of precipitation of CO_3^{2-} with Ca^{2+} **[6, 8]**. Thus, more free Ca^{2+} would be able to react with PO_4^{3-} **[6, 8]**. This deduction was not seen in these results due to perhaps low initial phosphate content to make significant difference.

The evolution of Cl species in the electrolytic system is plotted in **Figs. VII.11(a)**, **VII.11(c)** and **VII.11(e)**. At 0.8 mA cm^{-2}, only 1.1 ± 0.1% of the initially present Cl^- was converted to principally ClO_3^- (6.2 ± 2.3 mg L^{-1}; 2.6% of total Cl) after 5 h of electrolysis, with only 0.54 ± 0.22 mg-Cl_2 L^{-1} intermediary $HClO/ClO^-$ produced in the bulk (< 0.3% of total Cl). Low concentration of ClO_4^- was present at this j_{app}; 0.68 ± 0.48 mg L^{-1}, i.e. 0.24% of total Cl. Using higher applied current (4 mA cm^{-}

^{2}), 85.0 ± 2.6% of Cl^- was oxidized leading to the production of 21.6 mg-Cl_2 L^{-1} of HClO/ClO^- after 2 h of electrolysis (i.e., 10.1% of total Cl). The reactions of Cl^- and HClO/ClO^- (**Eqs. (VII.37)-(VII.38)** and **Eq. (VII.42)**) would then lead to continuous production of ClO_3^- (188.0 ± 2.5 mg L^{-1} after 5 h of electrolysis), which was the main chlorinated byproduct using 4 mA cm^{-2}. ClO_3^- was also the main precursor to the production of ClO_4^- (**Eqs. (VII.45)** and **(VII.68)**). 6.1 ± 1.1 mg L^{-1} of ClO_4^- was produced at the end of treatment (2.1% of total Cl) using 4 mA cm^{-2}. At the highest investigated j_{app} (16 mA cm^{-2}), the highest decline in Cl^- concentration was noted compared to the lower j_{app}. It diminished completely after 3 h of electro-oxidation. The production of free chlorine only took place at the first half hour of the process, accumulating up to only 5.55 ± 0.46 mg-Cl_2 L^{-1} (i.e., 2.8% of total Cl) before being consumed rapidly. Up to 1 h of electrolysis, Cl^- and free chlorine were rapidly converted to ClO_3^-, up to 168 ± 2 mg L^{-1} in the bulk (representing 67.4% of total Cl). ClO_4^- progressively started to accumulate after 0.5 h of electro-oxidation process. ClO_3^- as the intermediate started to decrease after 1 h of electrolysis and the accumulation of ClO_4^- went up to 223 ± 1 mg L^{-1} (71.3% of total chlorine) after 5 h of treatment. This time, ClO_4^- was the dominant chlorinated byproduct of electro-oxidation treatment when 16 mA cm^{-2} was adopted. Less than 12.6% of Cl-volatile was produced using 0.8 mA cm^{-2}, about 16.0% using 4 mA cm^{-2} and 43% when using 16 mA cm^{-2}. ClO_2^- was always below the value of limit of quantification owing to its rapid kinetics of reaction as previously discussed in **Section VII.3.2**. In the work of Bergmann et al. **[16]**, a synthetic solution initially containing 50 mg L^{-1} of Cl^- was electrolyzed using BDD rotating disk anode of 35 mm diameter (~10 cm^2 surface area, IrO_2 as cathode), at 20 mA cm^{-2}. In this condition, 9.5 mg L^{-1} of active chlorine was produced after 10 min of electrolysis before its concentration dropped drastically to yield 30 mg L^{-1} of ClO_3^-. Lower ClO_3^- was expected due to lower initial Cl^- content. In similar work, when drinking water (initial Cl^- content of 41 ppm) was electrolysed using similar electrolytic setup, 120 mg L^{-1} ClO_4^- was reported. In other work from Lacasa et al., an electrolyte initially containing 300 mg L^{-1} Cl^- was oxidized at 30 mA cm^{-2} in a cell with 78 cm^2 BDD (stainless steel as cathode) **[19]**. Very quick conversion of free chlorine to ClO_3^- occurred after 30 min of electrolysis producing 351 mg-ClO_3^- L^{-1}. Upon reaching this maximum concentration, ClO_3^- was converted to ClO_4^- and the latter reached its maximum concentration of 842 mg-ClO_4^- L^{-1} after 2 h of electrolysis. In another work from Scialdone et al. **[62]**, in a system where chloroacetic acid (473 mg L^{-1}) was treated electrochemically in a cylindrical undivided cell using BDD anode and stainless steel cathode (both possessing 3 cm^2 surface area), ClO_3^- and ClO_4^- were dosed at different applied current (20, 40 and 100 mA cm^{-2}). Approximately 232, 116 and 62 mg-ClO_3^- L^{-1} were produced in the ascending order of the investigated j_{app}. In the meantime, about 10 mg-ClO_4^- L^{-1} was produced using 20 mA cm^{-2} and 472 mg-ClO_4^- L^{-1} was formed at both 40 and 100 mA cm^{-2}. Separately, Herraiz-Carboné et al. reported a production of up to 49.6 mg-Cl_2 L^{-1} of HClO/ClO^- at 2.5 mA cm^{-2}, while treating synthetic

urine wastewater **[41]**. No presence of ClO_3^- and ClO_4^- at all was detected under their experimenting conditions (up to 5 mA cm^{-2}, BDD and stainless steel as anode and cathode, respectively). Upon comparison with literatures, suitable analogy could not be done due to dissimilarities in reactor design, applied operating conditions as well as initial chloride content in the electrolyte. Nonetheless, general conclusion of the evolution of chlorinated species could be drawn: (1) the reactivity of $HClO/ClO^-$ as intermediate product was rapid and it was quicker with increased current density and (2) the concentration of intermediate ClO_3^- as well as the subsequent ClO_4^- product were highly dependent on the initial Cl^- content as well as the current density adopted.

Figures VII.11(b), **VII.11(d)** and **VII.11(f)** depict the distribution percentages of N-species as a function of electro-oxidation treatment time at 0.8, 4 and 16 mA cm^{-2}. At the three investigated applied currents, the concentration of NO_3^- decreased slightly at the beginning of the process leading to the formation of NH_4^+ and N-volatile (**Eqs. (VII.9)-(VII.10)**) before reaching equilibrium in the bulk. No accumulation of NO_2^- was detected throughout the process, due to its low concentration and quick conversion to NO_3^- (**Eqs. (VII.12)** and **(VII.16)**) and NH_4^+ (**Eq. (VII.19)**). At the lowest current density (0.8 mA cm^{-2}), NH_4^+ was only partially removed in the electrolytic system, which was not the case at higher current density. It decreased by about 29.7% at the end of the electro-oxidation process. This finding can be attributed to lower conversion of Cl^- to $HClO/ClO^-$ (**Fig. VII.11(a)**). Using 4 mA cm^{-2}, NH_4^+ reacted rapidly with $HClO/ClO^-$ to form chloramines. At the highest applied current density tested (16 mA cm^{-2}), NH_4^+ was quickly consumed. However, starting from 1 h of treatment, NH_4^+ increased again. This particular observation was attributed to the depletion of $HClO/ClO^-$ in the bulk (**Fig. VII.11(e)**), thus there was less reactivity with NH_4^+ to form chloramines (**Eqs. (VII.26)-(VII.28)**). Furthermore, the higher accumulation of ClO_4^- in the bulk did not help to oxidize NH_4^+. Its reactivity with NH_4^+ was lower than HClO and Cl_2 due to its high activation energy **[19]**. In addition, slightly higher production rate of NH_4^+ than its reduction to NO_3^- and/or N_2 in the real effluent led to its accumulation in the electrolytic system. Moreover, when the production of N-volatile was compared at different j_{app} (**Figs. VII.11(b)**, **VII.11(d)** and **VII.11(f)**), it was found that N-volatile production increased with increasing applied current. 10.8, 31.1 and 40.3% of N-volatile were generated in the increasing order of the investigated j_{app}. N-combined (i.e., inorganic chloramines and organochloride compounds) was the major form of N-bearing byproducts after the electro-oxidation treatment of the tylosin-spiked wastewater effluent at all investigated j_{app}. The degradation and mineralization degree of the targeted model organic micropollutant is discussed in **Section VII.3.5.2**.

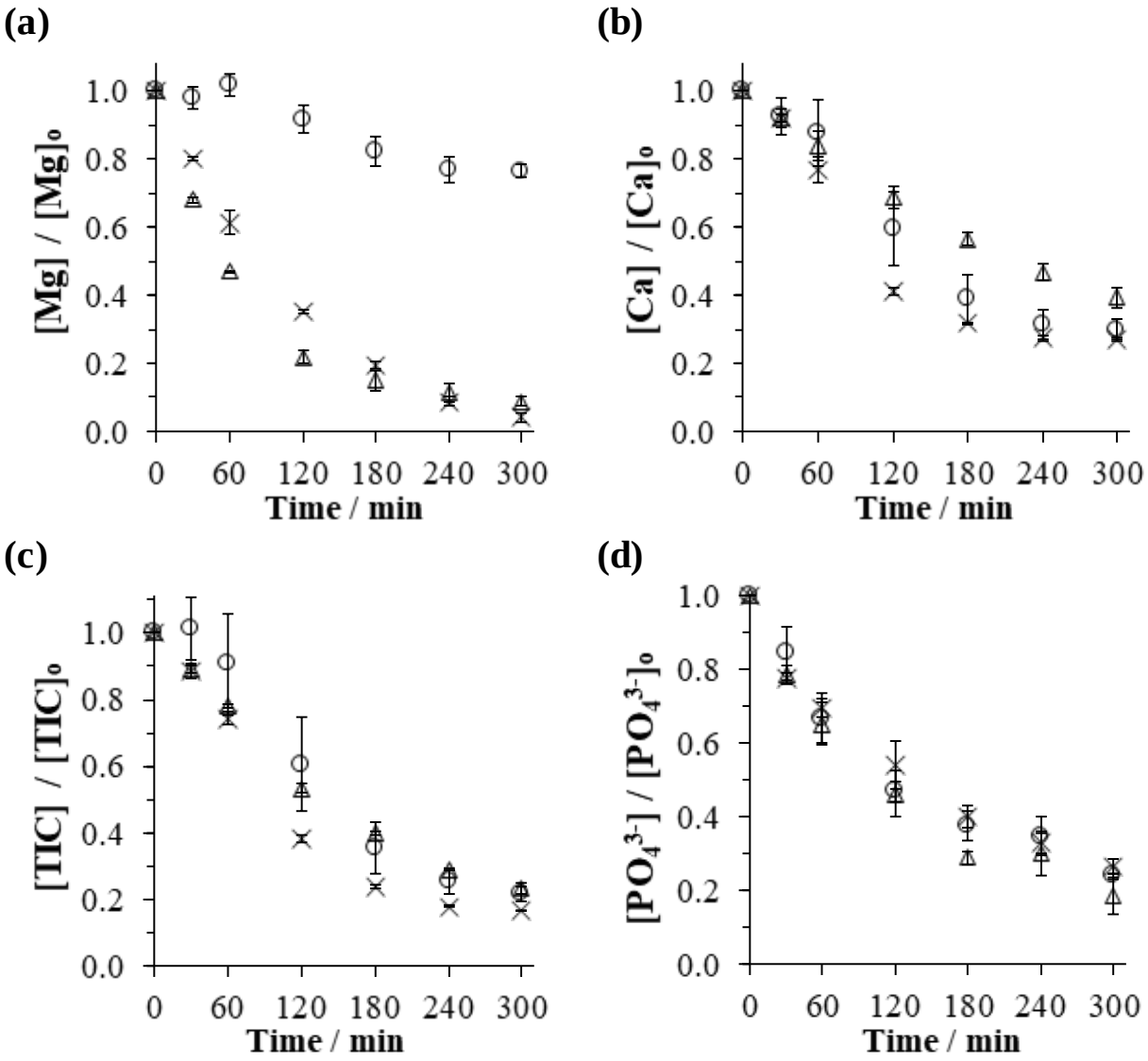

Fig. VII.10. Concentrations of **(a)** Mg^{2+}, **(b)** Ca^{2+}, **(c)** TIC and **(d)** PO_4^{3-} during the electrolysis of real effluent spiked with 10 mg L^{-1} tylosin at (○): 0.8, (×): 4 and (△): 16 mA cm^{-2}. Anode: BDD and cathode: stainless steel.

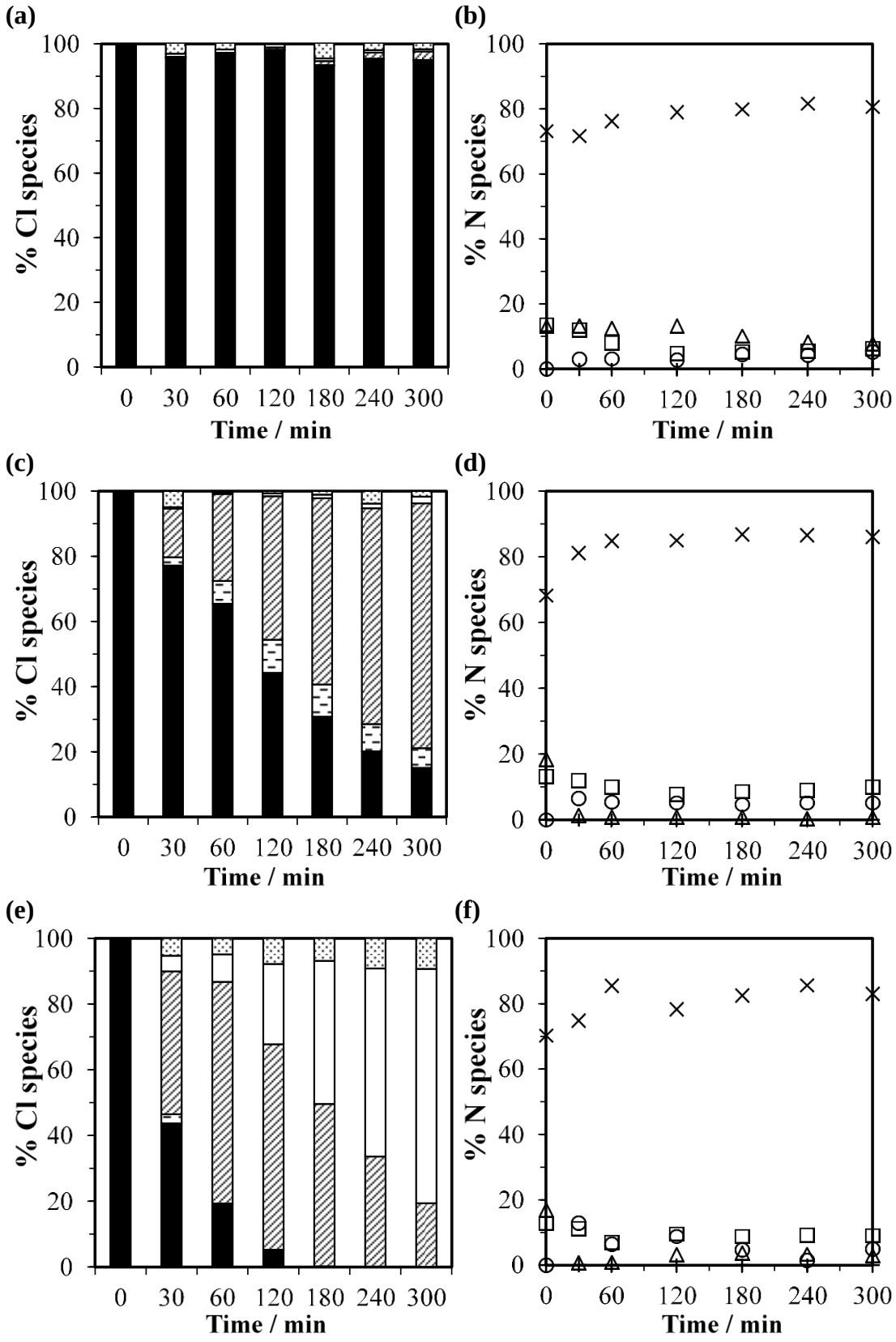

Fig. VII.11. Percentage of distributions of Cl-species during the electro-oxidation of real effluent spiked with 10 mg L^{-1} tylosin at **(a)** 0.8, **(c)** 4 and **(e)** 16 mA cm^{-2} as well as the distribution of N-species at **(b)** 0.8, **(d)** 4 and **(f)** 16 mA cm^{-2}. (■): Cl^-, (▬): HClO/ClO^-, (▦): ClO_2^-, (▨): ClO_3^-, (□): ClO_4^- and (▩): Cl-volatile, while (△): NH_4^+, (+): NO_2^-, (□): NO_3^-, (○): N-volatile and (×): N-combined. Anode: BDD and cathode: stainless steel.

VII.3.5.2. Kinetics and modeling of tylosin degradation as target micropollutant in reclaimed wastewater at different applied current densities

The plot of tylosin degradation as a function of time at the three j_{app} is given in **Fig. VII.12**. It can be observed that when the applied current corresponded to *DAC*=1 with respect to $j_{lim,0}$ (j_{app} = 0.8 mA cm^{-2}), the apparent degradation of tylosin decreased quasi-linearly over time up to 2 h of electrolysis. It was then followed by slower kinetics during the last three hours of electro-oxidation to reach 95% of abatement. This linear trend during the first 2 h of electro-oxidation was expected due to the applied j_{app}, which was lower or equal to the $j_{lim,0}$ of the initial COD of the tylosin. As a consequence, the oxidation of tylosin was limited by charge transfer **[56, 57, 63]**. During this period, tylosin degradation followed a zero-order kinetic rate with a kinetic constant of 0.0247 mg L^{-1} min^{-1} (R^2 = 0.98) (**Fig. VII.12(a)**). When the tylosin concentration decreased with treatment time, its limiting current density at time *t* ($j_{lim,t}$) also decreased. Once the j_{app} equaled to or was higher than the $j_{lim,t}$, tylosin degradation became mass transfer limited. As a result, its apparent kinetic degradation was no longer zero-order rate but followed pseudo-first order rate law **[56, 57, 63]**. From 2 h onwards (**Fig. VII.12(a)**), its decrease gave out first-order rate constant of 0.0138 min^{-1} (R^2 = 0.96). The deviation of modeled tylosin degradation curve at 0.8 mA cm^{-2} was compared with the experimental curve using RMSE (**Eq. (III.3)**). A deviation of 0.024 was evaluated which means that the theoretical model was conformed to the experimental data.

In contrast, using higher j_{app} of 4 mA cm^{-2} (*DAC* = 5), total degradation of tylosin parent molecule in RW was observed after 20 min of treatment (**Fig. VII.12(a)-(b)**). The degradation followed pseudo-first order kinetic rate with a rate constant of 0.17 min^{-1}. Tylosin abatement in simulated effluent (spiked with tylosin at 10 mg L^{-1}) at comparable current density was also investigated (**Fig. VII.12**). Slightly faster kinetics of elimination was noticed in the simulated matrix. Tylosin molecule was totally removed from the effluent after 15 min of electro-oxidation process. Consequently, the evolution of tylosin elimination could be fitted with marginally higher kinetic rate constant (i.e., 0.2191 min^{-1}) compared to the matrix of RW. Previously in **Section VII.3.4**, it has been demonstrated that more electro-precipitation took place in real wastewater effluent due to the more complex organic matrix in real waste effluent. Nevertheless, it has also been shown in **Chapter 6** that during 5-h of electro-oxidation, mineral scaling did not totally passivate the cathode surface. R_{CT} on electrode surface remained constant throughout the treatment. It suggests that the precipitation layer formed did not yet give major impact towards electronic exchanges for direct and mediated target pollutant degradation or organics mineralization in general. No fouling or deposition was observed on the anode. In conjunction with that, the slightly slower tylosin degradation observed in **Fig. VII.12(a)-VII.12(b)** was rather due to the presence of recalcitrant dissolved organic matter in the real

wastewater matrix. Its presence could compete with the degradation of tylosin molecule which led to slower removal of the target pollutant **[41, 53]**. The evolution of TOC during the electrolysis illustrated in **Fig. VII.12(c)** could give some insight towards the hypothesis. Under the polarization of 4 mA cm^{-2}, it was observed that more mineralization occurred in the real (35.1%) compared to the simulated (19.7%) effluents. The increase of TOC at the beginning of electro-oxidation was perhaps due to the breakdown of large tylosin parent compound (MW: 1066 g mol^{-1}). This resulted in an increase of dissolved organic content in the treated effluent. Here, it confirmed the competition between tylosin and dissolved organics since more mineralization occurred but slightly slower tylosin was removed. In both cases, the modeled curves of tylosin removal fitted well the experimental counterparts. RMSE were calculated at 0.021 and 0.048 in the real and simulated wastewater respectively. When the highest tested current density was applied (16 mA cm^{-2}), very quick tylosin degradation was observed. Total tylosin removal was already spotted during the first 5 min of treatment (**Fig. VII.12(a)-(b)**) with a kinetic rate constant of 1.2 min^{-1}.

Quick degradation of tylosin parent molecule demonstrated in this work corroborated the efficient treatment of tylosin by various advanced oxidation technologies documented in literature **[47, 49, 64-67]**. The only EAOP process to degrade tylosin was by EF reported by Ferrag-Siagh et al. **[49]**. 600 mL of synthetic solution containing 100 mg L^{-1} of tylosin and 300 mA applied current were used during the process. Complete tylosin degradation was noticed after 15 min of treatment. The tylosin degradation followed first-order kinetic law with 0.3083 min^{-1} rate constant. The kinetic rate constant was comparable with the one obtained in this work (i.e., 0.1750 to 0.2191 min^{-1} using 200 mA applied current). Slightly higher value reported in their work was due to higher applied current and could also be due to better performance of EF against EO as suggested by several authors **[68, 69]**.

In summary, it has been shown that after 5 h of electro-oxidation treatment, the quantity of electro-precipitation depended on the j_{app}. Nonetheless, the mineral scaling formed on cathode surface did not result in significant reduction in electronic transfer on electrode surface (after 5-h operation). No fouling or deposition was observed on anode. While treating real reclaimed wastewater, higher overall organic abatement was achieved but with slower target pollutant removal. Slower kinetics of the latter was due to the competition between persistent dissolved organics contained in the real wastewater matrix. Either way, the removal of tylosin using EAOP was efficient. Its removal could be estimated using first-order kinetic law but the kinetic constant might vary between EAOPs as function of applied operating conditions.

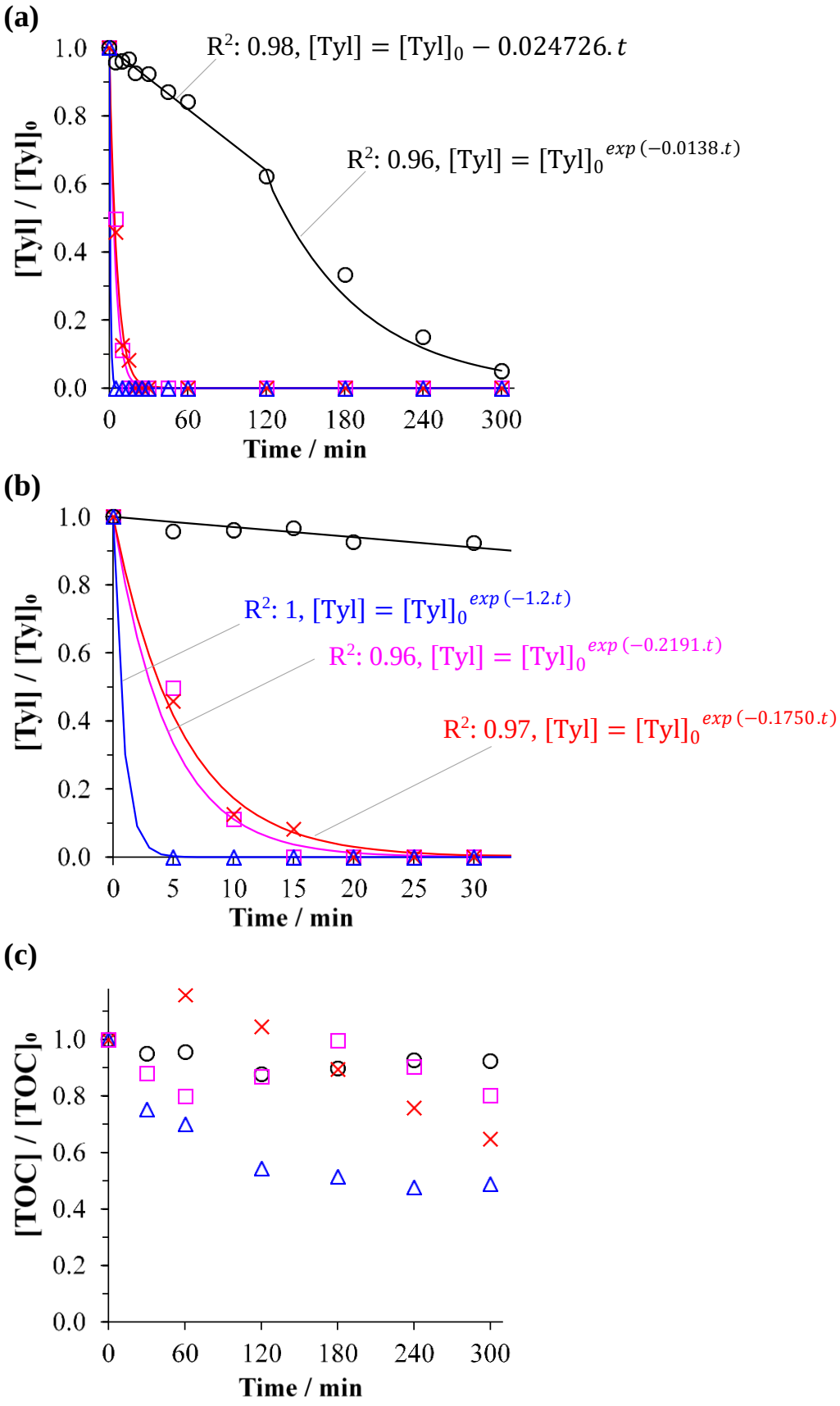

Fig. VII.12. Kinetics and modeling of **(a)** tylosin degradation, **(b)** zoom into the early kinetics of tylosin degradation and **(c)** mineralization during the electro-oxidation of RW containing 10 mg L^{-1} tylosin. (○, —): 0.8, (×, —): 4 and (△, —): 16 mA cm^{-2}. (□, —): simulated wastewater (SW) spiked with 10 mg L^{-1} tylosin (4 mA cm^{-2}). Anode: BDD and cathode: stainless steel.

VII.4. Conclusions

A bottom-up approach has been adopted to investigate thoroughly the influence of complex matrices of electrolyte on the formation of electro-precipitate, the degradation of target pollutant and overall organics mineralization inside microfluidic reactor. The main new insights are given hereinafter:

- Only $Mg(OH)_2$, $CaCO_3$ and $Ca_3(PO_4)_2$ were formed during the electro-oxidation process while the formation of struvite, $MgCO_3$, $CaMg(CO_3)_2$ and $Mg_3(PO_4)_2$ were not favoured. Similar deposition elements were found between submillimetric (this work) and centimetric (literatures) electrochemical reactor setups. Therefore, the anodic contribution in microfluidic configuration only affected the kinetics of electro-precipitation.
- The addition of multi-ions and organic matter onto the SW brought insignificant effect on the formation of electro-precipitate during the electrochemical treatment. High cathodic local pH dissipated the inhibiting capacity of organics towards the $Mg(OH)_2$, $CaCO_3$ and $Ca_3(PO_4)_2$ deposition.
- More mineral scaling occurred in RW compared to SW. It could be due to either (1) the presence of more complex dissolved organics in the wastewater that could most probably co-precipitate with Mg^{2+} and Ca^{2+} or (2) the high sulfate content in the simulated effluent that would inhibit on Mg and Ca precipitation.
- After 5 h of treatment, electro-deposition formed on cathode surface did not decrease the operation efficiency. Higher organic mineralization but slightly slower target pollutant degradation was noticed. The contrasting trend was attributed to the competition between persistent micropollutants with the target pharmaceuticals in the treated effluent.
- By applying the highest j_{app} (16 mA cm^{-2}), 51% of mineralization, 100% tylosin degradation and 45 mg of electro-precipitate were obtained after 5 h of electro-oxidation. Higher organic mineralization and lower mineral deposition were obtained in comparison with lower j_{app}.
- The highest energy consumption was procured using 16 mA cm^{-2} (41.2 kWh m^{-3} vs. 8.33 kWh (4 mA cm^{-2}) and 1.29 kWh m^{-3} (0.8 mA cm^{-2})). Moreover, the highest quantity of undesired byproducts (ClO_3^- + ClO_4^-) was also obtained under this condition (151 mg-Cl_2 L^{-1} vs. 82 (4 mA cm^{-2}) and 2.9 (0.8 mA cm^{-2}) mg-Cl_2 L^{-1}).

Upon these results, a j_{app} in the region of 1 to 2 mA cm^{-2} might be good compromise between organics abatement, scaling deposition and the yield of nuisance byproducts. The treatment duration ought to be longer to efficiently mineralize organic content. It would not be problematic to the submilimetric reactor judging from its very low electrical power consumption (e.g. 1.29 kWh m^{-3} during 5 h electro-oxidation at 0.8 mA cm^{-2}). Using the suggested j_{app} (1 to 2 mA cm^{-2}), the decrease in electro-oxidation

treatment efficiency by mineral scaling for a long-period operation should also be re-investigated more practically under continuous operating mode.

References

[1] J.N. Butler, Carbon dioxide equilibria and their applications, 1st ed., Taylor & Francis Group, New York: Routledge, 1991.
[2] K.J. Powell, P.L. Brown, R.H. Byrne, T. Gajda, G. Hefter, S. Sjöberg, H. Wanner, Chemical speciation of environmentally significant heavy metals with inorganic ligands. Part 1: The Hg^{2+}– Cl^-, OH^-, CO_3^{2-}, SO_4^{2-}, and PO_4^{3-} aqueous systems (IUPAC Technical Report), Pure and Applied Chemistry, 77 (2005) 739-800.
[3] C. Deslouis, I. Frateur, G. Maurin, B. Tribollet, Interfacial pH measurement during the reduction of dissolved oxygen in a submerged impinging jet cell, Journal of Applied Electrochemistry, 27 (1997) 482-492.
[4] M.M. Tlili, M. Benamor, C. Gabrielli, H. Perrot, B. Tribollet, Influence of the interfacial pH on electrochemical $CaCO_3$ precipitation, Journal of The Electrochemical Society, 150 (2003) C765.
[5] F.H. Adnan, E. Mousset, S. Pontvianne, M.-N. Pons, Mineral cathodic electro-precipitation and its kinetic modelling in thin-film microfluidic reactor during advanced electro-oxidation process, Electrochimica Acta, (2021) 138487.
[6] Y. Lei, I. Hidayat, M. Saakes, R. van der Weijden, C.J.N. Buisman, Fate of calcium, magnesium and inorganic carbon in electrochemical phosphorus recovery from domestic wastewater, Chemical Engineering Journal, 362 (2019) 453-459.
[7] K.S. Le Corre, E. Valsami-Jones, P. Hobbs, S.A. Parsons, Phosphorus recovery from wastewater by struvite crystallization: A review, Critical Reviews in Environmental Science and Technology, 39 (2009) 433-477.
[8] Y. Lei, J.C. Remmers, M. Saakes, R.D. van der Weijden, C.J.N. Buisman, Is there a precipitation sequence in municipal wastewater induced by electrolysis?, Environmental Science & Technology, 52 (2018) 8399-8407.
[9] J. Wang, S. Wang, Effect of inorganic anions on the performance of advanced oxidation processes for degradation of organic contaminants, Chemical Engineering Journal, 411 (2021) 128392.
[10] E. Mousset, L. Quackenbush, C. Schondek, A. Gerardin-Vergne, S. Pontvianne, S. Kmiotek, M.-N. Pons, Effect of homogeneous Fenton combined with electron transfer on the fate of inorganic chlorinated species in synthetic and reclaimed municipal wastewater, Electrochimica Acta, 334 (2020) 135608.
[11] L.C. Chow, E. Eanes, Solubility of calcium phosphates, Monographs in oral science, (2001) pp. 94-111.
[12] Y. Lei, M. Saakes, R.D. van der Weijden, C.J.N. Buisman, Effects of current density, bicarbonate and humic acid on electrochemical induced calcium phosphate precipitation, Chemical Engineering Journal, 342 (2018) 350-356.
[13] S. Garcia-Segura, M. Lanzarini-Lopes, K. Hristovski, P. Westerhoff, Electrocatalytic reduction of nitrate: Fundamentals to full-scale water treatment applications, Applied Catalysis B: Environmental, 236 (2018) 546-568.
[14] E. Mousset, S. Pontvianne, M.-N. Pons, Fate of inorganic nitrogen species under homogeneous Fenton combined with electro-oxidation/reduction treatments in synthetic solutions and reclaimed municipal wastewater, Chemosphere, 201 (2018) 6-12.
[15] M. Ghazouani, H. Akrout, L. Bousselmi, Nitrate and carbon matter removals from real effluents using Si/BDD electrode, Environmental Science and Pollution Research, 24 (2017) 9895-9906.
[16] M.E.H. Bergmann, J. Rollin, Product and by-product formation in laboratory studies on disinfection electrolysis of water using boron-doped diamond anodes, Catalysis Today, 124 (2007) 198-203.
[17] G. Pérez, R. Ibáñez, A.M. Urtiaga, I. Ortiz, Kinetic study of the simultaneous electrochemical removal of aqueous nitrogen compounds using BDD electrodes, Chemical Engineering Journal, 197 (2012) 475-482.
[18] A. Kapałka, A. Katsaounis, N.-L. Michels, A. Leonidova, S. Souentie, C. Comninellis, K.M. Udert, Ammonia oxidation to nitrogen mediated by electrogenerated active chlorine on Ti/PtO_x-IrO_2, Electrochemistry Communications, 12 (2010) 1203-1205.
[19] E. Lacasa, J. Llanos, P. Cañizares, M.A. Rodrigo, Electrochemical denitrificacion with chlorides using DSA and BDD anodes, Chemical Engineering Journal, 184 (2012) 66-71.
[20] M.J. Martin de Vidales, M. Millán, C. Sáez, P. Cañizares, M.A. Rodrigo, What happens to inorganic nitrogen species during conductive diamond electrochemical oxidation of real wastewater?, Electrochemistry Communications, 67 (2016) 65-68.

[21] G. Pérez, J. Saiz, R. Ibañez, A.M. Urtiaga, I. Ortiz, Assessment of the formation of inorganic oxidation by-products during the electrocatalytic treatment of ammonium from landfill leachates, Water Research, 46 (2012) 2579-2590.
[22] S. Garcia-Segura, E. Mostafa, H. Baltruschat, Could NO_X be released during mineralization of pollutants containing nitrogen by hydroxyl radical? Ascertaining the release of N-volatile species, Applied Catalysis B: Environmental, 207 (2017) 376-384.
[23] O. Azizi, D. Hubler, G. Schrader, J. Farrell, B.P. Chaplin, Mechanism of perchlorate formation on boron-doped diamond film anodes, Environmental Science & Technology, 45 (2011) 10582-10590.
[24] M.E.H. Bergmann, J. Rollin, T. Iourtchouk, The occurrence of perchlorate during drinking water electrolysis using BDD anodes, Electrochimica Acta, 54 (2009) 2102-2107.
[25] H. Bergmann, S. Koparal, The formation of chlorine dioxide in the electrochemical treatment of drinking water for disinfection, Electrochimica Acta, 50 (2005) 5218-5228.
[26] P. Duan, X. Liu, B. Liu, M. Akram, Y. Li, J. Pan, Q. Yue, B. Gao, X. Xu, Effect of phosphate on peroxymonosulfate activation: Accelerating generation of sulfate radical and underlying mechanism, Applied Catalysis B: Environmental, 298 (2021) 120532.
[27] M. Murugananthan, S.S. Latha, G. Bhaskar Raju, S. Yoshihara, Anodic oxidation of ketoprofen — an anti-inflammatory drug using boron doped diamond and platinum electrodes, Journal of Hazardous Materials, 180 (2010) 753-758.
[28] J. Radjenović, C. Sirtori, M. Petrović, D. Barceló, S. Malato, Solar photocatalytic degradation of persistent pharmaceuticals at pilot-scale: Kinetics and characterization of major intermediate products, Applied Catalysis B: Environmental, 89 (2009) 255-264.
[29] P. Valero, M. Verbel, J. Silva-Agredo, R. Mosteo, M.P. Ormad, R.A. Torres-Palma, Electrochemical advanced oxidation processes for Staphylococcus aureus disinfection in municipal WWTP effluents, Journal of Environmental Management, 198 (2017) 256-265.
[30] Y. Song, H.H. Hahn, E. Hoffmann, The effect of carbonate on the precipitation of calcium phosphate, Environmental Technology, 23 (2002) 207-215.
[31] H.R. Sindelar, M.T. Brown, T.H. Boyer, Effects of natural organic matter on calcium and phosphorus co-precipitation, Chemosphere, 138 (2015) 218-224.
[32] Y. Lei, B. Song, M. Saakes, R.D. van der Weijden, C.J.N. Buisman, Interaction of calcium, phosphorus and natural organic matter in electrochemical recovery of phosphate, Water Research, 142 (2018) 10-17.
[33] S. Garcia-Segura, E. Mostafa, H. Baltruschat, Electrogeneration of inorganic chloramines on boron-doped diamond anodes during electrochemical oxidation of ammonium chloride, urea and synthetic urine matrix, Water Research, 160 (2019) 107-117.
[34] Y. Ouarda, C. Trellu, G. Lesage, M. Rivallin, P. Drogui, M. Cretin, Electro-oxidation of secondary effluents from various wastewater plants for the removal of acetaminophen and dissolved organic matter, Science of the Total Environment, 738 (2020) 140352.
[35] Y. Takabe, N. Ota, M. Fujiyama, Y. Okayasu, Y. Yamasaki, M. Minamiyama, Utilisation of polarity inversion for phosphorus recovery in electrochemical precipitation with anaerobic digestion effluent, Science of the Total Environment, 706 (2020) 136090.
[36] C. Barchiche, C. Deslouis, O. Gil, P. Refait, B. Tribollet, Characterisation of calcareous deposits by electrochemical methods: Role of sulphates, calcium concentration and temperature, Electrochimica Acta, 49 (2004) 2833-2839.
[37] C. Barchiche, C. Deslouis, O. Gil, S. Joiret, P. Refait, B. Tribollet, Role of sulphate ions on the formation of calcareous deposits on steel in artificial seawater; the formation of green rust compounds during cathodic protection, Electrochimica Acta, 54 (2009) 3580-3588.
[38] Y. Tang, F. Zhang, Z. Cao, W. Jing, Y. Chen, Crystallization of $CaCO_3$ in the presence of sulfate and additives: Experimental and molecular dynamics simulation studies, Journal of Colloid and Interface Science, 377 (2012) 430-437.
[39] L. Fernández-Díaz, Á. Fernández-González, M. Prieto, The role of sulfate groups in controlling $CaCO_3$ polymorphism, Geochimica et Cosmochimica Acta, 74 (2010) 6064-6076.
[40] S.M. Hoseinieh, T. Shahrabi, Influence of ionic species on scaling and corrosion performance of AISI 316L rotating disk electrodes in artificial seawater, Desalination, 409 (2017) 32-46.
[41] M. Herraiz-Carboné, S. Cotillas, E. Lacasa, Á. Moratalla, P. Cañizares, M.A. Rodrigo, C. Sáez, Improving the biodegradability of hospital urines polluted with chloramphenicol by the application of electrochemical oxidation, Science of the Total Environment, 725 (2020) 138430.

[42] A. Fernandes, D. Santos, M.J. Pacheco, L. Ciríaco, A. Lopes, Nitrogen and organic load removal from sanitary landfill leachates by anodic oxidation at Ti/Pt/PbO_2, Ti/Pt/SnO_2-Sb_2O_4 and Si/BDD, Applied Catalysis B: Environmental, 148-149 (2014) 288-294.
[43] S. Garcia-Segura, J. Keller, E. Brillas, J. Radjenovic, Removal of organic contaminants from secondary effluent by anodic oxidation with a boron-doped diamond anode as tertiary treatment, Journal of Hazardous Materials, 283 (2015) 551-557.
[44] M.C. Dodd, M.-O. Buffle, U. von Gunten, Oxidation of antibacterial molecules by aqueous ozone: Moiety-specific reaction kinetics and application to ozone-based wastewater treatment, Environmental Science & Technology, 40 (2006) 1969-1977.
[45] L. Wojnárovits, T. Tóth, E. Takács, Critical evaluation of rate coefficients for hydroxyl radical reactions with antibiotics: A review, Critical Reviews in Environmental Science and Technology, 48 (2018) 575-613.
[46] L. Liu, W. Wu, J. Zhang, P. Lv, L. Xu, Y. Yan, Progress of research on the toxicology of antibiotic pollution in aquatic organisms, Acta Ecologica Sinica, 38 (2018) 36-41.
[47] M. Voigt, M. Jaeger, On the photodegradation of azithromycin, erythromycin and tylosin and their transformation products – A kinetic study, Sustainable Chemistry and Pharmacy, 5 (2017) 131-140.
[48] W. Baran, E. Adamek, M. Jajko, A. Sobczak, Removal of veterinary antibiotics from wastewater by electrocoagulation, Chemosphere, 194 (2018) 381-389.
[49] F. Ferrag-Siagh, F. Fourcade, I. Soutrel, H. Aït-Amar, H. Djelal, A. Amrane, Electro-Fenton pretreatment for the improvement of tylosin biodegradability, Environmental Science and Pollution Research, 21 (2014) 8534-8542.
[50] N.A. Sabri, H. Schmitt, B.M. van der Zaan, H.W. Gerritsen, H.H.M. Rijnaarts, A.A.M. Langenhoff, Performance of full scale constructed wetlands in removing antibiotics and antibiotic resistance genes, Science of the Total Environment, 786 (2021) 147368.
[51] N.A. Sabri, H. Schmitt, B. Van der Zaan, H.W. Gerritsen, T. Zuidema, H.H.M. Rijnaarts, A.A.M. Langenhoff, Prevalence of antibiotics and antibiotic resistance genes in a wastewater effluent-receiving river in the Netherlands, Journal of Environmental Chemical Engineering, 8 (2020) 102245.
[52] E. Mousset, M. Puce, M.N. Pons, Advanced electro-oxidation with boron-doped diamond for acetaminophen removal from real wastewater in a microfluidic reactor: Kinetics and mass-transfer studies, ChemElectroChem, 6 (2019) 2908-2916.
[53] F.C. Moreira, S. Garcia-Segura, R.A.R. Boaventura, E. Brillas, V.J.P. Vilar, Degradation of the antibiotic trimethoprim by electrochemical advanced oxidation processes using a carbon-PTFE air-diffusion cathode and a boron-doped diamond or platinum anode, Applied Catalysis B: Environmental, 160-161 (2014) 492-505.
[54] Y. Lan, C. Coetsier, C. Causserand, K. Groenen Serrano, On the role of salts for the treatment of wastewaters containing pharmaceuticals by electrochemical oxidation using a boron doped diamond anode, Electrochimica Acta, 231 (2017) 309-318.
[55] J. Alagesan, M. Jaisankar, S. Muthuramalingam, E. Mousset, P.V. Chellam, Influence of number of azo bonds and mass transport limitations towards the elimination capacity of continuous electrochemical process for the removal of textile industrial dyes, Chemosphere, 262 (2021) 128381.
[56] E. Mousset, Y. Pechaud, N. Oturan, M.A. Oturan, Charge transfer/mass transport competition in advanced hybrid electrocatalytic wastewater treatment: Development of a new current efficiency relation, Applied Catalysis B: Environmental, 240 (2019) 102-111.
[57] M. Panizza, P.A. Michaud, G. Cerisola, C. Comninellis, Anodic oxidation of 2-naphthol at boron-doped diamond electrodes, Journal of Electroanalytical Chemistry, 507 (2001) 206-214.
[58] F.H. Adnan, M.-N. Pons, E. Mousset, Mass transport evolution in microfluidic thin film electrochemical reactors: New correlations from millimetric to submillimetric interelectrode distances, Electrochemistry Communications, 130 (2021) 107097.
[59] H. Karoui, B. Riffault, M. Jeannin, A. Kahoul, O. Gil, M. Ben Amor, M.M. Tlili, Electrochemical scaling of stainless steel in artificial seawater: Role of experimental conditions on $CaCO_3$ and $Mg(OH)_2$ formation, Desalination, 311 (2013) 234-240.
[60] S.M. Hoseinieh, T. Shahrabi, B. Ramezanzadeh, M.F. Rad, The role of porosity and surface morphology of calcium carbonate deposits on the corrosion behavior of unprotected API 5L X52 rotating disk electrodes in artificial seawater, Journal of The Electrochemical Society, 163 (2016) C515-C529.
[61] J.M. Barazesh, C. Prasse, D.L. Sedlak, Electrochemical transformation of trace organic contaminants in the presence of halide and carbonate ions, Environmental Science & Technology, 50 (2016) 10143-10152.
[62] O. Scialdone, E. Corrado, A. Galia, I. Sirés, Electrochemical processes in macro and microfluidic cells for the abatement of chloroacetic acid from water, Electrochimica Acta, 132 (2014) 15-24.

[63] O. Scialdone, C. Guarisco, A. Galia, Oxidation of organics in water in microfluidic electrochemical reactors: Theoretical model and experiments, Electrochimica Acta, 58 (2011) 463-473.
[64] A.Y.-C. Lin, C.-F. Lin, J.-M. Chiou, P.K.A. Hong, O_3 and O_3/H_2O_2 treatment of sulfonamide and macrolide antibiotics in wastewater, Journal of Hazardous Materials, 171 (2009) 452-458.
[65] E. Chamberlain, C. Adams, Oxidation of sulfonamides, macrolides, and carbadox with free chlorine and monochloramine, Water Research, 40 (2006) 2517-2526.
[66] H. Dong, X. Guo, C. Yang, Z. Ouyang, Synthesis of g-C_3N_4 by different precursors under burning explosion effect and its photocatalytic degradation for tylosin, Applied Catalysis B: Environmental, 230 (2018) 65-76.
[67] X. Guo, H. Dong, T. Xia, T. Wang, H. Jia, L. Zhu, Highly efficient degradation toward tylosin in the aqueous solution by carbon spheres/g-C_3N_4 composites under simulated sunlight irradiation, ACS Sustainable Chemistry & Engineering, 6 (2018) 12776-12786.
[68] H. Olvera-Vargas, N. Oturan, E. Brillas, D. Buisson, G. Esposito, M.A. Oturan, Electrochemical advanced oxidation for cold incineration of the pharmaceutical ranitidine: Mineralization pathway and toxicity evolution, Chemosphere, 117 (2014) 644-651.
[69] S. Garcia-Segura, E.B. Cavalcanti, E. Brillas, Mineralization of the antibiotic chloramphenicol by solar photoelectro-Fenton: From stirred tank reactor to solar pre-pilot plant, Applied Catalysis B: Environmental, 144 (2014) 588-598.

VIII. Influence of cathode materials towards the formation of electro-precipitate

VIII.1. Introduction

Carbonaceous materials such as carbon felt, graphite felt and carbon sponge are well-known to inherit high porosity features that can overcome mass transfer limitation owing to their great specific surface **[1]**. They have also been the subject of research due to their high electrocatalytic properties, while offering low operating cost and environmentally-friendly properties compared to noble metals **[2]**. This can benefit wide range of prospective applications **[1, 3, 4]**, including in the water treatment domain **[5, 6]**.

In this chapter, the influence of the properties of carbonaceous materials on the occurrence of cathodic mineral scaling during the advanced electro-oxidation treatment of simulated and reclaimed wastewater was investigated for the first time. The cathode materials were firstly characterized using an electrochemical method before being subjected to electrolysis at different applied current densities. The role of electrode porosity was particularly explored and the amount of mineral electro-precipitation produced was systematically quantified.

Besides, another distinct characteristic of carbonaceous materials is that they possess lower overpotential for water reduction **[7]**. Consequently, wider potential window under cathodic range is achieved, prior to HER. Motivated by such additional interesting property of carbon material, the role of overpotential of H_2 evolution on the kinetics of electro-precipitation was further examined. The synergistic effect of HER overpotential coupled with the electrochemical configuration were discussed. The comparison between the occurrence of mineral scaling on different cathode materials inside submillimetric and millimetric d_{elec} was evaluated. Moreover, the new insights given by mechanistic understanding towards the electrochemical and chemical processes taking place at the electrode/electrolyte interface was substantiated with the *in-situ* electrochemical impedance analysis.

VIII.2. Experimental section

Stainless steel, graphite or carbon paper was used as cathode to investigate the influence of electrode material on the formation of electro-precipitate. CV was performed in a three-electrode configuration to estimate the electroactive surface of the different materials under study. 500 mL of solution containing 50 mM of $K_4Fe(CN)_6$ in 0.50 M of Na_2CO_3 was used **[7, 8]**. The cathode material to be characterized was used as WE, BDD was the CE and Ag-AgCl was the RE. The potential was swept between 0.6 and -0.8 V/Ag-AgCl with a scan rate of 10 mV s^{-1}. Interelectrode gap of 500 µm was

implemented during this characterization experiments. The electrolyte was circulated at 100 mL min^{-1}.

The electro-oxidation experiments were carried out using 500 mL solution containing 150 mg L^{-1} Ca^{2+}, 5 mg L^{-1} Mg^{2+} and 60 mg-C L^{-1} of TIC. It corresponds to the BE such used in **Chapters 4**, **6** and **7**. Galvanostatic electrolysis using two-electrode configuration was used to run the experiments. Two values of applied current were investigated: 20 (0.4 mA cm^{-2}) and 200 mA (4 mA cm^{-2}). BDD served as anode while stainless steel, graphite and carbon paper were used as cathode. The solution was recirculated at a flow rate of 100 mL min^{-1}. During the study of the role of interelectrode gap, three d_{elec} were investigated: 100 and 500 µm, representing submillimetric configurations, and 3000 µm representing the millimetric scale.

To characterize the electrochemical behavior of BE on the investigated cathodes during electrolysis, LSV was performed via a potentiostat under a three-electrode setup. A potential sweep between 0.5 and -1.8 V/Ag-AgCl with 10 mV s^{-1} scan rate was conducted. Stainless steel, graphite and carbon paper were used as the WE, BDD as CE and Ag-AgCl as RE. EIS was conducted in galvanostatic mode covering the frequency ranges between 100 kHz to 100 mHz. The perturbation amplitude (ΔI_{AC}) varied between 5 and 10 mA RMS according to EIS spectra with 10 ppd. The EIS analysis was programmed at regular interval during galvanostatic electrolysis at an applied direct current of 200 mA (i.e. 4 mA cm^{-2}). The EIS parameters were extracted by means of EEC model using ZSimpwin® commercial software.

Detailed analytical methods have been described in **Chapter 3**. Mg and Ca concentrations were quantified using ICP-OES. The evolution of TIC concentration was followed using TOC-TN analyzer. The morphology of electro-precipitate on carbon paper cathode surface was performed using SEM-EDX. During the electro-oxidation experiments of reclaimed wastewater (**Section VIII.3.1.3**), multi-ions were present. The evolution of anion concentrations (NO_3^-, NO_2^-, SO_4^{2-}, Cl^-, ClO_2^-, ClO_3^- and ClO_4^-) were measured using ionic chromatography. NH_4^+ was measured with HACH spectrophotometer, PO_4^{3-} was quantified using HACH PhosVer 3 method and free chlorine was dosed using HACH DPD method. TOC and TN complemented TIC analysis using TOC-TN analyzer (Shimadzu). Tylosin concentration was monitored using HPLC-UV (wavelength 290 nm).

VIII.3. Results and discussion

VIII.3.1. Influence of the porosity of cathode material on the formation of electro-precipitate

In this section, the influence of cathode porosity on the kinetics of electro-precipitate formation was thoroughly evaluated. Electrodes of different porosities, namely stainless steel, graphite and carbon paper were used as case study. These electrodes were firstly characterized by means of electrochemical method in **Section VIII.3.1.1**, before they were used as cathode and subjected to electrolysis at different applied currents (20 and 200 mA) in **Section VIII.3.1.2**. Finally, **Section VIII.3.1.3** was dedicated to a case study where the performance of porous cathode (carbon paper) as well as non-porous cathode (stainless steel) was compared regarding the electro-oxidation efficiency of reclaimed wastewater. The formation of electro-precipitation together with the fate of inorganic and organic species in the treated media were quantified.

VIII.3.1.1. Electroactivity of stainless steel, graphite and carbon paper characterized by electrochemical method

Redox reactions of $Fe(CN_6)^{3-}$ and $Fe(CN_6)^{4-}$ were used to estimate the electroactivity of the three investigated cathode surfaces. **Figure VIII.1** illustrates the voltammograms of stainless steel, graphite and carbon paper when they were subjected to CV. The peak current (I_P in A) is correlated to the electroactive surface area of an electrode by Randles-Sevcik equation (**Eq. (VIII.1)**) **[7-9]**:

$$I_P = 2.69 \times 10^5 \times A D_L^{1/2} n_e^{3/2} \gamma^{1/2} C_{SOL} \quad \text{(VIII.1)}$$

where A is the electroactive surface area (in cm^2), D_L is the diffusion coefficient of $Fe(CN_6)^{3-}$ /$Fe(CN_6)^{4-}$ in solution (6.48×10^{-6} cm^2 s^{-1} **[10-12]**), n_e equals to 1, γ is the scan rate (0.01 V s^{-1}) and C_{SOL} is 5×10^{-5} mol cm^{-3}.

From the values of I_P measured for the three cathode materials (**Fig. VIII.1**), their corresponding values of electroactive surface areas were determined. It was estimated that the stainless steel (**Fig. VIII.1(a)**), graphite (**Fig. VIII.1(b)**) and carbon paper (**Fig. VIII.1(c)**) possessed 80, 85 and 175 cm^2 of surface area, respectively. This trend is coherent with the increase of electrode porosity from stainless steel to graphite (~15%, Final Advanced Materials, Didenham, France) and carbon paper (~89%, Ion Power, München, Germany). There was only 6% difference between graphite and stainless steel despite the former being a carbonaceous material. This slightly higher electroactive surface of graphite was due to the fact that both stainless steel and graphite used in this work were solid plate electrodes. Porous properties of graphite gave slight advantage compared to the stainless

steel plate. Significant increase of electroactive surface area was provided by the carbon paper as expected. It was attributed to its high porosity which increased the number of electroactive sites at the cathode interface.

The LSV of the three investigated cathode materials in BE (150 mg L^{-1} Ca^{2+}, 5 mg L^{-1} Mg^{2+} and 60 mg-C L^{-1} of TIC) used to study the formation of electro-precipitation are given in **Fig. VIII.2**. From the LSV curves, the exchanged current (I_0) on stainless steel, graphite and carbon paper were estimated to be 1.2, 7.9 and 15.8 mA, respectively. I_0 indicated the easiness of electrons transfer that could occur at the electrode/electrolyte interface. From the values of I_0, charge transfer resistance (R_{CT}) could hence be estimated using **Eq. (VIII.2) [13, 14]**:

$$R_{CT} = \frac{RT}{n_e F I_0} \qquad \text{(VIII.2)}$$

where R_{CT} is in **Ω**, R is the gas constant (8.314), T is the temperature (in K) and n_e is the number of exchanged electrons for water reduction. Here, n_e equals to 2, due to the fact that water reduction by 2 electrons was the dominant faradaic reaction at the applied current investigated **[15]**.

By intermediary of **Eq. (VIII.2)**, R_{CT} on stainless steel, graphite and carbon paper were estimated to be 10.2, 1.62 and 0.81 **Ω**, respectively. These numbers foretell that electronic transfer is the easiest on carbon paper, followed by graphite and finally on stainless steel cathode. It tallies with the respective order of the above-mentioned surface of materials. The values of R_{CT} are compared with those measured with another technique (i.e., EIS) in **Section VIII.3.2.2**.

In the meantime, the role of cathode material on the kinetics of electro-precipitate during the electrolysis of solution containing 150 mg L^{-1} Ca^{2+}, 5 mg L^{-1} Mg^{2+} and 60 mg-C L^{-1} of TIC is scrutinized in the next section.

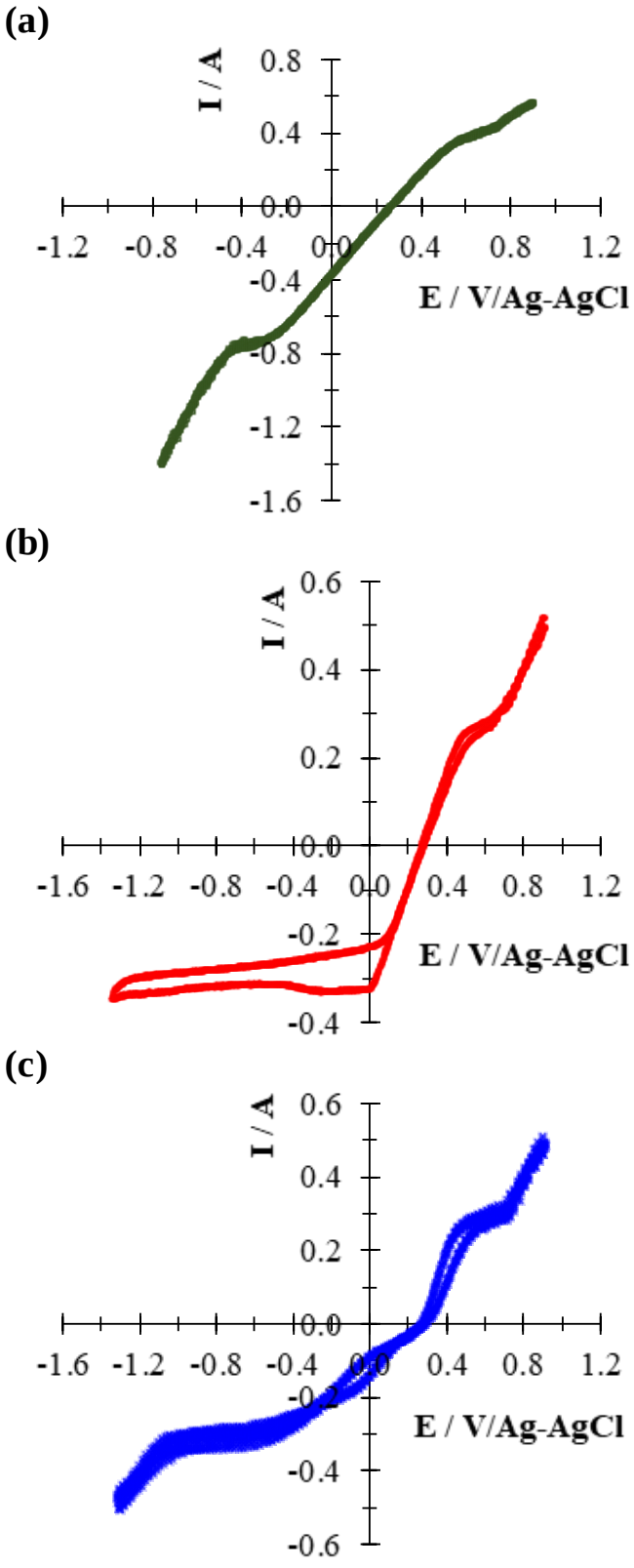

Fig. VIII.1. Voltammograms on **(a)** carbon paper, **(b)** graphite and **(c)** stainless steel for the determination of electroactive surface area. Electrolyte: 500 mL of 50 mM of $K_4Fe(CN)_6$ in 0.50 M of Na_2CO_3; potential sweep between 0.6 to -1.6 V/Ag-AgCl with a scan rate of 10 mV s^{-1}; CE: BDD and RE: Ag-AgCl; d_{elec}: 500 µm.

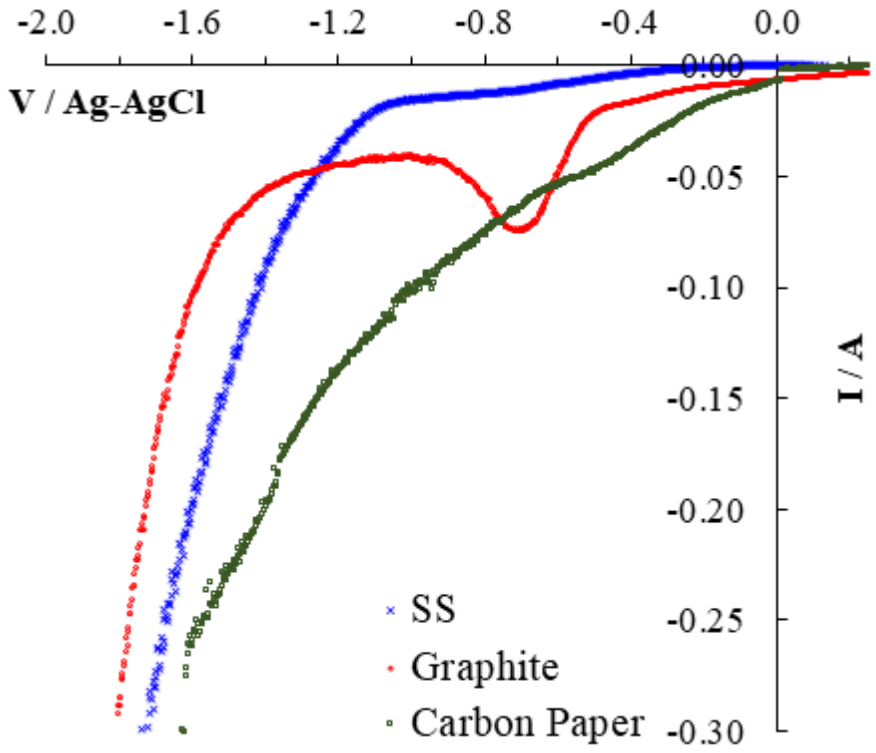

Fig. VIII.2. LSV of stainless steel, graphite and carbon paper. 500 mL solution containing 150 mg L^{-1} Ca^{2+}, 5 mg L^{-1} Mg^{2+} and 60 mg-C L^{-1} of TIC. Potential sweeps between 0.5 to -1.8 V/Ag-AgCl with a scan rate of 10 mV s^{-1}; CE: BDD and RE: Ag-AgCl; d_{elec}: 500 µm.

VIII.3.1.2. Electro-precipitation on different cathode materials at various applied current densities

In this section, the formation of electro-precipitate occurring on stainless steel, graphite and carbon paper under the polarization of different applied currents was evaluated. **Figure VIII.3** illustrates some photographs of mineral electro-precipitate that were formed on the investigated cathodes when BE was polarized at 200 mA. The scaling appeared whitish on stainless steel (**Fig. VIII.3(a)**) and graphite (**Fig. VIII.3(b)**), whereas the white appearance was not seen on carbon paper (**Figs. VIII.3(c)-VIII.3(d)**). Perhaps, the electro-precipitation took place within the pores using carbon paper. With the occurrence of mineral scaling being proven, its quantitative analysis on different cathode materials and applied current was conducted. The evolution of Mg^{2+}, Ca^{2+} and TIC concentrations during the 5 h of electrolysis at 20 and 200 mA are plotted in **Fig. VIII.4**. In **Fig. VIII.4(a)**, Mg^{2+} concentration decreased insignificantly for all three investigated cathode materials when 20 mA was applied. There was 5.2 $\pm$ 0.1% of decrease of Mg^{2+} concentration using stainless steel with 7% more decrease using graphite. Meanwhile, using carbon paper, Mg^{2+} concentration dropped by 2.1% after 3 h electrolysis before it re-dissolved into the solution. From these results, it could be deduced that little $Mg(OH)_2$ precipitation occurred on all cathode materials investigated at low applied current. With respect to the evolution of Ca^{2+} concentration (20 mA) as shown in **Fig.**

VIII.4(c), it decreased indifferently when stainless steel and graphite cathodes were used considering the standard deviations. It decreased to 45.8 ± 3.3% and to 47.8 ± 1.0% using stainless steel and graphite, respectively. Similar trend as the evolution of Mg^{2+} was observed in the case of carbon paper. Ca^{2+} concentration dropped by 11.2 ± 0.8% after 3 h of electrolysis before dissolving back into solution to yield only 1.3% of Ca precipitation on carbon paper at the end of electrolysis. The evolution of TIC concentration is given in **Fig. VIII.4(e)**. Their evolutions followed those of Ca^{2+} plotted in **Fig. VIII.4(c)** with the exception of carbon paper. It was observed that all TIC concentrations depleted after 5 h of electrolysis: 90 ± 18%, 94 ± 14% and 94 ± 7% of carbonates loss in the setup using stainless steel, graphite and carbon paper, respectively. Using stainless steel and graphite, the decrease of carbonates in conjunction with Ca^{2+} concentration confirmed the $CaCO_3$ electro-precipitation on both cathodes. Contrastingly, using carbon paper polarized at 20 mA, the TIC in the solution depleted but Ca^{2+} only precipitated by 1.3% at the end of electrolysis. Therefore, HCO_3^-/CO_3^{2-} might loss via an additional route, which is discussed later in this sub-section.

The evolution of Mg^{2+}, Ca^{2+} and TIC concentrations on stainless steel, graphite and carbon paper at higher applied current (200 mA) are shown in **Figs. VIII.4(b)**, **VIII.4(d)** and **VIII.4(f)**, respectively. From **Fig. VIII.4(b)**, it was observed that similar degree of precipitation of Mg^{2+} took place on the surface of stainless steel and graphite (91.0 ± 1.8% and 89.1 ± 2.2%, respectively). In contrast, lower Mg^{2+} precipitation was observed on carbon paper (i.e. 20.2 ± 1.1%). With regard to the evolution of Ca^{2+} concentration at 200 mA (**Fig. VIII.4(d)**), Ca^{2+} precipitated by 43.2 ± 5.6% and 46.7 ± 1.2% after 5 h of electrolysis when stainless steel and graphite were used as cathode, respectively. Thus, 3.5% more $CaCO_3$ precipitated on graphite in comparison to stainless steel. When carbon paper was adopted as cathode, Ca^{2+} precipitated by 48.2 ± 1.3% after just only 1 h of electrolysis. However, the precipitate re-dissolved into the bulk after 1 h of treatment and it ended with 40.0 ± 1.5% of Ca^{2+} precipitation, which was less than those found on stainless steel and graphite. **Figure VIII.4(f)** plots the evolution of TIC using the three cathode materials under the polarization of 200 mA. Comparable trends seen in the cases with 20 mA were observed. More precipitation of carbonates occurred using the graphite cathode setup (95.8 ± 5.4%) versus the stainless steel (89.4 ± 0.2%). This corroborated with the evolution of Ca^{2+} concentration where slightly more Ca^{2+} precipitated on graphite relatively to stainless steel. Regarding the TIC evolution under the carbon paper setup, as it was the case with Ca^{2+}, TIC depleted quickly down to 94.6 ± 0.9% just after 1 h of electrolysis. TIC decreased significantly faster at higher applied current in comparison to the case where 20 mA was applied (i.e., 4 h to deplete the TIC by 94% (**Fig. VIII.4(e)**)).

The peculiarity of the results obtained when carbon paper was adopted as cathode at both applied current could be justified by the trend of electrolytic solution pH over the course of electrolysis.

Figure VIII.5 plots the variation of electrolyte pH at both applied current investigated. It was observed that the bulk pH decreased the most using carbon paper as cathode regardless of applied current. Under the polarization of 20 mA using carbon paper (**Fig. VIII.5(a)**), the bulk pH decreased to an average pH value of 5.12 before it dropped to 3.38 after 4 h and further down to 3.12 after 5 h of electrolysis. This explained why there was a re-dissolution of Mg and Ca precipitates starting from 3 h of electrolysis in the case of 20 mA. Regarding the pH evolution at higher applied current (**Fig. VIII.5(b)**), it dropped rapidly to 3.76 after just 1 h of electrolysis, before settling at 3.56 at the end of the process. Similarly, this could explain the re-dissolution of Ca as well as quicker depletion of TIC after 1 h of electrolysis when 200 mA was applied. From these trends of bulk pH, it could be summarized that the carbonate loss in case of carbon paper was principally due to the conversion of HCO_3^- to H_2CO_3 ($pK_A = 6.3$ **[16]**) and then to CO_2 given the low pH environment (pH = 3.56) obtained using carbon paper. This was particularly true in the case of 20 mA where TIC was depleted by 94% but Ca^{2+} only precipitated by 11% (before re-dissolution). While applying 200 mA, Ca^{2+} quickly precipitated with CO_3^{2-} during the first hour of electrolysis before the pH environment got too low that it induced re-dissolution of $CaCO_3$ after 1 h of electrolysis.

The evolution of bulk pH when stainless steel and graphite were used as cathode are also depicted in **Fig. VIII.5**. It can be observed that, regardless of the value of applied current, the electrolytic bulk pH decreased in the increasing order of stainless steel > graphite > carbon paper. Comparing the porosity of the three cathode materials, it increased in the increasing order of stainless steel < graphite < carbon paper. Another particularity using porous electrode as cathode is that, it has been reported that the porous nature of the electrode would induce a retardation of OH^- diffusion flux from the porous cathode into the bulk **[17]**. As a consequence, more accumulation of OH^- in porous cathode due to the slower OH^- diffusion led to higher local pH on porous cathode. In the same time, the precipitation reactions near the cathode surface consumed OH^- **[18, 19]**. This consumption of OH^- combined with its slower diffusion into the bulk could have led to higher uncombined H^+ concentration in the bulk, which resulted in lower pH value. This could be the reason why lower bulk pH was obtained using carbon paper as cathode, followed by graphite and stainless steel. Moreover, the higher porosity of carbon paper could have led to a higher accumulation of OH^- in the pores, which could rapidly convert HCO_3^- to CO_3^{2-} for its reaction with Ca^{2+} to form $CaCO_3$. Consequently, rapid decrease of Ca^{2+} concentration was noticed (**Fig. VIII.4(d)**). Following similar principle, the porous nature of graphite plate led to slightly higher local OH^- concentration on graphite cathode relatively to the stainless steel plate which resulted in slightly higher $CaCO_3$ electro-precipitation on graphite as compared to stainless steel (**Figs. VIII.4(d)** and **VIII.4(f)**).

Contrastingly, the slow electro-precipitation of $Mg(OH)_2$ on carbon paper in comparison to graphite and stainless steel, came down to the applied cathode potential on carbon paper at 200 mA. It has been shown in literature that the precipitation of $Mg(OH)_2$ was highly dependent on applied current **[20-23]**, or more precisely to the cathode potential **[15]**. It was noticed in **Section VIII.3.1.1** that when 200 mA was applied, -1.54 V/Ag-AgCl was measured on stainless steel, -1.72 V/Ag-AgCl was measured on graphite, whilst -1.40 V/Ag-AgCl was measured on carbon paper (**Fig. VIII.2**). This higher applied cathode potential led to lower intensity of OH^- production from the reduction reactions of dissolved O_2 and water (**Eqs. (II.9)** and **(II.10)**). As a result, slower $Mg(OH)_2$ electro-precipitation was apparent with carbon paper.

Due to differences that porosity could bring towards the mechanism of electro-precipitation, electro-oxidation experiments to treat RW effluent using porous (carbon paper) and non-porous cathode (stainless steel) are compared in the next sub-section.

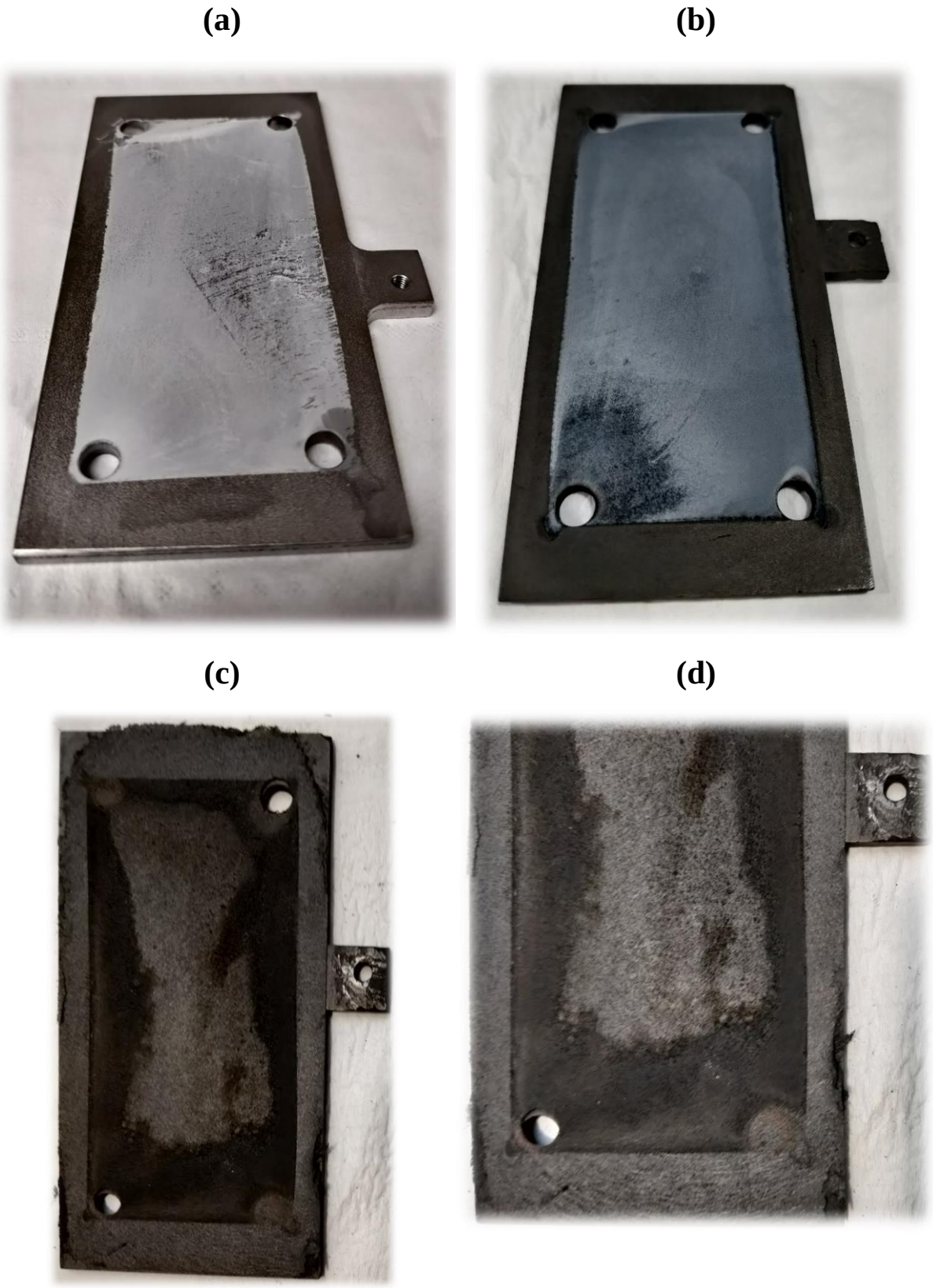

Fig. VIII.3. Photographs of mineral electro-precipitation occurring on **(a)** stainless steel, **(b)** graphite and **(c, d)** carbon paper cathodes after 5 h of electrolysis. d_{elec}: 500 µm. I_{app}: 200 mA.

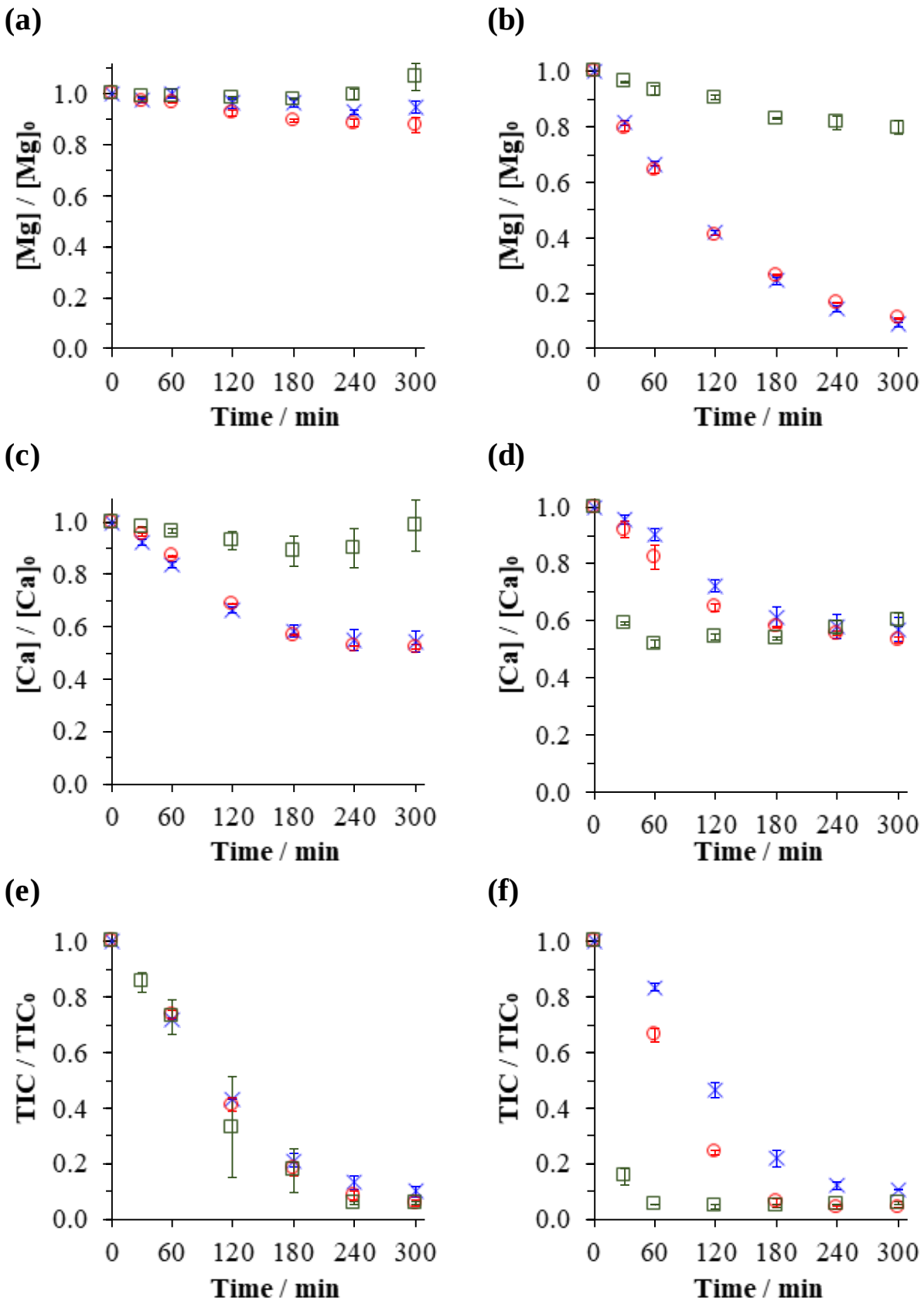

Fig. VIII.4. Concentrations of Mg^{2+}, Ca^{2+} and TIC during the electrolysis at 20 mA (**(a)**, **(c)**, **(e)**) and 200 mA (**(b)**, **(d)**, **(f)**). d_{elec}: 500 µm, (✕): stainless steel, (○): graphite and (□): carbon paper cathode. Electrolyte initially contained 150 mg L^{-1} Ca^{2+}, 5 mg L^{-1} Mg^{2+} and 60 mg-C L^{-1} of TIC.

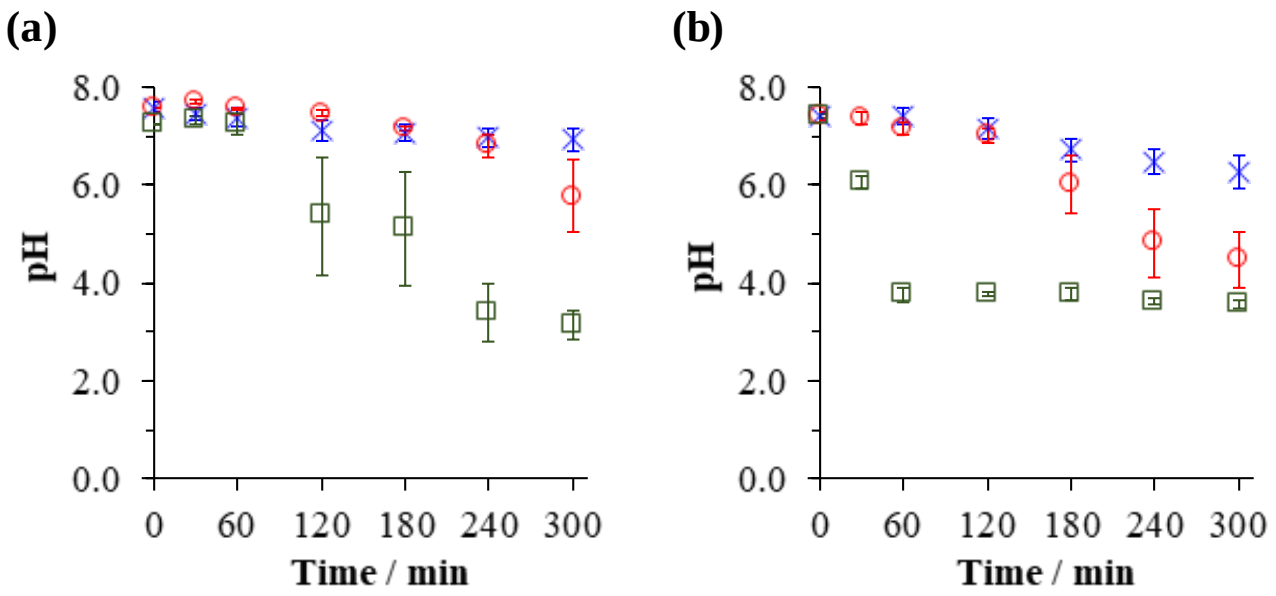

Fig. VIII.5. Evolution of bulk pH during the electrolysis at **(a)** 20 mA and **(b)** 200 mA. Cathode material: (✕): stainless steel, (○): graphite and (□): carbon paper.

VIII.3.1.3. Electro-precipitation on porous cathode during electro-oxidation of reclaimed wastewater

In this sub-section, the role of cathode porosity on the occurrence of electro-precipitate was further evaluated by treating RW effluent using an electro-oxidation process. The deposit formed on carbon paper (porous) and stainless steel (non-porous) along with the fate of inorganic and organic species in the treated media were quantified.

Figures VIII.6 and **VIII.7** plot the evolution of inorganic and organic species during the electro-oxidation of RW when carbon paper and stainless steel served as cathode. From **Fig. VIII.6(a)**, similar trend observed in BE was reproduced. Mg precipitated significantly on stainless steel cathode ($93.0 \pm 3.1\%$) but sluggishly on carbon paper (22.2%), which was ascribed to higher applied cathode potential on carbon paper as discussed previously (**Section VIII.3.1.2**). Moreover, similar conclusion could be drawn during the electrolysis of BE according to **Figs. VIII.6(b)** and **VIII.6(c)**. There was a rapid $CaCO_3$ deposition on porous carbon paper (63.4% of Ca and 88.4% of carbonate precipitation after 2 h of treatment) relatively to that occurring on stainless steel. Again, similar reasoning in relation to the retardation of OH^- diffusion to the bulk could be noticed. Thus, the accumulation of OH^- in porous cathode remains valid. However, slightly more Ca precipitation was observed on stainless steel than on carbon paper at the end of electro-oxidation treatment, i.e. 70.0% and 64.4% on stainless steel and carbon paper, respectively. Only slight re-dissolution of $CaCO_3$ occurred in the carbon paper configuration in the final hour of treatment. This was supposed to be due to a better buffering capacity of the wastewater effluent. It can be demonstrated by the evolution of bulk pH

during the electrolysis as depicted in **Fig. VIII.6(d)**. When carbon paper was used as cathode, the bulk pH equaled to 6.42 after 3 h of treatment. Then the pH dropped down to 4.37, when the electrolysis ended. In comparison, the bulk pH was equivalent to neutral pH (7) when stainless steel was used. **Figure VIII.6(e)** shows the evolution of phosphates during the electro-oxidation processes. It was noticed that the formation of calcium phosphate took place independently of the porosity of cathode. It has been reported that the deposition of $Ca_3(PO_4)_2$ was facilitated on cathode with larger surface area under identical applied current since it offered higher reactive surface **[24]**. Nevertheless, that enhancement could not be identified under our operating conditions due to low phosphate content. Then, in agreement with the TOC evolution illustrated in **Fig. VIII.6(f)**, marginally better mineralization took place with stainless steel on cathode (28.3% vs. 16.5% using carbon paper).

Figure VIII.7 illustrates the evolution of N and Cl species during the electro-oxidation process using carbon paper and stainless steel as cathode. **Figure VIII.7(a)** shows the concentration of NO_3^- during the treatment. Using stainless steel cathode, NO_3^- was only reduced by 9% after 1 h of electrolysis before its concentration increased progressively till the end of treatment. Meanwhile, when carbon paper replaced the stainless steel as cathode, NO_3^- concentration continuously decreased over the course of electro-oxidation reaching 95.6% of removal after 5 h of electrolysis. In conjunction with the evolution of NH_4^+ concentration illustrated in **Fig. VIII.7(b)**, in which NH_4^+ increased over the course of treatment, it could be deduced that the NO_3^- was reduced to yield NH_4^+ **[25-28]**. The reductions of NO_3^- to NH_4^+ and N_2 (**Eqs. (VI.9)-(VI.11)** and **Eq. (VIII.3)**) were fast and they led to efficient elimination of NO_3^- from the wastewater effluent.

$$NO_3^- + 10H^+ + 8e^- \rightarrow NH_4^+ + 3H_2O \quad \text{(VI.9)}$$

$$NO_3^- + 6H^+ + 5e^- \rightarrow \frac{1}{2}N_2 + 3H_2O \quad \text{(VI.10)}$$

$$NO_3^- + 2H^+ + 2e^- \rightarrow NO_2^- + H_2O \quad \text{(VI.11)}$$

$$NO_3^- + 10H^+ + 8e^- \leftrightarrow NH_4^+ + \bullet OH + 3H_2O \quad \text{(VIII.3)}$$

However, this evolution of NH_4^+ concentration was unexpected (**Fig. 7(b)**). Chloride was initially present in the RW ($N_{Cl^-}/N_{NH_4^+} \geq 100$), surpassing the break point of 7.6 **[29]**, but the NH_4^+ did not react with mediated chlorine oxidants to produce chloramines (**Eqs. (VII.26)-(VII.28)**), NO_3^- (**Eq. (VII.30)**) and N_2 (**Eq. (VII.31)**).

$$HClO + NH_4^+ \rightarrow NH_2Cl + H_2O + H^+ \quad \text{(VII.26)}$$

$$NH_2Cl + HClO \rightarrow NHCl_2 + H_2O \quad \text{(VII.27)}$$

$$NH_2Cl + HClO \rightarrow NCl_3 + H_2O \quad \text{(VII.28)}$$

$$NH_4^+ + 4HClO \rightarrow NO_3^- + H_2O + 6H^+ + 4Cl^- \quad \text{(VII.30)}$$

$$2NH_4^+ + 3HClO \rightarrow N_2 + 3H_2O + 5H^+ + 3Cl^- \quad \text{(VII.31)}$$

Consequently, NH_4^+ concentration increased over the course of electro-oxidation, unlike the case using stainless steel. This finding could be explained by a low production of free chlorine (0.43 mg-Cl_2 L^{-1}) when carbon paper was used compared with the stainless steel cathode (27.5 mg-Cl_2 L^{-1}) (**Fig. VIII.7(c)**). Despite of that, the Cl^- content of the effluent decreased by 18% more using carbon paper compared with stainless steel cathode (**Fig. VIII.7(d)**). In the meantime, the ClO_3^- and ClO_4^- concentrations increased. 179 mg-ClO_3^- L^{-1} and 11 mg-ClO_4^- L^{-1} were measured under carbon paper setup, whereas 193 mg-ClO_3^- L^{-1} and 4.7 mg-ClO_4^- L^{-1} were dosed under stainless steel configuration. Marginally lower ClO_3^- by 7.3% and 2.3 times more ClO_4^- were produced using carbon paper. It could be deduced that when porous carbon paper was used as cathode, the production of free chlorine via **Eqs. (VII.23)-(VII.25)** were much slower than the decomposition of free chlorine through **Eqs. (VII.37)-(VII.40)**, **Eqs. (VII.43)-(VII.44)**, **Eqs. (VII.53)-(VII.54)** and **(VII.56)-(VII.57)** as well as **Eqs. (VII.60)** and **(VII.66)**.

$$Cl^- \rightarrow Cl_2 + 2e^- \quad \text{(VII.23)}$$

$$Cl_2 + H_2O \rightarrow HClO + H^+ + Cl^- \quad \text{(VII.24)}$$

$$\frac{1}{2}Cl_2 + H_2O \rightarrow HClO + H^+ + e^- \quad \text{(VII.25)}$$

$$6HClO + 3H_2O \rightarrow 2ClO_3^- + 4Cl^- + \frac{3}{2}O_2 + 12H^+ + 6e^- \quad \text{(VII.37)}$$

$$HClO + 2ClO_2 + H_2O \rightarrow 2ClO_3^- + HCl + 2H^+ \quad \text{(VII.38)}$$

$$HClO \rightarrow ClO_3^- + HCl + Cl^- \quad \text{(VII.39)}$$

$$HClO + H_2O \rightarrow ClO_2^- + 3H^+ + 2e^- \quad \text{(VII.40)}$$

$$\frac{1}{2}Cl_2 + 3H_2O \rightarrow ClO_3^- + 6H^+ + 5e^- \quad \text{(VII.43)}$$

$$3Cl_2 + 3H_2O \rightarrow ClO_3^- + 5Cl^- + 6H^+ \quad \text{(VII.44)}$$

$$Cl_2 + 4H_2O \rightarrow 2ClO_2 + 8e^- \quad \text{(VII.53)}$$

$$\frac{1}{2}Cl_2 + 2H_2O \rightarrow HClO_2 + 3H^+ + 3e^- \quad \text{(VII.54)}$$

$$HClO + H_2O \rightarrow HClO_2 + 2H^+ + 2e^- \quad \text{(VII.56)}$$

$$HClO_2 \rightarrow ClO_2 + H^+ + e^- \quad \text{(VII.57)}$$

$$HClO + {\bullet}OH \rightarrow {\bullet}ClO + H_2O \quad \text{(VII.60)}$$

$$ClO^- + {\bullet}OH \rightarrow ClO_2^- + H^+ + e^- \quad \text{(VII.66)}$$

Moreover, the formation of ClO_3^- would not only be due to the fast oxidation of HClO/ClO^- and Cl_2 to ClO_3^- (**Eqs. (VII.37)-(VII.39)**) and (**Eqs. (VII.43)-(VII.44)**) respectively, but also from direct oxidation of Cl^- to ClO_3^- (**Eq. (VII.42)**):

$$Cl^- + 3H_2O \rightarrow ClO_3^- + 6H^+ + 6e^- \quad \text{(VII.42)}$$

Judging from higher concentration of ClO_4^- under the carbon paper compared with the stainless steel setup, it could also be concluded that the transformation of ClO_4^- from ClO_3^- (**Eqs. (VII.45)** and **(VII.68)**) were faster in the porous condition. It therefore contributed to higher ClO_4^- concentration and in the same time lower ClO_3^- content in the treated media (**Fig. VIII.7(e)** vs. **Fig. VIII.7(f)**).

$$ClO_3^- + H_2O \rightarrow ClO_4^- + 2H^+ + 2e^- \quad \text{(VII.45)}$$

$$ClO_3^- + \bullet OH \rightarrow ClO_4^- + H^+ + e^- \quad \text{(VII.68)}$$

Figure VIII.8 depicts the SEM images of precipitate formed on the porous carbon paper after the 5 h-electrolysis of BE and RW at 200 mA. SEM could only be done on the carbon paper because stainless steel cathode could not be cut into the form of the SEM sampler for the analysis without affecting its surface. The morphologies of the raw carbon paper (as control) at different magnifications are provided in **Figs. VIII.8(a)** and **VIII.8(b)**. With the benefit of EDX technique coupled to the SEM, 96.75 wt% of C was detected on the unused carbon paper sample with only 0.06 wt% Mg and 0.14 wt% Ca. After 5 h of electrolysis of BE (**Figs. VIII.8(c)** and **VIII.8(d)**), it was observed that $CaCO_3$ precipitated under cubic formed crystals typical of calcite allotropy. It was in agreement with the reports across literature given that the applied cathode potential (-1.40 V/Ag-AgCl) was in the region of reduction of water **[30, 31]**. It has also been reported that, in the presence of Mg^{2+}, the growth of calcite crystals was slowed down and $CaCO_3$ would preferentially take aragonite allotropy involving needle-like crystals **[20, 32-35]**. However, the Mg^{2+} concentration in our investigated system was too low to provoke significant change in calcite crystallography. Elementary analysis provided by EDX indicated that 1.23 wt% Mg and 40.39 wt% Ca was quantified on the carbon paper. The C wt% deposited on carbon paper that might belong to carbonate precipitate could not be precisely quantified due to the interference of C that might come from the carbon paper itself. In addition, **Figs. VIII.8(c)** and **VIII.8(d)** illustrate the morphology of electro-precipitate occurred after the electro-oxidation treatment of RW. It was noticed that in the presence of numerous ions and organics, the cubic feature of calcite allotropy slightly perished. Some part of the $CaCO_3$ deposition took irregular crystal form which might be a sign of co-precipitation with organic matter and/or phosphates as suggested by several authors **[19, 33, 34, 36-38]**. Further analysis using EDX indicated that 64.3 wt% of Ca and 0.90 wt% of Mg were present on the sampled carbon paper. About 0.61 wt% P was quantified compared to 0.08 wt% of P present on unused carbon paper control. However, the analyzed weight percentage of phosphorus presented high source of error since the concentration of PO_4^{3-} was very low relatively to that of Ca^{2+}. Moreover, the calcium phosphate deposition could take place anywhere on the 50 cm^2 geometric surface area of the carbon paper, i.e., 175 cm^2 electroactive surface area. This made difficult the detection of P within the material.

In summary, the use of highly porous cathode did not actually bring positive impact towards the minimization of electro-precipitation. This was due to (1) quicker $CaCO_3$ electro-precipitation that could occur when carbon paper served as cathode, (2) higher formation of ClO_3^- and ClO_4^- during the treatment, in addition to (3) the acidic environment produced at the end of the electrochemical process. Quick formation of $CaCO_3$ has to be avoided as it could rapidly passivate the cathode surface.

ClO_3^- and ClO_4^- are the well-known nocuous chlorinated byproducts and their formation is undesirable from the regulatory perspective. The acidic post-treatment condition might be favorable to re-dissolve the electro-precipitate formed on cathode surface, but it is not an efficient way to undo the passivated depositions. Most of the deposit remained on carbon paper despite minor re-dissolution into the bulk. Furthermore, the acidic environment would call for an additional treatment to neutralize the treated media before it could be released back into the environment.

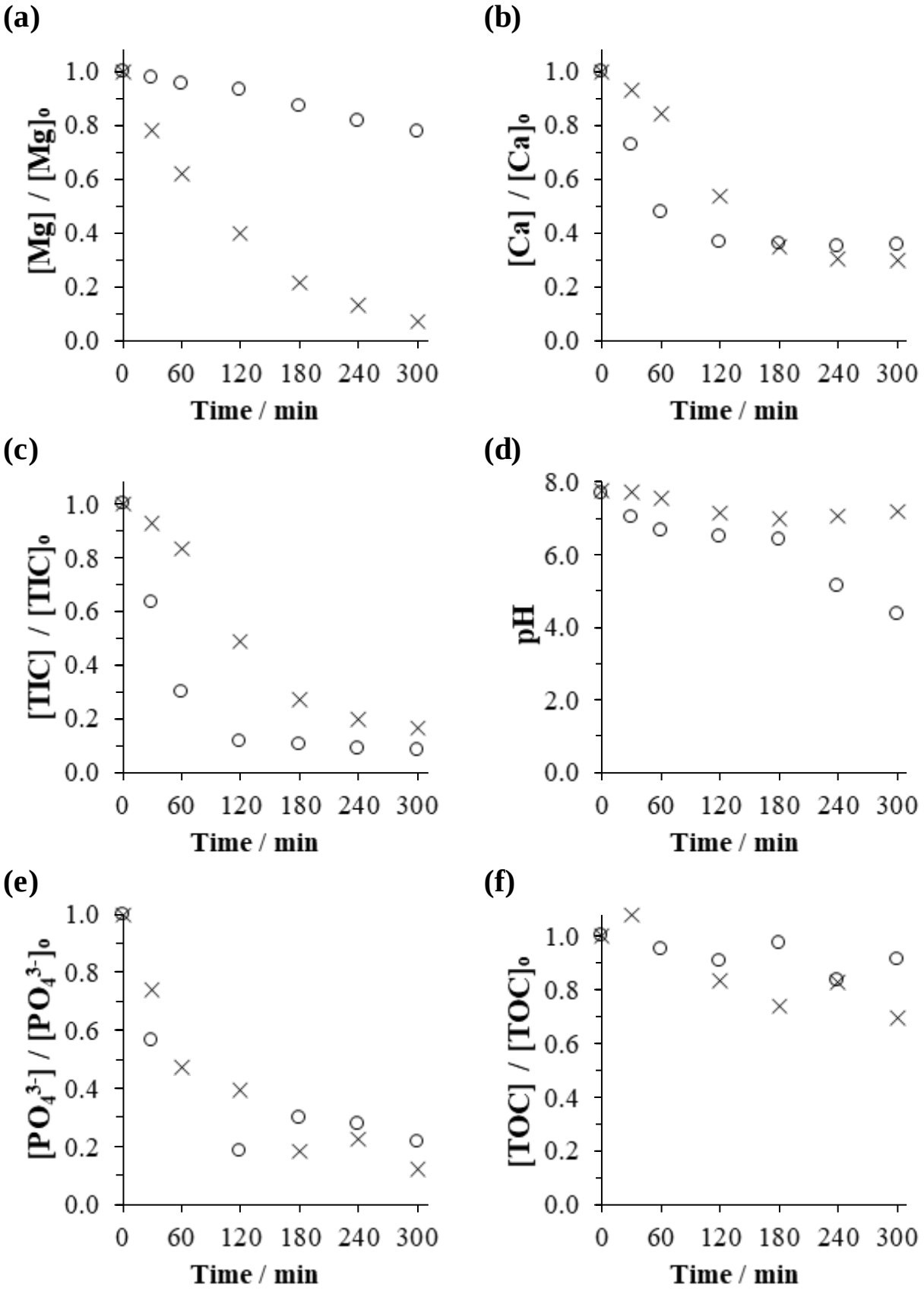

Fig. VIII.6. Concentrations of **(a)** Mg^{2+}, **(b)** Ca^{2+}, **(c)** TIC, **(d)** effluent bulk pH, **(e)** PO_4^{3-} and **(f)** TOC during the electro-oxidation treatment of RW at 200 mA applied current on (✕) stainless steel and (○) carbon paper cathode. The properties of RW are given in **Table VII.1** of **Section VII.2**.

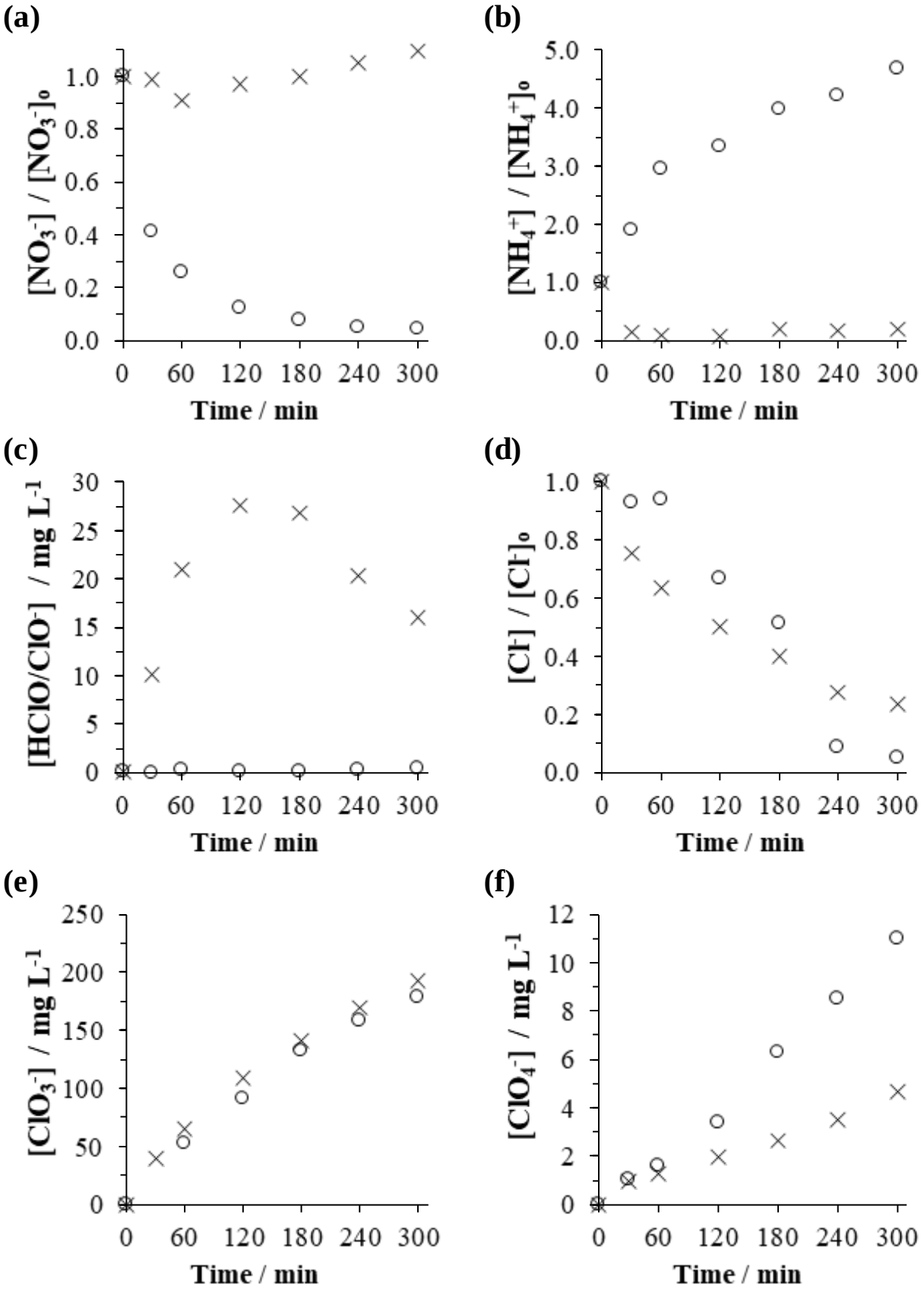

Fig. VIII.7. Concentrations of **(a)** NO_3^-, **(b)** NH_4^+, **(c)** HClO/ClO^-, **(d)** Cl^-, **(e)** ClO_3^- and **(f)** ClO_4^- during the electro-oxidation treatment of RW at 200 mA applied current on (✕) stainless steel and (○) carbon paper cathode. The properties of RW are given in **Table VII.1** of **Section VII.2**.

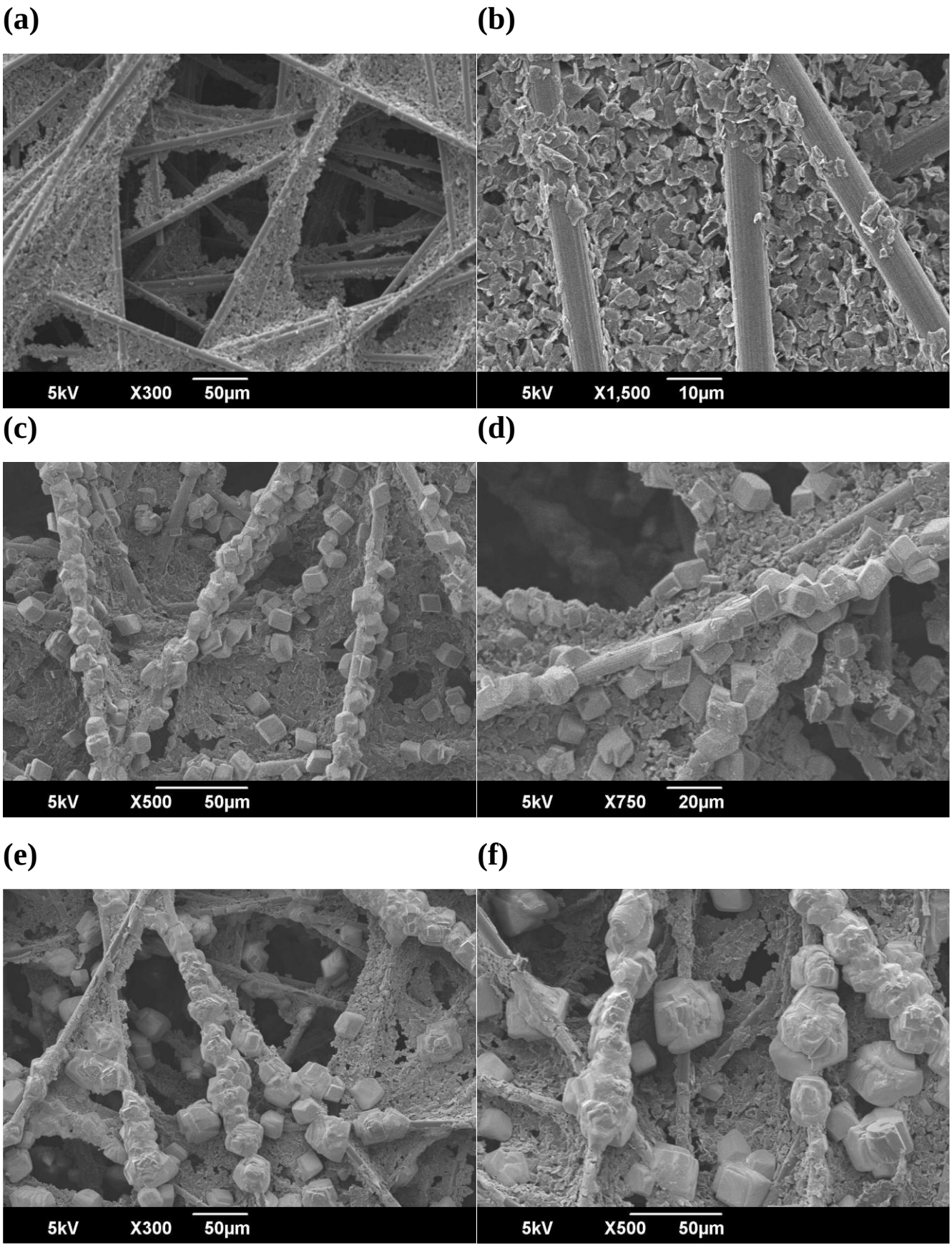

Fig. VIII.8. SEM of unused carbon paper (control) (**(a)**, **(b)**) and electro-precipitate formed on carbon paper after 5 h electrolysis of BE (**(c)**, **(d)**) and RW (**(e)**, **(f)**). I_{app}: 200 mA.

VIII.3.2. Role of H_2 evolution overpotential: synergistic effect of interelectrode distance and cathode material to reduce electro-precipitation

It has been demonstrated across **Section VIII.3.1** that by using a more porous cathode, it works in favor of mineral electro-precipitation. It corroborates the fact that porous cathode offers high electroactive surface, which enhances chemical and electrochemical reactions. As a consequence, if the formation of electro-precipitation is intended, porous cathode is the go-to option. Contrastingly, if the depreciation of mineral electro-precipitation is sought after, which is rather the case with the EAOPs in order to increase their life span, using cathode with high porosity might yield antagonistic consequences.

In this section, another property of carbonaceous material has been explored. Carbonaceous material such as carbon felt, graphite felt, vitreous carbon and graphite rod are known to possess higher overpotential for water reduction **[7]**. Consequently, wider potential window under cathodic range prior to H_2 evolution is achieved. That is the reason why carbonaceous materials have been receiving specific attention for a variety of applications (e.g. Fenton-based technology **[28, 39-42]**, non-Fenton catalytic degradation of organics **[43, 44]**, electrosorption **[45]** as well as fuel cells and batteries **[3, 46, 47]**) benefiting both their lower cost and environmentally-friendly properties. Moreover, it has been shown in **Chapter 6** that, the electro-precipitation occurs with concomitant HER **[20, 23, 32, 48, 49]** which results in deposit detachment from cathode surface **[23, 48, 50, 51]**. In that regards, carbonaceous cathode is of no exemption. Due to determinant role of concurrent gas evolution taking an effect on electro-precipitation formation, the overpotential of H_2 evolution offered by a carbonaceous material was further explored. Graphite plate, a low porosity carbonaceous electrode (~15%) was used as cathode to meet the objective. The kinetics of electro-precipitation taking place on graphite together with stainless steel plate were compared under both submillimetric and millimetric configurations to inspect the inter-relation between interelectrode gap and H_2 overpotential. The mechanistic understanding at the cathode/electrolyte interface is further deepened through electrochemical impedance analysis presented in **Section VIII.3.2.2**.

VIII.3.2.1. Electro-precipitation on stainless steel and graphite at different interelectrode distances

Figure VIII.9 shows the evolution of Mg^{2+}, Ca^{2+} and TIC deposited during the electrolysis at 200 mA, when either graphite or stainless steel plates were used as cathode. From the plot of Mg^{2+} concentration evolution in **Fig. VIII.9(a)**, it was observed that more Mg^{2+} electro-precipitated using 500 µm d_{elec} in comparison with 3000 µm setup. Using 500 µm, comparable Mg^{2+} electro-

precipitation was noticed between stainless steel (91.0 ± 1.8%) and graphite (89.1 ± 2.2%). When 3000 µm d_{elec} was equipped, Mg^{2+} precipitated by 81.1 ± 0.2% and 82.6 ± 2.8% on stainless steel and graphite, respectively. Under the 100 µm setup, a different behavior was noticed. 85.6 ± 2.6% of Mg^{2+} precipitated on stainless steel which was comparable to that evaluated using 500 µm setup considering the standard deviations. Contrastingly, only 6.3 ± 0.1% of Mg^{2+} was deposited on graphite cathode. In addition, the evolution of Ca^{2+} concentration is depicted in **Fig. VIII.9(b)**. Reproducible trends of Ca^{2+} deposition, relatively to the aforementioned Mg^{2+} deposition, were noted for the reactor configurations with both 500 µm and 3000 µm interelectrode gaps. More Ca^{2+} precipitation occurred under the configuration of 500 µm compared to that of 3000 µm. Under the 500 µm configuration, Ca^{2+} deposited by 43.2 ± 5.6% on stainless steel, whereas it precipitated slightly more on graphite cathode (i.e., by 46.7 ± 1.2%). In comparison with the 3000 µm d_{elec}, Ca^{2+} precipitated by 36.2 ± 1.6% on stainless steel versus 40.0 ± 3.3% on graphite. Surprisingly, when 100 µm d_{elec} was used, a conflicting behavior was noticed again. It corresponded to the configuration in which $CaCO_3$ electro-precipitate occurred the most at stainless steel cathode (55.1 ± 2.2%), compared with graphite electrode (9.0 ± 1.2%). The evolution of TIC concentrations illustrated in **Fig. VIII.9(c)** followed similar deduction drawn for the fate of Ca^{2+}. TIC decreased the most under the configuration of 100 µm d_{elec} with stainless steel as cathode. Comparatively, more carbonate deposition occurred under the 500 µm d_{elec} setup as compared to the 3000 µm, with marginally more electro-precipitation evaluated on graphite cathode in comparison to stainless steel for both d_{elec}.

To recapitulate, more electro-precipitates was formed under the 500 µm configuration (microfluidic) in comparison to that of 3000 µm (millimetric) and slightly more electro-precipitation took place on graphite cathode relatively to the stainless steel. The worst electro-precipitation occurred using 100 µm (microfluidic) d_{elec} but only when stainless steel was used as cathode. Contrastingly, the slowest electro-precipitation was found also using the 100 µm d_{elec} but with graphite on cathode. Upon these results, two general conclusions could be assumed: (1) interelectrode distance played determining role towards the formation of electro-precipitation and (2) under very particular operating condition (i.e., submillimetric d_{elec} equals or lower than 100 µm), graphite properties could help to reduce the kinetics of deposition unlike any other experimental conditions.

To further understand this disparity of electro-precipitation in function of cathode material as well as d_{elec}, the polarization curves in cathodic region on stainless steel and graphite at 100, 500 and 3000 µm gaps were performed (**Fig. VIII.10**). According to **Fig. VIII.10(a)**, it was observed that the HER overpotential was lower using graphite cathode in comparison to stainless steel at 500 µm d_{elec}. As a result, when 200 mA current was applied (i.e., 4 mA cm^{-2}), approximately -1.54 V/Ag-AgCl was measured on stainless steel, whilst -1.72 V/Ag-AgCl was quoted on graphite. Similarly, according to

Fig. VIII.10(b), when the cell was used with 3000 µm d_{elec}, the H_2 overpotential was also lower at 200 mA on graphite (-1.97 V/Ag-AgCl) than on stainless steel (-1.91 V/Ag-AgCl) cathodes. On one hand, the significantly lower applied cathode potential (into the water reduction region) measured under the macrometric reactor setup (3000 µm) could explain the lesser degree of electro-precipitation under this configuration. Intense competitive H_2 evolution on cathode surface reduced the reactive site for precipitating reactions and in the same time induced partial deposit detachment from the cathode surface. This observation follows the deduction made in **Chapter 6**, where the role of d_{elec} was thoroughly discussed and modeled. On the other hand, it was also noted that the applied cathode potential was marginally lower on graphite than on stainless steel (**Figs. VIII.10(a)** and **VIII.10(b)**). This led to slightly enhanced OH^- ions production from the water reduction reaction on graphite (**Eq. (II.10)**). As a consequence, there was a marginally higher driving force of thermodynamic shift of **Eqs. (II.11)-(II.13)** to the right, in the direction of mineral scaling production. Furthermore, it has been demonstrated that graphite inherits porous characteristic. It offered slightly enhanced electroactive surface area for electronic transfers (85 vs. 80 cm^2 of stainless steel (**Section VIII.3.1.1**)), which could lead to better electrochemical and/or chemical reactions. Local pH on graphite was also slightly higher than that achieved on stainless steel due to slight retardation of OH^- diffusion into the bulk. This led to better CO_3^{2-} conversion for $CaCO_3$ precipitation reaction in the case of graphite. These arguments could justify the fact that more deposition was quantified on graphite rather than on stainless steel at 3000 µm and 500 µm d_{elec}. On the contrary, reversal trend was noticed in the case where the microfluidic cell was equipped with 100 µm d_{elec}. In accordance with **Fig. VIII.10(c)**, it was observed that the HER overpotential was higher on graphite rather than on stainless steel cathode. Consequently, the cathode potential was measured at -1.33 V/Ag-AgCl on graphite against -1.45 V/Ag-AgCl on stainless steel when 200 mA was applied. Subsequently, less OH^- ions were produced on graphite, which significantly lowered the kinetics of $Mg(OH)_2$ and $CaCO_3$ deposition. Therefore, this finding might explain the contrasting observations made between the two cathode materials when 100 µm d_{elec} was adopted. This was the only condition where the carbonaceous graphite would substantially minimize the formation of mineral scaling.

The difference in the occurrence of mineral scaling on graphite and stainless steel inside microfluidic and millimetric reactors could be further emphasized by the evolution of bulk pH during the electrolysis (**Fig. VIII.9(d)**). The decreasing pH value correlated with the OH^- ion consumption by **Eqs. (II.11)** and **(II.12)** to form mineral precipitates. The more pH decreased, the more electro-precipitate formed on cathode surface, which was in agreement with the curves depicted in **Figs. VIII.9(b)** and **VIII.9(c)**. Only bulk pH corresponding to the microfluidic setup (100 µm) using graphite cathode increased over time. It corroborated with the fact that this was the only configuration where sluggish mineral scaling was observed (**Fig. VIII.9**). The pH evolution depicted in **Fig.**

VIII.9(d) again confirmed the accumulation of OH^- near porous cathode when graphite was used, which resulted in increasing H^+ accumulation in the bulk **[17]**. Thus, the pH dropped.

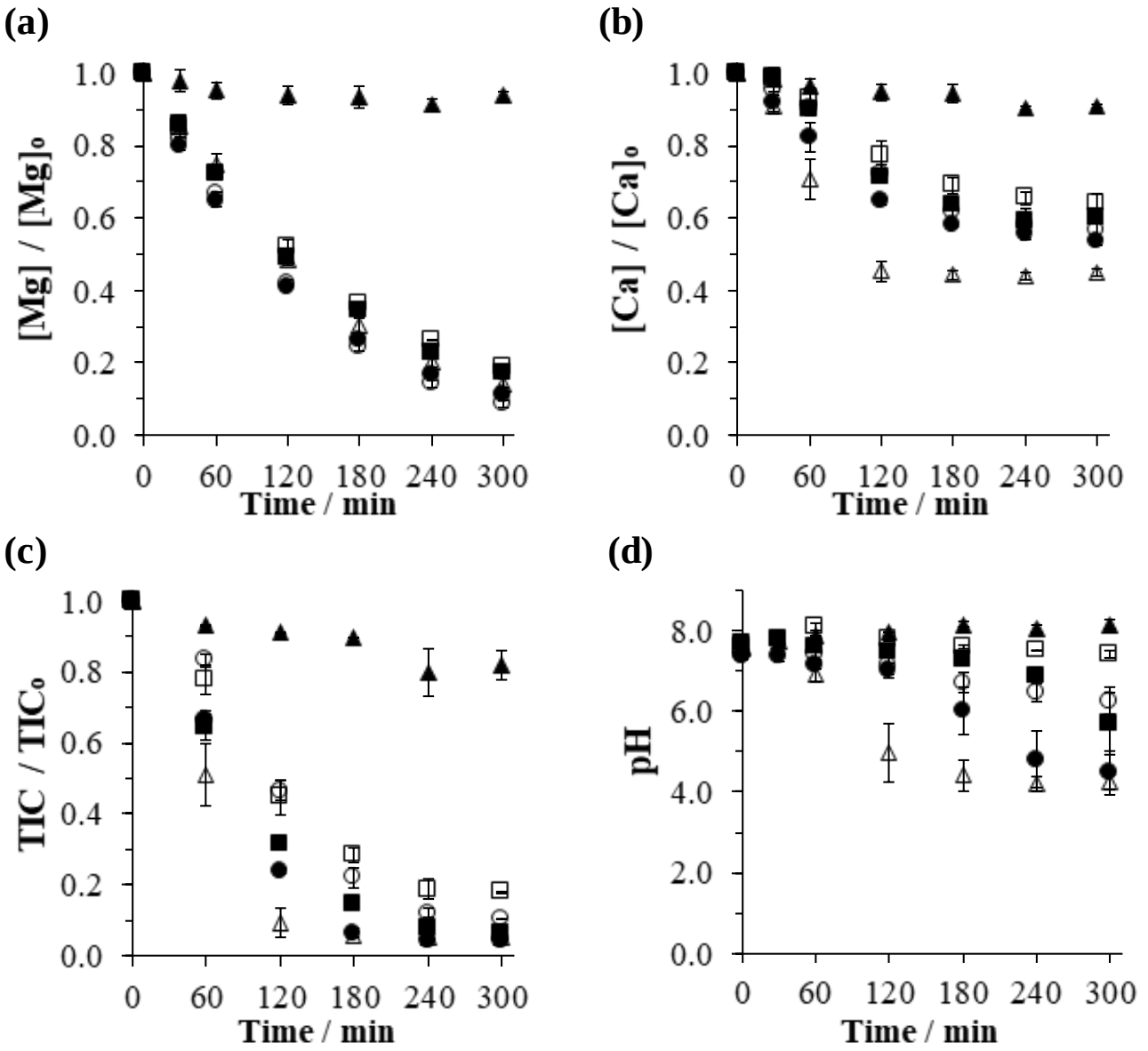

Fig. VIII.9. Concentrations of **(a)** Mg^{2+}, **(b)** Ca^{2+}, **(c)** TIC and **(d)** bulk pH during the electrolysis of solution initially containing 150 mg L^{-1} Ca^{2+}, 5 mg L^{-1} Mg^{2+} and 60 mg-C L^{-1} of TIC at 200 mA. d_{elec} of (△, ▲): 100, (○, ●): 500 and (□, ■): 3000 µm were evaluated using (▲, ●, ■): graphite and (△, ○, □): stainless steel cathode. Anode: BDD.

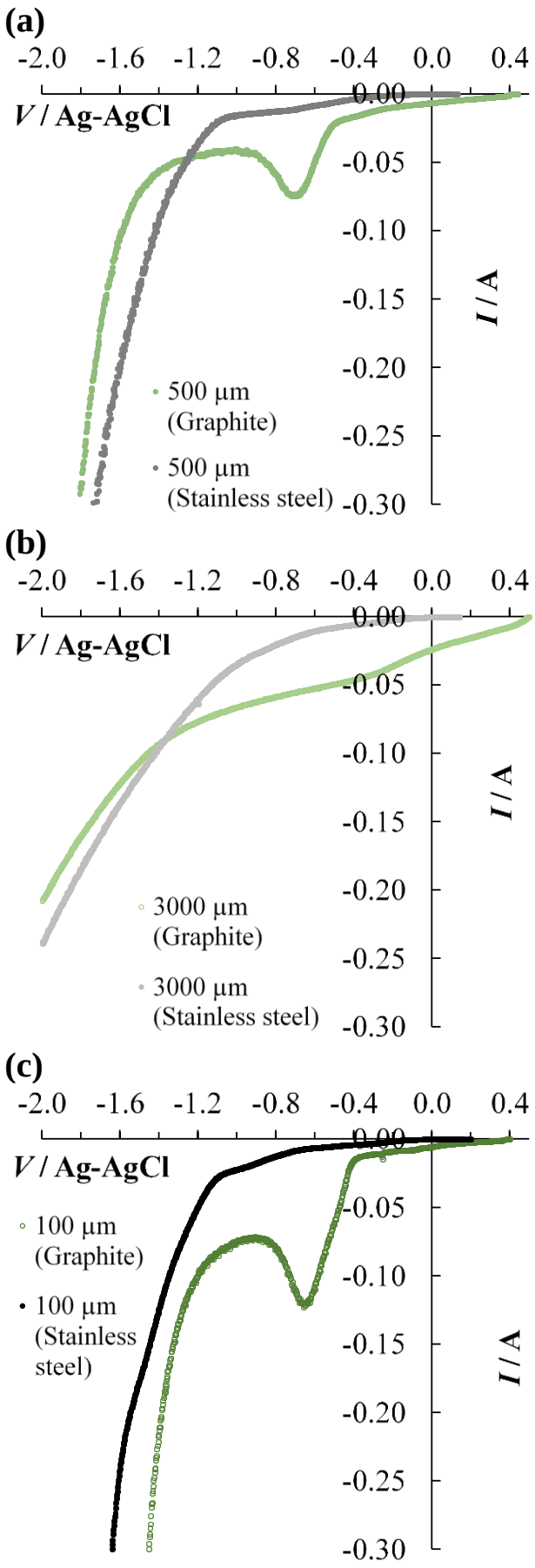

Fig. VIII.10. LSV of stainless steel and graphite plate cathodes when they were assembled in an electrochemical cell with **(a)** 500, **(b)** 3000 and **(c)** 100 µm d_{elec}. The potential was swept between 0.5 to -1.8 V/Ag-AgCl with a scan rate of 10 mV s^{-1}. CE: BDD, RE: Ag-AgCl.

VIII.3.2.2. Cathode/electrolyte interface study of electro-precipitation on graphite and stainless steel by electrochemical impedance technique

EIS analysis was performed on graphite and compared to stainless steel in order to characterize mineral electro-precipitation during the electrolysis at 100, 500 and 3000 µm interelectrode gaps. The evolutions of R_{CT} and C_{DL} using graphite cathode are plotted in **Fig. VIII.11**. It can be noticed that the values of R_{CT} appeared constant during the electrolysis for all three d_{elec} (**Figs. VIII.11(a)**, **VIII.11(c)** and **VIII.11(e)**). R_{CT} measured on graphite took the average values of 0.42 ± 0.10, 0.88 ± 0.05 and 2.96 ± 0.10 Ω respectively, when 100, 500 and 3000 µm d_{elec} were used. Despite the formation of electro-precipitation in the configurations of 500 and 3000 µm, the graphite surface was also not fully passivated. This was in-trend with the conclusion obtained in **Chapter 6**, using stainless steel as cathode. As for the evolution of C_{DL} illustrated in **Figs. VIII.11(b)**, **VIII.11(d)** and **VIII.11(f)**, it was noticed that they rather increased during the electrolysis unlike the evolution of C_{DL} on stainless steel cathode. It increased by 58, 76 and 37% in the respective order of 100, 500 and 3000 µm reactor configuration. This increase of C_{DL} values had no significant relation with the formation of electro-precipitate since it also increased when 100 µm d_{elec} was used (a condition where the least mineral scaling took place). Instead, it has something to do with the porosity of graphite and will be discussed shortly when it is compared to the stainless steel cathode. With respect to the evolution of film resistance (R_F) formed on graphite during the electrolysis plotted in **Fig. VIII.12**, it was observed that R_F increased during the first 2 h of electrolysis to 0.29 ± 0.01 and 0.43 ± 0.15 Ω for 500 and 3000 µm setup, respectively. It was expected to measure higher R_F value using 500 µm d_{elec} since marginally more scaling occurred at this distance, but the opposite trend was observed. Nonetheless, after 2 h electrolysis, reproducible trend was noticed on both interelectrode gaps in line with the kinetics of precipitation previously discussed in **Section VIII.3.1.2** and **Section VIII.3.2.1**. R_F values in both conditions decreased and it could be ascribed to the evolution of bulk pH in reference to **Fig. VIII.9(d)**. The fact that the electro-precipitate had the possibility to re-dissolve into the solution made decrease the apparent resistance related to the precipitated film. This might be the reason why R_F values decreased in both d_{elec} after 2 h of electrolysis as depicted in **Fig. VIII.12**.

Upon comparing the interfacial activities between graphite and stainless steel, some differences could be highlighted. The ratio of R_{CT} and C_{DL} values between graphite and stainless steel for all investigated d_{elec} configurations are illustrated in **Fig. VIII.11**. It can be observed that R_{CT} values on graphite were lower than those on stainless steel, i.e., averagely by 0.6-fold, 0.8-fold and 0.7-fold using 100, 500 and 3000 µm, respectively in all conditions. This lower R_{CT} value characterized by EIS on graphite relatively to that on stainless steel confirmed the similar deduction on R_{CT} comparison in **Section VIII.3.1.1** using I_0 method. On the contrary, C_{DL} values were higher on graphite in

comparison to the values measured on stainless steel by an average factor of 2.7, 1.1 and 1.5 using 100, 500 and 3000 µm, respectively. These differences were accounted for the porous properties of graphite. Due to the higher specific surface area of electrode/electrolyte interface using graphite (85 vs. 80 cm^2 for stainless steel, (**Section VIII.3.1.1**)), more active sites were available for electronic exchange at the interface. Consequently, R_{CT} decreased and C_{DL} increased. This finding was in agreement with the results documented by Da Silva et al. **[52]**. They found that C_{DL} value measured on porous metal oxide electrode was significantly reduced when the porosity of the electrode was decreased.

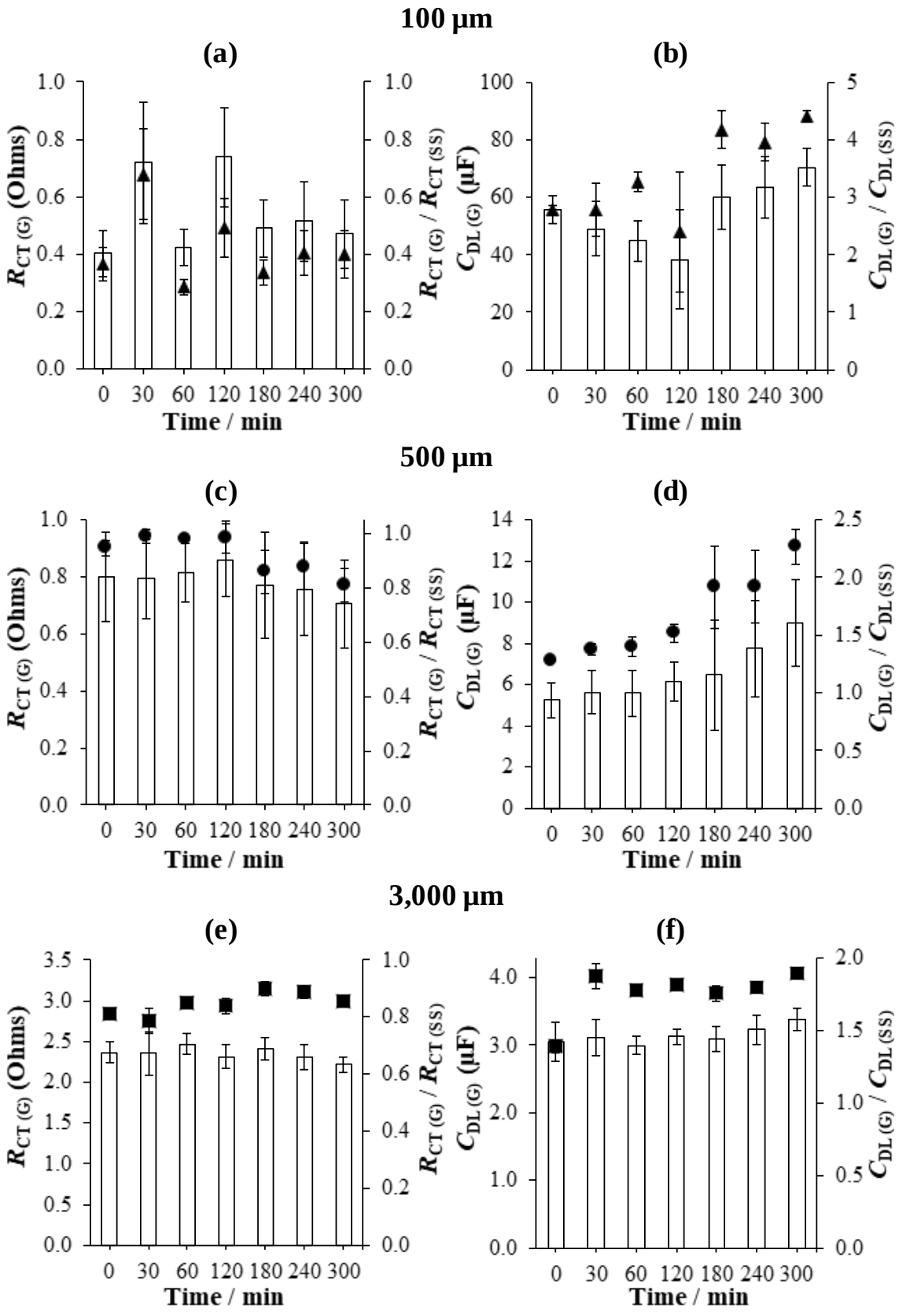

Fig. VIII.11. Evolutions of $R_{CT(G)}$ (▲, ●, ■) and $R_{CT(G)}/R_{CT(SS)}$ (□) (**(a)**, **(c)**, **(e)**) as well as $C_{DL(G)}$ (▲, ●, ■) and $C_{DL(G)}/C_{DL(SS)}$ (□) (**(b)**, **(d)**, **(f)**) during the electrolysis of solution containing Ca^{2+} 150 mg L^{-1}, Mg^{2+} 5 mg L^{-1} and TIC 60 mg L^{-1}. (▲): 100 µm (**(a)**, **(b)**), (●): 500 µm (**(c)**, **(d)**) and (■): 3000 µm (**(e)**, **(f)**). G: graphite and SS: stainless steel.

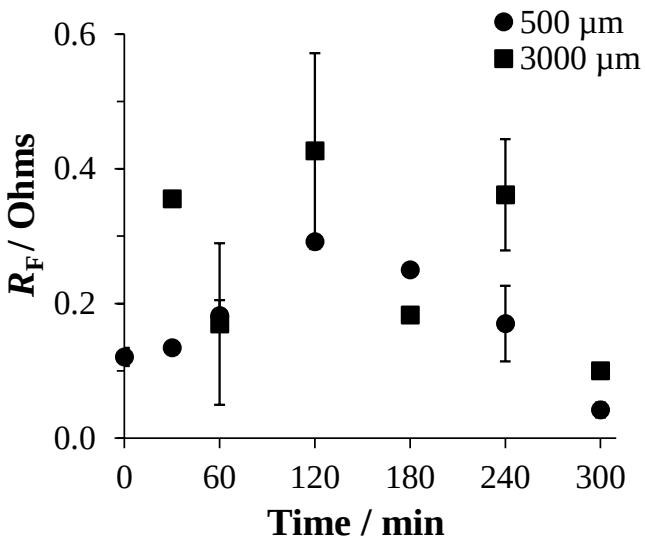

Fig. VIII.12. Evolutions of R_F during the electrolysis of solution initially containing Ca^{2+} 150 mg L^{-1}, Mg^{2+} 5 mg L^{-1} and TIC 60 mg L^{-1}. (●): 500 and (■): 3000 µm. WE: graphite, CE: BDD and RE: Ag-AgCl.

VIII.4. Conclusions

The role of cathode materials was meticulously investigated in this chapter. Non-porous and non-carbonaceous stainless steel as well as carbonaceous graphite plate and carbon paper which possessed different porosities were compared. The occurring electro-precipitation on different cathode materials was studied under submillimetric configuration, a condition in which no electro-precipitation results have yet been reported. Moreover, the influence of cathode material, particularly the porosity was examined using real RW. Simultaneously, the fate of chlorinated and nitrogenous inorganic byproducts were followed and quantified. Electroactive surface area of stainless steel, graphite and carbon paper were determined via electrochemical method. A value of 80, 85 and 175 cm^2 was obtained for stainless steel, graphite and carbon paper, respectively. It indicated that different cathode materials offered different number of sites for electronic exchanges on top of having different porosities. Principle results obtained using different cathode materials are as follows:

- $Mg(OH)_2$ precipitated little on stainless steel , graphite and carbon paper at low applied current (20 mA) whilst $CaCO_3$ electro-precipitation was formed only on stainless steel and graphite cathode but not on carbon paper.
- Using higher applied current (200 mA), significant precipitation of $Mg(OH)_2$ was observed on stainless steel and graphite, but low precipitation on carbon paper. However, quick $CaCO_3$ deposition was noted on carbon paper. Meanwhile, slightly favored $CaCO_3$ electro-precipitation on graphite in comparison to stainless steel was observed and it was ascribed to higher local pH due to porous characteristic of graphite.
- When porous carbon paper and non-porous stainless steel were used to treat RW, comparable mechanism of electro-precipitation was noticed compared to the BE. Marginal less organics mineralization was achieved using carbon paper.
- Lower HER overpotential would only lead to more formation of electro-precipitation. It was due to enhanced OH^- production that would consequently favor the mineral scaling. Slightly less mineral scaling could be achieved if the HER overpotential was very low into the water reduction region (where the competing H_2 evolution rigorously evolved on cathode surface).
- The role of HER overpotential was overshadowed by the additional rate limiting parameter, i.e., the E_C. When stainless steel was used as cathode under the 100 µm d_{elec} setup, the most electro-precipitation took place. Contrasting, by replacing stainless steel with graphite, the slowest mineral scaling was noticed. It was due to the alteration in cathode potential value where the OH^- production was less favorable.
- Using electrochemical impedance analysis, porous attribute of graphite was evidenced. Higher C_{DL} was determined on graphite compared to stainless steel. Lower R_{CT} measured on graphite

proved that better electronic transfers take place on graphite in comparison with stainless steel cathode.

In overall, due to rapid $CaCO_3$ deposition, high conversion rate of Cl^- into ClO_3^- and ClO_4^- as well as acidic post-treatment condition, porous carbon paper was not a suitable cathode to be opted for if the minimization of electro-precipitation is sought. Even though carbonaceous material such as graphite presents an economical edge, its use only resulted in worse appearance of mineral scaling. Nonetheless, it has been proven herein that slow kinetic growth of deposit could however be devised using graphite or other materials under the condition where the applied cathode potential does not favor the OH^- production.

References

[1] P. Simon, Y. Gogotsi, Materials for electrochemical capacitors, Nature Materials, 7 (2008) 845-854.
[2] R.L. McCreery, Advanced carbon electrode materials for molecular electrochemistry, Chemical Reviews, 108 (2008) 2646-2687.
[3] C. Hu, L. Dai, Carbon-based metal-free catalysts for electrocatalysis beyond the ORR, Angewandte Chemie International Edition, 55 (2016) 11736-11758.
[4] F. Yin, W. Yue, Y. Li, S. Gao, C. Zhang, H. Kan, H. Niu, W. Wang, Y. Guo, Carbon-based nanomaterials for the detection of volatile organic compounds: A review, Carbon, 180 (2021) 274-297.
[5] F.C. Moreira, R.A.R. Boaventura, E. Brillas, V.J.P. Vilar, Electrochemical advanced oxidation processes: A review on their application to synthetic and real wastewaters, Applied Catalysis B: Environmental, 202 (2017) 217-261.
[6] O. Garcia-Rodriguez, E. Mousset, H. Olvera-Vargas, O. Lefebvre, Electrochemical treatment of highly concentrated wastewater: A review of experimental and modeling approaches from lab- to full-scale, Critical Reviews in Environmental Science and Technology, (2020) 1-70.
[7] E. Mousset, Z. Wang, J. Hammaker, O. Lefebvre, Physico-chemical properties of pristine graphene and its performance as electrode material for electro-Fenton treatment of wastewater, Electrochimica Acta, 214 (2016) 217-230.
[8] T.X.H. Le, M. Bechelany, S. Lacour, N. Oturan, M.A. Oturan, M. Cretin, High removal efficiency of dye pollutants by electron-Fenton process using a graphene based cathode, Carbon, 94 (2015) 1003-1011.
[9] A.J. Bard, Faulkner, L.R., Double-layer structure and adsorption, in: J.W.S. Inc. (Ed.) Electrochemical methods: Fundamentals and applications, (2001), pp. 534.
[10] H. Saraç, M.A. Patrick, A.A. Wragg, Physical properties of the ternary electrolyte potassium ferri-ferrocyanide in aqueous sodium hydroxide solution in the range 10–90°C, Journal of Applied Electrochemistry, 23 (1993) 51-55.
[11] A.A. Wragg, A.A. Leontaritis, Local mass transfer and current distribution in baffled and unbaffled parallel plate electrochemical reactors, Chemical Engineering Journal, 66 (1997) 1-10.
[12] M. Griffiths, C.P. de León, F.C. Walsh, Mass transport in the rectangular channel of a filter-press electrolyzer (the FM01-LC reactor), American Institute of Chemical Engineers, 51 (2005) 682-687.
[13] A.J. Bard, Faulkner, L.R., Kinetics of electrode reactions, in: J.W.S. Inc. (Ed.) Electrochemical methods: Fundamentals and applications2001, pp. 87.
[14] K. Oldham, J. Myland, A. Bond, Electrode Polarization, Electrochemical science and technology: fundamentals and applications, John Wiley & Sons2011, pp. 193.
[15] F.H. Adnan, E. Mousset, S. Pontvianne, M.-N. Pons, Mineral cathodic electro-precipitation and its kinetic modelling in thin-film microfluidic reactor during advanced electro-oxidation process, Electrochimica Acta, (2021) 138487.
[16] J.N. Butler, Carbon dioxide equilibria and their applications, 1st ed., Taylor & Francis Group, New York: Routledge, 1991.
[17] Y. Lei, E. Geraets, M. Saakes, R.D. van der Weijden, C.J.N. Buisman, Electrochemical removal of phosphate in the presence of calcium at low current density: Precipitation or adsorption？, Water Research, 169 (2020) 115207.
[18] Y. Yu, H. Jin, X. Quan, B. Hong, X. Chen, Continuous multistage electrochemical precipitation reactor for water softening, Industrial & Engineering Chemistry Research, 58 (2019) 461-468.
[19] I. Sanjuán, D. Benavente, V. García-García, E. Expósito, V. Montiel, Electrochemical softening of concentrates from an electrodialysis brackish water desalination plant: Efficiency enhancement using a three-dimensional cathode, Separation and Purification Technology, 208 (2019) 217-226.
[20] H. Karoui, B. Riffault, M. Jeannin, A. Kahoul, O. Gil, M. Ben Amor, M.M. Tlili, Electrochemical scaling of stainless steel in artificial seawater: Role of experimental conditions on $CaCO_3$ and $Mg(OH)_2$ formation, Desalination, 311 (2013) 234-240.
[21] C. Deslouis, D. Festy, O. Gil, V. Maillot, S. Touzain, B. Tribollet, Characterization of calcareous deposits in artificial sea water by impedances techniques: 2-deposit of $Mg(OH)_2$ without $CaCO_3$, Electrochimica Acta, 45 (2000) 1837-1845.
[22] Y. Lei, I. Hidayat, M. Saakes, R. van der Weijden, C.J.N. Buisman, Fate of calcium, magnesium and inorganic carbon in electrochemical phosphorus recovery from domestic wastewater, Chemical Engineering Journal, 362 (2019) 453-459.

[23] S.M. Hoseinieh, T. Shahrabi, B. Ramezanzadeh, M.F. Rad, The role of porosity and surface morphology of calcium carbonate deposits on the corrosion behavior of unprotected API 5L X52 rotating disk electrodes in artificial seawater, Journal of The Electrochemical Society, 163 (2016) C515-C529.
[24] Y. Lei, J.C. Remmers, M. Saakes, R.D. van der Weijden, C.J.N. Buisman, Is there a precipitation sequence in municipal wastewater induced by electrolysis?, Environmental Science & Technology, 52 (2018) 8399-8407.
[25] G. Pérez, R. Ibáñez, A.M. Urtiaga, I. Ortiz, Kinetic study of the simultaneous electrochemical removal of aqueous nitrogen compounds using BDD electrodes, Chemical Engineering Journal, 197 (2012) 475-482.
[26] E. Lacasa, J. Llanos, P. Cañizares, M.A. Rodrigo, Electrochemical denitrificacion with chlorides using DSA and BDD anodes, Chemical Engineering Journal, 184 (2012) 66-71.
[27] M.J. Martin de Vidales, M. Millán, C. Sáez, P. Cañizares, M.A. Rodrigo, What happens to inorganic nitrogen species during conductive diamond electrochemical oxidation of real wastewater?, Electrochemistry Communications, 67 (2016) 65-68.
[28] E. Mousset, S. Pontvianne, M.-N. Pons, Fate of inorganic nitrogen species under homogeneous Fenton combined with electro-oxidation/reduction treatments in synthetic solutions and reclaimed municipal wastewater, Chemosphere, 201 (2018) 6-12.
[29] A. Kapałka, A. Katsaounis, N.-L. Michels, A. Leonidova, S. Souentie, C. Comninellis, K.M. Udert, Ammonia oxidation to nitrogen mediated by electrogenerated active chlorine on Ti/PtO_X-IrO_2, Electrochemistry Communications, 12 (2010) 1203-1205.
[30] J. Marin-Cruz, E. Garcia-Figueroa, M. Miranda-Hernández, I. Gonzalez, Electrochemical treatments for selective growth of different calcium carbonate allotropic forms on carbon steel, Water Research, 38 (2004) 173-183.
[31] C. Carré, A. Zanibellato, M. Jeannin, R. Sabot, P. Gunkel-Grillon, A. Serres, Electrochemical calcareous deposition in seawater. A review, Environmental Chemistry Letters, 18 (2020) 1193-1208.
[32] C. Barchiche, C. Deslouis, D. Festy, O. Gil, P. Refait, S. Touzain, B. Tribollet, Characterization of calcareous deposits in artificial seawater by impedance techniques: 3 — deposit of $CaCO_3$ in the presence of Mg(II), Electrochimica Acta, 48 (2003) 1645-1654.
[33] R. Jaouhari, A. Benbachir, A. Guenbour, C. Gabrielli, J. Garcia-Jareno, G. Maurin, Influence of water composition and substrate on electrochemical scaling, Journal of The Electrochemical Society, 147 (2000) 2151-2161.
[34] S. Xu, Structure and morphology of electrodeposited $CaCO_3$: X-ray diffraction and microscopy studies, Journal of The Electrochemical Society, 146 (1999) 3315.
[35] Y. Zhang, R.A. Dawe, Influence of Mg^{2+} on the kinetics of calcite precipitation and calcite crystal morphology, Chemical Geology, 163 (2000) 129-138.
[36] Y. Lei, B. Song, M. Saakes, R.D. van der Weijden, C.J.N. Buisman, Interaction of calcium, phosphorus and natural organic matter in electrochemical recovery of phosphate, Water Research, 142 (2018) 10-17.
[37] C. Deslouis, P. Falaras, O. Gil, M. Jeannin, V. Maillot, B. Tribollet, Influence of clay on calcareous deposit in natural and artificial sea water, Electrochimica Acta, 51 (2006) 3173-3180.
[38] Z. Belarbi, B. Sotta, L. Makhloufi, B. Tribollet, J. Gamby, Modelling of delay effect of calcium carbonate deposition kinetics on rotating disk electrode in the presence of green inhibitor, Electrochimica Acta, 189 (2016) 118-127.
[39] D. Li, T. Zheng, Y. Liu, D. Hou, H. He, H. Song, J. Zhang, S. Tian, W. Zhang, L. Wang, J. Ma, A cost-effective electro-Fenton process with graphite felt electrode aeration for degradation of dimethyl phthalate: Enhanced generation of H_2O_2 and iron recycling that simultaneously regenerates the electrode, Chemical Engineering Journal, 394 (2020) 125033.
[40] H. Dong, B. Dong, L. Sun, Z. Chi, M. Wang, H. Yu, Electro-UV/H2O2 system with RGO-modified air diffusion cathode for simulative antibiotic-manufacture effluent treatment, Chemical Engineering Journal, 390 (2020) 124650.
[41] E. Mousset, L. Frunzo, G. Esposito, E.D.v. Hullebusch, N. Oturan, M.A. Oturan, A complete phenol oxidation pathway obtained during electro-Fenton treatment and validated by a kinetic model study, Applied Catalysis B: Environmental, 180 (2016) 189-198.
[42] E. Mousset, L. Quackenbush, C. Schondek, A. Gerardin-Vergne, S. Pontvianne, S. Kmiotek, M.-N. Pons, Effect of homogeneous Fenton combined with electron transfer on the fate of inorganic chlorinated species in synthetic and reclaimed municipal wastewater, Electrochimica Acta, 334 (2020) 135608.
[43] H. Dong, X. Guo, C. Yang, Z. Ouyang, Synthesis of g-C_3N_4 by different precursors under burning explosion effect and its photocatalytic degradation for tylosin, Applied Catalysis B: Environmental, 230 (2018) 65-76.

[44] X. Guo, H. Dong, T. Xia, T. Wang, H. Jia, L. Zhu, Highly efficient degradation toward tylosin in the aqueous solution by carbon spheres/g-C_3N_4 composites under simulated sunlight irradiation, ACS Sustainable Chemistry & Engineering, 6 (2018) 12776-12786.
[45] X. Su, T.A. Hatton, Electrosorption at functional interfaces: from molecular-level interactions to electrochemical cell design, Physical Chemistry Chemical Physics, 19 (2017) 23570-23584.
[46] H.-D. Lim, D.H. Kim, S. Park, M.E. Lee, H.-J. Jin, S. Yu, S.H. Oh, Y.S. Yun, Magnesiophilic graphitic carbon nanosubstrate for highly efficient and fast-rechargeable Mg metal batteries, ACS Applied Materials & Interfaces, 11 (2019) 38754-38761.
[47] H. Zhou, Y. Shen, J. Xi, X. Qiu, L. Chen, ZrO_2-nanoparticle-modified graphite felt: Bifunctional effects on vanadium flow batteries, ACS Applied Materials & Interfaces, 8 (2016) 15369-15378.
[48] M. Piri, R. Arefinia, Investigation of the hydrogen evolution phenomenon on $CaCO_3$ precipitation in artificial seawater, Desalination, 444 (2018) 142-150.
[49] S.M. Hoseinieh, T. Shahrabi, Influence of ionic species on scaling and corrosion performance of AISI 316L rotating disk electrodes in artificial seawater, Desalination, 409 (2017) 32-46.
[50] C. Gabrielli, M. Keddam, A. Khalil, R. Rosset, M. Zidoune, Study of calcium carbonate scales by electrochemical impedance spectroscopy, Electrochimica Acta, 42 (1997) 1207-1218.
[51] J. Marin-Cruz, R. Cabrera-Sierra, M. Pech-Canul, I. Gonzalez, Characterization of different allotropic forms of calcium carbonate scales on carbon steel by electrochemical impedance spectroscopy, Journal of Applied Electrochemistry, 34 (2004) 337-343.
[52] L.A. da Silva, V.A. Alves, M.A.P. da Silva, S. Trasatti, J.F.C. Boodts, Electrochemical impedance, SEM, EDX and voltammetric study of oxygen evolution on Ir + Ti + Pt ternary-oxide electrodes in alkaline solution, Electrochimica Acta, 41 (1996) 1279-1285.

IX. General conclusions

IX.1. General overview

Submillimetric electrochemical reactors has bright potential to be used in the field of water/wastewater treatment. The micrometric d_{elec} not only intensifies mass transfer at the core of the electrochemical reactor, but also enhances redox reactions in between electrodes. Significant drop in interelectrode gap reduces internal resistance lowering notably the power consumption of the cell. Motivated by genuine interest in the use of microfluidic in the environmental domain, a thorough literature survey (**Chapter 2**) proved that little attention has been given on the occurrence of mineral deposition in submillimetric features. Consequently, it has been the principal goal of the PhD thesis to characterize the kinetics of electro-precipitation in such a reactor design and to explore the influencing parameters around it. The parametric approach has been proven correct as insightful experimental data were exploited. Moreover, theoretical models on mineral scaling kinetics as well as on interfacial properties of scaled cathode/effluent have been proposed.

IX.2. Kinetic models of mineral scaling inside microfluidic reactors

Reliable mathematical models have been proposed in **Chapter 4** and **Chapter 6** to predict the formation of electro-precipitation during the electro-oxidation process. The models took into consideration the j_{app}, electrolyte composition (Mg^{2+}, Ca^{2+}, OH^- and HCO_3^-/CO_3^{2-}) in the bulk as well as the d_{elec} by intermediary of concomitant evolving gas. Using the theoretical models, the experimental and model curves of precipitating Mg^{2+} and Ca^{2+} matched well. Moreover, the interfacial R_{CT} and C_{DL} properties at varying d_{elec} which were acquired experimentally using electrochemical impedance were also fitted under mathematic models. Consequently, the developed models would allow an estimation of the kinetics of mineral scaling as well as the values of R_{CT} and C_{DL} as function of large range of d_{elec} from submillimetric to millimetric ranges.

IX.3. Mass transfer evolution in submillmetric vs. millimetric configuration

Prior to the investigation of electro-precipitation occurring inside electrochemical reactors with varying d_{elec}, the mass transfer evolution while varying the d_{elec} was firstly looked into in **Chapter 5**. It has been demonstrated that k_m significantly increased with decreasing d_{elec}, particularly for interelectrode gap below 1000 µm. It thus defined a quantitative boundary between microfluidic and macrofluidic behaviors. Furthermore, a theoretical model that correlates k_m with a wide range of d_{elec} (100 to 3000 µm) was established. It would help an easy estimation of k_m for a given electrochemical cell equipped with a large range of d_{elec} working in parallel-plate mode. On top of that, mass transfer

correlation based on the Sherwood number in laminar regime was proposed. It took into consideration, not only fluid properties but also electrochemical reactor hydrodynamics and geometry for a convenient scale up or scale down application. Owing to the establishment of a k_m model with d_{elec}, its value could have been estimated when a d_{elec} of 50 µm was used. The determination of I_{lim} for k_m evaluation under this configuration was technically impossible due to the capacity limitation of the potentiostat.

IX.4. Fundamental role of interelectrode distance and energetic performance

Once the mass transfer characterization of the electrochemical cell with varying d_{elec} has been grasped, the research moved on to the role of d_{elec} on the formation of mineral electro-precipitation in **Chapter 6**. **Table IX.1** and **Fig. IX.1** illustrate the results of electro-precipitates formation and energetic performance during the electro-oxidation of a synthetic effluent under different d_{elec} configurations. They reflect the relationship of process efficiency and operational cost under different reactor configurations. From both **Table IX.1** and **Fig. IX.1**, no remarkable trend was seen on the evolution of mass of $Mg(OH)_2$ deposition as a function of d_{elec}. Meanwhile, insignificant quantity of $CaCO_3$ precipitation occurred using 50 µm due to non-faradaic conditions. It has been demonstrated in **Chapter 6** that increasing d_{elec} resulted in decreasing E_C into water reduction region. The least parasitic HER took place under the configuration of 100 µm. Consequently, the most $CaCO_3$ electro-precipitated using the 100 µm d_{elec} (35.3 mg). As the d_{elec} increased, the mass of $CaCO_3$ deposition decreased (down to 27.2 mg using 3000 µm setup) (refer **Table IX.1** and the relative trend plotted in **Fig. IX.1**. With regard to the power consumption (*PC*) during the electrolysis of 5 h across submillimetric into millimetric configurations, increasing trend of *PC* was evaluated in the increasing order of d_{elec}. The lowest *PC* was evaluated at d_{elec} = 50 µm (0.02 kWh m^{-3}) and it raised to 9.97 kWh m^{-3} using 3000 µm (**Table IX.1** and **Fig. IX.1**). This increasing trend of power consumption was in close relation with the variation of cell voltage (ΔU) (**Fig. IX.1**). ΔU was noticed to increase from 0.02 to 4.99 V when the reactor was used with d_{elec} of 50 and 3000 µm respectively. From the total amount of electro-precipitate (i.e., the sum of mass of $Mg(OH)_2$ and $CaCO_3$ deposit), specific power consumption for the formation of electro-precipitate (*SPCP*) during 5 h of electrolysis was evaluated. *SPCP* of 0.0117 and 0.1707 kWh g-precipitate^{-1} were obtained under d_{elec} = 50 and 3000 µm setup respectively (**Table IX.1**). The increasing trend of *SPCP* (**Fig. IX.1**) was due to (1) increasing *PC* as well as (2) decreasing quantity of electro-precipitate in the ascending order of d_{elec}.

Table IX.1. Electro-precipitation and energetic performance during 5 h of electrolysis in basic effluent (BE) across investigated d_{elec}.

	50 µm	100 µm	250 µm	500 µm	1,000 µm	3,000 µm
$Mg(OH)_2$ (mg)	0.00	2.00	2.22	1.97	2.16	2.02
$CaCO_3$ (mg)	1.610	35.28	34.18	30.29	29.20	27.18
ΔU (V)	0.0200	3.85	3.94	4.01	4.21	4.99
***PC* (kWh m^{-3})**	0.0380	7.70	7.88	8.03	8.41	9.97
***SPCP* (kWh g-precip.$^{-1}$)**	0.01170	0.1032	0.1083	0.1287	0.1300	0.1707

PC: specific power consumption per volume of effluent treated and ***SPCP***: specific power consumption per gram of electro-precipitate ($Mg(OH)_2$ + $CaCO_3$).

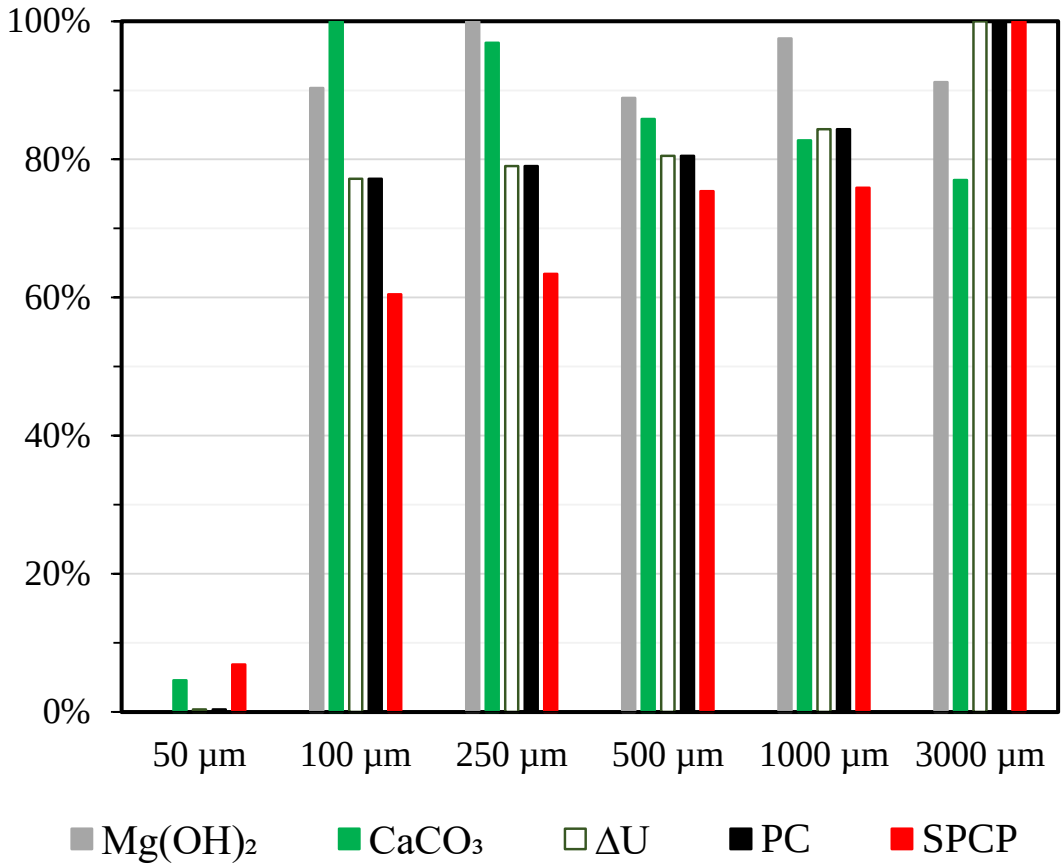

Fig. IX.1. Variation of $Mg(OH)_2$ and $CaCO_3$ electro-precipitation, cell voltage (ΔU), power consumption (*PC*) and specific power consumption per gram of precipitate (*SPCP*) as a function of d_{elec}. The reported value of a given parameter was relative to the highest one obtained with a given d_{elec} (**Table IX.1**).

IX.5. Technical aspects of electro-oxidation treatment of reclaimed wastewater at different applied current densities

The study was pursued with the characterization of mineral deposition in the matrix having increasing degree of complexity, close to the composition of a real effluent of municipal WWTP, and ended up with comparison with RW itself in **Chapter 7**. In regard to the theme of the thesis, simultaneous (1)

electro-precipitation, (2) organics mineralization, (3) removal of target pharmaceutical micropollutant and (4) fate of inorganic byproducts were quantified in submillimetric setup, a configuration distinguishable from any other work ever documented on the topic. To reach the objective, d_{elec} of 500 µm was selected to be in the microfluidic condition and in the same time having the least mineral scaling as deduced from **Chapter 6**. **Table IX.2** summarizes some evaluation aspects of the electro-oxidation of RW spiked with 10 mg L^{-1} tylosin at 0.8, 4 and 16 mA cm^{-2}. The highest degree of mineralization (51.1%) after 5 h of treatment was achieved using the highest j_{app} (16 mA cm^{-2}), whereas the lowest value (7.7%) corresponded to the lowest j_{app}, i.e., 0.8 mA cm^{-2}. The mass of electro-precipitation tabulated in **Table IX.2** corresponds to the total mass of $Mg(OH)_2$, $CaCO_3$ and $Ca_3(PO_4)_2$ precipitates. Marginally lower degree of electro-precipitation was observed after 5 h at 0.8 (53.1 mg) than at 4 mA cm^{-2} (56.6 mg), due to more OH^- production on cathode in the latter. Further increase in j_{app} (16 mA cm^{-2}) resulted in lower formation of electro-precipitation (47.1 mg) as the consequence of increasing competitive HER evolution on cathode surface. Next, harmful byproducts were quantified as the sum of ClO_3^- and ClO_4^- concentrations produced, expressed in mg-Cl_2 L^{-1}. It was noticed that the highest value (151 mg-Cl_2 L^{-1}) was obtained using 16 mA cm^{-2}, whilst the lowest (2.9 mg-Cl_2 L^{-1}) was yielded using the lowest j_{app}. In terms of power consumption performance during the 5-h electro-oxidation process, the highest *PC* was obtained by applying 16 mA cm^{-2} (41.2 kWh m^{-3}). On the other hand, the lowest *PC* was evaluated at 1.29 kWh m^{-3} upon applying 0.8 mA cm^{-2}. This trend was expected since the power consumption was proportionate to the applied current.

Total degradation of tylosin (100%) was obtained under the polarization of 4 and 16 mA cm^{-2} after 20 and 1 min of treatment, respectively, whereas 95% tylosin removal was noted after 5 h of electrolysis at 0.8 mA cm^{-2}. As a result, the specific power consumption for complete tylosin degradation (*SPCT*) was evaluated as function of not only the amount of tylosin removed (per gram of tylosin) but also of the applied current and the duration of the process. According to **Table IX.2**, the lowest *SPCT* (0.017 kWh g-Tyl^{-1}) was evaluated at 16 mA cm^{-2}, due to swift and total degradation of tylosin. Due to long treatment duration using 0.8 mA cm^{-2}, the highest *SPCT* was calculated using this j_{app} (0.18 kWh g-Tyl^{-1}), higher than *SPCT* at 4 mA cm^{-2} by 2.4-fold (0.069 kWh g-Tyl^{-1}). Similar approach was followed for the evaluation of specific power consumption for organic mineralization (*SPCM*) and electro-precipitation (*SPCP*). The extent of mineralization and electro-precipitation obtained after 5 h of electro-oxidation were used for the calculation of *SPCM* and *SPCP* respectively at the three investigated j_{app}. As expected, 0.8 mA cm^{-2} gave out the lowest *SPCM* (0.495 kWh g-TOC^{-1}) and *SPCP* (0.012 kWh g-$precipitate^{-1}$), whereas the highest *SPCM* (3.01 kWh g-TOC^{-1}) and *SPCP* (0.44 kWh g-$precipitate^{-1}$) were evaluated using 16 mA cm^{-2}. Similar remark can be made on the *SPCM* at 0.8 mA cm^{-2}, whereby owing to low *PC* under this configuration (1.29 kWh m^{-3} for 5 h

of treatment), it still has margin for longer treatment time to better mineralize organics in the wastewater. Regarding the evaluated *SPCP*, lower *SPCP* was achieved by applying 0.8 mA cm^{-2}. It is an inconvenience if the mineral scaling is unwanted, such with the case of EAOP. Electro-precipitation still occurred at about similar degree as 4 mA cm^{-2} despite lower current density used. However, this low *SPCP* would represent economical advantage if the electro-deposition on cathode was intended, e.g., in the applications of electro-precipitation for recovery or water softening. Finally, using these values of *SPC*, an estimation on energy consumption to (1) mineralize, (2) degrade pollutant or (3) remove/recover an amount of precipitate could be estimated as function of the duration of treatment performed.

Table IX.2. Summary of the evaluated parameters as the outcome of electro-oxidation of RW spiked with 10 mg L^{-1} tylosin at 0.8, 4 and 16 mA cm^{-2} during 5 h of treatment.

	0.8 mA cm^{-2} (*DAC*: 1)	**4 mA cm^{-2} (*DAC*: 5)**	**16 mA cm^{-2} (DAC: *20*)**
Mineralization (%)	7.7	35.1	51.1
Electro-precipitation (mg)	53.1	56.6	47.1
Tylosin degradation (%)	95.0	100	100
Undesirable byproducts (ClO_3^-+ClO_4^-) (mg-Cl_2 L^{-1})	2.9	82	151
***PC* (kWh m^{-3})**	1.29	8.33	41.2
***SPCM* (kWh g-TOC^{-1})**	0.495	1.27	3.01
***SPCT** (kWh g-Tyl^{-1})**	0.18	0.069	0.017
***SPCP* (kWh g-$precipitate^{-1}$)**	0.012	0.074	0.44

SPCM: specific power consumption per gram of TOC removed, ***SPCT***: specific power consumption per gram of tylosin degraded (*: the time depends on the duration of total tylosin removal) and ***SPCP***: specific energy consumption per gram of electro-precipitate formed.

From the values of performance provided in **Table IX.2**, **Fig. IX.2** is plotted to visualize relative distribution of parametric performances as function of different j_{app}. For that, the evaluated value at a given j_{app}, was expressed relatively to the highest one and it was done for all the inspected parameters. Thus, according to **Fig. IX.2**, it was clearly observed that 16 mA cm^{-2} outnumbered the other j_{app} in terms of energetic consumption (*PC*, *SPCM* and *SPCP*) due to high current applied. *SPCT* was the only exception, owing to very fast organic removal. The formation of undesirable byproducts occurred the most using this j_{app} as described previously. Highest organic mineralization was also obtained at 16 mA cm^{-2}, while slightly lower electro-precipitation occurred due to vigorous H_2 evolution. Contrastingly, minimal energy requirement was achieved using low j_{app}, but at the price of low organics and target pollutant removal. As a result, the *SPCT* was apparently the highest due to much slower kinetics of degradation.

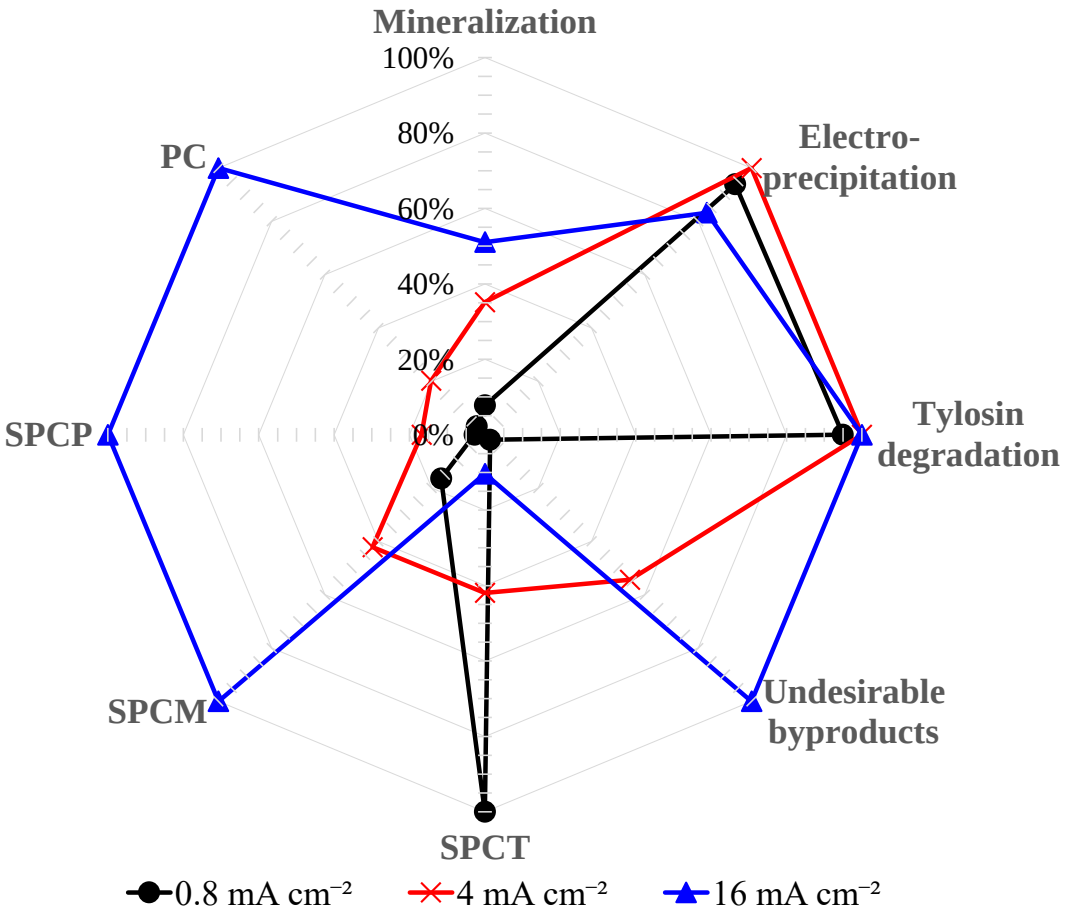

Fig. IX.2. Relative performances of the electro-oxidation of reclaimed wastewater spiked with 10 mg L^{-1} tylosin at 0.8, 4 and 16 mA cm^{-2} during 5 h of treatment.

IX.6. Porous cathode, the suitable candidate for electro-precipitation recovery

The kinetics of precipitation taking place on non-porous stainless steel was compared to that occurring on carbonaceous graphite plate and carbon paper. They all possessed distinct electroactive surface and porosity. It was demonstrated that the use of highly porous cathode such as carbon paper would only lead to a quickest $CaCO_3$ precipitation, a highest formation of toxic ClO_3^- and ClO_4^- byproducts as well as the necessity of post-treatment. Similarly, when graphite was employed as cathode, more mineral scaling was formed compared to the stainless steel, with the latter being less porous. The results suggested that stainless steel was the most suitable candidate to be used as cathode to minimize the electro-precipitation. Meanwhile, carbon paper and other porous materials would suit the purpose of the electro-precipitation for recovery process as the precipitation was more favorable when porous material acted as cathode.

IX.7. Perspectives

Short terms

Drastic trend of deposition as well as ohmic drop were observed between 50 and 100 µm d_{elec}. More experiments are needed for the distances in between for a better understanding on the involved mechanism. Improvement could still be made on the theoretical model involving Mg^{2+} because the experimental trend of $Mg(OH)_2$ as function of d_{elec} was not so apparent. In reality, $Mg(OH)_2$ is more amorphous relatively to $CaCO_3$, thus its stability was less reproducible. Furthermore, low Mg^{2+} concentration (5 mg L^{-1}) relatively to Ca^{2+} (150 mg L^{-1}) might complicate the result repeatability. Furthermore, the model could call for additional parameters coming from the contribution of anode especially from the provision of O_2. This provision should as well vary between interelectrode gaps. The influence of higher concentration of Mg^{2+}, Ca^{2+}, carbonates and other ions such as SO_4^{2-} could be further investigated. It has been understood from literature that the variation of each can influence the kinetics of precipitation of others. Hence, the robustness of models could be then tested correspondingly.

The experiments were conducted in batch recirculation mode throughout this work, which is a common practice during parametric studies. As a next step, the experiments shall be tested in continuous mode which reflects more on real case scenarii. The validity of developed model could also be tested. Additionally, a correlation to estimate the mass of precipitate deposited as a function of process duration and reactor geometry could be proposed.

A dimensionless *Sh* correlation was established in parallel-plate electrochemical reactor under laminar regime. Its application works best under similar reactor geometry but would require some corrections if it is to be applied for reactors with other geometries. Meanwhile, the mass transfer correlation under turbulent regime in microfluidic reactor has not yet been done. It would be an interesting contribution to the literature.

Medium terms

A program involving the overall modeling should be tempted and could not only consider the electro-precipitation but also the pollutants degradation together with the evolution of byproducts in real effluent at a given operating conditions. Besides, only inorganic byproducts were monitored during the EO process. The fate of organics, including organohalogen byproducts and any possible volatile organic compounds could also be quantified in order to get a complete mass balance. So, a complete comparison with the emission regulations could be made.

In addition, the tylosin parent molecule was efficiently degraded but its byproducts were not identified. The intermediates could be more toxic than the pristine compound. Therefore, it might be of particular interest to obtain a degradation pathway of tylosin by EAOP, since it has not yet been documented in literature. Moreover, the study of the removal of tylosin micropollutant (instead of spiked concentration) at a concentration typically detected in manure wastestream (in the order of µg L^{-1}) seems more practical. It was the initial objective of the thesis but could not be completed due to time constraints. To achieve the purpose, the use of powerful analytical tools, e.g., high performance liquid chromatography with tandem mass spectroscopy (LC-MS/MS) to follow its degradation and evolution of byproducts shall be required.

Long terms

After series of experiments with various j_{app} by treating synthetic and real wastewater, it has been shown that j_{app} in the region of 1 to 2 mA cm^{-2} might present a good compromise considering the overall power consumption, occurrence of mineral scaling, total organic mineralization, pharmaceuticals degradation as well as the evolution of undesirable byproducts. However, the outcome of this thesis suggested that, by drastically changing scale from millimetric to microfluidic environment, not only the mechanism of electro-precipitation remained the same, but its formation was also favored by less H_2 evolution activity and more favorable OH^- production on cathode surface. As a result, more deposition was generally observed under submillimetric configuration. At this stage, microfluidic feature might not be able to challenge the status quo of polarity reversal technique applied for descaling purpose as the quest to find its alternative shall continue.

In the meanwhile, a particular setup was found during the thesis work that could significantly slow down the kinetics of electro-precipitation. It involved the use of graphite as cathode with 100 µm interelectrode gap, a setup by which the formation of OH^- was minimized. Though, adopting such configuration seemed impractical to treat high volumes of effluent in real field water/wastewater treatment application, operating several microfluidic cells in parallel to improve productivity merits a trial. Total treatment duration ought to be longer to maximize organic removal but it would not cause energetic concern when submillimetric reactors are adopted. Furthermore, the deposits formed after 5-h of EO treatment did not result in noticeable decrease in charge transfer and organic degradation efficacy. Thus, it indicated that the electro-oxidation efficiency was not yet impacted by the cathodic scaling. This upscaling process shall be operated in continuous mode and at higher flow rates to get closer to the real field practice.